86

Characterizing Monoclonal Antibodies 3613

UV (215 nm)

LC-Electrospray MS
Total Ion Current

Glycopeptide-
selective trace
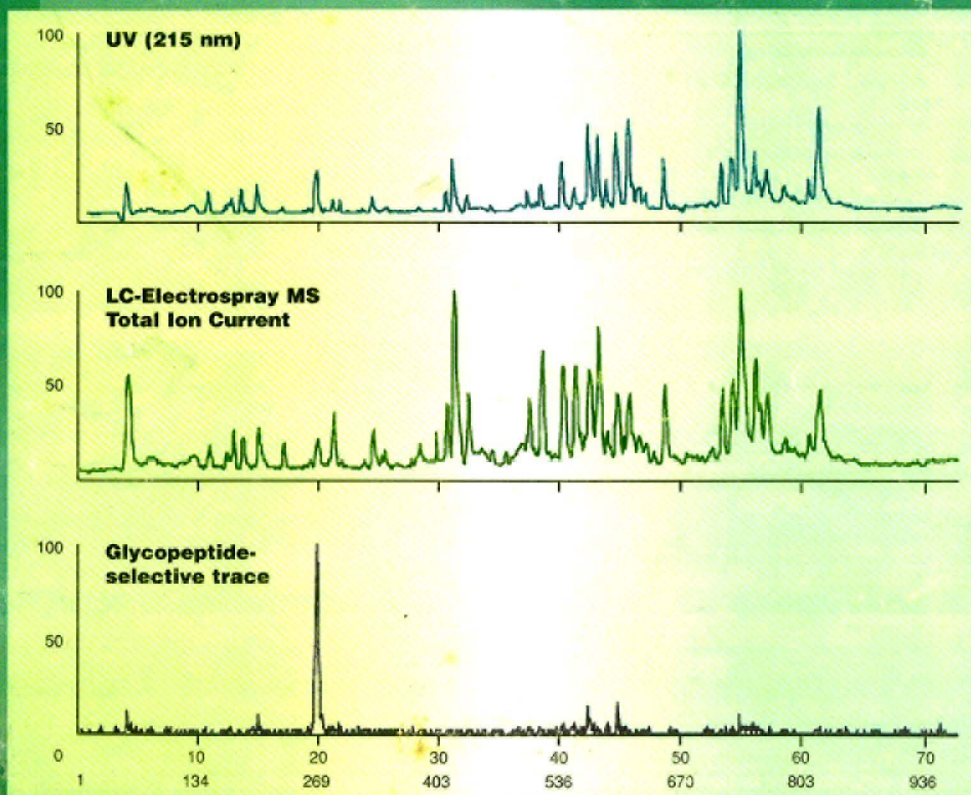
New Trace Analysis Products

As developments in analytical instrumentation for trace analysis push detection limits progressively lower, the lowest possible level of unwanted contaminants in standards becomes more critical. Aldrich is a unique source for both specially purified standard solutions and the highest purity raw materials for preparing standards. Some new additions to the Aldrich product line are listed below.

42,892-2	**Ammonium hydrogenphosphate matrix modifier solution,** 99.999% *(40% ammonium hydrogenphosphate in water)*	100mL	$150.00
		500mL	$375.00
42,893-0	**Ammonium nitrate matrix modifier solution,** 99.999% *(5% ammonium nitrate in 1% HNO₃)*	100mL	$100.00
		500mL	$250.00
42,886-8	**Calcium matrix modifier solution,** 99.9995% *(2% calcium in 1% HNO₃)*	100mL	$125.00
		500mL	$315.00
42,888-4	**Lanthanum matrix modifier solution,** 99.999% *(5% lanthanum in 1% HCl, specially purified to remove Ca and Mg)*	100mL	$90.00
		500mL	$225.00
42,887-6	**Lanthanum matrix modifier solution,** 99.999% *(5% lanthanum in 1% HNO₃, specially purified to remove Ca and Mg)*	100mL	$90.00
		500mL	$225.00
42,889-2	**Magnesium matrix modifier solution,** 99.9995% *(2% magnesium in 1% HNO₃)*	100mL	$75.00
		500mL	$187.50
42,890-6	**Nickel matrix modifier solution,** 99.999% *(5% nickel in 1% HNO₃, specially purified to remove Se)*	100mL	$125.00
		500mL	$315.00
42,891-4	**Palladium matrix modifier solution,** 99.999% *(2% palladium in 1% HNO₃, specially purified to remove As, Cu, Pb, Sb, Se, Tl; chloride-free)*	100mL	$225.00
		500mL	$565.00

42,931-7	**Environmental methods standard QC19** *(contains 100µg/mL each in 5% HNO₃: As, Be, Ca, Cd, Co, Cr, Cu, Fe, Mg, Mn, Mo, Ni, Pb, Sb, Se, Ti, Tl, V, Zn)*	100mL	$112.50
		500mL	$281.20
42,930-9	**Environmental methods standard QC21** *(contains 100µg/mL each in 5% HNO₃: As, Be, Ca, Cd, Co, Cr, Cu, Fe, Li, Mg, Mn, Mo, Ni, Pb, Sb, Se, Sr, Ti, Tl, V, Zn)*	100mL	$125.00
		500mL	$312.50
43,182-6	**Holmium ICP/DCP standard solution** *(10,000µg/mL Ho in 1-3 wt. % HNO₃)*	100mL	$45.00
43,181-8	**Lutetium ICP/DCP standard solution** *(10,000µg/mL Lu in 1-3 wt. % HNO₃)*	100mL	$115.00
43,179-6	**Thulium ICP/DCP standard solution** *(10,000µg/mL Tm in 1-3 wt. % HNO₃)*	100mL	$80.00
43,183-4	**Silicon ICP/DCP standard solution** *(10,000µg/mL Si, free of fluoride and alkali metal ions)*	100mL	$50.00
		500mL	$125.00

Introducing!

Aldrich's specially purified solutions (Figure 1), specially purified raw materials, expertise, and production facilities that are used to prepare our ICP/DCP and atomic absorption standards are also employed in preparing custom standards to your specifications with:

- prompt service
- Aldrich's committment to high quality

Please call our Technical Services Department at   and ask for a quotation for your custom standards requirements.
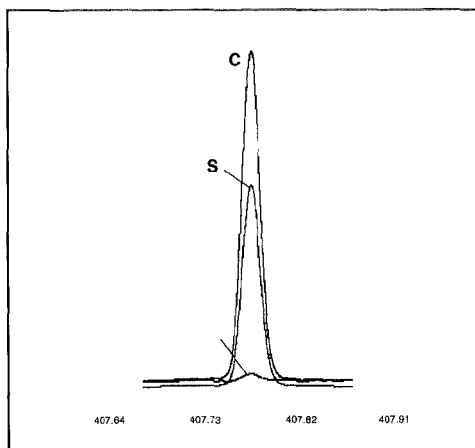
Figure 1. Strontium in Barium ICP Standards.
S, ICP signal for Sr at 407.7nm in a 0.1µg/mL Sr ICP standard; **C**, a commercial 1,000µg/mL Ba ICP standard prepared from Ba(NO₃)₂; and **A**, an Aldrich 1,000µg/mL Ba ICP standard (Aldrich Cat. No. 35,606-9) prepared from purified Ba(NO₃)₂.

1995 subscription rates include air delivery outside the U.S., Canada, and Mexico. Canadian subscriptions are subject to 7% GST.

	Members	Nonmembers (personal)	Nonmembers (institutional)
U.S.	$ 40	$ 85	$ 570
Canada and Mexico	77	122	607
Europe	123	168	653
Other countries	148	193	678

Members may share/donate their personal subscriptions with/to libraries and the like but only after 5 years from publication.

Nonmember rates in Japan: Rates above do not apply to nonmember subscribers in Japan, who must enter subscription orders with Maruzen Company Ltd., 3–10, Nihonbashi 2-chome, Chuo-ku, Tokyo 103, Japan. Tel: (03) 272-7211.

For multi-year and other rates, call toll free 800-227-5558 in the U.S. and Canada; in the Washington, DC, metropolitan area and outside the U.S., call 202-872-4363; fax 202-872-4615.

Single issues, current year, $24.00 except review issue, $50.00, and LabGuide, $50.00; **back issues and volumes and microform editions** available by single volume or back issue collection. For information or to order, call the number listed for subscription orders; or write the Microform & Back Issues Office at the Washington address.

Subscription orders by phone may be charged to VISA, MasterCard, or American Express. Call toll free 800-333-9511 in the continental U.S.; in the Washington, DC, metropolitan area and outside the continental U.S., call 202-872-8065. Mail orders for new and renewal subscriptions should be sent with payment to American Chemical Society, Department L-0011, Columbus, OH 43268-0011.

Changes of address must include both old and new addresses with ZIP code and a recent mailing label. Send all address changes to the ACS Columbus address. Please allow 6 weeks for change to become effective. **Claims for missing issues** will not be allowed if loss was due to failure of notice of change of address to be received in the time specified; if claim is dated (a) North America—more than 90 days beyond issue date, (b) all other foreign—more than 180 days beyond issue date. Hard copy claims are handled at the ACS Columbus address.

Instructions for authors of AC Research and guidelines for the Instrumentation, Report, Analytical Approach, and A/C Interface features are published in the Jan. 1 issue, p. 229, or can be obtained from our e-mail reflector "acinfo@acs.org" using the keyword phrases "ac research" or "ac apguide," respectively. Please consult these instructions prior to submitting a manuscript for consideration for publication.

Manuscripts for publication in AC Research (4 copies of text and illustrative material) should be submitted to the Editor at the University of North Carolina address. Please include a signed copyright status form; a copy of this document appears on p. 235 of the Jan. 1 issue. Manuscripts for publication in the A-page section should be submitted to the Washington editorial staff.

Supporting information is noted in the table of contents with a ■. It is available as photocopy ($12.00 for up to 3 pages and $1.50 per page for additional pages, plus $2.00 for foreign postage) or as 24× microfiche ($12.00, plus $1.00 for foreign postage). Canadian residents should add 7% GST. See supporting information notice at the end of journal article for number of pages. Orders must give complete title of article, names of authors, journal, issue date, and page numbers. Prepayment is required and prices are subject to change. In 1995, electronic supporting information is available to current journal subscribers via the Internet using either gopher or World Wide Web protocols. Most often, the material is available as PDF files, which may be viewed using Adobe's Acrobat Reader, a program that is freely available on the Internet. However, some articles may include computer programs, PostScript files, word-processing files, experimental data in a standard format (e.g., crystallographic parameters in CIF format), etc. In order to download the supplementary material files, users will need to enter their journal subscriber number, which can be found on the mailing label. Detailed instructions for using this service can be found on the Internet. With gopher, connect to pubs.acs.org, go to the "ACS Publications" selection, then to the "Supporting Information" selection. Read the README file in this directory for detailed instructions. When using a WWW client (e.g., Mosaic, Netscape), connect to the URL "http://pubs.acs.org/" and select the "Supporting Info. for Journals" link. For further information on electronic access, send electronic mail to gopher@acsinfo.acs.org, or phone (202) 872-4434. For information on microforms, contact Microforms & Back Issues at the ACS Washington address or phone (202) 872-4554. Supporting information, except structure factors, also appears in the microfiche edition.

The American Chemical Society and its editors assume no responsibility for the statements and opinions advanced by contributors. Views expressed in the editorials are those of the editors and do not necessarily represent the official position of the American Chemical Society.

ANALYTICAL CHEMISTRY ®

ACCELERATED ARTICLES

ARTICLES

CORRESPONDENCE

TECHNICAL NOTES

■ Supporting information for this paper is available separately (consult a current masthead page for ordering information). Supporting information is available to subscribers electronically via the Internet at http://pubs.acs.org (WWW) and pubs.acs.org (Gopher). All supporting information except for structure factor tables will also appear following the paper in the microfilm edition of the journal.

* In papers with more than one author, the asterisk indicates the name of the author to whom inquiries about the paper should be addressed.
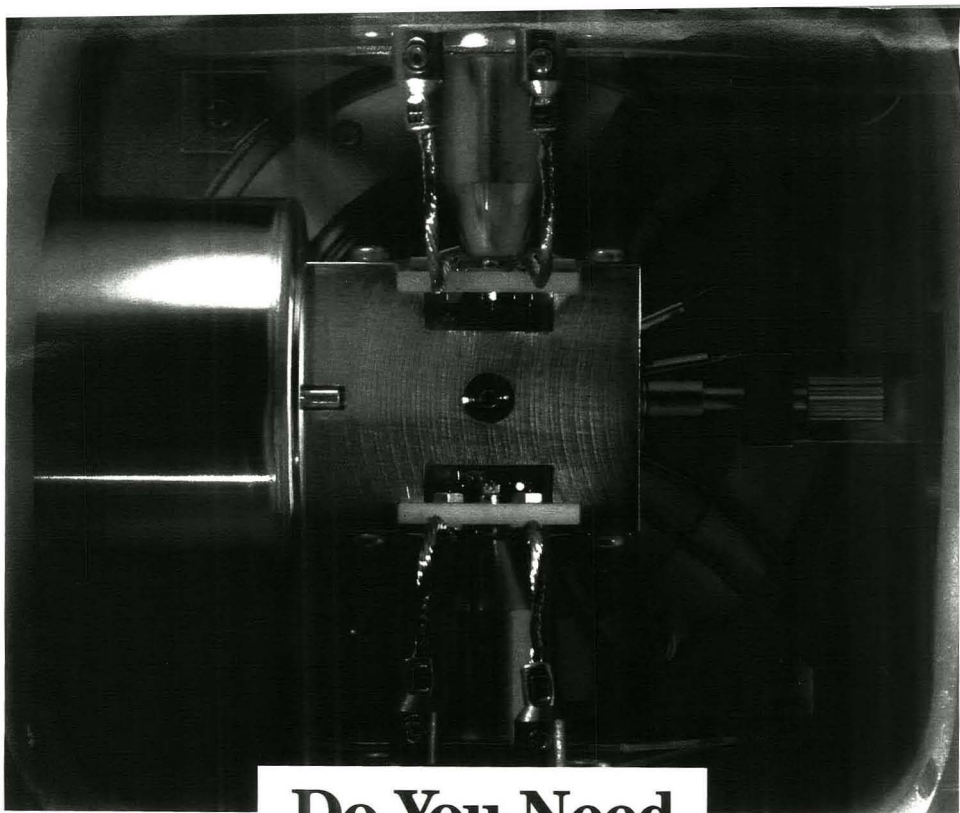
Do You Need
A Comprehensive GC/MS Solution?

The Shimadzu GC/MS QP-5000. The new generation. Compact and complete.

Regardless of whether you work in water, air, or soil analysis, or whether you are looking for environmental analysis, additives in food, or forensics drug abuse, our new GC/MS QP-5000 is sure to exceed your expectations. Its mass spectrometer, covering the range 10 amu to 700 amu, is coupled to the proven performance of the GC-17A gas chromatograph, including AFC for setting carrier related flows and pressures. Our new GC/MS QP-5000 has been designed for the most stringent analytical methodology as well as routine analytical laboratory work. Its compactness and range of features are truly impressive. The overall width of the GC and MS is just 72.5 cm (28.5"). All system operations are controlled by Microsoft® Windows™-based software. The GC/MS QP-5000 is a highly sensitive bench-top GC/MS with computer-simulation-optimized ion optics and fully automated vacuum control. Available options include a jet-separator interface, a high capacity turbomolecular pump, chemical-ionization, and a direct inlet system for low volatiles. Call your nearest Shimadzu Representative today for more details on the GC/MS QP-5000. You can count on a prompt response from us.
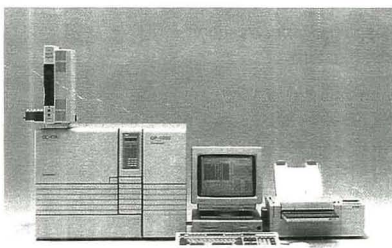
Microsoft® Windows™ is a registered trademark of Microsoft Corporation, Redmond, WA, USA.

This small EFTA cell...

...converts the best Trace Analyzer into a unique Flow-Through Trace Analyzer.

For excellent results where spectroscopy approaches its limits.

The new Metrohm Electrochemical Flow-Through Trace Analyzer (EFTA) uses a novel flow-through cell for determining trace metals (ppb) in different matrices.
Samples are introduced via a loop into the eluent stream.
Ions to be analyzed are preconcentrated as the sample passes the working electrode. Fresh eluent is introduced into the cell, the flow stopped and the concentration determined, all automatically.
EFTA gives convenient sample introduction and high throughput in an easy to use, precise system. To learn more about how EFTA can simplify your trace analysis, contact Metrohm at:

Get the product data you need fast...

By Phone: Use the reference list below, and contact the companies to fill an immediate need, or...
By Fax: Use the fax form on the opposite page to send a direct written request.

Company	Page	Issue	RSN	Data+	Phone	Fax	Contact
AC Analytical Controls	623 A	10/1/95	415		215-638-7078	215-638-7096	Jim McCormack
AccuStandard	503 A	8/1/95	416	●	800-442-5290	203-786-5287	Matt Bolgar
Aldrich Chemical	IFC	10/15/95	none	●	414-273-3850	414-273-2095	Rich Gross
Analytical Innovations	467 A	8/1/95	6		800-901-8576	513-298-4807	John H. Garrett
J. T. Baker	451 A	8/1/95	7	●	800-582-2537	908-859-9318	William Broad
Bear Instruments	503 A	8/1/95	417		408-773-0462	408-773-0463	Urs Steiner
Beckman Instruments	622 A	10/1/95	410	●	800-742-2345	714-773-8186	Amy Bratcher
Bioanalytical Systems	564 A	9/1/95	408	●	317-403-4572	317-497-1102	Craig Bruntlett
Bruker Instruments	498 A, 502 A	8/1/95	401, 411	●	508-667-9580	508-663-9177	Mark Chaykovsky
Bruker Instruments	560 A	9/1/95	401	●	508-667-9580	508-66-3954	Mark Chaykovsky
Carl Zeiss	565 A	9/1/95	415	●	800-356-1090	914-681-7443	Irv Toplin
Carl Zeiss Jena GmbH	623 A	10/1/95	417		49-3641-64-2500	49-3641-64-3311	Zeiss Gruppe
Cetac Technologies	502 A	8/1/95	413	●	800-369-2822	402-733-5292	John J. Uhr
Chem Service	538 A	9/1/95	1	●	800-452-9994	610-692-8729	Ron Gray
Comstock	498 A	8/1/95	402	●	615-483-7690	615-481-3884	Susan Zell
EG&G Instruments (Princeton)	475 A	8/1/95	8	●	609-530-1000	609-883-7259	Ruth Rearick
EG&G Instruments (Princeton)	610 A	10/1/95	10, 11	●	609-530-1000	609-883-7259	Ruth Rearick
Finnigan MAT	459 A, 502 A	8/1/95	5, 408	●	408-433-4800	408-433-4823	Gary Spear
Finnigan MAT	498 A	8/1/95	403	●	44-1442-233555	44-1442-233666	Stan Evans
Finnigan MAT	529 A	9/1/95	9	●	408-433-4800	408-433-4823	Gary Spear
Finnigan MAT	574 A	10/1/95	9	●	408-433-4800	408-433-4823	Gary Spear
Finnegan/Tremetrics	565 A	9/1/95	411	●	512-251-1555	512-251-1597	Elaine Moody
Fisons Instruments	499 A	8/1/95	404	●	508-524-1000	508-524-1100	Cathy Schaub
Fisons Instruments	622 A	10/1/95	413	●	508-524-1000	508-524-1100	Cathy Schaub
Fisons Instruments	618 A	10/1/95	401	●	508-524-1000	508-524-1100	Cathy Schaub
Fluka Chemie	509 A	9/1/95	5		41-81-7552511	41-81-7565449	
Fluka Chemie	571 A	10/1/95	1	●	41-81-7552511	41-81-7565449	
Galileo Electro-Optics	503 A	8/1/95	418	●	508-347-9191	508-347-3849	Laurie Placella
Hamamatsu	487 A	8/1/95	none		800-524-0504	908-231-1218	Robert Wisner
Hamilton	IFC	8/1/95	9	●	800-648-5950	702-856-7259	B. Milne/R. Beavers
Hamilton	OBC	9/1/95	8	●	800-648-5950	702-856-7259	B. Milne/R. Beavers
Hewlett-Packard	499 A	8/1/95	415	●	415-857-5603	415-857-8228	Doug Forsyth
Hewlett-Packard	618 A	10/1/95	402	●	415-857-5603	415-857-8228	Doug Forsyth
Hiden Analytical	623 A	10/1/95	416		44-1925-445225	44-1925-416518	Ian D. Neale
Hinds Instruments	564 A	9/1/95	410	●	503-690-2000	503-690-3000	Ted Oakberg
Hi-Tech Scientific	564 A	9/1/95	409	●	44-722-323643	44-722-412153	David Mitchell
IN/US Systems	622 A	10/1/95	407	●	800-875-4687	813-620-3708	John Hnizdil
Isco	502 A	8/1/95	412	●	402-464-0231	402-464-0318	Gary Bakken
Jeol USA	OBC	8/1/95	10	●	508-535-5900	508-536-2205	Brian Musselman
Jeol USA	561 A	9/1/95	402	●	508-535-5900	508-536-2205	Robert DiPasquale
Jeol USA Inc.	OBC	10/1/95	7	●	508-535-5900	508-536-2205	Brian Musselman
John Wiley & Sons	581 A	10/1/95	5	●	212-850-6137	212-850-6264	S. NelsonK&M
Electronics	475 A	8/1/95	2	●	413-781-1350	413-737-0608	Rick Brighenti
Labsphere	622 A	10/1/95	412	●	603-927-4266	603-927-4694	Joan A. Beaulieu
Macherey-Nagel	580 A	10/1/95	2		(02421) 969-0	(02421) 969-199	
McPherson	502 A	8/1/95	411	●	800-255-1055	508-263-1458	Christi Schoeffel
Melles Griot	622 A	10/1/95	409		800-835-2626	714-261-7589	Lynn Strickland
Metrohm	454 A	8/1/95	1	●	41-071-538-585	41-071-538-9041	R. Steiner
Metrohm	512 A	9/1/95	2	●	41-071-538-585	41-071-538-9041	R. Steiner
Metrohm	584 A	10/1/95	3	●	41-071-538-5	41-071538-90	R. Steiner
Metrohm	6 C	10/15/95	none	●	41-071-538-5	41-071538-90	R. Steiner
Mettler-Toledo	565 A	9/1/95	412	●	800-638-8537	609-426-0121	Al Beronio
Molecular Dynamics	564 A	9/1/95	407		800-333-5703	408-773-1493	Jim Bull
PE Nelson	618 A	10/1/95	403	●	408-577-2200	408-894-9307	Alycia Cortez-Frank
Perkin-Elmer	OBC	9/15/95	none	●	203-761-2574	203-762-6000	Mary Cooke-Kager
Perkin-Elmer	IBC	9/15/95	none	●	415-570-6667	415-638-6199	Valerie Tucker
Perkin-Elmer	502 A	8/1/95	410	●	203-761-2574	203-762-6000	Carol Blaszczynski
Perkin-Elmer	589 A	10/1/95	6	●	415-570-6667	415-638-6199	Valerie Tucker
Perkin-Elmer	OBC	10/15/95	none	●	203-761-2574	203-762-6000	Mary Cooke-Kager
Perkin-Elmer	IBC	10/15/95	none	●	415-570-6667	415-638-6199	Valerie Tucker
PerSeptive Biosystems	499 A	8/1/95	406	●	800-899-5858	508-383-7885	Charles Cuneo
Photometrics	564 A	9/1/95	405	●	602-889-9933	602-573-1944	Michelle Downs
Quadrex Corporation	503 A	8/1/95	414	●	800-275-7033	203-393-0391	John Lipsky
Sapidyne Instruments	622 A	10/1/95	408		208-345-7677	208-392-4985	Steve Lackie
Scott Specialty Gases	IFC	9/1/95	7	●	215-766-8861	215-766-0320	Donna M. Vito
Scott Specialty Gases	599 A	10/1/95	8	●	215-766-8861	215-766-0320	Donna M. Vito
Shandon Lipshaw	565 A	9/1/95	413		800-547-7429	412-788-1138	Beverly Miller
Shimadzu Scientific Instruments	499 A	8/1/95	407	●	800-477-1227	410-381-1222	Roger Greathead
Shimadzu Scientific Instruments	IFC	9/15/95	none	●	800-477-1227	410-381-1222	Roger Greathead
Shimadzu Scientific Instruments	IFC	10/1/95	4	●	800-477-1227	410-381-1222	Roger Greathead
Shimadzu Scientific Instruments	5 C	10/15/95	none	●	800-477-1227	410-381-1222	Roger Greathead
Siemens Industrial Automation	622 A	10/1/95	411	●	404-740-3931	404-740-3998	Herbert Stuhler
Supelco	623 A	10/1/95	414	●	800-247-6628	800-447-3044	Michael Gray
Teledyne Electronic Technologies	521 A	9/1/95	3	●	415-962-6526	415-967-4353	Sharon Gomez
Thermo Separation Products	619 A	10/1/95	404	●	800-532-4752	408-526-9810	Brent Davis
Topac Scientific Instruments	565 A	9/1/95	414		617-740-8778	617-740-8779	Antoni Drybanski
Upchurch Scientific	503 A	8/1/95	415	●	800-426-0191	800-359-3460	Amy King
Varian Associates	561 A	9/1/95	403, 404	●	415-424-6786	415-858-0480	Carl Hadjis
Varian Associates	619 A	10/1/95	405	●	415-242-6880	510-945-2335	Deborah Kohnstamm
Varlen Instruments	564 A	9/1/95	406		800-729-4447	815-729-3700	Steve Klinger
Waters	619 A	10/1/95	406	●	800-252-4752	508-482-2674	Tony Lewtas

Data+ Column: A bullet indicates that additional product and company information is available in the 1996 *Analytical Chemistry* LabGuide Edition.
RSN: Reader Service Number

Accelerated Articles

An Integrated Strategy for Structural Characterization of the Protein and Carbohydrate Components of Monoclonal Antibodies: Application to Anti-Respiratory Syncytial Virus MAb

Gerald D. Roberts, Walter P. Johnson, Sudhir Burman, Kalyan R. Anumula, and Steven A. Carr*

SmithKline Beecham Pharmaceuticals, King of Prussia, Pennsylvania 19406-0939

The relatively rapid and extensive characterization of the amino acid sequence and site-specific carbohydrate structures of a recombinant, reshaped human monoclonal antibody directed against respiratory syncytial virus (RSHZ19) is presented. The integrated strategy used a combination of mass spectrometric and conventional methodologies. Liquid chromatography/electrospray mass spectrometry was used for peptide mapping and selective identification of glycopeptides, and Edman degradation and tandem mass spectrometry were used to define the sequences of selected peptides. Matrix-assisted laser desorption/ionization mass spectrometry provided the M_r of the intact protein and was used to characterize endo- and exoglycosidase digests of isolated glycopeptides to identify the glycosylation-site peptide and define the structures of the carbohydrates at that site. These experiments verified 99.1% of the light- and 99.3% of the heavy-chain amino acid sequences. The N and C termini of both chains were confirmed, and the nature and extent of heterogeneity at the N and C termini of the heavy chain were determined. Oxidation of a specific methionine residue to the sulfoxide was demonstrated by sequencing the N-terminally blocked peptide by tandem MS. Carbohydrate was found exclusively at Asn^{296} of the heavy chain. There was no evidence for a nonglycosylated form of the molecule or for the presence of O-linked carbohydrate. The qualitative distribution of glycoforms at this site was determined by MS of the isolated, tryptic glycopeptide and compared with results obtained by high-performance anion exchange chromatography and high-resolution gel permeation chromatography of oligosaccharides released by hydrazinolysis. The sequence and linkage of individual glycan species were determined using matrix-assisted laser desorption/ionization MS to monitor the results of a series of controlled digestions with specific exoglycosidases. The set of glycoforms consists predominantly of biantennary, core fucosylated carbohydrates lacking sialic acid. The present study is one of the first to directly evaluate the quantitative as well as qualitative consistency of the MS methods with conventional methods for carbohydrate analysis.

Respiratory syncytial virus (RSV) is the major cause of serious lower respiratory tract disease in infants and young children worldwide.[1] Infection can lead to bronchiolitis and pneumonia and results in an estimated 91 000 hospitalizations and 4500 deaths annually in the United States alone.[2] Outbreaks of the disease occur in a predictable yearly fashion, coincident with outbreaks of the other major respiratory viruses, influenza and parainfluenza.[3] No vaccine is presently available for RSV, and the only approved treatment is with a relatively nonselective anti-viral agent ribavirin, a drug that has gained only limited acceptance in the medical community.[1,4]

The World Health Organization and National Institute of Allergy and Infectious Diseases have given a high priority to development of effective methods to prevent and treat RSV infection. Several active and passive immunization strategies are

(1) Levin, M. J. *J. Pediatr.* 1994, *124*, S22–S27.
(2) Heilman, C. A. *J. Infect. Dis.* 1990, *161*, 402–406.
(3) Hall, C. B. *Science* 265, 1994, 1393–1394.
(4) Chanock, R. M.; Parrott, R. H.; Connors, M.; Collins, P. L.; Murphy, B. R. *Pediatr.* 1992, *90*, 137–143.

being explored in this regard.[1,5,6] Active immunization methods include use of formalin-inactivated vaccines, subunit vaccines, or live attenuated virus strains. Passive immunization therapies have focused on neutralization of the glycoproteins expressed on the surface of the virus. The genome of RSV encodes for 10 proteins of which 4 are glycoproteins displayed on the outer membrane of the virus.[7-9] Two of these proteins, the F and G envelope glycoproteins are of particular interest because polyclonal and monoclonal antibodies to these proteins alone have been shown to confer protective immunity in animal models.[7,9,10] The G glycoprotein is believed to be important for attachment of virus to the cell, while the F glycoprotein mediates cell fusion and formation of the giant, multinucleated cells from which the virus derives its name. Particular attention has focused on the F glycoprotein because its amino acid sequence is highly conserved (~90% identical) between the two antigenic subgroups A and B, whereas the sequence of the G glycoprotein is not (~50% identical).[11-14]

We have been developing a reshaped human monoclonal antibody (MAb) directed against the highly conserved F glycoprotein for passive immune therapy of RSV infection. The molecule, which we refer to here as RSHZ19, consists of two IgG1 heavy chains and two light (κ) chains in which the complementarity determining regions from an F-protein-specific murine MAb have been substituted into otherwise human variable framework regions.[15] The protein, which has been cloned and expressed at high levels in Chinese hamster ovary cells, is presently in clinical trials for treatment of infants and young children with RSV infection and prophylaxis in patient populations at high risk due to preexisting conditions such as bronchopulmonary dysplasia or congenital heart disease. RSHZ19 is effective at preventing or clearing pulmonary infection in animal models of RSV infection.[15]

As with all recombinant proteins, it is necessary to rigorously characterize the structure of RSHZ19 to satisfy the requirements of regulatory agencies when approving these forms of therapy. A number of diagnostic imaging and human therapeutic products based on MAbs have already been introduced, and many more are nearing or are in clinical trials. Mass spectrometry has been extensively used to determine the molecular weights of MAbs and subunits derived therefrom.[16-22] None of these reports has been especially exhaustive, particularly with regard to characterizing the oligosaccharide component, and only one group has

described the use of MS to study a MAb at the peptide level.[23] While molecular weight information is extremely valuable, it cannot be substituted for more detailed analysis of the protein in order to detect and characterize covalent modifications or variants of the protein that may be present.[23] Because of the increasing interest in this class of molecule in industry and academia, we have tried to develop a generally applicable, comprehensive strategy to characterize the amino acid sequence of MAbs and to identify modifications such as glycosylation, truncation, oxidation, deamidation, etc., that might be present. The overall strategy includes the following steps: (1) M_r measurement of the intact MAb by MS; (2) separation and M_r measurements by MS of each of the separated light and heavy protein chains produced by reduction and alkylation of the intact MAb; (3) high-performance liquid chromatography/electrospray (LC/ES) MS analysis of the separated reduced and S-carboxymethylated light and heavy chains with stepping of the collisional excitation potential to produce carbohydrate-specific marker ions at low m/z; (4) a detailed sequence and linkage determination of the oligosaccharide structure using high-performance anion exchange chromatography, high-resolution gel permeation chromatography, and matrix-assisted laser desorption/ionization (MALDI) MS for analysis of the products arising from reaction of the isolated glycopeptides with glycosidases of known specificity; and (5) Edman degradation and tandem MS to define the sequences of selected peptides. This strategy is presented here for the reshaped human MAb, RSHZ19.

EXPERIMENTAL PROCEDURES

Materials. Reshaped, human monoclonal antibodies against the F glycoprotein of RSV (RSHZ19) were produced in Chinese hamster ovary cells as previously described[15] (RSHZ19 is described as HuRSV19VHFNS/VK in this reference). All chemicals and reagents used were of the highest purity commercially available. Proteolytic enzymes used were "sequencing grade" from Boehringer-Mannheim (Indianapolis, IN). Recombinant peptide N-glycosidase F (PNGase F) was obtained from Genzyme (Cambridge, MA). Exoglycosidases were obtained from Oxford Glycosystems (Rosedale, NY). Model glycopeptides were obtained from Accurate Chemical (Westbury, NY) or were derived from RNase B or fetuin as previously described.[24,25]

Reduction, Alkylation, and Separation of Light and Heavy Chains. Native RSV was reduced and S-carboxymethylated (RCM) using published procedures.[26,27] The chains were separated using two TSK G3000SW size exclusion columns (Supelco,

(5) Groothius. J. R. *J. Pediatr.* **1994**, *124*, S28–S34.
(6) Du, R-P.; Jackson, G. E. D.; Wyde, P. R.; Yan, W.-Y.; Wang, Q.; Gisonni, L.; Sanhueza, S. E.; Klein, M. H.; Ewasyshyn, M. E. *Bio/Technology* **1994**, *12*, 813–817.
(7) Olmsted, R. A.; Elango, N.; Prince, G. A.; Murphy, B. R.; Johnson, P. R.; Moss, B.; Chanock, R. M.; Collins, P. L. *Proc. Natl. Acad. Sci. U.S.A.* **1986**, *83*, 7462–7466.
(8) Walsh, E. E.; Cote, P. J.; Fernie, B. F.; Schlessinger, J. J.; Brandris, M. W. *J. Gen. Virol.* **1986**, *67*, 505–513.
(9) Walsh, E. E.; Hall, C. B.; Briselli, M.; Brandris, M. W.; Schlessinger, J. J. *J. Infect. Dis.* **1987**, *155*, 1198–1204.
(10) Johnson, P. R.; Collins, P. L. *J. Gen. Virol.* **1988**, *69*, 2623–2628.
(11) Epp, O.; Colman, P.; Fehlammer, H.; Bode, W.; Schiffer, M.; Huber, R. *Eur. J. Biochem.* **1974**, *45*, 513–524.
(12) Saul, F.; Amzel M.; Poljak R. *J. Biol. Chem.* **1978**, *253*, 585–597.
(13) Taylor, G.; Stott. E. J.; Furze, J. Ford, J.; Sopp, P. *J. Gen. Virol.* **1992**, *73*, 2217–2223.
(14) Arbizi, J.; Taylor, G. Lopez, J. A.; Furze, J.; Wyld, S.; Whyte, P.; Stott, E. J.; Wertz, G.; Sullender, W.; Trudel, M.; Melero, J. *J. Gen. Virol.* **1992**, *73*, 2225–2234.
(15) Tempest, P. R.; Bremmer, P.; Lambert, M.; Taylor, G.; Furze, J. M.; Carr, F. J.; Harris, W. J. *Biotechnology* **1991**, *9*, 266–271.
(16) Siegel, M. M.; Tsao, R.; Doelling, V. W.; Hollander, I. J. *Anal. Chem.* **1990**, *62*, 1536–1542.

(17) Siegel, M. M.; Hollander, I. J.; Hamann, P R.; James, J. P.; Hinman, L.; Smith, B. J.; Farnsworth, A. P. H.; Phipps, A.; King, D. J.; Karas, M.; Ingendoh, A.; Hillenkamp, F. *Anal. Chem.* **1991**, *63*, 2470–2481.
(18) Feng, R.; Konishi, Y.; Bell, A. W. *J. Am. Soc. Mass Spectrom.* **1991**, *2*, 387–401.
(19) Feng, R.; Konishi, Y. *Anal. Chem.* **1992**, *64*, 2090–2095.
(20) Feng, R.; Konishi, Y. *Anal. Chem.* **1993**, *65*, 645–649.
(21) Jiskoot, W.; van de Werken, G.; Martin J. M. C.; Green, B. N.; Deuvery. E. C.; Crommelin, D. J. A. *Pharm. Res.* **1992**, *9*, 945–951.
(22) Lewis, D. A.; Guzzetta, A. W.; Hancock, W. S.; Costello. M. *Anal. Chem.* **1994**, *66*, 585–595, 1994.
(23) Carr, S. A.; Hemling, M. E.; Bean, M. F.; Roberts, G. D. *Anal. Chem.* **1991**, *63*, 2802–2824.
(24) Carr, S. A.; Roberts, G. D. *Anal. Biochem.* **1986**, *157*, 396–406.
(25) Carr, S. A.; Huddleston, M. J.; Bean, M. F. *Protein Sci.* **1993**, *2*, 183–196.
(26) Garvey, J. S.; Cremer, N. E.; Sussdorf, D. H. *Methods in Immunology. A Laboratory Text for Instruction and Research.* 3rd ed.; W. A. Benjamin, Inc.: Reading, MA, 1977.
(27) Jaton, J. C.; Brandt, D. C.; Vassalli In *Immunological Methods*; Lefkowits, I., Pernis, B., Eds.; Academic Press: New York, 1979.

Bellefonte, PA) coupled in series and operating isocratically, using 3.0 M guanidine hydrochloride in 50 mM sodium phosphate buffer, pH 6.2. Fractions containing the RCM light and RCM heavy chains were desalted by dialysis into 1.0 M acetic acid (500 mL × 4) over 48 h.

MALDI-MS of Intact RSHZ19. Approximately 3 pmol of the sample was examined in a matrix of sinapinic acid on the VG TofSpec laser desorption mass spectrometer. Light from a 337-nm pulsed N₂ laser was focused on the target, and a laser energy setting of 3:126 and an acceleration voltage of 27 kV were used. A total of 48 laser shots were averaged to produce the spectrum. The mass scale was calibrated externally with bovine serum albumin.

ESMS of Intact RSHZ19. Stabilizing buffers and impurities were removed from a solution (10 mg/mL) of the intact protein by centrifugal ultrafiltration with a Centricon-10 small-volume concentrator (Amicon, Inc., Beverly, MA) having a molecular weight cutoff of 30 000. The purified protein was collected in 10% acetic acid. The solution was adjusted to ~27% acetonitrile in 30% acetic acid and, using flow injection, was examined by ESMS on a PE-Sciex API-III triple–quadrupole mass spectrometer fitted with a fully articulated ion spray probe and an atmospheric pressure ionization source (PE-Sciex, Ontario, Canada). The mass spectrometer was scanned continuously from m/z 1800 to 2400 with a scan step of 0.2 and a dwell time per step of 3.0 ms resulting in a scan duration of 9.29 s. The orifice voltage was set at 100 V. The mass scale was calibrated as previously described.[25,28] It is important to note that automatic mass assignment algorithms applied to ESMS data have difficulty in properly assigning peak centroids—and, therefore, charge state—to broad, statistical m/z peaks such as those typically produced for large glycoproteins (see Discussion). In such cases we find that manual centroid assignment produces better M_r values with lower standard deviation.

ESMS of Separated Light and Heavy Chains. Each of the samples was examined by ESMS on the Sciex electrospray MS system. The RCM light chain was flow injected in 1.0 M acetic acid, and the RCM heavy chain was infused in a solution of ~22% acetonitrile in 25% acetic acid. A high concentration of acid was used to denature the protein and to maximize the degree of protonation/charging. For the RCM light chain, the mass spectrometer was scanned continuously from m/z 400 to 2400 with a scan step of 0.2 and a dwell time per step of 1.0 ms resulting in a scan duration of 10.55 s. The orifice voltage was set at 80 V. For the RCM heavy chain, the mass spectrometer was scanned continuously from m/z 600 to 2000 with a scan step of 0.2 and a dwell time per step of 1.93 resulting in a scan duration of ~14 s. The orifice voltage was set at 90 V.

Reversed Phase LC/ESMS of Tryptic Digests of Light and Heavy Chains. A 160 μL aliquot of a tryptic digest solution (110 pmol/μL) of the RCM light chain or 150 μL of a tryptic digest solution (120 pmol/μL) of the RCM heavy chain was analyzed using a 4.6 mm × 25 cm Vydac C₁₈ column connected to the Sciex API-III electrospray MS system. The column was heated to 45 °C. The HPLC system (Beckman System Gold) was operated at a flow rate of 1 mL/min beginning with a mobile phase of 100% solvent A (0.1% TFA), which was increased linearly to 50% solvent B (80% CH₃CN, 0.1% TFA) in 65 min. A 142:1 split was used

postcolumn to divert 993 μL/min to a UV detector (λ = 215 nm) and fraction collector, and 7 μL/min to the Sciex mass spectrometer. The mass spectrometer was scanned continuously from m/z 140 to 2400 with a scan step of 0.2 m/z and a dwell time per step of 0.32 ms resulting in a scan duration of 4.5 s. The orifice voltage was changed during each scan from a value of 135 V between m/z 140 and 400 to a value of 65 V from m/z 401 to 2400. This was done to increase fragmentation of glycopeptides to enhance their detectability as previously described.[25,28] All significant peaks appearing in the UV trace were fraction collected and kept at −70 °C for further analysis as might be deemed necessary.

Electrospray Tandem MS. Selected HPLC fractions were concentrated to near dryness on a Speed-Vac centrifuge (Savant Instruments, Farmingdale, NY) and reconstituted in ~20−100 μL of 1:1 methanol/H₂O (v/v), 0.2% in formic acid. Approximately 1−5 μL of each sample was introduced into the mass spectrometer by either flow injection or infusion. The mobile phase (1:1 methanol/H₂O v/v, 0.2−8% in formic acid) was delivered using a infusion pump (Harvard Apparatus, South Natick, MA) at a flow rate of 1 μL/min. Doubly-charged parent ions, $(M + 2H)^{2+}$, were selected with Q1 for collision-induced decomposition in Q2 of the triple–quadrupole. Quadrupole-3 of the triple–quadrupole system was scanned from m/z 10 to 2400 with a mass step of 0.25 Da and 10 ms dwell/step. Argon was used as the collision gas with a calculated collision energy of ~50 eV. Parent ion transmission was maximized by reducing the resolution of Q1 to transmit a ~2−3 m/z window about the selected parent ion. Daughter ion spectra were obtained from an injection of 1−5 μL of the samples at a concentration of ~2.5−10 pmol/μL.

MALDI-MS of Peptides and Analysis of Metastable Ions. MALDI-MS analyses of peptides were carried out using a Fisons VG TofSpec SE mass spectrometer (Manchester, UK), a single-stage reflectron instrument with a maximum resolution in the reflecting mode of $m/\Delta m$ 6000 (fwhm) using photon irradiation from a 337-nm pulsed nitrogen laser and 25-keV accelerating energy. The instrument was externally mass calibrated in the linear and reflectron modes using a mixture of peptides of known M_r. Aliquots of the HPLC fractions were mixed (1:2 v/v) with α-cyano-4-hydroxycinnamic acid (10 mg/mL in 1:1 CH₃CN/H₂O), spotted onto the stainless steel target and allowed to air-dry prior to insertion into the mass spectrometer. Structural information may be discerned from MALDI-MS by analysis of metastable ions formed in the field-free drift region of the time-of-flight analyzer.[51] Metastable ion mass spectra were acquired in eight consecutive, overlapping mass scale segments, each representing a 25% mass change from the previous segment. The segments were combined and externally mass calibrated (vs a metastable ion spectrum of a model peptide such as renin tetradecapeptide or substance P, residues 2−11) by the data system.

Carbohydrate Composition Analysis. The carbohydrate composition of anti-RSV-MAb was determined using methods previously described.[29] The method involves release of monosaccharides by acid hydrolysis followed by their derivatization with anthranilic acid to yield fluorescent derivatives.

Hydrazinolysis Release of Carbohydrates from the Glycoprotein and Separation and Analysis of Carbohydrates by High-Performance Anion Exchange Chromatography. Oligosaccharides were isolated from the glycoprotein using Glycoprep 1000 (Oxford Glycosystems, Oxford, UK), which operates

(28) Huddleston, M. J.; Bean, M. F.; Carr, S. A. *Anal. Chem.* **1993**, *65*, 877−884.

(29) Anumula, K. R. *Anal. Biochem.* **1994**, *220*, 275−283.

using the hydrazinolysis methodology developed by Kobata and colleagues.[30] Samples for hydrazinolysis were prepared by organic solvent precipitation in the reactor vessels (glass screw-cap tubes 13 × 65 mm). Less than 2.0 mg each of the glycoproteins was made up to 0.5 mL using a fresh 1% NH_4HCO_3 solution. Glycoproteins were precipitated using 4 volumes of ethyl alcohol/ethyl acetate (1:1) containing 1% acetic acid mixture at room temperature for 30 min. Precipitated proteins were collected by centrifugation (table top) and were resuspended in 0.5 mL of NH_4HCO_3 solution. A total of three precipitations was found to be satisfactory for oligosaccharide release by removing the interfering substances such as buffer salts, excipients, and detergents from the samples. The glycoprotein precipitates were dried using a vacuum centrifuge (Savant, with no heat) for at least 3 h. The samples were installed into the Glycoprep 1000, which was set up to release oligosaccharides using the "N" program option according to the manufacturers instructions. Oligosaccharide pools were dried by lyophilization and an aliquot (~5–10%) was analyzed by high-performance anion exchange chromatography with pulsed amperometric detection (HPAE-PAD) as previously described.[29]

Hydrazinolysis Release of Carbohydrates from the Tryptic Glycopeptide and Analysis of Fluorescently Labeled Carbohydrates by HPLC and High-Resolution Gel Permeation Chromatography. Oligosaccharides were also released by hydrazinolysis from glycopeptides identified in the LC/ESMS experiments. Dry glycopeptide samples supplied to Oxford GlycoSystems (12 nmol) were transferred to the GlycoPrep 1000 reactor vessels using TFA (0.1% v/v), and the oligosaccharides released and recovered using the "N + O" program. The sample was fluorescently labeled by reductive amination with 2-aminobenzamide, and derivatized oligosaccharides were separated from excess reagents using Whatman 3MM chromatography paper and subjected to ascending paper chromatography using 1-butanol/ethanol/water (4:1:1). The 2-aminobenzamide-labeled oligosaccharides remained at the origin and were subsequently eluted with water. An aliquot of the total pool of this sample was separated by HPLC on a 4.6 mm × 100 mm GlycoSep C column using acetonitrile and ammonium formate as eluent according to the standard experimental protocol ASP00C1 from Oxford Glycosystems. A second aliquot of the sample was subjected to high-resolution gel permeation chromatography. To accomplish this, the fluorescently labeled oligosaccharides were suspended in an aqueous solution of a partial acid hydrolysate of dextran (internal standards for glucose units) and applied to a gel permeation column in the RAAM 2000 Glycosequencer (Oxford Glycosystems). The column was eluted with water at 55 °C at a flow rate of 30 μL/min over 21.6 h. Detection was by an in-line fluorescence flow detector and an in-line differential refractometer.

Exoglycosidase Digestion of the Glycopeptide. In three different experiments the glycopeptide isolated from the tryptic digest was subjected to digestion with individual or combinations of the exoglycosidases β-galactosidase (source, *Streptococcus pneumoniae*; specificity, Galβ1-4GlcNAc) and β-N-acetylhexosaminidase (source, *S. pneumoniae*). The latter enzyme is specific for GlcNAcβ1-2Man at low enzyme concentration (0.01 milliunit/μL), while it exhibits broader specificity for GlcNAc-β1-2,4, or 6Man at high concentration (0.1 milliunit/μL). The final incubation

(30) Takasaki, S.; Mizuochi, T.; Kobata, A. *Methods Enzymol.* 1982, 83, 268–277.

Table 1. Determined M_r Values on Anti-RSV MAb and the Reduced and Alkylated Light and Heavy Chains

sample	ESMS	MALDI-MS[b]
anti-RSV Mab (intact)	149265 ± 100[c]	149519 ± 300[c]
light chain (reduced, alkylated)	24368 ± 3[a]	nd[c]
heavy chain (reduced, alkylated)	51250 ± 50[a]	nd[c]

[a] Estimated error (Da). [b] Calibrated with bovine serum albumin. [c] Not determined.

solution (total volume, 10 μL) of the first experiment consisted of a β-galactosidase concentration of 0.08 milliunit/μL and a substrate concentration of 10 mM. The final incubation solution (total volume = 10 μL) of the second experiment consisted of a β-galactosidase concentration of 0.08 milliunit/μL, a β-N-acetylhexosaminidase concentration of 0.1 milliunit/μL, and a substrate concentration of 10 mM. A third experiment was performed identically to the second, except the β-N-acetylhexosaminidase was used at a 10-fold lower concentration to obtain highly specific cleavage. At time points T = 0, 2, 4, 8, and 24 h, 0.5-μL aliquots of the digests were removed and spotted on a laser target with a matrix of α-cyano-4-hydroxycinnamic acid and examined by MALDI-MS.

RESULTS

The M_r values of the intact glycoprotein and the separated light and heavy chains (following reduction and S-carboxymethylation) were determined by ESMS and MALDI-MS and are shown in Table 1. The M_r of the polypeptide chain of RSHZ19 deduced from the cDNA sequence is 146 242. This value takes into account 16 disulfides formed by the 32 Cys present. The measured M_r values of the intact glycoprotein obtained by ESMS (Figure 1a) and MALDI-MS differ from the calculated value by 3023 and 3277 Da, respectively, indicating the presence of a modification having substantial mass, presumably carbohydrate. The M_r of the reduced and S-carboxymethylated light chain obtained by ESMS (Figure 1b) was within 1 Da of the predicted value (24 367 Da), whereas the M_r of the reduced and S-carboxymethylated heavy chain was heavier than the mass calculated for the reduced and alkylated polypeptide chain (49 699 Da) by 1551 Da (Figure 1c). The 1551-Da difference must be multiplied by 2 to take into account that there are two heavy chains (and two light chains) in the intact MAb. The 3102 Da so obtained accounts well for the total mass discrepancy observed for the intact MAb and suggests that all of the modifications present reside on the heavy chain.

Establishing the M_r values for the intact MAb and its heavy and light chains rapidly provides important information in the characterization of the MAb structure. However, it is necessary to further characterize the glycoprotein by conducting studies on smaller fragments in order to locate posttranslational modifications such as sites of glycosylation, ragged termini, and sites of oxidation or deamidation. This is readily accomplished using LC/ESMS with in-line UV detection on mixtures of relatively small peptides generated by use of a proteolytic enzyme that will cleave predictably and with reasonable specificity.[23,31-33] The reduced

(31) Hemling, M. E.; Roberts, G. D.; Johnson, W.; Carr, S. A. *Biomed. Environ. Mass Spectrom.* 1990, 19, 677–691.
(32) Covey, T. R.; Huang, E. C.; Henion, J. D. *Anal. Chem.* 1991, 63, 1193–1200.
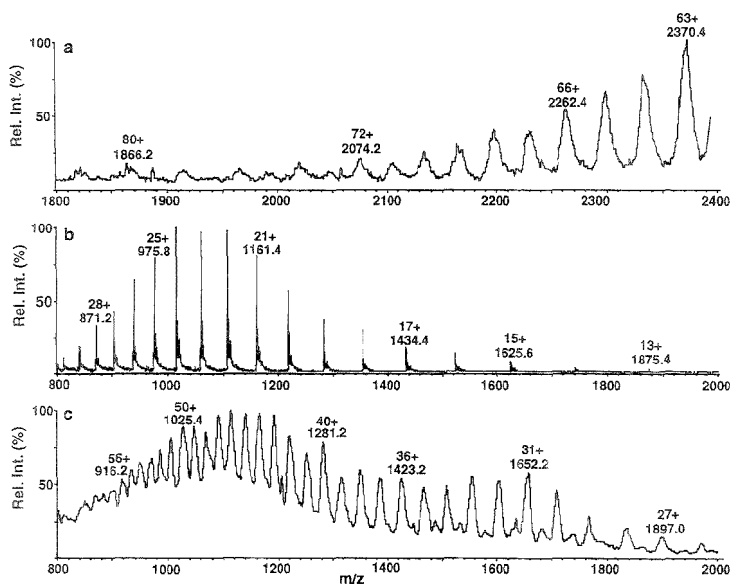
Figure 1. (a) ES mass spectrum of native RSHZ19. Because the m/z range of the mass spectrometer used is limited to m/z 2400, peaks with fewer than 63 charges are not observed. (b) ES mass spectrum of reduced and S-carboxymethylated RSHZ19 light chain. (c) ES mass spectrum of reduced and S-carboxymethylated RSHZ19 heavy chain. Labels on peaks correspond to the observed m/z and the determined charge states. The major satellite peaks to the high-mass side of each of the main ion series peaks correspond to $(M + H_{n-1} + K)^{n+}$.

and carboxymethylated light and heavy chains were digested in separate experiments with trypsin and then analyzed by LC/ESMS. The UV and total ion current (TIC) traces produced during the analyses of the light- and heavy-chain digests are presented in Figures 2 and 3, respectively. Peptide signals were assigned to specific sequence locations with the aid of an interactive computer program developed in-house.[34] The program (Rosetta, available commercially from PE-Sciex as PeptideMap) determines the M_r of all of the peptides in the LC/ESMS data set and matches them, if possible, to the calculated M_r of all peptides that would be expected to form based on the reaction conditions used and the predicted sequence. The following cleavage site criteria were used to make assignments: (1) a tryptic site at both ends; (2) a tryptic site at one end and a chymotryptic site at the other; (3) a chymotryptic site at both ends; and (4) any of the above with one uncleaved, internal tryptic site (e.g., Arg-Glu).

The predicted sequences of the heavy and light chains are shown in Figures 4 and 5, respectively. Peptides identified in the LC/ESMS experiments are indicated with their determined M_r and the scan numbers at which they were found. In general, the determined M_r values were ≤ 0.2 Da of calculated. The data obtained by the LC/ESMS of the mixtures of tryptic peptides provided 99.1% coverage of the 219 amino acid light chain and 99.3% of the 446 amino acid sequence of the heavy chain. Only two of the 22 predicted unique tryptic fragments of the light-chain sequence were not detected. One of these corresponds to a single

(33) Ling, V.; Guzetta, A. W.; Canova-Davis, E.; Stults, J. T.; Hancock, W. S. *Anal. Chem.* 1991, *63*, 2909–2915.

(34) Soneson, K. K.; Carr, S. A.; Hemling, M. E.; Taylor, A.; Bonner, R.; Roberts, G. D.; Bean, M. F.; Annan, R. S.; Johnson, W. *Proceedings of the 42nd ASMS Conference on Mass Spectrometry and Allied Topics;* Chicago, IL, 1994; p 662.

arginine (Arg[113]); however this residue is detected in a partial tryptic fragment (Val[109]–Arg[113]) formed by incomplete cleavage between two consecutive tryptic sites. The other corresponds to a dipeptide (His[194]–Lys[195]). Except for two, all of the 37 predicted unique tryptic fragments of the heavy chain were detected (analysis of the glycopeptide is described below). These correspond to a single lysine (Lys[213]) and a dipeptide (Ser[414]–Arg[415]). It is often difficult to detect dipeptides by LC/ESMS since they usually elute in the high-aqueous portion of the chromatogram where buffer salts present in the sample also elute. These excipients tend to suppress peptide-related signals. In cases where the determined M_r was higher than the predicted M_r by more than 0.5 Da, deamidation of Asn to Asp was suspected to have occurred (see peptides identified with a subscript d in Figures 4 and 5). The M_r of these peptides were redetermined by infusion of the corresponding fractions to confirm the observed mass shift.

There is generally excellent agreement between the UV traces and the total ion current traces from the LC/ESMS experiments with respect to the presence and relative abundances of peaks. However, discrepancies can arise because the detectors are measuring different physical parameters of the molecules. The UV response is a product of concentration and molar absorptivity at the given wavelength, while the response in MS is a function of the number of ions produced within the mass range monitored. In the UV trace of the light chain (Figure 2), the peak at a retention time of ~24.2 min is very strong, whereas in the TIC trace it is very weak. The observed M_r of this component is 560.4, which corresponds to a predicted tryptic tetrapeptide (Val[151]–Lys[154]). The sequence of this peptide was confirmed by electrospray tandem MS (ESMS/MS; see below) and by analysis of metastable ions in MALDI-MS (the so-called postsource decay
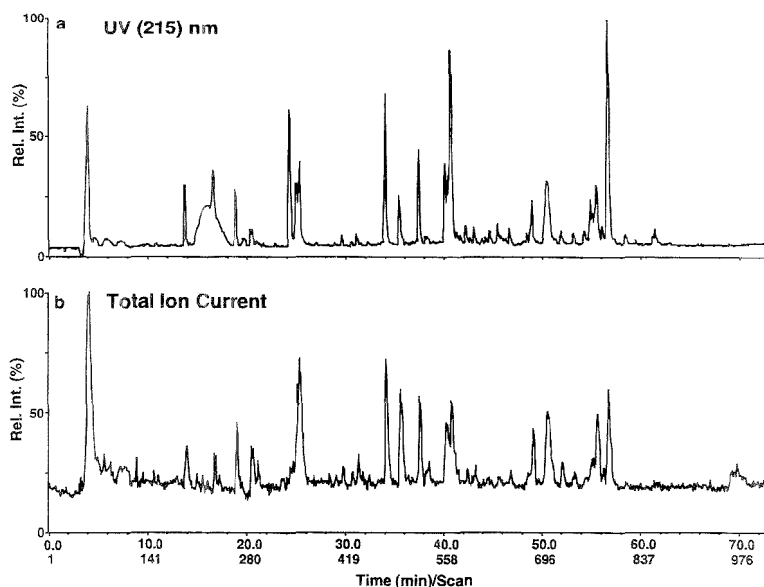
Figure 2. On-line LC/UV/ESMS analysis of a tryptic digest of RSHZ19 reduced and S-carboxymethylated light chain: (a) UV trace at 215-nm absorbance; (b) total ion current trace produced by the mass spectrometer. Chromatographic peaks appear in the UV trace ~0.4 min later than they appear in the TIC trace.

Figure 3. On-line, LC/UV/ESMS analysis of a tryptic digest of RSHZ19 reduced and S-carboxymethylated heavy chain: (a) UV trace at 215-nm absorbance; (b) total ion current trace produced by the mass spectrometer; (c) glycopeptide-selective trace (see text). Chromatographic peaks appear in the UV trace ~0.4 min later than they appear in the TIC trace.

technique).[51] In this case, the considerable difference in response is due to the presence of the strong UV absorber Trp in the small peptide. The raised baseline at ~17 min in the UV chromatogram of the light chain was most likely caused by an air bubble and

was not reproduced in subsequent injections of this same sample.

The expected N and C termini of both chains were identified on the basis of the observed M_r in the LC/ESMS data (Figures 4 and 5). A peptide 16 Da heavier than the predicted, blocked

```
            10          20          30          40          50          60
DIQLTQSPSSLSASVGDRVTITCRSSQTLVHTDGNTYLEWYQQKPGKAPKLLIYRVSNRF
<———————1860.0———————><—749.4—><———2681.4(ave)———————><314><676.4><—474><
    (523-529)            (352-360)    (564-574)              (78-105)(496-503)(100-116)
<..........................>                                              <...>

            70          80          90          100         110         120
SGVPSRFSGSGSGTDFTFTISSLQPEDIATYYCFQGSHLPRTFGQGTKVEIKRTVAAPSV
—748.4—<———————3876.0(ave)———————————————————————————><—737.4—><—643p—><—————
  (352-360)         (789-797)                             (265-270) (295-298)
                                                              <.....>

            130         140         150         160         170         180
FIFPPSDEQLKSGTASVVCLLNNFYPREAKVQWKVDNALQSGNSQESVTEQDSKDSTYSL
—1945.0(ave)————><———1798.0d———————><346><—559><——————————————2136.4(ave)d—><———
  (699-719)           (771-783)      (65-80)(340-349)              (349-353)
                                        <.>

            190         200         210
SSTLTLSKADYEKHKVYACEVTHQGLSSPVTKSFNRGEC
—1502.0————><—624.2>  <————————1876.0————————><522><365>
 (560-566)   (194-198)        (475-481)     (233-237)(101-113)
                                             <........>
```

Figure 4. Predicted amino acid sequence of RSHZ19 reduced and S-carboxymethylated light chain indicating the peptides (underlined) identified by RP-HPLC/ESMS of a tryptic digest. Sequences identified by Edman degradation are underlined with a dotted line. The values given in parentheses represent the range of scans over which the indicated component was observed to elute. The M_r values are monoisotopic molecular masses unless otherwise noted. Partial cleavages (i.e., one or more uncleaved tryptic sites) are denoted with the subscript p. The subscript d denotes that possible deamidated forms of the peptide were detected.

N-terminal tryptic peptide of the heavy chain was also observed in the LC/ESMS data eluting ~2 min prior to the predicted N-terminal peptide (58.5 vs 60.6 min, Figure 3). Attempts to sequence this peptide by Edman degradation failed, presumably due to the presence of a blocked N terminus. The sequences of this peptide, and that of the blocked N-terminal peptide with the expected M_r, were established by mass spectrometric peptide sequencing by electrospray tandem MS.[23] Both peptides produced an identical series of N-terminal (b_1-b_5) fragment ions, demonstrating that the peptides have the same sequence through residue 5 (data not shown). Similarly, the C-terminal (y_2-y_4) fragment ions corresponding to the partial sequence HisTrpValArg were obtained for both peptides. However, beginning at y_5, the y fragment ions in the spectrum of the earlier eluting peptide shift upward by 16 Da relative to those in the spectrum of the predicted N-terminal peptide, demonstrating that Met^{34} is oxidized. The sequence of the predicted N-terminal peptide was also corroborated by Edman degradation following treatment with pyroglutamate aminopeptidase to remove $<Glu^1$ at the N terminus. The ratio of the predicted N-terminal peptide to the modified N-terminal peptide is ~1.8:1 based on the ion current response for the respective $(M + 3H)^{3+}$ ions.

Two forms of the heavy-chain C-terminal tryptic peptide were also observed by LC/ESMS: $Ser^{439}-Gly^{445}$ and $Ser^{439}-Lys^{446}$. Approximately 85% of the heavy chain is in the des-Lys form based on the ion current response and the UV absorbance for the respective forms of the peptide. Partial removal of the C-terminal Lys of the heavy chain of MAbs has been previously reported and may be due to carboxypeptidase B-like activity present during the fermentation process.[22] Similarly, the predicted amino terminus, Asp^1-Arg^{18}, and the carboxyl terminus, $Gly^{217}-Cys^{219}$, of the light chain were identified by mass spectrometry and, in these cases, confirmed by Edman degradation.

A variety of techniques yielding an increasing level of structural detail were employed to study the glycosylation of the RSHZ19. Carbohydrate composition analysis obtained on the intact MAb indicated the presence of the following sugars in moles of carbohydrate per mole of MAb: fucose (Fuc) 1.8; N-acetylglucosamine (GlcNAc) 6.4; galactose (Gal) 1.2; mannose (Man) 4.9; and N-acetylneuraminic acid (NANA) 0.1. These values are not corrected for the losses encountered during hydrolysis.[29] These data are consistent with the presence of complex, N-linked

oligosaccharide; the absence of galactosamine suggests that no O-linked carbohydrates of the usual type are present.

LC/ESMS was used to locate glycopeptides in the complex digest mixtures and to preparatively fractionate them for further structural studies. We recently described a general approach for selective detection of a variety of posttranslational modifications in proteins during LC/ESMS analysis of digests.[25,28] The method relies on the formation and detection of low-mass fragment (marker) ions that are specific for the modification(s) of interest. The natural abundance of these low-mass marker ions in normal electrospray mass spectra is often quite low, but their abundance can be significantly enhanced by collision-induced decomposition of the parent ions. This is accomplished by stepping the potential that controls the extent of collision-induced decomposition of source-produced ions from a high voltage, to maximize fragment ion production during acquisition of low m/z ions, to a lower voltage to yield intact ionized molecules during the remainder of the scan. In this way, both intact parent ions and abundant marker ions are observed in the same m/z scan. A selected ion current trace for one or more of the marker ions reveals where in the chromatogram the modified peptide is eluting. Glycopeptides in complex mixtures may be selectively detected on the basis of production of diagnostic sugar oxonium ions, particularly the $HexNAc^+$ and $Hex-HexNAc^+$ fragments.

The elution position of the glycopeptide in the HPLC separation of the tryptic digest of the heavy chain was established by plotting a selected ion current (SIC) trace for the sum of the m/z 366 $HexHexNAc^+$ and m/z 168 $(HexNAc - 2H_2O)^+$ carbohydrate marker ions produced in the manner described above. These ions maximize at ~19.5 min in the chromatogram (Figure 3c). The mass spectrum obtained by averaging the scans representing the entire glycopeptide peak envelope (UV retention times of 19.1–19.6 min.) is shown in Figure 6. Clusters of ions are observed in three distinct regions of the mass spectrum which correspond to the $(M + 3H)^{3+}$, $(M + 2H)^{2+}$ and $(2M+3H)^{3+}$ of the glycopeptide. The ions in each of these clusters are separated by the incremental masses of various monosaccharides. For example, the peaks at m/z 1398.8 and 1317.8 differ by 81 Da; because these ions are doubly charged, the true mass difference is 162, which corresponds to the incremental mass of a hexose (e.g., Gal or Man). The observed distribution of peaks provides a snapshot of the glycoform heterogeneity at this specific site. We also routinely

Figure 5. Predicted amino acid sequence of RSHZ19 heavy chain indicating the peptides (underlined) identified by reverse phase LC/ESMS of a reduced and S-carboxymethylated tryptic digest of reduced and S-carboxymethylated protein. Dotted underlines correspond to sequences identified by Edman degradation. The N-terminal amino acid is pyroglutamic acid (<E). The values given in parentheses represent the range of scans over which the indicated component was observed to elute. The M_r values are monoisotopic molecular masses unless otherwise noted. Partial cleavages (i.e., one or more uncleaved tryptic sites) are denoted with the subscript p. A compound with an M_r value equivalent to the tetrapeptide Val[214]–Lys[217] elutes in scans 162–166 and 180–185. CHO at Asn[296] denotes the determined glycosylation site. The M_r value determined from the mass spectrum of scans 61–75 is 307.1 and corresponds to the dipeptide Cys[320]–Lys[321]. The apparent elution of the peptide, Thr[392]–Lys[408], at two slightly different retention times is possibly a result of cis/trans isomerization of Pro residues in the peptide. The subscript d denotes that possible deamidated forms of the peptide were detected. The large peptide, Leu[83]–Lys[120], tailed severely in the LC chromatogram and was detected only through a selected ion current plot of the mass of the predicted $(M + 3H)^{3+}$.

reanalyze small aliquots of the HPLC fraction(s) containing the entire glycopeptide pool(s) by infusion ESMS to determine whether minor glycoforms may be present that have gone undetected due to the relatively fast scan conditions employed in the LC/ESMS analyses. In the present case, the infusion data (data not shown) and the LC/ESMS data for the glycopeptide pool showed the same distribution of M_r for the glycoforms.

The only consensus sequence for N-glycosylation (Asn-X-Ser/Thr, where X = any amino acid except Pro) in the protein is Asn[296], which is found in the tryptic peptide Glu[292]–Arg[300]. The identity of this glycopeptide was established by digestion of a small portion of the fraction with peptide-*N*-glycosidase F. This releases the entire carbohydrate en bloc from the peptide and converts the attachment site Asn to Asp.[24] Analysis of the digest by MALDI-MS after ~1 min of reaction time revealed the presence of a new $(M + H)^+$ signal at m/z 1191.2 (calculated, m/z 1191.2) corresponding uniquely to the $(M + H)^+$ for Glu[292]–Arg[300] in which Asn[296] had been converted to Asp. The $(M + H)^+$ for Glu[292]–Arg[300] in which Asn[296] is unsubstituted was not detected in the LC/ESMS data, and therefore, we conclude that the protein is fully glycosylated at this site. Subtracting the peptide mass from the determined glycoform masses yields a series of residual carbohydrate masses. All potential carbohydrate compositions that fit these masses were generated with the computer program

Gretta's Carbos (Wade Hines and Brad Gibson, UCSF). Unique compositions were identified for each parent glycoform. The predominant anti-RSV carbohydrates have compositions of Hex$_4$-HexNAc$_4$dHex (39%) and Hex$_3$HexNAc$_4$dHex (37%), presumably corresponding to highly processed biantennary, core fucosylated structures (see below). The mixture of carbohydrates attached to the intact MAb was also released by hydrazinolysis and analyzed by HPAE-PAD. The retention times of the major species correspond to neutral, biantennary oligosaccharides, core fucosylated carbohydrates lacking sialic acid, in agreement with the MS data. Carbohydrate analysis was also performed on oligosaccharides released from the tryptic glycopeptide sample and analyzed by HPLC anion exchange chromatography and gel permeation chromatography. The anion exchange chromatography indicated that the oligosaccharides are largely neutral (>95%). Consequently, deacidification was deemed unnecessary prior to gel permeation analysis. By high-resolution gel permeation chromatography, at least six components are indicated with hydrodynamic volumes ranging from 8.0 glucose units to 15.3 glucose units (data not shown). These data are in agreement with the ESMS, MALDI-MS, and the HPAE-PAD data (Table 2).

To further elucidate the oligosaccharide structure in terms of sequence and linkage information, aliquots of the HPLC fraction known to contain the glycopeptides were digested with specific

$(M+2H)^{2+}$

100

1317.8
x = 3
y = 4

1398.8
x, y = 4

E^{292}
$(Hex)_x(HexNAc)_y(dHex)-N^{296}$
R^{300}

Relative Intensity (%)

50

$(M+3H)^{3+}$
933.0
x, y = 4

x = 4
y = 3
1297.0

x = 5
y = 4
1480.0

$(2M+3H)^{3+}$
(x=3, y=4)
+
(x, y=4)

x = 3
y = 4
879.4

x = 5
y = 4
987.4

1216.0

x,y = 3

1757.6
x = 3
y = 4

1811.2

x,y = 4
1865.6

800   1000   1200   1400   1600   1800   2000
m/z
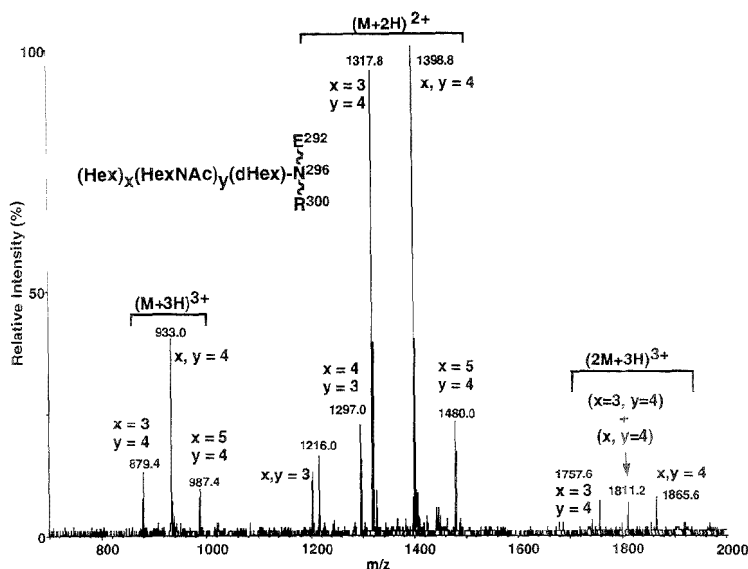
Figure 6. LC/ES mass spectrum of the glycosylated primary tryptic peptide (Glu[292]—Arg[300]) identified in the LC/ESMS data (Figure 3c). The set of peaks produced by the 2+ charge state is the most abundant and indicates the presence of at least five glycopeptides that differ in the number of monosaccharide units that comprise the oligosaccharide segment (see text).

Table 2. Carbohydrate Structures of Anti-RSV MAb

ESMS		proposed structure[a]	rel % composition carbohydrate			
$(M+2H)^{2+}$	M_r (Det.)		ESMS	HPAE-PAD[b]	MALDI-MS	HRGP[c]
1480.0	2958.0	Gβ1-4GNβ1-2Mα-1 ... Fα1 Arg[300] / Mβ1-4GNβ1-4GN-Asn[296] / Gβ1-4GNβ1-2Mα-1 ... Glu[292]	8	14	6	7
1407.8	2813.6	−F	3	nd[d]	1	nd
1398.8	2795.6	−G	36	45	36	39
1326.0	2650.0	−G, −F	3	nd	4	nd
1317.8	2633.6	−2G	34	30	36	25
1297.0	2592.0	−G, −GN	8	5	7	8
1245.0	2488.0	−2G, −F	1	nd	4	nd
1216.0	2430.0	−2G, −GN	6	2	6	8

[a] The first entry in the column is the most heavily glycosylated structure observed. All subsequent entries differ from the first entry by the loss of the indicated sugars. [b] High-performance anion exchange chromatography with pulsed amperometric detection. Equal responses are assumed for all the oligosaccharides. HPAE-PAD detected <5% monosialyated oligosaccharides. [c] High-resolution gel permeation chromatography. [d] nd, not determined.

exoglycosidases. The time course of these reactions was monitored by MALDI-MS.[35] The mixture of glycopeptides was subjected to concurrent, controlled digestion with two highly specific exoglycosidases, a β-galactosidase (specificity, Galβ1-4GlcNAc and Galβ1-4GalNAc) and a β-N-acetylhexosaminidase (specificity, GlcNAcβ1- 2Man under low enzyme-to-substrate ratio conditions). These enzymes were chosen on the basis of the structural types proposed from the ESMS and MALDI-MS analyses of the glycopeptide pools, as well as the HPAE-PAD data. The resulting products were then analyzed directly by MALDI-MS. These results indicate that in a sample of the digest taken immediately all of the terminal Gal residues and a minor amount of terminal

GlcNAc residues were removed from the glycopeptide. At 8 h most of the GlcNAc residues were removed, and at 24 h digestion of the oligosaccharide by both enzymes appeared to be complete (Figure 7). Complete removal of GlcNAc with the 1—2 specific enzyme rules out the presence of bisecting GlcNAc which, if present, would be linked 1—4 to the β-linked Man of the trimannosyl core. The RSV glycopeptide was also evaluated using three different α-fucosidases: chicken liver α-fucosidase (specificity = Fucα1-2,4,6)), bovine epididymis α-fucosidase (specificity = Fucα1-6(>2,3,4)), and almond meal α-fucosidase (specificity = Fucα1-3/4). Unfortunately, the results obtained with these enzymes were inconclusive. The enzyme with the broadest specificity released a significant amount of Fuc, but not all (Figure 8d). Furthermore it was found to be contaminated with galac-

(35) Sutton, C. W.; O'Neill, J. A.; Cottrell, J. S. *Anal. Biochem.* **1994**, *218*, 34—46.
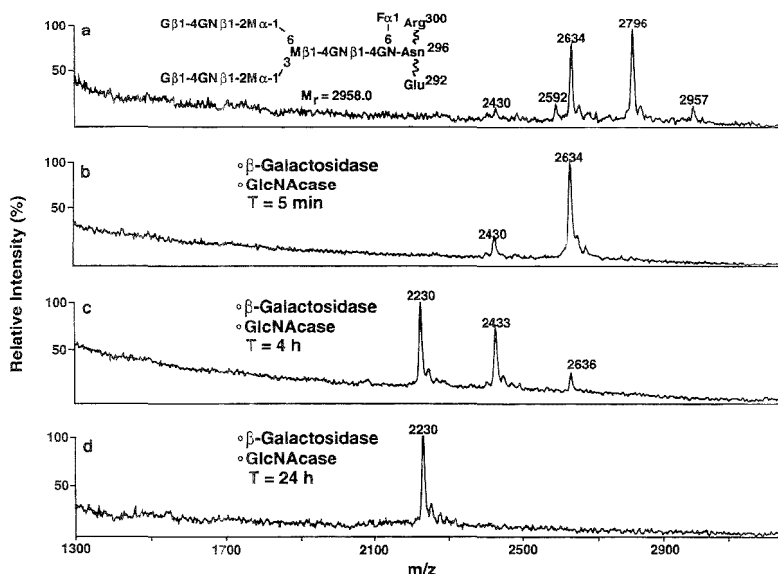
Figure 7. MALDI mass spectra of (a) the mixture of tryptic glycopeptides of RSHZ19 and (b–d) the same glycopeptides following digestion with two exoglycosidases at various time points. The spectra show the transformation of the glycopeptides due to the loss of terminal monosaccharide residues beginning at essentially $T = 0$ to $T = 24$ h.
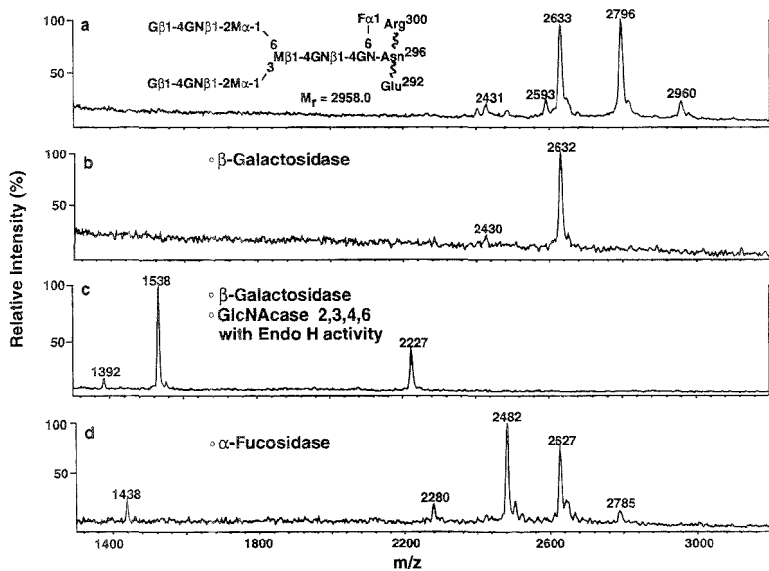
Figure 8. MALDI mass spectra of (a) the mixture of tryptic glycopeptides of RSHZ19 and the same glycopeptides following digestion with (b) β-galactosidase and (c) β-galactosidase combined with β-N-acetylhexosaminidase. Panel d is the glycopeptide after digestion with α-fucosidase from chicken liver.

tosidase. A small but significant amount of Fuc was removed after 22 h using the 1–6-specific enzyme, whereas no reaction was obtained with the 1–3/4-specific enzyme. These data are most consistent with attachment of Fuc to the 6-position of GlcNAc, but we cannot rule out attachment to the 3-position as well.

These results demonstrate that RSHZ19 is glycosylated with a family of core fucosylated, (predominantly) nonsialylated, biantennary oligosaccharides having $Gal\beta1$-4GlcNAc$\beta1$-2Man as the outer chains. The electrospray, MALDI-MS, HPAE-PAD, and gel permeation data are summarized in Table 2. Eight glycoforms

are detected by MS, while at least five and six different glycoforms were observed by HPAE-PAD and gel permeation chromatography, respectively. The relative ratios of the glycoforms are derived from the peak heights of the respective components in the MALDI-MS and ESMS data (2+ series) and the peak areas from the HPAE-PAD and gel permeation data. These ratios are generally in very close agreement with each other, with the MS discerning a few additional minor glycoforms (Table 2).

It is now possible to reevaluate the determined M_r of the intact glycoprotein to see whether the modifications to the polypeptide chain determined to be present fully account for the mass difference of 3023 Da (determined by ESMS) to the calculated mass of the protein. The studies described above have established that (1) the heavy chain has pyroglutamic acid (<Glu) at the N terminus; (2) ~88% of the heavy chain (predicted to be 446 amino acids long) lacks the C-terminal Lys residue; (3) the light chain is 219 amino acids long and corresponds precisely to the sequence predicted by the cDNA; (4) there is one N-linked glycosylation site located on each heavy chain; and (5) the distribution of glycoforms at each of the two N-linked sites in the intact MAb is identical with an average incremental mass of 1601 Da based on ESMS analysis of tryptic glycopeptides (see below). This number is also consistent with that calculated from the observed relative molar ratios of carbohydrate obtained by carbohydrate composition analysis (see above). The M_r calculated for the intact protein taking these modifications into account (assuming 100% of heavy chain is des-Lys) is 149 154 Da. The M_r determined by ESMS is within 111 Da or 0.07% of this value, whereas the MALDI-MS value is within 365 Da or 0.2% (Table 1). The close agreement between the calculated and predicted M_r provides a high degree of confidence that all modifications with significant mass have been accounted for and that the overall sequence has a very high degree of fidelity to that predicted from the cDNA.

DISCUSSION

We have demonstrated that the primary structure of large glycoproteins like the anti-RSV-MAb described here may be extensively characterized through a combination of LC/ESMS and MALDI-MS, supplemented as necessary with Edman degradation and tandem MS to aid in the sequence analysis of specific peptides. To our knowledge, the present study is one of the most detailed characterizations of the primary structure of a humanized MAb and its posttranslational modifications. These experiments verified 99.1% of the light- and 99.3% of the heavy-chain amino acid sequences, confirmed the N and C termini of both chains, and demonstrated the nature and relative extent of heterogeneity at the N and C termini of the heavy chain. A previous LC/ESMS study achieved only 81% coverage of the molecule and reported only very limited characterization of the carbohydrate.[22] The study of RSHZ19 reported here illustrates some of the unique capabilities that mass spectrometry provides for identifying sites and structures of modifications such as glycosylation, N-terminal blocking groups, and C-terminal proteolytic clipping. While it would be possible, in principal, to use conventional methodologies for confirmation of amino acid sequence, the various modifications noted above that were identified in RSHZ19 would have been difficult to detect and characterize without MS. In addition to improving the completeness and accuracy of the structural characterization, the use of MS also greatly increased the speed of the overall analysis.

To our knowledge, the present study is the first to directly compare MALDI-MS and ESMS of glycopeptides with high-performance gel permeation chromatography and HPAE-PAD of enzymatically and chemically released carbohydrates to assess the capabilities of the respective techniques for providing quantitative as well as qualitative information on the carbohydrates present. These data indicate that, for oligosaccharides of the types found in MAbs, the agreement among these techniques is very good (Table 2). The relative ratios of the glycoforms are derived from the peak heights of the singly charged (M + H)$^+$ in the MALDI-MS, the (M − 2H)$^{2+}$ in the ESMS data, and the peak areas from the HPAE-PAD and gel permeation data. Quantification of the entire carbohydrate distribution requires that the glycopeptide sample analyzed contain all of the heterogenous carbohydrate species present at that site. Isolation of the glycopeptide pool(s) from the glycoprotein digest is greatly simplified by the stepped collision energy scan employed here during the LC/ESMS analyses.[25,28] This technique selectively identifies glycopeptides and the start and end points of their elution profiles in the chromatographic data. In general, we select the lowest charge state with good ion statistics that is observed in ESMS to correlate peak height with relative solution concentration. By choosing the lowest charge state, we minimize any effect that charging of the carbohydrate structures may have on the apparent glycopeptide distribution. Such differences in charging can affect the observed peak ratios, as illustrated by the ratio of the glycoform peaks in the (M + 3H)$^{3-}$ cluster vs those of the (M + 2H)$^{2+}$ cluster in Figure 6. An assumption of this method is that the peptide picks up charge at low pH more readily than does the carbohydrate and dominates the charge character of the glycopeptide. This assumption is supported by the higher relative gas phase basicities of the primary amine (NH$_2$ terminus and Lys) and/or guanido (Arg) functionalities present on the peptide[36] vs the lower gas phase basicities of the N-acetyl groups of the carbohydrate.[37] In the case of carbohydrates (as opposed to glycopeptides), the relative abundances of peaks of a given charge state in the ESMS data cannot be used for quantitation because carbohydrates with additional chargeable groups (like sialic acid or HexNAc) will have charge distributions different from those with fewer chargeable groups. Summing the abundances at each charge state has been suggested as a means of obtaining quantitative information in this case.[38]

Another unique aspect of the work described here was the use of MALDI-MS to monitor the results of a series of controlled digestions with specific exoglycosidases.[35] The mass shifts observed provided the sequence and linkage of individual glycan species. Direct analysis of the glycopeptide by MS has several advantages over these approaches. First, it is unnecessary to have a method for quantitatively releasing the oligosaccharides without degrading them. Both chemical and enzymatic methods of release have specific drawbacks with respect to these issues.[39] Second, as demonstrated here, the glycopeptide is amenable to either sequential or parallel exoglyosidase digestion with MALDI-MS readout of the structural information. Importantly, there is no need to purify the product prior to analysis by MALDI-MS if

(36) Wu, Z.; Fenselau, C. *Rapid Commun. Mass Spectrom.* 1992, *6*, 403–405.
(37) Meot-Ner (Mautner), M. *J. Am. Chem. Soc.* 1994, *106*, 278–283.
(38) Linsley, K. B.; Chan, S.-Y.; Reinhold, B. B.; Lisi, P. J.; Reinhold, V. N. *Anal. Biochem.* 1994, *219*, 207–217.
(39) Dwek, R. A.; Edge, C. J.; Harvey, D. J.; Wormald, M. R.; Parekh, R. B. *Ann. Rev. Biochem.* 1993, *62*, 65–100.

suitable care has been taken to control the amount of salt in the digests (see below). The peptide portion of the molecule serves as a "derivative", which allows the conjugate to ionize and desorb efficiently, and it also shifts the region in which ions from the molecule are observed to higher mass, effectively eliminating potential problems with low-mass interferences such as the matrix used in MALDI-MS. Third, the exoglycosidase sequencing experiments may be carried out on simple mixtures of oligosaccharides attached to a common peptide backbone (Figures 7 and 8). Mixture analysis is possible whenever the resulting products of a given digest have masses different from other sample constituents. In contrast, conventional approaches for the analysis of either sequential or parallel exoglycosidase digests may only be reliably used to sequence pure oligosaccharides.[39,40] It is important to note that the MS techniques readily detected several minor glycoforms which were not discerned by either of the conventional techniques. This may be due to overlap of the chromatographic peaks of these carbohydrates with those of other carbohydrate constituents of the sample. Small peaks are often present in the chromatograms, particularly in the HPAE-PAD technique, which are due to degradation of the carbohydrate or which are non-carbohydrate in origin.[41,42] These peaks can also obscure minor carbohydrate components or make the analyst overlook them.

The validity of using exoglycosidases to provide detailed structural information hinges on the use of highly pure enzyme preparations that do not contain unacceptably high levels of contaminating glycosidases. Several sources of highly purified glycosidases are now available commercially, but it is well advised to be skeptical of the claimed specificities and lack of contamination. For example, we have confirmed the observation[35] that certain preparations of S. pneumoniae β-N-acetylhexosaminidase are contaminated with an endoglycosidase H-like enzyme. In an 8-h digest of the RSV glycopeptide with this enzyme at the higher E:S ratio, a strong peak is observed at m/z 1538 that corresponds to $(M + H)^+$ for the tryptic peptide with only one GlcNAc and one Fuc residue still attached, indicating that cleavage has occurred between the GlcNAc residues of the chitobiose unit (Figure 8c). In this case, the presence of the unexpected endoglycosidase H-like activity provided additional sequence information, placing the Fuc on the ultimate GlcNAc residue. The peak at m/z 1392 indicates a minor amount of the analogous des-Fuc glycopeptide. Similarly, digestion of the RSV glycopeptide with a chicken liver α-fucosidase advertised as specific for Fuc linked α-1-2,4,6 to GlcNAc removed a significant amount of the Gal in addition to Fuc following a 22-h digest (Figure 8d). Another problem with commercially available exoglycosidases is that they contain buffers such as sodium citrate/phosphate which at relatively high concentrations can cause problems in obtaining useful MALDI-MS signals due to signal suppression. Use of lower levels of enzyme than recommended by the supplier decreases the ratio of salt to analyte and frequently results in sufficient cleavage to provide diagnostically useful analytical data. Clearly, mass spectrometry is an exquisitely sensitive method for detecting aberrant glycosidase activity as long as that aberrant activity produces a species having a unique mass. When possible,

suitable model studies should be performed and the products analyzed by MS to confirm the cleanliness and specificities of the enzymes used. In the present study, the galactosidases and N-acetylhexosaminidases were checked using commercially available model glycopeptides whose structures have been corroborated by NMR or glycopeptides derived from well-characterized glycoproteins such as RNase B or fetuin.

The carbohydrates of IgG have been shown to have a role in the binding and activation by the antibody of complement, binding to macrophage Fc receptors, and antibody-dependent cellular cytotoxicity.[43] Abnormal glycosylation of IgG has also been associated with specific disease states such as rheumatoid arthritis.[44,45] The structures of the carbohydrates on recombinant glycoproteins vary depending upon the specific cell expression system and the culture conditions used. For these reasons, it is important to characterize the glycosylation of recombinant MAbs. The pool of carbohydrate structures identified in IgGs purified from human, rabbit, and bovine sera contain predominantly biantennary structures, with significant populations of species having core fucosylation, terminal sialic acid, and bisecting GlcNAc.[46] The carbohydrate structures determined here are most similar to the carbohydrate structures found in the mouse[47] in that they are highly fucosylated and do not contain bisecting GlcNAc. Sialic acid appears to be absent from the carbohydrates of RSHZ19 expressed in CHO cells. The absence of sialic acid is consistent with the structures of N-linked carbohydrate found in a MAb directed against the interleukin 2 receptor expressed in Sp2/0 cells[22] and in a humanized murine anti-CD18 MAb expressed in NS/O mouse myeloma cells.[48] Significant amounts of oligomannose structures were also reported in the NS/O mouse myeloma-derived MAb. Highly sialylated tri- and tetrantennary structures (some having two sialic acids on a single branch) were reported for the mouse MAb OKT3 isolated from hybridoma culture fluid.[49]

The analyses described here were all carried out using nanomole levels of glycoprotein. We and others have shown that detailed characterization of large glycoproteins by MS can be accomplished with picomole quantities of starting material.[21,25,31,50] The sensitivity in ESMS is more closely related to the sample concentration than mass flow into the mass spectrometer. Therefore, when only small amounts of sample are available (<100 pmol), it is necessary to use small internal diameter HPLC columns (≤1 mm), which operate at lower flow rates (≤40 μL/min), and small UV detector flow cells (≤1 μL). Lower flow rates put increased demands on the flow rate stability of the pumps,

(40) Kobata, A.; Yamashita, K.; Takasaki, S. Methods Enzymol. 1987, 138, 84–94.
(41) Lee, Y. C. Anal. Biochem. 1990, 189, 151–162.
(42) Hardy, M. R.; Townsend, R. R. Proc. Natl. Acad. Sci. U.S.A. 1988, 85, 3289–3293.
(43) Rademacher, T. W.; Parekh, R. B.; Dwek, R. A. Annu. Rev. Biochem. 1988, 57, 785–838.
(44) Parekh, R. B.; Dwek, R. A.; Sutton, B. J.; Fernandes, D. L.; Leung, A.; Stanworth, D.; Rademacher, T. W.; Mizuochi, T.; Taniguchi, T.; Matsuda, K.; Takeuchi, F.; Nagano, Y.; Miyamoto, T.; Kobata, A. Nature 1985, 316, 452–457.
(45) Kobata, A. Glycobiology 1990, 1, 5–8.
(46) Tandai, M.; Endo, T.; Sasaki, S.; Masuho, Y.; Kochibe, N.; Kobata, A. Arch. Biochem. Biophys. 1991, 291, 339–348.
(47) Mizuochi, T.; Hamako, J.; Titani, K. 1987, Arch. Biochem. Biophys. 257, 387–394.
(48) Yu Ip, C. C.; Miller, W. J.; Silberklang, M.; Mark, G. E.; Ellis, R. W.; Huang, L.; Glushka, J.; Van Halbeek, H.; Zhu, J.; Alhadeff, J. A. Arch. Biochem. Biophys. 1994, 308, 387–399.
(49) Krotkiewski, H.; Gronberg, G.; Krotkiewska, B.; Nilsson, B.; Svensson, S. J. Biol. Chem. 1990, 265, 20195–20201.
(50) Henzel, W. J.; Bourell, J. H.; Stults, J. T. Anal. Biochem. 1990, 187, 228.
(51) Della-Negra, S.; LeBeyec, Y. Anal. Chem. 1985, 57, 2035. Tang, X.; Ens, W.; Standing K. G.; Westmore J. B. Anal. Chem. 1988, 60, 1791. Spengler B.; Kirsch, D.; Kaufmann R. J. Phys. Chem. 1992, 96 , 9678.

and the ability of the mixer to mix mobile phases produces reproducible gradients. However, when recombinant MAb's (or other recombinant proteins) are characterized for regulatory purposes, it is generally unnecessary to use such small amounts of sample since they must be produced in quantities that are very large by MS standards. This is important because there are specific advantages to using larger amounts of sample for the LC/ESMS as well as many of the conventional analyses described. For example, standard internal diameter HPLC columns (2.1 or 4.6 mm) may be used rather than columns with internal diameters of 1 mm or less. The larger internal diameter columns are more robust, and it is easier to obtain reproducible, high-resolution separations on these columns using standard HPLC equipment. Furthermore, because there is no significant benefit in directing more than a small percentage of the column flow to the mass spectrometer for LC/MS, the majority of the sample may, simultaneous to the LC/MS experiment, be fraction collected for additional experiments such as tandem MS, infusion of selected fractions to obtain better ion statistics (important for glycopeptides), Edman degradation, carbohydrate analysis, etc., as required, based on the observed molecular species in each fraction. All of the LC/ESMS experiments described here were performed in this manner.

The ease with which the M_r of large glycoproteins may now be obtained by MS has provided a degree of mass measurement accuracy heretofore unavailable. However, the amount of structural information provided by such a measurement is still limited by the relatively poor capability to resolve variants of very large molecules that have slightly different masses than that of the parent protein. In both ESMS and MALDI-MS, the width of the unresolved parent molecular ion envelope of large, unmodified proteins is almost always greater than calculated on the basis of the natural abundance of the isotopes present and the resolution of the analyzer. This is due to significant gas phase adduction of alkali metals (e.g., Na), small molecules (e.g., NH_3), or the matrix used for the MALDI-MS experiment (e.g., sinapinic acid). These adducts are usually not resolved from the $(M + H)^+$ envelope, and their contribution causes an unpredictable shift upward in mass of the apparent centroid of the molecular ion cluster. The presence of actual heterogeneity in the protein structure only amplifies this effect. Analysis of the intact MAb provided no information regarding the heterogeneity due to carbohydrate, ragged termini, and deamidation. Analysis of the separated light and heavy chains was a significant improvement, permitting sequence variants of the light chain and some level of heterogeneity of the heavy-chain carbohydrate to be observed. However, neither the true extent of heterogeneity nor its origins could be ascertained with certainty until the protein was cleaved to peptides of mass spectrometrically manageable size where the accuracy and resolution permitted single dalton differences to be readily determined.

GLOSSARY

RSV	respiratory syncytial virus
MAb	monoclonal antibody
RSHZ19	a reshaped human MAb specific for the fusion (F) protein of RSV
LC/ESMS	liquid chromatography/electrospray mass spectrometry
MALDI-MS	matrix-assisted laser desorption/ionization mass spectrometry
PNGase F	peptide N-glycosidase F
RNase B	ribonuclease B
RCM	reduced and carboxymethylated
HPAE-PAD	high-performance anion exchange with pulsed amperometric detection
HPLC	high-performance liquid chromatography
TIC	total ion chromatogram
MS/MS	tandem mass spectrometry
HRGP	high-resolution gel permeation
<E and <Glu	pyroglutamic acid

Monitoring of IgG Antibody Thermal Stability by Micellar Electrokinetic Capillary Chromatography and Matrix-Assisted Laser Desorption/Ionization Mass Spectrometry

Anthony J. Alexander* and David Emlyn Hughes*

Bristol-Myers Squibb, Analytical Research & Development, Pharmaceutical Research Institute, P.O. Box 4755, Syracuse, New York 13221-4755

Monitoring the stability of immunoglobulin G (IgG) type antibodies is a crucial analytical issue spanning a wide variety of immunological/biotechnological studies, which includes the analysis of conjugated IgG's for drug delivery. Capillary electrophoresis (CE) has proven valuable for the analysis of proteins and has the potential to separate and detect native antibody components. An ideal complement to CE, which is capable of providing the desired detection specificity to provide species identification information, is matrix-assisted laser desorption/ionization mass spectrometry (MALDI-MS). Utilizing these two techniques we have developed an antibody examination procedure and monitored the degradation of an internalizing chimeric (human/mouse) monoclonal antibody (BR96). Electropherograms of the antibody after up to 166 h of thermal stress are presented; MALDI mass spectra of the stressed antibody were acquired at the same time points. At 166 h, the percentage of ionization carried by the intact antibody molecular ions M^-, M^{2-}, etc., had clearly decreased, while that due to additional ion species had significantly increased. Ions corresponding in mass to loss of one light chain, loss of an F_{ab} arm to yield an $F_{ab/c}$ type fragment, and formation of separated heavy-chain and light-chain moieties were observed. Several of these fragments result from simple disulfide linkage disruption. In addition, species less in mass than common antibody subunits were also observed, demonstrating peptide as well as disulfide bond cleavage. The observation that a small number of well-defined species were formed during the study suggests that the cleavage induced by thermal stress is very site-specific within the IgG.

The analytical examination of an immunoglobulin (IgG) antibody represents a substantial challenge. These large proteinaceous species consist principally of two larger heavy-chain strands covalently attached to two smaller light-chain strands by disulfide bonds, as depicted in Figure 1. The variable carbohydrate content is typically present only on the heavy chain.[1] Since IgG antibodies possess an average molecular mass of 150 000 Da and multiple forms varying only slightly in amino acid and carbohydrate content, examinations based on molecular weight

(MW) differences alone would not be expected to be useful. Liquid chromatographic separatory procedures, principally size exclusion, ion-exchange, affinity, hydrophobic interaction, and hydroxylapatite chromatography, have proven useful for antibodies.[2] Of these techniques, ion-exchange chromatography, is possibly the most selective procedure for large proteins, perhaps implying that charge-dependent separations show substantial promise. Capillary electrophoresis (CE), which separates species on the basis of molecular mass and net charge, has been used for analysis of peptides and a few proteins such as adrenocorticotropin, transferrin, ribonuclease, insulin, and growth hormone.[2,3]

CE peptide separation studies have principally involved synthetic (or known) species[4,5] and peptides resulting from protein digestion. CE tryptic mapping procedures are available for human recombinant insulin-like growth factor I (rhIgG-I),[6] myoglobin,[7] hemoglobins,[8] α-1-acid glycoprotein, and human growth hormone (hGH).[9,10] Comparisons of enzymatic digestion protocols have previously been performed,[11] as well as alternative forms of detection.[12] Comparison of the selectivity of CE peptide separations with the more established liquid chromatographic techniques has generally supported the primary or complimentary use of the CE technique.[4,7,8,13]

Large proteins, glycoproteins, and metal-associated proteins require particularly selective techniques of analysis to represent the multiple, closely related forms present in actual samples. Importantly, protein studies performed by CE have been shown to be able to separate the major species arising from degradative deamidation and amino acid and glycan microheterogeneity.[14] Whereas peptide CE separations have often been adequately

(2) Guttman, A.; Paulus, A.; Cohen, A. S.; Karger, B. L.; Rodriques, H.; Hancock, W. S. In *Electrophoresis 88*; VCH Publishers: New York, 1988; pp 151–160.

(3) Grossman, P. D.; Colburn, J. C.; Lauer, H. H.; Nielson, R. G.; Riggin, R. M.; Sittampalam, G. S.; Rickard, E. C. *Anal. Chem.* 1989, *61*, 1186.

(4) Zhang, Y. K.; Chen, N.; Wang, L. *Biomed. Chromatogr.* 1993, *7* (2), 75–77.

(5) Gaus, H. J.; Beck-Sickinger, A. G.; Bayer, E. *Anal. Chem.* 1993, *65*, 1399–1405.

(6) Hilser, V. J.; Worosila, G. D.; Rudnick, S. E. *J. Chromatogr.* 1993, *630*, 329–336.

(7) Cassiano, L.; Rabine, R.; Rossetti, D. V.; Bassi, F. A. *J. Chromatogr.* 1991, *572*, 51–58.

(8) Ross, G. A.; Lorkin, P.; Perrett, D. J. *Chromatogr.* 1993, *636*, 69–79.

(9) Nashabeh, W.; el Rassi, Z. *J. Chromatogr.* 1991, *536*, 31.

(10) Nielsen, R. G.; Rickard, E. C. *J. Chromatogr.* 1990, *516*, 99.

(11) Cobb, K. A.; Novotny, M. V. *Anal. Chem.* 1992, *64*, 879.

(12) Lee, T. T.; Lillard, S. J.; Yeung, E. S. *Electrophoresis* 1993, *14*, 429.

(13) Sutcliffe, N.; Corran, P. H. *J. Chromatogr.* 1993, *636*, 95.

(14) Compton, B. J.; O'Grady, E. A. *Anal. Chem.* 1991, *63*, 2597.

(1) Gooding, K. M.; Regnier, F. E. In *HPLC of Biological Macromolecules*; Marcel Dekker: New York, 1990; pp 487–528.
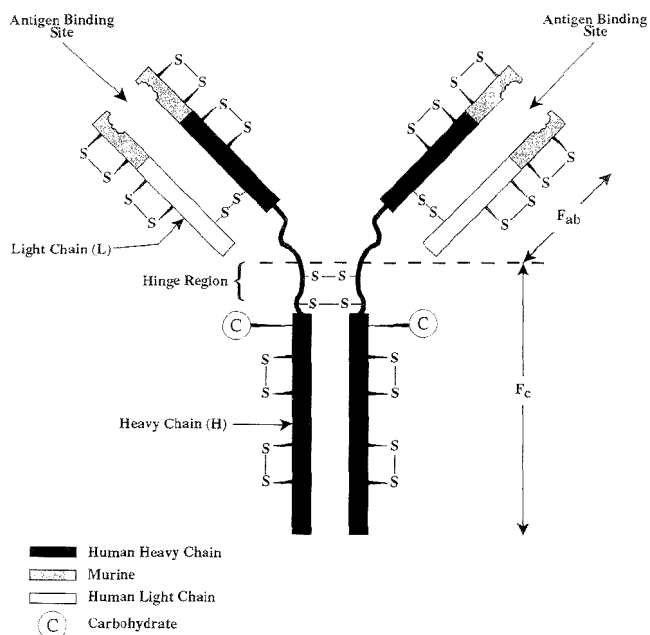
Figure 1. Schematic representation of chimeric BR96 (human/mouse) monoclonal antibody.

described by simple charge and mass electrophoretic models[15] (although the exponent of the mass in the defining equation is not firmly established), proteins require a more complex separation model. Even in peptide separations, the importance of hydrophobicity and conformation has been observed.[5] Specificity related to conformation presumed to occur due to different hydrodynamic profiles for different conformers has been observed in protein studies. The unfolding of human serum transferrin has been studied by CE and found to be dependant on iron content, but independent of carbohydrate content.[16] Similarly, free solution CE has been used to monitor the temperature-dependent unfolding of lysozyme[17] at low pH.

Although CE studies on antibodies are not abundant, one combined theoretical and empirical study[18] demonstrated that a single amino acid difference in a chimeric IgG antibody form was detectable. In a second study, a micellar CE procedure was developed that was capable of separating IgG monoclonal antibody, alkaline phosphatase (MW 140 000), and an alkaline phosphatase—IgG conjugate.[19] Micellar CE procedures have also been developed for the analysis of recombinant proteins in fermentation broth[7] and a chimeric monoclonal antibody—cytotoxin conjugate.[20]

Matrix-assisted laser desorption/ionization mass spectrometry (MALDI-MS) generates molecular ions of predominantly low charge state (MH^{n+} with $n = 1-4$), which are generally detected

with a mass accuracy of ±0.1%, or better, using a time-of-flight (TOF) mass analyzer.[21] The technique is extremely sensitive, requiring low picomole to subpicomole amounts of material, and has a mass range in excess of 200 000 Da. It is also particularly well suited to the analysis of large biomolecules, as it is relatively insensitive to the presence of buffering agents, salts, and denaturants, which are often essential to maintain sample stability.[22] A significant exception to this is the influence of sodium dodecyl sulfate (SDS), which causes spectral degradation at levels as low as 0.01%,[22] which is unfortunate, as this detergent is used extensively in CE separations. For this reason, no attempt was made in this study to directly peak collect and analyze the CE fractions by MALDI-MS. Several off-line CE/MALDI-MS studies have been reported in the literature;[23-25] however, these have predominantly addressed the separation and detection of peptides and small proteins (<~30 kDa). As far as we are aware, extension of this methodology to antibodies has yet to be demonstrated. Relatively few studies involving the application of MALDI-MS to the characterization of intact IgG's have been reported. Siegel et al.[26] showed it to be a particularly elegant method for determining

(15) Wu, S. L.; Teshima, G.; Cacia, J.; Hancock, W. S. *J. Chromatogr.* **1991**, *559*, 357.

(16) Kilar, F.; Hjerten, S. *J. Chromatogr.* **1993**, *638*, 269.

(17) Hilser, V. J.; Worosila, G. D.; Freire, E. *Anal. Biochem.* **1993**, *208*, 125.

(18) Compton, B. J. *J. Chromatogr.* **1991**, *559*, 357.

(19) Harrington, S. J.; Varro, R.; Li, T. M. *J. Chromatogr.* **1991**, *559*, 385.

(20) Hughes, D. E.; Richberg, P. *J. Chromatogr.* **1993**, *635*, 313.

(21) Hillenkamp, F.; Karas, M.; Beavis, R. C.; Chait, B. T. *Anal. Chem.* **1991**, *63*, 1193A–1203A.

(22) Mock, K. K.; Sutton, C. W.; Cottrell, J. S. *Rapid Commun. Mass Spectrom.* **1992**, *6*, 233–238.

(23) Keough, T.; Takigiku, R.; Lacey, M. P.; Purdon, M. *Anal. Chem.* **1992**, *64*, 1594–1600.

(24) Van Veelen, P. A.; Tjaden, U. R.; Van der Greef, J.; Ingendoh, A.; Hillenkamp, F. *J. Chromatogr.* **1993**, *647*, 367–374.

(25) Castoro, J. A.; Chiu, R. W.; Monnig, C. A.; Wilkins, C. L. *J. Am. Chem. Soc.* **1992**, *114*, 7571–7572.

(26) Siegel, M. M.; Hollander, I. J.; Hamann, P. R.; James J. P.; Hinman, I.; Smith B. J.; Farnsworth, A. P. H.; Phipps, A.; King D. J.; Karas, M.; Ingendoh, A.; Hillenkamp, F. *Anal. Chem.* **1991**, *63*, 2470–2481.

the carbohydrate and drug content of a range of conjugated monoclonal IgG's. Other, more recent studies have concentrated on developing comprehensive strategies, of which MALDI-MS molecular weight determination on the intact antibody and subunits is an integral part, for the characterization of monoclonal IgG's of therapeutic interest.[27,28] To date, however, we have not located any papers in which this technique has been applied to the analysis of degraded antibodies.
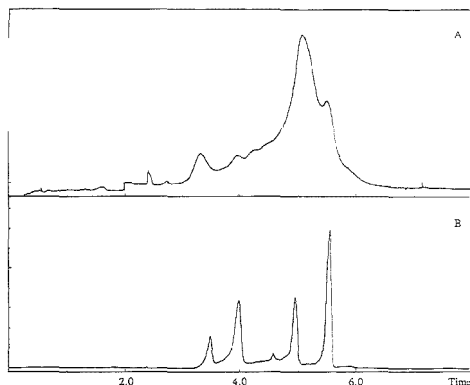
Utilizing MALDI-MS in conjunction with CE , we have developed a general antibody examination procedure and monitored the heat degradation of an internalizing chimeric (human/mouse) monoclonal IgG. A preliminary report of part of this work was presented previously.[29]

EXPERIMENTAL SECTION

Material and Reagents. All reagents were analytical grade. Sodium citrate, sodium chloride, and sodium borate were obtained from Fisher Scientific. Sodium dodecyl sulfate was electrophoresis grade from Sigma Chemical Co. and sinapinic acid was purchased from Aldrich Chemical Co. Polyclonal antibodies (horse, mouse, dog, goat, bovine, rat, sheep, rabbit, cat, pig, chicken, guinea pig) were obtained from Sigma Chemical Co. while monoclonals were obtained from Calbiochem (La Jolla, CA) except for chimeric BR96, which was manufactured by Bristol-Myers Squibb Co.

CE Instrumentation. The CE separation was performed using a Beckman P/ACE system with a 50 cm × 75 μm i.d. uncoated fused-silica capillary. The mobile phase was 12 mM sodium borate buffered to pH 9.4 containing 25 mM SDS. After pressure injection, the separation was performed at 30 kV for 8 min at 25 °C and monitored at 214 nm. Lyophilized samples were diluted with water to a concentration of 1 mg/mL prior to injection. Neutral species were determined to migrate at 2.3 min.

Mass Spectrometry Instrumentation. MALDI mass spectra were obtained using a Bruker Instruments Reflex TOF mass spectrometer, equipped with a nitrogen laser (337 nm). Spectra were obtained using an ion extraction voltage of 30 kV and a transient recorder time resolution of 10 ns. The detector response from low-mass matrix ions was minimized by the application of a 5 μs deflection pulse. The onset for ion attenuation from this pulse extends to ~7000 Da. Spectra were externally calibrated using the singly and doubly charged ions from bovine albumin dimer (MW 133 048[30]). Samples containing ~1–10 mg/mL protein were typically diluted 10:1 or 20:1 with an aqueous saturated solution of sinapinic acid (SA) containing 25–33% acetonitrile. A 1.0 μL sample of this mixture was deposited on a stainless steel sample stage and allowed to air-dry. Both the in-house and commercial monoclonal IgG samples used in this study contained either 15 mM phosphate or 25 mM citrate stabilizing buffers. These buffers were *not* removed prior to analysis. Polyclonal IgG samples were dissolved in water to a concentration of 1 mg/mL. The spectra shown were obtained using the linear detector and represent the summation of 20 consecutive laser shots. A nine-

(27) Ashton, D. S.; Beddell, R. C.; Cooper, D. J.; Craig, S. J.; Lines, A. C.; Oliver, R. W. A.; Smith. M. A. *Anal. Chem.* **1995**, *67*, 835–842.

(28) Johnston, W. P.; Roberts, G. D.; Burman, S.; Carr, S. A. *Proceedings of the 42st ASMS Conference on Mass Spectrometry and Allied Topics*, Chicago, IL, May 29–June 3, 1994; ASMS: East Lansing, MI, 1994; p 669.

(29) Alexander, A. J.; Hughes, D. E. *Proceedings of the 41st ASMS Conference on Mass Spectrometry and Allied Topics*, San Francisco, CA, May 30–June 4, 1993; ASMS: East Lansing, MI. 1993; pp 420a–420b.

(30) Blackledge, J. A.; Alexander, A. J. *Anal. Chem.* **1995**, *67*, 843–848.

Figure 2. Typical electropherograms obtained from the CE analysis of polyclonal guinea pig IgG (A) and monoclonal anti-(human-α-1-antitrypsin) murine IgG (B).

point smoothing function was applied to the raw data prior to plotting.

IgG Degradation Conditions. A chimeric (human/mouse) monoclonal antibody at a concentration of 10 mg/mL in a 25 mM sodium citrate/250 mM sodium chloride aqueous buffer at pH 8.5 was heat-stressed at 60 °C for a period of 166 h. At discrete time points, sample aliquots were removed and analyzed by CE and MALDI-MS. In each case, the aliquoted material was diluted 20-fold with matrix solution prior to analysis by MALDI-MS. The commercially available monoclonal and polyclonal IgG's were used without further purification or exchange of buffers and diluted in a manner similar to the chimeric antibody.

RESULTS AND DISCUSSION

The experimental procedure was applied to the analysis of 16 polyclonal and monoclonal antibodies. All of the antibodies were able to be examined without modifying the CE conditions. One typical monoclonal and a polyclonal antibody are analyzed by both CE and MALDI-MS in the next two sections. Attention is then turned to the chimeric (human/mouse) monoclonal IgG BR96 and the four conformation peaks identified; the antibody is thermally degraded and the identity of the resulting peaks in the electropherogram inferred by MALDI-MS.

Capillary CE Separations of Monoclonal and Polyclonal Antibodies. Figure 2 presents typical electropherograms obtained from the CE analysis of polyclonal guinea pig IgG and monoclonal anti-(human-α-1-antitrypsin) murine IgG. Both electropherograms are complex. The monoclonal IgG exhibits at least four well-resolved peaks with a main peak efficiency of ~40 000 theoretical plates/m. On the basis of protein unfolding studies performed on the BR96 antibody (see below) and a common molecular weight, these species are postulated to be protein conformers. Polyclonal guinea pig IgG is characterized by several poorly resolved peaks with a main peak efficiency of ~500 theoretical plates/m. One of these peaks is of particular interest in that it is relatively intense and also appears at the characteristic migration time of separated light chain (~5.7 min). The electropherograms are consistent with the expected presence of a family of related IgG molecules in the case of the polyclonal and distinct species in the case of the monoclonal antibodies.

Figure 3. MALDI mass spectra of polyclonal guinea pig IgG (upper spectrum) and monoclonal anti-(human-α-1-antitrypsin) murine IgG (lower spectrum). In each case, 3.5 pmol of the antibody was loaded on the probe tip. Matrix, sinapinic acid.

MALDI Mass Spectra of Monoclonal and Polyclonal Antibodies. Figure 3 illustrates the MALDI mass spectra obtained from the above samples and are typical of spectra obtained from a range of polyclonal and monoclonal antibodies, respectively. Each spectrum was obtained under identical conditions from 3.5 pmol of material loaded on the probe tip. In addition to the charged molecular ions M^+, M^{2+}, M^{3+}, M^{4+}, and $2M^{3+}$, typically present in MALDI mass spectra of monoclonal antibodies,[26,27] there are other significant, but less abundant ions, present in the mass spectrum. Of these, ions corresponding in mass to loss of one light chain, $(M - LC)^+$, $(M - LC)^{2+}$, and the separated light chain $(LC)^-$ are clearly discernable. As IgG molecules are constructed from LC and HC subunits that differ in molecular weight by a factor of ~2, the possibility exists that ion signals resulting from multiple charging of the intact antibody (M^{2+}, M^{3+}, etc.) could also arise from singly charged fragments generated by disulfide bond cleavages. Such species would not be distinguishable due to the relatively low resolution of the MALDI-TOF experiment ($M/\Delta M < 1000$). For example, a fragment corresponding to $(LC + HC)^+$, i.e., half the molecule, would have an m/z value very similar (within 50 Da) to that of the doubly charged intact molecule (M^{2+}). This ambiguity can generally be resolved by examination of the peak widths of the ion signals, since these will decrease proportionally with increasing charge for multiply charged ions. Peak widths for M^{2+}, M^{3+}, and M^{4+} ions will be $^1/_2$, $^1/_3$, and $^1/_4$, respectively, of the peak width for the M^+ ion signal. This is clearly evident in the spectra of monoclonal IgG's (Figure 3, lower spectrum), although it can be less discernable

in the case of polyclonal species (Figure 3, upper trace) due to the greater asymmetry of the ion signals.

In the spectra of polyclonal species, the LC^+ signal was found to vary widely in intensity compared to that observed for most monoclonal IgG's. In many samples studied by both CE and MALDI, the presence of the LC species in the sample solution has been inferred from the CE chromatogram, although it cannot be ruled out that there might be some contribution to the LC^- ion intensity from MALDI-induced dissociation of the disulfide-linked antibody. The presence of an ion corresponding to separated LC was observed previously in the MALDI mass spectra of monoclonal antibodies, even when no LC was observed in the samples by traditional bioanalytical methods.[26] Monoclonal anti-(human-α1-antitrypsin) murine IgG, has been previously examined by electrospray ionization after removal of the stabilizing buffer.[31] Using 242 pmol of sample, a molecular mass of $148\,484 \pm 4$ Da was established.

In general, the MALDI ion signals from the polyclonal species are wider and more asymmetric than those obtained from monoclonal IgG antibodies. This is consistent with the increased microheterogeneity of the polyclonal sample. For the majority of polyclonal samples studied, the signal/noise was a factor of 5–10 times less than that obtained for monoclonal species using the same experimental conditions.

Thermally Induced Chaotropic Unfolding of the BR96 Antibody. BR96 antibody in solution is represented in the CE

(31) Feng, R.; Konishi, Y. Anal. Chem. 1992, 64, 2090–2095.
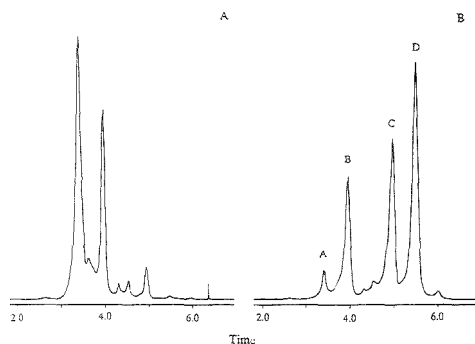
Figure 4. Thermally induced unfolding of the chimeric BR96 antibody in the presence of the chaotropic agent sodium dodecyl sulfate: (A) CE separation at initial conditions; (B) CE separation after 2 min at 80 °C.

electropherogram by multiple peaks (See Figure 4A). To determine which peaks simply represent conformational forms of the antibody (and not, for example, impurities), a sample solution containing the chaotropic agent SDS at a concentration of 12 mM was heated for 2 min at 40, 60, and 80 °C. The critical micellar concentration for SDS is 8 mM. The antibody progressively distributed itself into species with longer migration times as the temperature was increased; the highest temperature (80 °C for 2 min) is represented in Figure 4B. The conclusion is that the SDS/thermally induced IgG unfolding allowed greater antibody/SDS interaction, resulting in a larger net negative charge on the unfolded conformer and hence longer migration times during cathodic electrolysis. The peaks identified as A–D are hence assumed to be conformational isomers of intact antibody. Although this could not be directly confirmed by MALDI-MS due to the presence of SDS, this assumption is supported by the fact that only one molecular species, of mass 149 671 ±127 Da (n = 4, average determined from M^+ and M^{2+} ion signals), was observed for chimeric BR96 IgG in the absence of SDS. This value is also in good agreement (−145 Da, 0.10%) with that calculated for the glycosylated antibody derived from the theoretical mass of the cDNA sequence plus the experimentally derived N-linked carbohydrate mass (data not shown).

Heat Degradation of a Chimeric (Mouse/Human) Monoclonal IgG and Parallel Examination of Products by CE and MALDI-MS. Electropherograms of the undegraded IgG and the antibody after 47, 94, and 166 h of thermal stress are shown in Figure 5. As illustrated, the unstressed antibody is represented by four major peaks (peaks A–D, assumed to be conformers) and a relatively low level of antibody-related species. Note that the electropherograms for chimeric BR96 in Figures 4A and 5 (t = 0) are dissimilar despite the identical separatory conditions. The difference is due to the initial conditions to which the IgG was subjected. In Figure 4A, the dissolution buffer was 25 mM sodium citrate/250 mM sodium chloride, pH 5.5, in the presence of SDS. In Figure 5 (t = 0), the dissolution buffer was 25 mM sodium citrate/250 mM sodium chloride, pH 8.5 (to promote the ensuing thermal degradation). The distribution of conformers A–D and the presence or absence of minor species is therefore not identical for the two samples, with perhaps the most striking difference the preference at pH 8.5 for conformers C and D. As
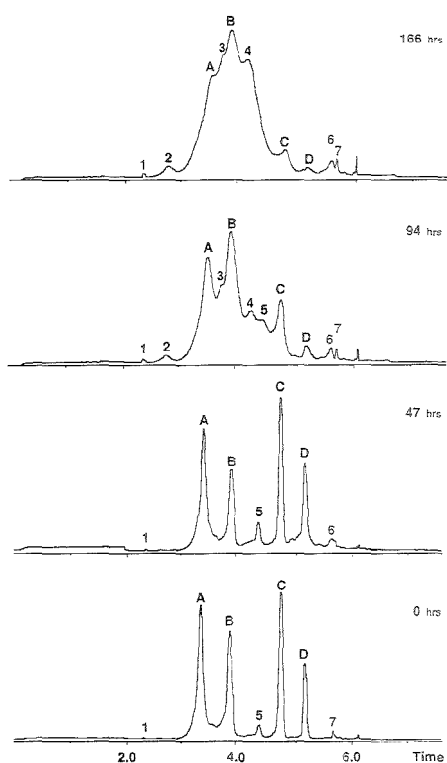
Figure 5. CE electropherograms of heat-degraded chimeric BR96 monoclonal antibody after 0, 47, 94, and 166 h of thermal stress at 60 °C.

Table 1[a]

electrophoretic peak no.	mass assigned (Da)	structural assignment
1	not obsd	multimer aggregate
2	not obsd	multimer aggregate
3	not obsd	noncovalent dimer[d]
4	101 850	IgG − F_{ab} type fragment[c]
5	125 540	IgG − one light chain[d]
6	50 980	IgG heavy chain
7	24 070	IgG light chain

[a] Note: Under the CE conditions employed, early migrating species have been shown to be of higher molecular weight; hence peaks 1 and 2 would be expected to be due to aggregated species. No ions corresponding to these species were observed, or would be expected, using MALDI, as these species are generally not covalently linked and thus do not survive the ionization process (see text for further discussion). [b] Deduced from size exclusion measurements (data not shown). [c] Tentative assignment only—within mass measurement accuracy other possibilities exist—such as loss of both light chains. [d] Tentative assignment only—within mass measurement accuracy other possibilities exist,— such as loss of an N-terminus fragment from a heavy chain.

degradation proceeds, peaks 2, 4, 6, and 7 are formed. Peaks 1, 3, and 5 also increase in height.

Figure 6 illustrates the MALDI mass spectra of the heat-stressed antibody at the same (0–166 h) time points. The initial spectrum (t = 0) was obtained from 3.3 pmol of IgG loaded on
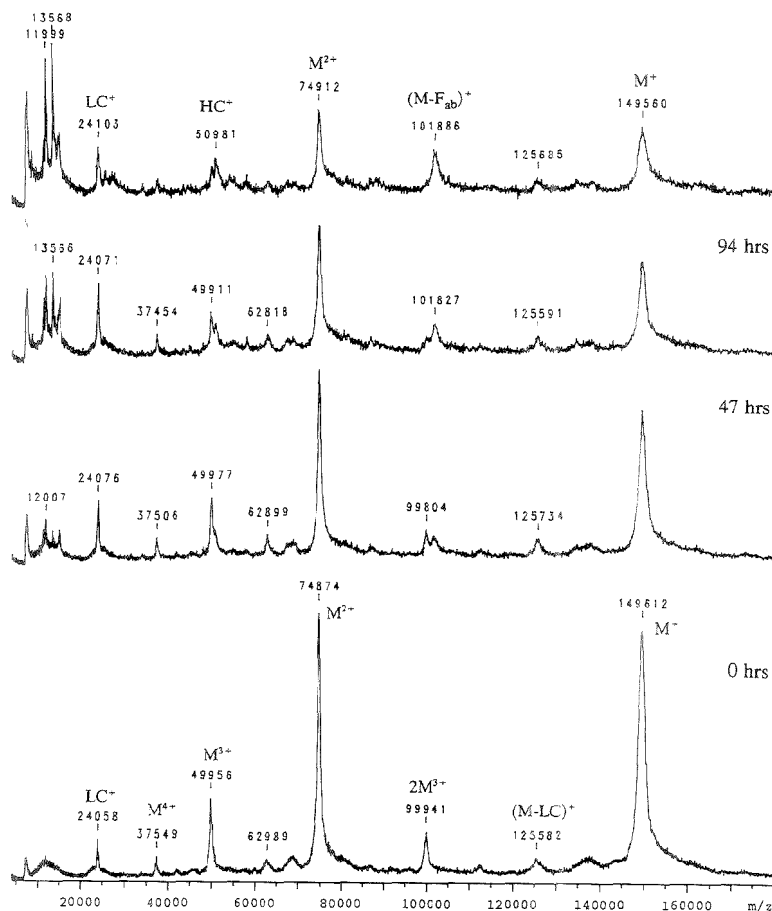
Figure 6. MALDI mass spectra of heat-degraded chimeric BR96 monoclonal antibody obtained from the samples shown at the same time points in Figure 5. The initial spectrum ($t = 0$) was obtained from 3.3 pmol of IgG loaded on the probe tip. Matrix, sinapinic acid.

the probe tip; subsequent spectra were obtained with progressively less intact IgG as the degradation progressed. Comparing the 0 and 166 h data, the percentage of ionization carried by the molecular ions M^+, M^{2+}, M^{3+}, and M^{4+} has clearly decreased while that due to additional ion species, particularly below m/z 16 000, has significantly increased. On closer examination of the plots, several ion signals at m/z 125 600, 101 800, 50 900, and 24 070 progressively increase with time. This is illustrated graphically in Figure 7. These ions correspond in mass to loss of one light chain from the antibody $(M - LC)^+$, loss of an F_{ab} arm to yield an $F_{ab/c}$ type fragment $(M - F_{ab})^-$, and formation of separated heavy-chain (HC^+) and light-chain (LC^+) moieties, respectively. Although the terms F_{ab} and F_c refer to IgG fragments specifically generated by papain cleavage of both heavy chains at specific sites in the hinge region (as illustrated in Figure 1), they are used here in the generic sense, without reference to the exact sites of cleavage. An $F_{ab/c}$ type fragment, formed after loss of one F_{ab}

arm, would therefore consist of the second F_{ab} arm, plus the remaining F_c portion of the IgG. The above types of fragments have been previously identified in monoclonal antibody degradation studies, although the authors note that such degradation processes are antibody dependent.[32,33] By comparison of the MALDI-MS and CE data at the respective time points, and since the CE migration rates have been shown for this system to increase with decreasing fragment mass, tentative mass assignments have been made for some of the CE peaks. These are presented in Table 1. Within the accuracy of the mass measurement, and considering the multitude of possible degradative pathways available, these structural assignments are only tentative. However, despite this limitation, it is clear that MALDI-MS

(32) Jiskoot, W.; Beuvery, E. C.; de Koning, Ada A. M.; Herron, J. N.; Crommelin, D. J. A. *Pharm. Res.* **1990**, *7*, 1234–1241.
(33) Roa, P. E.; Kroon, D. J. In *Stability of Protein Pharmaceutical Case Histories*; Wang, J., Born, M. P., Eds.; Plenum: New York, 1992.
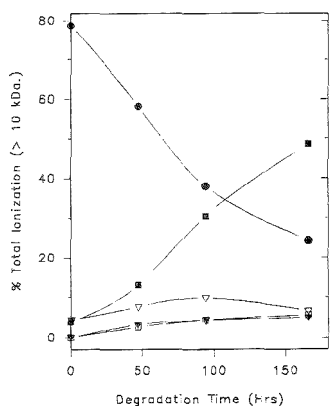
Figure 7. Plot of selected ion intensities from Figure 6, as a percentage of total IgG ionization (sum of ion intensities >10 kDa) versus IgG degradation time: (●) sum of molecular ion intensities M^{n+} for $n = 1-3$; (■) sum of fragment ions in mass range 10 000–20 000 Da; (△) LC fragment ion intensity; (▲) HC fragment ion intensity; (□) $(M - F_{ab})^+$ type fragment ion intensity.

provides a very useful "fingerprint" for assessing degradative change in such studies.

The increasing solution phase aggregation, typical of stressed antibodies[34] and apparent by CE (peaks 1–3, Figure 5), was not observed by MALDI-MS. This is not apparent from Figure 6 as the spectra are shown truncated at ~180 000 Da for the sake of clarity, however, data were acquired to >400 000 Da. This observation is consistent with the majority of the dimer (peak 3) and higher order aggregates (peaks 1 and 2) being present as noncovalently linked species. In our experience, such species are not detected by MALDI-MS, whereas covalently bound antibody-type molecules generally survive the desorption/ionization process and are detected predominantly as intact molecular ions, in both linear and reflectron modes of operation (data not shown). Thus, the low-intensity ions at about 99 000 ($2M^{3+}$), 222 750 ($3M^{2+}$), and 297 000 Da ($2M^+$) observed in Figure 3B and in other published MALDI-MS spectra of antibodies[26] presumably arise from gas phase reactions in the relative high pressure "plume" of material desorbed by the laser pulse.

It is also interesting to note that the same degradation species are present after 166 h; that is, no significant new peaks were observed in the CE electropherogram or the MALDI mass spectrum at masses greater than the pulser cutoff mass (~7000 Da). This suggests that the cleavage induced by thermal stress is very site-specific within the antibody. Also, the intensities of the species at m/z 15 202, 13 568, and 11 999 correlate with increasing hours of thermal stress (see Figure 7). These species are all significantly less in mass than any of the common antibody

(34) Paborji, M.; Pochopin, N. L.; Coppola, W. P.; Bogardus, J. B. *Pharm. Res.* 1994, *11*, 764–71.

subunits (light and heavy chains) and thus must result from cleavage of peptide bonds rather than just disulfide linkages.

Electropherograms of monoclonal antibodies were invariably characterized by a set of relatively well-resolved peaks (see Figures 2 and 5), whereas polyclonal antibody electropherograms, apparently due to extensive microheterogeneity, were invariably similar to the guinea pig IgG shown in Figure 2. The migration times for all antibodies studied and their degradation products were within 8 min, allowing the CE procedure to be generally useful for IgG analysis. Due to the extensive microheterogeneity of the polyclonal antibodies, degradation into fragments was less dramatic than with monoclonal antibodies since the polyclonal-related species formed were often not well resolved from the intact IgG. Hence, with both polyclonal and monoclonal species, comparison with the intact (undegraded) IgG is strongly recommended to estimate the state of degradation of a given sample.

CONCLUSIONS

A generally applicable analytical protocol for CE and MALDI-MS has been developed to examine both polyclonal and monoclonal IgG antibodies. Sixteen antibodies have been successfully examined by the combined procedure. The thermal stability of one of the monoclonal antibodies (chimeric BR96) was then studied in detail. In comparison to traditional electrophoretic and liquid chromatographic methods of analysis, CE provides the very selective separation of antibody-related chains and fragments required for the examination of degraded samples. MALDI-MS provides a complimentary "fingerprint" or impurity profile of an antibody from which it is possible to assess the degree of degradation and gain specific molecular weight information on the resulting species formed.

In the case of chimeric BR96 IgG, heat degradation at 60 °C for a period of 166 h produced only a few well-defined fragments. Despite the size and complexity of the antibody, the bonds cleaved by thermal stress are apparently very site-specific within the molecule.

Electrochemical Detection of Exocytosis at Single Rat Melanotrophs

Charina D. Paras and Robert T. Kennedy*

Department of Chemistry, P.O. Box 117200, University of Florida, Gainesville, Florida 32611-7200

Amperometry at a carbon fiber microelectrode was used to monitor secretion of peptide hormone from single melanotrophs of the intermediate lobe of the rat pituitary. The method is based on electrochemical oxidation of tryptophan and tyrosine residues of small proopiocortin-derived peptides secreted from these cells. For single-cell measurements, the electrode, which had a sensing diameter of ~9 μm and a total tip diameter of 30 μm, was positioned ~1 μm away from single melanotrophs. When cells were stimulated by application of 64 mM K$^+$, a series of randomly occurring current spikes with an average area of 34 ± 6 fC was observed. The current spikes were strongly dependent on the presence of Ca^{2+}. Current spikes of nearly identical area and shape were also elicited by mechanical stimulation. Cyclic voltammograms obtained from cell releasates confirmed that the substance detected was a tryptophan- or tyrosine-containing peptide. On the basis of amperometric tests of the most abundant peptides in melanotrophs, it is concluded that the current spikes are due to detection of primarily α-melanocyte stimulating hormone. The spike area corresponds to 0.32 amol of α-melanocyte stimulating hormone. It is concluded that the current spikes represent detection of concentration pulses that are expected following exocytosis events.

Peptide hormones secreted from pituitary cells control a wide variety of biological functions. In addition, these cells serve as useful models for the study of neurons. An understanding the regulation and mechanism of secretion of these peptides is therefore of considerable interest. A significant limitation in the study of pituitary cells has been the lack of methods to monitor peptide release on the same time scale that cells regulate secretion. For example, although it is generally agreed that pituitary cells release peptide by exocytosis, the direct measurement of peptide secretion with the temporal and spatial resolution to detect single exocytosis events has not been accomplished. The most commonly used method for monitoring secretion is to assay fractions collected from perfusion of large collections of cells.[1-5] This method provides temporal resolution on the minute time scale and is not compatible with single cells. Cell capacitance measurements have allowed secretory activity at single cells to be measured; however, for pituitary cells the sensitivity has not been sufficient to detect single exocytosis events.[6]

Several recent reports have focused on the use of microelectrodes for detection of exocytosis at single cells.[7-12] In this technique, an electrode, typically a carbon fiber microelectrode of about the same size as the cell, is positioned adjacent to a single cell. Substances secreted from the cell are detected after they diffuse the short distance between the cell and electrode. Exocytosis of epinephrine and norepinephrine from adrenal cells,[7,8] dopamine from PC12 cells,[10] serotonin from mast cells,[11] and insulin from pancreatic β-cells[12] has been detected using electrochemical methods. Both amperometry and voltammetry have been used for detection. For both methods, high temporal resolution and mass sensitivity results from the close proximity of the cell and electrode and the fast response time of the electrodes. When used to measure exocytotic release, stimulation of a cell results in a series of current spikes observed at the electrode. It has been demonstrated that the current spikes correspond to direct detection of multimolecular packets released from vesicles. In many cases, it is found that isolated current spikes correspond to single exocytosis events.

In this report, we describe the extension of this technique to monitoring α-melanocyte stimulating hormone (α-MSH) and related peptides secreted from single melanotrophs of the pars intermedia of the rat pituitary gland. We have found that current spikes are obtained at carbon fiber microelectrodes following stimulation of melanotrophs which correspond to detection of concentration pulses resulting from exocytosis. The observations are the highest resolution yet obtained for detection of α-MSH secretion and demonstrate the first direct detection of peptide secreted from pituitary cells at the level of single exocytosis events. Since the exocytosed material is detected directly, this method should allow the kinetics of release separate from the kinetics of pore openings and endocytosis to be studied. Thus, the method provides information complementary to the cell capacitance method of monitoring secretion in these cells.

(1) Munemura, M.; Eskay, R. L.; Kebabian, J. W. *Endocrinology* 1980, *106*, 1795.
(2) Tsuruta, K.; Grewe, C. W.; Cote, T. E.; Eskay, R. L.; Kebabian, J. W. *Endocrinology* 1982, *110*, 1133.
(3) Jackson, S.; Lowry, P. J. *Neuroendocrinology* 1983, *37*, 248.
(4) Raymond, V.; Lepine, J.; Giguere, V.; Lissitzky, J.-C.; Cote, J.; Labrie, F. *Mol. Cell. Endocrinol.* 1981, *22*, 295.
(5) Kongsamut, S.; Shibuya, I.; Uehara, M.; Douglas, W. W. *Endocrinology* 1993, *133*, 336.

(6) Thomas, P.; Surprenant, A.; Almers, W. *Neuron* 1990, *5*, 723.
(7) Leszczyszyn, D. J.; Jankowski, J. A.; Viveros, O. H.; Diliberto, E. J.; Near, J. A.; Wightman, R. M. *J. Biol. Chem.* 1990, *265*, 14736.
(8) Wightman, R. M.; Jankowski, J. A.; Kennedy, R. T.; Kawagoe, K. T.; Schroeder, T. J.; Leszczyszyn, D. J.; Near, J. A.; Diliberto, E. J.; Viveros, O. H. *Proc. Natl. Acad. Sci. U.S.A.* 1991, *88*, 10754.
(9) Chow, R. H.; von Ruden, L.; Neher, E. *Nature* 1991, *356*, 60.
(10) Chen, T. K.; Luo, G.; Ewing, A. G. *Anal. Chem.* 1994, *66*, 3031.
(11) Alvarez de Toledo, G.; Fernandez-Chacon, R.; Fernandez, J. M. *Nature* 1993, *363*, 554.
(12) Kennedy, R. T.; Huang, L.; Atkinson, M. A.; Dush, P. *Anal. Chem.* 1993, *65*, 1882.

EXPERIMENTAL SECTION

Cell Isolation and Culture. Melanotrophs were isolated and dispersed using a procedure similar to that described elsewhere.[6] Pituitaries were obtained from three adult male Sprague-Dawley rats weighing 200–300 g. The pituitaries were washed with a Ca^{2+}-free balanced salt solution (137 mM NaCl, 5 mM KCl, 0.7 mM Na_2HPO_4, 25 mM HEPES, 10 mM glucose, adjusted to pH 7.25). The neurointermediate (NI) lobe was separated from the anterior lobe under a dissecting microscope. The isolated NI lobes were rinsed twice with the Ca^{2+}-free balanced salt solution and then transferred into a sterilized centrifuge tube with a siliconized Pasteur pipet. The tissues were digested in 0.5 mL of collagenase (2 mg/mL in Ca^{2+}-free balanced salt solution) at 37 °C for 30 min. They were then digested in 0.5 mL of trypsin (0.5 mg/mL in Ca^{2+}-free balanced salt solution) at 37 °C for 15 min. During digests the cells were triturated three times using a fire-polished, siliconized Pasteur pipet. After each digest, the cells were centrifuged at 550g for 4 min at room temperature. After dispersion, the cells were washed with Dulbecco's modified Eagle's medium (DMEM; GIBCO Catalog No. 11885) and plated in small spots on seven polylysine-coated Petri dishes. The cells were incubated at 37 °C, 100% humidity, and 5% CO_2 in DMEM containing 10% fetal calf serum. 100 μM glutamine, 0.081 g/L nonessential amino acid supplement (Sigma Chemical Co., Catalog No. 2025), 100 000 units/L penicillin, and 100 mg/L streptomycin. Cells were used on days 2–6 of culture.

Electrode Preparation and Testing. Glass-encased carbon fiber microelectrodes were prepared using previously described techniques.[13] Briefly, a glass capillary (AM systems) containing a single, carbon fiber of 9 μm diameter (P-55S from Amoco Performance Products) was pulled to a fine tip on a commercial pipet puller (Narishige PE-2). The carbon fibers were sealed in the pipet tip by dipping them in epoxy. Once the epoxy was cured, the electrodes were polished at a 30–45° angle on a micropipet beveler (Sutter Instruments). Immediately after polishing, electrodes were dipped in 2-propanol for 10–15 min and then ultrasonicated in H_2O for 5 min.

Calibration and other electrode tests were performed using a flow injection apparatus similar to that described elsewhere.[12] This system consisted of a syringe pump (Harvard Apparatus 11) connected to a two-position, six-port valve (Valco AC6UHC) equipped with a 1 mL sample loop. The outlet of the valve emptied into a glass cell via 0.25 mm inner diameter tubing. The working electrode was positioned in the outlet of the tubing using a micromanipulator. The entire flow injection system was housed in a Faraday cage. Data were collected using an EI-400 potentiostat (Ensman Instrumentation, Bloomington, IN). For amperometric recordings, the electrode was poised at +0.80 V (all potentials are versus sodium-saturated calomel electrode). Amperometric data were collected at 300 Hz and low-pass filtered with a cutoff frequency of 100 Hz. The data were collected by an IBM-compatible personal computer (Gateway 2000 486-66 MHz) via a National Instruments multifunction board.

Fast-scan cyclic voltammetry was performed as described elsewhere.[14] Briefly, the potential on the electrode was linearly scanned from 500 to 1100 mV and back to 500 mV at a rate of 300 V/s. Each scan took 3.3 ms, and scans were obtained at a rate of

10 Hz. All voltammograms shown are background subtracted. The background was obtained prior to application of substances to the electrode or, in the case the single cell measurements, prior to the stimulation. The cyclic voltammograms were filtered at 2 kHz.

The number of electrons transferred per mole (n) was determined using chronoamperometry at a microelectrode according to a previously described method.[15] For this experiment, the background-subtracted steady state current (Δi) was measured following a potential step from +0.40 to +0.80 V. Values for n were calculated according to the following equation: $n = \Delta i / 4rCDF$, where r is the radius of the electrode (disk carbon electrodes were used for these experiments), C is the concentration of α-MSH, D is the diffusion coefficient, and F is the Faraday constant.

The diffusion coefficient for α-MSH used for these calculations was 3.75×10^{-6} cm^2/s. This value was calculated by measuring the dispersion of an α-MSH concentration pulse as it flowed through a capillary tube. At sufficiently high flow rates, the Golay equation[16] simplifies to $D = d^2v/(96H)$, where d is the inner diameter of the capillary, v is the flow velocity in the capillary, and H is plate height. Details of using this method are given elsewhere.[17]

Single-Cell Measurements. Single-cell measurements were performed in a manner similar to that described elsewhere.[7,8] Petri dishes containing the cells were rinsed three times with balanced salt solution (same composition as the solution used for cell isolation except 2.0 mM $CaCl_2$ was also added). The dish was filled with the balanced salt solution and placed in a microincubator (Medical Systems, Inc.) on the stage of an inverted microscope (Zeiss Axiovert 35). The microincubator maintained the temperature at 34 °C. To perform measurements, a cell was located with the microscope and a working microelectrode brought to within 1 μm of a cell using a micropositioner (Burleigh PC-1000).

Substances were applied to individual cells by pressure-ejecting solutions from the tips of micropipets which were positioned ~30 μm from the cell. Flow rates through the pipet tips were ~1 nL/s. Stimulants were dissolved in balanced salt solution. For K+ stimulation, 64 mM KCl was added to the balanced salt solution with an equivalent amount of NaCl removed. For mechanical stimulation, the electrode was pressed against the cell, usually until current spikes were observed, and then retracted until the electrode was ~1 μm away from the cell.

All cell data are reported as the mean $\pm$ 1 standard deviation. Spikes were counted and measured only if their peak height was 3 times the peak-to-peak noise.

Chemicals. Unless stated otherwise, all chemicals used for standards and buffers were obtained from Sigma Chemical Co. (St. Louis, MO) and cell culture chemicals and media were obtained from GIBCO (Grand Island, NY).

RESULTS AND DISCUSSION

Electrochemical Detection of α-MSH. Melanotrophs secrete a collection of peptides derived from the cleavage of proopiocortin. Primary secretory products are α-MSH, corticotro-

(13) Kelly, R. S.; Wightman, R. M. *Anal. Chim. Acta* **1986**, *187*, 79.
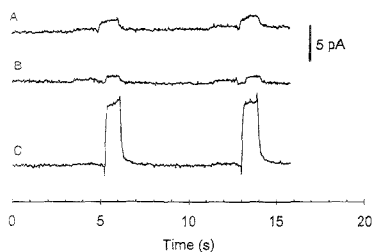(14) Bauer, J. E.; Kristensen, E. W.; May, L. M.; Wiedemann, D. J.; Wightman, R. M. *Anal. Chem.* **1991**, *60*, 1268.

(15) Heinze, J. *Angew. Chem., Int. Ed. Engl.* **1993**, *32*, 1268.
(16) Golay, M. In *Gas Chromatography 1958*; Desty, D. H., Ed.; Butterworths: London, 1959; p 36.
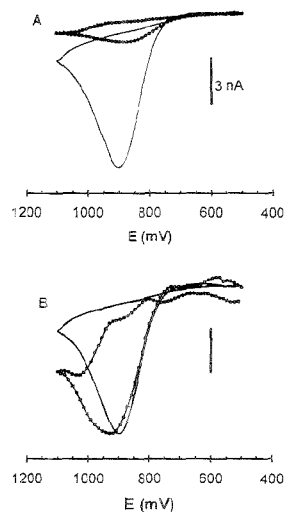(17) St. Claire, R. L., III Ph.D. Dissertation, University of North Carolina at Chapel Hill, 1986.

Figure 1. Flow injection analysis of proopiocortin peptides. Substances were injected at 1.0 μM each. Duplicate injections were performed ~8 s apart. Substances injected are (A) β-endorphin, (B) CLIP, and (C) α-MSH.

phin-like intermediate lobe peptide (CLIP), lipotropin (γ-LPH), and β-endorphin or variants of these peptides with posttranslational modifications.[18-20] In addition, a 16 kDa fragment (16K) of proopiocortin is also a major vesicle component.[18-20] It is well-known that small peptides containing tryptophan and tyrosine can be detected by oxidation at carbon electrodes.[21-23] Since many of the secretory products of melanotrophs contain these amino acids, it seemed reasonable that it would be possible to detect secretory activity at a carbon microelectrode through detection of one or more of these products.

Figure 1 illustrates flow injection analysis for α-MSH, CLIP, and β-endorphin. In this experiment, the electrode potential was fixed at +0.80 V and 1 μM of each peptide was injected. At this potential, α-MSH gave a signal 9 times higher than β-endorphin and 10 times higher than CLIP. (γ-LPH produced no signal under these conditions.) This selectivity is partially attributed to the presence of tryptophan in α-MSH. Of the two electroactive residues, tryptophan gives 5 times the current at carbon fiber microelectrodes for a given concentration, as illustrated in the cyclic voltammograms in Figure 2A. α-MSH contains a single tryptophan while the other electroactive peptides contain no tryptophan and just single tyrosine residues. The selectivity for tryptophan is useful in this case, but surprising, since other types of carbon electrodes have much less selectivity for tryptophan over tyrosine.[2] The other factor contributing to selectivity for α-MSH is its relatively small size, 13 amino acids, compared to β-endorphin (31 amino acids), CLIP (21 amino acids), and γ-LPH (58 amino acids). The likelihood of electroactivity being observed in a peptide decreases with increasing size since in larger peptides the electroactive residues may be sterically hindered from interacting with the electrode surface.

Figure 2B illustrates a background-subtracted fast-scan cyclic voltammogram of 100 μM α-MSH obtained by flow injection analysis. The voltammogram is compared to that obtained for tryptophan at 100 μM. The similarity in the shape of the voltammograms supports the idea that the electroactivity observed is due to the tryptophan residue. α-MSH, which has the structure

(18) Smelik, P. G.; Berkenbosch, F.; Vermes, I.; Tilders, F. J. H. In *The Anterior Pituitary Gland*; Bhatnagar, A. J., Ed.; Raven Press: New York, 1983; p 113.
(19) Glembotski, C. C. *J. Biol. Chem.* **1981**, *260*, 7433.
(20) Mains, R. E.; Eipper, B. A. *J. Biol. Chem.* **1979**, *254*, 7885.
(21) Bennet, G. W.; Brazell, M. P.; Marsden, C. A. *Life Sci.* **1981**, *29*, 1001.
(22) Sauter, A.; Frick, W. *J. Chromatogr.* **1984**, *297*, 215.
(23) Drumheller, A. L.; Bachelard, H.; St-Pierre, S.; Jolicoeur, F. B. *J. Liq. Chromatogr.* **1985**, *8*, 1829.

Figure 2. Background-subtracted fast-scan cyclic voltammograms for (A) 0.1 mM tyrosine (solid circles) and 0.1 mM tryptophan (solid line) and (B) 0.1 mM α-MSH (solid circles) and 0.1 mM tryptophan (solid line). The current bar is 3 nA for tryptophan and 0.1 nA for α-MSH. Each voltammogram is the average of 10 scans.

of N-acetyl adrenocorticotropin hormone 1–13, is actually one of three peptides with the same amino acid sequence released from melanotrophs. In addition, N,O-diacetyl α-MSH and desacetyl α-MSH are found.[24] Approximately 86% of the α-MSH-like material released is N,O-diacetyl α-MSH.[24] Only ~9% of the α-MSH-like substance is α-MSH, which is the form used for calibrations. However, all forms of α-MSH are detected equally (results not shown) because the modifications do not affect the tryptophan or its access to the electrode surface.

For amperometry, linear calibration curves were obtained for α-MSH over the range of 10 nM to 1 μM. A typical line had a slope of 10.9 pA/μM, a y-intercept of 0.71 pA, and a correlation coefficient of 0.994. The relative standard deviation at all concentrations was less than 0.1%. For cyclic voltammetry, the current at +0.9 V could be used to generate a calibration curve. Calibrations were linear from the range of 10 nM to ~0.6 μM. A typical line had a slope of 301 pA/μM, a y-intercept of 24 pA, and a correlation coefficient of 0.994. Negative deviations from linearity were observed above 0.6 μM which were apparently due to adsorption of the peptide or its oxidized product on the electrode surface. When the current at +0.9 V was measured for cyclic voltammetry, the relative standard deviation was less than 2% at all concentrations and the detection limit was 10 nM. Although 10 nM was the detection limit when just the current at +0.9 V was measured, recognizable voltammograms could only be obtained if the concentration was greater than 50 nM and if at least 10 scans were averaged together. For single scans, ~150 nM was required to obtain a useful voltammogram.

In both amperometry and cyclic voltammetry, it was found that exposures of the electrode to concentrations over 10 μM would decrease the response of the electrode, indicating fouling of the

(24) Goldman, M. E.; Beaulieu, M.; Kebabian, J. W.; Eskay, R. L. *Endocrinology* **1983**, *112*, 435.

Figure 3. Amperometric current recordings made at single melan-otrophs with the electrode at +0.80 V. (A) Stimulation was by application of 64 mM K+ in balanced salt solution. Stimulation indicated by the solid line. All other details of the experiment are given in the Experimental Section. (B) Current trace from mechanical stimulation, which was initiated ~30 s prior to the current recording.
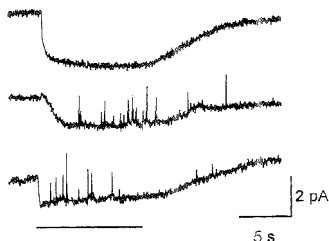
Figure 4. Current recordings made at a single melanotroph during stimulation with 64 mM K+ in Ca2+-free media. All recordings are made at the same cell. The recordings were made in order from top to bottom with 5 min between each stimulation. The first stimulation was with 64 mM K+ with no Ca2+; the next two recordings were with 64 mM K+ with 2.4 mM Ca2+ in the stimulation medium. The bar indicates the time of the stimulation.

Figure 5. Cyclic voltammetric recordings from mechanical stimula-tion at a single melanotroph. (A) Cyclic voltammograms were obtained every 100 ms, and the current at +0.9 V (the peak voltage for α-MSH) from each voltammogram was plotted. (B) Comparison of background-subtracted cyclic voltammograms obtained during single-cell stimula-tion (dashed line) and for authentic α-MSH (solid line). For the voltammogram from the cell, the five cyclic voltammograms that were recorded near the peak of the current trace in (A) were averaged. The background voltammograms were obtained from 1 s prior to the increase in current seen in (A). The voltammogram for authentic α-MSH was obtained by applying 10 μM α-MSH in balanced salt solution from a micropipet onto the electrode using the same pressure ejection system as used for applying stimuli. The current bar is 1 nA for the standard α-MSH and 0.1 nA for the cell recording.

electrode surface. The mechanism of fouling is presumably adsorption of the oxidized tryptophan on the electrode surface.[25]

Detection of Secretion. Figure 3A illustrates amperometric current recordings observed after application of 64 mM K+ to a cell. As shown, current spikes in the range of 0.5−5 pA height are observed following stimulation. Current spikes were rarely observed without stimulation of the cell. Also, current spikes were not observed if the electrode potential was insufficient to oxidize α-MSH. The occurrence of current spikes was strongly dependent on the presence of Ca2+ in the extracellular fluid. Figure 4 illustrates a series of K+ stimulations performed in Ca2+-free media. Application of 64 mM K+ without Ca2+ typically produced no spikes, while application of 64 mM K+ with 2.4 mM Ca2+ produced a series of spikes of varying number. The average number of spikes observed with Ca2+ was 15 ± 3.8 while that observed without Ca2+ was 1.4 ± 0.81 (n = 7).

An example of an amperometric recording following mechan-ical stimulation is shown in Figure 3B. Mechanical stimulation, although not well characterized physiologically, has proven useful in adrenal medullary chromaffin cells as a method of eliciting exocytosis for electrochemical detection.[8] Using mechanical stimulation at melanotrophs, it was found that, after an initial series

of spikes, a low frequency of spikes continued for over 60 s (Figure 3B). This time course of spike activity is in marked contrast to that with K+ stimulation, which only occurred during the stimula-tion and for a short time after the cessation of K+ application. In spite of the different time course, the spikes had similar shapes and sizes. For example, the average width at half-height for spikes elicited by mechanical stimulation was 36 ± 4 ms (n = 20) and for spikes elicited by K+ stimulation it was 36 ± 6 ms (n = 24). The average areas under spikes elicited by mechanical stimulation was 38 ± 5 fC (n = 19), and by K+ stimulation, the average spike area was 34 ± 6 fC (n = 35). (A random selection of spikes that were well-resolved from other spikes were used for these calcula-tions.)

Cyclic Voltammetry at Single Cells. Attempts made to monitor secretion following K+ stimulation by cyclic voltammetry were unsuccessful. The difficulty was that voltammograms were obtained every 100 ms, which was too infrequent to detect spikes. In addition, the spikes were so narrow that it was impossible to signal average multiple cyclic voltammograms obtained during a single spike. Thus, the sensitivity by cyclic voltammetry is likely to be low enough to prevent observing a voltammogram on a single spike. Using mechanical stimulation, however, it was often possible to generate large, broad spikes that were apparently due to the overlap of many spikes.[8] This is illustrated in Figure 5A.

(25) Brabec, V.; Mornstein, V. *Biophys. Chem.* **1980**, *12*, 159.

which shows the current at +1.0 V in a series of cyclic voltammograms obtained after a mechanical stimulation. Figure 5B shows a cyclic voltammogram that was obtained at the peak of the spike shown in Figure 5A. The voltammogram is overlaid with that obtained for authentic α-MSH at the same electrode at the end of the experiment. The change in shape for the voltammogram shown in Figure 5B relative to those shown in Figure 2 for α-MSH was usually observed after the electrode had been exposed to the cells.

It is difficult to establish unequivocally the identity of the substances contributing to the current signals observed; however, the data strongly support the conclusion that the main source of current spikes is detection of α-MSH and its derivatives. Cyclic voltammograms obtained from the single-cell releasates match that for α-MSH and are indicative of a small peptide containing tryptophan or tyrosine. From the amperometric experiments, we know that of the five peptides present in greatest abundance in rat melanotroph vesicles (α-MSH, CLIP, β-endorphin, γ-LPH, and 16K), the electrode can detect α-MSH, CLIP, and β-endorphin; however, the electrode is 9−10 times more sensitive to α-MSH than to the other two detectable peptides. Given that the peptides are secreted in an equimolar ratio,[3,20] we can estimate that ~86% of the signal is due to α-MSH (and its derivatives) and the remaining percentage split is almost equally between the other two peptides.

Detection of Exocytosis. The current spikes observed by amperometry have many of the characteristics that are expected for detection of exocytosis events. Their occurrence is closely related to stimulation and is strongly dependent on external Ca^{2+}. In addition, their shape is the same as that expected qualitatively based on diffusion of detected material from the cell to the electrode. The fact that the area of the spikes is independent of the stimulation method also supports the idea that the spikes are a detection of exocytosis events. The area under the current spikes corresponds to the amount detected according to Faraday's law. Thus, if the current spikes are due to exocytosis, then the spike area should reflect vesicular content, which should not change with different acute stimulations. Therefore, the spike area should be independent of the stimulation method for detection of exocytosis events, as observed.

The average area of the current spikes that we measured was 36 fC. This value can be used to provide an approximate estimate of the amount of α-MSH-like peptide in melanotroph vesicles as follows. From the discussion above, we can estimate that 86% of this area, or 31 fC, is due to detection of α-MSH and its derivatives. We measured n for α-MSH to be 0.96 ± 0.04 at +0.80 V ($n = 4$); therefore, 31 fC from Faraday's law corresponds to detection of 0.32 amol of α-MSH. Assuming that a spike corresponds to the detection of all of the vesicle content,[7,8] this leads to a conclusion that the vesicles contain 0.32 amol of α-MSH-like peptide.

We can estimate the amount expected per vesicle from previous studies as follows. Previous measurements of the basal secretion rate of dispersed melanotrophs have been reported and are consistent if the values are normalized to time of incubation and numbers of cells.[1,2] A typical value is 1.31 ng/2 × 10^4 cells·20 min.[2] Assuming the rate of basal release is constant, and using a molecular mass of 1665 g/mol for α-MSH, this secretion rate corresponds to 118 amol/cell.[2] Basal secretion in dispersed melanotrophs corresponds to ~0.9% of total hormone content per hour.[6,20] Thus, if 118 amol/cell corresponds to 0.9% of α-MSH content released per hour, then the cell content is 13 fmol. On the basis of electron micrographs of rat melanotrophs,[26] it has been estimated that rat melanotrophs contain 80 000 vesicles.[6] Assuming that all of the hormone is found in the vesicle, this corresponds to a vesicular content of 0.16 amol. Taking into account the limitations of the calculations, this value is in reasonable agreement with the value of 0.32 amol that we obtained. The value that we measured could be high for two reasons. One is that part of the spike could be due to detection of substances that we have not accounted for in our calculations. In addition, the average spike area we obtained may be skewed to higher values because smaller spikes, which could result from smaller vesicles, may not be detected because of a poor signal-to-noise ratio. Nevertheless, the good agreement between the two estimates of vesicle content supports the idea that the spikes are of the appropriate size to correspond to detection of the exocytosis of single vesicles in rat melanotrophs.

CONCLUSIONS

It has been demonstrated that exocytosis can be detected at single melanotrophs using amperometry at a carbon fiber microelectrode. The resolution and stimulation conditions allow single events to be observed. Cyclic voltammetry indicates that the detected substances are small tryptophan- or tyrosine-containing peptides. Based on previous studies of melanotroph vesicle content and amperometry, the chemical origin of the signal is primarily α-MSH-like peptides with much smaller contributions from CLIP and β-endorphin.

(26) Chronwall, B. M.; Bishop, J. F.; Gehlert, D. R. *Peptides* 1988, *9* (Suppl. 1), 169.

Analysis of High-Mass Biomolecules Using Electrostatic Fields and Matrix-Assisted Laser Desorption/Ionization in a Fourier Transform Mass Spectrometer

Jie Yao, Michael Dey, Salvador J. Pastor, and Charles L. Wilkins*

Department of Chemistry, University of California, Riverside, California 92521

A new decelerating technique that places dc potentials on the orthogonal excitation and receiver plates as well as the rear trapping plate (conductance limit) of the source cell of a dual cubic cell has been applied to the standard matrix-assisted laser desorption/ionization Fourier transform mass spectrometry technique. When this five-plate trapping method is applied, high-mass ions with large translational kinetic energies can be trapped efficiently and detected. Using this approach, low-resolution spectra of carbonic anhydrase (MW = 29 000), egg albumin (MW = 45 000), and bovine albumin (MW = 66 000) have been obtained. Because the new decelerating method requires no modification to the existing cell, it is also possible to obtain high-resolution spectra for compounds with masses of ca. 14 000 Da and lower. Utilizing the five-plate trapping method, a bovine insulin spectrum with a resolving power of 20 000 was obtained. It is not yet possible to obtain higher resolution for the higher mass proteins. The reasons for this difficulty are currently being investigated.

A current limitation of matrix-assisted laser desorption/ionization Fourier transform mass spectrometry (MALDI-FTMS) measurements is the inherent difficulty in trapping high-mass species. Due to the MALDI desorption process, molecules and ions are ejected from the matrix surface with kinetic energies that scale directly with their mass.[1] As a consequence, ions of higher m/z and accordingly higher kinetic energies are inefficiently trapped if standard low-voltage FTMS trapping potentials are used. A number of researchers have devoted considerable effort to examining kinetic energy distributions and trapping efficiencies for ions with higher translational energies.[2–5] The trapping problem was partially solved by introduction of a gated trapping

protocol in which a 9-V deceleration potential is applied to the rear trapping plate of a cubic cell to slow ions entering the cell. Using this method, Castoro and co-workers[2,3] successfully analyzed singly charged biomolecules with molecular masses as great as that of carbonic anhydrase (MW = 29 000). However, for higher mass ions it was necessary to increase the trapping voltage and to average multiple spectra in order to improve the signal-to-noise ratio, because very few ions are trapped. Nikolaev and co-workers[4] utilized a method to trap low-mass ions scattered from a surface with kinetic energies up to 500 eV by simply biasing the sample relative to all the plates of the cell. Hettich and Buchanan[5] varied the potential difference between the sample probe and the front trapping plate. These workers found that use of retarding fields lower than 10 V did not significantly affect trapping efficiencies. These studies suggested that it might be profitable to examine the use of higher decelerating potentials than had previously been used to trap MALDI-generated ions.

Until recently, there was slow progress in addressing the problem of achieving high-mass analysis for singly charged ions by Fourier transform mass spectrometry, in spite of the fact that it is capable of providing extremely high resolving power and mass accuracy in the low part-per-million (ppm) range.[6–9] The majority of recent high-mass work has focused on the use of electrospray ionization (ESI) to produce multiple charge states, allowing detection in a m/z range more suited to FTMS. These efforts have resulted in ultra-high-resolution mass spectral measurements.[10–14] McLafferty and co-workers[15] reported isotopic resolu-

(1) Beavis, R. C.; Chait, B. T. *Chem. Phys. Lett.* 1991, *181*, 479–484.
(2) Castoro, J. A.; Köster, C.; Wilkins, C. *Rapid Commun. Mass Spectrom.* 1992, *6*, 239–241.
(3) Castoro, J. A.; Wilkins, C. *Anal. Chem.* 1993, *65*, 2621–2627.
(4) Nikolaev, E. N.; Mordehai, A. V.; Frankevich, V. E., Jr. *Rapid Commun. Mass Spectrom.* 1991, *5*, 260–262.
(5) Hettich, R. L.; Buchanan, M. V. *Int. J. Mass Spectrom. Ion Processes* 1991, *111*, 365–380.

(6) Guan, S.; Marshall, A. G. *Rapid Commun. Mass Spectrom.* 1993, *7*, 857–860.
(7) Pastor, S. J.; Castoro, J. A.; Wilkins, C. L. *Anal. Chem.* 1995, *67*, 379–384.
(8) McIver, R. T.; Li, Y.; Hunter, R. L. *Rapid Commun. Mass Spectrom.* 1994, *8*, 237–241.
(9) McIver, R. T.; Li, Y.; Hunter, R. L. *Int. J. Mass Spectrom. Ion Processes* 1994, *132*, L1–L7.
(10) Fenn, J. B.; Mann, M.; Meng, C. K.; Wong, S. F.; Whithouse, C. M. *Science* 1989, *246*, 64–71.
(11) Kebarle, P.; Tang, L. *Anal. Chem.* 1993, *65*, 972A–986A.
(12) Senko, M. W.; Beu, S. C.; McLafferty, F. W. *Anal. Chem.* 1994, *66*, 415–417.
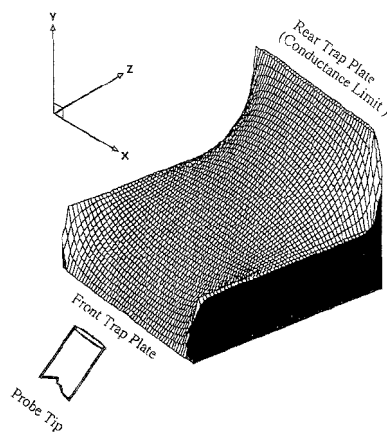(13) Senko, M. W.; Speir, J. P.; McLafferty, F. W. *Anal. Chem.* 1994, *66*, 2801–2808.
(14) Winger, B. E.; Hofstadler, S. A.; Bruce, J. E.; Udseth, H. R.; Smith, R. D. *J. Am. Soc. Mass Spectrom.* 1993, *4*, 566–577.

tion of ions derived from porcine albumin (MW 66 000). Hofstadler and Laude[16] were able to detect ions corresponding to a dimer of bovine albumin (m/z 132 kDa). Recently, Smith and co-workers[17] detected individual T4 DNA ions (mass 110 MDa), demonstrating the capability of ESI-FTMS in the 10^8-Da mass range and representing the highest mass yet determined by mass spectrometry. Although electrospray ionization has excellent mass range capabilities, ionization efficiency can be suppressed by solution reagents, such as detergents and salts, which are commonly used in biochemistry.[18,19]

MALDI, the topic of this paper, represents an alternative and complementary approach to electrospray ionization of high-mass species. Generally, there are two types of MALDI ion generation sources. An external ion source creates ions outside the magnetic field, and the ions are subsequently guided into the cell by utilizing an ion guide or lenses. The primary advantage of an external ion source is that it facilitates generation of a collimated beam during the ion transfer process. On the other hand, ions generated directly within the magnetic field (internal ion source) are available for immediate analysis. Internal sources avoid possible problems that may arise during ion transmission from an external ion source, where molecules can experience mass discrimination due to flight-time effects, as well as increased metastable decay. The main drawback of internal MALDI ion generation is the large spatial distribution of ions of the same m/z ratio, making ion coherence for excitation/detection less than optimal. There is continued research interest in finding ways to "axialize" or cool the ions within the cell to a better collimated starting position. Such an approach combines the simplicity of internal ion generation with the advantage of a collimated beam characteristic of an external source.

The theoretical upper mass limit for thermal ions in a Fourier transform mass spectrometer is high and has been approximated to be at least 300 000 Da in a 7-T FTMS.[20,21] In a recent paper, Solouki, Gillig, and Russell[22] demonstrated the feasibility of high-mass FTMS analysis. In their research, they positioned a copper wire ion guide parallel to the magnetic field lines within a cylindrical cell and reported success in detecting singly charged biomolecule ions with masses as great as 157 kDa (transferrin dimer). Use of the copper wire guide poses some problems because it alters the electric field experienced by the ions. Positive ions attracted to a negatively biased ion guide must be repelled by a positive voltage before subsequent dipolar excitation. As a consequence of the changing electric field and corresponding shifts in frequency, accurate mass calibration is difficult.

Reported here is a possible approach to further extend the detectable mass range of singly charged ions using MALDI-FTMS, employing an electrostatic field deceleration method, where decelerating voltages up to 75 V are applied not only to the rear trapping plate of the source region of a dual cubic cell but also to the excitation and receiver plates of the cubic cell. This "five-

(15) Speir, P. J.; Senko, M. W.; Little, D. P.; Loo, J. A.; McLafferty, F. M. *J. Mass Spectrom.* **1995**, *30*, 39–42.
(16) Hofstadler, S. A.; Laude, D. A., Jr. *Anal. Chem.* **1992**, *64*, 569–572.
(17) Chen, R.; Cheng, X.; Mitchell, D. W.; Hofstadler, S. A.; Wu, Q.; Rockwood, A. L.; Sherman, M. G.; Smith, R. D. *Anal. Chem.* **1995**, *67*, 1159–1163.
(18) Kay, I.; Mallet, A. I. *Rapid Commun. Mass Spectrom.* **1993**, *7*, 744–746.
(19) Schindler, P. A.; Van Dorsselaer, A. *Anal. Biochem.* **1993**, *213*, 256–263.
(20) Gross, M. L.; Rempel, D. L. *Science* **1984**, *226*, 261–268.
(21) Wood, T. D.; Schweikhard, L.; Marshall, A. G. *Anal. Chem.* **1992**, *64*, 1461–1469.
(22) Solouki, T.; Gillig, K. J.; Russell, D. H. *Anal. Chem.* **1994**, *66*, 1583–1587.

Figure 1. Five-plate trapping field lines calculated by MacSimion (Version 2.03, Montech Pty Ltd.) for 50 V on the rear trapping plate and 20 V on both the excitation (yz-plane) and receiver (xz-plane) plates. The magnetic field lies along the z-axis.

plate" trapping method shows improved trapping efficiency during the ionization event. Simulations (MacSimion, Version 2.03, Montech Pty Ltd., Monash University, Victoria, Australia) suggest that application of voltages to five of the six plates of the FTMS cell forms a "cuplike" electrostatic field in which ions can be more efficiently trapped. Simulated ion calculations show a much improved potential surface which should be more conducive to better trapping because off-axis ions are less likely to be ejected (neutralized on cell plates). Figure 1 is a simulation of the field map that results if 50 V is applied to the rear trapping plate and 20 V to both the excitation and receiver plates. The five-plate trapping approach does not require cell modification. Instead, dc pulses and excitation pulses are separated in time and controlled by existing FTMS software. This setup allows maximum flexibility and control for an FTMS experiment without impairing the ability to do lower mass high-resolution work.

EXPERIMENTAL SECTION

Instrumentation. Experiments were carried out using a Waters-Extrel (Madison, WI) FTMS-2000 Fourier transform mass spectrometer operating at 6.2 T and equipped with an automatic solids probe. The source and analyzer cells of the cubic dual cell are separated by a conductance limit with a 2-mm-diameter hole. A Lambda Physik EMG-201-MSC excimer laser (Lambda Physik, Gottingen, Germany) operating at a wavelength of 308 nm with a pulse width of 28 ns was used. The laser beam enters the mass spectrometer through a fused-silica window and is focused to a 500-μm-diameter beam spot upon a sample probe tip using a 12.5-cm focal length fused-silica lens. Laser energies were attenuated to between 20 and 30 mJ/pulse. The vacuum chamber is pumped by two diffusion pumps (Edwards Diffstak, Model 160) with maximum pumping speeds of 700 L/s. Spectra reported here were obtained using source cell detection. Five-plate trapping is achieved by using a modified high-power excitation amplifier (Waters-Extrel) that can switch between a dipolar excitation configuration and a dc-only configuration to the transmitter plates of the source cell of a dual cubic cell. Direct current voltages on

Figure 2. Diagram of connections for five-plate trapping. Voltage 1 is the dc voltage applied to the rear trapping plate. Voltage 2 is the dc voltage applied to both the excitation and receiver plates.

the receiver plates and rear trapping plate (conductance limit of a dual cell) are supplied through voltage-sensitive switches by two external power supplies (Power Designs Inc., Modes 105TA, New York). Additional electronics protect the preamplifier and direct the signal to and from the cell controller, where the sequence can be controlled with existing Odyssey software (Version 3.0, Waters-Extrel FTMS). The instrument has been described in detail previously.[2,23] MacSimion (MacSimion, Version 2.03, Montech Pty Ltd.) was used to calculate the potential surfaces for five-plate deceleration experiments.

Experimental Sequence. A diagram of the five-plate deceleration connections to the cell appears in Figure 2. The decelerating voltage, up to 75 V, is applied not only to the rear trapping plate but also to the excitation and receiver plates of a cubic FTMS cell. The deceleration dc pulse and the excitation pulse on the excitation plates are simply separated in time. To deal with the high kinetic energies of MALDI ions, which increase as ion mass increases, larger dc potentials are applied to the rear trapping plate (plate opposite to sample probe) and the excitation/receiver plates to facilitate efficient trapping. To trap positive ions, the front trapping plate is set to 0.0 V, the rear trapping plate is set between 30 and 75 V, and the excitation/receiver plates are set between 2 and 75 V prior to firing the laser. These decelerating potentials are maintained for $100-300$ μs. Subsequently, the potentials of the front and the rear plates are adjusted to between 0.5 and 3 V, suitable for FTMS observations, while the dc voltages on the excitation and receiver plates are switched off. The ability to trap "hot" ions is accomplished by the increased electrostatic potentials during the desorption/ionization event. Once trapped, the ions lose their excess energy either through collisional cooling with background neutrals in the source cell (5×10^{-8} Torr is typical pressure) or through infrared emission. In addition, trapped ions establish an equilibrium with the different ion motional modes. As a consequence, translational energy is redirected from the z-axis, permitting detection at much lower trapping potentials. For the mass spectral observations reported here, ions were excited by a chirp excitation with a general range of 50–100 KHz and a sweep rate of 230 Hz/μs. All detection was done in direct mode. The experimental sequence shown in Figure 3 was employed using a data acquisition rate of 1 MHz and collecting 32K data points.

Sample Preparation. The matrix used for all experiments was 2,5-dihydroxybenzoic acid (DHB; Fluka Chemical Co., Buchs, Switzerland). D-Fructose was used as a co-matrix because it has been demonstrated to cool biomolecules during the MALDI
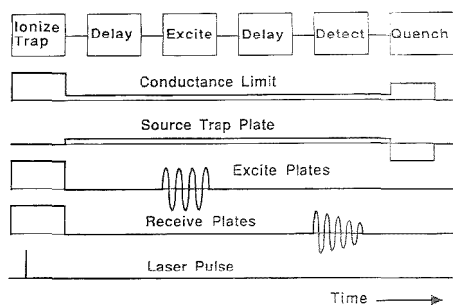
Figure 3. Experiment event sequence for five-plate trapping experiment. The differences between the five-plate trapping method and a standard FTMS experiment are the conditions for the ionization event. To trap high-mass ions, instead of applying a dc voltage only on the rear trapping plate, a dc voltage controlled by the software is also applied to the excitation/receiver plates. The dc pulse is maintained for 100–300 μs. Subsequently, a dipolar chirp excitation is applied to the excitation plates to excite the ions to a larger radius, which are then detected by the receiver plates. The last event is the quench pulse used to remove ions from the cell.
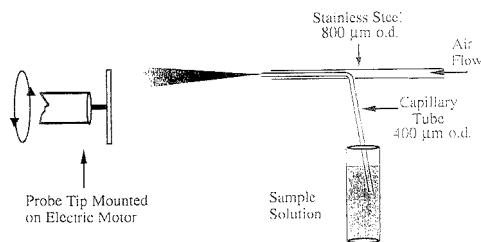
Figure 4. Aerosol spray sample preparation. Air flow tubing is made from a stainless steel syringe and the sample aspiration tubing is made from a fused-silica capillary.

process.[2,23] Bovine insulin, carbonic anhydrase, egg albumin, and bovine albumin were purchased from Sigma Chemical Co. (St. Louis, MO). A 50 mM DHB matrix was prepared by dissolving 0.410 of DHB in 50 mL of methanol. A 50-μL aliquot of trifluoroacetic acid (TFA) was added to give an overall 0.1% TFA (v/v) concentration to enhance ionization efficiency. A 50 mM D-fructose stock solution was prepared by dissolving 0.450 g in 50 mL of methanol. Bovine insulin (1 mg) was dissolved in 5 mL of methanol. Solutions of carbonic anhydrase, egg albumin, and bovine albumin were made by dissolving 1 mg of protein in 2 mL of water. The bovine insulin, DHB, and fructose solutions were combined to form a solution with an analyte/matrix/co-matrix molar ratio of 1:5000:2500. Similarly, carbonic anhydrase was prepared for analysis by using solutions with an analyte/matrix/ co-matrix molar ratio of 1:8000:4000. For egg albumin and bovine albumin, an analyte/matrix/co-matrix molar ratio of 1:10 000:5000 was used. For analysis, each mixture was aerosprayed onto a rotating stainless steel probe tip using the arrangement diagrammed in Figure 4. As the biomolecule mass increases, aerosol spraying becomes more critical. The air flow rate should be very low to obtain a homogeneous crystal layer on the probe tip. Following deposition, samples were introduced into the vacuum

(23) Köster, C.; Castoro, J. A.; Wilkins, C. L. *J. Am. Chem. Soc.* 1992, *114*, 7572–7574.
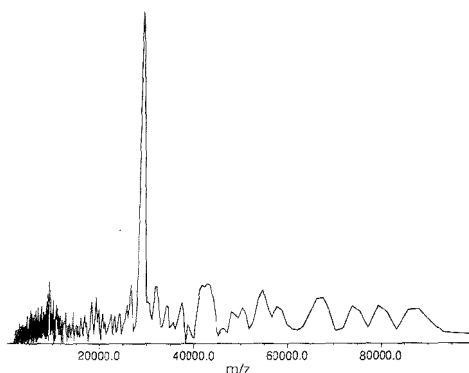
Figure 5. MALDI–FT mass spectrum of carbonic anhydrase (MW = 29 000). Five-plate trapping voltages were 30 V on the rear trapping plate and 10 V on the excitation and receiver plates. For spectral data acquisition, a trapping voltage of 2 V was applied to both the front and rear trapping plates.
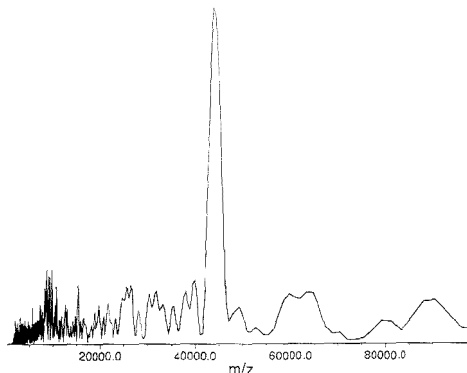
Figure 6. MALDI–FT mass spectrum of egg albumin (MW = 45 000). Five-plate trapping voltages were 50 V on the rear trap plate and 35 V on the excitation and receiver plates. For spectral data acquisition, a trapping voltage of 3 V was applied to both the front and rear trapping plates.

system and the system allowed to pump to a pressure of 5×10^{-8} Torr before analysis.

RESULTS AND DISCUSSION

High-Mass Analysis. As mentioned earlier, Russell and co-workers[22] extended the analytical mass range by placing an ion guide in a cubic cell. Here, the mass range was extended using an unmodified standard FTMS cubic cell. By replacing the single-plate deceleration event of a MALDI-FTMS experiment with the five-plate trapping method, trapping efficiency is improved, as seen in the carbonic anhydrase spectrum in Figure 5. To obtain the spectrum in Figure 5, it was necessary to average four time-domain scans taken at sequential probe positions. This procedure was necessary due to presence of the D-fructose co-matrix. Although the D-fructose provides collisional cooling of the protein,[2,23] its presence appears to limit the number of shots available per spot. The averaging of 4 scans is a significant reduction from the averaging of 10–30 scans needed to produce similar signal-to-noise ratios for this compound's spectrum in previous studies.[3] The best spectrum was obtained for deceleration conditions of 10 V on the excitation and receiver plates and 30 V on the rear trapping plate. For spectral data acquisition, ions were detected under standard 2-V trapping conditions. Figure 6 shows the spectrum of egg albumin with a molecular ion of $m/z = 45\ 000$. To decelerate these higher mass species, the rear trapping plate (conductance limit) was held at 50 V and the side plates held at 35 V. It appears that the trapping of high-mass ions is simply an electrostatic potential matching problem.[24,25] The ultimate solution may be to use the highest decelerating voltages that one has available. One frequently overlooked detail is the role of the laser's interaction with the matrix and initial ion velocities. Most matrix studies have focused on testing families of compounds for their efficiency of the ionization of analytes and determination of the optimum mixture ratios. The researchers in these studies have made use of the various types of lasers including nitrogen

Figure 7. MALDI–FT mass spectrum of bovine insulin (MW = 5734). Five-plate trapping voltages were 9.5 V on the rear trap plate and 4 V on the excitation and receiver plates. For spectral acquisition, a trapping voltage of 0.6 V was applied to the front and rear trapping plates. Resolving power is 20 000.

lasers (337.1 nm), Nd–YAG (357 nm, tripled harmonic), and dye lasers (355 nm using 2,2′′′-dimethyl-p-quaterphenyl (BMQ)). However, there is some evidence that the choice of the laser wavelength may play a significant role in establishment of the initial ion velocities,[26–28] previously assumed to be 760-1000 m/s for all cases. Because kinetic energy scales directly with mass, it seems probable that lowering the initial desorption velocity would greatly increase the detectable upper mass range of current systems.

High-Resolution Analysis. As mentioned earlier, the five-plate trapping method allows MALDI-generated ions to be trapped efficiency and guides ions close to the center of the cell. Figure 7 shows a bovine insulin five-plate trap MALDI-FT mass spectrum with an average resolving power of 20 000 and an isotope peak distribution that is in good agreement with the theoretical distribution. This spectrum was obtained by careful adjustment

(24) Hanson, D. H.; Kerley, E. L.; Castro, M. E.; Russell, D. H. *Anal. Chem.* **1989**, *61*, 2040–2046.

(25) Solouki, T.; Russell, D. H. *Proc. Natl. Acad. Sci. U.S.A.* **1992**, *89*, 5701–5704.

(26) Ens, W.; Mao, Y.; Mayer, F.; Standing, K. G. *Rapid Commun. Mass Spectrom.* **1991**, *5*, 117–123.

(27) Spengler, B.; Cotter. R. J. *Anal. Chem.* **1990**, *62*, 793–796.

(28) Pan, Y.; Cotter, R. J. *Org. Mass Spectrom.* **1992**, *27*, 3–8.
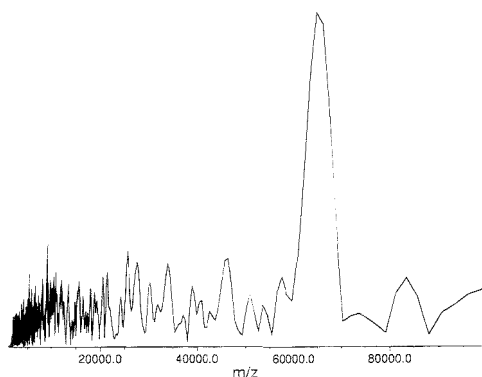
Figure 8. MALDI–FT mass spectrum of bovine albumin (MW = 66 000). Five-plate trapping voltages were 50 V on the rear trapping plate and 35 V on the excitation and receiver plates. For spectral data acquisition, a trapping voltage of 3 V was applied to both the front and rear trapping plates.

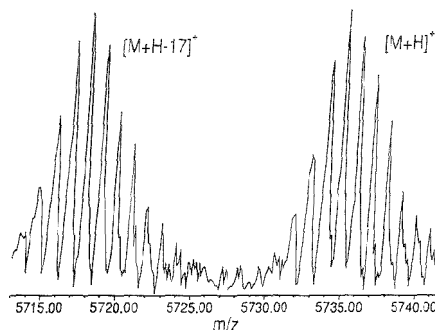of the trapping voltage on both the excitation and receiver plates (4 V) and also on the rear trapping plate (9.5 V). A trapping voltage of 0.6 V was used on the front and rear trapping plates during normal excitation/receive events to trap an optimum number of ions allowing measurement of this high-resolution spectrum. The principal advantage of the five-plate trapping method over standard FTMS experiments employing gated trapping is that higher mass ions can be trapped and detected because the upper kinetic energy trapping limit for ions has been extended from 9.5[29] to 75 eV. Figure 8 is an extremely low-resolution MALDI-FT mass spectrum of bovine albumin (MW = 66 000). To decelerate these ions, the rear trapping plate was held at 50 V while the excitation and receiver plates were held at 35 V. Clearly, the mass resolving power shown in this spectrum

is unimpressive. However, it does demonstrate the efficacy of the five-trap approach for capturing at least some of these massive ions. In that sense, these results are encouraging, giving evidence that the detectable mass range in FTMS can be extended by this new method. Obviously, it remains to achieve high-resolution spectra for high-mass molecules. Some of the probable causes of the extremely poor mass resolution include the following: (1) the large collisional cross section of the high-mass ions, which can cause loss of coherence during the detection event as a result of collisions with neutrals;[30] (2) possible enhancement of meta-stable decay of the molecular ions, caused by internal excitation during the MALDI process; and (3) difficulties in exciting high-mass ions into coherence. Several groups have developed potential means of addressing some of these problems. Rempel and Gross[31-33] devised a radio frequency-only mode FTMS experiment to manipulate the broadly distributed ion cloud to improve detection of ions initially located away from the center of the trap. Solouki and Russell[34] demonstrated a method to dampen the translational energies in a "waiting room" prior to the excitation and detection events. Marshall and co-workers[35-37] have shown promising results based upon use of a quadrupolar excitation pulse and buffer gas to relax ions to the center of the FTMS cell. We are currently investigating the combination of quadrupolar excitation with the five-plate deceleration method described here.

CONCLUSION

It appears from the present results that five-plate deceleration shows much promise for MALDI-FTMS of high-mass compounds. Because high-voltage deceleration occurs only during the MALDI step, the rest of the mass spectral measurement can proceed as usual. Moreover, this protocol does not involve modification to the existing cell. Based upon the present successes in analyzing singly charged high mass species, future prospects are promising. Because high-mass ions can be trapped, it will be particularly interesting to study the effects of collision-induced or surface-induced dissociation upon these large molecules.

ACKNOWLEDGMENT

(29) Dey, M.; Castoro, J. A.; Wilkins, C. L. *Anal. Chem.* **1995**, *67*, 1575–1579.
(30) Covey, T.; Douglas, D. J. *J. Am. Soc. Mass Spectrom.* **1993**, *4*, 616–623.
(31) Rempel, D. L.; Gross, M. L. *J. Am. Soc. Mass Spectrom.* **1992**, *3*, 590–594.
(32) Holliman, C. L.; Rempel, D. L.; Gross, M. L. *J. Am. Soc. Mass Spectrom.* **1992**, *3*, 460–463.
(33) Jacoby, C. B.; Holliman, C. L.; Rempel, D. L.; Gross, M. L. *J. Am. Soc. Mass Spectrom.* **1993**, *4*, 186–189.
(34) Solouki, T.; Russell, D. H. *Appl. Spectrosc.* **1993**, *47*, 211–217.
(35) Guan, S.; Wahl, M. C.; Wood, T. D.; Marshall, A. G. *Anal. Chem.* **1993**, *65*, 1753–1757.
(36) Guan, S.; Wahl, M. C.; Marshall, A. G. *J. Chem. Phys.* **1994**, *100*, 6137–6140.
(37) Huang, Y.; Pasa-Tolic, L.; Guan, S.; Marshall, A. G. *Anal. Chem.* **1994**, *66*, 4385–4389.

Electrochemistry Combined On-Line with Electrospray Mass Spectrometry

Feimeng Zhou[†] and Gary J. Van Berkel*

Chemical and Analytical Sciences Division, Oak Ridge National Laboratory, Oak Ridge, Tennessee 37831-6365

In this paper a variety of methods to couple electrochemistry on-line with electrospray mass spectrometry (EC/ES-MS) are presented, and the fundamental and analytical utility of this hybrid technique is illustrated. The major problems encountered in coupling EC and ES-MS are discussed, and means to overcome them are presented. Three types of electrochemical flow cells, viz., a thin-layer electrode flow-by cell, a tubular electrode flow-through cell, and a porous electrode flow-through cell, are discussed in regard to their suitability for this coupling. Methods for coupling each of these electrochemical cells on-line with ES-MS, either floated at or decoupled from the ES high voltage and controlled by a constant current supply, a constant potential supply, or a potentiostat are presented. Three applications are used to illustrate the utility and versatility of the EC/ES-MS combination: (1) the ionization of neutral analytes (i.e., perylene) for detection by ES-MS, (2) the study of the products of electrode reactions (i.e., nickel(II) octaethylporphyrin oxidation products), including relatively short-lived products (i.e., β-carotene oxidation products), and (3) the enhanced determination of metals (i.e., elemental silver) achieved by coupling anodic stripping voltammetry on-line with ES-MS.

The analytically powerful combination of electrochemistry (EC) on-line with mass spectrometry (MS) has received scant attention, given that the two techniques were first coupled by Bruckenstein and Gadde[2] over 20 years ago. This lack of attention stems largely from the fact that, until recently, studies performed with this combination were limited to the analysis of volatile species due to difficulties in interfacing the liquid environment of EC with the gas-phase environment of MS.[2,3] However, over the past decade, several types of ionization methods and interfaces have been developed that allow mass spectrometers to sample and analyze nonvolatile species, both organic and inorganic, originally present in a liquid solution.

Using one such ionization method/interface, viz., thermospray (TS),[4] Hambitzer and Heitbaum[5] were the first to couple EC on-line with MS and study nonvolatile solution species. Yost, Brajter-

Toth, and co-workers[3,6-10] refined this EC/TS-MS methodology, also combining it with HPLC, and demonstrated it to be an especially powerful tool in the study of biological redox reactions. Another approach was taken by Bartmess and Phillips,[11] who combined EC and fast atom bombardment (FAB)-MS.[12] In their work, EC was used to assist the ionization of neutral analyte species in the liquid FAB matrix prior to sputtering of the sample with the atom beam. Attempts have also been made to couple EC with MS using the particle beam interface,[13] and one would expect that flow-FAB[14] and atmospheric pressure chemical ionization (APCI)[15] would also be viable ionization methods/interfaces for EC/MS.

Electrospray[16-20] (ES) also holds promise for coupling EC on-line with MS, as demonstrated in several preliminary reports.[21-24] Electrospray is an atmospheric pressure technique that makes use of an electrostatic sprayer to assist the transfer of ionic analytes initially present in solution into the gas phase for mass analysis (ES-MS). This technique is rapidly becoming the ionization method/interface of choice for analyzing nonvolatile, polar, and thermally labile compounds, especially high molecular weight biopolymers, and for coupling liquid separation methods

(6) Volk, K. J.; Lee, M. S.; Yost, R. A.; Brajter-Toth, A. *Anal. Chem.* 1988, *60*, 722−724.
(7) Volk, K. J.; Yost, R. A.; Brajter-Toth, A. *Anal. Chem.* 1989, *61*, 1709−1717.
(8) Volk, K. J.; Yost, R. A.; Brajter-Toth, A. *J. Chromatogr.* 1989, *474*, 231−243.
(9) Volk, K. J.; Yost, R. A.; Brajter-Toth, A. *J. Electrochem. Soc.* 1990, *137*, 1764−1771.
(10) Zhu, S.-M.; Brajter-Toth, A. *Anal. Chim. Acta* 1990, *237*, 305−310.
(11) Bartmess, J. E.; Phillips, L. R. *Anal. Chem.* 1987, *59*, 2012−2014.
(12) Barber, M.; Bordoli, R. S.; Elliott, G.; Sedgwick, R. D.; Tyler, A. N. *Anal. Chem.* 1982, *54*, 645A−657A.
(13) Jones, J. A.; Yost, R. A. *Proceedings of the 40th ASMS Conference on Mass Spectrometry and Allied Topics*, Washington, DC, May 31−June 5, 1992; ASMS: Santa Fe, NM, 1992; pp 1711−1712.
(14) Caprioli, R. M. *Anal. Chem.* 1990, *62*, 8, 477A−485A.
(15) Huang, E. C.; Wachs, T.; Conboy, J. J.; Henion, J. D. *Anal. Chem.* 1990, *62*, 713A−725A.
(16) Fenn, J. B.; Mann, M.; Meng, C. K.; Wong, S. K.; Whitehouse, C. M. *Science* 1989, *246*, 64−71.
(17) Fenn, J. B.; Mann, M.; Meng, C. K.; Wong, S. K.; Whitehouse, C. M. *Mass Spectrom. Rev.* 1990, *9*, 37−71.
(18) Smith, R. D.; Loo, J. A.; Edmonds, C. G.; Barinaga, C. J.; Udseth, H. R. *Anal. Chem.* 1990, *62*, 882−899.
(19) Mann, M. *Org. Mass Spectrom.* 1990, *25*, 575−587.
(20) Kebarle, P.; Tang, L. *Anal. Chem.* 1993, *65*, 972A−986A.
(21) Van Berkel, G. J.; McLuckey, S. A.; Glish, G. L. *Proceedings of the 39th ASMS Conference on Mass Spectrometry and Allied Topics*, Nashville, TN, May 19−24, 1991; ASMS: Santa Fe, NM, 1991; pp 1237−1238.
(22) Asano, K. G.; Van Berkel, G. J. *Proceedings of the 41st ASMS Conference on Mass Spectrometry and Allied Topics*, San Francisco, CA, May 31−June 5, 1993; ASMS: Santa Fe, NM, 1993; pp 1068a−1068b.
(23) Zhou, F.; Van Berkel, G. J. *Proceedings of the 42nd ASMS Conference on Mass Spectrometry and Allied Topics*, Chicago, IL, May 29−June 4, 1994; ASMS: Santa Fe, NM, 1994; p 1002.
(24) Bond, A. M.; Colton, R.; D'Agostino, A.; Downard, A. J.; Traeger, J. C. *Anal. Chem.* 1995, *67*, 1691−1695.

(1) Bruckenstein, S.; Gadde, R. R. *J. Am. Chem. Soc.* 1971, *93*, 793−794.
(2) Bittins-Cattaneo, B.; Cattaneo, E.; Königshoven, P.; Vielstich, W. In *Electroanalytical Chemistry*; Bard, A. J., Ed.; Marcel Dekker: New York, 1991; Vol 17, pp 181−220.
(3) Volk, K. J.; Yost, R. A.; Brajter-Toth, A. *Anal. Chem.* 1992, *64*, 21A−33A.
(4) Blakley, C. R.; Vestal, M. L. *Anal. Chem.* 1983, *55*, 750−754.
(5) Hambitzer, G.; Heitbaum, J. *Anal. Chem.* 1986, *58*, 1067−1070.

with MS.[16-20] In contrast to many of the ionization methods/ interfaces mentioned above, ES involves no heating of the solvent, gas-phase reactions of the analytes are minimal, and a wider variety of solvent systems can be used.

Over the last several years, our investigation of the EC/ES-MS combination has found that several problems must be overcome or at least recognized to successfully couple EC to ES-MS.[21-23] First, since the ES source normally operates at a very high voltage (3–5 kV), the EC system must be either floated at or be decoupled from the ES high voltage. Second, the level of supporting electrolyte normally used in electrochemical experiments (50–100 mM) can plug the atmospheric sampling interface and necessitate frequent cleaning of the interface. Furthermore, the addition of such "foreign" electrolytes to the electrospray solvent system can severely suppress the gas-phase ion signal from the analyte of interest.[25] Therefore, means to alleviate the problems for ES-MS operation caused by typical EC electrolyte systems must be developed. Third, the ES device itself is an electrochemical cell,[26-30] and thus, analytes may be oxidized/ reduced in the metal ES capillary. The possibility of this "electrochemical interference" occurring in EC/ES-MS experiments must be recognized.

In this paper, we describe several methods to couple and operate three different types of electrochemical flow cells on-line with ES-MS and the means to overcome each of the aforementioned problems in coupling EC to ES-MS. Data from a variety of EC/ES-MS experiments are presented to illustrate the fundamental and analytical utility, as well as the versatility, of this new hybrid technique.

EXPERIMENTAL SECTION

Chemicals. All analytes, HPLC-grade methylene chloride, and HPLC-grade acetonitrile were purchased from commercial suppliers and used as received. Silver solutions were prepared by diluting a 1000 ppm silver standard solution (High Purity Standard, Inc., Charleston, SC) with acetonitrile, Milli-Q (Millipore Corp., Bedford, MA) purified water, and nitric acid (trace element analysis grade, J. T. Baker) to obtain a final acetonitrile/water/ nitric acid composition of 95/5/0.1 (v/v/v).

Electrochemical Cells. The thin-layer electrode flow cell (Bioanalytical Systems, Inc., West Lafayette, IN) consisted of a glassy carbon working electrode (6 mm diameter) embedded in PEEK, separated from a stainless steel auxiliary electrode by a Teflon gasket (0.01 in. thick), and a Ag/AgCl reference electrode contacting the solution through a small hole in the auxiliary electrode (Figure 1a). The tubular electrode cell was constructed in-house by connecting two stainless steel metal capillaries (6.5 cm long, 127 μm i.d., 500 μm o.d.; Scientific Instrument Services, Ringoes, NJ) to each end of a PEEK low dead-volume connector (0.254 μm through-hole; Upchurch Scientific, Oak Harbor, WA) (Figure 1b). The porous electrode cell (ESA, Inc., Bedford, MA) consisted of a porous graphite working disk electrode (0.8 mm long, 2.5 mm diameter, 0.1–3 μm diameter pores), and palladium auxiliary and reference electrodes (Figure 1c).

Figure 1. Schematic representation of the electrochemical flow cells used on-line with ES-MS: (a) thin-layer electrode cell, (b) tubular electrode cell, and (c) porous electrode cell.

Cyclic Voltammetry. The cyclic voltammogram (CV) of β-carotene (acetonitrile/methylene chloride (9/1 v/v), 40 mM lithium triflate) was recorded at 1.0 V/s using a 6 mm diameter glassy carbon working electrode, a platinum auxiliary electrode, and a silver quasi-reference electrode under the control of a PAR 173 potentiostat (Princeton Applied Research Corp., Princeton, NJ) with a PAR 175 universal programmer. Decamethylferrocene was added to the analyte solution and used as the reference redox system. The simulated CV for β-carotene was obtained using the same parameters as above, assuming an $E_rE_rC_iE_r$ mechanism.

On-Line EC/ES-MS. A Finnigan-MAT ion trap mass spectrometer (ITMS), modified for pneumatically assisted ES-MS, was used in this work.[33-35] For experiments employing continuous infusion, a syringe pump (Harvard Apparatus, Inc., Cambridge, MA) was used to deliver the analyte solution, through 250 μm i.d. Teflon tubing, to the electrochemical cell. In the floated mode, the solution either exited directly from the cell and was sprayed (tubular electrode cell) or exited the cell and was sprayed from a short piece (~7.0 cm) of 100 μm i.d. (370 μm o.d.) fused silica capillary (Polymicro Technologies, Inc., Phoenix, AZ) taking the place of the metal capillary in the ES source (thin-layer and porous electrode cells). In the decoupled mode, the solution exited the cell through 30 cm of 100 μm i.d. fused silica capillary that attached to a stainless steel spray capillary (6.5 cm long, 127 μm i.d., 500 μm o.d.; Scientific Instrument Services) within the ES source.

For constant potential electrolysis (CPE) experiments in the three-electrode configuration, the electrochemical cell and a home-

(25) Tang, L.; Kebarle, P. *Anal. Chem.* 1993, 65, 3654–3668.
(26) Blades. A. T.; Ikonomou, M. G.; Kebarle, P. *Anal. Chem.* 1991, 63, 2109–2114.
(27) Van Berkel, G. J.; McLuckey, S. A.; Glish, G. L. *Anal. Chem.* 1992, 64, 1586–1593.
(28) Xu. X.; Nolan, S. P.; Cole, R. B. *Anal. Chem.* 1994, 66, 119–125.
(29) Van Berkel, G. J.; Zhou, F. *Anal. Chem.* 1995, 67, 2916–2923.
(30) Van Berkel, G. J.; Zhou, F. *Anal. Chem.*, in press.

(31) Štulík K.; Pacáková, V. *Electroanalytical Measurements in Flowing Liquids*; John Wiley & Sons: New York, 1987.
(32) Wang, J. *Stripping Analysis: Principles, Instrumentation and Applications*; VCH Publishers: Deerfield Beach, FL, 1985.
(33) Van Berkel, G. J.; Glish, G. L.; McLuckey, S. A. *Anal. Chem.* 1990, 62, 1284–1289.
(34) McLuckey, S. A.; Van Berkel, G. J.; Glish, G. L.; Henion, J. D.; Huang, E. C. *Anal. Chem.* 1991, 63, 375–383.
(35) Van Berkel, G. J.; McLuckey, S. A.; Glish, G. L. *Anal. Chem.* 1991, 63, 1098–1109.
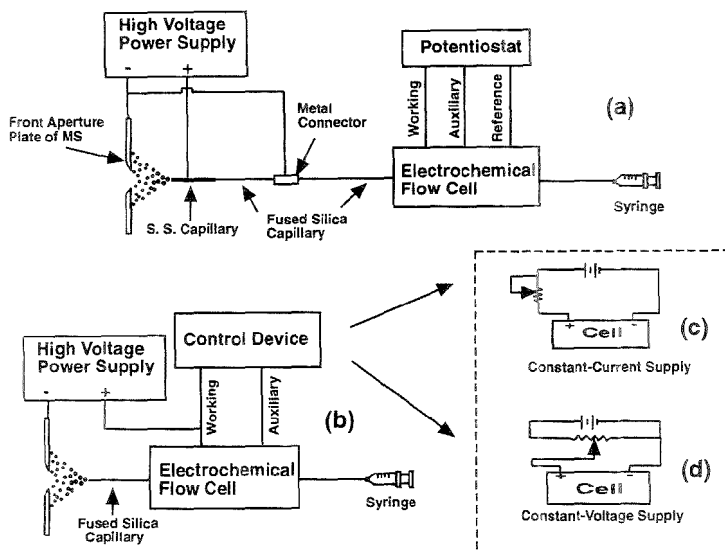
Figure 2. Schematic representations showing the methods used to connect the electrochemical flow cells on-line with the ES source. (a) The decoupled mode, in which a metal connector is connected to the ground of the electrospray high-voltage power supply, and the solution is sprayed from a metal capillary that is connected to the high-voltage end of the supply. In this particular setup, a potentiostat is used to control the working electrode potential in the three-electrode configuration. (b) The floated mode, in which the electrochemical flow cell and the control device are floated at the high voltage of the ES source. The control device in this case was either (c) a constant current supply or (d) a constant potential supply.

built potentiostat were decoupled from the ES high voltage (Figure 2a). A grounded stainless steel zero dead-volume connector (Upchurch Scientific) was connected to the cell exit via a 5.0 cm length of 100 μm i.d. fused silica capillary. The other end of the connector was attached to the metal spray capillary via 30 cm of 100 μm i.d. fused silica capillary. When the floated mode of operation was used (Figure 2b), the cells and circuitry floating at the ES voltage were contained in separate plexiglass boxes with insulated electrode leads used to connect the circuitry (Figure 2c,d) to the electrodes. The constant current source used for constant current electrolysis (CCE) in the two-electrode configuration was a modest voltage supply (i.e., several 9 V batteries) and a 2 MΩ variable resistor (Figure 2c). The circuit used for CPE in the two-electrode configuration consisted of a voltage divider and several 9 V batteries (Figure 2d).

Anodic stripping voltammetry (ASV) of silver on-line with ES-MS was performed in the decoupled mode using the thin-layer cell in the three-electrode configuration. The syringe pump and a plastic syringe were used to deliver a carrier solution (acetonitrile/water/nitric acid (95/5/0.1 v/v/v)) at 40 μL/min to a Rheodyne (Cotati) Model 7066 injector, equipped with a controller and a 1.0 mL sample loop used to inject the analyte solution into the electrochemical cell. Following electrochemical preconcentration of silver from the analyte solution at −2.0 V, the silver was electrochemically stripped (1.0 V) back into the analyte solution for detection by ES-MS.

RESULTS AND DISCUSSION

Electrochemical Flow Cells and On-Line Coupling with ES-MS. Electrochemical flow cells of three different designs, as shown in Figure 1, were used in the present work. The thin-layer electrode cell (Figure 1a), in which solution flows through a thin channel that separates the planar working electrode from the auxiliary electrode, is a typical flow-by cell normally used as an amperometric detector.[31] The tubular electrode cell (Figure 1b) is a very simple flow-through cell based on two tubular electrodes. The downstream electrode is the working electrode, and the upstream electrode serves as the auxiliary electrode. The porous electrode cell (Figure 1c) is also a flow-through cell with solution flowing through the small pores in the porous working electrode and passing by the cylindrical auxiliary and reference electrodes. A cell of this design is typically used as a coulometric detector.[31]

To couple any one of these cells on-line with ES, the cell and the circuitry that operates it must be either floated at the ES high voltage (i.e., 3–5 kV) or somehow decoupled from this voltage. Figure 2 shows our decoupled arrangement (Figure 2a) and the arrangement that we used to float the cells and circuitry at the ES high voltage (Figure 2b). In terms of response time for gas-phase detection, the floated mode is most advantageous since a long transfer line from the cell to the ES source is avoided (see β-carotene data below). Once they were coupled on-line, we were able to operate the cells in two different electrochemical modes, viz., two-electrode CCE or CPE in a two- or three-electrode configuration.[36] The circuitry associated with these different modes of operation is also illustrated in Figure 2. In terms of carrying out EC experiments on-line with ES-MS, we found that

(36) Bard, A. J.; Faulkner, L. R. *Electrochemical Methods: Fundamentals and Applications;* Wiley: New York, 1980.

when either CCE or CPE could be used for an experiment, the CCE mode of operation offered several advantages. These advantages included, among others, the fact that (1) the simple circuitry for CCE is more easily floated at the high ES voltage than the potentiostat required for three-electrode CPE, (2) the reference electrode required for three-electrode CPE is not needed in CCE, (3) CCE is more easily performed in resistive solutions than CPE (i.e., less electrolyte is needed for CCE which benefits ES-MS), and (4) the problem of potential drift in resistive solutions that plagues two-electrode CPE, and can also hinder three-electrode CPE, is avoided in CCE. The latter two advantages are discussed in more detail below. Moreover, disadvantages associated with CCE that make it less commonly used in conventional electrochemical experiments (e.g., detection problems caused by large double-layer charging effects and ill-defined potential–time responses) are not problematic in EC/ES-MS experiments, because detection is accomplished via the mass spectrometer.[36]

Supporting Electrolyte. The 50–100 mM concentration of nonvolatile electrolyte normally used in EC experiments causes problems with plugging and degraded performance of the ES atmospheric sampling interface. Even more significant is suppression of the analyte gas-phase ion signal that can result from this high electrolyte concentration.[20,25] The most commonly used electrolytes (e.g., quaternary ammonium salts) have a very large propensity for gas-phase ion formation, and concentrations even as low as ten to a few hundred micromolar can lead to significant signal suppression.[24] Fortunately, less commonly used but no less functional electrolytes, such as alkali metal salts, e.g., lithium triflate and lithium hexafluorophosphate, have a much lower suppression effect,[20,25] which enabled their use in the present studies at concentrations as high as a few millimolar.[23,30] Moreover, these electrolytes are suitable for use in both aqueous and nonaqueous solvent systems. For aqueous systems, nitric acid at an appropriately low concentration is another suitable electrolyte (see silver data below).

The necessity of using a supporting electrolyte at relatively low concentration (a few millimolar) in EC/ES-MS can compromise the electrochemical portion of the experiment because of high solution resistance. As alluded to above, high solution resistance is more detrimental in CPE than CCE, because the large "iR drop" in resistive solutions makes the actual electrode potential differ significantly from the applied potential. Also, because deviation of the actual electrode potential from the applied potential varies with the magnitude of the faradaic current, the electrode reactions can be difficult to control. High solution resistance is less problematic in CCE since the required current for efficient electrolysis may be supplied by simply increasing the output of the current supply.[36]

Selected Applications of EC/ES-MS. *Electrochemical Ionization of Neutral Compounds.* Previous work has shown that certain types of neutral compounds (e.g., aromatic, heteroaromatic, and other highly conjugated molecules) that are not normally amenable to analysis by ES-MS can be ionized in solution and detected using one of two different electron transfer chemistries, viz., chemical redox reactions[37–42] and the electrolysis process
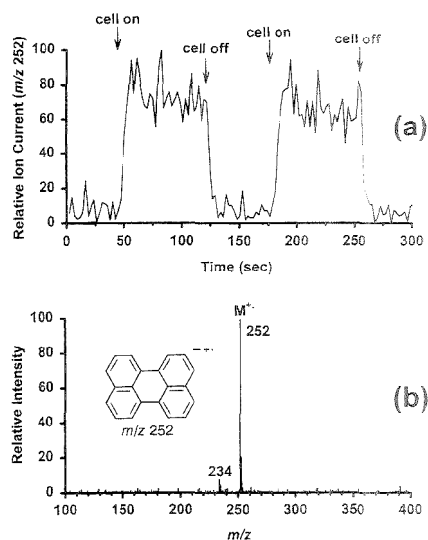
Figure 3. (a) EC/ES-MS extracted ion current profile for the radical cation of perylene (*m/z* 252), demonstrating the electrochemical ionization of perylene using the tubular electrode cell in the floated constant current operational mode. A 0.06 mM solution of perylene (acetonitrile/methylene chloride (1/1 v/v), 40 mM lithium triflate) was continuously infused (40 μL/min) through the cell, and the cell current (140 μA) was turned on and off as indicated. (b) ES mass spectrum obtained with the cell current on.

inherent to ES.[27,28,30] In principle, the same compound types are amenable to ionization and detection using EC/ES-MS. Relative to the use of chemical redox reactions, the EC/ES-MS approach eliminates solution mixing, sample dilution, and the use of highly reactive reagents (e.g., antimony pentafluoride). Furthermore, in some cases, appropriate reagents for analyte ionization may not be available. In comparison to the use of the inherent electrolysis process, the EC/ES-MS approach should afford a higher electrolysis efficiency (because the efficiency of the inherent ES electrolysis process is current-limited)[29,30] and a greater degree of ionization selectivity.

The EC-ES/MS approach for neutral analyte ionization is demonstrated here using the tubular electrode cell operated in the floated CCE mode. Figure 3a is the extracted ion current profile for the radical cation of perylene (*m/z* 252) obtained in a continuous infusion experiment (0.06 mM perylene) in which the cell current (140 μA) was turned on and off. Some amount of radical cation is detected with the cell off. This "electrochemical interference" is due to oxidation of the perylene via the electrolysis process inherent in ES. Because the ES current is low (<1 μA) and the majority of this current is supplied by the oxidation of iron in the stainless steel ES capillary,[26,29] only a small fraction of perylene can be oxidized with the cell off. The constant current source attached to the dual-tube cell supplies a current more than 2 orders of magnitude greater than the ES current. Thus, with

(37) Van Berkel, G. J.; McLuckey, S. A.; Glish, G. L. *Anal. Chem.* **1991**, *63*, 2064–2068.
(38) Van Berkel, G. J.; Asano, K. G.; McLuckey, S. A. *J. Am. Soc. Mass Spectrom.* **1994**, *5*, 689–692.
(39) Van Berkel, G. J.; Asano, K. G. *Anal. Chem.* **1994**, *66*, 2096–2102.
(40) Van Berkel, G. J.; Zhou, F. *Anal. Chem.* **1994**, *66*, 3408–3415.

(41) Zhou, F.; Van Berkel, G. J.; Donovan, B. T. *J. Am. Chem. Soc.* **1994**, *116*, 5485–5486.
(42) Bond, A. M.; Colton, R.; Fiedler, D. A.; Kevekordes, J. E.; Tedesco, V.; Mann, T. F. *Inorg. Chem.* **1994**, *33*, 5761–5766.

the cell current on, a large fraction of the perylene is electrochemically ionized ($E \approx 1.0$ V vs SCE[43]), and the radical cation signal increases by about an order of magnitude.

For reference, Figure 3b is the ES mass spectrum obtained with the cell on. The only other ion observed besides the perylene radical cation is due to an unknown at m/z 234, which is present at the same intensity even with the cell off. Of note in this spectrum is the absence of ions associated with the supporting electrolyte (40 mM lithium triflate) and the excellent signal-to-background levels obtained with just 0.06 mM perylene. In contrast, Bond et al.,[24] using a similar tubular electrode cell online with ES-MS for ionization of neutrals (i.e., diethyldithiocarbamate complexes, 0.2 mM), made use of tetrabutylammonium hexafluorophosphate (0.2 mM) as the supporting electrolyte. The base peak in their spectrum was due to the tetrabutylammonium cation (m/z 242), and they reported significant analyte ion signal suppression. Thus, the data in Figure 3 demonstrate the advantage for EC/ES-MS in choosing an electrolyte for the electrochemistry that also benefits the ES-MS portion of the experiment.

Although not demonstrated here, this or another EC/ES-MS configuration might be used in conjunction with an on-line separation for selective analyte ionization/detection. One might differentiate among those individual compounds in the separated mixture that are ionic (detection unaffected by cell) and those compounds that are neutral but ionizable by electrochemical oxidation/reduction. Appropriate control of cell currents or working electrode potentials should allow for selective ionization/detection among the neutral compounds on the basis of their respective redox potentials.

EC/ES-MS for the Study of Electrode Reactions. The electrochemical ionization data presented above are, in effect, studies of electrode reactions via EC/ES-MS. However, the experimental results presented below illustrate in more detail the variety of information about electrode reactions that can be provided by this technique. Nickel(II) octaethylporphyrin (Ni^{II}OEP) is used as the model compound to demonstrate the utility of EC/ES-MS for the detection of electrochemically generated species via stepwise electron transfer reactions. Ni^{II}OEP is known to undergo two reversible one-electron oxidation reactions ($E_r E_r$ mechanism) in a variety of nonaqueous solvents.[40,44] The peak potential of the first oxidation reaction (E_{pa1}) is 0.84 V, while that of the second oxidation reaction (E_{pa2}) is about 1.37 V (both vs SCE).[40] Because the products of interest are stable, and therefore do not require rapid detection, this work was carried out with the porous electrode cell in the decoupled, three-electrode operational mode.

The plots in Figure 4 show the mass spectral intensities of the monocation (M$^{\bullet+}$, m/z 590) and the dication (M^{2+}, m/z 295) of Ni^{II}OEP (each normalized with respect to the largest signal intensity of the respective species) as a function of the working electrode potential. The respective intensities of these ions with the cell on were extracted from the total ion current profile obtained during continuous infusion (40 μL/min) of a 20 μM Ni^{II}OEP solution (acetonitrile/methylene chloride, 1.0 mM lithium triflate), with the working electrode potential stepped to the appropriate value from open circuit for 10 s and then back to open circuit. Plots such as these are often referred to as mass spectrometric hydrodynamic voltammograms.[3] The CV of

(43) Janz, G. J.; Tomkins, R. P. T. *Nonaqueous Electrolyte Handbook*; Academic Press: New York, 1973; Vol. II.
(44) Fuhrhop, J.-H.; Mauzerall, D. *J. Am. Chem. Soc.* **1969**, *91*, 4174–4181.
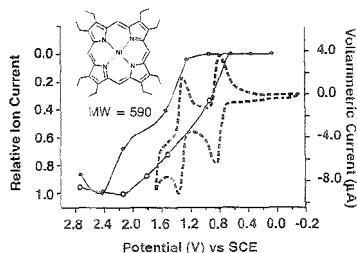
Figure 4. EC/ES-MS hydrodynamic voltammograms for the monocation (m/z 590, ○) and the dication (m/z 295, ●) of Ni^{II}OEP, obtained using the porous electrode flow cell in the decoupled, three-electrode operational mode. The cyclic voltammogram of Ni^{II}OEP obtained in a separate off-line experiment (dotted curve) is also shown. See text for experimental details.

Ni^{II}OEP obtained off-line[40] is also shown in Figure 4 to illustrate the correlation with the hydrodynamic voltammograms. The mass spectrometric hydrodynamic voltammograms, like the CV, clearly indicate that the mono- and dication are formed at two different electrode potentials, the difference in these electrode "appearance potentials" being 0.5 V, which is in good agreement with the peak potential difference measured from the CV (i.e., 0.53 V).

Given the high electrolysis efficiency of the porous electrode cell (approaching 100%), the observation of the monocation at potentials beyond those necessary to form the dication was not expected. Only beyond the potential where the dication reached its maximum level did the signal from the monocation begin to decrease. We attribute this observation largely to the following disproportionation reaction:

$$(\text{Ni}^{II}\text{OEP})^{2+} + \text{Ni}^{II}\text{OEP} \rightarrow 2(\text{Ni}^{II}\text{OEP})^{\bullet+}$$
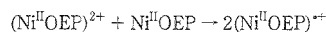
Supporting evidence for the occurrence of this reaction was the peak tailing of the Ni^{II}OEP monocation and dication signals observed after the cell was turned off. We believe this peak tailing is indicative of adsorption of the dication onto the porous graphite working electrode. In this situation, the adsorbed dication would be available for reaction with the neutral Ni^{II}OEP continuously flowing through the electrode.

To illustrate the utility of EC/ES-MS for the study of electrode reactions involving the generation of relatively short-lived species, we chose to study β-carotene. From previous studies, it is known that β-carotene undergoes a two-electron transfer reaction, forming the dication,[40,45–48] which then rapidly undergoes one or more irreversible chemical follow-up reactions, and the products of the follow-up reactions can be reduced ($E_r E_r C_i E_r$ mechanism). The specific follow-up reactions and their rates depend on the solvent system. In methylene chloride, the CV suggested that the follow-up reaction was relatively slow (an estimated dication half-life of several seconds), given that an appreciable reduction wave could

(45) Mairanovsky, V. G.; Engovatov, A. A.; Ioffe, N. T.; Samokhvalov, G. I. *J. Electroanal. Chem.* **1975**, *66*, 123–137.
(46) Grant, J. L.; Kramer, V. J.; Ding, R.; Kispert, L. D. *J. Am. Chem. Soc.* **1988**, *110*, 2151–2157.
(47) Khaled, M.; Hadjipetrou, A.; Kispert, L. D. *J. Phys. Chem.* **1990**, *94*, 5164–5169.
(48) Khaled, M.; Hadjipetrou, A.; Kispert, L. D.; Allendoerfer, R. D. *J. Phys. Chem.* **1991**, *95*, 2438–2442.
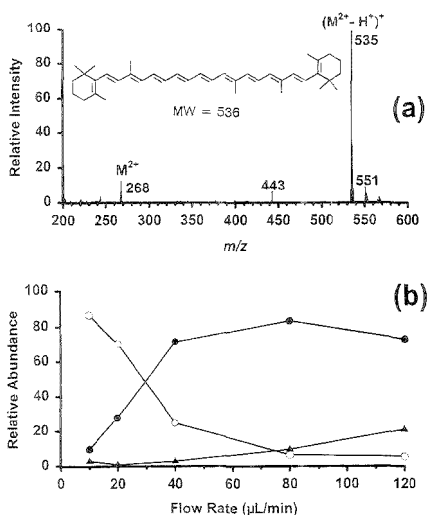
Figure 5. Electrochemical oxidation behavior of β-carotene studied using on-line EC-ES/MS. (a) The ES mass spectrum obtained in an EC/ES-MS experiment, in which a solution of β-carotene (107 μM, acetonitrile/methylene chloride (9/1 v/v), 1.0 mM lithium triflate) was continuously infused (80 μL/min) through the thin-layer cell operated in the floated constant current (9 μA) mode. (b) Plot showing the relative abundances of the three major peaks observed in the EC/ES-MS mass spectra, viz., m/z 268 (▲), 535 (●), and 551 (○), as a function of flow rate.

be observed during the reverse scan at relatively slow scan rates (e.g., 100 mV/s).[40] The CV obtained in acetonitrile/methylene chloride (9/1 v/v, 40 mM lithium triflate, CV not shown) is very similar, except that higher scan rates must be employed to observe a similar reduction wave during the scan reversal, indicating that the lifetime of the dication in this solvent system is significantly shorter than that in methylene chloride. On the basis of a CV simulation using the $E_r E_r C_i E_r$ mechanism for the electrochemical behavior of β-carotene, the half-life of the dication in this solvent system was estimated to be only 0.2 s.

Due to the fact that the dication of β-carotene is short-lived, the thin-layer cell in the floated CCE mode of operation was employed in this EC/ES-MS study. This setup, because of a small dead-volume (~2 μL), minimized the transit time for the electrochemically generated species from the cell to the gas phase. Figure 5a is the mass spectrum obtained by continuously infusing 107 μM β-carotene at 80 μL/min with the cell current on (9 μA). The small peak at m/z 268 corresponds to the dication, M^{2+}. The base peak in the spectrum corresponds in mass to $(M - 1)^+$ and has been previously identified as $(M^{2+} - H^+)^{\bullet +}$ in our work[40] and the work of others.[45-48] The other peak of relatively high abundance in the spectrum, viz., m/z 551, is probably also due to a follow-up reaction of the dication. These identifications are substantiated by the plots in Figure 5b, which show that the relative abundances of these ions (i.e., m/z 268, 535, and 551) are quite dependent on the flow rate, which correlates with reaction time. For flow rates of 10, 20, 40, 80, and 120 μL/min, the respective reaction times (i.e., travel time of analyte from electrochemical cell to tip of spray capillary) are 12, 6.0, 3.0, 1.5, and 1.0 s. Therefore, as might be expected, the abundance of

m/z 268 relative to the products of the follow-up reactions (m/z 535 and 551) is low at low flow rate (longer reaction times) but increases as flow rate increases (shorter reaction times).

Anodic Stripping Voltammetry for Enhanced Trace Element Determination. Methods for the analysis and quantification of elemental species by ES-MS are only in the development stage, and the factors affecting the precision and accuracy of ES-MS in elemental determinations remain to be fully elucidated.[49-51] Nevertheless, ES-MS has shown considerable promise in this area, particularly for elemental speciation and for the determination of elements that have traditionally been difficult to determine by other elemental MS techniques (e.g., halides by inductively coupled plasma MS (ICPMS)). Possibly the most severe limitations for elemental ES-MS of real-world samples will be the need to analyze aqueous-based samples and samples with high salt content (e.g., sea water or urine). Either situation can lead to severe signal suppression.[20,25] One route to circumvent these problems is to employ an on-line preconcentration/cleanup routine along with matrix exchange. In this way, the species of interest can be removed from the troublesome matrix and liberated into a more amenable ES-MS solvent system. An appropriate electrochemical method for this purpose is ASV[32] coupled to ES-MS using the thin-layer flow cell in the three-electrode, decoupled operational mode. In the ASV portion of the experiment, the element of interest is first selectively deposited (reduced/oxidized through control of the electrode potential) onto the working electrode from the flowing sample solution, while any interfering matrix constituents or other elements flow to waste. Next, a clean carrier solution is introduced (if necessary), and the deposited element is selectively oxidized/reduced, i.e., stripped, from the electrode (again through control of the electrode potential) into the solvent system for detection by the downstream mass spectrometer.

Demonstrated here is the ASV/ES-MS analysis of elemental silver (Ag^+). This particular example represents an ideal situation for the ES-MS detection portion of the experiment with our ES instrumentation. Our "home-made" ES interface performs best with singly charged metals. For example, our ES-MS detection levels for doubly charged metals that might also be analyzed by ASV, such as Pb^{2+} and Hg^{2+}, are about an order of magnitude or more higher than the detection levels for Ag^+. In addition, the stripping step in the ASV analysis of Ag^+ (as well as the preconcentration step) can be performed in a solvent system composed of mainly organic solvent. Typically, signal levels for species sprayed from organic solvents (regardless of the ES instrumentation) are an order of magnitude greater than the same species sprayed from water.[20] Most other elements one might analyze by ASV would have to be preconcentrated from and stripped into an aqueous solvent system.

We found that the mixed solvent system of acetonitrile/water (95/5 v/v), containing 0.1% nitric acid provided the best ES signal stability and lowest detection levels for Ag^+ in continuous infusion and flow injection modes of analysis (~10 ppb, 3σ/sensitivity), while also enabling the requisite electrochemistry to be carried out. The nitric acid serves in this case both as the supporting electrolyte for the ASV experiment and as a reagent to keep Ag^+ in solution. Figure 6a shows the overlaid time-resolved response

(49) Agnes, G. R.; Horlick, G. *Appl. Spectrosc.* **1994**, *48*, 649-654.
(50) Agnes, G. R.; Horlick, G. *Appl. Spectrosc.* **1994**, *48*, 655-661.
(51) Stewart, I. I.; Horlick, G. *Anal. Chem.* **1994**, *66*, 3983-3993.
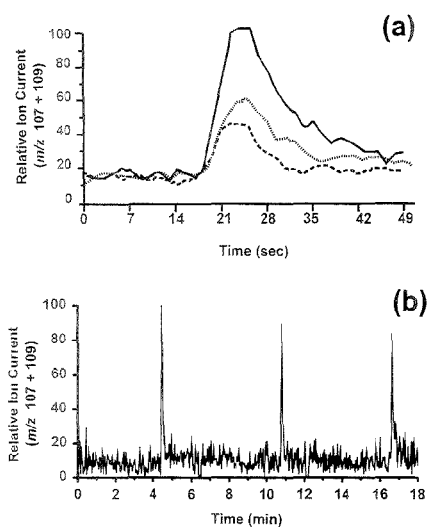
Figure 6. (a) Overlaid, time-resolved ion current responses for Ag^+ (m/z 107 + 109) obtained from three separate ASV/ES-MS experiments in which Ag^+ was preconcentrated from a 100 ppb silver solution (acetonitrile/water/nitric acid (95/5/0.1 v/v/v)) for 1.5 min (dashed curve), 3 min (dotted curve), and 6 min (solid curve) and then stripped into the same solution. (b) Time-resolved ion current response for Ag^+ (m/z 107 + 109) obtained from three sequential ASV/ES-MS experiments in which Ag^+ was preconcentrated from a 1.0 ppb silver solution (acetonitrile/water/nitric acid (95/5/0.1 and v/v/ v)) for 3 min and then stripped into the same solution. The ASV portion of these experiments was carried out using the thin-layer flow cell operated in the decoupled, three-electrode constant potential mode. Preconcentration was performed at −2.0 V and stripping at 1.0 V.

for Ag^+ (m/z 107 + 109) obtained in three separate ASV/ES-MS experiments in which Ag^+ was preconcentrated from a 100 ppb silver solution for 1.5 min (60 μL of sample consumed), 3 min (120 μL of sample consumed), and 6 min (180 μL of sample consumed) and then stripped from the electrode back into the same solvent system. These plots show that as the preconcentration time increased, both the height and area of the stripping peaks increased. This is expected because as the preconcentration time increased, the amount of silver deposited on the electrode also increased. A plot of the peak heights as a function of preconcentration time yielded a linear plot (slope = 1.29) and the preliminary indication of the quantitative nature of the method. Use of an internal standard as described by Agnes and Horlick[49]

(52) Zhou, F.; Van Berkel, G. J.; Morton, S. J.; Duckworth, D. C.; Adenini, W. K.; Keller, . M. *Special Publication of the American Standards and Technology of Materials*, in press.

would be expected to provide the best levels of precision and accuracy in quantitative determinations by ASV/ES-MS.

Figure 6b is the time-resolved response for Ag^+ (m/z 107 + 109) obtained during three sequential ASV/ES-MS experiments in which Ag^+ was preconcentrated from a 1.0 ppb Ag^+ solution for 3 min (baseline of plot before peaks) and then stripped into the same solvent system (peaks in plot). This concentration of Ag^+ is below our ES-MS detection limit of 10 ppb Ag^+. Note that the Ag^+ stripping peak intensities are quite reproducible and about 10 times greater than the signal levels for Ag^+ without preconcentration (baseline of the plot after each stripping peak). This example serves to illustrate that with only a 3 min preconcentration (consuming ~120 μL of sample), the concentration detection levels for Ag^+ may be effectively lowered from 10 ppb without preconcentration to 1 ppb or less with preconcentration. Although not carried out here, the preconcentration coupled with matrix exchange might have been used to eliminate detrimental effects on the ES process due to the sample matrix (e.g., high salt content).[52]

CONCLUSIONS

The results in this paper demonstrate that the problems encountered in coupling EC on-line with ES-MS can be successfully overcome, and any one of a variety of electrochemical flow cells, with various operational modes and coupling methods, can be used in EC/ES-MS for both fundamental and analytical studies. On the basis of this work, the EC/ES-MS hybrid methodology would appear to have the potential to develop into a very versatile and analytically useful EC/MS coupling for the analysis of nonvolatile solution species.

ACKNOWLEDGMENT

High-Resolution Selected Ion Monitoring in a Quadrupole Ion Trap Mass Spectrometer

Greg Wells* and Chuck Huston

Varian Chromatography Systems, Walnut Creek, California 94598

A new method of selected ion monitoring was described that was capable of unit mass isolation throughout the operational mass range of an ion trap mass spectrometer. The trap was first selectively filled with ions via the application of a broad-band waveform to the end caps during ionization. A second isolation step completed the unit mass isolation, leaving only the desired ions in the trap. Following the accumulation and isolation steps, the intensity of the isolated ions was determined by resonantly scanning them from the trap for detection. As many as 10 different masses could be monitored by sequentially applying these steps. The ionization time for each mass was individually adjusted to optimize the filling of the trap with the selected ions; this increased the dynamic range for the set of ions. The individual spectra for each mass could then be added together to form a mass spectrum containing all specified ions.

Selected ion monitoring is a common mass spectrometry technique that is used to increase the signal-to-noise ratio (S/N) of ions (relative to their full scan values). The S/N improvement results from increased transmission efficiency and a reduction in noise due to the increased dwell time associated with the measurement of the selected ion. Ion trap mass spectrometers generally work on a different principle than transmission instruments. Ions are formed in the electron ionization mode by pulsing the ionizing electron beam into the trap for a short period of time to ionize the sample. All of the ions that will contribute to the resulting mass spectrum are formed during this time interval. The trapped ions are then sequentially scanned from the trap for detection in increasing mass order. Since the ions must be scanned from the trap for detection, the signal-to-noise ratio for a particular ion can only be improved by increasing the number of ions of a particular mass-to-charge ratio that are stored.

The storage of large numbers of ions in the trap will result in Coulombic interactions that degrade the sensitivity and resolution of the device. The need to utilize the limited ion storage capacity of the trap has resulted in the development of several techniques to eliminate unwanted ions from the trap and selectively accumulate only specified target ions. Radio frequency (rf) isolation techniques have been used to selectively trap and accumulate ions.[2-4] These techniques establish trap conditions that destabilize

unwanted ions. A significant limitation to this approach is the requirement of moving the operating point of the selected ion close enough to at least one instability boundary so that ions adjacent to the selected ion are removed from the trap by instability ejection.

Ions trapped in a quadrupolar trapping field have amplitude oscillations whose characteristic (or secular) frequencies are functions of the mass-to-charge ratio of the ion and the frequency and voltage of the rf trapping field.[1] The radial or axial motion of the ions can be increased, via resonance excitation, by subjecting the ions to a field whose frequency matches the characteristic frequency of the ion motion. The selectivity of resonance ejection was utilized in early studies of ion trapping processes to eliminate interfering ions.[5] In these studies, a supplemental voltage was added to the end-cap electrodes of the trap to create a dipole field whose frequency matched the secular frequency of the ion to be ejected. The ions in resonance with this field increased their amplitudes in the axial direction until they were ejected. Swept frequency techniques[6,7] for ion ejection have met with limited success due to the low duty cycle for ejection. More recently, broad-band resonance excitation techniques have been described that use inverse Fourier transform (SWIFT) waveforms,[8-12] constructed waveforms,[13-15] or filtered noise.[16-17]

The techniques utilizing broad-band resonance excitation are all similar in that the waveforms have numerous frequency components to eject unwanted ions and notches in the frequency spectrum corresponding to the secular frequencies of the target ions. The waveforms are applied during the ionization period to continuously eject the unwanted ions. Efficient isolation of the target ions requires very narrow notches with frequency compo-

(4) Weber-Grabau, M. U.S. Patent 4,818,869, 1989.
(5) Fulford, J. E.; Hoa, D. N.; Hughes, R. J.; March, R. E.; Bonner, R. F.; Wong, G. J. *J. Vac. Sci. Technol.* 1980, *17*, 829—835.
(6) McLuckey, S. A.; Goeringer, D. E.; Glish, G. L. *J. Am. Soc. Mass Spectrom.* 1991, *2*, 11—21.
(7) Schwartz, J. C.; Jardine, I. *Rapid Commun. Mass Spectrom.* 1992, *6*, 313.
(8) Marshall, A. G.; Ricca, T. L.; Wang, T. L. U.S. Patent 4,761,545, 1988.
(9) Goodman, S.; Hanna, A. U.S. Patent 4,945,234, 1990.
(10) Guan, S.; Marshall, A. G. *Anal. Chem.* 1993, *65*, 1288—1294.
(11) Jullian, R. K.; Cooks, R. K. *Anal. Chem.* 1993, *65*, 1827—1833.
(12) Soni, M. H.; Cooks, R. G. *Anal. Chem.* 1994, *66*, 2488—2496.
(13) Franzen, J.; Gabling, R. H.; European Patent Application EP 0 362 432 A1, 1988.
(14) Shaffer, B. A.; Karnicky, J.; Buttril, S. E., Jr. *Proceedings of the 41st ASMS Conference on Mass Spectrometry and Allied Topics*, May 31—June 4, 1993; pp 802a—802b.
(15) Wells, G.; Huston, C., submitted for publication in *J. Am. Soc. Mass Spectrom.*
(16) Garrett, A. W.; Cisper, M. E.; Nogar, P. H.; Hemberger, P. H. *Rapid Commun. Mass Spectrom.* 1994, *8*, 174—178.
(17) Kelley, P. E.; Hoekman, D.; Bradshaw, S. *Proceedings of the 41st ASMS Conference on Mass Spectrometry and Allied Topics*, May 31—June 4, 1993, 453a—453b.

* Address reprint requests to Varian Chromatography Systems, 2700 Mitchell Dr., Walnut Creek, CA 94598.

(1) March, R. E.; Hughes, R. J. *Quadrupole Storage Mass Spectrometry*; Wiley: New York, 1991.
(2) Fulford, J. E.; March, R. E. *Int. J. Mass Spectrom. Ion Phys.* 1978, *26*, 155.
(3) Eades, D. E.; Yates, N. A.; Yost, R. A. *Proceedings of the 39th ASMS Conference on Mass Spectrometry and Allied Topics*, May 19—24, 1991; p 1491.

nents on each side of the target ion secular frequency to eject the corresponding ions with masses above and below it. The Coulombic influence of space charge on the ion secular frequency, however, can shift the frequency as though a dc field were present.[2] Since there is a finite time required to eject unwanted ions from the trap by resonance excitation, there is some average space charge, throughout the ionization period, in excess of that due only to the target ions. The space charge can shift the secular frequency of the target ions from the theoretical value used to determine the center frequency of the notch. Thus, when narrow notches are used for isolation and a large amount of space charge is present, the secular frequencies of many of the ions may be shifted outside of the notch, causing these ions to be ejected. More recently it has been recognized that, in nonideal ion traps possessing an octopole distortion, the secular frequency of the ion depends on the amplitude.[18] Thus, ions formed far from the center of the trap (e.g., during electron ionization or ion injection processes) will have secular frequencies that are different from the values that they would have at the center of the trap. The use of a buffer gas in ion traps for collisional dampening of the ion oscillations is advantageous for both electron ionization[5,6,19] and ion injection processes.[20-23] It would be expected that ions formed or injected far off center followed by collisional dampening to the center would experience a time-dependent shift in their secular frequencies. Again, the initial frequencies would be different from those located at the center of the notch, causing ejection of some of the target ions.

The most severe limitation to using broad-band waveforms to accomplish both selective ion accumulation and ion isolation is the inability to achieve unit mass isolation at higher masses. In these methods, the rf storage voltage is held constant during the application of the waveforms. Since the electron energy distribution depends on the amplitude of the rf storage voltage, a relatively low value is required to obtain EI spectra that are similar to those obtained from other types of mass spectrometers. The operating point of an ion (the "q_z" value) decreases as the mass increases. This results in a decrease in mass dispersion with increasing mass. Therefore, a waveform with a fixed notch width will trap an increasing mass range as the ion mass increases. For example, ions with $m/z = 100$ and 101 have secular frequencies separated by 2000 Hz at a rf storage voltage of 450 V_{pp}; ions with $m/z = 500$ and 501 have frequencies separated by only 100 Hz. A broad-band waveform that has a 2 kHz wide notch centered at frequencies corresponding to $m/z = 100$ and 500 will isolate $m/z = 100$ from adjacent integer masses, but a range of ions (approximately 20 Da) will be trapped at $m/z = 500$.

This work overcame the limitations that occurred when simultaneous isolation of several ions of greatly differing mass-to-charge ratios was attempted. The method employed in this work utilized a three-step process in which the trap was first selectively filled with the target ion by the application of a broad-band waveform to the end caps of the trap during ionization. The

waveform served to eliminate the unwanted ions from the trap and accumulated ions in a small mass range about the target ion. A second isolation step ejected all remaining unwanted ions and left only the desired ions in the trap. Following the storage and isolation steps, the intensity of the isolated ions was determined by resonantly scanning the ions from the trap for detection. As many as 10 different masses could be monitored by sequentially applying these steps. The ionization time for each mass was individually adjusted to optimize the filling of the trap with the target ions, thus increasing the dynamic range for the set of ions. The individual scans for each mass could then be added together to form a mass spectrum containing all specified ions.

EXPERIMENTAL SECTION
All experiments were performed using a Varian Saturn 3 ion trap (Varian Chromatography Systems, Walnut Creek, CA) and prototype Selected Ion Storage (SIS) software. The Saturn system contained a built-in arbitrary waveform generator (Wave~Board) that applied a waveform to the end-cap electrodes to create a dipolar field. Memory on the Wave~Board allowed for the storage and application of 10 different scan groups and their associated waveforms. Each scan group contained the instrument scan parameters that were required to optimally fill the trap and isolate the selected ions. Additional scan groups and waveforms could be downloaded to the instrument at specified times during a chromatographic run (up to a maximum of 200 acquisition segments) or in real time instrument control. For data taken at slower or faster scan rates than are found in the standard ion trap, data were acquired using a Tektronix digitizing signal analyzer, DSA 601 with a 7A22 differential amplifier (Tektronix Inc., Beaverton, OR).

RESULTS AND DISCUSSION
The motion of an ion in a quadrupole field can be determined from the solution to the Mathieu equation.[1] The stable solutions to the equation are characterized by the parameters q_z and a_z that define the operating point of the ion within the stability region. These parameters are defined as:

$$q_z = 8eV/m(r_0^2 + 2z_0 12)/\Omega^2 \qquad (1)$$

$$a_z = -16eU/m(r_0^2 + 2z_0^2)/\Omega^2 \qquad (2)$$

where V is the amplitude (0 to peak) of the rf potential applied to the ring electrode, U is the dc potential, m is the mass-to-charge ratio (m/z), r_0 is the radius of the ring electrode, z_0 is the inscribed radius of the end-cap electrodes, and Ω is the rf drive frequency. The secular frequency of an ion, ω_z, can be determined from the value of β_z:

$$\omega_z = (\beta_z/2)\Omega \qquad (3)$$

The value of β_z is a function of the operating point in (a_z, q_z) space and can be computed from a well-known continuing fraction.[1] In this work no dc field was applied; thus $a_z = 0$.

Figure 1 shows the general scan function used for this work.[24-26] A broad-band multifrequency waveform WF1 was

(18) Franzen, J. *Int. J. Mass Spectrom. Ion Processes* **1991**, *106*, 63-78.
(19) Stafford, G. C.; Kelley, P. E.; Stephens, D. R. U.S. Patent 4,540,884, 1985.
(20) Van Berkel, G. J.; Glish, G. L.; McLuckey, S. A. *Anal. Chem.* **1990**, *62*, 1284-1295.
(21) Louris, J. N.; Amy, J. W.; Ridley, T. Y.; Cooks, R. G. *Int. J. Mass Spectrom. Ion Processes* **1989**, *88*, 97.
(22) McLuckey, S. A.; Glish, G. A.; Asano, K. G. *Anal. Chim. Acta* **1989**, *225*, 25.
(23) Pedder, R. E.; Yost, R. A.; Weber-Grabau, M. *Proceedings of the 37th ASMS Conference on Mass Spectrometry and Allied Topics*, May 21-26, 1989; p 468.

(24) Bolton, B.; Wells, G.; Wang, M. *Proceedings of the 41st ASMS Conference on Mass Spectrometry and Allied Topics*, May 30-June 1, 1993; p 133.
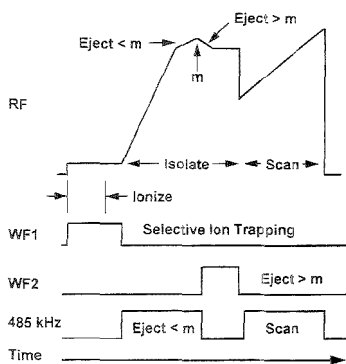
Figure 1. SIM scan function.

applied during the ionization period and for a short "cool time" after the end of ionization. This waveform was constructed of discrete frequency components to resonantly eject ions of mass-to-charge ratio above and below the target ion. This step filled the trap with predominantly the target ions. The remaining ions with masses below the target ion were next removed by resonantly scanning them out of the trap by applying a single-frequency dipole field (485 kHz) to the end caps of the trap and moving the operating point of the ion to $q_z = 0.901$ by increasing the rf trapping voltage V. The remaining ions with masses above the target ion were removed by lowering the operating point of the ion to $q_z = 0.84$ coincident with the application of a broad-band waveform containing frequencies between 20 and 400 kHz with a 500 Hz spacing. Upon reaching $q_z = 0.84$ the rf field was held constant for 2 ml while the waveform remains on. The isolated target ions were then scanned from the trap for detection. This process could be repeated for a maximum of 10 different ions to produce a contiguous series of "group spectra". Each analytical scan was preceded by a prescan which also selectively filled the trap with the target ion and isolated the target ion as in the analytical scan. Thus, the ionization time in the analytical scan was based on the intensity of the mass isolated ion obtained in the prescan. After the individual group spectra were stored to the MS workstation disk, each unique set of group spectra could be added to form a single merged spectrum that contained up to 10 ion mass-intensity pairs.

Figure 2A shows a background spectrum of polysiloxane column bleed from a DB5 column (J&W Scientific, Folsom CA), showing target ions $m/z = 406$, 415, and 431 taken in the ion profile mode. Figure 2B shows the selected ion storage of $m/z = 415$ using a broad-band notched waveform applied to the trap during the ionization period.[15] A notch width of 3.0 kHz and a cutoff mass of 48 Da was used. The observed mass range stored was approximately 10 Da. Narrower notches would improve the isolation slightly but at the expense of the loss of a significant number of the target ions. No measurable ions were stored if a notch width of less than 1 kHz was used. Figure 2C shows the sequential isolation of $m/z = 406$, 415, and 431 (insets). The increased ionization time and the attendant increase in signal-to-
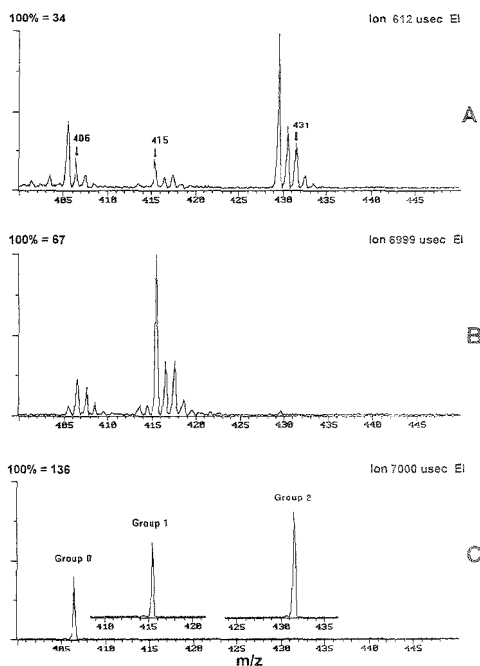
Figure 2. (A) Background spectrum of polysiloxane colum bleed in the ion profile mode. (B) SIS isolation of $m/z = 415$; frequency notch width 3 kHz. (C) Sequential isolation of $m/z = 406$ (group 0); inset $m/z = 415$ (group 1); inset $m/z = 431$ (group 2).

noise ratio was approximately the same for the latter two methods. However, the two-step method used in Figure 2C has the additional advantage of unit mass isolation. This method of selective ion accumulation and isolation has previously been studied as a means of parent ion isolation for GC/MS/MS and was found to have excellent sensitivity and linearity in a variety of complex matrices.[27-30]

Individual spectra could not be merged in the profile mode since these data were not stored to the hard disk. Figure 3A shows the sequential acquisition of the three target ions prior to merging the spectra. Figure 3B shows the results of merging the individual spectra to form merged spectra files containing $m/z = 406$, 415, and 431.

An important application of selected ion monitoring is the detection of co-eluting compounds, particularly isotopically labeled compounds. Figure 4A shows the unmerged chromatogram and spectra of 500 pg of phencyclidine (PCP) and 50 pg of deuterated phencyclidine (D-5 PCP). The ion monitored for the unlabeled PCP was $m/z = 200$ (loss of C_3H_7); the D-5 PCP was monitored using $m/z = 205$. In this example the peak width at half-maximum was approximately 2 s. Eight data points were obtained during

(25) Bolton, B.; Wells, G.; Wang, M. *Proceedings of the 42st ASMS Conference on Mass Spectrometry and Allied Topics*, May 29–June 3, 1994; p 710.
(26) Wells, G. *Quadrupole Ion Trap Improved Technique For Ion Isolation*. U.S. Patent No. 5,198,665, 1993.

(27) Schachterle, S.; Brittain, R. D. *Proceedings of the 41st ASMS Conference on Mass Spectrometry and Allied Topics*, May 30–June 1, 1993, p 178.
(28) Schachterle, S.; Brittain, R. D., Mills, J. *J. Chromatogr. A* 1994, *683*, 185–193.
(29) Feigel, C.; Brittain, R. D. *Proceedings of the 42st ASMS Conference on Mass Spectrometry and Allied Topics*, May 29–June 3, 1994; p 253.
(30) Bolton, B.; Brittain, R. D. M. *Proceedings of the 42st ASMS Conference on Mass Spectrometry and Allied Topics*, May 29–June 3, 1994; p 720.
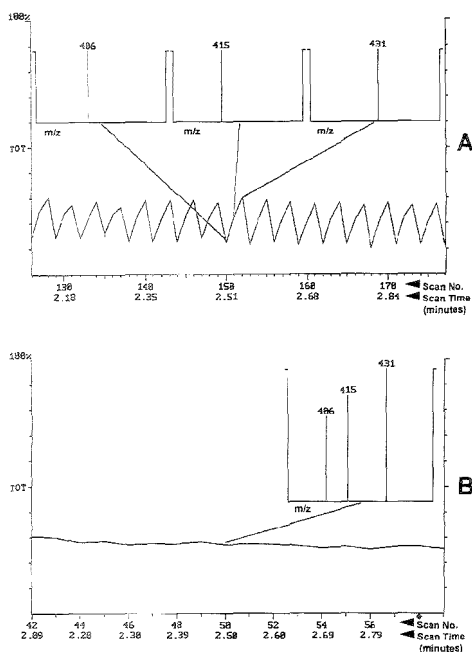
Figure 3. (A) Sequential group spectra in the aquisition centroid mode. (B) Merged spectra from groups 0, 1, and 2.

the half-width (16 across the entire peak), which is adequate for quantitation. Each data point is the result of averaging five microscans of 50 ms duration. Averaging several microscans increases the signal-to-noise ratio and increases the stability of the mass intensity. Reducing the number of microscans would allow more data points to be obtained across a chromatographic peak. The maximum ionization time and peak centroiding represents the majority of the scan cycle time. Experiments that are currently in progress have decreased the cycle time to 16 ms while maintaining the same signal-to-noise ratio. This would allow an acquisition rate greater than 60 Hz for a single mass or over 10 Hz for six different masses. This data frequency is adequate for most applications of capillary chromatography.

Figure 4B shows the chromatogram and spectra from the merged group spectra. The small difference in retention times between PCP and D-5 PCP could easily be seen as a change in relative ion ratios. The difference in retention times was even more apparent in Figure 5, which shows the reconstructed single-ion mass chromatograms for $m/z = 200$ and 205. The minimum detectable amount of PCP was 5 pg (10:1 S/N) injected on-column, and the linear range extended to 1.0 ng (no data greater than 1.0 ng were obtained).

Sequential isolation and detection of each ion had the inherent advantage of allowing the analytical ionization time to be adjusted independently for each ion, thus increasing the useful dynamic range for the set of selected sample ions. The independent adjustment of the ionization time resulted in the complete filling of the trap with ions of a single mass-to-charge ratio. The signal increased linearly with ionization time, and the noise decreased (at most) by the square root of the number of scans that are co-
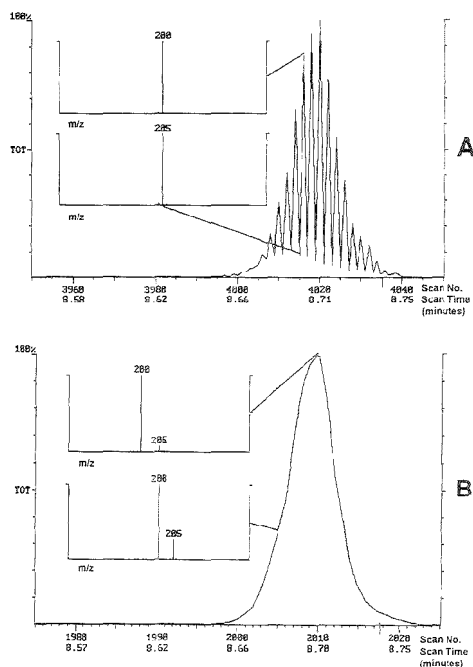
Figure 4. (A) Mass chromatogram of coeluting PCP and D-5 PCP before merging spectra. (B) Mass chromatogram of coeluting PCP and D-5 PCP after merging spectra.
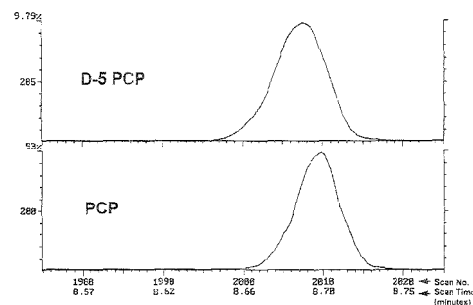
Figure 5. Reconstructed single-ion mass chromatogram for $m/z = 200$ and 205.

added. Therefore, the signal-to-noise ratio will improve faster by maximizing the number of ions of a given mass-to-charge ratio than by averaging several mass scans.

The utility of this method of selected ion monitoring can be better appreciated when the affects of space charge due to background ions from the sample matrix and column are considered. Excess space charge, particularly from masses greater than the target mass, creates a dc field that results in a finite value of a_z (eq 2), even if there is no applied dc voltage to the trap electrodes. The secular frequency (ω_z in eq 3) depends on the operating point (a_z, q_z). The effect of the space charge is to shift the secular frequency to smaller values (toward higher mass). If the space charge distortion is severe, mass peak shapes
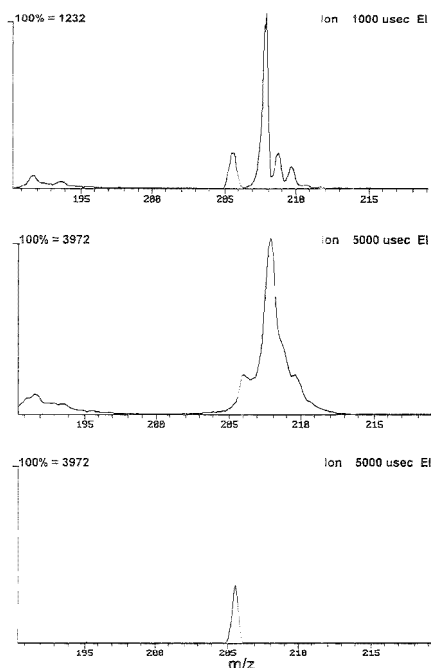
Figure 6. Spectra of D-5 PCP with polysiloxane column bleed background: (A) ionization time 1000 μs.; (B) ionization time 5000 μs; (C) ionization time 5000 μs with m/z = 205 isolated.

Figure 7. (A) HCB and polysiloxane at m/z = 282 isolated to a range of 1 Da and mass scanned at 550 Da/s. (B) HCB isolated and scanned at 550 Da/s. (C) HCB isolated and scanned at 11 000 Da/s.

will be distorted. Figure 6A shows the spectrum of D-5 PCP (m/z = 205) in the presence of polysiloxane column bleed (m/z = 207). Increasing the ionization time (Figure 6B) to increase the sensitivity results in a loss of mass resolution due to space charge effects. When the ion was mass isolated to remove the excess space charge from the m/z = 207 ion, the resolution and sensitivity was restored (Figure 6C). Ions with masses below the target ion do not affect the target ion since they are first removed by resonant scanning. The broad-band waveform (WF2 in Figure 1) was applied at an operating point ($q_z = 0.901$) greater than than the final value ($q_z = 0.84$). At this point, the highest frequency component of the waveform was in resonance with ions several daltons above the target ion mass. The rf field was lowered to slowly reduce the operating point to the final value, resulting in the ejection of high-mass ions in descending mass order. As the unwanted space charge was ejected from the trap, the secular frequency of the target ion shifted back to higher frequencies (toward lower mass) and the resolution and mass position was restored. A notched broad-band waveform utilizing a 2 kHz notch width would still not separate m/z = 205 from m/z = 207 sufficiently to prevent distortion of the PCP ion, particularly when the mass from the polysiloxane is in great excess.

An extension of this technique can be used to obtain high-resolution selected ion monitoring. It is known that increased mass resolution is possible by reducing the rf scan rate during mass analysis.[31-33] It is also possible to increase the resolution during the mass isolation step[34] by reducing the rates at which the rf field is changed. Polysiloxane column bleed interferes with
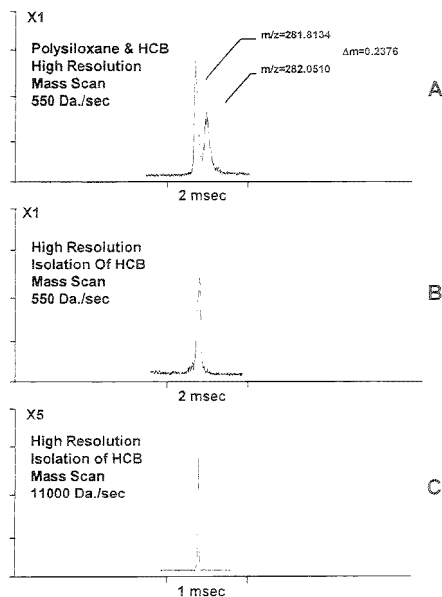
the measurement of ions of hexachlorobenzene (HCB) at the nominal integer mass of m/z = 282. HCB has a mass of 281.8134 Da and the polysiloxane ion has a mass of m/z = 282.0510 Da. Figure 7A shows the high mass resolution scan of these ions at a scan rate of 550 Da/s (10 times slower than the normal scan rate) following isolation of a mass range of 1 Da. Isolation of the HCB ion and high mass resolution scanning (Figure 7B) would reduce space charge effects as in the previous example.[34] Although these ions are resolved, the slow scan rate results in the peak width (at the base) being increased from the normal 180 to 750 μs/Da. If the same number of ions are isolated and scanned out for detection, the peak sensitivity would be reduced by over a factor of 4 due to the slower scan rate. Since it is possible to achieve high mass resolution during the isolation step, it should not be necessary to also scan the ions out of the trap under high-resolution conditions. In Figure 7C the HCB ion is first isolated under high-resolution conditions as in Figure 7B, followed by mass scanning at a rate of 11 000 Da/s (90 μs/Da). A factor of 8 increase in sensitivity was expected to be obtained in this manner. The observed increase was only a factor of 7. It is believed that the peak response at these scan rates was limited by the bandwidth of the electrometer, since the predicted factor of 4 increase was observed when the scan rate was reduced to 180 μs/Da.

(31) Schwartz, J. C.; Syka, J. E. P.; Jardine, I. J. Am. Soc. Mass Spectrom. 1991, 2, 198–204.
(32) Williams, J. D.; Cox, K. A.; Cooks, G. R.; Kaiser, R. E., Jr.; Schwartz, J. C. Rapid Commun. Mass Spectrom. 1991, 5, 327–329.
(33) Londry, F. A.; Wells, G. J.; March, R. E. Rapid Commun. Mass Spectrom. 1993, 7, 43–45.
(34) Schwartz, J. A.; Jardine, I. Rapid Commun. Mass Spectrom. 1992, 6, 313–317.

A significant unknown in this method is the ultimate accuracy of the mass isolation step at very high resolution. The effects of space charge on resolution and mass accuracy become more pronounced as the number of ions in the trap is increased. Traldi[35] reported mass shifts that are related to ion structure. These effects are not completely understood and are the subject of current research.

CONCLUSIONS

A new method of selected ion monitoring was demonstrated that combined the sensitivity enhancement of selective ion accumulation and the specificity of unit mass isolation. Future improvements to this technique would involve the use of higher resolution in the isolation step and faster scanning during the

detection step to reduce the cycle time. Increasing the ionization efficiency would reduce the ionization time required and further reduce the total cycle time for a given mass. The current maximum ionization time that is used is 25 ms. An increase in ionization efficiency by a factor of 5 would allow the maximum ionization time to be reduced to 5 ms while maintaining the same number of ions produced, and thus maintaining a constant signal-to-noise ratio.

(35) Traldi, P.; Cururuto , O.; Bortolini,O. *Rapid Commun. Mass Spectrom.* 1992, 6, 410.

Capillary Electrochromatography–Electrospray Mass Spectrometry: A Microanalysis Technique

Karl Schmeer, Beate Behnke, and Ernst Bayer*

Institut für Organische Chemie, Universität Tübingen, Auf der Morgenstelle 18, 72076 Tübingen, Germany

An electrospray mass spectrometer was coupled to an capillary electrochromatographic system. Peptides were analyzed in a capillary column packed with 1.5-μm reversed phase stationary phase at flow rates of 1−2 μL/min. Supplementary pressure was applied to stabilize the electrochromatographic performance. The interface employed allowed fast and simple installation of the electrochromatographic system to the mass spectrometer, requiring neither sheath flow nor long transfer capillaries. This CEC−MS coupling allows the routine detection of picomole quantities.

Capillary electrochromatography[1-6] can be considered as a variant of reversed phase liquid chromatography performed in packed capillary columns. An electric field is applied across the length of the columns to transport the eluent by electroosmosis. The velocity of the electroosmotic flow is independent of the particle size of the stationary phase over a wide range, thus allowing the use of columns packed with 1.5-μm particles up to a length of 0.5 m. With such columns, efficiencies of more than 200 000 plates/column can be attained,[1-3] comparable to those obtainable in capillary zone electrophoresis (CZE) and thus exceeding by far the efficiency of 30 000 plates generally obtained in HPLC. The use of such small particles in pressure-driven HPLC requires uncomfortably high pressure.

Separation of hydrophobic analytes is easily performed in capillary electrochromatography (CEC) with up to 90% modifier, typically acetonitrile. An instrumentation for gradient elution in CEC has been described recently[4] which allows very flexible tuning of the selectivity analogous to its effect in HPLC. In addition, the selectivity in analysis of charged analytes can be increased by electromigration of the sample molecules comparable to CZE.

To minimize Joule heat, CEC columns with inner diameters of 50−100 μm are generally applied. The flow rate of up to 2 μL/min and loadability of sample quantities in the nanogram range are considerably higher than in CZE, where flow rates in the nanoliter per minute and sample amounts in the picogram range are common. In HPLC, the inner diameter of the columns can be varied over a wide range and correspondingly also the flow rate and loadability. Capillary electrochromatography offers the possibility of sample preconcentration from diluted solutions

analogous to HPLC. This is especially convenient in the gradient elution mode.

A major drawback of pure CEC was the difficulty of obtaining stable flow conditions. As recently demonstrated, this problem is readily overcome by using supplementary pressure.[3-6]

Electrochromatography provides several advantages for coupling to the mass spectrometer. With capillary columns of 100-μm i.d., flow rates of 1−2 μL/min are obtained, a value almost ideal for electrospray-MS. Therefore no interface like a liquid sheath flow analogue to CZE is required. Sintered silica gel frits allow the direct coupling of the packed capillary columns without additional transfer capillaries. The spray is thus formed directly at the outlet side of the column.

On-line coupling of micellar electrokinetic capillary chromatography (MECC) is usually restricted to MS detection due to incompatible amounts of compounds necessary for micelle formation, typically anionic surfactants. A coupling method for hydrophobic analytes in electrodriven techniques has been missing. CEC is closing this gap.

A technique related to CEC is pseudoelectrochromatography.[7,8] Here the eluent is transported by pressure analogous to conventional HPLC, and therefore, the same restrictions to column length, particle size of the stationary phase, and efficiency apply. An electrical field is used for tuning the selectivity in separations of charged analytes.

The first coupling of a pseudoelectrochromatographic system to a FAB-MS was carried out by van der Greef et al. in 1991.[7] The columns used had an inner diameter of 220 μm. These large inner diameters were necessary to provide a flow rate of 5−15 μL/min suitable for the CF-FAB interface. Coupling of a pseudoelectrochromatographic system with columns of the same internal diameter to an electrospray-MS with a sheath flow interface was also demonstrated by the same group in 1993.[8]

A coupling of pure electrochromatography to FAB-MS was reported in 1994 by Gordon and Lord.[9] They presented a separation of steroids in a capillary column of 50-μm i.d. packed to a length of 35 cm with 3-μm particles.

In all approaches published so far,[7-9] transfer capillaries were required to connect the separation columns with the mass spectrometer resulting in loss of efficiency.

In this paper we present and discuss the fist coupling of electrochromatography with supplementary pressure to an electrospray-MS. As will be demonstrated, the eluent is mainly transported by the electroosmotic flow and pressure is only employed to stabilize the EOF at high electrical field strength.

(1) Knox, J. H.; Grant, J. H. *Chromatographia* 1991, *32*, 317−328.
(2) Yamamoto, H.; Baumann, J.; Erni, F. *J. Chromatogr.* 1992, *593*, 313−319.
(3) Smith, N. W.; Evans, M. B. *Chromatographia* 1994, *38*, 649−657.
(4) Behnke, B.; Bayer, E. *J. Chromatogr. A* 1994, *680*, 93−98.
(5) Tsuda, T. *LC-GC* 1992, *5*, 26−36.
(6) Behnke, B.; Bayer, E. *J. Chromatogr.*, in press.
(7) Verheij, E. R.; Tjaden, U. R.; Niessen, W. A. M.; van der Greef, J. *J. Chromatogr.* 1991, *554*, 339−349.

(8) Hugener, M.; Tinke, A. P.; Niessen, W. M. A.; Tjaden, U. R.; van der Greef, J. *J. Chromatogr.* 1993, *647*, 375−385.
(9) Gordon, D. B.; Lord, G. A. *Rapid Commun. Mass Spectrum.* 1994, *8*, 544−548.

The combination of packed capillary columns and interface described provides an optimum of efficiency and sensitivity.

MATERIAL AND METHODS

Preparation of the Packed Capillary Columns. Fused-silica capillaries of 100-μm i.d. and 360-μm o.d. were obtained from Polymicro Technology (Phoenix, AZ). The frits consisted of sintered fused-silica gel (Gromsil, $d_p = 5$ μm; Grom, Herrenberg, FRG) as described in ref 4. The capillary columns for coupling to the mass spectrometer were made by first sintering a frit on the outlet side, slurry packing with reversed phase silica gel (Gromsil ODS-2, $d_p = 1.5$ μm; Grom), and then preparing of the inlet frit. The capillary columns for the UV detection mode were produced as described in ref 4.

Apparatus. The electrochromatographic system consists of a modular capillary electrophoresis system (Grom) combined with a standard HPLC system (Sykam, Gilching, FRG). A Chromatopac C-R6A (Shimadzu, Kyoto, Japan) was used for data processing. Solvent splitting is accomplished by a stainless steel T-piece and a resistance capillary of 50-μm i.d. and 50-cm length. A split ratio of ~1:2000 is obtained at zero electric field strength. The eluent is filtered by a guard column before entering the injection device. The T-piece is grounded to protect the HPLC system from possible damage caused by the high voltage. Injection of ~0.1 μL was accomplished by filling the electrolyte reservoir on the inlet side with 5 μL of sample and pressurizing for 10 s at 200 bar. The reservoir was then flushed with eluent.

Electrochromatography. For the on-line peptide separation, a chromatographic column of 20-cm overall length and 100-μm i.d. was packed to a length of 19 cm with 1.5-μm reversed phase particles. The length of the frits was 0.3 cm each. The supplementary pressure was 180 bar at 0.5 mL/min flow rate of the pump. Separation of peptides in conventional HPLC is usually carried out with acetonitrile water mixtures containing 1 mL/L trifluoroacetic acid (TFA). To avoid bubble formation resulting from excessive Joule heating, the TFA concentration was reduced to 0.07 mL/L. The eluent was acetonitrile–water + TFA (80:20). The concentrations of the peptides were 20 μg/mL each in acetonitrile–water (40:60). Dissolution of analytes in a solvent of lower elution strength than the eluent results in focusing of the sample at the beginning of the stationary phase. Electrochromatography was performed at 20.2 kV and 0.8 μA. The applied potential gradient is given by the difference of +25 kV of the power supply and –4.8 kV of the steel needle.

Mass Spectrometry. All mass spectra were recorded on a Sciex API III triple–quadrupole mass spectrometer, having an electrospray ion source (Sciex, Toronto, Canada) and a m/z range of 2400 dalton. Calibration was carried out with a NaI solution. Spectra were recorded in positive mode (dwell time 0.5–1 ms, step size 0.5–1 amu; data acquired to disk). For data acquisition, data processing and the control of the mass spectrometer a MacIntosh IIx was employed. The orifice voltage was held at 70 V and the needle voltage at 4.8 kV.

EC–MS Interface. The electrochromatographic system was connected to the MS so that the outlet of the separation column was positioned within the inner steel needle of the ion source, thus avoiding long connection capillaries (Figure 1).

The anode was connected to the electrolyte reservoir on the inlet side. To insulate the mass spectrometer against the high voltage, a 1-cm-thick rubber mat was attached to the front side of the mass spectrometer and the column was passed through a
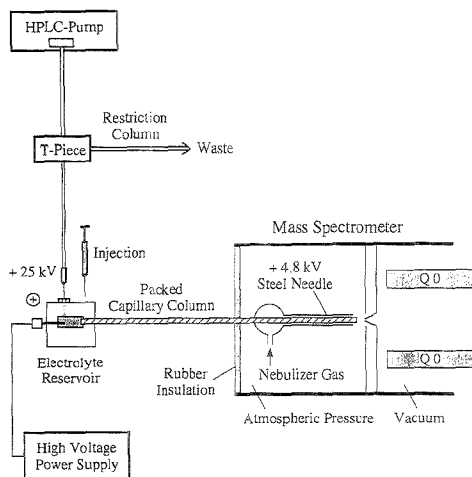
Figure 1. Schematic representation of the setup for capillary electrochromatography–mass spectrometry.
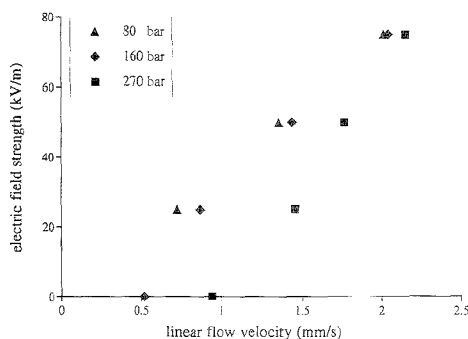
Figure 2. Influence of supplementary pressure and electric field strength on the flow velocity: column, fused silica, 100-μm i.d., 40-cm length, packed for 23 cm, $d_p = 1.5$ μm; buffer, 2.5 mM phosphate, 80% acetonitrile, pH 4; pressure, 80–270 bar with 0.25–1 mL/min.

3-mm hole therein into the interface. Between the power supply for the needle voltage (of the MS) and the steel needle, a 60-MΩ load resistor was inserted.

Chemicals. The peptides were synthesized on an ABI 431A peptide synthesizer using Fmoc chemistry. The Fmoc amino acids were purchased from Nova Biochem (Läufelfingen, Switzerland) and Rapp Polymere (Tübingen, Germany). All other chemicals were products of Fluka (Buchs, Switzerland) and Merck (Darmstadt, Germany). All chemicals for buffer preparation were of research grade.

RESULTS AND DISCUSSION

In electrochromatography with supplementary pressure, the flow velocity is a function of the electric field strength and the applied pressure as shown in Figure 2. Surprisingly, the contributions of pressure-driven and electrodriven flow are not additive. With increasing electroosmotic flow, the influence of the pressure decreases. At an electric field strength of 100 kV/m, the overall
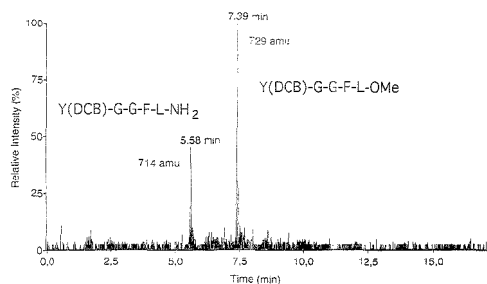
Figure 3. Extracted mass electrochromatogram of *m/z* 714 and 729 for the on-line peptide separation. Conditions as described in the experimental section.

flow velocity is thus almost independent of the applied pressure. For this reason, the ion current detected by the MS collapsed immediately when the anode voltage was switched off.

The high selectivity and separation power of the electrochromatography is demonstrated with a mixture of enkephalin methyl ester and enkephalin amide (Figure 3). The selectivity of the separation is enhanced by electromigration of the sample molecules. At low pH, the amide carries an additional positive partial charge, migrates faster to the cathode, and is therefore eluted first. The electric field strength of 100 kV/m is significantly higher than the 20—60 kV/m typically used in capillary electrophoresis. Thus, the separation was strongly influenced by an electrophoretic separation mechanism.

Here, the first coupling of an electrospray-MS with an electrochromatographic system in which the flow is mainly carried by the electroosmotic flow is presented. Additional sheath flow, which is usually required in CE—MS coupling, is unnecessary on account of the relatively high flow rate of 1—2 µL/min. In addition, the frit at the end of the column enhances the process of spraying, thus also improving the signal intensities in the MS. Therefore, the focused peak reaches the mass spectrometer undiluted. The absence of transfer capillaries eliminates additional postcolumn dispersion. For these reasons, the mass spectrometer detects very narrow peaks of only 4—8-s peak width.

The mass spectra of the corresponding peaks (Figure 4) show a high abundance of Na^+ and K^+ adducts, reducing significantly

(10) Wahl, J. H.; Goodlett, D. R.; Udseth, H. R.; Smith, R. D. *Anal. Chem.* **1992**, *64*, 3194—3196.
(11) Henion, J. D.; Mordehai, A. V.; Cai, J. *Anal. Chem.* **1994**, *66*, 2103—2109.
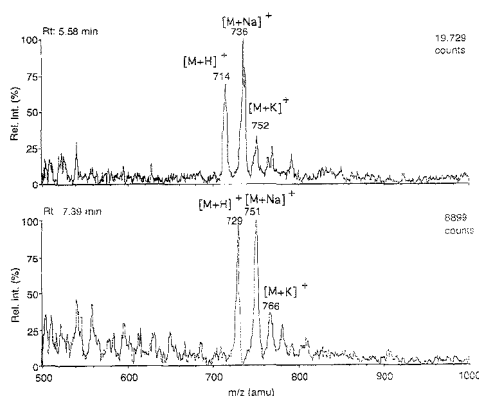
Figure 4. Mass spectra taken from the chromatographic peaks in Figure 3.

the intensity of the protonated species. In order to detect the small amounts of peptide injected (3 pmol) it was found necessary to decrease the resolution of the MS, thus increasing its sensitivity. The alkali metal ions possibly originate from the underivatized silica spheres in the frits. Deactivation by silanization should prevent this phenomenon. Further improvement of the sensitivity is expected by gold coating and narrowing of the outlet side of the capillary column.[5]

With such measures attomole-level detection limits have recently been obtained in CZE—MS coupling.[10,11]

In summary, the coupling of electrochromatography with electrospray mass spectrometry can be regarded as a very promising method. The small amount of sample and the enormous separation power of the CEC combined with the information provided by the MS represent an excellent combination, especially for microanalysis.

ACKNOWLEDGMENT

Determination of Nanogram per Liter Concentrations of Volatile Organic Compounds in Water by Capillary Gas Chromatography and Selected Ion Monitoring Mass Spectrometry and Its Use To Define Groundwater Flow Directions in Edwards Aquifer, Texas

Paul M. Buszka*,†

U.S. Geological Survey, 8011 Cameron Road, Austin, Texas 78754

Donna L. Rose*

U.S. Geological Survey, National Water Quality Laboratory, 5293 Ward Road, Arvada, Colorado 80002

George B. Ozuna and George E. Groschen‡

U.S. Geological Survey, 435 Isom Road, Suite 234, San Antonio, Texas 78216

A method has been developed to measure nanogram per liter amounts of selected volatile organic compounds (VOCs) including dichlorodifluoromethane, trichlorofluoromethane, cis-1,2-dichloroethene, trichloroethene, tetrachloroethene, and the isomers of dichlorobenzene in water. The method uses purge-and-trap techniques on a 100 mL sample, gas chromatography with a megabore capillary column, and electron impact, selected ion monitoring mass spectrometry. Minimum detection levels for these compounds ranged from 1 to 4 ng/L in water. Recoveries from organic-free distilled water and natural groundwater ranged from 70.5% for dichlorodifluoromethane to 107.8% for 1,4-dichlorobenzene. Precision was generally best for cis-1,2-dichloroethene, tetrachloroethene, and the dichlorobenzene isomers and worst for dichlorodifluoromethane and trichlorofluoromethane. Blank data indicated persistent, trace-level introduction of dichlorodifluoromethane, 1,4-dichlorobenzene, and tetrachloroethene to samples during storage and shipment at concentrations less than the method reporting limits. The largest concentrations of the selected VOCs in 27 water samples from the Edwards aquifer near San Antonio, TX, were from confined-zone wells near an abandoned landfill. The results defined a zone of water with no detectable VOCs in nearly all of the aquifer west of San Antonio and from part of the confined zone beneath San Antonio.

Studies in Europe and the United States have found an association between detections of volatile organic compounds (VOCs) in groundwater from unconfined aquifers and urban land uses.[1−4] Potentially important sources of VOCs to groundwater include septic tanks and cesspools, seepage from leaking underground storage tanks, leakage of leachate from landfills, contaminants in urban runoff, and other point sources. Application of sensitive analytical techniques to detect VOCs in groundwater can define their migration and identify sources and processes affecting their concentrations.

Previous investigations of the effects of wastewater on groundwater quality have emphasized determinations of nitrogen and phosphorus species, detergents, fecal coliform bacteria, and VOCs. The nutrient, detergent, and bacterial constituents may be useful only as indicators of pollution after contamination is widespread. In addition, VOCs may be sporadically disposed, not detected by random sampling, or present in concentrations less than the limits of detection of commonly used analytical methods. For example, VOCs used as septic tank cleaners include 1,1-dichloroethane, dichloroethene, 1,1,1-trichloroethane, trichloroethene, and tetrachloroethene.[3,5] Other organic compounds such as the 1,2 and 1,4 isomers of dichlorobenzene and 2,6-di-tert-butyl-p-benzoquinone, have been useful in tracing sewage-contaminated groundwater.[6] These compounds originate from household cleaners, detergents, and disinfectants. They were detected during several of these investigations[1,4,6] at concentrations less than the standard reporting limits of 0.2 μg/L by Method 524.2 of the U.S.

(1) Rivett, M. O.; Lerner, D. N.; Lloyd, J. W.; Clark, L. J. Hydrol. (Amsterdam) 1990, 113, 307−323.
(2) Fusillo, T. V.; Hochreiter, J. J.; Lord, D. G. Ground Water 1985, 23, 354−360.
(3) Eckhardt, D. A.; Flipse, W. J.; Oaksford, E. T. U.S. Geological Survey, Water-Resources Investigations Report 86-4142; U.S. Government Printing Office: Washington, DC, 1986; 35 pp.
(4) Buszka, P. M. U.S. Geological Survey, Water-Resources Investigations Report 87-4116; U.S. Government Printing Office: Washington, DC, 1987; 100 pp.
(5) Canter, L. W.; Knox, R. C. Septic tank system effects on ground-water quality. Lewis Publishers: Chelsea, MI, 1985; 336 pp.
(6) Barber, L. B., II; Thurman, E. M.; Schroeder, M. P.; Leblanc, D. R. Environ. Sci. Technol. 1988, 22, 205−211.

Present address: U.S. Geological Survey, 5957 Lakeside Blvd., Indianapolis, IN 46278.
Present address: U.S. Geological Survey, 102 E. Main St., 4th Floor, Urbana, IL 31801.
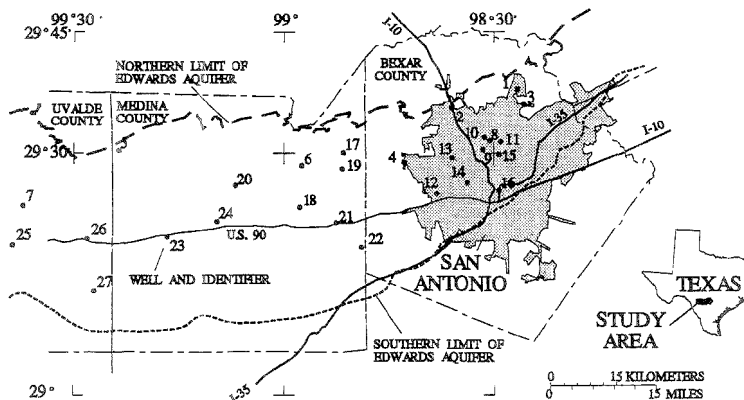
Figure 1. Location of study area, the Edwards aquifer, and wells sampled for this study.

Environmental Protection Agency (USEPA).[7] A reliable method to detect VOCs at smaller, nanogram per liter detection limits could give a useful early warning of water quality degradation to scientists and managers who work with environmental data.

This paper describes a method for determining concentrations of VOCs in water ranging from about 2 to 250 ng/L. This method extracts VOCs from a 100 mL water sample using purge-and-trap techniques. The compounds are separated and identified by gas chromatography/mass spectrometry (GC/MS) in the selected ion monitoring (SIM) mode. The instrumental time of 55 min/sample allows the automated analysis of several samples per day. This procedure, identified as the SIM method, was applied to analyses for nine target VOCs. The target compounds included *cis*-1,2-dichloroethene (*c*-DCE), dichlorodifluoromethane (DCDFM), 1,2-dichlorobenzene (1,2-DCB), 1,3-dichlorobenzene (1,3-DCB), 1,4-dichlorobenzene (1,4-DCB), 2,6-di-*tert*-butyl-*p*-benzoquinone (DBQ), tetrachloroethene (PCE), trichloroethene (TCE), and trichlorofluoromethane (TCFM).

Several methods have been reported to determine VOCs in natural water. These include purge-and-trap extraction of 25 mL samples with conventional GC/MS analysis (PT),[8] adsorption—thermal desorption (ATD) onto a sorbent trap with GC/MS analysis (ATD),[9] pentane extraction followed by GC analysis with electron capture detection (ECD),[10] and extraction by closed-loop stripping with GC/MS analysis (CLS).[11] The SIM method should have lower reporting limits than PT because of the greater sensitivity of SIM and the larger mass of potentially extractable VOCs in a 100 mL sample. The SIM method uses a more commonly available extraction apparatus than the ATD method.

Recoveries of target compounds by purge-and-trap extraction are generally superior to those reported for CLS.[11] Reporting limits of the SIM method should be comparable to those of the ECD method because of the enhanced sensitivity of the MS detector when run in the SIM mode.[12] The SIM method, unlike ECD, limits the chance for mistaken identification of coeluting compounds as target VOCs by identifying the target VOCs from their retention times and from the masses of selected ion fragments. These characteristics indicate the potential of the SIM method to detect nanogram per liter concentrations of VOCs in water. These very small concentrations may be sufficiently small to warn of groundwater contamination in its early stages.

The SIM method was applied to determine potential VOC tracers of groundwater flow and potential contamination in water from 27 domestic and public supply wells in the Edwards aquifer in Bexar, Medina, and Uvalde Counties near San Antonio, TX (Figure 1). The Edwards aquifer is a very permeable, dissolution-modified, and faulted limestone and is the sole source of water for about 1.5 million people in the city of San Antonio and most of the adjacent counties to the west and northeast.

Outcrop and hydraulically unconfined parts of the aquifer under urbanized areas have been previously demonstrated to contain VOCs in concentrations that are generally less than $2\,\mu g/L$.[4] No VOCs were observed in water from deeper, hydraulically confined parts of the aquifer below central San Antonio.[4] Hydraulically confined zones of the aquifer provide the best productivity for water supply. Vertical displacements of 50% or more along faults through the aquifer have been hypothesized as barriers to groundwater flow. These barriers would redirect groundwater flow containing VOCs toward the northeast, away from the confined zone under San Antonio. The aim of this application was to determine whether SIM method analyses were useful in defining regionally important sources of recharge and fault barriers to contaminant flow.

EXPERIMENTAL SECTION

Note: Use of firm or trade names in this article is for identification purposes only and does not constitute endorsement

(7) Guidelines establishing test procedures for the analysis of pollutants under the Clean Water Act. *Code of Federal Regulations*, Part 136, Oct 26, 1984; U.S. Government Printing Office: Washington, DC, 1984; *Fed. Regist.* **1984**, *40*, 198–199.

(8) Wershaw, R. L.; Fishman, M. J.; Grabbe, R. R.; Lowe, L. E., Eds. U.S. Geological Survey, Techniques of Water-Resources Investigations, Book 5; U.S. Government Printing Office: Washington, DC, 1987; Chapter A3, 80 pp.

(9) Pankow, J. F.; Isabelle, L. M.; Hewetson, J. P.; Cherry, J. A. *Ground Water* **1985**, *23*, 775–782.

(10) Eklund, G.; Joseffson, B.; Roos, C. *J. High Resolut. Chromatogr., Chromatogr. Commun.* **1978**, *7*, 34–40.

(11) Barber, L. B., II. Geochemistry of organic and inorganic compounds in a sewage contaminated aquifer, Cape Cod, Massachussets. M.S. Thesis, University of Colorado, Boulder, CO, 1985.

(12) Millington, D. S.; Norwood, D. L. In *Organic Carcinogens in Drinking Water: Detection, Treatment and Risk Assessment*; Ram, N. M., Calabrese, E. J., Christman, R. F., Eds.; John Wiley and Sons: New York, 1986; pp 131–152.
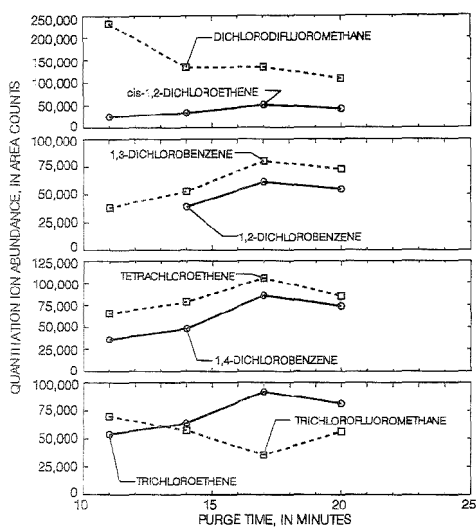
Figure 2. Variation of compound abundance with purge time from 50 ng/L spiked samples.

by the U.S. Geological Survey.

Apparatus. The equipment used for the SIM procedure included the following items: (1) a purge-and-trap unit, Tekmar Models LSC 2000 and ALS 2032; (2) purge vessels with a 100 mL capacity with fritted glass at the sparge inlet; (3) a 0.2667 cm i.d. trap that was packed to a total length of 25 cm with one-third each of Tenax, silica gel, and charcoal, followed by a 1 cm length of OV-1 column packing; (4) a gas chromatograph/mass spectrometer (Hewlett Packard 5996) equipped with a jet separator; and (5) a DB-624 megabore capillary column, 30 m × 0.53 mm i.d., with a 3 μm film thickness.

To determine the best purge time, four 50 ng/L standards containing the eight target compounds were purged with helium at a flow rate of 40 mL/min for 11, 14, 17, and 20 min. The amount of each compound purged from the standards was determined by the abundance of the quantitation ion for each compound. The greatest amounts of *c*-DCE, 1,2-DCB, 1,3-DCB, 1,4-DCB, PCE, and TCE were purged from the standards using a 17 min purge time (Figure 2). The greatest amounts of DCDFM and TCFM were removed from the sample using a purge time of 11 min (Figure 2). A purge time of 15 min was selected for the SIM method as a compromise.

The VOCs were collected on the trap at room temperature and desorbed onto the GC column at 180 °C for 4 min. The transfer line extending from the purge-and-trap unit to the megabore column was composed of silica (0.32 mm i.d.), externally coated with aluminum. The transfer line was inserted directly into the column, eliminating the injection port. The transfer line and valve temperatures were set at 100 °C.

The gas chromatograph was operated using the following program: isothermal operation at 10 °C for 5 min, heated using a linear temperature increase to 190 °C (6 °C/min), and then isothermal operation at 190 °C for 2 min. The trap was baked at 225 °C for 8 min after desorption to prepare the trap for the next analysis. The oven was then allowed to cool for 10 min before

the next sample injection. The total time required for each analysis was 55 min. The carrier gas was helium at a flow rate of 15 mL/min. The instrument was tuned to pass bromofluorobenzene criteria[7] in the full-scan mode.

The SIM mode was chosen for this analysis to get the greatest analytical sensitivity from the GC/MS equipment. Three ions were chosen for each compound. These ions were scanned for 333 ms each, for a total scan time of 1 s. The ion chosen for quantitation was usually the base peak. When a target compound interfered with the base peak scan, a secondary ion was used for quantitation. The quantitation ion, the secondary ions, and the retention time for each of the target VOCs are listed in Table 1. The source and analyzer temperatures were both 200 °C, and the GC/MS transfer line temperature was 170 °C.

Reagents. All stock standards described in this method were made using commercially available, high-purity, purge-and-trap grade methanol. Five microliter aliquots of a 1 μg/mL solution containing the surrogate and internal standards (SURRIS) were added to every standard and sample to check the performance of the operating system. The internal standards were 1,2-dichloroethane-d_4 and 1,2-dichlorobenzene-d_4. The surrogate standards were fluorobenzene, toluene-d_8, and 1,4-bromofluorobenzene. A quality control check standard containing 5 μg/mL each of the VOCs was prepared from standards obtained from the USEPA.

Organic-free distilled water for field and equipment blanks was prepared by boiling distilled water for 1 h and chilling the water with ice. The water was analyzed and determined to be free of contaminants. The water was bottled in cleaned and burned 1 L glass bottles with Teflon-lined septum plastic lids. All instrument blanks were prepared using 100 mL of organic-free distilled water spiked with SURRIS.

Laboratory Procedures. To ensure the integrity of the analytical procedure, several steps were taken to lessen background interferences. Each vessel was purged with helium for 25 min before the analysis. After all the purge vessels had been cleaned, the trap was baked for 30 min at 225 °C. An instrument blank was analyzed before sample analysis to determine if instrument and laboratory background concentrations of the target VOCs were acceptable. Separate 250 mL syringes were used for loading samples and standards. The syringes were cleaned before and after each use with sequential rinses of methanol, organic-free water, and sample.

To prepare the sample at the laboratory for analysis, 100 mL was introduced into a clean 250 mL syringe equipped with a Luer-Lock fitting. The plunger was inserted, and residual air was vented through the syringe valve. Five microliters of the SURRIS standard was injected through the syringe valve. The sample was transferred into a clean 100 mL purge vessel and analyzed using the protocol described in the Apparatus section. The groundwater samples were analyzed in duplicate or triplicate within 12 days of collection.

A five-point calibration curve was generated before analysis for each of the chlorinated VOCs using a concentration range from 10 to 250 ng/L. The calibration curve for DBQ ranged from 200 to 2000 ng/L. Working standards were prepared by spiking 100 mL portions of organic-free distilled water in a 250 mL syringe with the appropriate amounts of SURRIS and stock solutions. The standard was transferred to a clean 100 mL purge vessel and analyzed according to the protocol in the Apparatus section. A response factor (RF) was determined for each target compound

Table 1. Retention Times of the Target, Internal Standard, and Surrogate Standard Compounds and Their Characteristic Quantitation and Secondary Ions

compound name	absolute retention time (min)	m/z^a quantitation ion	m/z^a secondary ions	internal standard reference[b]
		Target Compounds		
cis-1,2-dichloroethene	9.72	96	60, 61*	1
1,2-dichlorobenzene	23.90	146*	148	2
1,3-dichlorobenzene	23.11	146*	111, 148	2
1,4-dichlorobenzene	22.89	146*	111, 148	2
dichlorodifluoromethane	2.30	85*	50, 87	1
2,6-di-tert-butyl-p-benzoquinone	34.49	177	135, 220	2
tetrachloroethene	16.35	166*	164, 166	2
trichloroethene	12.76	132	130*, 132	1
trichlorofluoromethane	4.19	101*	66, 103	1
		Internal Standard Compounds		
1,2-dichlorobenzene-d_4	23.85	152	150*	2
1,2-dichloroethane-d_4	11.34	65*	67, 102	1
		Surrogate Standard Compounds		
1,4-bromofluorobenzene	23.85	95*	174, 176	na
fluorobenzene	12.01	96*	50, 70	na
toluene-d_8	15.97	98*	70, 100	na

[a] An asterisk indicates the ion is the base peak for that compound. [b] na, not applicable.

at each concentration using the following calculation:

$$RF = \frac{A(c)\,C(i)}{A(i)\,C(c)}$$

where $A(c)$ is the GC peak area of the quantitation ion for the compound or surrogate standard, $A(i)$ is the GC peak area of the quantitation ion for the internal standard, $C(i)$ is the concentration of the internal standard (in ng/L), and $C(c)$ is the concentration of the compound or surrogate standard (in ng/L).

The quantitation ion and internal standard assignment for each VOC are listed in Table 1. If the relative standard deviation (RSD) of the response factors was <20%, the average response factor was used for quantitation. If the RSD was >20%, a first or second degree curve was used for quantitation.

A daily standard, prepared at a concentration of 50 ng/L, was analyzed to determine if the instrument was operating within specifications. A response that was within 30% of the average response factor in the calibration curve was achieved by this method. A response within 40% of the concentration of a daily quality control standard was also achieved by the method. These responses meet the guidelines set by the USEPA for Method 524.2.[7]

Method detection levels (MDLs) were determined using standard procedures.[7] Method precision was determined by analyzing seven spiked replicates at two concentrations, 10 and 200 ng/L, in organic-free distilled water and a natural groundwater from the project area. The natural groundwater was collected from well TD-68-33-202. It had, at the time of collection, a pH of 7.1, a temperature of 22.5 °C, a specific conductance of 456 µS/cm, and a dissolved oxygen concentration of 4.4 mg/L.

To identify a VOC in a sample, the retention time of the VOC had to agree within 0.1 min of the daily standard, and the ion abundances in the mass spectrum had to agree with their abundances in the daily standard. If a VOC was detected at or near the MDL, a duplicate, and in some cases a triplicate, was analyzed. All samples were also analyzed by USEPA Method 524.2.[7] In this manner, the identity of each VOC was confirmed by a full-scan spectrum if the amount detected was >10–20 ng/

L. Once an identification was made, the amount present was quantified using the following formula:

$$C = \frac{C(i)A(c)}{RF(c)A(i)}$$

where C is the concentration of the VOC in the sample in ng/L, $C(i)$ is the concentration of the internal standard in ng/L, $A(i)$ is the area of the quantitation ion of internal standard, $RF(c)$ is the average response factor for the VOC detected, and $A(c)$ is the area of the quantitation ion of the VOC.

If any VOCs were detected in the daily blank, the amount detected was considered when reviewing data at the MDL. For example, if TCE was detected at 2 ng/L in the daily blank, and it was detected in the sample at 4 ng/L, the concentration of TCE would be reported as <4 ng/L.

Field Procedures. Groundwater samples were collected from large-capacity public supply wells and from domestic wells. Samples were collected after the water temperature, specific conductance, and pH were observed to stabilize and after at least three casing volumes had been purged. Samples were collected from faucets located at the wellhead using cleaned and burned, washerless brass hose bibs and copper tubing. The sample bottles were slowly filled from the bottom and allowed to overflow before being sealed. Five bottles were filled consecutively from each site and are called "replicate samples". All samples were chilled to 4 °C immediately after collection and stored at that temperature until analysis. Chemical preservatives were not added to the samples collected for this study.

The potential intrusion of the target organic compounds into the sample during storage and shipment was tested using a set of three, triplicate trip-blanks. Organic-free water was sequentially prepared at the laboratory and shipped to the USGS office in San Antonio. From the office, it was transported to well 6 and poured into nine 250 mL sample vials. The sample vials consisted of precleaned 250 mL amber glass bottles that were sealed with a Teflon-lined septum lid cap. One set of three trip-blanks was immediately chilled and shipped for next-day delivery in iced, sealed coolers to the USGS National Water Quality Laboratory in

Table 2. Method Statistics for the Target Compounds

compound name and concn in water matrix[a]	organic-free distilled water matrix		natural groundwater matrix		minimum detectable concn[a]
	% recvrd	RSD	% recvrd	RSD	
cis-1,2-dichloroethene					
10	104.4	8.2	103.8	8.3	2
200	100.6	3.7	103.8	2.2	
1,2-dichlorobenzene					
10	100.5	7.3	98.4	7.5	1
200	106.2	7.5	107.3	3.2	
1,3-dichlorobenzene					
10	94.3	6.0	95.3	5.9	1
200	100.4	5.3	102.9	2.3	
1,4-dichlorobenzene					
10	90.8	6.3	98.4	7.5	1
200	106.	5.5	107.8	2.2	
dichlorodifluoromethane					
10	81.6	24.2	96.8	11.0	4
200	70.5	18.9	91.4	7.6	
2,6-di-*tert*-butyl-*p*-benzoquinone					
500	93.5	16.9	61.8	14.4	180
2000	88.2	8.8	87.3	11.3	
tetrachloroethene					
10	106.6	7.2	98.5	3.1	2
200	90.8	6.4	93.1	4.4	
trichloroethene					
10	99.5	20.1	99.8	8.9	4
200	112.1	16.8	101.7	2.4	
trichlorofluoromethane					
10	82.9	16.9	97.1	4.7	3
200	84.4	10.1	91.6	6.6	

[a] Concentrations are in nanograms per liter.

Arvada, CO, for analysis. The other two sets of three samples were held for 1 and 2 days, respectively, before shipment in a refrigerator at the San Antonio office to determine sample storage interferences. All trip-blanks were analyzed immediately upon arrival at the laboratory. Data from these analyses were compared with those from an analysis of organic-free water that had been stored in the San Antonio office refrigerator for 34 days. The "34-day" water was stored without headspace in a 1 L precleaned glass bottle with a standard Teflon-lined cap.

RESULTS AND DISCUSSION

Laboratory Study. The MDLs determined for the SIM method ranged from 1 ng/L for 1,2-DCB and 1,4-DCB to 4 ng/L for TCE and DCDFM (Table 2). These values represent the MDL with a 99% confidence interval. The typical reporting limit for standard PT analyses of these VOCs by USEPA Method 524.2 is 200 ng/L.[7] The lower MDLs for SIM analyses are from 50–200 times lower than the MDLs from standard PT analyses. The primary reason for the lower detection limits is the use of SIM as compared to the scanning mass spectrometry that is used in standard PT analyses. The occasional presence of smaller concentrations of these target compound in the laboratory environment prevents the achievement of an additional decrease in MDLs that is possible using the SIM method as compared to the full-scan mode.[12]

Recoveries of the seven spiked replicates in two matrices ranged from 82 to 112% for all the chlorinated VOCs except DCDFM (Table 2). The recoveries of DCDFM at 200 and 10 ng/L concentrations in organic-free distilled water were 71 and 82%, respectively. The recoveries of DCDFM from the natural matrix at the same concentrations were 97 and 91%, respectively. Larger

recoveries of TCFM also were obtained from the natural matrix than from the organic-free distilled water (Table 2). The lower recoveries of DCDFM and TCFM may reflect their enhanced solubility in a matrix with fewer dissolved solids. These recoveries are all within recommended tolerances for EPA Method 524.2 for these same compounds.[7]

The MDL for DBQ was 180 ng/L (Table 2). DBQ is more polar and less volatile than the chlorinated VOCs, enhancing its retention in the aqueous phase and increasing the difficulty of its desorption from the trap. Consequently, DBQ was not purged or desorbed as efficiently as chlorinated VOCs, resulting in a higher MDL. The calibration curve had a RSD ranging from about 20 to 40%. A second-degree equation was used for quantitation.

The recoveries of the seven spike replicates ranged from 62 to 94% for DBQ. The recovery of DBQ at a concentration of 500 ng/L from the natural groundwater matrix was 62%. The recovery of DBQ at 2000 ng/L from the natural matrix was 87%. The recoveries were 94 and 88%, respectively, for the same concentrations from the organic-free distilled water matrix.

This method is suitable for samples containing <1 μg/L of the selected chlorinated VOCs but has not been evaluated for greater concentrations. EPA Method 524.2 is more suited to detect concentrations of VOCs that are >1 μg/L. All samples in this groundwater study were first analyzed by EPA Method 524.2 to determine if concentrations of VOCs greater than 1 μg/L were present.[7] Concentrations of VOCs greater than 10 μg/L could easily saturate the mass spectrometer using the SIM method.

The amount of water vapor that is transferred during the desorb cycle also can interfere with the SIM analysis. This was shown by a shift of the baseline between 10 to 14 min and a significant increase in the amount of water seen in the ion source

Table 3. Summary Statistics for Concentrations of the Target Compounds in Laboratory-Prepared Blank and Field-Prepared Trip-Blank Samples

| | laboratory-prepared blank sample | | | | field-prepared trip-blank sample | | | |
| | | concn (ng/L)[a] | | | | concn (ng/L)[a] | | |
compound name	no. of samples	min	med	max	no. of samples	min	med	max
cis-1,2-dichloroethene	37	<2	<2	<2	14	<2	<2	<2
1,2-dichlorobenzene	37	<1	<1	4	14	<1	<1	<1
1,3-dichlorobenzene	37	<1	<1	4	14	<1	<1	<1
1,4-dichlorobenzene	37	<1	<1	4	14	<1	2	12
dichlorodifluoromethane	37	<2	2	23	14	<4	<4	106
2,6-di-*tert*-butyl-*p*-benzoquinone					14	<180	<180	<180
tetrachloroethene	37	<1	1	4	14	<1	2	4
trichlorofluoromethane	37	<1	<1	7	14	<3	<3	13
trichloroethene	37	<2	2	9	14	<4	<4	<4

[a] Min, minimum; med, median; max, maximum.

while monitoring for mass 18. This baseline shift or "water bump" is caused by the gradual elution of water vapor from the GC column during heating. Trichloroethene and fluorobenzene (SS1) were the only compounds that eluted near the water bump. The daily response factors were sensitive to the position of the water bump. Using a shorter desorption time may reduce the size of the water bump and associated interferences but may also decrease the recovery of the less volatile target compounds.

The concentrations of all target compounds except DCDFM, PCE, and TCE in the laboratory blanks generally remained below their respective MDLs. The median concentrations of DCDFM, PCE, and TCE in the laboratory blanks were equal to their MDLs (Tables 2 and 4). The MDLs of DCDFM, PCE, and TCE were limited by chemical interferences rather than instrumental sensitivity. All target compounds except *c*-DCE were detected in at least one sample in concentrations greater than the MDL. Laboratory blanks were analyzed daily and before and after analysis of groundwater samples or standards to determine background levels of target compounds. Over the course of the project, a total of 37 laboratory blanks were analyzed (Table 3). As a precaution, the minimum reportable concentration for target compounds in water samples, called the "method reporting limit", was set to twice the interfering concentration when it exceeded the MDL. These data indicate the need for analysis of blanks immediately before, during, and immediately after analyses of samples to identify background interferences.

Field Study. 1,4-DCB and PCE were detected in more than 50% of the 14 trip-blanks analyzed by this study (Table 3). DCDFM, 1,4-DCB, and TCFM were present at the highest concentrations of any target compounds in the trip-blanks. When a target compound was detected in a trip-blank, its reporting limit for that set of samples was adjusted to twice the interfering concentration.

An analysis of the trip-blank data revealed persistent, trace-level introduction of DCDFM, 1,4-DCB, and PCE to the samples during storage and shipment (Figure 3). Shipping-related contamination is indicated by the detection of 1,4-DCB and PCE in the samples not held at the San Antonio office before shipment to the laboratory (0 days stored, Figure 3). Storage-related contamination is indicated by the increase in DCDFM and PCE concentrations with the time held in the San Antonio office refrigerator. These three compounds were not detected in the organic-free distilled water before it was shipped to the San Antonio office. These data all indicate that the sample containers
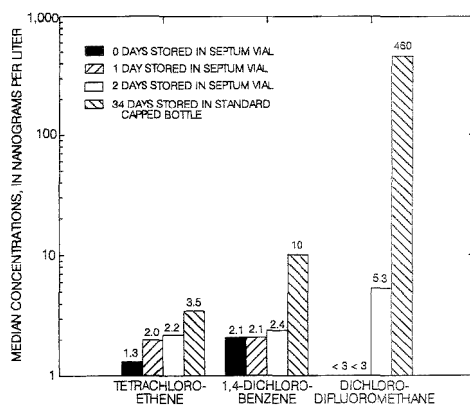
Figure 3. Changes in concentrations of selected target compounds in trip-blank samples with respect to duration of refrigerator storage.

are permeable to trace concentrations of the target compounds in the shipping and office environments. 1,4-DCB is commonly used as a fumigant and as a disinfection agent in washrooms.[13] DCDFM is common in the environment because of its use and release from refrigeration devices.[13,14] PCE is a commonly used solvent and degreaser.[13] Contamination attributable to storage at the laboratory before analysis was not noted, possibly because of the more stringent monitoring and restrictions on use of these compounds at the laboratory. These data show that rapid shipment of all samples and stringent monitoring of blank samples must be an integral part of the SIM method if septum vials are used.

Samples were held in the San Antonio office for 2 days or less before shipment to the laboratory. The trip-blank data indicate that potential contamination of these samples by entry of target compounds into the vials is less than the method reporting limits (Figure 3, Table 4).

Specific conductance values in groundwater samples ranged from 450 μS/cm at well 9 to 607 μS/cm at well 10. The pH values in water from these wells ranged from 6.7 at wells 7 and 25 to 7.7 at wells 18 and 19. The water samples all contained calcium and

(13) Montgomery, J. H.; Welkom, L. M. *Groundwater chemicals desk reference*; Lewis Publishers: Chelsea, MI, 1989; 640 pp.
(14) Thompson, G. M.; Hayes, J. M. *Water Resour. Res.* 1978, 15, 546–554.

Table 4. Analyses of Selected Organic Compounds in Water from the Edwards Aquifer

well no.	local well identifier	date well sampled[a]	no. of replicate analyses	concn (ng/L)[b]							
				c-DCE	1,2-DCB	1,3-DCB	1,4-DCB	DCDFM	PCE	TCE	TCFM
			Unconfined-Zone Wells, Residential and Range Land Use, Bexar County								
1	AY-68-21-804	900604	3	<2	<1	<1	7	<4	4	<4	<3
2	AY-68-28-102	900605	3	<2	<1	<1	<4*	<4	4	<4	4
3	AY-68-29-210	900606	3	<2	<1	<1	<4*	<4	7	5	<3
4	AY-68-35-102	900522	2	<2	<1	<1	6	<4	2	<4	<4
			Unconfined-Zone Wells, Range and Agricultural Land Use, Medina and Uvalde Counties								
5	TD-68-29-901	900529	3	<2	<1	<1	<4*	<4	<2	<5*	<3
6	TD-68-33-202	900613	2	<2	<1	<1	<4*	<4	<2	<4	<3
7	YP-69-36-702	900611	2	<2	<1	<1	<4*	<4	<2	<4	<3
			Confined-Zone Wells near Abandoned Landfill, Bexar County								
8	AY-68-28-904	900516	3	17	2	2	6	310	600	27	28
9	AY-68-28-909	900625	3	<2	<1	<1	<4*	<8	290	11	25
10	AY-68-28-919	900516	3	<2	<1	<1	<4	42	290	<4	130
11	AY-68-29-703	900814	3	3	<1	<1	<4*	47	190	8	17
			Confined-Zone Wells, Bexar County								
12	AY-68-35-913	900625	2	<2	<1	<1	<4	<4	<2*	<4	<4
13	AY-68-36-102	900625	3	<2	<4*	<4*	<4*	<8	350	6	18
14	AY-68-36-502	900625	2	<2	<1	<1	<4	<4	<2*	<4	<3
15	AY-68-37-101	900814	3	<2	<1	<1	<4	<4	43	<4	3
16	AY-68-37-404	900814	3	<2	<1	<1	<4	<4	<2	<4	<3
			Confined-Zone Wells, Medina and Uvalde Counties								
17	TD-68-26-701	900619	2	<2	<1	<1	<4	<4	<2	<4	<3
18	TD-68-33-701	900604	2	<2	<1	<1	<4*	<4	<2	<4	<3
19	TD-68-34-104	900521	3	<2	<1	<1	<4*	<4	<2	<4	<3
20	TD-69-40-403	900604	2	<2	<1	<1	<4*	<4	<2	<4	<3
21	TD-58-41-303	900619	2	<2	<1	<1	<4	<4	<2	<4	<3
22	TD-58-42-506	900604	2	<2	<1	<1	<4*	<4	<2	<4	<3
23	TD-69-46-601	900529	2	<2	<1	<1	<4*	<4	<2	<4	<3
24	TD-69-47-301	900530	3	<2	<1	<1	<4	<4	<2	<4	<3
25	YP-69-43-606	900611	2	<2	<1	<1	<4*	<4	5	<4	<3
26	YP-69-45-405	900611	2	<2	<1	<1	<4*	<4	<2	<4	<3
27	YP-69-53-202	900611	2	<2	<1	<1	<4*	<4	<2	<4	<3
			Method Reporting Limits for Target Compounds								
			c	<2	<1	<1	<4	<4	<2	<4	<3

[a] Date in year, month, day format (YYMMDD). [b] An asterisk indicates compound detection may be due to lab or shipping contaminant. [c] Measurement not made.

bicarbonate ion as the major dissolved cation and anion and had a chemistry that is typical of water from the parts of the Edwards aquifer used for public supply.[4]

Several target compounds, including PCE, 1,4-DCB, TCE, and TCFM, were determined in SIM analyses of groundwater from unconfined-zone wells in north and northeast Bexar County (Figure 4). None of the target compounds were detected in these water samples using EPA Method 524.2. PCE was detected in all four wells sampled from this area in concentrations ranging from 2 to 7 ng/L (Table 4). Land use over the unconfined-zone in north and northeast Bexar County has historically had little residential development,[15] with some recent residential and commercial development during the 1980s. No target compounds were detected in three water samples from unconfined-zone wells in Medina and Uvalde Counties. These latter areas have historically been used as undeveloped range land and for agricultural land uses.[15] The contrast in target compound concentrations between the Bexar County unconfined-zone wells and the Medina and Uvalde unconfined-zone wells was not sufficiently large, however, to allow the use of PCE, 1,4-DCB, TCE, or TCFM as tracers to distinguish different recharge sources.

(15) Texas Department of Water Resources. Land use/land cover maps of Texas: Report LP-62. Texas Dept. of Water Resources: Austin, TX, 1978; 47 maps.

Water samples collected in Bexar County from confined-zone wells 8 and 10 near an abandoned landfill and from well 2 had the largest concentrations and number of target compounds detected by this study (Table 4). All target compounds except DBQ were detected in a sample from well 8 that was closest to the abandoned landfill. Concentrations of 14 of the 19 compounds detected in water from the 4 wells near the abandoned landfill were less than the 0.2 μg/L reporting limit of EPA Method 524.2; the SIM method is better able to define occurrences of VOCs that may reflect regional contamination.

Application of the SIM method was useful in distinguishing relatively VOC-free groundwater recharge from west of San Antonio and contaminant-affected recharge from northern Bexar County and San Antonio. Only one detection was made of any target compound in water from three unconfined-zone wells and 11 confined-zone wells from Medina and Uvalde counties (Table 4). Water from three confined-zone wells, 12, 14, and 16, also had no detectable concentrations of target compounds, indicating their source as the relatively organic-free groundwater from west of San Antonio. In contrast, water from updip and upgradient wells 13 and 15 and wells near the abandoned landfill contain detectable concentrations of VOCs. The distribution of VOCs in these water samples agrees with flow directions postulated for groundwater

Figure 4. Location of sampled wells and symbols indicating where selected organic compounds were detected in groundwater samples.

by Maclay and Land.[16] The area west of San Antonio contributed an estimated 67% of the average 635.5 acre-feet/year of recharge to the Edwards aquifer between 1933 and 1988.[17]

The SIM method analyses allowed two differing sources of the target compounds in groundwater to be distinguished. The presence of human-influenced concentrations of TCFM had been previously described for water samples collected during 1978 from well 13.[14] The water samples from this well and from wells 9 and 15 did not contain c-DCE and DCDFM. These latter samples differ from those obtained from wells 8, 10, and 11 near the abandoned landfill which contain c-DCE and DCDFM. All these wells were identified as part of a zone of TCFM-affected water that was previously defined as extending from well 13 to northeastern parts of the aquifer.[14]

The detection of c-DCE in SIM analyses of water from wells 8 and 11 indicates that anaerobic microbial degradation of PCE and TCE may have occurred in the aquifer or in the methanogenic environment of the abandoned landfill. This degradation has been observed to occur in other anaerobic environments by microbially mediated dehalogenation reactions.[18] In contrast, aerobic conditions prevailed in all sampled groundwaters with dissolved oxygen concentrations ranging from 2.6 mg/L at well 17 to 8.4 mg/L at well 14. Previous analyses of groundwater from the abandoned landfill also detected undifferentiated cis or trans isomers of 1,2-dichloroethene.[4] Gases vented from the abandoned landfill contain sufficient methane to be burned at the site and are evidence of anaerobic conditions in the landfill.

DBQ was not detected in any of the groundwater samples using this technique. DBQ had previously been detected using the CLS method at concentrations ranging from <10 to 30 ng/L in water from two wells in the Edwards aquifer near Austin, Texas.[19] Solvent extraction with the SIM method may recover DBQ from water more efficiently than purge-and-trap methods.

The degree of sorptive retardation of organic compounds in groundwater is an important factor in evaluating a potential tracer of groundwater flow. Sorptive retardation of organic compounds increases directly with their octanol–water partition coefficient and the organic carbon content of aquifer–solid surfaces.[20] The log octanol–water partition coefficients of the target compounds detected in groundwater by this study range from 2.09 for c-DCE to 3.44 for 1,4-DCB.[12] According to this scheme, c-DCE would be least affected, and 1,4-DCB would be most affected by sorptive retardation. The amount of organic carbon on pore surfaces in freshwater parts of the Edwards aquifer has not been reported in the literature.

The long-term persistence of the target organic compounds in the aquifer and their use in trace concentrations as ambient tracers are also functions of their resistance to biotransformation. For example, PCE and TCE persist in water during batch microcosm and field-infiltration studies conducted under aerobic conditions.[20,21] Isomers of dichlorobenzene are degradable under aerobic conditions in laboratory conditions and in field infiltration experiments.[22] No data on the biotransformations of DCDFM and TCFM were found. These compounds have structures similar to that of carbon tetrachloride. Carbon tetrachloride is resistant to biotransformation under aerobic conditions.[13] The prevalence of aerobic conditions in the aquifer would therefore favor the resistance of DCDFM, PCE, TCE, and TCFM to biotransformation.

CONCLUSIONS

A convenient and reproducible method has been described to detect and quantify volatile organic compounds in water samples with a minimum detectable level ranging from 1 to 4 ng/L. The sensitivity of the method was enhanced by increasing the volume of water extracted to 100 mL, by optimizing the purge time for the target compounds, and by monitoring ambient laboratory conditions to ensure the lack of interferences during the analytical procedure. The requirement that a positive response be observed for three characteristic ions lessens the possibility of false results in comparison with analytical methods that use an electron capture detector.

(16) Maclay, R. W.; Land, L. F. U.S. Geological Survey, Water-Supply Paper 2336-A; U.S. Government Printing Office: Washington, DC, 1988; 48 pp.

(17) Nalley, G. M. Edwards Underground Water District Bulletin 48; Edwards Underground Water District: San Antonio, TX. 1989; p 15.

(18) Smith, L. R.; Dragun, J. Environ. Int. 1984, 291–298.

(19) Buszka, P. M.; Zaugg, S. D.; Werner, M. G. Bull. Environ. Contam. Toxicol. 1990, 45, 507–515.

(20) Schwarzenbach, R. P.; Giger, W.; Hoehn, E.; Schneider, J. K. Environ. Sci. Technol. 1983, 17, 472–479.

(21) Parsons, F.; Wood, P. R.; DeMarco, J. J. Am. Water Works Assoc. 1984, Feb, 56–59.

(22) Barber, L. B., II. Ground Water 1988, 6, 696–702.

Application of the SIM method to the analysis of groundwater samples provides more information regarding flow directions in the aquifer than did standard techniques. For example, the selective application of SIM analyses in groundwater quality surveys near the fringes of a contaminant plume would enhance determinations of contaminant migration. This was principally because the method reporting limits for SIM determinations were 50–200 times lower than those for standard PT methods. Because the SIM method is not specific to chlorinated compounds, it is adaptable to a wide range of VOCs. The SIM method, therefore, offers better sensitivity and selectivity for trace-level VOC determinations than previously used methods.

Analyses of laboratory and trip-blank samples determined that entry of interfering concentrations of the target compounds into the sample vials was possible. Applications of the SIM method to environmental studies should be preceded by a trip-blank study to identify environmental influences during sample shipment, collection, and storage. The development of sample containers with better integrity than the septum vials used for this work would lessen the need for the stringent blank control.

Detection of Hypoglycemic Drugs in Human Urine Using Micellar Electrokinetic Chromatography

M. Núñez, J. E. Ferguson, D. Machacek, G. Jacob, R. P. Oda, G. M. Lawson, and J. P. Landers*

Clinical Capillary Electrophoresis Facility, Department of Laboratory Medicine and Pathology, Mayo Foundation/Mayo Clinic, Rochester, Minnesota 55905

Micellar electrokinetic chromatography (MEKC) is evaluated as a potential analytical method for the separation and detection of a series of sulfonylurea drugs used in the treatment of hyperglycemia. These drugs are often surreptitiously abused, producing extremely low blood glucose levels and symptoms indistinguishable from those associated with an insulin-secreting tumor. Separation buffer containing 50 mM sodium dodecyl sulfate (SDS) was found to be adequate for the MEKC separation of the third generation drugs (glipizide and glyburide) but not the second generation drugs (acetohexamide, chlorpropamide, tolazamide, and tolbutamide). At a pH of 8.5 in the presence of 20 mM borate/20 mM phosphate and 150 mM SDS, all seven components were adequately resolved with an analysis time of 17 min. Altering the concentration of the buffering components to either 5 mM borate/5 mM phosphate or 40 mM borate alone reduced the analysis time to less than 10 min with no observable loss in resolution. A series of other micelle-forming surfactants were evaluated, and only sodium cholate provided an improvement over the SDS-based system. Optimal separation was obtained with 75 mM sodium cholate and led to complete analysis with baseline resolution of all seven components in less than 8 min. These conditions were shown to be adequate for the detection of the hypoglycemic drugs spiked into normal urine and in patients taking these drugs. The precision associated with nine consecutive injections of six samples ($n = 54$) was found to be acceptable with percent coefficient of variance for absolute migration times (MT_{abs}) for all peaks averaging 0.89 with peak area and peak height being 8.49 and 8.26, respectively. The between-sample precision was found to average 0.92% for MT_{abs} and 8.56% and 8.45%, respectively, for the relative peak area and peak height. With a detection limit for the drugs in urine (following extraction) in the 50 ng/mL range, the potential exists for an MEKC-based assay for the detection of sulfonylurea drugs in urine.

High-performance capillary electrophoresis (HPCE or CE) is a relatively new analytical technique that avoids many of the problems known to plague slab gel electrophoresis[1] and has been shown to be useful for analytes as diverse as ions,[2] small organic molecules,[3] sugars,[4] peptides,[5,6] oligonucleotides,[7] and proteins.[8,9] The inability of the most universal mode, capillary zone electro-

phoresis (CZE), which separates analytes based on charge-to-mass ratio, to resolve uncharged analytes has led to the development of micellar electrokinetic chromatography (MEKC).[10] Separation of uncharged or neutral analytes by MEKC occurs primarily due to a "hydrophobic partitioning effect" as a result of micelle-forming surfactants [e.g., sodium dodecyl sulfate (SDS)] added to the separation buffer. Under these conditions, differential partitioning of the analytes into the micelles as governed by their hydrophobicity allows for their separation. MEKC is particularly useful for the analysis of drugs, both uncharged and weakly charged, and this is reflected in the literature with the MEKC-based analysis of a variety of drugs.[11-16]

Sulfonylurea drugs have been utilized over the past four decades in the treatment of hyperglycemia. While this manifestation is typically associated with maturity-onset diabetes mellitus,[17] it is also observed in nondiabetic patients, primarily due to drug abuse. "Factitious" or "drug-induced" hypoglycemia has been reported as a result of the surreptitious use of sulfonylurea drugs. Problems associated with their surreptitious abuse arise from a diagnostic perspective. In the differential diagnosis of hypoglycemia, failure to detect surreptitious abuse of sulfonylurea drugs can result in an erroneous diagnosis of insulinoma (pancreatic tumor).[18] There have been instances where exploratory surgery and even partial removal of the pancreas (subtotal pancreatectomy) had been done before sulfonylurea drug abuse could be discovered.[19] The psychological basis of "factitious hypoglycemia" is still not understood, but its predominance for afflicting women in the allied health field (85% of all cases) can clearly be linked to accessibility to the drug. The strikingly large number of cases

(1) Landers, J. P. BioEssays 1991, 13, 253–258.
(2) Jones, W. R.; Jandik, P.; Pfeifer, R. Am. Lab. 1991, 23, 40–46.
(3) Carney, S. L.; Osborne, D. J. Anal. Biochem. 1991, 195, 132–140.

(4) Liu, J.; Shirota, O.; Novotny, M. Anal. Chem. 1991, 63, 413–417.
(5) Grossman, P. D.; Colburn, J. C.; Lauer, H. H.; Nielsen, R. G.; Riggin, R. M.; Sittampalam, G. S.; Rickard, E. C. Anal. Chem. 1989, 61, 1186–1194.
(6) Oda, R. P.; Madden, B. J.; Morris, J. C.; Spelsberg, T. C.; Landers, J. P. H. J. Chromatogr. 1994, 680, 341–351.
(7) Ulfelder, K. J.; Schwartz, H. E.; Hall, J. M.; Sunzeri, F. J. Anal. Biochem. 1992, 200, 260–267.
(8) Bushey, M.; Jorgenson, J. J. Chromatogr. 1989, 480, 301–310.
(9) Cohen, N.; Grushka, E. J. Capillary Electrophor. 1994, 215, 112–115.
(10) Terabe, S.; Otsuka, K.; Ishikawa, K.; Tsuchiya, A.; Ando, T. Anal. Chem. 1984, 56, 111–113.
(11) Johansson, I. M.; Pavelka, R.; Henion, J. D. J. Chromatogr. 1991, 559, 515–528.
(12) Garcia, L. L.; Shihabi, Z. K. J. Liq. Chromatogr. 1993, 16, 2049–2057.
(13) Morita, J.; Sawada, J.-J. J. Liq. Chromatogr. 1993, 641, 375–381.
(14) Gariel, P.; Grammond, J. P.; Guyon, F. J. J. Chromatogr. 1993, 615, 317–325.
(15) Schwartz, M. E.; Merion, M. J. Chromatogr. 1993, 632, 209–213.
(16) Wernly, P.; Thormann, W. Anal. Chem. 1992, 64, 2155–2159.
(17) O'Sullivan, D. I.; Cashman, W. F. Br. Med. 1970, 2, 572–575.
(18) Alquist, D. A.; Nelson, R. L.; Callaway, C. W. Ann. Intern. Med. 1980, 93, 281–282.
(19) Jordan, R. M.; Kammer, H.; Riddle, M. R. Arch. Intern. Med. 1977, 137, 390–393.

of drug-induced hypoglycemia, combined with the difficulty in distinguishing this problem from an insulinoma, has prompted the need for the development of a rapid, sensitive assay for these drugs in urine or serum.

Relatively few studies have been published describing effective analytical methodologies for detecting sulfonylurea drugs in biological fluids. Shenfield et al.[20] described a semiquantitative HPLC method for clinically active concentrations of five sulfonylurea drugs. In their study, a methodology was described for effectively detecting plasma chlorpropamide in the four case histories that were presented. However, the plasma concentration of 10 μg/mL was dramatically higher than the urinary levels expected with glipizide or glyburide, which would ~20–100 times lower (100–500 ng/mL). Recently, an HPLC method was reported that provided limited means for the detection of low concentrations of glyburide and its metabolites.[21] Attempts to utilize other analytical techniques have also been unproductive. GC/MS has proven problematic as a result of the nonvolatility and difficulty in derivitizing the sulfonylurea drugs, while LC/MS is not widely used. It is for these reasons that capillary electrophoretic analysis of these compounds has been pursued. With the resolution and rapid analysis time afforded by MEKC, capillary electrophoresis was explored as an alternative technology for providing an assay for second- and third-generation sulfonylurea drugs. In this study, we describe the capillary electrophoretic separation of six sulfonylurea drugs using MEKC. Under the appropriate conditions and with the addition of sodium cholate as a micelle-forming surfactant in the separation buffer, resolution of six sulfonylurea drugs and an internal standard is achieved as a result of both electrophoretic mobility and chromatography (due to partitioning of the analyte into micelles). Included in these are four of the most commonly prescribed drugs: chlorpropamide, glyburide, glipizide, and tolbutamide.

EXPERIMENTAL SECTION

Materials. Boric acid, borax (sodium tetraborate), sodium cholate, SDS, glyburide (Gb), sodium hydroxide, tolbutamide (Tb) and tolazamide (Ta) were obtained from Sigma (St. Louis, MO). Chlorpropamide (Cp) was obtained from Pfizer, Inc. (New York, NY). Acetohexamide (Ah) was obtained from ICN Pharmaceuticals, Inc. (Costa Mesa, CA). Sodium phosphate, HPLC-grade acetonitrile, and HPLC-grade methanol were purchased from Fisher Scientific (Fairlawn, NJ). Glipizide was obtained from Research Biochemicals, Inc. (Natick, MA), N-acetyl-4-(2,3-dichlorophenylureido)benzenesulfonamide internal standard was obtained from Aldrich Chemical Co. (Milwaukee, WI). Burdick and Jackson high-purity solvents (Muskegon, MI) were used for chromatography and sample extraction. The Bond Elut sample extraction cartridges (200 μg; 3 mL syringe cartridge volume) were from Varian (Harbor City, CA). Fused-silica capillaries were purchased from Polymicro Technologies (Phoenix, AZ).

Buffer and Sample Preparation. Separation buffers were prepared from 500 mM stock solutions. Borate buffer stock was prepared by mixing 500 mM boric acid with the appropriate amount of 125 mM sodium tetraborate until a pH of 8.5 was obtained. The phosphate buffer was prepared by solubilizing the

appropriate amount of disodium phosphate to make a 500 mM solution. All buffers were made with Milli-Q (Millipore, Bedford, MA) water, and filtered through an 0.2 μm filter (Gelman) before use. Sulfonylurea drug standards and the internal standard were prepared at a concentration of 1 mg/mL in methanol (HPLC-grade); they were kept at 4 °C when in use and at −20 °C when not in use.

Solid Phase Extraction Procedure. Internal standard (100 μL of a 10 μg/mL stock solution) was added to 10 mL of urine in a 15 mL beaker. After the pH of the urine was adjusted to 2.0 with concentrated HCl, the urine was transferred to a 60 mL separatory funnel containing 15 mL of chromatographic-grade methylene chloride. The mixture was shaken vigorously by hand for 2 min. After allowing 5 min for the phases to separate, the lower organic phase was transferred to a 15 mL conical tube and dried under a stream of nitrogen gas at 45 °C. The dried urine extract was reconstituted with 400 μL of 50:50 methanol/water and transferred to a 200 μg C_{18} Bond Elut cartridge that had been prewashed with 1 mL of acetonitrile. The cartridge was washed with 1.25 mL of 10% (v/v) acetonitrile/water followed by 1.0 mL of 40% (v/v) acetonitrile/water. After the wash fractions were discarded, the analytes were eluted from the cartridge with 1 mL of acetonitrile. The eluate was dried under nitrogen in a 300 μL limited-volume vial, where it was stored at −20 °C until required for CE analysis. For analysis of one of the drugs in patient urine, a random urine was obtained from a patient taking 100 mg of chlorpropamide daily. For the extraction process, 10 mL, 1 mL, and 100 μL of a random urine was used and the extract was redissolved in 30 μl of 100% methanol.

High-Performance Liquid Chromatography Conditions. Ten milliliters from a random urine collection was spiked with 1 μg each of glipizide, glyburide, and the internal standard to simulate a 100 ng/mL concentration. A two-step urine purification procedure was used as described in the Solid Phase Extraction Procedure section. An injected volume of 50 μL was analyzed using a Shimadzu SIL-9A autoinjector onto a Beckman Ultrasphere C_{18} 5 μm particle size column (250 × 4.6 mm). Chromatography was obtained with an isocratic elution with a Shimadzu LC-600 pump using 38% (v/v) acetonitrile in 0.1 M ammonium acetate, pH 7.2, at room temperature with a flow rate of 1.0 mL/min. Detection was with a Shimadzu SPD-M6A photodiode array UV detector.

Capillary Electrophoresis Instrumentation. MEKC was carried out on a Beckman P/ACE System 2100 or System 5510 (Beckman Instruments, Fullerton, CA) and interfaced with an IBM 55SX or 486 Value Point computer utilizing System Gold software (V. 8.1) for control and data collection. Detection was carried out either at a single wavelength of 200 nm or with scanning diode array detection at 200 −350 nm. Peak migration times, integrated areas and height were obtained through the System Gold software. The P/ACE instrument was equipped with a sample cooling tray that maintained samples at ~4 °C, enabling overnight runs without significant evaporation of the sample.

Capillary Electrophoresis Separation Conditions. New capillaries were conditioned by a 20 column volume rinse each with 0.1 M NaOH, water, and the separation buffer (in order). For a typical analysis, the following method was used: a three column volume rinse with running buffer, 1–3 s pressure injection (0.5 psi) of sample, 1 s pressure injection of separation buffer, separation at 25 kV (constant voltage), a three column volume

(20) Shenfield, G. M.; Boutagy, J. S.; Webb, C. *Ther. Drug Monit.* 1990, *2*, 393–397.
(21) Rydberg, T.; Wåhlin-Boll, E.; Melander, A. *J. Chromatogr.* 1991, *564*, 223–233.
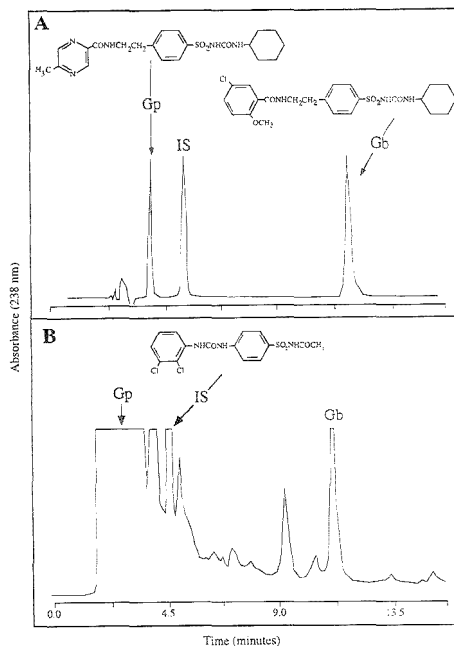
wash with 0.1 M NaOH followed by a momentary dip into distilled water, and a three column volume rinse with running buffer. With buffers containing micelle-forming detergents (e.g., SDS or SC), an additional rinse step was included in the method. The capillary was rinsed with 10 column volumes of a solution that was 10 times the buffer concentration of the separation buffer. For example, a method involving use of a 5 mM borate/5 mM phosphate/150 mM SDS buffer would employ a rinse step with 50 mM borate/50 mM phosphate/150 mM SDS solution at the same pH. Polyimide-coated, fused-silica capillaries (Polymicro Technologies) were 50 μm i.d., and either 27 or 47 cm in length (20 and 40 cm, respectively, to the detector). Polarity was such that the inlet was the anode and the outlet was the cathode. The capillary temperature was maintained at 25 °C. Detection was measured by absorbance at 200 nm.

Evaluation of Reproducibility. Evaluation of the migration time reproducibility with drug standards using the SDS-containing buffer was carried out with 10 consecutive injections of the standards in methanol at a concentration of 143 μg/mL. For evaluation of the separation conditions involving sodium cholate as a surfactant, a pooled urine that had been spiked with each of the drugs at a concentration of 500 ng/mL was divided into 11 equal aliquots and extracted as described above. Each individual sample was redissolved in 300 μl of methanol and transferred to a 500 μL Eppendorf tube and dried under nitrogen. The residue was resuspended in 30 μl of 5 mM borate/5 mM phosphate/25 mM cholate and vortexed/sonicated until solubilized. Each sample was injected for 4 s, 0.5 psi, for nine consecutive injections with each of six samples. Reproducibility was determined for migration time, integrated peak area, and peak height in comparison with the internal standard, which was added to the original urine sample so that the final concentration was 500 ng/mL.

RESULTS AND DISCUSSION

Sulfonylurea drugs have been used extensively for the control of hyperglycemia associated with maturity-onset diabetes.[22] Over the course of the last 40 years there have been several "generations" of sulfonylurea drugs. These include carbutamide (first generation), acetohexamide/chlorpropamide/tolazamide/tolbutamide (second generation) and most recently, glipizide and glyburide (third generation). The third-generation hypoglycemic drugs are much more potent and, subsequently, are effective at lower concentrations. Concentrations in the plasma and urine rarely exceed 300–500 ng/mL with a 5 mg oral dose of the drug.[23] It is for this reason that most analytical techniques have been found to be ineffective in detecting these drugs in biological samples.

Defining MEKC Conditions. In our initial studies, conditions were sought for the separation of glipizide and glyburide since these are the most commonly prescribed sulfonylurea drugs.[24] Reverse phase HPLC conditions can be defined for the effective separation of glipizide and glyburide from the internal standard (which will be referred to as IS in this study)] (Figure 1A). The migration order of glipizide, IS, and glyburide reflects the hydrophobic character of these compounds. When spiked into normal urine at a concentration of 100 ng/mL and extracted on a solid phase cartridge as described in the Experimental Section,

(22) Batey, R. G. *Drugs* **1977**, *14*, 116–119.
(23) Adams, W. J.; Skinner, G. S.; Bombardt, P. A.; Courtney, M.; Brewer, J. E. *Anal. Chem.* **1982**, *54*, 1287–1291.
(24) Melander, A.; Bitzen, P.-O.; Faber, O.; Groop, L. *Drugs* **1989**, *37*, 58–72.

Figure 1. High-performance liquid chromatography of glipizide, glyburide, and the internal standard. (A) Chromatography of the standard compounds in methanol (10 μg/mL). (B) Chromatography of normal urine spiked with the three standard compounds at 100 ng/mL. Conditions as described in the *Experimental* section.

recovery of the compounds was found to be ~80–90%. However, while analysis of this sample is completed in a reasonable time frame, only glyburide is clearly resolved (Figure 1B). It would be difficult, if not impossible, to identify glipizide and the IS among the other urinary components which coelute in the same region.

Using the conditions reported by Nishi et al.[25] as a starting point, separation of standard glipizide, glyburide, and IS was carried out in a 50 μm × 20 cm (effective length) capillary using a buffer composed of 20 mM borate and 20 mM phosphate, pH 8.9, with SDS added at a concentration of 50 mM. SDS is a well-established anionic surfactant which forms typical spherical micelles with a hydrophobic interior and a hydrophilic exterior at a critical micelle concentration (cmc) of ~8 mM. As shown in Figure 2A, baseline separation of all three compounds is accomplished in less than 130 s. To test the effectiveness of the extraction procedure and the initial CE separation conditions, the IS was spiked into buffer and normal human urine at a concentration of 250 ng/mL, extracted, redissolved in 20 μL of methanol, and analyzed. When hydrodynamically injected into the capillary, the IS is clearly seen and can be identified by its migration time of 88 s (Figure 2B and C for extracted buffer and urine, respectively). Analysis of the spiked urine shows that IS can be identified despite the number of other urinary components that are present. However, it was clear that, with such a narrow

(25) Nishi, H.; Fukuyama, T.; Matsuo, M.; Terabe, S. *J. Chromatogr.* **1990**, *498*, 313–323.
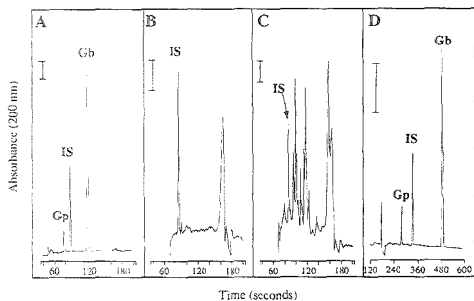
Figure 2. High-performance capillary electrophoretic separation of third-generation sulfonylurea drugs. (A) Separation of glipizide (100 μg/mL in methanol), glyburide (500 μg/mL in methanol), and the internal standard (250 μg/mL in methanol). (B) Separation of extract resulting from 1 mL of buffer spiked with the internal standard (250 μg/mL). Extract was redissolved in 20 mL of methanol. (C) Separation of extract resulting from 1 mL of normal urine spiked with the internal standard (250 ng/mL). Extract was redissolved in 20 mL of methanol. (A–C) involved separation in a 50 μm × 20 cm bare fused-silica capillary. (D) Separation of glipizide (100 μg/mL in methanol), glyburide (500 μg/mL in methanol), and the internal standard (250 μg/mL in methanol) in 50 μm × 40 cm bare fused-silica capillary. All separations were carried out in 20 mM borate/20mM phosphate/50 mM SDS, pH 8.5. Samples were in 100% methanol and hydrodynamically injected for 3 s. A constant voltage of 30 kV was applied to the system (16 μA) with the capillary temperature maintained at 20 °C. The bar represents 0.010 absorbance unit. All figures to follow involve the use of a 50 μm × 40 cm (effective length) bare fused-silica capillary. Key: Gp, glipizide; Gb, glyburide; IS, internal standard.

window, resolution would be poor and identification of the drug(s) difficult. As a result, separation was examined in a capillary with twice the effective length (40 cm). At the cost of a significantly longer analysis time (9 min), glipizide, glyburide, and the IS are well-resolved in a window that should allow for sulfonylurea drug identification in the presence of a number of other urinary components (Figure 2D).

In order that the CE-based assay for hypoglycemic drug detection be universal, the second-generation drugs (tolbutamide, tolazamide, chlorpropamide, and acetohexamide), which are still prescribed to some extent, were prepared as a mixture and analyzed under similar conditions . When separated at 30 kV in the buffer described above (20 mM borate/20 mM phosphate/50 mM SDS, pH 8.9; 40 cm capillary), only two peaks were resolved, one containing acetohexamide and tolazamide and the other tolbutamide and chlorpropamide (Figure 3A). Decreasing the voltage to 25 kV had a small but significant effect, allowing for the partial resolution of tolbutamide and chlorpropamide but not acetohexamide and tolazamide (Figure 3B). Changing the hydrophobic character of the separation buffer with the addition of 20% acetonitrile further resolved tolbutamide from chlorpropamide but, again, did little for the resolution of tolazamide and acetohexamide (Figure 3C). Further increases in acetonitrile concentration did not aid in the resolution of tolazamide and acetohexamide. Other organic additives were tested, and as with acetonitrile, none effected the resolution of tolazamide and acetohexamide. Subsequently, the addition of organic solvents was not pursued further. Adequate resolution was finally obtained by increasing the SDS concentration to 200 mM (Figure 3D). However, the prolonged migration times for glipizide, glyburide,
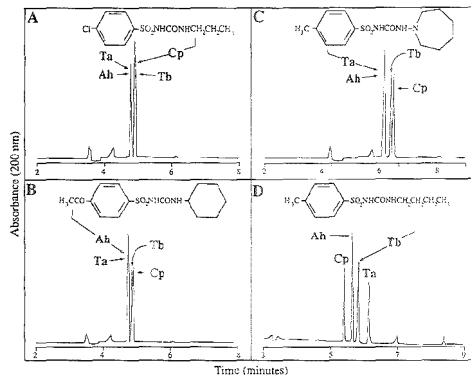
Figure 3. Capillary electrophoretic separation of second-generation sulfonylurea drugs. (A) Separation was carried in 20 mM borate/20 mM phosphate/50 mM SDS, pH 8.5; 30 kV; 20 °C; detection at 200 nm. (B) As with (A) except with an applied voltage of 25 kV. (C) As with (B) with the addition of 20% acetonitrile to the buffer. (D) As with (A) with the SDS concentration increased to 200 mM. Other parameters as described for Figure 2. Key: Tb, tolbutamide; Cp, chlorpropamide; Ah, acetohexamide; Ta, tolazamide.

and the internal standard under these conditions were considered unacceptable (data not shown).

Effect of Buffer Type, pH, and [SDS]. Since several studies have shown the dramatic effect that micelle concentration has on the resolution in MEKC,[26,27] and the data given in Figure 3D indicated that higher SDS concentrations may be key to the separation of all of the sulfonylurea drugs (including the IS), the SDS concentration was varied in order to identify conditions for optimal separation. While equations have been derived to predetermine the micelle concentration for the optimal resolution of solutes, a prerequisite is that the partition coefficients of the solutes and other system values are known.[28] Difficulty in obtaining hydrophobicity information about the analytes forced the empirical determination of an optimal SDS concentration. Since the aim of this study was to develop an assay that would provide a single screen for both second- and third-generation sulfonylurea drugs, conditions were sought for the separation of all six drugs and the internal standard. The standard mixture containing the second- and third-generation drugs as well as the IS was separated in a series of 20 mM borate/20 mM phosphate buffers (pH 8.5) containing various SDS concentrations. As expected from the results illustrated in Figure 3A–C, lower concentrations of SDS (3 and 10 mM) were ineffective for complete resolution of either the second- or third-generation drugs (Figure 4). At SDS concentrations less than 100 mM, acceptable resolution of glipizide, glyburide, and the internal standard was obtained but tolbutamide, tolazamide, chlorpropamide and acetohexamide were not resolved (Figure 4A–D). Adequate resolution of all seven components was obtained in a buffer containing an SDS concentration of 150 mM or greater (Figure 4E and F). Under these conditions, the migration times for glipizide, glyburide, and IS were significantly longer than observed at lower SDS concentrations and considered undesirable from an assay development perspective.

(26) Sepaniak, M. G.; Cole, R. O. Anal. Chem. 1987, 59, 472.
(27) Khaledi, M. G.; Smith, S. C.; Strasters, J. K. Anal. Chem. 1991, 63, 1820–1830.
(28) Foley, J. P. Anal. Chem. 1990, 62, 1302–1308.
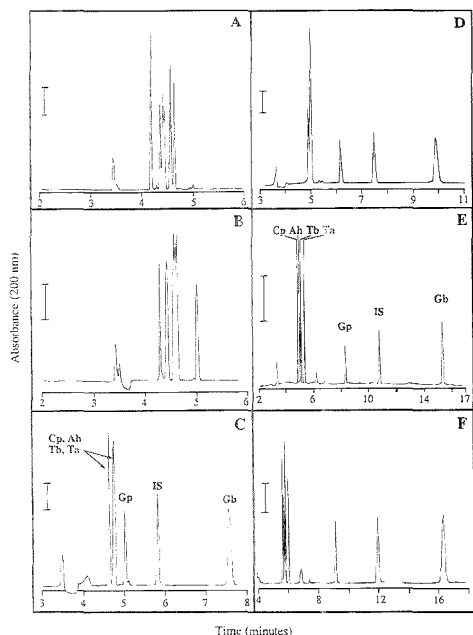
Figure 4. Effect of buffer SDS concentration on separation at pH 8.5. Separation was carried out with SDS concentration equal to 3 (A), 10 (B), 50 (C), 100 (D), 150 (E), and 200 mM (F). The system current associated with each of these separations was 40, 42, 51, 62, 87, and 120 μA, respectively. All other conditions as defined in Figure 2. The bar represents 0.005 absorbance unit.

Having determined the optimal SDS concentration (≥150 mM), the effect of other parameters on the separation was evaluated. Through the testing of a series of 20 mM borate/20 mM phosphate/200 mM SDS buffers having pH's 6.98, 7.52, 8.18, 8.51, 9.06, and 10.13, it became clear that optimal separation was obtained in the pH range of 8.5 (data not shown). The influence of buffer component concentration was also evaluated with a series of buffers containing 150 mM SDS at a pH of 8.5 but varying in the borate/phosphate composition. Since SDS was the main contributor to the buffer ionic strength, it was not surprising that the current did not change significantly (2/2, 64.2 μA; 5/5, 71.5 μA; 10/10, 83.9 μA; 40/0, 69.4 μA) with the only exception being 0 mM borate/40 mM phosphate (0/40, 158 μA), which stressed the capacity of the system for thermostating the capillary at 20 °C. With respect to buffer concentration, optimal resolution was observed with a borate/phosphate combination of either 5 mM/5 mM or 40 mM/0 mM (data not shown) and the former was used for further studies providing a single screen assay for six sulfonylurea drugs in less than 10 min.

As a final attempt at further decreasing the analysis time, several other anionic detergents were evaluated. On the basis of previous studies, which have shown that selectivity changes may accompany the use of different surfactants,[29] sodium cholate (SC), sodium glycodeoxycholate (SGDC), and sodium taurocholate (STC) were evaluated for their effectiveness in resolving the

(29) Terabe, S.; Otsuka, K.; Ando, T. *Anal. Chem.* 1985, *57*, 834–841.
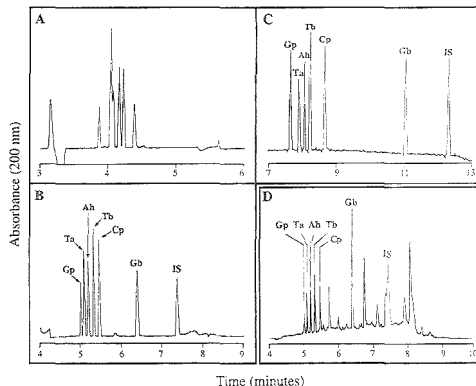
Figure 5. Decreased analysis time associated with the use of sodium cholate as the surfactant. Separation of standards was carried out in 5 mM borate/5 mM phosphate, pH 8.5, containing sodium cholate at concentrations equal to 20 (A), 75 (B), and 150 mM (C). Analysis of an extracted urine containing all hypoglycemic drugs and the IS at a concentration of 100 ng/mL except for Gb which was at 200 ng/mL (D). Separation was carried out in 5 mM borate/5 mM phosphate/ 75 mM sodium cholate (25 kV, 61 μA) following a 2 s hydrodynamic injection of the reconstituted extract (total volume 20 μL). All other conditions as defined in Figure 2.

sulfonylurea drugs (data not shown). While that latter two detergents showed little promise for affording resolution of the drugs, SC provided separation that was comparable or better than the SDS system with respect to analysis time. Although an anionic detergent like SDS, sodium cholate is a bile salt with a planar steroid-like structure presenting a polar and nonpolar face. It does not form spherical SDS-like micelles but instead, at a cmc of ~14 mM, forms aggregates (typically dimers to octamers) that are held together primarily by hydrogen bonding. Figure 5 shows the separation of a standard mixture of sulfonylurea drugs in separation buffer consisting of 5 mM borate/5 mM phosphate, pH 8.5, and SC at concentrations of 20, 75, and 150 mM (Figure 5A–C, respectively). Excellent resolution of all compounds is obtained with the SC buffer in less time than with SDS (which was ~10 min) and with half the detergent concentration (75 mM). All peaks were baseline-resolved with the slowest migrating peak detectable in less than 8 min. Figure 5D shows that these conditions are amenable to detection of these drugs in human urine. Following extraction, normal urine spiked with glipizide, IS, acetohexamide, chlorpropamide, tolazamide, and tolbutamide at 100 ng/mL and glyburide at 200 ng/mL was analyzed by MEKC using the sodium cholate system. Each of the drugs were clearly resolved in the presence of a number of unidentified peaks in the urine extract with the glyburide peak having a peak area approximately twice that of the other drugs. Peak identification was possible based on the MTs for the individual components and these correlated well with those observed for the standards alone. Absolute peak identification was accomplished through co-injection of individual drug standards with the extract and through an increase in peak height/area. Under these conditions, the lower limit of detection for drugs in urine (following extraction) was found to be ~50 ng/mL.

As a means of simplifying peak identification, separation of the sulfonylurea drug standards was monitored with scanning diode

A

B
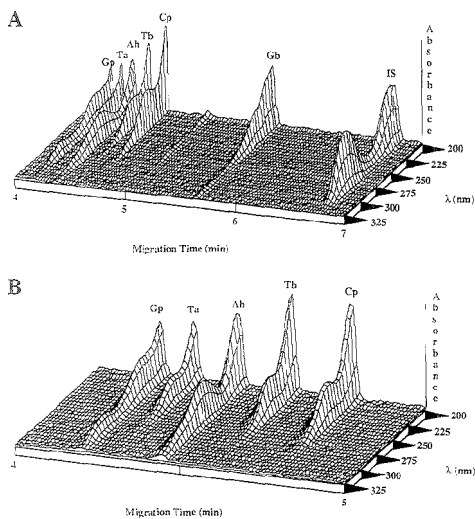
Figure 6. Analysis of sulfonylurea drugs using scanning diode array detection. (A) Three-dimensional spectral profile for sulfonylurea drugs migrating (4–7 min). (B) Expanded scale for migration time 4–5 min. Separation was carried out in 5 mM borate/5 mM phosphate/75 mM sodium cholate (25 kV, 61 μA) following a 2 s hydrodynamic injection of the standard mixture containing each of the sulfonylurea drugs and the internal standard at a concentration of 125 μg/mL. All conditions as defined in Figure 2 except that detection was scanning diode array from 190 to 350 nm.

Figure 7. Detection of chlorpropamide in an extracted patient urine using MEKC. (A) Analysis of hypoglycemic drug standards in methanol at a concentration of 143 μg/mL each. (B) Analysis of an extracted patient urine (total volume 30 μl; 3 s injection by pressure). Separation was carried out in 5 mM borate/5 mM phosphate/75 mM sodium cholate (25 kV, 61 μA). All other conditions as defined in Figure 2.

array detection from 190–350 nm. Figure 6A shows that several of the sulfonylurea drugs have characteristic spectra in this region, which allows for identification without total reliance on MT_{abs} or the requirement for spiking experiments. Tolazamide, tolbutamide, and glyburide all have similar, unremarkable spectral characteristics with an absorbance peak at 230 nm. However, several of the other components have unique spectral characteristics. Glipizide has a substantial absorbance at 225 and 280 nm, acetohexamide at 252 nm, while the internal standard used in this study has a uniquely strong absorbance at 212 and 272 nm (Figure 6B). Clearly, diode array detection has the potential for providing additional confirmatory information for some of the sulfonylurea drugs that may be observed in patient urine.

Analysis of Hypoglycemic Drugs in Patient Urine. As a final test of this CE-based method for hypoglycemic drugs in urine, a random urine sample was obtained from a patient who was ingesting 100 mg of chlorpropamide daily. Extraction was carried out with 10 mL, 1 mL, and 100 μL of the patient urine as given in the Experimental Section. Analysis of the extract (dissolved in methanol) from the 10 mL sample produced a peak that exceeded the range of the detector. Analysis of the extract for the 1 mL urine sample easily allowed for identification of chlorpropamide by comparing the MT_{abs} with that of the drug standards (Figure 7). The MT_{abs} for the peak in the patient urine was 7.28 min and correlated well with chlorpropamide in the standard mixture (7.29 min). Similar analysis of the 100 μL urine sample showed that chlorpropamide could also be easily detected despite the small sample volume used. This confirmed the utility of the MEKC-based system for the identification of hypoglycemic drugs in urine.
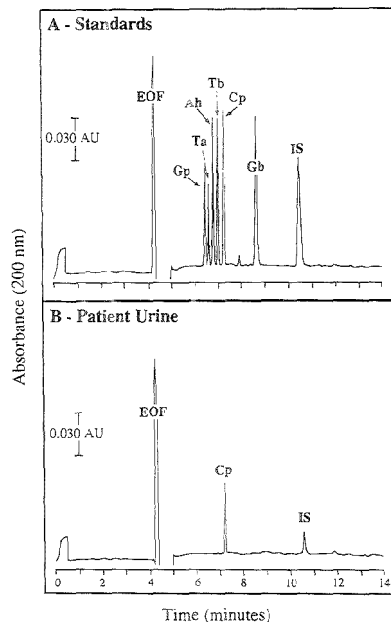
Reproducibility. Although the goal of this project was to develop a method to detect, and not necessarily quantify, hypoglycemic drugs in urine, it was still important to determine the precision associated with the assay. The absolute peak migration time (MT_{abs}; not corrected) reproducibility associated with separation using the 150 mM SDS system was determined with a series of consecutive analyses ($n = 10$) of the same sample containing all seven drug standards in methanol. Initial evaluation showed that, with a simple 0.1 M NaOH rinse and reequilibration with separation buffer between runs, MT_{abs} reproducibility was unimpressive [percent coefficient of variance (% CV) of 2–7%]. However, incorporation of a rinse step using a 50 mM borate/50 mM phosphate/150 mM SDS solution (i.e., 10× separation buffer), dramatically improved the MT_{abs} reproducibility. The percent CV ($n = 10$) for each of the peaks of chlorpropamide, acetohexamide, tolbutamide, tolazamide, glipizide, IS, and glyburide was found to be 0.27, 0.29, 0.28, 0.30, 0.84, 0.69, and 1.6, respectively. The somewhat higher percent CV for glyburide was curious and coincided with the observation that this peak always tended to be broader than glipizide. The detection sensitivity for the direct injection of these compounds was ~1–3 μg/mL (3 s hydrodynamic injection at 0.5 psi = 4 nL). The fact that the samples were in 100% methanol drastically limited the volume that could be injected without loss of resolution. With urine containing sulfonylurea drugs, the limit of detection (following extraction) was ~50 ng/mL.

Table 1. Reproducibility (% CV) for the Absolute Migration Time, and the Peak Area/Peak Height Relative to the Internal Standard Multiple Injections (*n* = 9) with a Single Urine Extract

peak	% CV		
	MT_{abs}	PA_{rel}	PH_{rel}
glipizide	0.11	1.59	2.37
tolazamide	0.11	3.44	3.72
acetohexamide	0.12	1.86	2.61
tolbutamide	0.13	2.42	2.58
chlorpropamide	0.13	2.13	2.04
glyburide	0.14	1.81	2.21
internal standard	0.16		

Table 2. Reproducibility (% CV) for the Absolute Migration Time, and the Peak Area/Peak Height Relative to the Internal Standard Multiple Injections (*n* = 54) with Six Identical but Distinct Samples

peak	% CV		
	MT_{abs}	PA_{rel}	PH_{rel}
glipizide	0.78	6.87	7.01
tolazamide	0.78	6.72	9.15
acetohexamide	0.82	5.23	5.97
tolbutamide	0.85	5.52	5.49
chlorpropamide	0.87	8.49	7.60
glyburide	1.03	18.11	14.36
internal standard	1.12		

The precision associated with the 75 mM sodium cholate system was evaluated more comprehensively by determining the percent CV values for MT_{abs} as well as peak area and height. A spiked pooled urine (500 ng/mL for each drug and the IS) was divided into multiple aliquots, each of which was taken through the extraction procedure described in the Experimental Section. In contrast to the reproducibility study described above, the dried extracts from six samples were solubilized in 5 mM borate/5 mM phosphate/25 mM cholate as the sample matrix, since reproducibility was poorer with samples dissolved in methanol as a result of its volatility. From these experiments, reproducibility associated with (1) nine consecutive injections of the sample, (2) a single injection of six individual samples (between-sample precision), and (3) multiple injection (*n* = 9) of six individual samples (total *n* = 54) was determined. The reproducibility associated with nine consecutive injections of a single sample is given in Table 1. The MT_{abs} reproducibility for each drug peak in the urine extract was significantly improved over that observed with the standard drugs solubilized in methanol (average % CV of 0.13 in aqueous vs 0.61% in methanol). The reproducibilities for the peak area PA_{rel} (average 2.21%) and peak height PH_{rel} (average 2.59%) relative to the internal standard were equally as good and likely reflect the more suitable nature of an aqueous sample matrix over a volatile organic matrix. The between-sample precision calculated from the results of a single injection of each of the six samples was found to be acceptable with the MT_{abs} reproducibility ranging from 0.89 to 1.28% (average 1.02%) while the PA_{rel} and PH_{rel} ranged from 5.06 to 19.28 (average 8.70%) and 5.29 to 13.95 (average 8.32%), respectively. Multiple injection of each of six samples allowed for an estimate of the collective reproducibility (n=54) for MT_{abs}, PA_{rel}, and PH_{rel}, which is given in Table 2. These values did not differ dramatically from those calculated between-sample averaging 0.86% for Mt_{abs}, 8.49% for PA_{rel}, and 8.26% for PH_{rel}. These values are acceptable in light of the fact that this also reflects sample-to-sample differences inherent in the extraction procedure. For reasons that are not clear, the PA_{rel} and PH_{rel} values for glyburide were somewhat higher than the values associated with the other drugs. This likely reflects the dissimilarities in extraction efficiency between glyburide and the internal standard which, apparently, is minimal with the other drugs. This may also correlate with the fact that glyburide always appeared as a broader peak and, hence, may be interacting to some extent with the capillary wall. In general, the reproducibility was found to be acceptable and, with some fine tuning, may be amenable to extrapolation into a more quantitative assay.

Mechanistic Aspects of Hypoglycemic Drug Separations. From a mechanistic perspective, several observations character-

istic to the MEKC separation of the sulfonylurea drugs are curious. In general, resolution of analytes in MEKC is dependent on both the nature of the surfactant head group (charged or uncharged) and the hydrophobic moiety.[30] By this virtue, MEKC is applicable not only to the separation of uncharged analytes through micelle/aqueous partitioning but also to the separation of charged analytes through surface adsorption and/or comicellization. As a result, polar analytes tend to be more susceptible to changes in the surfactant head group than to alterations in the hydrophobic environment within the micelle. The sulfonyl urea drugs in this study are generally considered to be weak acids with pK values in the 5.0–6.0 range[31] and, therefore, are expected to behave as nonpolar, weakly charged analytes. At a pH of 8.5 in the absence of surfactant, all of the sulfonylurea drugs migrate slower than an endoosmotic flow (EOF) marker but are not resolved; this observation correlates with expected behavior of weak, negatively charged analytes.

The relatively small size of the charged head group of SDS and an aggregation number of 60 allows for the formation of a micelle with a surface containing a substantial negative charge density and a relatively hydrophobic interior.[32] Hence, it is unlikely that the observed separation in the presence of 150 mM SDS is due to significant interaction of the negatively charged drugs with the micelle and is most likely due to micellization due to their hydrophobic nature. It is interesting that the second- and third-generation drugs are grouped in the MEKC separation using an SDS system. Glipizide, glyburide, and the internal standard are clearly retained to a greater extent by the SDS micelles than acetohexamide, chlorpropamide, tolbutamide, and tolazamide. The fact that they spend less time micellized (i.e., their partition coefficient is lower) explains why a higher concentration of SDS is required for their separation. Using the retention on reverse phase HPLC as a general indicator of hydrophobicity of these compounds, the migration order in the SDS-based MEKC system correlates well with the exception of tolazamide, which appears to have a higher affinity for the micelles than would be predicted. The presence of a seven-membered ring in this structure may impart more hydrophobic character to this drug than the others of the same generation and this subtlety may be exacerbated in MEKC.

Despite the fact that both SDS and SC are anionic surfactants, their structures differ significantly, and hence, it is not surprising

(30) Khaledi, M. G. In *Handbook of Capillary Electrophoresis*; Landers, J., Ed.; CRC Press: Boca Raton, FL, 1993; pp 43–94.
(31) Wahlin-Boll, E.; Melander, A. *J. Chromatogr.* 1979, *164*, 541–546.
(32) Neugebauer, J. M. *Methods Enzymol.* 1990, *182*, 239–282.

that such dramatic changes in selectivity were observed. The planar steroid-like structure of SC and its low aggregation number (2−3) make it difficult for micellization of analytes to occur.[30] Hence, most of the SC-induced changes in selectivity are likely due to (hydrophobic) interaction of the analyte with the micelle surface. Comparing the peak order with that observed by HPLC, the presence of SC in the separation buffer has a marked effect on the migration behavior of chlorpropamide, glipizide, and the internal standard. Two of these structures (chlorpropamide and the internal standard) have their migration dramatically retarded. This may be due the presence of chloride functional groups (one on chlorpropamide; two on glipizide) which may increase the hydrophobic nature of the compound and, hence, increase the amount of time spent in the micelles. Clearly, the presence of chloride groups alone cannot account for mobility in the SC-containing buffers since glipizide, which has a single chloride, appears to have less affinity for the SC micelles than it does for micellar SDS. The significance of this observation is unclear at the present time but emphasizes the changes in selectivity that can accompany the use of different micelle-forming surfactants.

CONCLUSIONS

This study has demonstrated the potential utility of MEKC for the detection of sulfonylurea drugs in human urine. The development of an MEKC-based method for urinary hypoglycemic drug detection highlights the ability of CE to provide a rapid assay with a detection sensitivity in the 50 ng/mL range. These data present the possibility of using MEKC for the detection of drugs in the urine of patients who may be suffering from drug-induced hypoglycemia and to rule out insulinoma. Studies are currently underway to test the effectiveness of this assay on a variety of clinical samples as well as to determine the identity of potential interfering substances. Studies attempting to decrease the effort required in concentrating the sample using "off-line" solid phase extraction procedures are also in progress. With this approach, it may be possible to concentrate and partially purify comparatively large volumes of urine (1−5 μL) "on-line" using solid phase extraction-capillary electrophoresis (SPE-CE), which involves the use of a solid phase extraction device connected at the capillary inlet.[33] This will improve the feasibility of the assay for use in the clinical laboratory.

(33) Strausbauch, M. A.; Madden, B. J.; Wettstein, P. J.; Landers, J. P. *Electrophoresis* 1995, *16*, 541−548.

Ultra-High-Speed DNA Sequencing Using Capillary Electrophoresis Chips

Adam T. Woolley and Richard A. Mathies*

Department of Chemistry, University of California, Berkeley, California 94720

DNA sequencing has been performed on microfabricated capillary electrophoresis chips. DNA separations were achieved in $50 \times 8 \mu m$ cross-section channels microfabricated in a 2 in. $\times$ 3 in. glass sandwich structure using a denaturing 9% T, 0% C polyacrylamide sieving medium. DNA sequencing fragment ladders were produced and fluorescently labeled using the recently developed energy transfer dye-labeled primers. Sequencing extension fragments were separated to ~433 bases in only 10 min using a one-color detection system and an effective separation distance of only 3.5 cm. Using a four-color labeling and detection format, DNA sequencing with 97% accuracy and single-base resolution to ~150 bases was achieved in only 540 s. A resolution of greater than 0.5 was obtained out to 200 bases for both the one- and four-color separations. The prospects for enhancing the resolution and sensitivity of these chip separations are discussed. This work establishes the feasibility of high-speed, high-throughput DNA sequencing using capillary array electrophoresis chips.

Capillary electrophoresis (CE) is a powerful technique for DNA analysis, which has been applied to restriction fragment sizing, PCR product analysis, forensic identification, and DNA sequencing.[1] CE separations are much faster than those in slab gels, because higher electric fields can be applied; however, conventional CE has the disadvantage that it only allows the analysis of one sample or lane at a time. Our group has addressed this issue by developing capillary array electrophoresis (CAE)[2] in which separations are performed in a bundle of parallel silica capillaries, and we have demonstrated the use of CAE for DNA sequencing,[3,4] restriction fragment sizing,[5] and short tandem repeat analysis.[6] In CAE, the lane width is reduced from the ~1 mm typical for slab gels to ~100 μm. Further miniaturization of electrophoretic separations to increase the number of lanes, as well as the speed and throughput of the separations will be necessary to meet the needs of the Human Genome Project.[7,8] Therefore, we have recently focused on the use of microfabrication techniques to produce miniaturized capillary arrays.

The use of microfabrication to produce electrophoretic separation capillaries was first introduced in 1992 by Manz and Harrison.[9] Subsequently, capillary zone electrophoresis separations of fluorescent dyes[10] and of fluorescently labeled amino acids[11,12] were performed in individual microfabricated capillaries on glass chips. Our own efforts have been directed toward producing microfabricated capillary arrays on chips and using them for high-resolution separations of DNA restriction fragments and PCR products.[13] Separations of small, fluorescently labeled phosphorothioate oligonucleotides have also recently been performed on a microfabricated chip.[14] These results suggest that if the sensitivity and resolution were enhanced it might even be possible to perform DNA sequencing on chips. To enhance the sensitivity of these separations, we have exploited the recently developed energy transfer dye-labeled sequencing primers[15,16] and employed confocal fluorescence detection.[13,16] In addition, techniques for filling microfabricated channels with denaturing polyacrylamide matrices, loading DNA sequencing samples on a chip, injecting the samples, and performing sequencing separations have been developed. These studies show that we can achieve single-base resolution of DNA sequencing samples to ~200 bases on chips in only 10 min separations. The prospects for increasing the read lengths on CE chips to ~500 bases are also discussed. The demonstration of high-speed DNA sequencing on CE chips is the first step toward miniaturizing the entire DNA sequencing procedure on microfabricated devices.

EXPERIMENTAL SECTION

Sequencing Sample Preparation. DNA sequencing samples were generated using standard dideoxy sequencing chemistry and energy transfer dye-labeled primers;[15,16] the other reagents used to prepare the sequencing samples were obtained from Amersham Life Science (Cleveland, OH). The DNA sequencing fragments used in the one-color separations were made using 2.4 pmol of the fluorescently labeled F10F primer (see ref 15 for nomenclature), 10 μg of single-stranded M13mp18 DNA template, and they

' Dedicated to our friend and colleague Dr. Huiping Zhu (1959–1995).
(1) Monnig, C. A.; Kennedy, R. T. Anal. Chem. 1994, 66, 280R–314R.
(2) Mathies, R. A.; Huang, X. C. Nature 1992, 359, 167–169.
(3) Huang, X. C.; Quesada, M. A.; Mathies, R. A. Anal. Chem. 1992, 64, 967–972.
(4) Huang, X. C.; Quesada, M. A.; Mathies, R. A. Anal. Chem. 1992, 64, 2149–2154.
(5) Clark, S. M.; Mathies, R. A. Anal. Biochem. 1993, 215, 163–170.
(6) Wang, Y.; Ju, J.; Carpenter, B. A.; Atherton, J. M.; Sensabaugh, G. F.; Mathies, R. A. Anal. Chem. 1995, 67, 1197–1203.
(7) Hunkapiller, T.; Kaiser, R. J.; Koop, B. F.; Hood, L. Science 1991, 254, 59–67.
(8) Smith, L. M. Science 1993, 262, 530–532.

(9) Manz, A.; Harrison, D. J.; Verpoorte, E. M. J.; Fettinger, J. C.; Paulus, A.; Ludi, H.; Widmer, H. M. J. Chromatogr. 1992, 593, 253–258.
(10) Jacobson, S. C.; Hergenroeder, R.; Koutny, L. B.; Warmack, R. J.; Ramsey, J. M. Anal. Chem. 1994, 66, 1107–1113.
(11) Harrison, D. J.; Fluri, K.; Seiler, K.; Fan, Z.; Effenhauser, C. S.; Manz, A. Science 1993, 261, 895–897.
(12) Effenhauser, C. S.; Manz, A.; Widmer, H. M. Anal. Chem. 1993, 65, 2637–2642.
(13) Woolley, A. T.; Mathies, R. A. Proc. Natl. Acad. Sci. U.S.A. 1994, 91, 11348–11352.
(14) Effenhauser, C. S.; Paulus, A.; Manz, A.; Widmer, H. M. Anal. Chem. 1994, 66, 2949–2953.
(15) Ju, J.; Ruan, C.; Fuller, C. W.; Glazer, A. N.; Mathies, R. A. Proc. Natl. Acad. Sci., U.S.A. 1995, 92, 4347–4351.
(16) Ju, J.; Kheterpal, I.; Scherer, J. R.; Ruan, C.; Fuller, C. W.; Glazer, A. N.; Mathies, R. A. Anal. Biochem.. in press.
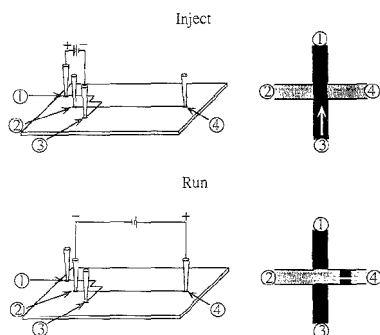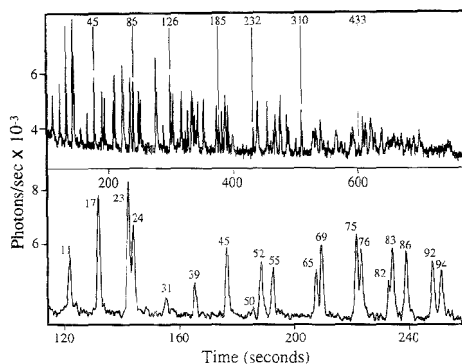
Figure 1. Schematic diagram of the electrophoresis chip indicating the injection procedure. The injection channel connects reservoirs 1 and 3, and the separation channel connects reservoirs 2 and 4. In the inject mode, a field is applied between reservoirs 1 and 3, causing the DNA to migrate through the gel-filled intersection toward reservoir 1. In the run mode, a field is applied between reservoirs 2 and 4, causing the DNA fragments in the intersection region to migrate toward reservoir 4 through the gel in the separation channel. The actual devices had 15 electrophoresis systems integrated on each chip.


Figure 2. One-color DNA sequencing fragment separation on a CE chip. (top) Electropherogram of M13mp18 A sequencing fragments generated with the primer F10F. (bottom) Expanded view of the peaks corresponding to the first 100 bases, demonstrating single-base resolution. The sample was injected by electrophoresing it through the cross channel at 170 V/cm for 60 s and separated at 250 V/cm in a 9% T, 0% C polyacrylamide-filled channel. Excitation was at 488 nm and fluorescence from 515 to 545 nm was detected. The effective separation length of the 50 μm wide and 8 μm deep channel was 3.5 cm.

were terminated using ddATP. The F10F primers are labeled with 6-carboxyfluorescein (FAM) at the 5′ end, with a second FAM attached to the tenth nucleotide from the 5′ end of the primer on a modified T residue. The samples used in the four-color DNA sequencing experiments were generated using dITP sequencing chemistry with 4.8 pmol of fluorescently labeled primer and 4.8 μg of single-stranded M13mp18 DNA template for each of the four reaction mixtures. The primers used for the four-color reactions were F10F, F10J, F10T, and F10R. These primers are labeled at the 5′ end as described above and have either FAM, 2′,7′-dimethoxy-4′,5′-dichloro-6-carboxyfluorescein (JOE), N,N,N',N'-tetramethyl-6-carboxyrhodamine (TAMRA), or 6-carboxy-X-rhodamine (ROX) attached to the tenth nucleotide from the 5′ end of the primer on a modified T residue. For the four-color experiments, the mixtures were pooled, and then for both the one- and four-color experiments, the DNA fragments were precipitated, washed with ethanol, and resuspended in 2 μL of 95% formamide/2.5 mM EDTA. The samples were denatured at 90 °C for 2 min and immediately placed on ice prior to injection.[16]

Electrophoresis Procedures. Electrophoresis chips were fabricated and the channel surfaces were derivatized using [γ-(methacryloxy)propyl]trimethoxysilane as described previously.[13] An aqueous solution of acrylamide (9% T, 0% C) in 45 mM Tris/45 mM borate/1 mM EDTA/8.3 M urea (pH 8.3) was filtered with a 0.2 μm pore diameter filter (Millipore, Bedford, MA) and then degassed under vacuum for 1 h. Polymerization was initiated by adding 2.5 μL of 10% ammonium persulfate and 1.5 μL of N,N,N',N'-tetramethylethylenediamine (TEMED) to a 1-mL aliquot of acrylamide solution, which was then drawn into all the channels by placing the solution in reservoir 4 and applying vacuum to the other reservoirs (see Figure 1 for labeling). The acrylamide was allowed to polymerize overnight at 4 °C, and the channels were preelectrophoresed at 100 V/cm for 15 min prior to use.

To perform an injection, reservoir 3 was rinsed with 95% formamide and then 1.0 μL of sequencing sample was pipeted

into the reservoir. The other three reservoirs were filled with 45 mM Tris/45 mM borate/1 mM EDTA (pH 8.3); to establish electrical contacts on the chip, wires were inserted into the cutoff pipet tips which formed the four reservoirs. In the one-color sequencing separation, the sample was "plug" injected[13] by applying 170 V/cm between reservoirs 1 and 3 for 60 s and run by applying 250 V/cm between reservoirs 2 and 4. In the four-color sequencing separation, the sample was injected for 30 s in the same manner and run at 200 V/cm.

Instrumentation. The detection system used for the one-color sequencing separations has been described previously;[13] the instrumentation used for the four-color sequencing separations has also been described.[16] Briefly, the 488-nm line from an argon ion laser was focused within the channel using a 20× NA 0.5 objective. Fluorescence was collected by the objective and passed through a series of dichroic filters to divide the fluorescent signal into four spectral regions (510–540, 545–570, 570–590, and 590–660 nm). The fluorescent signal in the first three spectral regions was filtered by a band-pass filter; the fourth region was filtered with a long-pass filter; a 100-μm confocal pinhole spatially filtered the fluorescence in all four spectral channels before photomultiplier detection. The analog output from the photomultipliers was filtered with a low-pass filter having a 0.2-s time constant and sampled at 10 Hz with a 16-bit ADC board (NB-MIO-16XL-18, National Instruments, Austin, TX) controlled by a program written in LabVIEW running on a Macintosh IIci. Additionally, a 660-nm short-pass filter was placed before the longest wavelength detector to reduce background fluorescence from the glass. The raw data were Fourier transformed, the high-frequency (>0.5 Hz) noise was removed, and then an inverse Fourier transform was performed. After background subtraction, the smoothed data were transformed using a multicomponent matrix transformation.[17] The transformation matrix was formed using the fluorescence

(17) Smith, L. M.; Kaiser, R. J.; Sanders, J. Z.; Hood, L. E. Methods Enzymol. 1987, 155, 260–301.
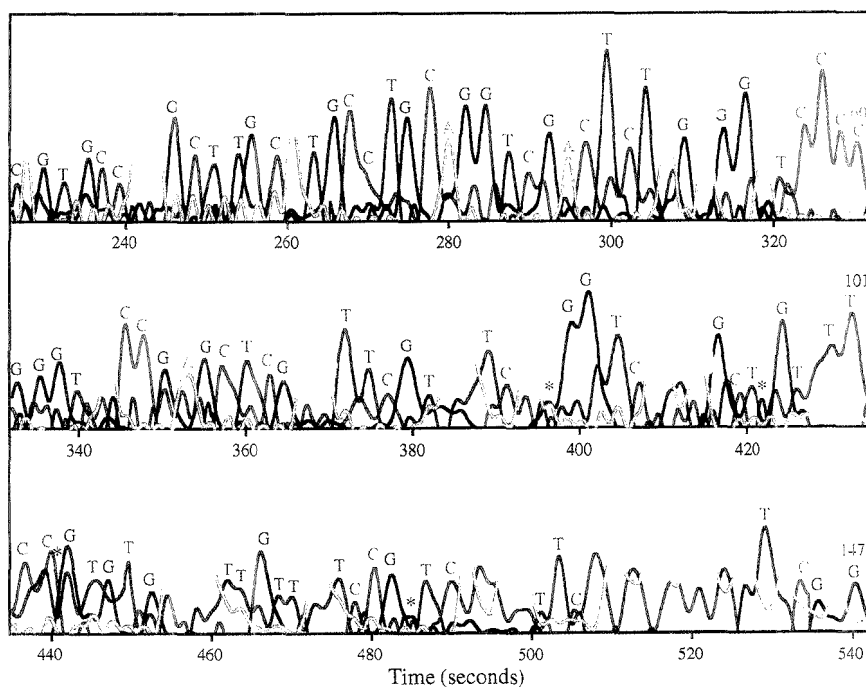
Figure 3. Analyzed four-color DNA sequencing data from M13mp18 DNA labeled using the F10F, F10J, F10T, and F10R energy transfer primers and separated on a CE chip. The raw fluorescence data were transformed as described in the Experimental Section to present a plot of relative concentration of each of the labeled DNA fragments as a function of time. The bases are identified by the color of the peaks: blue (F10F) C; green (F10J) T; black (F1CT) G; red (F10R) A. The three bases that were not called, T at 397 s, T at 441 s, and C at 484 s and a C incorrectly called at 422 s are indicated by a black asterisk. Weak signal from the C- and T-terminated peaks was most likely the cause of these errors. The sample was injected by electrophoresing it through the cross channel at 170 V/cm for 30 s and separated at 200 V/cm in a 9% T, 0% C polyacrylamide-filled channel. Excitation was at 488 nm and detection was at 510—540 nm for C, 545—570 nm for T, 570—590 nm for G, and 590—660 nm for A. The effective separation length of the 50 μm wide and 8 μm deep channel was 3.5 cm .

signals in each spectral channel from known single DNA fragment peaks terminated at C, T, G, and A nucleotides. Transforming the data from the four spectral channels yields information about the relative concentrations of the four sets of dye-labeled DNA fragments.[16] The plot of these concentration data as a function of time was corrected for the mobility differences of the dye-labeled fragments by adding 2.2 s to the migration times of the fragments labeled with F10T and F10R, yielding the analyzed four-color sequencing profile.

Safety Considerations. Microfabricated CE chips could be mass produced inexpensively, so a prefilled, disposable chip would minimize the user's exposure to hazardous chemicals such as acrylamide, a neurotoxin and carcinogen. Furthermore, the small volumes of solutions required to fill microfabricated channels decrease the quantities of all reagents used (hazardous or not). The short length of these microfabricated channels allows separations at 200 V/cm with a lower applied voltage (1 kV), reducing the hazard of electrical shock.

RESULTS AND DISCUSSION

Figure 2 presents a separation of F10F-labeled, ddATP-terminated DNA sequencing fragments on a CE chip. The fragments were separated in a channel 50 μm wide and 8 μm deep

with a distance from injection to detection of only 3.5 cm. The peaks are visible starting at ~100 s, and all the peaks have been detected by 800 s. The peak corresponding to 433 bases after the primer is detected at 602 s. The lower portion of Figure 2 presents an expanded view of the peaks corresponding to the first 100 bases, separated in ~4 min. Single-base resolution was obtained throughout this region; for example, bases 23 and 24, bases 75 and 76, and bases 82 and 83 are all resolved.

Figure 3 presents a four-color sequencing run using a CE chip. These data have been analyzed by applying a matrix transformation to the fluorescence data to correct for cross talk. Single-base resolution was obtained throughout the region shown; there were four errors in the base calls, or 97% accuracy out to 147 bases, with a separation time of just 9 min. The signals for the C- and T-terminated fragments became too weak to distinguish from the background noise beyond this region, so the sequence could be read only as far as shown. However, the signal strength for the A- and G-terminated fragments was strong enough to distinguish peaks to ~400 bases at a separation time of 15 min.

Figure 4 presents an analysis of the resolution in the four-color sequencing separation. The figure shows a plot of resolution as a function of base number, with a least-squares exponential fit to the data. A resolution of at least 0.5 between adjacent peaks is
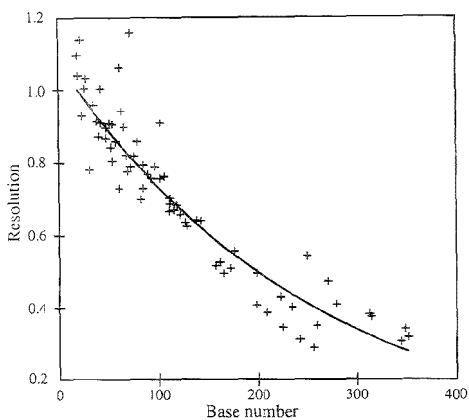
Figure 4. Plot of resolution as a function of base number for the four-color sequencing run. The solid line is a least-squares fit of an exponential function to the data: ($y = 1.0762e^{-0.0038503x}$, $R = 0.94$) Resolution was normalized to single-base spacing when the bases analyzed were not adjacent. Peak parameters for the resolution calculations were determined by fitting a Gaussian function to peaks in the raw data. The resolution of two peaks was calculated by taking the difference of the migration times and dividing by 4 times the mean of the variances of the peaks. The resolution of nonadjacent bases was normalized by dividing the calculated resolution by the base spacing between the fragments.

necessary to obtain peak information from the data;[18] from the least-squares fit, the resolution in this run was above 0.5 out to 200 bases. Similar results were obtained for the one-color run with a resolution greater than 0.5 out to 215 bases. The maximum number of theoretical plates for a band was 1.1×10^6, corresponding to 3.1×10^7 plates/m.

We have demonstrated that high-speed DNA sequencing can be performed using microfabricated CE chips. DNA sequencing with 97% accuracy has been demonstrated, and single-base resolution to >200 bases has been demonstrated in only 7 min (1700 bases/h per lane), using an effective separation distance of only 3.5 cm. DNA sequencing fragments as long as 433 bases can be detected in ~10 min separations (2400 bases/h per lane). By comparison, DNA sequencing using slab gel electrophoresis yields 500 bases of sequence in ~8–10-h (50–60 bases/h per lane), and sequencing with capillary electrophoresis yields 500 bases of sequence in ~1–2 h (250–500 bases/h per lane). This comparison makes it clear that the use of microfabricated capillaries may lead to a significant improvement in DNA sequencing technology.

The ability to read the sequence past ~200 bases was limited in these experiments by the signal in the first two spectral channels. The raw signal in these channels was a factor of ~2 less than in the other channels because the sensitivity of these two photomultipliers was less than that of the others by a factor of 2–3. The dyes that primarily fluoresce in the wavelength range collected in the first two spectral channels, F10F and F10J, were used to label the C- and T-terminated fragments, hence the lower sensitivity for these fragments. The length of the read for these

fragments would have been approximately the same as for the A- and G-terminated fragments (~400 bases) if a 2-fold higher concentration of the C- and T-terminated fragments had been used in this run or if the detection sensitivity were improved.

In order to achieve adequate signal, 12 times more primer and DNA template were used for sequencing on the CE chip than for conventional capillaries.[16] The reduced sensitivity with chips is due to the smaller injection and detection volumes; for example, the cross-sectional area of a $50 \times 8 \mu m$ channel is 20 times smaller than that of a 100-μm-i.d. capillary. The detection sensitivity could be improved and the amount of reagents could be reduced through several modifications to the experiments. For example, <10% of the channel width was illuminated by the laser in the current setup. By using a cylindrically focused beam and a confocal slit matching the channel width, the signal could be increased by a factor of 10. Also, making the channels 20 μm deep instead of 8 μm would raise the signal by a factor of 2.5 more. These two improvements alone would produce a 5-fold increase in the signal-to-noise ratio. Finally, improved matching of the volume of sample placed on the chip (1 μL) to the volume of sample actually injected (~100 pL) would significantly reduce the quantities of reagents used. The reagent volumes could be reduced through integration of the sequencing reactions onto the chip. These improvements should allow DNA sequencing to be performed on CE chips with sensitivity and quantities of reagents comparable to other techniques.

Although the resolution was adequate to call only ~200 bases in these runs, there are several possible ways to extend the resolution to 400–500 bases. Increasing the separation distance, decreasing the length of the injected plug,[19] or using a sieving medium that is better optimized for longer DNA fragments[20] can all increase the range of acceptable resolution. Using the peak variances and published values for diffusion coefficients of single-stranded DNA in denaturing polyacrylamide gels,[19] we calculated the length of the injected plug to be $101 \pm 6 \mu m$ from the 50-μm-wide injection channel. By using a 20–30-μm-wide injection channel or controlling the potentials at all reservoirs during injection,[10] the plug length could be decreased to <50 μm. With a 50-μm plug length and a 7-cm effective separation distance, the resolution for adjacent fragments would be at least 0.5 out to ~320 bases, which is near the limit of resolution for 9% T, 0% C polyacrylamide in longer capillaries.[4] However, the limit of resolution in capillaries can be extended to ~500 bases by using cross-linked polyacrylamide at lower concentrations.[16] The increased length would double the time required for separation; nevertheless, these separations would still be significantly faster than the current methodologies. These considerations suggest that it should be possible to obtain single-base resolution to ~500 bases on CE chips by optimizing the channel length, injection, and sieving medium.

CONCLUSIONS

The demonstration of high-speed DNA sequencing on microfabricated capillary electrophoresis chips paves the way to a variety of important applications. Once the resolution and run length are improved, and a more facile method of loading samples is devised, it is reasonable to think that we could make a 2-in. × 3-in. CAE

(18) Best, N.; Arriaga, E.; Chen, D. Y.; Dovichi, N. J. *Anal. Chem.* **1994**, *66*, 4063–4067.

(19) Luckey, J. A.; Norris, T. B.; Smith, L. M. *J. Phys. Chem.* **1993**, *97*, 3067–3075.

(20) Figeys, D.; Dovichi, N. J. *J. Chromatogr.* **1993**, *645*, 311–317.

chip that would perform parallel DNA sequencing of 32 or more different samples in ~15 min. The detection region for 32 closest-packed channels would be ~3 mm wide, which could be detected in a scanning format with a duty cycle per channel of ~2%. Alternatively, by using a multiple array detector, nearly a 100% duty cycle could be achieved. Assuming a read length of 400 bases in 20 min for 32 parallel channels yields a raw DNA sequencing rate of ~40 000 bases/h for a single chip. Furthermore, recent work has demonstrated that simple chemical reactions can be combined with free zone electrophoresis separations on chips.[21,22] Coupling more complex reactions involving DNA sample preparation with our high-speed, high-resolution separation technology could drastically simplify DNA analysis. This integration on a large scale could lead to low-cost, disposable microfabricated devices which combine DNA sample preparation, amplification, injection, separation, and detection with analysis times of just a few minutes. The development of these microfabricated integrated DNA analysis systems will be an important step in the Human Genome Project.

(21) Jacobson, S. C.; Koutny, L. B.; Hergenroeder, R.; Moore, A. W., Jr.; Ramsey, J. M. *Anal. Chem.* **1994**, *66*, 3472–3476.
(22) Jacobson, S. C.; Hergenroeder, R.; Moore, A. W., Jr.; Ramsey, J. M. *Anal. Chem.* **1994**, *66*, 4127–4132.

Pyrolysis with a Solvent Trapping Technique. Qualitative Identification of Acrylic Acid and Methacrylic Acid in Emulsion Polymers

Frank Cheng-Yu Wang,* Bruce Gerhart, and Charles G. Smith

Analytical Sciences Laboratory, Michigan Division, The Dow Chemical Company, Midland, Michigan 48667

A technique that combines pyrolysis of a polymer with trapping of the pyrolysis products in a solvent followed by analysis of the solvent by gas chromatography or liquid chromatography has been developed. Two vinyl acids (acrylic acid and methacrylic acid) as low-level additives polymerized into polymer chains were qualitatively identified in latex particles using this technique and compared to results obtained for direct pyrolysis-gas chromatography of the polymer. Although the percent conversion to the acid monomers through pyrolysis of the acids contained in the emulsion polymers was low, detectable signals and well-resolved peaks were obtained when solvent trapping of the pyrolysis products was applied. The advantages and disadvantages of the trapping technique are discussed, and proposals are made for future developments.

Pyrolysis-gas chromatography (Py-GC), and pyrolysis-gas chromatography/mass spectrometry (Py-GC/MS) are two techniques used to qualitatively and quantitatively identify major components in polymers.[1-3] Both techniques utilize thermal energy to break down polymers to monomers and small oligomers in the gas phase. Those gases are directly passed into a gas chromatograph to achieve the separation. Presently there exists a lot of polymer modifiers that have a decidedly different polarity than the major monomers and that are polymerized into the polymer backbone at relatively low levels. Those low-level modifiers frequently appear with poor peak shape under the chromatographic environments established for analysis of the major monomers. Sometimes, changing the chromatographic environment (for example, change to a different polarity capillary column) to accommodate the low-level modifiers will result in poor separation of all major components. Low-level organic acids in emulsion polymers are good examples of this situation.

Organic acids (especially vinyl carboxylic acids) are added with other monomers into emulsion polymer (latex) systems to increase copolymer strength, provide stability, enhance adhesion, expand swellability in water, and define the surface chemistry. Acrylic acid and methacrylic acid are two vinyl acids commonly used in these emulsion polymerizations. Because these acids are normally added at low concentration (2-10% by weight), the qualitative and quantitative identification of these acids is a challenging task for the analyst.

In an emulsion polymer system, the unreacted acid monomers are dissolved in the serum or liquid phase. The aqueous serum phase can be extracted and filtered to permit identification and quantitative determination of residual acid by a suitable liquid chromatography (LC) technique. The analysis of acids in the solid polymer particles, however, is typically determined by acid/base titration. Even with end-point titration curve analysis, which may provide information on the cumulative strengths of the polymerized acids, there is no effective direct technique for the qualitative and quantitative identification of these vinyl acids in the solid polymer phase.

Other techniques are being used to analyze the latex particles, such as infrared spectroscopy (IR) and nuclear magnetic resonance spectroscopy (NMR). Both techniques are able to identify the existence of the acid functional groups at the concentration levels examined here, but they are inadequate for use in further qualitative identification because of a lack of significantly different functional groups between the vinyl acids and/or interferences from other monomers in the latex polymer and lack of sensitivity at lower acid concentrations.

Py-GC and Py-GC/MS are two of the generally used techniques to qualitatively and quantitatively identify major monomers in the solid phase of emulsion polymers.[1] Major components in commercial emulsion polymers are nonpolar monomers such as styrene, butadiene, acrylate, and methacrylate esters.[4] Because of the polar nature of vinyl acids, however, they are normally not well separated on nonpolar chromatographic columns which are usually used to separate major nonpolar products derived from the pyrolysis of the solid phase of the emulsion polymer. Even where there is a chromatographic column capable of performing an acceptable separation with suitable peak shape, the direct Py-GC analysis still suffers from two major disadvantages. First, the detector response for acids is normally low because of low pyrolysis conversion to the basic monomer, and second, interferences occur from other components. As a result, the acid components in the pyrogram exist as small peaks buried under or assimilated with other primary and secondary pyrolysis product peaks.

The major pyrolysis reaction mechanism for acids in the polymer chain results in formation of carbon dioxide, water, and related aliphatic counterparts (the decarboxylation reaction). The analysis of acids in the polymer chain has been achieved by the derivatization method, whereby methylation is performed on the

(1) Irwin, W. I. *Analytical Pyrolysis: A Comprehensive Guide;* Marcel Dekker: New York, 1982.

(2) Liebman, S. A.; Levy, E. J. *Pyrolysis and FC in Polymer Analysis;* Marcel Dekker: New York, 1985.

(3) Wampler, T. P. *J. Anal. Appl. Pyrolysis* 1989, 16, 291.

(4) Sudol, E. D.; Daniel, E. S.; El-Aasser, M. S. In *Polymer Latex;* Sudol, E. D., Daniel, E. S., El-Aasser, M. S., Eds.: ACS Symposium Series 492; American Chemical Society: Washington, DC, 1992; p 1.

acid groups on the particle surface.[5,6] Simultaneous pyrolysis methylation (SPM) or other derivatization reactions are reported for polyesters, phenolic resins, and other materials that yield polar, poorly separated pyrolysis products.[7-9] The methylated monomers or other derivatives survive the pyrolysis reaction to give the ester products, which are very stable for GC and GC/MS analysis. However, the path to direct production of the acid monomer (depolymerization reaction) still exists, and with competition from the decarboxylation reaction, this path has been generally overlooked by the analyst. This depolymerization reaction path may be utilized for the qualitative identification of acids in the solid polymer phase. The effectiveness of this technique depends on the efficiency of conversion to the acid monomer, the resolution of the monomers from potentially interfering pyrolysis products, and the availability of detectors sensitive enough to detect the low yields of these acid monomers.

Pyrolysis, instead of being viewed as part of a Py-GC technique, can be utilized as a sample preparation technique for the investigation of the basic monomer units. The pyrolysis reaction is merely a mechanism of applying thermal energy to cleave the polymer chains into fragments, monomers, and other secondary reaction products. Considering the number and variety (polar and nonpolar) of pyrolysis fragments, monomers, and secondary reaction products that could potentially be produced, one chromatographic column (either GC or LC) certainly cannot effectively separate all of them. However, if a preliminary separation is performed prior to the formal chromatographic separation, the components that would potentially overlap/interfere during the separation could be greatly reduced, resulting in a more effective separation.

A stepwise pyrolysis-LC study of polystyrene[10] utilizing the trapping technique followed by LC as a supplemental method to study the pyrolysis products of polystyrene that were not suitable for the gas chromatography conditions has been reported. The capability of investigating higher boiling fragments, which were not suitable for GC, is another advantage of the pyrolysis, solvent-trapping technique.

In this study, pyrolysis products were trapped into an aqueous solution followed by GC and LC separations in order to identify acrylic acid or methacrylic acid contained in the solid phase of two latex products. The advantages and disadvantages of this method were studied in comparison to direct Py-GC. This pyrolysis-solvent trapping method with strict operating controls may provide a technique for quantitative determination of the individual acids in the polymer chain. In addition, improving the trap design may lead to complete computer control and an automated process for this analysis.

EXPERIMENTAL SECTION

Sample Preparation. (1) **Latex Solid.** Two latexes, A and B, were made in our laboratories. Latex A had 44.8% solid polymer, which contained by weight 50% styrene, 47% butadiene, and 3% acrylic acid, while latex B had 56.3% polymer solids, which

(5) Cutié, S. S.; Buzanowski, W. C.; Berdasco, J. A. *J. Chromatogr.* **1990**, *513*, 93.
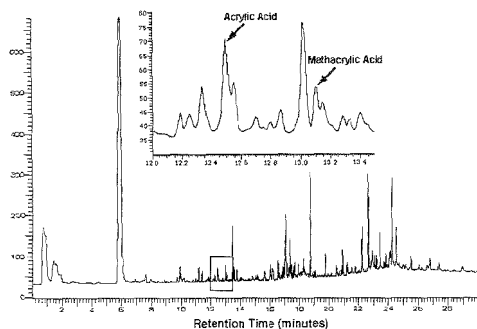(6) Buzanowski, W. C.; Cutié, S. S.; Howell, R.; Papenfuss, R. *J. Chromatogr A.* **1994**, *677*, 355.
(7) van der Peyl, G. L. Q.; Linnartz, T. C. T.; van Rossum. C. A. J. J.; Zeelenberg, M. *J. Anal. Appl. Pyrolysis* **1991**. *19*, 279.
(8) Challinor, J. M. *J. Anal. Appl. Pyrolysis* **1991**, *20*, 15.
(9) Challinor, J. M. *J. Anal. Appl. Pyrolysis* **1991**, *16*, 323.
(10) Lai, S.; Locke, D. C. *J. Chromatogr.* **1983**, *255*, 511.
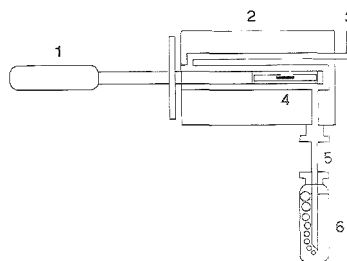
Figure 1. Setup of pyrolysis-liquid-trapped system: (1) pyroprobe, (2) pyroprobe interface, (3) helium carrier gas inlet, (4) latex sample, (5) output needle, and (6) liquid collection vial.

contained by weight 68% styrene, 25% 2-ethylhexyl acrylate, and 7% methacrylic acid. Each latex (2 g) was mixed with 10 mL of methanol (containing 1% KBr), shaken for 5 min, and centrifuged with collection of the solid portion. This "washing" process was repeated two more times and then the solid phase was dried at 80 °C in a vacuum oven for 1 h. The dried solid was stored in a humidity-controlled environment (humidity 50%) for 48 h before use. The solid samples were heated at 220 °C for 10 min prior to pyrolysis to ensure there were no detectable residual acids left from the aqueous phase.

(2) **Standard Solution of Acids.** Acrylic acid (99%) and methacrylic acid (99%), purchased from Aldrich Chemical Co., were used without further purification. A standard solution containing acrylic acid and methacrylic acid was prepared by diluting the concentrated acid with the appropriate amount of 0.01 N H_2SO_4 solution to obtain the desired concentration.

Pyrolysis-Gas Chromatography. Samples of dried latex were weighed into quartz tubes and equilibrated for 10 min in a 220 °C interface connected to the injection port of a HP5890 gas chromatograph equipped with a flame ionization detector (FID). Samples were pyrolyzed (CDS 120 Pyroprobe Pt coil) at a set temperature of 700 °C with a maximum heating ramp for a 20-s interval. The pyrolysis products were split 1:10 in the 220 °C injection port, separated on a fused-silica capillary column (J&W DB-FFAP, 15 m × 0.32 mm i.d., 0.25-μm film) using a linear temperature program (40 °C for 4 min and then 20 °C/min ramp to 220 °C with a 17-min hold), the head pressure was approximately 10 psi, and a FID detector was used.

Pyrolysis-Aqueous Solution Trapping. The pyrolysis-liquid trapping system setup is shown in Figure 1. Samples of dried latex were weighed into quartz tubes and equilibrated for 10 min in a 220 °C interface with the output needle (Yale hypodermic needle, 24G1 regular bevel) of the interface immersed into a vial containing 200 μL of solution (in this study, the solutions used were 0.01 N sulfuric acid, methanol, or methylene chloride). The helium carrier gas flow was 30 mL/ min. Samples were pyrolyzed (CDS 120 Pyroprobe Pt coil) at a set temperature of 700 °C with a maximum heating ramp for a 20s interval. The pyrolysis products carried out by the helium passed through the needle and then were bubbled through the aqueous solution for approximately 1 min. The vial was sealed with a septum and aluminum closure ring for further use in the LC or GC separations.

Gas Chromatography. The pyrolysis products trapped in the aqueous solution were separated using the previously described instrument, but the Pyroprobe interface was replaced by the HP

Figure 2. Pyrogram from direct PY-GC of latex A (containing acrylic acid). The inset shows the retention time between 12.0 and 13.5 min. The acrylic acid retention is 12.45 min, and the methacrylic acid is 13.02 min.

7673 autosampler. Vials containing the aqueous solution of pyrolysis products were analyzed using a 2-μL injection volume. All the other experimental conditions (injector temperatures, column, flow, oven temperature programming, and detector) remained the same.

Liquid Chromatography. An HP1090 liquid chromatograph was used for the LC analysis of the aqueous solution containing the trapped pyrolysis products. The injection volume was set at 20 μL. The separation was performed on an Aminex 100 mm × 7.8 mm (HPX-87H) Fast Acid column (Bio-Rad), using a 0.01 N H_2SO_4 mobile phase with 0.7 mL/min flow rate, and ultraviolet (UV) detection monitored at 210 nm.

RESULTS AND DISCUSSION

Trapping pyrolysis products into a solvent has five major advantages over conventional direct Py-GC. They are as follows: (1) the capability of studying higher boiling pyrolysis products which were not suitable for the GC conditions; (2) the pyrolysis products getting preselected/separated through the selection of the trapping solvent as long as the analyte under consideration is trapped (dissolved) with a high efficiency; (3) the flexibility of further separations and identification techniques, such as GC, LC, SFC, etc.; (4) the flexibility to adjust sample intensities by dilution to reduce the trapping solution concentration or by multiple pyrolysis to increase the concentration in the trapping solution; and (5) pyrolysis and separation discerned as two events, providing an easily manageable experimental time and design. The first advantage has been discussed in the literature,[10] and will not be the focus in this study.

Figures 2 and 3 show the pyrograms for the direct Py-GC of latex solid A and B. The portion of the pyrograms containing the acrylic acid and methacrylic acid peaks have been amplified and placed into an inset frame. Based on chromatography of the standard acid mixture injected into the chromatograph, the retention time of acrylic acid was 12.40 ± 0.05 min and the retention time of methacrylic acid was 13.02 ± 0.05 min. Because the FFAP is a column suitable for separation of relatively polar components, some peaks exhibited poor peak shape. Since all components produced in the pyrolysis flow through the chromatography column, the separation of acrylic acid and methacrylic acid was not base-line resolved. The qualitative identification of
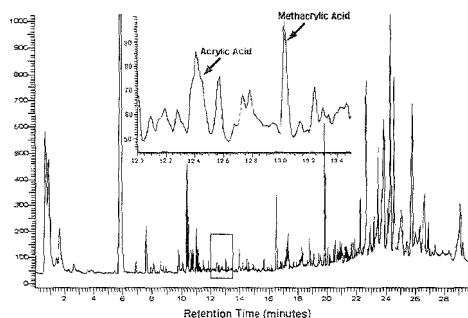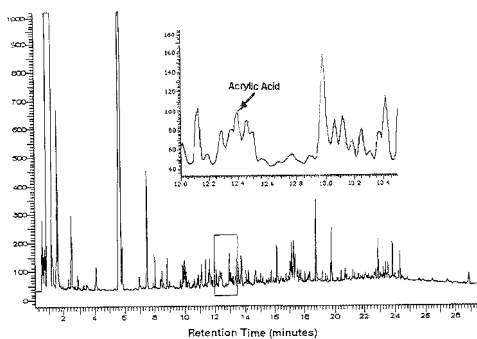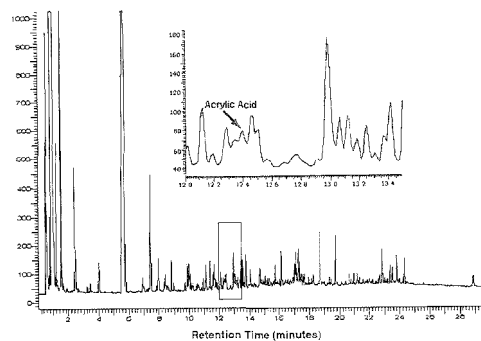

Figure 3. Pyrogram from direct Py-GC of latex B (containing methacrylic acid). The inset shows the retention time between 12.0 and 13.5 min. The acrylic acid retention is 12.45 min, and the methacrylic acid is 13.02 min.
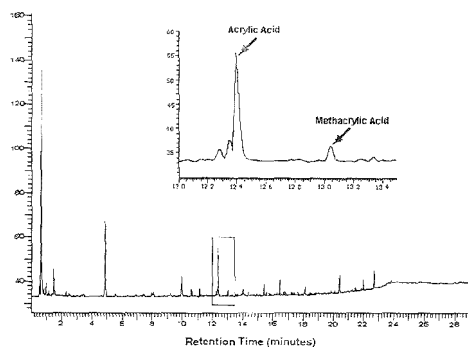
Figure 4. Chromatogram of pyrolysis-0.01 N H_2SO_4 solution-trapped GC of latex A (contain acrylic acid). The inset shows the retention time between 12.0 and 13.5 min. The acrylic acid retention is 12.40 min, and the methacrylic acid is 13.02 min.

acrylic acid or methacrylic acid was not possible. Owing to interferences from other components in the pyrogram, the peak area of acrylic acid and methacrylic acid could not be measured without further separation or specific detection such as GC/MS.

Figures 4–9 show the gas chromatograms of pyrolysis products trapped in 0.01 N H_2SO_4 solution, methanol, and methylene chloride for acrylic acid containing latex A and methacrylic acid containing latex B, respectively. In the latex A case (Figures 4–6), comparing these three gas chromatograms with the direct Py-GC pyrograms, the 0.01 N H_2SO_4 solution-trapped products revealed a significant reduction in complexity of peaks and the acrylic acid and methacrylic acid peaks are better resolved from other pyrolysis products. This is a direct result of the low solubility of the nonpolar pyrolysis products in the polar solution. In contrast, the methanol and methylene chloride-trapped products exhibit gas chromatograms of about the same complexity as direct Py-GC pyrograms. This indicates that the selection of 0.01 N H_2SO_4 solution as the trapping solvent can properly separate the acrylic acid or methacrylic acid from an abundance of other components. Trapping, especially in the 0.01 N H_2SO_4 solution, improved the efficiency of separation/identification of the acrylic acid and methacrylic acid. The selection of the solvent for the trapping can depend on the components desired, the type of polymer, and the purpose of the analysis. In another way, the

Figure 5. Chromatogram of pyrolysis-methanol solution-trapped GC of latex A (contain acrylic acid). The inset shows the retention time between 12.0 and 13.5 min. The acrylic acid retention is 12.40 min.
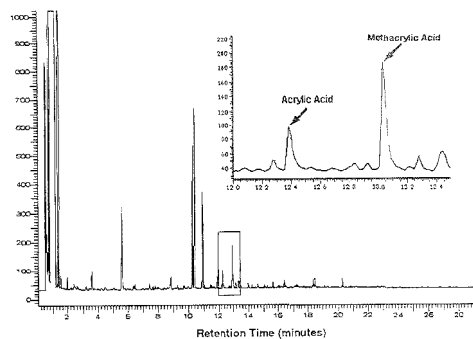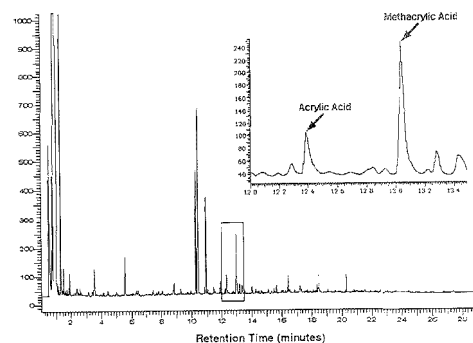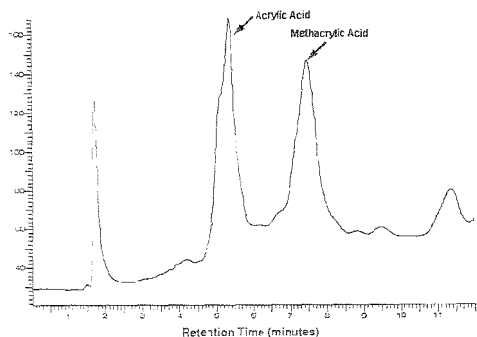

Figure 6. Chromatogram of pyrolysis-methylene chloride solution-trapped GC of latex A (contain acrylic acid). The inset shows the retention time between 12.0 and 13.5 min. The acrylic acid retention is 12.40 min.
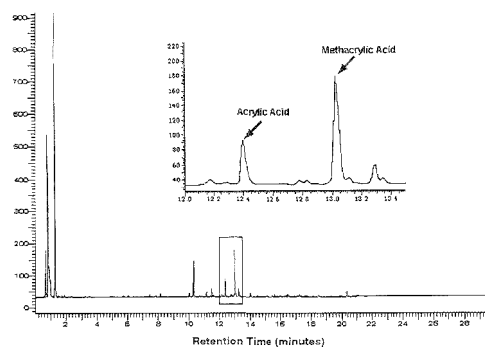
Figure 7. Chromatogram of pyrolysis-0.01 N H_2SO_4 solution-trapped GC of latex B (contain methacrylic acid). The inset shows the retention time between 12.0 and 13.5 min. The acrylic acid retention is 12.40 min, and the methacrylic acid is 13.02 min.
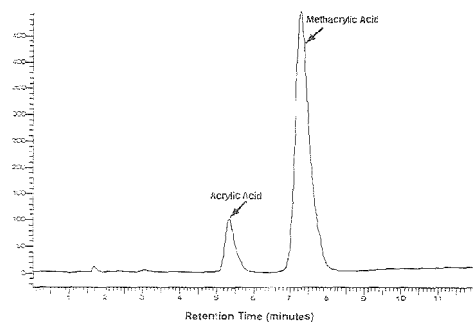

Figure 8. Chromatogram of pyrolysis-methanol solution-trapped GC of latex B (contain methacrylic acid). The inset shows the retention time between 12.0 and 13.5 min. The acrylic acid retention is 12.40 min, and the methacrylic acid is 13.02 min.

Figure 9. Chromatogram of pyrolysis-methylene chloride solution-trapped GC of latex B (contain methacrylic acid). The inset shows the retention time between 12.0 and 13.5 min. The acrylic acid retention is 12.40 min, and the methacrylic acid is 13.02 min.
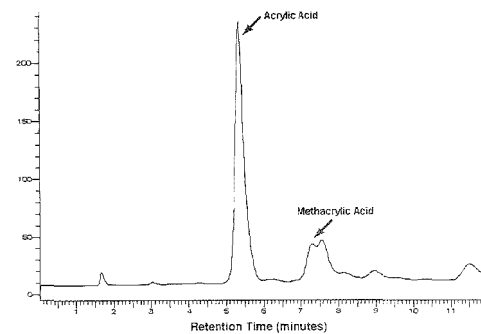
Figure 10. Chromatogram of pyrolysis-0.01 N H_2SO_4 solution-trapped LC of latex A (contain acrylic acid). The acrylic acid retention is 5.34 min, and the methacrylic acid is 7.28 min.

trapping procedure can be thought of as a sample preparation/ screening process. In the latex B case (Figures 7–9) , all three chromatograms are similar. This means the solvent selection is not as critical as in the latex A case.

Trapping the pyrolysis products into solution provided a significant advantage by allowing a choice for subsequent separa-

tion techniques. Instead of the separation being performed by GC, the separation also can be accomplished by LC. Figures 10–13 show the liquid chromatograms of the pyrolysis products trapped in 0.01 N H_2SO_4 and methanol for latex A and latex B, respectively. The acrylic acid and methacrylic acid retention times with these experimental conditions matched those of the standards

Figure 11. Chromatogram of pyrolysis-methanol solution-trapped LC of latex A (contain acrylic acid). The acrylic acid retention is 5.34 min, and the methacrylic acid is 7.28 min.

Figure 12. Chromatogram of pyrolysis-0.01 N H_2SO_4 solution-trapped LC of latex B (contain methacrylic acid). The acrylic acid retention is 5.34 min, and the methacrylic acid is 7.28 min.
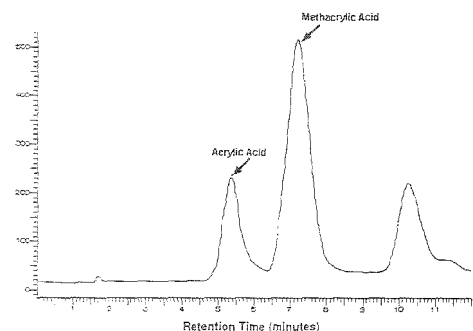
Figure 13. Chromatogram of pyrolysis-methanol solution-trapped LC of latex B (contain methacrylic acid). The acrylic acid retention is 5.34 min, and the methacrylic acid is 7.28 min.

at 5.34 and 7.28 min, respectively. In the 0.01 N H_2SO_4 solution case, the conversion percentage for acrylic acid was calculated as 0.004% and for methacrylic acid was calculated at 0.005%. Compared with the GC separation, the LC procedure supplied two additional separation advantages. The ion exclusion column used for the LC separation excluded any nonpolar components, and the UV detector (210 nm) discriminated against any non-UV-absorbing components. Consequently, the LC method provided

a cleaner chromatogram for easier identification and eliminated many possible interferences resulting in well-resolved peaks for area measurement and the foundation for further quantitative analysis.

The fourth advantage of the trapping process is that sample concentration can be adjusted to meet the separation/identification requirement. The solution concentration can be increased through pyrolysis of multiple samples or decreased by diluting with solvent. This is normally not an option with a direct Py-GC interface. In order to obtain the best separation/identification results, the capability of complete sample concentration control is a big advantage.

In conventional direct Py-GC, once the chromatographic experiment starts, both pyrolysis interface unit and chromatograph are locked into the experiment. This is true even with the several models of automatic pyrolysis units commercially available, which in general laboratory practice can be an inefficient means of utilizing instruments. In the solvent trapping technique, the pyrolysis process is separated from the separation/chromatography process. This translates to flexibility in choosing the separation technique and highly efficient instrument usage and time.

The detection limits or the minimum amount of acrylic and methacrylic acid that could be detected in the GC and LC method based on the 0.01 N H_2SO_4 solution case were calculated. These calculations were based on the analyte concentration giving a signal (peak height) greater or equal to the blank signal plus 10 standard deviations of the blank.[11] For acrylic acid, the GC detection limit was 2.29 pg and the LC detection limit was 7.73 pg of acrylic acid. For methacrylic acid, the GC detection limit was 2.58 pg and the LC limit 7.14 pg.

From the acrylic acid and methacrylic acid peaks in all the figures, no matter which acid in the latex was identified by the GC or LC separation, every chromatogram contained both acrylic acid and methacrylic acid peaks. This strongly suggested there was a methylation/demethylation reaction taking place during pyrolysis or the acids used in polymerization contained both monomeric species. The methyl group may be contributed from the fragmentation of other major components in the solid latex system such as styrene, butadiene, and methyl methacrylate.[12] The demethylation process can be viewed as another path of fragmentation of acid monomer which occurs during pyrolysis. The degree of methylation will highly depend on the pyrolysis environment especially if methyl groups are abundantly available during the pyrolysis reaction, such as pyrolyzing a latex with methyl methacrylate as a major component.

Because of the proposed methylation/demethylation process observed in this study, it is apparent that when one examines a latex suspected to contain both acrylic and methacrylic acids a suitable polymer standard needs to be used for peak ratio comparison. This standard should have the same fundamental polymer composition as the sample in question, thereby duplicating the potential methylation/demethylation reaction. With such a standard identified and analyzed by the same chromatographic conditions, the comparison of acrylic/methacrylic acid peak ratios should lead to a viable conclusion as to the existence of one or both acids in the emulsion polymer. For example, if the acrylic/methacrylic acid peak ratio matches that of a standard having

(11) Miller, J. C.; Miller, J. N. *Statistics for Analytical Chemistry*, 2nd ed.; John Wiley & Sons: New York, 1988; p 115.
(12) Sousa Pessoa de Amorium, M. T.; Bonster, C.; Veron, J. *J. Anal. Appl. Pyrolysis* **1981**, *3*, 19.

either one of the acids, then that one acid most likely exists alone in the polymer. Any significant deviation from this ratio would likely indicate that both acids are present.

CONCLUSION

The pyrolysis method should always be considered as a sample preparation technique especially for qualitative and quantitative analyses of vinyl acids in a solid polymer. The pyrolysis-liquid trapping method not only serves as a mechanism to collect pyrolysis products in the solvent matrix for the added flexibility of further analysis but also performs the first selection process (dissolve or not dissolve) for the pyrolysis products. The trapping system can be well designed and computer automated based on the application. In this study, the method of pyrolysis with trapping in 0.01 N H_2SO_4 solution for the purpose of analyzing acrylic acid and methacrylic acid in the latex solid phase has shown some distinct advantages over conventional pyrolysis techniques.

Theoretical Model of Electroosmotic Flow for Capillary Zone Electrophoresis

Marina F. M. Tavares[†] and Victoria L. McGuffin*

Department of Chemistry, Michigan State University, East Lansing, Michigan 48824-1322

A mathematical model of electroosmotic flow in capillary zone electrophoresis has been developed by taking into consideration of the ion-selective properties of silica surfaces. The electroosmotic velocity was experimentally determined, under both constant voltage and constant current conditions, by using the resistance-monitoring method. A detailed study of electroosmotic flow characteristics in solutions of singly charged, strong electrolytes (NaCl, LiCl, KCl, NaBr, NaI, NaNO$_3$, and NaClO$_4$), as well as the phosphate buffer system, revealed a linear correlation between the ζ potential and the logarithm of the cation activity. These results suggest that the capillary surface behaves as an ion-selective electrode. Consequently, the ζ potential can be calculated as a function of the composition and pH of the solution with the corresponding modified Nernst equation for ion-selective electrodes. If the viscosity and dielectric constant of the solution are known, the electroosmotic velocity can then be accurately predicted by means of the Helmholtz–Smoluchowski equation. The proposed model has been successfully applied to phosphate buffer solutions in the range of pH from 4 to 10, containing sodium chloride from 5 to 15 mM, resulting in ~3% error in the estimation of the electroosmotic velocity.

Over the past decade, capillary zone electrophoresis (CZE) has emerged as a very resourceful alternative for the separation of charged biomolecules. Relevant aspects of the technique, such as high efficiency, high resolving power, high speed, full automation, and a variety of injection and detection schemes, have been extensively investigated.[1] In addition to these technological developments, much research in capillary zone electrophoresis has been directed toward demonstrating the versatility of the technique for routine applications.[2,3] However, despite the past considerable effort toward the description of the electrokinetic phenomena,[4,5] there is still a scarcity of fundamental studies to provide greater understanding of the physicochemical nature of the separation process at the capillary surface and in solution.

In capillary zone electrophoresis, a background electrolyte with adequate buffering properties forms a continuum along the migration path. Under the influence of a tangentially applied electric field, two mechanisms of migration occur.[1,4,5] The field exerts an electric force on charged molecules, which migrate with a constant velocity that is characteristic of the molecular charge, size, and shape. Concomitant to the electrophoretic migration, a flow of solution as a bulk is induced by the electric field. This migration, regarded as electroosmosis, is dependent on the characteristics of the capillary surface as well as the composition of the conducting medium.

The existence of electroosmotic flow in fused-silica capillaries has contributed significantly to the full automation of capillary electrophoresis, allowing for on-line sample injection and detection as well as simultaneous analysis of cations and anions in favorable cases.[1–3] The electroosmotic flow has a substantial influence on the time the analytes reside in the capillary. However, because of the flat velocity profile, electroosmotic flow theoretically introduces no broadening. The same velocity component is added to all solute molecules, regardless of their radial position. Consequently, analysis time and efficiency benefit from a rapid electroosmotic flow, although resolution may be compromised.

The understanding and control of electroosmotic flow have critical implications in the design of electrophoretic separations. In recent years, several strategies have been developed to exert a proper control of the electroosmotic flow. Perhaps the most effective means is to alter the chemical and physical properties of the buffer solution. In this context, changes in the pH, concentration, and ionic strength of the buffer[6,7] and in the type and concentration of inert electrolyte or organic additive,[8–11] as well as changes in solvent viscosity, dielectric constant,[12] and temperature,[13] have all been successfully demonstrated. Another simple approach to alter or ultimately inhibit the electroosmotic flow involves changing the chemical composition of the capillary material and, hence, the surface charge density. Fused-silica, glass, and Teflon capillaries have been employed for this purpose.[14] In fused-silica capillaries, the nature of the capillary wall can be further modified by physical coating and chemical deriva-

† Current address: Instituto de Química, Universidade de São Paulo, São Paulo, Brazil.

(1) Grossman, P. D.; Colburn, J. C. *Capillary Electrophoresis—Theory and Practice*; Academic Press Inc.: San Diego, CA, 1992.

(2) Kuhr, W. G.; Monnig, C. A. *Anal. Chem.* **1992**, *64*, 389R–407R.

(3) McLaughlin, G. M.; Nolan, J. A.; Lindahl, J. L.; Palmieri, R. H.; Anderson, K. W.; Morris, S. C.; Morrison, J. A.; Bronzert, T. J. *J. Liq. Chromatogr.* **1992**, *15*, 961–1021.

(4) Hiemenz, P. C. *Principles of Colloid and Surface Chemistry*, 2nd ed.; Marcel Dekker: New York, 1986.

(5) Bier, M. *Electrophoresis—Theory, Methods and Applications*; Academic Press Inc.: New York, 1959.

(6) Vindevogel, J.; Sandra, P. *J. Chromatogr.* **1991**, *541*, 483–488.

(7) VanOrman, B. B.; Liversidge, G. C.; McIntire, G. L.; Olefirowicz, T. M.; Ewing, A. G. *J. Microcolumn Sep.* **1990**, *2*, 176–180.

(8) Atamna, I. Z.; Metral, C. J.; Muschik, G. M.; Issaq, H. J. *J. Liq. Chromatogr.* **1990**, *13*, 2517–2527.

(9) Atamna, I. Z.; Metral, C. J.; Muschik, G. M.; Issaq, H. J. *J. Liq. Chromatogr.* **1990**, *13*, 3201–3210.

(10) Green, J. S.; Jorgenson, J. W. *J. Chromatogr.* **1989**, *478*, 63–70.

(11) Fujiwara, S.; Honda, S. *Anal. Chem.* **1987**, *59*, 487–490.

(12) Schwer, C.; Kenndler, E. *Anal. Chem.* **1991**, *63*, 1801–1807.

(13) Kurosu, Y.; Hibi, K.; Sasaki, T.; Saito, M. *J. High Resolut. Chromatogr.* **1991**, *14*, 200–203.

(14) Lukacs, K. D.; Jorgenson, J. W. *J. Chromatogr.* **1985**, *8*, 407–411.

tization methods.[15-17] Other strategies, such as the application of an external electric field across the capillary wall, can also be used to influence the electroosmotic flow.[18,19]
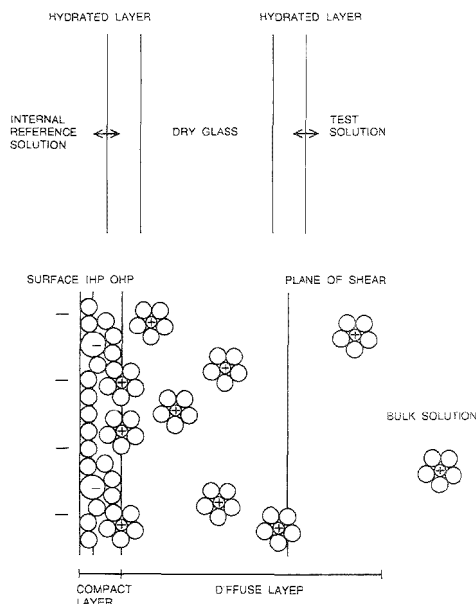
At the present time, mathematical modeling of electroosmotic flow has been achieved by solution of the fundamental laws describing mass transport and chemical equilibria.[20,21] Other approaches rely on the estimation of parameters related to the electrical double layer.[22] In most instances, the resulting equations are not trivial, and their solution can be approached only by computationally intensive numerical methods. Therefore, a simpler and more practical means of describing the migration process is highly desirable.

In this work, the nature of electroosmotic migration in fused-silica capillaries is examined from theoretical and experimental perspectives. A physically meaningful model is proposed, where the response of the capillary surface to changes in buffer composition and pH is treated in analogy to an ion-selective electrode. The prediction of electroosmotic flow is evaluated under both constant voltage and constant current conditions. The validity of the model is confirmed using phosphate buffer solutions in the pH range from 4 to 10, with a controlled total concentration of sodium ion.

THEORY

Ion-Selective Membranes. The ion-selective properties of glass membranes have been exploited for the construction of a variety of chemical sensors.[23-25] Among the many representative examples, the pH-sensing glass electrode is one of the most common. A typical pH electrode consists of a thin glass membrane sealed at the end of a tube containing an appropriate standard solution and an internal reference electrode. During the measurements, the complete assembly is immersed in a test solution, and the potential is registered with respect to an external reference electrode. A schematic diagram of the glass membrane in contact with the internal reference solution and the test solution is shown in the top part of Figure 1.

Many of the properties that confer sensitivity and selectivity to such membranes are associated with the chemical structure of the glass.[24] Silicate glasses are composed of an irregular three-dimensional network of silicon and oxygen atoms with nominal composition $(SiO_2)_x$. The holes or defects in this structure are occupied by cations, held more or less strongly by electrostatic attraction to the neighboring oxygen atoms. Doubly and triply charged cations are strongly held and do not contribute to the electrical conduction properties of the glass. However, singly charged cations, which are quite mobile within the lattice, are primarily responsible for charge transport in the interior of the glass membrane.

(15) Schomburg, G. Trends Anal. Chem. 1991, 10, 163–169.
(16) Hjerten, S. J. Chromatogr. 1985, 347, 191–198.
(17) McCormick, R. Anal. Chem. 1988, 60. 2322–2328.
(18) Lee, C. S.; McManigill, D.; Wu, C. T.; Patel, B. Anal. Chem. 1991, 63, 1519–1523.
(19) Hayes, M. A.; Ewing, A. G. Anal. Chem. 1992, 64, 512–516.
(20) Dose, E. V.; Guiochon, G. A. Anal. Chem. 1991, 63, 1063–1072.
(21) Bier, M.; Palusinski, O. A.; Mosher, R. A.; Saville, D. A. Science 1983, 219, 1281–1287.
(22) Salomon, K.; Burgi, D. S.; Helmer, J. C. J. Chromatogr. 1991, 559, 69–80.
(23) Bard, A. J.; Faulkner, L. R. Electrochemical Methods—Fundamentals and Applications; John Wiley & Sons: New York, 1980.
(24) Koryta, J. Ion-Selective Electrodes. 2nd ed.; Cambridge University Press: London, 1975.
(25) Freiser, H. Ion-Selective Electrodes in Analytical Chemistry; Plenum Press: New York, 1978.

Figure 1. Schematic diagrams of an ion-selective glass membrane (top) and the electrical double-layer structure at silica surfaces (bottom). These diagrams are not on the same distance scale but are drawn to emphasize the regions of behavioral analogy according to the proposed model.

Exposure of the glass to water causes the formation of a hydrated gel layer. At the outer edge of this layer in contact with the solution, the singly charged sites are predominantly occupied by hydrogen ions. Within the gel layer, there is a continuous decrease in the number of hydrogen ions and an increase in the number of other cations. In the interior of the glass, such sites are occupied exclusively by cations.

The exchange of cations in the hydrated gel layer with cations in the solution is responsible for the pH response and alkaline error that are characteristic of glass membranes. If sodium is considered to be the only active cation in the membrane, the ion-exchange reaction can be written as

$$H^+(glass) + Na^+(soln) \leftrightarrow H^+(soln) + Na^+(glass) \quad (1)$$
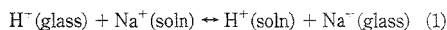
with the associated equilibrium constant

$$K = \frac{a_H(soln)a_{Na}(glass)}{a_H(glass)a_{Na}(soln)} \quad (2)$$

where a_H and a_{Na} represent the activities of hydrogen and sodium ions, respectively, in solution (soln) and in the interior of the glass membrane (glass). The equilibrium constant for this reaction is quite small, favoring the incorporation of hydrogen rather than

sodium ions into the silicate lattice in close contact with the solution.[23]

When a pH difference exists between the test and the internal reference solutions, a boundary potential develops across the glass membrane. This boundary potential (E_b) is given by the Nernst equation, modified to include the contribution of the sodium ions to the pH response:[23]

$$E_b = E' + \frac{2.303RT}{zF} \log[a_H(\text{soln}) + k^{pot} a_{Na}(\text{soln})] \quad (3)$$

where z is the ionic charge, T is the absolute temperature, R is the gas constant, and F is the Faraday constant. The constant term (E') includes contributions to the boundary potential from hydrogen and sodium ions in the internal reference solution, as well as from the reference electrode, junction, and asymmetry potentials. Equation 3 shows that the membrane is responsive to both hydrogen and sodium ions in the test solution, where the degree of selectivity is dictated by the magnitude of k^{pot}. The quantity k^{pot} is defined as the potentiometric constant of the determinand H^+ with respect to the interferent Na^- and may assume values that range from zero (no interference) to greater than unity, depending upon the composition of the membrane.[24,25] The potentiometric constant is comprised of the ratio of ionic mobilities (μ) in the membrane as well the exchange equilibrium constant defined by eq 2:

$$k^{pot} = K \frac{\mu_{Na}(\text{glass})}{\mu_H(\text{glass})} \quad (4)$$

Equation 3 leads to interesting predictions concerning the glass membrane response. If the product of k^{pot} and a_{Na} is sufficiently small compared to a_H, the membrane is primarily responsive to hydrogen ions, constituting a pH-selective glass electrode. Conversely, when the product of k^{pot} and a_{Na} surpasses a_H, the membrane responds primarily to sodium ions, constituting a sodium-selective glass electrode.

Electrical Double-Layer Structure. Silica surfaces are characterized by the presence of several types of silanol groups (SiOH), which are weakly acidic in character.[27] In contact with an aqueous medium, some of the silanol groups are ionized and cause the surface to be negatively charged.[28] As a result, a nonhomogeneous spatial distribution of charge originates within the solution in immediate proximity to the surface, designated as the electrical double layer. Much theoretical work has been concerned with describing the interface between the surface and the solution, including evaluation of the potential and concentration profiles as a function of distance.[4,5,23] Some of the presently accepted features of the electrical double-layer structure are illustrated in the bottom part of Figure 1.

The region adjacent to the surface is occupied by layers of strongly oriented water molecules and some ions, presumably dehydrated, tightly held to the surface by electrostatic and other cohesive forces (specific adsorption). The center of these ions defines a plane known as the inner Helmholtz plane (IHP).

(26) Buck, R. P.; Boles, J. H.; Porter, R. D.; Margolis, J. A. *Anal. Chem.* **1974,** *46,* 255–261.

(27) Unger, K. K. *Porous Silica;* Journal of Chromatography Library 16; Elsevier Scientific Publishing Co.: New York, 1979.

(28) Lyklema, J. *J. Electroanal. Chem.* **1968,** *18,* 341–348.

Hydrated ions approach the surface by a distance correspondent to their hydration radius. These ions are loosely bound, and their interaction with the surface is independent of their chemical properties (nonspecific adsorption). The plane defined by the center of the hydrated ions is known as the outer Helmholtz plane (OHP), or Stern layer, and delimits the compact region of the double layer. Due to the finite temperature and associated random thermal motion, some of the ions diffuse further into solution. As the distance from the surface increases, the concentration decreases and ultimately approaches the bulk value. This region is referred to as the diffuse part of the double layer.

When an electric field is imposed tangentially to the surface, the electrical forces act upon the spatial distribution of charge within the diffuse layer, causing the unilateral movement of ions toward the oppositely charged electrode.[4,5] During their migration, these ions transport the surrounding solvent molecules, inducing the overall movement of solution known as electroosmotic flow. Due to differences in the magnitude of electrical and frictional forces within the double layer, a velocity gradient originates. The flow velocity is zero at the surface, increases inside the double-layer region, and reaches a maximum value at a certain, very small distance from the charged surface. The remainder of the solution migrates with this maximum velocity. The location at which the mobile portion of the diffuse layer can slip or flow past the charged surface is characterized as the plane of shear. The potential developed at the plane of shear is known as the electrokinetic or ζ potential. Its magnitude has important implications on the development and characterization of electroosmotic flow (vide infra).

The potential distribution in the double layer can be derived by solving the Poisson–Boltzmann equation for limiting cases. If the surface potential (Ψ_0) is sufficiently low (<50 mV), the potential profile with distance (x) can be approximated by the Debye–Huckel theory:[4,23]

$$\Psi = \Psi_0 \exp(-\kappa x) \quad (5)$$

One of the most important quantities to emerge from the Debye–Huckel theory is the parameter κ, which correlates properties of the solution with the double-layer dimensions:

$$\kappa^2 = \frac{1000e^2 N_A}{\epsilon kT} \sum z_i^2 M_i \quad (6)$$

where z_i is the charge and M_i the molarity of ion i, ϵ is the dielectric constant of the medium, e is the elemental charge, N_A is Avogadro's number, k is Boltzmann's constant, and T is the absolute temperature. The quantity κ^{-1}, known as the Debye length, is often used to characterize the thickness of the double layer.

Analogy between Ion-Selective Membranes and Double-Layer Structure at Silica Surfaces. The proposed model for electroosmotic flow is based on behavioral analogies between an ion-selective membrane and the double-layer structure at the fused-silica capillary surface, as illustrated in Figure 1. In analogy to the internal reference solution of a pH-sensing glass electrode, the compact region of the double layer is modeled as a reference layer for the bulk solution. The establishment of the compact layer is dictated primarily by the extent of ionization of the silica

surface, which is affected by the pH but not by the ionic character and content of the bulk solution. Therefore, the potential within the compact layer responds only to changes in pH of the bulk solution. At the plane of shear, which is a physical boundary between the immobile and mobile parts of the solution, an exchange equilibrium between hydrogen and sodium ions occurs. Therefore, the potential at the plane of shear the ζ potential, is responsive to both hydrogen and sodium ions in the bulk solution, in a mechanism analogous to that which accounts for the alkaline error in glass membranes. The proposed model thus comprises two fundamental ways to manipulate electroosmotic flow in capillary zone electrophoresis: the judicious choice of pH (a coarse adjustment) and the selection of an appropriate sodium concentration (a fine adjustment).

EXPERIMENTAL SECTION

Capillary Zone Electrophoresis System. A regulated high-voltage dc power supply (Model EH50R0.19XM3; Glassman High Voltage Inc., Whitehouse Station, NJ) is operated in either constant current (0–190 μA) or constant voltage (0–50 kV) mode. The operator is protected from accidental exposure to high voltage by enclosing the CZE system in a Plexiglas box equipped with safety interlocks. The power supply is connected via platinum rod electrodes to two small reservoirs containing the solution under investigation. Fused-silica capillary tubing (Polymicro Technologies, Phoenix, AZ), with dimensions 75 μm i.d., 375 μm o.d., and 110 cm total length, is immersed at each end in the solution reservoirs. In order to minimize thermal effects, the capillary is maintained at 25.0 °C during operation by means of a thermostatically controlled water bath (Model RTE 9B; Neslab Instruments, Portsmouth, NH).

The standard procedure to condition the capillary surface prior to flow measurement consisted of washing with 1 M sodium hydroxide for 10 min, followed by washing with the solution under investigation, preferably overnight but at least for a 2 h period, at 20 psi. In the studies on the effect of cation type, an acid wash with 10^{-2} M hydrochloric acid was performed prior to the alkaline wash with a solution of the appropriate cation hydroxide. In the studies on phosphate buffers, the standard conditioning procedure was performed only when the pH of the buffer was changed. When not in use, the capillary was rinsed with deionized water and dried under helium.

Flow Measurement. The electroosmotic flow was measured by a modification of the procedure introduced by Huang et al.[29] Initially, the capillary and the outlet reservoir are filled with a solution that is 2% higher in concentration than the nominal or desired value. The inlet reservoir is then replenished with a solution of the same composition but 2% lower than the nominal concentration. Under the applied electric field, the dilute solution continuously migrates into the capillary and displaces an equivalent volume of the more concentrated solution, thereby causing the resistance to change. If the power supply is operated in the constant voltage mode, the changes in resistance can be followed by recording the changes in current. Conversely, if the instrument is operated in the constant current mode, the changes in resistance can be followed by recording the changes in voltage. A 0–10 V dc signal, in direct proportion to either the output current (0–190 μA) or the output voltage (0–50 kV), is available at the remote terminal of the power supply. This signal is subsequently divided

(29) Huang, X.; Gordon, M. J.; Zare, R. N. *Anal. Chem.* **1988**, *60*, 1837–1838.

to 0–1 V and displayed on a recorder (Model 3392A; Hewlett-Packard Co., Avondale, PA). Note that when the current is monitored, the signal decreases with time until the entire capillary is filled with the dilute solution, after which the signal becomes constant. Under the same conditions, when the voltage is monitored, the signal initially increases and then becomes constant. The inflection point represents the time (t) required to complete the filling of the capillary by electroosmosis. Thus, with knowledge of the capillary length (L), the electroosmotic velocity can be calculated ($v_{osm} = L/t$). Provided that the velocity is linearly related to concentration over the small interval ($\pm 2\%$) used for the measurement, no determinate error is introduced by the resistance-monitoring method.

Reagents. All electrolyte solutions were prepared from analytical grade reagents and deionized water, preadjusted to pH 9 with 0.1 M sodium hydroxide solution. The buffer systems (pH 4–10) were prepared from sodium mono-, di-, and triphosphates and sodium chloride salts. The buffer solutions were formulated in order to contain a specific total sodium ion concentration (5–15 mM).

Physical Measurements. The absolute viscosity of sodium chloride solutions was determined by measurements of kinematic viscosity and density.[30] A constant value of 0.8755 ± 0.0017 cP at 25 °C was obtained for all solutions in the concentration range from 1 to 10 mM. The dielectric constant of sodium chloride solutions was evaluated by the heterodyne beat method[30] using a beat-frequency oscillator (Model DM01; Wiss. Tech. Werkstatten, Weilheim Obb., Germany). Due to inherent limitations of this method when applied to solutions of high conductance, the measurements could not be performed at concentrations greater than 0.1 mM. A constant value of 78.5 ± 1 at 25 °C was obtained for all solutions in the concentration range from 0.001 to 0.1 mM.

Data Processing. All data processing and numerical calculations were performed on a 80–386 microprocessor-based computer in a spreadsheet format (Microsoft Excel, version 4.0; Microsoft Corp., Redmond, WA).

RESULTS AND DISCUSSION

The characterization of electroosmotic flow depends on how distinctly the effect of a given variable can be isolated from others. For this reason, the proper selection of the conducting medium and the control of its composition are extremely important. Conducting media with buffering properties are commonly used in capillary zone electrophoresis because of the dual effect of pH on the extent of ionization of the solutes and the silanol groups. However, the complexity of buffer systems and the diversity with which a buffer solution can be formulated make it difficult to isolate the effect of a single variable such as pH from other changes that may occur concomitantly when pH is varied, such as ionic strength, buffer concentration and capacity, cation and anion type, etc. Therefore, in order to characterize the electroosmotic flow, a simpler electrolyte system seems to be a more appropriate choice. In this work, the preliminary studies were performed using solutions of singly charged, strong electrolytes. In later studies, the electroosmotic flow was characterized in the phosphate buffer system, and a comprehensive model was developed to predict the flow magnitude under a variety of operational conditions.

(30) Weissberger, A. *Physical Methods of Organic Chemistry*, 3rd ed.; Interscience Publishers Inc.: New York, 1959.

The experimental validation of the proposed model relies on the precision and accuracy with which the electroosmotic flow can be determined. It is well accepted[7,12,31,32] that the electroosmotic flow is strongly dependent on the manner in which the capillary surface has been conditioned. In the absence of a systematic procedure, the electroosmotic flow could be measured in the same day with ±10% RSD, and the day-to-day reproducibility was ±20% RSD. When the capillary surface was conditioned properly, as described previously, the single-day reproducibility was better than ±1% RSD, and the day-to-day reproducibility was better than ±3% RSD over a period of 6 months.

The reliability of the model for the electroosmotic flow also depends on the method selected to evaluate the flow magnitude. In this work, several of the most common methods were compared, including the neutral-marker method,[14] the weighing procedure,[31] and the resistance-monitoring method.[29] When a large pH range was inspected, the monitoring of resistance changes in the conducting medium was found to be the most reliable method. The modifications introduced in this work extend the use of the resistance-monitoring method to both constant voltage and constant current conditions. This enables the direct comparison of results obtained under both conditions for the development and evaluation of the proposed model of electroosmotic flow.

Preliminary Studies of Electroosmotic Flow under Constant Voltage Conditions. In the constant voltage operation of the power supply, the electroosmotic flow is evaluated by means of the Helmholtz–Smoluchowski equation,[4,5] which relates the linear velocity (v_{osm}) and the electric field strength (E) according to

$$v_{osm} = -\frac{\epsilon\epsilon_0\zeta}{\eta}E = \mu_{osm}\frac{V}{L} \tag{7}$$

where V is the applied voltage and L is the total capillary length. The proportionality term, which represents the electroosmotic mobility (μ_{osm}), is comprised of several constants such as the dielectric constant (ϵ) and the viscosity (η) of the medium, the permittivity of the vacuum (ϵ_0), and the ζ potential (ζ). The Helmholtz–Smoluchowski equation is valid when the radius of the capillary (r) is large compared to the double-layer thickness (κ^{-1}, eq 6), or when the product (κr) is much larger than 100. In the theoretical derivation of eq 7, no assumptions are made regarding the structure of the double layer except for the existence of a plane of shear. It is implied, however, that the dielectric constant and viscosity of the bulk solution are applicable within the double layer. It is interesting to note that when the velocity and electric field vectors are in the same direction, a negative value for ζ potential is required.

According to the Helmholtz–Smoluchowski equation, a linear relationship between the electroosmotic velocity and field strength is expected. However, when the velocity is displayed as a function of the applied voltage (Figure 2), the slope shows a dependence on the concentration of sodium chloride in aqueous solutions. Therefore, it is important to examine in more detail the effect of concentration on each constant in the slope of the Helmholtz–

(31) Lambert, W. J.; Middleton, D. L. *Anal. Chem.* **1990**, *62*, 1585–1587.
(32) Smith, S. C.; Strasters, J. K.; Khaledi, M. G. *J. Chromatogr.* **1991**, *559*, 57–68.
(33) Altria, J. D.; Simpson, C. F. *Anal. Proc.* **1986**, *23*, 453–454.
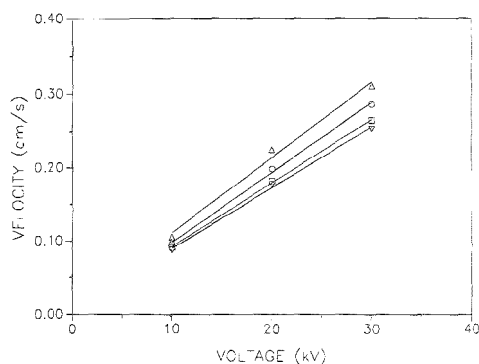
Figure 2. Dependence of electroosmotic velocity on the applied voltage for aqueous sodium chloride solutions of concentration (△) 1, (○) 2, (□) 3, and (▽) 4 mM.

Smoluchowski equation. In order to accommodate the large concentration range studied, the results are plotted in a semilogarithmic manner in Figure 3. As intrinsic properties of the solution, the dielectric constant and viscosity are expected to be dependent on the solution composition.[30] However, within the concentration range studied, both the dielectric constant and the viscosity are shown to be fairly constant and approach the values for pure water. The ζ potential was calculated from eq 7, where the slope of the graph of electroosmotic velocity versus applied voltage was used, together with the measured values of viscosity and dielectric constant. As an interface potential, the ζ potential is expected to be influenced by both the solution composition and the surface characteristics. Indeed, the ζ potential shows a marked dependence on the concentration of the solution in Figure 3. These results identify the ζ potential as the most important parameter to understand the development of electroosmotic flow and the mechanism by which the surface responds to changes in the electrolyte composition. Furthermore, the dependence of the ζ potential on the logarithm of the sodium concentration characterizes an ion-selective type of response.

With the intent of exploring in more detail the ion-selective behavior of the capillary surface, the ζ potential was determined in other singly charged electrolyte systems. Figure 4a presents the influence of the cation type on the magnitude of the ζ potential for aqueous solutions of lithium, sodium, and potassium chloride. Within the concentration range studied, the ζ potential varied linearly with the logarithm of the cation concentration, which verifies that the capillary surface responds to each cation in a Nernstian manner. However, at any given concentration, no statistically significant variation in the magnitude of the ζ potential was observed. This behavior implies that the surface does not distinguish between cation types, regardless of their chemical diversity. Two possible explanations are proposed to justify this behavior: either the site-binding characteristics of lithium, sodium, and potassium are similar or the cations are totally precluded from specific adsorption within the compact layer. The latter conclusion seems to be more reasonable in view of the previous work of Li and Bruyn,[34] where radiometric measurements at quartz surfaces revealed the presence of sodium ions only in the diffuse region

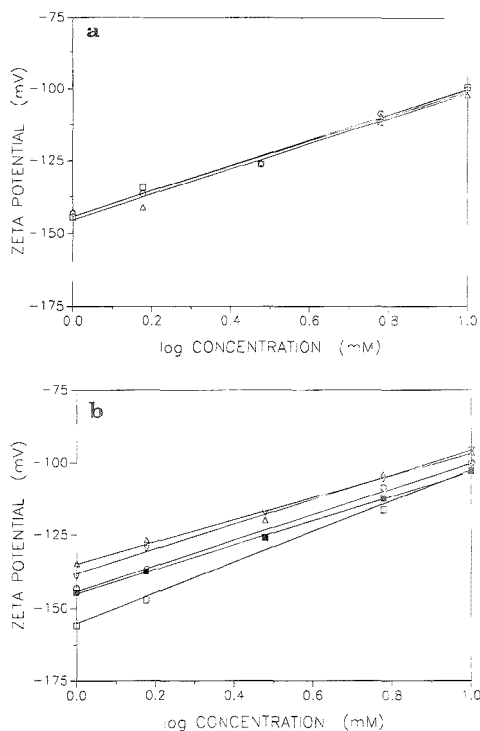(34) Li, H. C.; Bruyn, P. L. *Surf. Sci.* **1966**, *5*, 203–220.
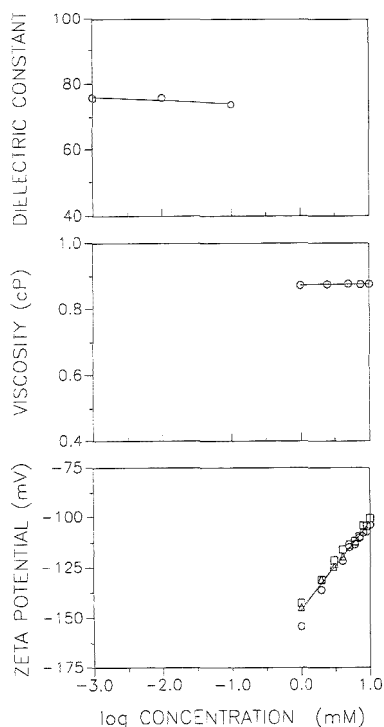
Figure 3. Evaluation of dielectric constant, viscosity, and ζ potential of aqueous sodium chloride solutions at pH 9. The ζ potential was evaluated under constant voltage conditions at ($\triangle$) 10, (O) 20, and ($\square$) 30 kV.

Figure 4. (a) Effect of cation type on the magnitude of the ζ potential under constant voltage conditions at 20 kV. Aqueous solutions at pH 9 of ($\triangle$) LiCl, ($\square$) KCl, and (O) NaCl. (b) Effect of anion type on the magnitude of the ζ potential under constant voltage conditions at 20 kV. Aqueous solutions at pH 9 of (O) NaCl, ($\triangle$) NaBr, ($\blacksquare$) NaI, ($\square$) NaNO₃, and ($\triangledown$) NaClO₄.

of the double layer. It is noteworthy that several recent studies in capillary zone electrophoresis have reached conclusions different from those reported here. Salomon et al.[22] reported that electroosmotic velocity increased with the hydrated radius of the cation, whereas Atamna et al.[8] observed the opposite behavior. Based on our experience, the method of conditioning the capillary surface is particularly important when the cation type is altered. An acid wash is necessary to remove the cations in the immobile region of the diffuse layer, so that they can be replaced completely with the appropriate cation during the alkaline wash. In the absence of this treatment, a mixed composition of cations is obtained at the capillary surface, which compromises the reliability and long-term reproducibility of the electroosmotic flow.

Figure 4b presents the influence of the anion type on the magnitude of the ζ potential for aqueous solutions of sodium chloride, bromide, iodide, nitrate, and perchlorate. The ζ potential varied markedly with the anion type, particularly in the low concentration range. These results suggest that the anion is involved, in some manner, in the development of the double-layer structure. The exact origin of this effect is not known, however, as there is no apparent correlation of the ζ potential with the hydrated radius,[35,36] the mobility,[23] or the adsorption properties[37,38] of the anion. There appears to be a great deal of controversy in

the literature to date regarding the effect of anion type on the development of the electroosmotic flow. Atamna et al.[9] observed strong differences in the electroosmotic flow using common sodium buffer solutions. VanOrman et al.[7] found that buffers with several different anion types can produce the same electroosmotic velocity, provided that the ionic strength is carefully controlled. Green and Jorgenson[10] concluded that differences in anion type are unimportant if the concentration of an inert electrolyte is at least 3-fold higher than the concentration of the operating buffer. Despite these prior observations, our data suggest that even solutions of inert electrolytes with well-controlled ionic strength exhibit a distinct influence of the anion type on the electroosmotic flow.

In conclusion, the results presented herein clearly sustain the possibility of predicting electroosmotic flow by modeling the ζ potential as a function of the logarithm of the cation concentration. It has been shown that the capillary surface responds to the

(35) McConnell, B. L.; Williams, K. C.; Daniel, J. L.; Stanton, J. H.; Irby, B. N.; Dugger, D. L.; Maatman, R. W. *J. Phys. Chem.* **1964**, *68*, 2941–2946.

(36) Melchior, D. C.; Bassett, R. L. *Chemical Modeling of Aqueous Systems II*; ACS Symposium Series 416; American Chemical Society: Washington, DC, 1990.

(37) Schultze, J. W.; Koppitz, F. D. *Electrochim. Acta* **1976**, *21*, 327–336.

(38) Habib, M. A.; Bockris, J. O. In *Comprehensive Treatise of Electrochemistry*; Bockris, J. O., Conway, B. E., Yeager, E., Eds.; Plenum Press: New York, 1980; Vol. 1, Chapter 4.

solution concentration in a Nernstian manner, regardless of the electrolyte type employed. There is no apparent selectivity of the surface toward the cation; however, the ζ potential magnitude is affected by the anion identity. Therefore, under constant voltage conditions, the prediction of electroosmotic flow is restricted by the ionic character of the electrolyte system.

Preliminary Studies of Electroosmotic Flow under Constant Current Conditions. In order to describe electroosmotic flow under constant current conditions, Ohm's law must be incorporated into the Helmholtz–Smoluchowski equation (eq 7):

$$v_{osm} = -\frac{\epsilon\epsilon_0\zeta}{\eta}\frac{RI}{L} \qquad (8)$$

where R is the resistance of the medium, I is the applied current, and all other variables are previously defined. The resistance is given by

$$\frac{1}{R} = k\frac{A}{L} \qquad (9)$$

where A is the cross-sectional area of the capillary and k is the conductivity of the solution. The conductivity is related to the electrophoretic mobility (μ_i) of the individual ionic species as follows:

$$k = F\sum|z_i|\mu_i M_i \qquad (10)$$

By combining eqs 8–10, the following expression results:

$$v_{osm} = -\frac{\epsilon\epsilon_0\zeta}{\eta}\frac{I}{Ak} = \frac{\mu_{osm}}{AF\sum|z_i|\mu_i M_i}I \qquad (11)$$

Equation 11 predicts a linear relationship between electroosmotic velocity and the applied current. The influences of the capillary dimensions, solution properties, and surface characteristics are clearly evident in the derivation of eq 11.

According to eq 11, the electrophoretic mobility is one of the intrinsic characteristics of the electrolyte that is expected to affect the electroosmotic velocity. To examine the extent of this effect, the electroosmotic velocities of sodium nitrate and sodium bromide solutions were measured in reference to sodium chloride solutions. Nitrate and bromide are the anions whose solutions presented the greatest difference in electroosmotic behavior in the previous study under constant voltage conditions. The electroosmotic velocity under constant current conditions, shown in Figure 5, varied linearly with the applied current and seems to be independent of the type of anion. Therefore, it is valid to conclude that the differences in anion mobility[23] were not sufficiently large to affect the electroosmotic velocity under the experimental conditions employed in this work.

As shown in eq 11, another means to affect the electroosmotic flow is by altering the charge of the electrolyte. This is particularly important when studying the electroosmotic behavior of more complex electrolytes such as buffer systems, where several species with different charge and mobility are likely to be present. However, by addition of a substantial amount of a singly charged, strong electrolyte, the electroosmotic velocity of the buffer solution can be controlled. Figure 6 shows the results of flow measure-
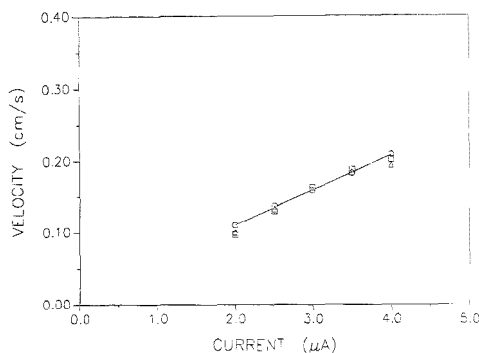
Figure 5. Effect of anion type on the electroosmotic velocity under constant current conditions. Aqueous solutions at pH 9 with 3 mM concentration of (O) NaCl, ($\triangle$) NaBr, and ($\square$) NaNO$_3$.
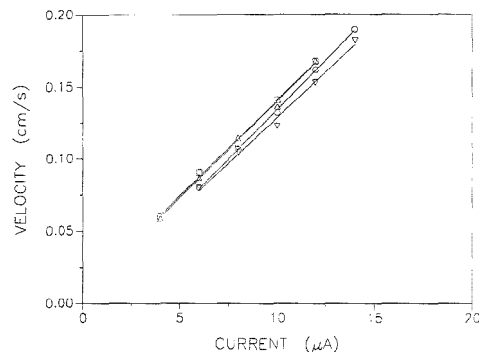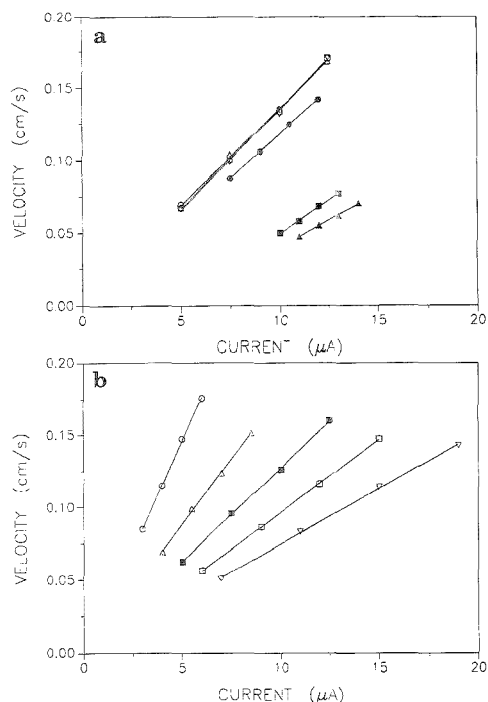

Figure 6. Effect of the ratio of Na(NaCl) to Na(buffer salts) on electroosmotic velocity under constant current conditions for phosphate buffer solutions at pH 9 with 10 mM total sodium concentration: ($\triangledown$) 0:10, (O) 5:5, ($\square$) 6.5:3.5, and ($\triangle$) 10:0.

ments in phosphate buffer solutions at pH 9 (where the highly charged PO_4^{3-} and HPO_4^{2-} species predominate over $H_2PO_4^-$ and H_3PO_4), with increasing amounts of sodium chloride. When the concentration of sodium chloride exceeds the concentration of the buffer salts, the electroosmotic velocity approaches that of a sodium chloride solution.

The studies under constant current conditions have shown that the ion-selective behavior of the capillary surface applies to strong electrolytes as well as to buffer systems. In buffers, however, the differences in charge and mobility of the individual species must be masked by addition of an excess of a singly charged, strong electrolyte. Therefore, under carefully controlled experimental conditions, the proposed model of electroosmotic flow can be explored in more detail to represent the behavior of complex buffer systems.

Validation of the Ion-Selective Model. The effects of pH and composition of phosphate buffer solutions were examined separately under constant current conditions. These solutions were prepared in such a way that the ratio of sodium from sodium chloride and the sodium buffer salt was maintained constant and equal to unity. For a constant concentration of sodium, shown for a representative case in Figure 7a, the electroosmotic velocity increased nonlinearly from pH 4 to 10. The pH affects the
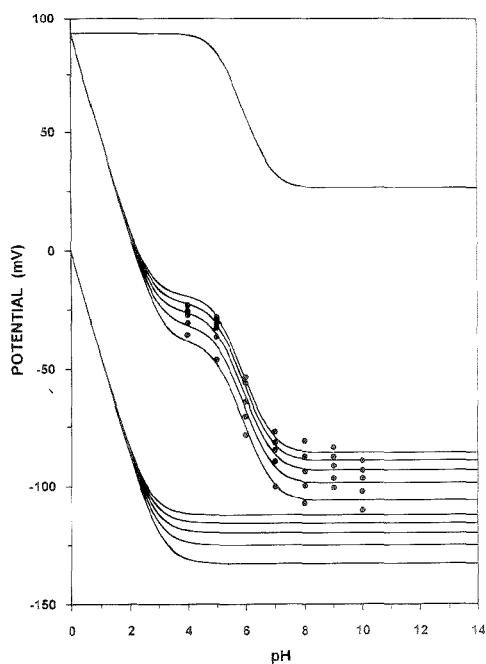
Figure 7. (a) Effect of pH on electroosmotic velocity under constant current conditions for phosphate buffer solutions with 10 mM total sodium concentration and 1:1 ratio of Na(NaCl) to Na(buffer salts): (▲) pH 4, (■) 5, (●) 6, (▽) 7, (○) 8, (□) 9, and (△) 10. (b) Effect of total sodium concentration on electroosmotic velocity under constant current conditions for phosphate buffer solutions at pH 7 with 1:1 ratio of Na(NaCl) to Na(buffer salts): (○) 5, (△) 7.5, (■) 10, (□) 12.5, and (▽) 15 mM.

Figure 8. Comparison of experimental data with the ion-selective model for ζ potential as a function of pH from 4 to 10 and total sodium concentration from 5 to 15 mM (bottom to top data sets). The individual ζ_0 term and logarithmic activity term from eq 12 are shown separately in the top and bottom curves, respectively, with their summation in the center curves. Experimental conditions as given in Figure 7.

electroosmotic flow by influencing the extent of ionization of the silica surface and, thus, altering the surface potential. When the pH is much lower than the pK_a of the silica surface, extensive protonation of the silanol groups occurs, which reduces the charge density in the double layer. Consequently, the ζ potential is lowered and the electroosmotic flow decreases. A change in the electrolyte concentration produced the opposite effect, as illustrated for a representative case in Figure 7b. For a constant value of pH, which defines a constant surface potential, the electroosmotic velocity decreased proportionately with the total sodium concentration from 5 to 15 mM. As the concentration of the bulk solution increases, compression of the double layer occurs, and the electroosmotic flow decreases.

The combined effects of pH and composition of the buffer solution on the magnitude of the ζ potential are illustrated in Figure 8. These experimental data were fit to an equation analogous to that describing the ion-selective behavior of glass membranes (eq 3):

$$\zeta = \zeta_0 + \text{slope} \log(a_H + k^{pot}a_{Na}) \qquad (12)$$

The potential ζ_0 is mathematically described by a Gaussian

probability integral or error function (erf), which is sigmoidal in shape:[39]

$$\zeta_0 = [\text{erf}(A_0 \, pH + B_0)]C_0 + D_0 \qquad (13)$$

The parameters A_0 and B_0 are related to the mean and standard deviation of the distribution. The parameter C_0 confers the height to the sigmoidal curve, and the parameter D_0 provides the displacement in the ζ potential axis. The unknown parameters of eqs 12 and 13 were searched numerically, and the best fit was determined by means of the least-squares method.[40] The magnitudes of these parameters as well as the sum of the squared residuals (SSE) are presented in Table 1. The statistical evaluation of the ion-selective model is summarized in Table 2. Within the experimental range of buffer pH and composition, the model predicts with good accuracy the ζ potential and, hence, the electroosmotic velocity.

To understand the physical basis of this model, it is instructive to interpret separately the contribution of each term in eq 12. The logarithmic term, which represents the ion-selective behavior of the surface, is shown in the bottom part of Figure 8. At very low

(39) Spanier, J.; Oldham, K. *An Atlas of Functions*; Hemisphere Publishing Corp.: Washington, DC, 1987.
(40) Devore, J. L. *Probability and Statistics for Engineering and the Sciences*, 2nd ed.; Brooks/Cole Publishing Co.: Monterey, CA, 1987.

Table 1. Parameters of the Ion-Selective Model

parameter	value	parameter	value
A_0	−0.86	slope	44.4
B_0	5.11	k^{pot}	0.22
C_0	33.2	SSE	247
D_0	59.7		

Table 2. Comparison of the Experimentally Determined ζ Potential with Values Calculated from the Ion-Selective Model

nominal pH	a_H (M)	a_{Na} (M)	ζ potential (mV) exptl	calcd[a]	% error[b]
4	1.98×10^{-4}	4.63×10^{-3}	-35.7 ± 1.2	−38.5	−7.8
	1.75×10^{-4}	6.84×10^{-3}	-30.6 ± 1.1	−31.6	−3.3
	1.52×10^{-4}	9.00×10^{-3}	-27.3 ± 0.75	−26.6	2.6
	1.51×10^{-4}	1.11×10^{-2}	-25.7 ± 0.68	−22.7	12
	1.55×10^{-4}	1.32×10^{-2}	-23.3 ± 0.42	−19.5	16
5	2.19×10^{-5}	4.63×10^{-3}	-46.3 ± 1.3	−47.9	−3.5
	1.95×10^{-5}	6.84×10^{-3}	-36.8 ± 1.5	−40.7	−11
	1.82×10^{-5}	9.00×10^{-3}	-32.8 ± 0.94	−35.2	−7.3
	1.58×10^{-5}	1.11×10^{-2}	-31.1 ± 0.77	−31.1	0.0
	1.50×10^{-5}	1.32×10^{-2}	-28.5 ± 0.85	−27.8	2.5
6	1.65×10^{-6}	4.63×10^{-3}	-78.7 ± 2.3	−74.8	5.0
	1.50×10^{-6}	6.84×10^{-3}	-70.5 ± 1.8	−67.3	4.5
	1.45×10^{-6}	9.00×10^{-3}	-64.2 ± 2.1	−62.0	3.4
	1.36×10^{-6}	1.11×10^{-2}	-56.3 ± 2.3	−57.9	−2.8
	1.35×10^{-6}	1.32×10^{-2}	-53.6 ± 2.9	−54.6	−1.9
7	1.83×10^{-7}	4.63×10^{-3}	-100.3 ± 1.6	−99.6	7.0
	1.66×10^{-7}	6.84×10^{-3}	-89.7 ± 1.5	−92.1	−2.7
	1.39×10^{-7}	9.00×10^{-3}	-85.0 ± 1.5	−86.8	−2.1
	1.27×10^{-7}	1.11×10^{-2}	-81.6 ± 1.5	−82.7	−1.3
	1.35×10^{-7}	1.32×10^{-2}	-77.3 ± 1.8	−79.4	−2.7
8	1.85×10^{-8}	4.63×10^{-3}	-107.5 ± 1.6	−105.8	1.6
	1.58×10^{-8}	6.84×10^{-3}	-99.9 ± 1.4	−98.3	1.6
	1.43×10^{-8}	9.00×10^{-3}	-93.7 ± 1.3	−93.0	0.75
	1.33×10^{-8}	1.11×10^{-2}	-87.6 ± 1.2	−88.9	−1.5
	1.29×10^{-8}	1.32×10^{-2}	-81.0 ± 1.2	−85.6	−5.7
9	3.72×10^{-9}	4.63×10^{-3}	-100.8 ± 2.8	−106.2	−5.4
	2.93×10^{-9}	6.84×10^{-3}	-96.7 ± 1.5	−98.7	−2.1
	2.31×10^{-9}	9.00×10^{-3}	-91.6 ± 1.6	−93.4	−2.0
	1.98×10^{-9}	1.11×10^{-2}	-87.8 ± 2.0	−89.3	−1.7
	1.85×10^{-9}	1.32×10^{-2}	-83.7 ± 2.4	−86.0	−2.7
10	1.76×10^{-10}	4.63×10^{-3}	-110.4 ± 2.1	−106.2	3.8
	1.50×10^{-10}	6.84×10^{-3}	-102.3 ± 2.1	−98.7	3.5
	1.39×10^{-10}	9.00×10^{-3}	-96.8 ± 1.9	−93.4	3.5
	1.31×10^{-10}	1.11×10^{-2}	-93.4 ± 2.0	−89.3	4.4
	1.21×10^{-10}	1.32×10^{-2}	-89.4 ± 1.7	−86.0	3.8

[a] Calculated by using eq 12 with the parameters given in Table 1. [b] % error = (exptl − calcd)/exptl × 100.

pH, the ζ potential responds exclusively to the logarithm of the hydrogen ion activity. As the pH increases, the contribution of sodium to the overall potential increases dramatically and predominates shortly after pH 4. This behavior is attributed in part to the relative magnitude of the hydrogen and sodium ion activity, but primarily to the magnitude of the potentiometric constant. According to the proposed model k^{pot} carries information on the exchange equilibrium between sodium and hydrogen ions at the plane of shear. The value 0.22 is appreciably higher than the potentiometric constant of a pH-sensing glass electrode ($k^{pot} = 10^{-12}$–10^{-13})[25,26] and, indeed, more closely approximates that of a sodium-selective glass electrode ($k^{pot} = 2.5 \times 10^{-4}$–$0.55$).[26,41,42] This result suggests that both hydrogen and sodium ions contribute significantly to the transport of charge across the plane of shear.

(41) Phang, S.; Steel, B. J. Anal. Chem. 1972, 44, 2230−2232.
(42) Wilson, M. F.; Haikala, E.; Kivalo, P. Anal. Chim. Acta 1975, 74, 395−410.

The ion-selective model in eq 12, when applied to the phosphate buffer system, gives a slope of 44.4 mV per 10-fold change in concentration. It is noteworthy that a slope of 43.7 mV was observed in the studies with pure electrolyte systems (Figure 3). The influence of electrolyte concentration on the ζ potential of silica surfaces has been the subject of many studies.[43−45] and there is substantial evidence to support the departure of the slope from the value of 59 mV expected for ideal Nernstian behavior. Several models have been proposed to account for this phenomenon, where the rate of change of the ζ potential with the logarithm of concentration ($d\zeta/d(\log C)$) is correlated with important parameters of the double layer. An explanation proposed by Hunter and Wright[46] is that conductance at the silica surface alters the surface charge density, such that the classical equations[23] describing the potential profile in the double layer are no longer strictly applicable. This concept is further supported by the theoretical model of Lyklema,[28,48] who postulated the existence of an amorphous gel layer at the silica surface in which the potential is affected by the degree of penetration of certain cations.

The ion-selective behavior of the surface alone, as represented by the second term of eq 12, is not sufficient to explain the sigmoidal contour of the experimental data. It is the first term, ζ_0, that imparts this feature to the ζ potential curve, as demonstrated in the top part of Figure 8. Among the many possible mathematical functions with sigmoidal shape,[39] the error function was chosen because of its physical meaning. Another way to interpret the ζ potential curve as a function of pH is to recognize that it represents a titration curve of the acidic sites at the silica surface. The acidic sites are assumed to be silanol groups in slightly differing environments, whose abundance is normally distributed. The inflection point of the titration curve gives an overall pK_a that is representative of the average acidity of the surface. The experimentally determined pK_a of 5.9 is in good agreement with previously reported values for silica materials determined by electrophoretic,[12,14] spectroscopic,[49] and potentiometric methods.[3,50] A more detailed inspection of Figure 8, however, reveals that the experimental data appear to diverge somewhat from the model in the vicinity of pH 8−10. This behavior, which is statistically significant and reproducible, may be indicative of a second distinct type of acidic site. The existence of multiple types of acidic sites at silica surfaces has been postulated by several research groups.[27,51−53] The present model may be readily extended to consider multiple sites in eq 13, with better correspondence to the experimental data.

The modeling of the response of the capillary surface as an ion-selective membrane leads to interesting observations. For instance, inspection of Figure 8 reveals that all curves tend toward the same point as the ζ potential approaches zero. At this point,

(43) Parks, G. A. Chem. Rev. 1965, 65, 177−198.
(44) Wiese, G. R.; James, R. O.; Healy, T. W. Faraday Discuss. Chem. Soc. 1971, 52, 302−311.
(45) Rutgers, A. J.; De Smet, M. Trans. Faraday Soc. 1945, 41, 758−771.
(46) Hunter, R. J.; Wright, H. J. L. J. Colloid Interface Sci. 1971, 37, 564−580.
(47) Churaev, N. V.; Sergeeva, I. P.; Sobolev, V. D.; Derjaguin, B. V. J. Colloid Interface Sci. 1981, 84, 451−460.
(48) Tadros, T. F.; Lyklema, J. J. Electroanal. Chem. 1968, 17, 267−275.
(49) Hair, M. L.; Hertl, W. J. Phys. Chem. 1970, 74, 91−94.
(50) Strazhesko, D. N.; Strelko, V. B.; Belyakov, V. N.; Rubanik, S. C. J. Chromatogr. 1974, 102, 191−195.
(51) Ong, S.; Zhao, X.; Eisenthal, K. B. Chem. Phys. Lett. 1992, 191, 327−335.
(52) Nawrocki, J. Chromatographia 1991, 31, 177−192.
(53) Nawrocki, J. Chromatographia 1991, 31, 193−205.

the double layer has collapsed to an infinitesimally thin layer of ions, and the electroosmotic flow ceases. The pH corresponding to the point where the ζ potential reaches zero is known as the point of zero charge (PZC). For colloidal silica, the PZC is believed to occur approximately at pH 2.5,[43,47] which is in good agreement with that predicted from this model. It is necessary to emphasize that caution must be exercised in the physical interpretation and application of the model beyond this point. The model predicts positive values for the ζ potential and, hence, a reversal of electroosmotic flow at pH values less than the PZC. For this to occur in practice, a layer of cations would have to adsorb specifically at the silica surface, thereby reversing its charge.

CONCLUSIONS

The prediction of electroosmotic flow in capillary zone electrophoresis under both constant voltage and constant current conditions has been successfully achieved through the development of a simple but physically meaningful model. The proposed model is based on the evaluation of the ζ potential as a function of the buffer composition in a manner analogous to that which describes the ion-selective behavior of glass membranes. The ζ potential, together with the dielectric constant and viscosity of the buffer solution, can then be used to calculate the electroosmotic velocity from the Helmholtz—Smoluchowski equation. The model has been fully supported by experimental data in the pH range from 4 to 10, which is most useful in capillary zone electrophoresis, resulting in ~3% error in the estimation of the electroosmotic velocity.

Capillary Electrophoresis Study of the Hydrolysis of a β-Lactamase Inhibitor

George N. Okafo,[†] Paul Cutler,[†] David J. Knowles,[‡] and Patrick Camilleri*,[†]

SmithKline Beecham Pharmaceuticals, The Frythe, Welwyn, Herts AL69AR, U.K., and SmithKline Beecham Pharmaceuticals, Brockham Park, Betchworth, Surrey RH3 7AJ, U.K.

(5R)-6(Z)-[(1-Methyl-1,2,3-triazol-4-yl)methylene]penem-3-carboxylic acid monohydrate (BRL 42715) is a potent β-lactamase inhibitor. We report a study on the hydrolysis of the four-membered lactam ring of this compound mediated either by Tris buffer or by Tem-2 β-lactamase. In both studies free-zone capillary electrophoresis proved to be ideal in the identification of the products of reaction, the interpretation of the mechanism of hydrolysis, and the determination of kinetic parameters and stoichiometry.

β-Lactam antibiotics are commonly used in the treatment of bacterial infections. However, the elaboration of hydrolytic enzymes (β-lactamases) by many bacterial pathogens renders many such antibiotics ineffective in the clinical environment. The discovery of β-lactamase inhibitors, such as clavulanic acid,[1–3] led to the successful development of a variety of antibiotic/inhibitor combinations for therapeutic use.[4,5] The majority of known β-lactamase inhibitors, including all those used clinically, contain the characteristic four-membered β-lactam ring and act as suicide inhibitors; cleavage of the β-lactam amide bond gives rise to a stably inhibited enzyme species, acylated on the active site serine. Such inhibitors frequently exhibit branched kinetic pathways with appreciable turnover (acylation/deacylation) before the stably inhibited enzyme species is trapped.[6–8]

More recently, a novel class of β-lactamase inhibitors, the 6-(substituted methylene) penems, have been reported.[9] One such inhibitor, BRL 42715 [(5R)-(Z)-6-(1-methyl-1,2,3-triazol-4-yl)-methylene]penem-3-carboxylic acid], is highly potent with an initial stoichiometry of inhibition of Tem-2 β-lactamase of 1:1. Regeneration of active enzyme has been found to be slow and incomplete, suggesting partitioning of the inhibited enzyme to give a very stable inactivated species.[10]

One of the simplest methods commonly used to follow a reaction in solution is to monitor directly changes in the ultraviolet absorbance of either a reactant or a product with time.[11,12] This methodology is especially useful when the reaction followed is first order or pseudo first order, and there is no interference due to absorbance by other species. In cases where it is not possible to choose an appropriate wavelength to follow a reaction due either to more than one absorbing species in a reaction mixture or to consecutive reactions, the change in concentration–time profile of reactants and products is commonly determined using high-performance liquid chromatography (HPLC)[13,14] with UV detection. This separation technique is reliable and is ideal when relatively hydrophobic and neutral molecules are involved.

The more recently introduced analytical technique of capillary electrophoresis (CE)[15,16] is complementary to HPLC. CE can be most effective in providing high resolution of both neutral and ionic species when used in the micellar electrokinetic capillary electrophoresis (MECC) or free-zone electrophoresis modes, respectively. This technique can also be fast, allowing more frequent sampling during the time course of a reaction. It is also allows the decay or formation of both simple and much more complex molecules to be monitored simultaneously.

We now report the use of free-zone CE to study the mechanism of hydrolysis of the β-lactam ring of BRL-42715 catalyzed either by tris(hydroxymethyl)aminomethane (Tris) or by Tem-2 β-lactamase. Unlike conventional direct UV spectral analysis, our investigations have allowed the simultaneous analysis of BRL-42715, enzyme, intermediates, and products with high resolution and low sample consumption.
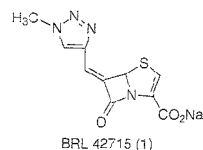
BRL 42715 (1)

EXPERIMENTAL SECTION

Materials. Buffer constituents used in capillary and gel electrophoresis were of Analar grade and were purchased from BDH (Lutterworth, U.K.) and from Sigma (Poole, U.K.). BRL 42715 and the dihydrothiazepine derivative BRL 44516 were supplied by the Medicinal Chemistry Department at SmithKline

† SmithKline Beecham Pharmaceuticals, Surrey.
‡ SmithKline Beecham Pharmaceuticals, Herts.
(1) Howarth, T. T.; Brown, A. G.; King, T. J. J. Chem. Soc., Chem. Commun. 1976, 266–269.
(2) Reading, C.; Cole. M. Antimicrob. Agents Chemother. 1970, 11, 852–857.
(3) Hunter, P. A.; Coleman, K.; Fisher, J.; Taylor, D. J. Antimicrob. Chemother. 1980, 6, 455–470.
(4) English, A. R.; Retsema, J. A.; Girard, A. E.; Lynch, J. E.; Bath, W. E. Antimicrob. Agents Chemother. 1978, 14, 414–419.
(5) Aronoff, S. C.; Jacobs, M. R.; Johenning, S.; Yamabe, S. Antimicrob. Agents Chemother. 1984, 26, 580–582.
(6) Knowles, J. R. Antibiotics. Vol. 6: Modes and Mechanisms of Microbial Growth Inhibitors; Hahn, B., Ed.; Springer-Verlag: New York, 1992; pp 99–107.
(7) Cartwright, S. J.; Waley, S. G. Med. Res. Rev. 1983, 3, 341–382.
(8) Reading, C.; Cole. M. J. Enzyme Inhib. 1986, 1, 83–104.
(9) Bennet, I. S.; Brooks, G.; Broom, N. J.; Calvert, S. N.; Coleman, K.; Francois, I. J. Antibiot. 1991, 44, 969–978.

(10) Farmer, T. H.; Page, J. W. J. Payne, D. J.; Knowles, D. J. C. Biochem. J., in press.
(11) Jencks, W. P. Catalysis in Chemistry and Enzymology; McGraw-Hill: New York, 1969; Chapter 11.
(12) Kandanarachchi, P.; Sinnott, M. L. J. Am. Chem. Soc. 1994, 116, 5592–5600.
(13) Breslow, R; Xu, R. J. Am. Chem. Soc. 1993, 115, 10705–10713.

Beecham. Tem-2 β-lactamase (75% protein by weight) from *Escherichia coli* was obtained from Porton as a white lyophilized powder containing potassium phosphate.

Equipment. The CE system consisted of a Beckman P/ACE Model 5000 equipped with an autosampler, diode array detector, and temperature-controlled sampler carousel equilibrated at 20 °C. The conditions used in the study of the reaction of BRL 42715 with Tris were as follows: capillary, 27 cm × 50 μm i.d. untreated fused-silica capillary (effective length, 20 cm); buffer, 20 mM sodium phosphate, pH 7.30; separation voltage, 10 kV; detection, UV absorbance at a wavelength of 200 nm; temperature, 37 °C; sample introduction, 1 s hydrodynamic pressure (0.5 psi) injection of the reaction solution. The hydrolysis of BRL 42715 by Tem-2 was studied under the following CE conditions: capillary, 24 cm × 50 μm i.d. (effective length, 17 cm) untreated fused-silica capillary; buffer, 20 mM sodium dihydrogen phosphate, pH 7.3; detection, UV absorbance, 200 nm; applied voltage, gradient voltage separation of 1 kV min^{-1} over 15 min; temperature, 22 °C; sample, the Tem-2/BRL 42715 1:1 complex was injected hydrodynamically as before.

Isoelectric Focusing (IEF). Samples were focused on precast agarose gels (FMC Bioproducts) against an ampholyte pH gradient covering the p*I* range 3.0–10.0 at 1.5 kV, 20 mA, 25 W for 30 min at 9 °C. Protein bands were visualized by staining by either Coomassie Blue or silver stain. The gels were loaded with 10 μg of protein per track (unless otherwise stated). A reference sample of proteins of defined p*I*s (Pharmacia LKB) was run on each gel, and the banding patterns were compared by eye.

Hydrolysis of BRL 42715 Mediated by Tris. BRL 42715 (1.28 mg, 4.21 μmol) was dissolved in an aliquot of 80, 300, 450, or 600 mM Tris (pH 9.54, equilibrated at 20 °C) to give a final concentration of 4.96 mM. The solution was then immediately transfered to a plastic vial and analyzed by CE at 20 min intervals for a total time of 300 min.

The reaction product was isolated as follows: solid Tris (9.6 mg, 79.3 μmol) was dissolved in a glass vial containing distilled water (1 mL). The solution was adjusted to pH 9.54 using dilute HCl before transfer to another vial containing BRL 42715 (10 mg, 32.9 μmol). An aliquot (200 μL) of the solution was immediately placed in a CE vial and the reaction monitored by CE until the inhibitor had been consumed. After 2 h, the resulting solution was acidified by the addition of 1.0 M HCl (200 μL) and then evaporated to dryness (Genevac centrifugal evaporator). The residue was extracted twice with methanol (2 × 500 mL) and dried in a stream of N$_2$ gas. The structure of the resulting solid was then determined by proton and ^{13}C NMR and mass spectrometric analysis: H (400 MHz; D$_2$O) δ 7.82 (1H, C=CH), 7.58 (1H, NCH=C), 6.38 (1H, SCH=C), 5.84 (1H, SCH), 4–4.1 (2H, OCH$_2$C), ~4.00 (3H, CH$_3$), 3.4 (3 × 2H, CH$_2$O); C (100 MHz; D$_2$O) δ 171.25 (C=O), 171.05 (C=O), 153.06 (RC=), 144.98 (NHC=), 141.55 (=C(NH)carboxylic), 126.78 (NC=), 112.46 (SC=), 109.67 (R=C-carboxylic), 68.16 (C-O (Tris moiety), 65.78 (CH$_2$OH), 58.63 (C(NH$_2$)), 44.42 (OCO), 39.38 (NCH$_3$). FAB (nitrobenzyl alcohol matrix), *m/z* 386 (M + H)$^+$.

(14) Martin, M. T.; Angeles, T. S.; Sugasawara, R.; Aman, N.I.; Napper, A. D.; Darsley, M. J.; Sanchez, R.I.; Booth, P.; Titmas, R. C. *J. Am. Chem. Soc.* **1994**, *116*, 6508–6512.

(15) Jorgenson, J. W.; Lukacs, K. D. *Anal. Chem.* **1991**, *63*, 802–807.

(16) Camilleri, P., Ed. *Capillary Electrophoresis: Theory and Practice*; CRC Press: Boca Raton, FL, 1993.

Tem-2 β-Lactamase-Mediated Hydrolysis of BRL 42715. BRL 42715 (0.86 mg, 2.83 mmol) was dissolved in a volume (27.2 mL) of 5 mM Tris buffer adjusted to pH 7 using dilute HCl to give a final concentration of 104 μM. An aliquot (104 μL, representing 10.8 nmol of inhibitor) of solution was then transferred to a CE vial and allowed to equilibrated to 30 °C within the Beckman P/ACE sample tray. A separate Tris solution containing 1 molar equiv (0.40 mg, 10.8 nmol dissolved in 104 mL of Tris buffer) of Tem-2 β-lactamase, preincubated at 30 °C, was also prepared. Both the enzyme and the inhibitor solutions were then mixed thoroughly on a vortex mixer before incubation at 30 °C and CE analysis. The reaction was sampled every 60 min for 24 h and then finally after 48 h.

RESULTS AND DISCUSSION

The proposed mechanism of action of BRL 42715 with Tem β-lactamase is the rapid formation of an acyl enzyme species. At low inhibitor/enzyme ratios, free enzyme is slowly regenerated.[10] Spectroscopic data suggest that the reaction proceeds via the formation of the seven-membered dihydrothiazepine. BRL 44156,[17] as was shown unequivocally for the interaction of BRL 42715 with K1 β-lactamase.[18] The interaction of a 20-fold molar excess of BRL 42715 to Tem β-lactamase led to irreversible inhibition.[16] The amino acid residue participating[19] in the acylation of the main β-lactamases is serine-70. The possible involvement of the stronger alkoxide nucleophile rather than the hydroxy group of this amino acid may be related to the fact that a common feature present around the serine-70 active site is a lysine residue (Lys 73 or Lys 83 in class A and class C enzymes, respectively). The facile protonation of the amino group of lysine can stabilize a zwitterionic form where the negative charge lies on the alkoxide form of serine-70. As a simple model for the interaction of BRL 42715 with β-lactamase, we studied the reaction of this compound with Tris. The nature of the product of reaction provides information on whether one of the hydroxyl groups (in the neutral or anionic form) or the amino group is involved in nucleophilic attack. The alternative products are the dihydrothiazepine derivatives **2** and **4**, respectively. We have used free-zone capillary electrophoresis to distinguish between these two possible products and the free acid BRL 44516, using the expected charge density differences of these species at alkaline pH.
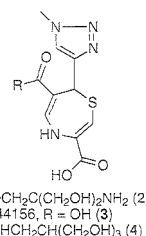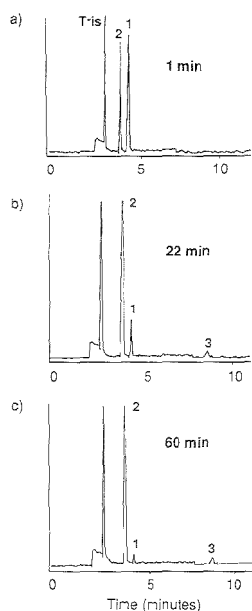

R = OCH$_2$C(CH$_2$OH)$_2$NH$_2$ (**2**)
BRL 44156, R = OH (**3**)
R = NHCH$_2$CH(CH$_2$OH)$_3$ (**4**)

Figure 1 shows typical electropherograms of samples from a reaction of BRL 42715 (4.96 mM) dissolved in Tris buffer (600

(17) Farmer, T. H.; Knowles, D. J. C., unpublished observation.

(18) Broom, N. J. P.; Farmer, T. H.; Osborne, N. F.; Tyler, J. W. *J. Chem. Soc., Chem. Commun.* **1992**, 1663–1664.

(19) Joris, B.; Ghuysen, J.; Dive, G.; Renard, A.; Dideberg, O.; Charlier, P.; Frere, J.; Kelly, J. A.; Boyington, J. C.; Moews, P. C.; Knox, J. R. *Biochem. J.* **1988**, *250*, 313–324.

Figure 3. Linear plot of the dependence of the first-order rate constant, k, for the hydrolysis of BRL 42715 with Tris concentration.
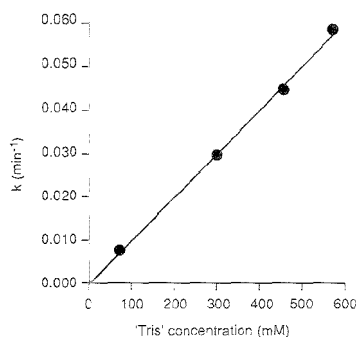
Figure 1. Electropherograms showing the hydrolysis of BRL 42715 (1) to form the Tris adduct (2) as the major product and BRL 44156 (3) after (a) 1, (b) 22, and (c) 60 min. The identity of BRL 44156 was confirmed from migration time and diode array characteristics of an authentic sample.
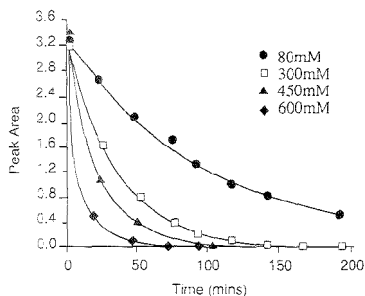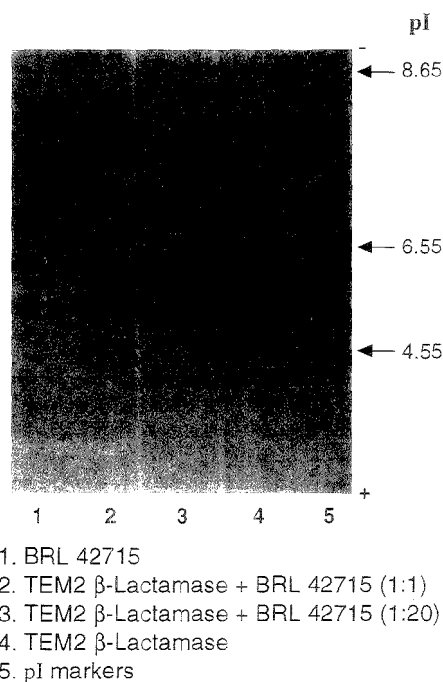

Figure 2. Kinetic profiles for the hydrolysis of BRL 42715 at different Tris concentrations.

1. BRL 42715
2. TEM2 β-Lactamase + BRL 42715 (1:1)
3. TEM2 β-Lactamase + BRL 42715 (1:20)
4. TEM2 β-Lactamase
5. pI markers

Figure 4. Isoelectric focusing gel showing the appearance of a second more acidic band due to the presence of the β-lactamase—BRL 42715 adduct.

mM) at pH 9.54, after incubating at 20 °C. Under these conditions Tris (pK_a 8.1) is largely neutral, comigrating with mesityl oxide (data not shown). BRL 42715 migrates after the electroosmotic front due to its negative charge density. At longer times of reaction, BRL 44156 is seen as a minor product. This molecule carries two negative charges so that it migrates well after BRL 42715. The formation of BRL 44156 is due to attack by hydroxide anions. The major product of this reaction was found to be the Tris adduct 2 and not 4. The structure of 2 was confirmed by conducting the reaction on a larger scale (see Experimental Section) and NMR and MS analysis.

The migration time of 2 is also consistent with a molecule that is zwitterionic in character. As expected, the rate of reaction of BRL 42715 with excess Tris follows first-order kinetics (Figure

2). Rate constants, determined from the plots in Figure 2, were plotted against the Tris concentration to give the linear relationship (r, 0.998) shown in Figure 3. The line passes through the origin: the bimolecular reaction of BRL 42715 with Tris is much faster than with specific base at the much higher concentrations of buffer used in these experiments. The formation of 2 indicates that one of the oxygen atoms of Tris is a stronger nucleophile toward the carbonyl group on the β-lactam ring of BRL 42715 than the more basic amine nitrogen. This in turn almost certainly signifies that the nucleophile is not the hydroxyl moiety but the oxygen anion in the zwitterionic form of Tris, that is (+)NH$_3$C(CH$_2$OH)$_2$CH$_2$O-
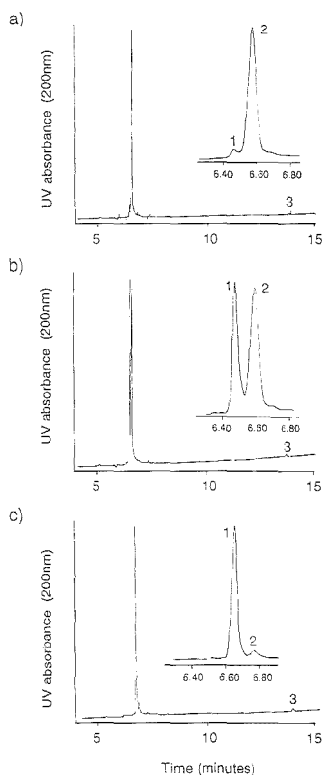
Figure 5. Capillary electrophoresis analysis of the decomposition of the β-lactamase–BRL 42715 complex to give free enzyme and BRL 44156 after (a) 30, (b) 240, and (c) 660 min of reaction. Insets show the relative proportions of the free enzyme and the enzyme–drug complex on an expanded time scale. The labels **1**, **2**, and **3** refer to free enzyme, enzyme–BRL 42715 complex, and BRL 44156, respectively.

Scheme 1

(3)
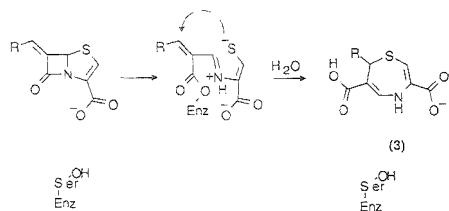
(−). Such differences have been reported[20] previously for hydroxylamine where the overall reactivity of this molecule has been found to be more than 2 orders of magnitude larger than that of an amine of comparable basicity. The mechanism of hydrolysis of BRL42715 catalyzed by Tris is in agreement with recent studies on the inactivation of β-lactamase[21] by BRL42715. Both these studies and the X-ray structure[22] of a closely related β-lactamase

(20) Jencks, W. P.; Carriuolo. J. *J. Am. Chem. Soc.* 1960, *82*, 178–184.
(21) Bulychev, A.; Massova, I.; Lerner. S. A.; Mobashery, S. *J. Am. Chem. Soc.* 1995, *117*, 4797–4801.
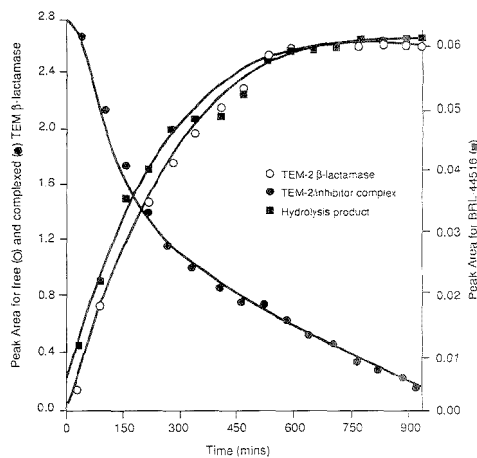
Figure 6. Area–time profiles showing the decay of the enzyme–drug complex and the formation of free enzyme and BRL 44156.

clearly show that, besides the lysine residues mentioned earlier, Arg 244 is close in space to Ser 70, the amino acid involved in the acylation by BRL42715.

Because of the encouraging results obtained using capillary electrophoresis to follow the reaction of BRL 42715 with Tris, we used this technique to study the hydrolysis of the complex of this drug with Tem-2 β-lactamase. The formation of this complex can be seen from isoelectric focusing as shown in Figure 4. The IEF pattern for TEM-2 β-lactamase indicates a major band with an apparent p*I* of approximately 5.8. On addition of BRL 42715 at a ratio of either 1:1 or 1:20, an extra, more acidic band is generated. This results from interaction of the drug with the enzyme leading to the generation of a more acidic species (Scheme 1). Although the IEF results are good evidence for the formation of an enzyme–inhibitor complex, analysis by this technique is slow and not quantitative. Moreover, this technique does not allow monitoring of BRL 44516 (3), the seven-membered ring product of hydrolysis.

Free-zone CE was found to offer very clear advantages over IEF and has allowed the simultaneous monitoring with time of the disappearance of the BRL 42715–inhibitor complex and the appearance both of free enzyme and of BRL 44516 (3). As the three analytes are negatively charged at the pH of this study, they all migrate after the electroosmotic front. The order of migration can also be interpreted from expected charge densities. Thus, assuming that the volumes of enzyme and enzyme–inhibitor complex are of similar magnitude, the charge density of the latter is larger than that of the enzyme alone. The considerably longer migration time of BRL 44516 is due to its much smaller volume and the two negative charges carried by this molecule. Electropherograms obtained at three time intervals are shown in Figure 5. For an equimolar molar ratio of Tem-2 and BRL 42715, no free enzyme or drug was observed at the start of the reaction. This observation is in line with 1:1 stoichiometry. The kinetic profile for the interaction of BRL 42715 with Tem-2 is given in Figure 6. From the time–response curves it was found that the half-lives

(22) Jelsch, C.; Mourney, L.; Masson, J. M.; Samama, J. P. *Proteins: Struct. Funct. Genet.* 1993, *16*, 364–371.

for the disappearance of the TEM-2 β-lactamase inhibitor complex and the appearance of free TEM-2 β-lactamase and the hydrolysis product BRL 44516 are both of the order of about 170 min, again confirming a 1:1 stoichiometry.

CONCLUSION

We have successfully used free-zone CE to determine some of the kinetic parameters for the reaction of BRL-42715 (a β-lactamase inhibitor) with either Tris or Tem-2 β-lactamase. The acquisition of data using this analytical technique was found to be fast, compared to other more common electrophoretic techniques such as IEF. Moreover, the methodology developed allowed the facile and simultaneous determination of changes in the concentration of both simple and more complex analytes with time.

Analytical Magnetapheresis of Ferritin-Labeled Lymphocytes

Maciej Zborowski,*,† Chwan Bor Fuh,† Ralph Green,‡ Liping Sun,§ and Jeffrey J. Chalmers§

Departments of Biomedical Engineering, Clinical Pathology, and Cell Biology, The Cleveland Clinic Foundation, 9500 Euclid Avenue, Cleveland, Ohio 44195, and Department of Chemical Engineering, The Ohio State University, 140 West 19th Avenue, Columbus, Ohio 43210-1180

Analytical magnetapheresis is a technique for analyzing magnetic particles in suspension. The magnetically susceptible particles form a deposition pattern from the suspending medium under carefully controlled flow and magnetic field conditions. This technique was used to determine the effective magnetic volumetric susceptibility, $\Delta\chi$, of human lymphocytes labeled with an iron-rich protein, ferritin. Dynabeads M450, monodisperse polymeric beads doped with magnetite, of a diameter 4.5 μm, close to that of human lymphocytes, were used as a reference. The experiment showed an almost complete deposition of ferritin-labeled lymphocytes at an average flow velocity of 0.28 mm/s, a representative magnetic field of 1.67 T, and a magnetic field gradient of 2.57 T/mm. The calculated $\Delta\chi$ was $(2.92 \pm 0.24) \times 10^{-6}$[SI] (ferritin-labeled lymphocytes), and the corresponding number of ferritin molecules per lymphocyte was $(1.75 \pm 0.44) \times 10^{7}$. In comparison, an almost complete deposition of the Dynabeads was observed at a much higher average flow velocity, 15 mm/s, a much lower field, 0.164 T, and a much lower field gradient, 0.025 T/mm. These results corresponded to a much higher $\Delta\chi = 0.245$[SI] (Dynabeads M450). These results offer important guidelines in evaluating the use of ferritin as a soluble magnetic cell label.

Magnetic separation has played an important role in the manufacturing and mining industries since the nineteenth century.[1] Only recently has it been introduced to the life sciences, where it has been growing in popularity in the past decade, in particular as a technique for cell separation.[2–6] Compared to other more conventional methods of cell separation, magnetic separation is relatively simple and fast. The static magnetic field does not interfere with the movement of ions and charged solutes in aqueous solutions (at low flow rates) as does the electric field. Furthermore, the large differences between magnetic permeabilities of the magnetic and nonmagnetic materials can be exploited in developing highly selective separation methods. This high selectivity can be achieved with other separation methods only through extensive and costly instrumentation development.

Industrial magnetic separators are typically challenged by ferromagnetic particles. Almost all biological material, however, such as proteins, DNA, and cells, are either diamagnetic or slightly paramagnetic and therefore require a magnetic support for separation.[7] Notable exceptions are erythrocytes and magnetotactic bacteria because of their high iron content.[7–9] Diamagnetic substances are characterized by a negative magnetic susceptibility, χ, whereas paramagnetic substances have a positive magnetic susceptibility. The magnetic support is provided either by particulate suspension of large polymeric particles doped with magnetite or by solutions or colloidal suspension of paramagnetic compounds.

The application of large magnetic particles as a magnetic support evolved from particle-based immunoassays and tests.[3,10,11] Polymeric particles or beads are rendered magnetically susceptible by doping the polymer with magnetite. The magnetic susceptibility of such particles, typically of the order of $\chi_p = 10^{-1}$[SI], is several orders of magnitude higher than the net magnetic susceptibility of deoxygenated erythrocytes in aqueous medium, 5.17×10^{-6}.[7] (The SI unit system and the volumetric magnetic susceptibility, χ, are used throughout this study unless otherwise indicated. If χ' is in em cgs units, then χ[SI] = $4\pi\chi'$[em cgs].) The magnetic susceptibility of the aqueous medium (water) is $\chi_{aq} = -9.05 \times 10^{-6}$ (diamagnetic).[7,13] The diameter of the magnetic beads is of the order of 1 μm, and the beads have functionalized surfaces allowing for conjugation with antibodies. The combination of a large surface area and the magnetic susceptibility of the dispersed solid phase dramatically decreases the assay time and simplifies the separation steps.[14] These large magnetic particles are rapidly displaced from a solution, even by relatively weak magnetic fields and low gradients, typically 0.1 T and 10 T/m, respectively.

(1) Mitchell, R.; Bitton, G.; Oberteuffer, J. A. *Sep. Purif. Methods* 1975, *4*, 267–303.
(2) Hirschbein, B. L.; Brown, D. W.; Whitesides, G. M. *CHEMTECH* 1982, March, 172–179.
(3) Funderud, S.; Nustad, K.; Lea, T.; Vartdal, F.; Guadernack, G.; Stensted, P.; Ugelstad, L. In *Lymphocytes: A Practical Approach*; Klaus G. G. B., Ed.; Oxford University Press: New York, 1987; pp 55–61.
(4) Lau, H. P.; Charlton, R. R.; Yang, E. K.; Miller, W. K. *Targeted Diagn. Ther.* 1989, *2*, 201–216.
(5) Hancock, J. P.; Kemshead, J. T. *J. Immunol. Methods* 1993, *164*, 51–60.
(6) Battye, F. L.; Shortman, K. *Curr. Opin. Immunol.* 1991, *3*, 238–241.

(7) Graham, M. D. *J. Phys., Colloq.* 1984, *45* (Suppl. au no. 1), C1:779–C1:784.
(8) Okazaki, M.; Maeda, N.; Shiga, T. *Experientia* 1986, *42*, 842–843.
(9) Meldrum, F. C.; Mann, S.; Heywood, B. R.; Frankel, R. B.; Bazylinski, D. A. *Proc. R. Soc. London Ser. B* 1993, *251*, 231–236.
(10) Bangs, L. B. *J. Intern. Fed. Clin. Chem.* 1991, *2*, 188–193.
(11) Vaccaro, D. E. *Amer. Biotechnol. Lab.* 1990, *8*, 30–35.
(12) Gee, A. P.; Mansour, V.; Weiler, M. *J. Immunogen.* 1989, *16*, 103–115.
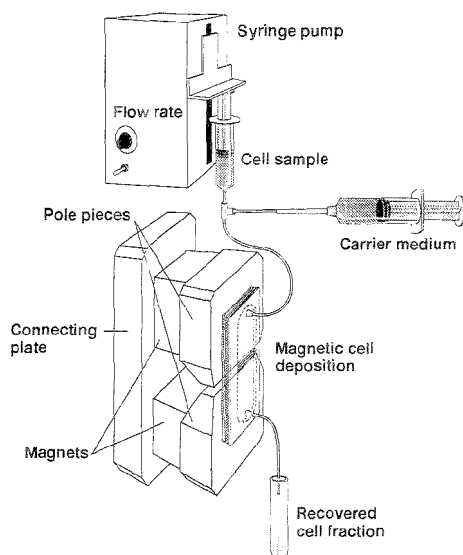(13) *CRC Handbook of Chemistry and Physics*, 67th ed.; Weast, R. C., Ed.; CRC Press: Boca Raton, FL, 1986; p E-123.
(14) *Current Protocols in Immunology*; Coligan, J. E., Kruisbeek, A. M., Margulies, D. H., Shevach, E. M., Strober, W., Eds.; John Wiley and Sons: New York, 1992; pp 7.4.1–7.4.6.

The successful application of magnetic particles to immunoassays led to the evaluation of their ability to tag cells. At present, there are at least two types of particle-based immunomagnetic cell separation systems commercially available that are used in laboratory and clinical applications, Dynal MPC (Dynal, Great Neck, NY), and MaxSep magnetic cell separator (Baxter Co., Deerfield, IL). Both systems are typically used in combination with monodisperse polystyrene beads, 4.5 μm in diameter, doped with magnetite at 23% (w/v) (Dynabeads M450, Dynal A.S., Oslo, Norway). With their increasing use for cell tagging, it becomes apparent that the size of the magnetic beads, comparable to that of the cell, is an important limitation in the magnetic separation efficiency.[5] A number of studies have been reported recently in which smaller, colloidal magnetic cell labels were investigated to determine the efficiency of cell tagging.[4,15,16] A magnetic separation system based on a colloidal 50 nm diameter magnetic microbead became commercially available recently (MiniMACS, Miltenyi Biotec Inc., Sunnyvale, CA).

The rapid integration of magnetic separation techniques and new magnetic labels in biotechnology requires parallel development of analytical methods to measure and optimize the magnetic separation process. The limitation of the currently used magnetic separators is that they do not allow direct observation of the magnetic fraction. Information about the performance of such separators is always inferred indirectly from the difference in the cell population composition before and after the magnetic separation. We developed a system in which the magnetically separated cells are directly accessible to cytological and cytochemical examination on the microscopic slide. Such a system offers higher sensitivity in detecting the magnetic cell separation than the current systems. Conceptually, this system evolved from ferrography, an analytical method based on the magnetic deposition of particles in a free-flowing, open stream.[17-20] We propose the term "analytical magnetapheresis" (from Greek *apheresis*, to take off or isolate) to describe the process of magnetic separation for analytical purposes.[21-23]

The magnetic deposition system comprised intersecting fluid flow path and the magnetic interpolar gap of a permanent magnet (see Figure 1). The magnetic field of the interpolar gap was characterized by the saturation field deep inside the interpolar gap, B_0, and the interpolar gap width, $2a$. The fluid flow was contained inside a parallelpiped channel of known width, w, and height, h. A homogeneous population of cells (human lymphocytes) was magnetically labeled using a high iron content protein, cationized ferritin. Ferritin is a naturally occurring, soluble iron storage protein in mammals.[24] The cell type and the ionic character of the magnetic label binding ensured uniform magnetization of all cells in the sample. The suspensions of magnetically

(15) Miltenyi, S.; Müller, W.; Weichel, W.; Radbruch, A. *Cytometry* 1990, *11*, 231–238.
(16) Yau, J. C.; Reading, C. L.; Thomas, M. W.; Davaraj, B. M.; Tindle, S. E.; Jagannath, S.; Dicke, K. A. *Exp. Hematol.* 1990, *18*, 219–222.
(17) Seifert, W. W.; Westcott, V. C. *Wear* 1972, *21*, 27–42.
(18) Evans, C. H.; Tew, W. P. *Science* 1981, *213*, 653–654.
(19) Nair, K. *Basic Fluid Power Res. J.* 1980, *13*, 281–294.
(20) Russell, A. P.; Westcott, V. C.; Demaria, A.; Johns, M. *Wear* 1983, *90*, 159–165.
(21) Zborowski, M.; Malchesky, P. S.; Jan, T.-F.; Hall, G. S. *J. Gen. Microbiol.* 1992, *138*, 63–68.
(22) Zborowski, M.; Tada, Y.; Malchesky, P. S.; Hall, G. S. *Appl. Environ. Microbiol.* 1993, *59*, 1187–1193.
(23) Zborowski, M.; Tada, Y.; Malchesky, P. S.; Hall, G. S. *Colloids Surf. A: Physicochem. Eng. Aspects* 1993, *77*, 209–218.

Figure 1. Principal components of analytical magnetapheresis. Before magnetic separation, the entire fluid path is filled with carrier medium. The cell sample is held in a syringe. At a controlled rate, using a syringe pump, cells are pumped into a thin parallelpiped channel placed over the magnet. The deposition of the magnetic material forms at the interpolar gap of the magnet. The magnetically trapped cells adhere to the bottom wall of the channel, after which the cells are air-fixed, stained, and mounted on slides, allowing for microscopic analysis and storage. The cells escaping the magnetic entrapment are collected in a tube past the magnet and counted.

labeled cells were pumped through the channel at various volumetric flow rates, Q. For each value of Q, the cells were counted before and after the magnetic deposition. The number of cells recovered past the magnet after the deposition, relative to the number of cells before the deposition, was defined as the fractional cell (or particle) recovery, ϵ. As a result, the rate of change of ϵ with the variation of Q was characteristic of the average net magnetic susceptibility of the cell, $\Delta\chi$. Monodisperse magnetic microspheres, Dynabeads M450, of well-characterized dimension and the magnetic susceptibility, were used as a control.[12]

The objectives of this study were to show that the magnetic field used in magnetapheresis may be mapped to a very high degree of accuracy, that such magnetic field is amenable to a highly accurate theoretical description allowing computations of the magnetic force field in the vicinity of the interpolar gap, and that the interposition of a well-defined laminar flow on the magnetic field leads to a highly controlled magnetic deposition system. We also show that the magnetically deposited cell fraction is amenable to routine cytological examination.

1. THEORY

1.1. Description of the Model. Due to high viscous forces acting on the micrometer-size cells (or particles) in the aqueous

(24) Harrison, P. M.; Andrews, S. C.; Artymiuk, P. J.; Ford, G. C.; Lawson, D. M.; Smith, J. M. A.; Treffry, A.; White, J. L. In *Iron Transport and Storage*; Ponka, P., Schulman, H. M., Woodworth, R. C., Eds.; CRC Press: Boca Raton, FL, 1990; pp 81–102.

medium, the magnetic cells moved in a quasi-static motion (no inertial effects). Therefore, the viscous drag, $\mathbf{F}_D$, equals the magnetic force, $\mathbf{F}_m$, and the cell motion was described by the equation

$$\mathbf{F}_D = \mathbf{F}_m \qquad (1)$$

The magnetic force, $\mathbf{F}_m$, acting on a cell labeled with N_{fer} identical ferritin molecules is a sum of the magnetic forces acting on each ferritin molecule, $\mathbf{F}_{fer}$:[25]

$$\mathbf{F}_m = \sum_{fer}^{N_{fer}} \mathbf{F}_{fer} \qquad (2)$$

The magnetic force acting on the ferritin molecule, $\mathbf{F}_{fer}$, is the force of an external, nonuniform magnetic field, $\mathbf{B}$, acting on a magnetic dipole, μ. The magnetic dipole moment of ferritin, μ_{fer}, is induced by the external magnetic field of strength $\mathbf{H}$, and $\mu_{fer} \propto \mathbf{H}$ (paramagnetic ferritin). In a diamagnetic medium, such as water, $\mathbf{B} = \mu_0\mathbf{H}$. The magnetic moment, magnetostatic potential energy, U, and magnetic force, $\mathbf{F}_{fer}$, acting on the ferritin molecule are expressed by the following formulae:[25]

$$\mu_{fer} = V_{fer}\Delta\chi_{fer}\frac{\mathbf{B}}{\mu_0}, \quad U = -\frac{1}{2}\,\mu_{fer}\cdot\mathbf{B} \qquad (3a)$$

$$\mathbf{F}_{fer} = -\nabla U = \frac{1}{2}\frac{V_{fer}\Delta\chi_{fer}}{\mu_0}\nabla B^2 \qquad (3b)$$

where V_{fer} is ferritin volume, $\Delta\chi_{fer} = \chi_{fer} - \chi_{aq}$ is the net ferritin magnetic cell susceptibility in the aqueous solution, and μ_0 is the magnetic permeability of vacuum. The cell size is small with respect to spatial variations of B, and therefore the same field and gradient are acting on each ferritin molecule on the cell. Substitution of eq 3b into eq 2 yields

$$\mathbf{F}_m = N_{fer}\mathbf{F}_{fer} = \frac{1}{2}N_{fer}\frac{V_{fer}\Delta\chi_{fer}}{\mu_0}\nabla B^2 \qquad (3c)$$

The magnetic force acting on the cell also can be expressed by an effective cell magnetic susceptibility, $\Delta\chi$. The term "effective" here means relative to the medium (water) and averaged over the cell volume. The cell motion in the external magnetic field stems from its effective magnetic susceptibility, $\Delta\chi$, and the resulting magnetic force $\mathbf{F}_m$:

$$\mathbf{F}_m = \frac{1}{2}\frac{\Delta\chi V}{\mu_0}\nabla B^2 \qquad (4)$$

where V is cell volume. Native lymphocytes have a magnetic susceptibility equal to that of water, and therefore their effective susceptibility, $\Delta\chi = 0$. Since the effective magnetic cell susceptibility is the result of binding of the ferritin molecules, it follows that the right-hand sides of eqs 3c and 4 are equal, from which one obtains

(25) Becker, R. *Electromagnetic Fields and Interactions*; Dover Publications, Inc.: New York, 1982; Chapter CIII.

$$N_{fer}\Delta\chi_{fer}V_{fer} = \Delta\chi V$$

$$N_{fer} = \frac{\Delta\chi}{\Delta\chi_{fer}}\frac{V}{V_{fer}} = \frac{\Delta\chi}{\Delta\chi_{fe4}}\left(\frac{R}{R_{fer}}\right)^3 \qquad (5)$$

where R and R_{fer} are cell and ferritin radii, respectively. The ferritin molecule comprises a protein shell of a molecular weight of 450 000 and an outer radius of 6 nm. It contains an iron core of a varying number of iron atoms, depending on species and metabolic state of the organism.[24] The commercial horse spleen ferritin preparation used in this experiment contains varying numbers of iron atoms in one ferritin molecule, from 1000 to up to 4000, with an average of 2000. This corresponds to 20% (w/w) iron content, ferritin specific gravity of 2.37 g/cm^3, and molecular weight of 560 000. The reported specific magnetic susceptibility of horse spleen ferritin at room temperature is 7.5×10^{-6}[em cgs] (no information about iron load was provided).[26] The reported molar magnetic susceptibility of the ferritin iron core is 5900 $\times$ 10^{-6}[em cgs] at 2000 iron atoms/ferritin molecule, corresponding to a lower value of the ferritin specific susceptibility of 2.95 $\times 10^{-6}$[em cgs].[33] The corresponding value of the volumetric magnetic susceptibility in SI units, used in the subsequent calculations, is $\chi_{fer} = 4\pi(2.37)(2.95 \times 10^{-6}) = 87.9 \times 10^{-6}$. Thus, the net volumetric magnetic susceptibility of ferritin molecule in aqueous solution is $\Delta\chi_{fer} = \chi_{fer} - \chi_{aq} = 87.9 \times 10^{-6} - (-9.05 \times 10^{-6}) = 96.9 \times 10^{-6}$. In calculating N_{fer}, we used the reported average lymphocyte radius of 5 μm,[27] which was somewhat higher than the value measured in our laboratory, 4.2 ± 0.4 μm (data not shown). The error of N_{fer} relative to the presence of cells other than lymphocytes (mostly monocytes) in the lymphocyte preparation, which also bind ferritin, was accounted for by assuming the same dispersion of cell radii around the mean as observed in our laboratory, 0.4 μm (data not shown).

The source of the magnetic field is the interpolar gap of a half-width equal to a, and the saturation field deep inside the gap equal to B_0. Such a gap can be approximated by an infinite slot in a complex z-plane. The magnetic field can be described using a scalar potential P.[28] The field lines and the equipotential lines for the infinite slot were obtained using the complex potential function P of a single line current in a complex w-plane:

$$P = \Phi + j\Theta = -\frac{j}{\pi}(\Phi_2 - \Phi')\ln w + \Phi' \qquad (6)$$

where Φ_2 and Φ' are constants. The constant field lines, $\Phi =$ const, and the constant potential lines, $\Theta =$ const, in the w-plane were transformed back to the complex z-plane using the conformal mapping function for an infinite slot:[28]

$$z = a + 2j\frac{a}{\pi}[\sqrt{1 - w^2} + \ln w - \ln(1 + \sqrt{1 - w^2})] \quad (7)$$

The maps of the magnetic field around the interpolar gap in the

(26) Blaise, A.; Chappert, J.; Girardet, J.-L. *C. R. Acad. Sci. Paris* **1965**, *261*, 2310–2313.
(27) *Hematology*; Williams, W. J.; Beutler, E.; Erslev, A. J.; Lichtman, M. A., Eds.; McGraw-Hill Co.: New York, 1990; Chapter 100.
(28) Weber, E. *Electromagnetic Fields. Theory and Applications. Vol. I—Mapping of Fields*; John Wiley & Sons, Inc.: New York, 1960; p 344.
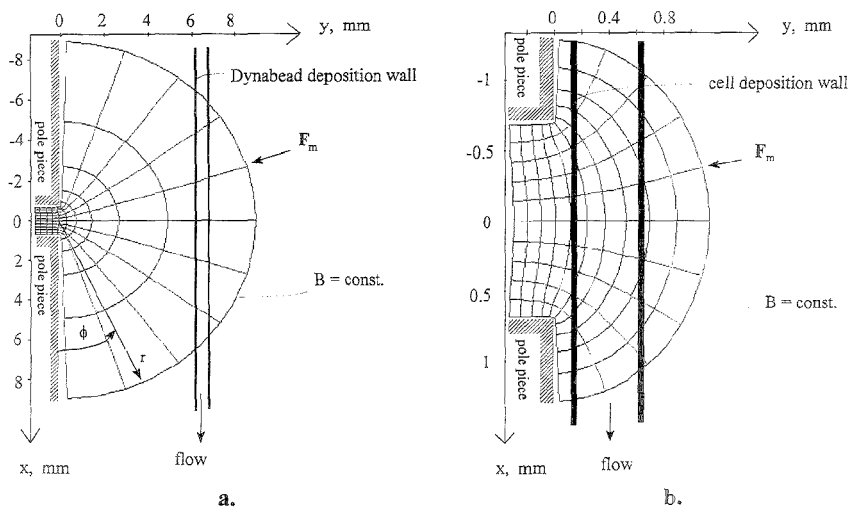
Figure 2. Magnetic field around the interpolar gap. The field lines, B, and the equipotential lines orthogonal to the field lines were generated using a solution for an infinite slot, eqs 6 and 7. The arrow shows direction of the magnetic force, F_m, acting on a small paramagnetic particle in the far field. The position of the flow channel is indicated by a pair of thick lines. The direction of the carrier medium flow is indicated by an arrow. (a) Far field, used in the Dynabead deposition experiments. The field lines are concentric semicircles, and equipotential lines are radial lines from the origin. The polar coordinates [r,ϕ] were used in the far-field approximation, eq 8. (b) Near field, used in the cell deposition experiments.

z-plane are shown in Figure 2 parts a (far from the interpolar gap) and b (near the interpolar gap).

The surfaces of the pole pieces near the gap may be treated as the equipotential surfaces.[28] At distances greater than a, the near-field map shown in Figure 2b was approximated by the far-field map shown in Figure 2a. For the far field, the following relationship holds:[28]

$$\mathbf{B} = \frac{2aB_0}{\pi} \frac{1}{r} \frac{\mathbf{r}}{r} \tag{8}$$

where $\mathbf{r} = [x,y]$ is the position vector of the magnitude $r = (x^2 + y^2)^{1/2}$.

The cell motion in the viscous medium was approximated by that of a rigid sphere of radius R. The cell motion was within the Stokes region, since the product of the cell velocity relative to that of medium, Δv, and cell diameter, $2R$, was less than about 0.01 cm^2/s.[29] The viscous drag force was represented by the Stokes formula:

$$\mathbf{F}_D = 6\pi R\eta\Delta v \tag{9}$$

The carrier medium velocity distribution in a parallelepiped channel of very large aspect ratio (width to height, $w/h \approx 12$)) was parabolic, thus,

$$v_x(y) = -\frac{4v_{max}}{h^2}(y - y_1)(y - y_2) \tag{10a}$$

(29) Bird, B. R.; Stewart, W. E.; Lightfoot, E. N. *Transport Phenomena*; John Wiley and Sons: New York, 1950; Chapter 2.3.

$$v_{max} = \frac{3}{2}\frac{Q}{wh} \tag{10b}$$

where v_{max} is the maximum flow velocity, $h = y_2 - y_1$ is the height of the rectangular channel, w is the width of the channel, and Q is the volumetric flow rate of the carrier medium.

1.2. Trajectories of the Magnetically Labeled Cells in the Magnetic Field and the Fractional Cell Recovery, ϵ. The fractional cell recovery, ϵ, was defined as the ratio of cell concentration in the eluate, c_{out}, to that in the feed, c_{in}:

$$\epsilon = c_{out}/c_{in} \tag{11}$$

The value of ϵ was computed numerically by simulating particle trajectories in the magnetic and flow fields. The trajectories were simulated for different initial positions of the particle (cell) upstream, far away from the interpolar gap. The initial position of the cell with respect to the deposition wall was defined by the parameter λ, $0 < \lambda < 1$, so that $y_0 = y_1 + \lambda h$ is the initial y-coordinate of the cell, where y_1 is the position of the deposition wall, and h is the channel height (see Figure 2). The initial position of the cell the most distant from the deposition wall, trapped by the magnetic field, was denoted λ_0. For a parabolic flow velocity distribution, eq 10, one obtains

$$\epsilon = c_{out}/c_{in} = 1 - \frac{\int_{y_1}^{y_1+\lambda_0 h} c_{in} v_x(y)\ \mathrm{d}y}{\int_{y_1}^{y_2} c_{in} v_x(y)\ \mathrm{d}y} = 1 - (3\lambda_0^2 - 2\lambda_0^3) \tag{12}$$

where $y_2 = y_1 + h$.

Equation 1, with the substitutions of eqs 4, 8, 9, and 10, was solved in the $x'y'$-plane, using dimensionless variables x', y', t', and

B', defined as follows:

$$x' = x/a, \quad y' = y/a, \quad t' = (v_{max}/a)t,$$
$$B' = B/B_0 = (2/\pi)(1/r') \tag{13}$$

The relationship between the primed and nonprimed time and spatial derivatives has the following form:

$$
\begin{cases}
\dot{x}' = \dfrac{dx'}{dt'} = \dfrac{1}{v_{max}}\dfrac{dx}{dt} = \dfrac{1}{v_{max}}\dot{x} \\[2mm]
\dot{y}' = \dfrac{dy'}{dt'} = \dfrac{1}{v_{max}}\dfrac{dy}{dt} = \dfrac{1}{v_{max}}\dot{y}
\end{cases}
\tag{14a}
$$

$$
\begin{cases}
\dfrac{\partial B'^2}{\partial x'} = \dfrac{a}{B_0^2}\dfrac{\partial B^2}{\partial x} = -\dfrac{8}{\pi^2}\dfrac{x'}{r'^4} \\[2mm]
\dfrac{\partial B'^2}{\partial y'} = \dfrac{a}{B_0^2}\dfrac{\partial B^2}{\partial y} = -\dfrac{8}{\pi^2}\dfrac{y'}{r'^4}
\end{cases}
$$

where $r' = (x'^2 + y'^2)^{1/2}$. The dimensional parameters of the system were conveniently grouped in the dimensionless number ζ, defined as follows:

$$\zeta = {}^1/_9 \frac{R^2}{\eta v_{max}}\frac{\Delta\chi}{\mu_0}\frac{B_0^2}{a} \tag{14b}$$

The equations describing the cell motion, and the initial conditions take the following form:

$$
\begin{cases}
\ddot{x}' = -\zeta\dfrac{\partial B'^2}{\partial x'} - 4\dfrac{a}{h}(y' - y'_1)(y' - y'_2) \\[2mm]
\ddot{y}' = -\zeta\dfrac{\partial B'^2}{\partial y'}
\end{cases}
\tag{15}
$$

$$
\begin{cases}
x'(0) = \dfrac{x_0}{a} \\[2mm]
y'(0) = \dfrac{y_0}{a} = y'_1 + \lambda\dfrac{h}{a}, \quad 0 < \lambda < 1
\end{cases}
$$

The solution of eqs 15 also determined cell trajectories and their end points in terms of parameters λ and ζ. There were two trajectory end points significant for the present analysis: either on the deposition wall, corresponding to the cell capture, or in infinity, resulting in cell recovery. By running a series of simulations for the increasing values of λ, at constant ζ, an escape value of λ_0 was determined for which the trajectory end point jumped from the deposition wall to infinity. The value of λ_0 was used subsequently to calculate ϵ, eq 12. The procedure was then repeated for a number of values of parameter ζ, resulting in a range of values of ϵ, from that approaching 0 to that approaching 1. The whole process led to the determination of a theoretical dependence of ϵ on ζ, which was conveniently presented as a plot $\epsilon = \epsilon(\zeta)$. In the remainder of the text, such plots are referred to as "calibration plots". In experiments with the ferritin-labeled lymphocytes, the calibration plot was obtained using a trial value of $\Delta\chi = 10^{-6}$. The numerical values of other parameters used in the calculations are shown in Table 1. Considering that ζ is inversely proportional to v_{max}, eq 14b, and therefore to Q, eq 10b, the relationship between ϵ and ζ could also be determined

experimentally. Fitting the theoretical curve, $\epsilon = \epsilon(\zeta)$, to the experimental data was done by correcting the trial value of $\Delta\chi$ to a value for which the theoretical curve best approximates the experimental data (see below). The trial value of $\Delta\chi$ for the Dynabead M450 was set equal to the value provided by the manufacturer, $\Delta\chi = 0.245$, and no further fitting was done. Examples of cell trajectories for different values of λ_0 are shown in Figure 3.

1.3. Fitting the Calibration Curve $\epsilon = \epsilon(\zeta)$ **to the Experimental Data.** Two different calibration curves, $\epsilon = \epsilon(\zeta)$, one for Dynabead M450 and one for the cell, were calculated. The relative positions of the flow channel and the interpolar gap used in the calculations are shown in Figures 2, parts a and b, correspondingly. The value of λ_0, describing the most distant cell captured in the magnetic field, was evaluated with an accuracy of ±0.01. The numerical calculations and trajectory plotting were performed using MapleV release 2 software package (MathSoft Inc., Cambridge, MA), on an IBM-compatible PC. The computer program is available from the authors on request. The sample results are illustrated in Figure 3.

Comparison between the calculated and the experimentally measured values of ϵ was made possible by expressing ζ as a function of Q. Substituting the expression for v_{max}, eq 10b, into the definition of ζ, eq 14b, yields

$$\zeta = \frac{2}{27}\frac{whR^2}{\eta}\frac{\Delta\chi}{u_0}\frac{B_0^2}{a}\frac{1}{Q} = \zeta_Q\frac{1}{Q} \tag{16}$$

For Dynabead M450, the computed relationship $\epsilon = \epsilon(\zeta)$ was linear for the entire range of ϵ, $0 < \epsilon < 1$. The proportionality constant, ζ_Q, eq 16, was calculated using the numerical value of $\Delta\chi_D \approx \chi_D = 0.245$, and was $\zeta_Q = 211$ mL/min. Numerical values of other constants used in the calculations are shown in Table 1. The experimental values of ϵ vs Q for Dynabeads were plotted directly onto the Dynabead calibration curve $\epsilon = \epsilon(\zeta)$ using the relationship $\zeta = \zeta_Q(1/Q)$.

For the cell, the computed relationship $\epsilon = \epsilon(\zeta)$ was almost linear in the range $0 < \epsilon \le 0.6$. Therefore, it was approximated by the following equation:

$$\epsilon = \epsilon(\zeta) = m\zeta + b \tag{17}$$

where m is the slope and b is the intersect determined by the regression analysis for a set of points $[\zeta_i, \epsilon_i(\zeta_i)]$, $i = 1, \ldots, 10$, selected from the curve $\epsilon = \epsilon(\zeta)$, $0 < \epsilon \le 0.6$. These values were $m = -5.41 \pm 0.25$, $b = 0.695 \pm 0.027$, and $r^2 = 0.987$. The proportionality constant, ζ_Q, calculated using the trial value of $\Delta\chi = 10^{-6}$, was equal to 2.25×10^{-3} mL/min. Other constants are shown in Table 1.

The experimental value of the cell magnetic susceptibility, $\Delta\chi$, was determined as follows. By substituting the expression for ζ, eq 16, into the expression for ϵ, eq 17, one obtains

$$\epsilon = m\zeta + b = m\zeta_Q\frac{1}{Q} + b \qquad \text{theory} \tag{18}$$

$$\epsilon_E = m_E\zeta_E + b_E = m_E\zeta_{QE}\frac{1}{Q_E} + b_E$$

$$= m'\frac{1}{Q_E} + b_E \qquad \text{experiment}$$

Table 1. Material and Geometric Parameters of the Analytical Magnetapheresis

parameter	notation	numerical value	SI units
	A. Magnetic Separation System		
interpolar gap width	a	0.7	mm
saturation magnetic field	B_0	2.433 ± 0.037	Tesla (tesla) $= \mathrm{N\ A^{-1}\ m^{-1}}$
magnetic permeability of vacuum	μ_0	$4\pi \times 10^{-7}$	T·m/A
water viscosity	η	10^{-3}	$\mathrm{kg\ m^{-1}\ s^{-1}}$
flow channel height	$h = y_2 - y_1$	0.5	mm
flow channel width	w	6	mm
	B. Dynabead Calibration Plot Parameters		
magnetic susceptibility	$\Delta\chi_D \approx \chi_D$	0.245	1
density	ϱ	1.5×10^3	$\mathrm{kg/m^3}$
radius	R_D	2.25	$\mu m = 10^{-6}\ m$
volumetric flow rate of the medium	Q	2.7–20	mL/min
average flow velocity	$v_{av} = 10^3/60\ Q/w\ h$	15–110	mm/s
initial conditions	$x_0 = -10a$	$y_1 = 6.1$	mm
	$y_1 < y_0 < y_2$	$y_2 = 6.6$	
	C. Cell Calibration Plot Parameters		
effective magnetic susceptibility (trial value)	$\Delta\chi$	10^{-6}	1
density	ϱ	10^3	$\mathrm{kg/m^3}$
radius	R	5	$\mu m = 10^{-6}\ m$
volumetric flow rate of the medium	Q	0.05–0.24	mL/min
average flow velocity	$v_{av} = 10^3/60\ Q/w\ h$	0.28–1.33	mm/s
initial conditions	$x_0 = -4a$	$y_1 = 0.15$	mm
	$y_1 < y_0 < y_2$	$y_2 = 0.65$	
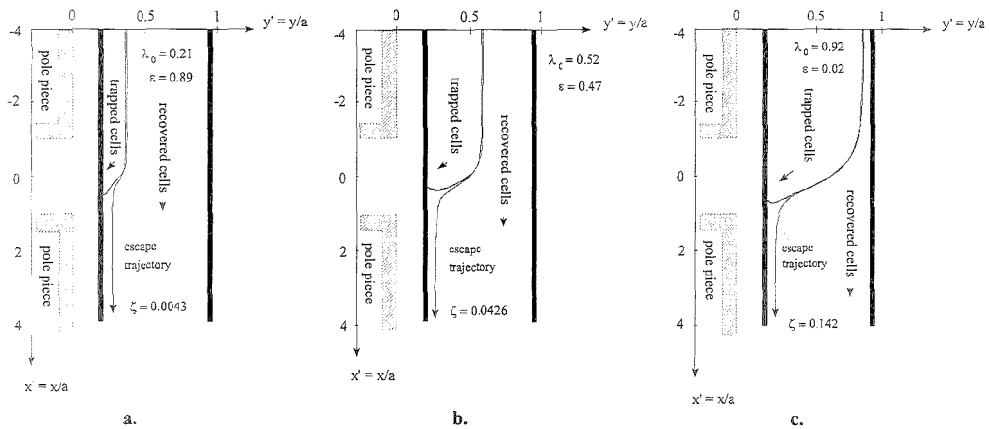
Figure 3. Examples of cell trajectories as a function of the dimensionless number ζ, defined in eq 14b. The trapped cell trajectory end points are on the deposition wall. The escape trajectory end points are in infinity. Parameter λ_0 describes the initial position at entry of the most distant cell from the deposition wall that becomes trapped. The flow of the carrier medium is from top to bottom. The panels a, b, and c are in the order of decreasing fractional cell recovery, ϵ, corresponding to increasing ζ. These panels are examples of a series of plots used to establish the Dynabead and cell calibration curves $\epsilon = \epsilon(\zeta)$, as described in the text.

The symbols with subscript E relate to the experimental quantities. The symbols without subscripts relate to the theoretical quantities. The slope, $m' = m_E\ \zeta_{QE}$, and the intersect, b_E, were determined experimentally by the regression analysis on the data points $[1/Q_E, \epsilon_E]$.

The theoretical regression line fits the experimental points if the following conditions hold true:

$$m_E = m \qquad \zeta_E = \zeta + (b - b_E)/m \qquad (19)$$

From eqs 16, 18, and 19,

$$\frac{\Delta\chi_E}{\Delta\chi} = \frac{\zeta_{QE}}{\zeta_Q} \qquad \zeta_{QE} = \frac{m'}{m_E} = \frac{m'}{m} \qquad (20)$$

from which one arrives at the following relationship between the experimental (corrected), $\Delta\chi_E$, and the trial, $\Delta\chi$, values of the magnetic susceptibility:

$$\Delta\chi_E = \frac{m'}{m}\frac{\Delta\chi}{\zeta_Q} \qquad (21)$$

where m' is determined from experiment (see eq 18), and m, $\Delta\chi$, and ζ_Q are known from theory. Equations 19 allow one to plot the experimental data $[\zeta_E, \epsilon_E]$ against the theoretical curve $\epsilon - \epsilon(\zeta)$.

1.4. Error Analysis. All experimental measurements were done at least in duplicate. Dynabead and ferritin-labeled lymphocyte counts were repeated eight times for each value of the volumetric flow rate Q. The results are presented as averages $\pm$ standard deviation. The correlation between variables was analyzed using regression analysis at the confidence level $p = 0.05$. The regression plots show average values of the dependent variable and standard deviations. For fewer than eight measurements per independent variable, all the data points are shown. The error of the compound variable was calculated using the compound error of a function.[30] The standard deviation of the regression slope and the regression constant were used in calculating the error of the compound variable, where applicable.

2. EXPERIMENTAL SECTION

2.1. Magnetic Field Measurements. A magnetic field was generated with a permanent magnet assembly consisting of two pairs of neodymium–iron–boron magnets characterized by a maximum energy product of 2.23×10^5 T·A/m. The magnets were connected by soft iron pole pieces conducting the magnetic flux lines to the interpolar gap (see Figure 1). The length of the interpolar gap along the Oz-coordinate, 25 mm, was much larger than its width along the Ox-coordinate, $2a = 1.4$ mm (compare Figure 2), and therefore the magnetostatic field **B** was two-dimensional, in the Oxy-plane, near the center of the interpolar gap. The depth (along the Oy-coordinate) to width ratio of the interpolar gap, 6 mm:1.4 mm, was sufficient to assume that the interpolar gap field was equivalent to a field of an infinite slot. The magnetic field map shown in Figure 2 was obtained using the solutions for an infinite slot, eqs 6 and 7.

The magnetic field measurements were performed using a Gaussmeter and a Hall-effect probe (Model 9200 Gaussmeter and transverse probe STG920404, F. W. Bell, Orlando, FL). The probe measured magnetic flux perpendicular to a sensing area of a diameter 0.89 mm, located 0.37 mm from the end of the rectangular probe stem. Polar coordinates $[r,\phi]$ (see Figure 2a) were used to define the location of the center of the sensing area. The dimensions of the stem were length 100 mm, width 3.8 mm, and thickness 1.0 mm. One set of field measurements was performed along selected isomagnetic lines, $B = $ const, far from the interpolar gap. In the far-field region, the isomagnetic lines form concentric semicircles centered on the origin, similar to the field lines B (see Figure 2b). The measurements were performed at three different distances from the center of the interpolar gap, $r = 5$, 10, and 20 mm, and for varying ϕ at constant r, from $\phi = 15°$ to 165°, in 15° increments. The probe was mounted on a cutout which assured the perpendicular orientation of the probe sensing area to the magnetic field lines at any given set of the polar coordinates $[r,\phi]$. A separate set of measurements was performed for varying r at constant ϕ, from $r = 0$ to 20 mm, in increments from 0.02 mm in the fast changing field region to 0.4 mm in the slow changing region. The probe was mounted on a micrometer stage (Klinger Scientific, Richmond Hill, NY).

The saturation field deep inside the gap, B_0, was calculated by analyzing the dependence of B over $1/r$. The slope of the regression line B over $1/r$, in the linear range of B vs $1/r$, determined the value of B_0 for the known value of a, see eq 8. The $B \propto 1/r$ approximation of the magnetic field was accurate

for experiments with Dynabeads for which the deposition channel was placed in the far field of the slot, from $y_1 = 6.1$ mm to $y_2 = 6.6$ mm. The $B \propto 1/r$ approximation could be used down to distances of $r = (0.34)2a = 0.68 \times 0.7$mm $= 0.48$ mm, at which the slot flux changes character to the tooth tip flux.[28] This approximation was also used in calculating the reference cell calibration curve, $\epsilon = \epsilon(\zeta)$. The error in using expressions 8 instead of the exact solution of eq 6 and 7 was approximately 10% (data not shown) for the most distant cell from the interpolar gap, for which $y_0 = 0.65$ mm. The large errors in predicting ϵ at high flow rates due to the contribution of cells close to the slot was avoided by limiting the analysis to $\epsilon \leq 0.6$.

The characteristic values of the magnetic field, B, and gradient, $|\nabla B|$, see eqs 8, were determined at the field line corresponding to the most distant cell trajectory from the interpolar gap. In Dynabead experiments, this corresponded to the distance $r = 6.6$ mm; for experiments with the ferritin-labeled lymphocytes, this corresponded to the distance $r = 0.65$ mm.

2.2. Flow Channel. The flow channel consisted of top and bottom plates and a silicone rubber spacer. The spacer was sandwiched between the top and bottom plates. The top plate had two drilled holes to connect the tubing used as an inlet and an outlet for the channel. The bottom plate was made of a thin glass, 150 μm thick (Fisher Finest Premium Cover Glass No.1, Fisher Scientific, Pittsburgh, PA), and was used to collect the magnetic deposition. The cutout of the silicone rubber sheet (Silastic 0.02 in., Dow Corning Corp., Midland, MI) of length 40 mm and width 6 mm was used as a flow channel chamber. The spacer thickness defined the flow channel height, $h = 0.5$ mm.

The flow channel was positioned at two different distances from the magnet surface. In the experiments with ferritin-labeled lymphocytes, the distance from the inner surface of the deposition plate to the magnet was $y_1 = 0.15$ mm. In experiments with the M450 beads, this distance was $y_1 = 6.1$ mm.

The volumetric flow rates used in the lymphocyte experiments were $Q = 0.05$, 0.07, 0.10, 0.15, and 0.24 mL/min. These flow rates corresponded to the linear velocity range of 0.28–1.3 mm/s. The volumetric flow rates used for the experiments with M450 beads were $Q = 2.7$, 3.9, 5.9, 8.8, 13, and 20 mL/min, corresponding to the linear flow velocity range of 15–110 mm/s.

The flow channel was positioned such that the flow direction was parallel to gravity to avoid interference from gravitational sedimentation. After each experiment, the bottom plate was disassembled and stained with Modified Wright stain (Sigma Chemical Co., St. Louis, MO) before being mounted on microscope slides.

2.3. Lymphocytes and M450 Reference Beads. Freshly drawn blood was obtained from consenting, healthy volunteer donors according to institutional guidelines. Peripheral lymphocytes were isolated from whole blood using density gradient centrifugation (Ficoll-Hypaque, Pharmacia, Piscataway, NJ) immediately after blood donation. The residual erythrocytes were lysed by exposure for 1 min to an osmotic shock buffer (RBC Lysing Buffer, Sigma Chemical Co.). The lymphocytes were washed several times with phosphate-buffered saline (PBS, GIBCO, Grand Island, NY) and kept on ice until needed for use. The composition of the cell sample was evaluated for selected samples using an automated cell counter (Technicon Co., Tarrytown, NY), and it showed 95% lymphocytes (including both T and B subpopulations); the remaining fraction was mostly monocytes

---

(30) Margenau, H.; Murphy, G. M. *The Mathematics of Physics and Chemistry*; D. Van Nostrand Co.: Princeton, NJ, 1962; Chapter 13.

with a small number of neutrophils. The magnetic labeling technique, described below, was not specific to the cell surface markers: therefore, on average, the amount of the label bound per cell surface area was approximately the same for all markers. Larger cells, such as monocytes, would acquire more label and therefore contribute more to the deposition than their fractional concentration in solution. This effect of the cell size on the cell susceptibility analysis was considered small, however, due to only a small number of monocytes in the sample and the uniform size of the normal peripheral lymphocytes.[27]

The lymphocytes were incubated with cationized horse spleen ferritin (Sigma Chemical Co.) in 25 mM HEPES and 150 mM NaCl solution (pH = 7.5) at room temperature for 15 min. The cationized ferritin is supplied as a N,N-dimethyl-1,3-propanediamine derivative of the native horse spleen ferritin, and it exhibits a net positive charge at pH 7.5. Under these conditions, the cationized ferritin readily formed ionic bonds with the anionic sites on the cell membrane.[33] The concentration of ferritin was 0.001% (v/v). Following incubation, lymphocytes were washed with 150 mM NaCl to remove ferritin from solution. The lymphocyte counts were performed using a hemacytometer (Reichert, Buffalo, NY) before and after the magnetic deposition experiments. The sample volume was 0.5 or 1.0 mL. The initial lymphocyte concentration was 2×10^6 cells/mL; the initial M450 bead concentration was 1×10^6 beads/mL. The fractional cell recovery, ϵ, in the fraction collected past the magnet was calculated as the ratio of cell counts in the recovered cell sample to cell counts in the initial cell sample, in accordance with eq 11. The values of ϵ were plotted as a function of $1/Q$ and fitted to the reference cell calibration curve $\epsilon = \epsilon(\zeta)$ as discussed in section 1.3 above.

3. RESULTS

3.1. Magnetic Field.
The magnetic field as a function of ϕ, $B = B(\phi)_r$, at three different polar distances r from the interpolar gap center, is shown in Figure 4a. As expected from the theory, there was very little variation in B as a function of ϕ in the far-field region. The following averages were obtained at different distances r from the center of the gap: $\langle B(\phi)_r \rangle = 0.316 \pm 0.014$ T at $r = 5$ mm, $\langle B(\phi)_r \rangle = 0.175 \pm 0.010$ T at $r = 10$ mm, and $\langle B(\phi)_r \rangle = 0.0894 \pm 0.0070$ T at $r = 20$ mm. The magnetic field variation with distance r at $\phi = 0$ is shown in Figure 4b. The far-field approximation, $B \propto 1/r$, starts to break down at distances of ~1 mm, where the field bends toward a plateau inside the interpolar gap. The far-field region is shown in Figure 4c using a plot of B on $1/r$, at $\phi = 0$, for $r = 1-20$ mm. Again, the departure from nonlinearity is noticeable at $r = 1$ mm. The slope of the regression line of B on $1/r$ at $\phi = 0$ was used to determine the saturation magnetic field, B_0. The extrapolated value of the saturation magnetic field $B_0 = 2.433 \pm 0.027$ T, $n = 201$. The magnetic field B and gradient $|\nabla B|$, representative of experiments with Dynabeads (at $r = 6.6$ mm), were $B = 0.1642 \pm 0.0056$ T and $|\nabla B| = 0.024\,88 \pm 0.000\,85$ T/mm. The field and gradient representative of experiments with the ferritin-labeled lymphocytes ($r = 0.65$ mm) were $B = 1.667 \pm 0.057$ T and $|\nabla B| = 2.565 \pm 0.088$ T/mm.

3.2. Dynabead M450 Fractional Recovery.
The experimental fractional recovery values, ϵ_E, were plotted as a function of ζ_E, calculated from eq 18, based on the constants listed in Table 1. The experimental points $[\zeta_E, \epsilon_E]$ were plotted directly onto the calibration curve $\epsilon = \epsilon(\zeta)$ predicted from theory, as described in section 1.3 (see Figure 5a). The theoretically predicted calibration curve was inside the 95% confidence intervals of the mean ϵ_E for

a.

b.

c.
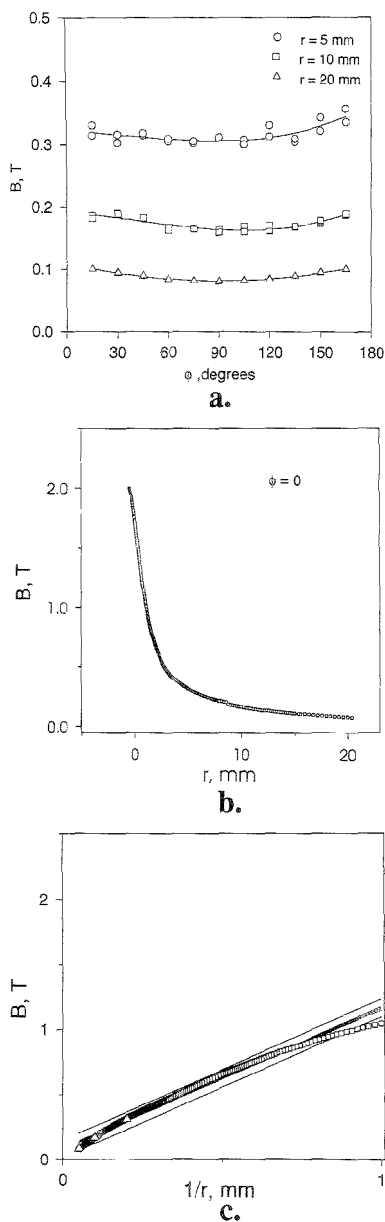
Figure 4. (a) Magnetic field, B, around the interpolar gap as a function of position in polar coordinates $[r, \phi]$ defined in Figure 2a. The field was measured along the field lines, B (see Figure 2a). Variations of the field with ϕ at constant r illustrate deviations of the experimental data from the potential field model (far field). (b) Magnetic field as a function of r, at $\phi = 0$, $n = 256$. (c) Magnetic field as a function of $1/r$ at $\phi = 0$. The triple line represents linear regression of B on $1/r$, slope = 1.083 ± 0.012, constant = 0.081 ± 0.042, $r^2 = 0.984$, and $n = 201$. The single lines represent the 95% confidence interval from the regression line. Open triangles represent average values of B shown in panel a.
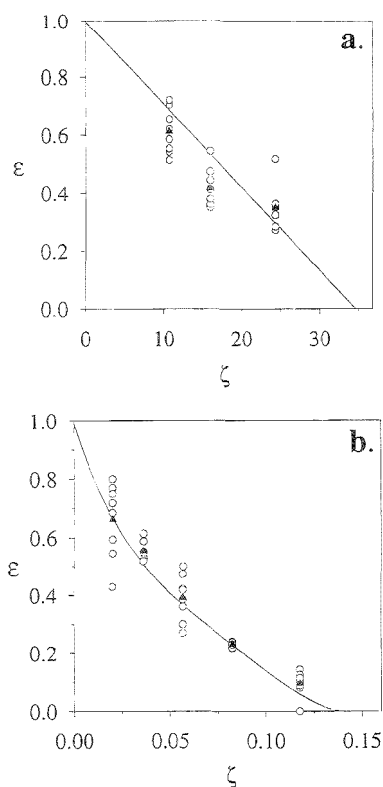
Figure 5. Calibration curve of fractional recovery, ϵ, as a function of parameter ζ, $\epsilon = \epsilon(\zeta)$. Solid lines represent theoretical prediction, open circles represent experimental observations, and solid triangles are averages for each value of ζ. (a) Dynabead M450: the theoretical values fall within the 95% confidence interval of the average experimental observations. (b) Ferritin-labeled lymphocytes: the experimental data were fitted to the theoretical calibration curve using eqs 18, see text.

all three values of ζ_E and is shown in Figure 5a, $n_E = 24$. The agreement between the predicted and measured values of the reference particle recovery, to within the experimental error, supports the validity of the results obtained for the ferritin-labeled lymphocytes.

3.3. Ferritin-Labeled Lymphocytes Fractional Recovery. The experimental points [ζ_E, ϵ_E] were fitted onto the calibration curve $\epsilon = \epsilon(\zeta)$ predicted from theory, as described in section 1.3 (see Figure 5b). The parameters of the regression line ϵ_E on $1/Q_E$, eq 18, were the following: $m' = -(3.55 \pm 0.24) \times 10^{-2}$, $b_E = 0.773 \pm 0.043$, and $n_E = 40$. The corresponding net magnetic susceptibility of the ferritin-labeled lymphocytes was obtained from eq 21: $\Delta\chi = (2.92 \pm 0.24) \times 10^{-6}$. The corresponding average number of ferritin molecules per ferritin-labeled lymphocyte was obtained from eq 5: $N_{fer} = (1.75 \pm 0.44) \times 10^{7}$.

Figure 6a shows the macroscopic appearance of the magnetic deposition of M450 beads, obtained at the flow velocity of 15 mm/s. It is worth noting that this deposition was obtained when the flow channel was kept at 6.1 mm away from the magnet, as depicted in Figure 2a. The loss of beads in parts of the deposition

band was an artifact of channel handling caused by the lack of bead adhesion to the channel surface.

The magnetic deposition zone for ferritin-labeled lymphocytes, after staining and mounting on the substrate slide, is shown in Figure 6c. A series of depositions is shown in order of decreasing flow velocity, from 0.83 through 0.28 mm/s. As flow velocity decreased, the density of the deposition increased. These changes corresponded to the changes in the recovered cell fraction counts, ϵ, which decreased with the decreasing flow velocity (and increasing ζ); see Figure 5b. One may also distinguish increased deposition at the edges of individual deposition bands, corresponding to the edges of the interpolar gap, (compare Figure 2b). This increase suggests that at distance a very close to the edges of the interpolar gap, the tooth tip flux dominates over the slot field flux, and the approximation $B \propto 1/r$ is no longer valid.[28] The near-field map shown in Figure 2b illustrates well the increased concentration of field lines and equipotential lines around the edge tip corresponding to the increased magnetic field, gradient, and force at the tip. However, the overall magnetic deposition appearance in Figure 6c shows the predominance of the slot effects, over tooth tip effects which supports the validity of the theoretical approach in describing the magnetic deposition process.

The microscopic appearance of cells and M450 beads in the magnetic deposition is shown in Figure 7. A concatenation of the M450 beads in the direction of the magnetic flux lines is clearly visible; it was caused by attraction between the high magnetic moments of the individual beads.

4. DISCUSSION

Analytical magnetapheresis of ferritin-labeled lymphocytes allowed close scrutiny of the magnetic separation process. The apparatus and magnetic separation were amenable to a detailed experimental and theoretical analysis. Such an analysis is rarely possible with existing magnetic separators, and relatively few attempts of such an analysis have been reported in the literature.[7,8,31-35] The measurement was done against a control provided by the reference magnetic particles, Dynabeads M450.[12] Analytical magnetapheresis allowed us to perform measurements under conditions matching possible applications of ferritin as a magnetic cell label. Low flow velocity, 0.28 mm/s, and high field intensity, 1.67 T, and high gradient, 2.57 T/mm, were required to remove ferritin-labeled lymphocytes from solution. In contrast, the M450 beads were removed almost completely at a much higher flow velocity, 15 mm/s, lower magnetic field intensity, 0.16 T, and lower gradient, 0.025 T/mm.

The low magnetic susceptibility of the ferritin-labeled cells requires that a high magnetic gradient be used to displace the cells from solution. The motion of low-susceptibility particles in the vicinity of a high-gradient magnetic field has been studied in the past using high-permeability intrusion (typically, a wire) in the magnetic field.[32-34] Use of a single wire allowed direct

(31) Hardwick, R. A.; Prisco, M. R.; Shah, D. O. *Artif. Organs* 1990, 14, 342–347.

(32) Takayasu M.; Duske, N.; Ash, S. R.; Friedlaender, F. J. *IEEE Trans. Magn.* 1982, 18, 1520–1522.

(33) Odette, L. L.; McCloskey, M. A.; Young, S. H. *Biophys. J.* 1984, 45, 1219–1222.

(34) Takayasu, M.; Kelland, D. R. *IEEE Trans. Magn.* 1986, 22, 1125–1127.

(35) Liberti, P. A.; Feeley, B. P. In *Cell Separation Science and Technology*; Compala D. S., Todd, P., Eds.; ACS Symposium Series 464; American Chemical Society: Washington, DC, 1991; pp 269–289.
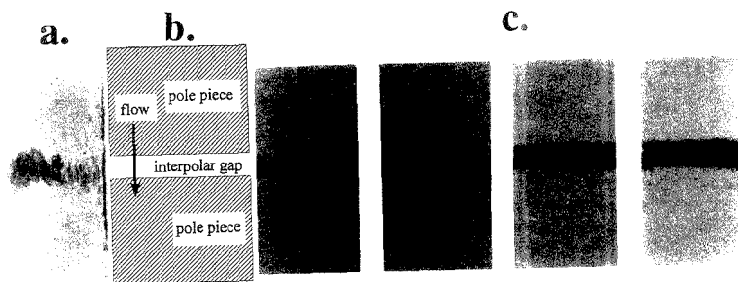
Figure 6. Macroscopic appearance of the magnetic deposition zone. The sample flow was from top to bottom. (a) M450 beads, without staining or mounting. (b) Diagram of the magnetic deposition zone, shown on the same scale as parts a and c of this figure. (c) Ferritin-labeled lymphocytes, after being stained and mounted on a microscopic slide, in the order of decreasing flow velocity, v_{av} = 0.83, 0.56, 0.39, and 0.28 mm/s, respectively. Cell deposition increased as flow velocity decreased.
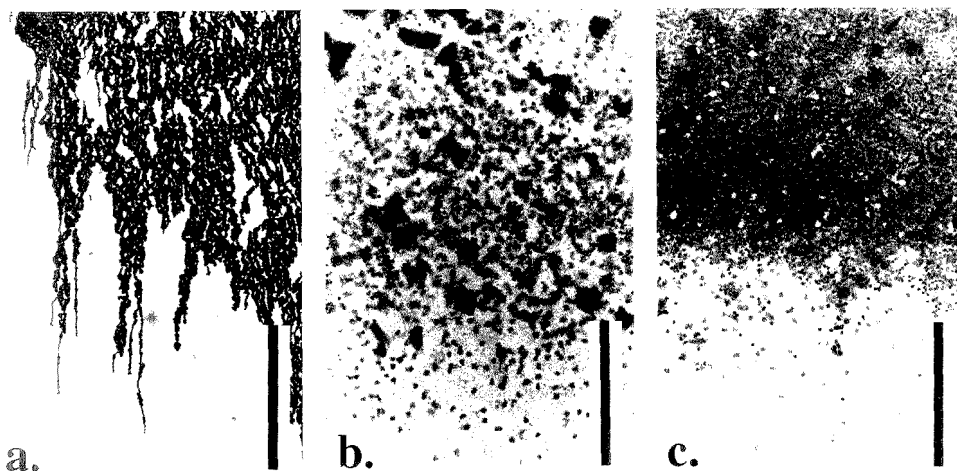
Figure 7. Microscopic appearance of the magnetic deposition shown in Figure 6. The scale bar represents 500 μm. (a) M450 Dynabeads. (b) Ferritin-labeled lymphocytes, v_{av} = 0.83 mm/s. (c) Ferritin-labeled lymphocytes, v_{av} = 0.28 mm/s. Note the comparable size of lymphocytes and M450 beads and the concatenation of M450 beads in the direction of the magnetic flux lines.

observation, on a microscopic scale, of particle deposition on the wire surface. The single high-permeability wire exposed to a homogeneous magnetic field offered a relatively simple model of the distribution of the magnetic field and forces.[36] The laminar flow of a carrier medium perpendicular to the straight, infinite wire provided a relatively simple model of the magnetic force in those studies. The formidable difficulties in extending such a model to the packed-bed, high-gradient magnetic separators and other types of magnetic separators currently in use hampered extending such an analysis to practical devices.

In this study, we used analytical magnetapheresis to compare magnetic properties of a well-characterized magnetic polymeric bead and a high iron content protein, ferritin. The use of ferritin as a magnetic cell label has been proposed before.[33,37,38] Ferritin offers several potential advantages over particulate magnetic labels

and other currently evaluated colloidal magnetic labels. The structure of the protein shell of ferritin molecules provides monodisperse molecular size distribution and good solubility under physiological conditions.[24] The surface of the protein shell may be modified to form direct or indirect binding with antibodies against selected cell or tissue surface receptors. Ferritin-conjugated antibodies have been routinely used as immunological markers in transmission electron microscopy studies of cellular substructures.[39]

The studies of the magnetic properties of mammalian ferritins by Mössbauer spectroscopy and NMR spectroscopy showed that the ferrihydrite crystal has a single-domain antiferromagnetic character, accounting for the paramagnetic behavior of mammalian ferritin in the magnetic field at room temperature.[40] The chemical composition and crystalline structure of the iron compound inside the ferritin protein shell are fairly labile and may be modified to

(36) Watson, J. H. P. *J. Appl. Phys.* **1973**, *44*, 4209−4213.
(37) Russell, A. P.; Evans, C. H.; Westcott, V. C. *Anal. Biochem.* **1987**, *164*, 181−189.
(38) Zborowski, M.; Malchesky, P. S.; Savon, S. R.; Green, R.; Hall, G. S.; Nosé, Y. *Wear* **1990**, *142*, 135−149.
(39) de Petris, S.; Raff, M. C. *Eur. J. Immunol.* **1972**, *2*, 523−535.
(40) Bizzi, A.; Brooks, R. A.; Brunetti, A.; Hill, J. M.; Alger, J. R.; Miletich, R. S.; Francavilla, T. L.; Di Chiro, G. *Radiology* **1990**, *177*, 59−65.

form a single superparamagnetic magnetite crystal.[41]

Analytical magnetapheresis allowed us to calculate the magnetic susceptibility of the ferritin-labeled lymphocytes and to estimate the number of ferritin molecules per lymphocyte necessary for the magnetic cell deposition. Previous studies evaluated the feasibility of ferritin as a label for magnetic cell separation without providing information on the cell ferritin load needed to achieve separation.[33,37,38] Under the present experimental conditions, the net magnetic susceptibility of the ferritin-labeled lymphocytes in aqueous solution was 2.92×10^{-6}, and the ferritin load was 1.75×10^7 molecules/cell. The net magnetic susceptibility of the ferritin-labeled lymphocytes was comparable to that of the deoxygenated erythrocytes, 5.17×10^{-6}.[7] It is interesting to note that for a reported lower ferritin load of 2.8×10^4 ferritin molecules/cell, the paramagnetic susceptibility of ferritin was not sufficient to offset the diamagnetic susceptibility of the cell (assumed to be equal to that of the water, $\chi_{aq} = -9.05 \times 10^{-6}$), with a resulting predicted net magnetic susceptibility of the ferritin-loaded cell equal to -8.2×10^{-6} (diamagnetic).[37] The measured number of ferritin molecules per cell used in this study for magnetic separation provides the information needed for further applications of ferritin as a magnetic label and, in particular, in considering ferritin as an immunomagnetic label.

ACKNOWLEDGMENT

GLOSSARY

a	interpolar gap half-width, eqs 7 and 8
b	intercept of the regression ϵ on ζ, eq 17
B	magnetic field intensity, eq 8
c	particle (cell) concentration
F	force
h	channel height
H	magnetic field strength
m	slope of the regression line ϵ on ζ, eq 17
n	sample size
r	radial coordinate, or correlation coefficient
N	number of ferritin molecules per lymphocyte, eq 5
P	complex potential, eq 6
Q	volumetric flow rate
R	hydraulic radius of the particle, eq 5
v	flow velocity
V	particle (cell) volume
w	channel width, or complex number on the w-plane, eqs 6 and 7

x,y	Cartesian coordinates
z	complex number on the z-plane, eqs 6 and 7

Greek Characters

ϵ	fractional cell recovery, eq 11
Θ	potential function in the complex potential P, eq 6
λ	relative distance from the deposition plate at entry, upstream and far away from the interpolar gap, eq 15 and Figure 3
λ_0	value of λ for the most distant trajectory ending at the deposition wall
$\Delta\chi$	effective magnetic susceptibility, averaged over particle volume, equal to a difference between the magnetic susceptibility of the particle and that of the medium (aqueous solution)
μ	magnetic moment
μ_0	magnetic permeability of vacuum. $4\pi \times 10^{-7}$ T/m·A
ϱ	specific density
η	viscosity of water
ζ	dimensionless number grouping the material and geometric constants of the magnetic deposition system
ζ_Q	proportionality constant between ζ and $1/Q$
ϕ	angular coordinate
Φ	field function in the complex potential P, eq 6

Subscript, Superscript, and Special Characters

aq	aqueous
av	average
D	viscous drag, or relating to the Dynabead
E	experimental
fer	ferritin
i	summation index
in, out	pertaining to quantities far away from the magnetic field
m	magnetic
0	saturation or initial value
1	relating to the proximal (deposition) wall of the deposition channel relative to the magnet surface
2	relating to the distal wall of the deposition channel relative to the magnet surface
'	dimensionless coordinate
$\langle\,\rangle$	average over spatial coordinates
boldface	vector quantity

(41) Meldrum, F. C.; Heywood, B. R.; Mann, S. *Science* 1992, *257*, 522–523.

Direct Determination of Inorganic Ions at Sub-ppb Levels by Ion Chromatography Using Water as a Mobile Phase

Wenzhi Hu,*,† Akira Miyazaki,† Hiroaki Tao,† Akihide Itoh,‡ Tomonari Umemura,‡ and Hiroki Haraguchi‡

National Institute for Resources and Environment, 16-3 Onogawa, Tsukuba, Ibaraki 305, Japan, and Department of Applied Chemistry, School of Engineering, Nagoya University Furo-cho, Chikusa-ku, Nagoya 464-01, Japan

Electrostatic ion chromatography (EIC) was used for determination of trace level inorganic ions. EIC is a new method of separating ions based on simultaneous electrostatic attraction and repulsion interactions between analyte ions and fixed positive/negative charges of a stationary phase, having the special advantage of using only water as the mobile phase. Initial results showing two elutions of the same analyte gave new insights into the mechanism of EIC. It suggests that the zwitterionic stationary phase, like a single charged stationary phase, has a Stern layer and a diffuse layer. The first elution is from the diffuse layer, and the second is from the Stern layer. As simpler analysis is facilitated by a single elution, a new species of inorganic salt with a longer elution time was added to the original sample solution in order to release analyte ions from the Stern layer to the diffuse layer. The newly introduced salt is called a sacrifice species. Without preconcentration, inorganic ions at sub-ppb levels were successfully detected by this method.

The desirability of an ion chromatography (IC) technique using only water as the mobile phase is summarized by Small:[1] "There are a number of ion chromatographic techniques that, though not widely used, deserve mention because of their simplicity and their potential for further development. All use water or other polar solvent as the sole component of the mobile phase. This not only eliminates the need for electrolytes and precise eluent make-up, but it avoids many of the detection problems that ionic eluents can impose. Detection can be expected to be very sensitive since the background is essentially deionized water."

In an earlier paper dealing with the results of ion separation achieved using water as the mobile phase, published in 1977,[2] the stationary phase used was a crown ether bonded one. Later, Small et al.[3] reported that inorganic ions could also be separated using water as the mobile phase when a very weak ion exchange resin stationary phase was used. The separations achieved using both of these methods, however, were poor compared with the results of the separation of the same ions using the conventional ICs (using an ion exchange stationary phase with a mobile phase containing the replacing ions).

A new approach for separating ions, also using water as the mobile phase but employing a zwitterionic stationary phase, has been developed by Hu et al.[4] When a small amount of aqueous solution containing an analyte (cations and anions) is passed through a zwitterionic stationary phase, neither the analyte cations nor the analyte anions can get close to the opposite charge fixed on the stationary phase, because another charge on the same molecule, fixed on the stationary phase, repels the analyte ions simultaneously. The analyte cations and anions are forced into a new state of simultaneous electrostatic attraction and repulsion interaction in the column. This was termed an "ion-pairing-like form". This method of separation was termed electrostatic ion chromatography (EIC).[4] The previous studies[4,5] demonstrated that the separation of inorganic ions (with the exception of cations having the same charge) using EIC is comparable to separations of the same ions obtained using conventional ICs. In previous studies,[4,5] samples having high concentrations (mmol/L) of analyte ions were used in order to understand the mechanism. In those studies, samples with low concentrations of ions were not investigated.

In this study, attention was turned to the determination of trace level inorganic ions using EIC. Initial results showing separate elution times for the same analyte gave new insights into the mechanism of EIC and led to the development of a new technique for simpler determination of trace level inorganic ions.

EXPERIMENTAL SECTION

Apparatus. The HPLC system used in this study was the same system used previously.[5] It was a Shimadzu (Kyoto, Japan) LC-6A system equipped with a Shimadzu LC-7A pump, a SIL-6A autoinjector, a SCL-6A system controller, and a CDD-6A conductivity detector connected with a SPD-M6A photodiode array UV–vis detector. An ICP-AES (Model 075 Plasma Atomcomp MKII; Thermo Jarrell-Ash, Franklin, MA) was also connected to this HPLC system for the detection of the cations. Two ODS-packed columns (L-Column, 4.6 × 250 mm; Chemical Inspection and Testing Institute, Tokyo, Japan), the first coated with CHAPS micelles and the second coated with Zwittergent-3-14 micelles, were prepared and used as the separation columns. The proce-

† National Institute for Resources and Environment.
‡ Nagoya University Furo-cho.
(1) Small, H. *Ion Chromatography*; Plenum: New York, 1989; p 132.
(2) Blasius, E.; Janzen, K.-P.; Adrian, W.; Klautke, G.; Lorscheider, R.; Maurer, P.-G.; Nguyen, V. B.; Nguyen Tien, T.; Scholten, G.; Stockemer, J. *Z. Anal. Chem.* 1977, 284, 337.
(3) Small, H.; Soderquist, M. E.; Pischke, J. W. U.S. Patent 4,732,686, 1988.

(4) Hu, W.; Takeuchi, T.; Haraguchi, H. *Anal. Chem.* 1993, 65, 2204.
(5) Hu, W.; Tao, H.; Haraguchi, H. *Anal. Chem.* 1994, 66, 2514.
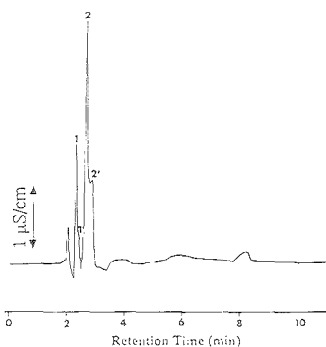
Figure 1. Chromatogram of an aqueous solution containing 1.0 μM each of NaCl and CaCl$_2$. Column, ODS-packed column (250 $\times$ 4.6 mm) coated with Zwittergent-3-14 micelles; mobile phase, pure water; flow rate, 1.0 mL/min; sample injection, 100 μL; detection, conductivity. (1, 1′) Na$^+$$-Cl^-$ and (2, 2′) Ca^{2+}$-$2Cl$^-$.

dure for the preparation of the columns was described in previous papers.[4,6]

Reagents. The zwitterionic detergents of CHAPS {3-[(3-cholamidopropyl)dimethylammonio]-1-propanesulfonate} and Zwittergent-3-14 were obtained from Dojin (Kumamoto, Japan). Inorganic salts used as the analytes were purchased from Wako (Osaka, Japan). All of these reagents were used as received. Pure water used as the mobile phase and to dissolve the reagents was prepared in the laboratory using a Milli-Q purification system (Millipore, Bedford, MA). All of the samples and the pure water used as the mobile phase were stored in clear polypropylene bottles (wall thickness, 0.7 mm).

RESULTS AND DISCUSSION

An aqueous solution containing 1.0 μmol/L each of NaCl and CaCl$_2$ was prepared and separated using EIC. The chromatogram shows main peaks (1 and 2) and secondary peaks (1′ and 2′) for both Na$^+$$-Cl^-$ and Ca^{2+}$-$2Cl$^-$ (Figure 1). These secondary peaks have not been observed in previous studies. Furthermore, when concentrations of NaCl and CaCl$_2$ in the sample solution were lower than 0.4 μmol/L, the main peaks (1 and 2) were never observed, while the secondary peaks (1′ and 2′) were always observed. This phenomenon provides new insights into the mechanism of EIC.

To investigate this phenomenon further, this EIC system was connected with photodiode array UV$-$vis and ICP-AES detectors. Standard solutions containing barium nitrate with a concentration range of 1.0 μmol/L$-$10.0 mmol/L were prepared and analyzed using the Zwittergent-3-14 micelle-coated column and the CHAPS micelle-coated column. Barium nitrate was chosen because barium is a very sensitive element for the ICP-AES and nitrate ions are easily identified using the UV$-$vis detector. A main peak (peak A) and a secondary peak (peak A′) were observed when a Zwittergent-3-14 micelle-coated column and a CHAPS micelle-coated column were used. The retention time of peak A is shorter than that of peak A′. The results obtained using these three detectors indicate that both main and secondary peaks correspond to the same ionic association of Ba^{2+}$-$2NO$_3^-$. The peak areas of

A and A′ are directly proportional to the concentration of Ba(NO$_3$)$_2$ in the original sample solution. But the peak areas of A′ become constant when the concentration of Ba(NO$_3$)$_2$ is larger than 120 μmol/L. When the concentration of Ba(NO$_3$)$_2$ is relatively high (>0.3 mmol/L), the ratio of A′/A (peak areas) is very small (<0.6%). On the contrary, when the concentration of Ba(NO$_3$)$_2$ is relatively low (low μmol/L level), the ratio of A′/A is very large. When the concentration of the analyte is low, the secondary peak becomes critical.

Standard solutions containing other species of inorganic salts were also prepared and examined, and similar results were obtained.

To explain the occurrence of a main and a secondary elution, the Stern model of an electrical double layer was employed. This double layer of ions around a single charged stationary phase has been described by many authors.[7-19] Results of the present study show that an electrical double layer also exists in the EIC column, but it differs from the classical electrical double layer in a single charged stationary phase in the following ways:

(1) The electrostatic fields are larger (the positive field and the negative field), because both of the analyte ions (cations and anions) can be retained with the single zwitterionic stationary phase. In conventional ICs, when positive charges are fixed on the stationary phase, the original counterions of the analyte anions are eluted immediately from the column, i.e., only the analyte anions can be retained with the stationary phase. When negative charges are fixed on the stationary phase, only the analyte cations can be retained.

(2) There are simultaneous electrostatic attraction and repulsion interactions between both of the analyte ions and the charged particles fixed on the stationary phase, because electrostatic interactions between analyte ions and the zwitterionic stationary phase are very soft. The transfer of the analyte ions between the double layer and the bulk solution can be achieved with only the swashing power of the pure water mobile phase.

(3) Two elution times occur for each analyte in EIC. Analyte ions eluted from the diffuse layer are observed to have a shorter retention time than analyte ions eluted from the Stern layer. In conventional ICs, there is no difference in elution time between diffuse and Stern layers, because a large number of replacing ions are contained in the mobile phase. But in EIC, using only water as the mobile phase, very few ions exist ([H$^+$] = [OH$^-$] = 10^{-7} mol/L); hence, the differences between the two layers can easily be observed.

(4) When both the analyte and the stationary phase are hydrophobic, the Stern layer in EIC is strongly accentuated. This is because hydrophobic and electrostatic interactions occur simultaneously, resulting in much stronger retention of the analyte.

(6) Hu, W.; Tao, H.; Tominaga, M.; Miyazaki, A.; Haraguchi, H. *Anal. Chim. Acta* **1994**, *299*, 249.

(7) Cantwell, F. F.; Puon, S. *Anal. Chem.* **1979**, *51*, 623.
(8) Afrashtehfar, S.; Cantwell, F. F. *Anal. Chem.* **1982**, *54*, 2422.
(9) Liu, H.; Cantwell, F. F. *Anal. Chem.* **1991**, *63*, 993.
(10) Liu, H.; Cantwell, F. F. *Anal. Chem.* **1991**, *63*, 2032.
(11) Stahlberg, J. *J. Chromatogr.* **1986**, *356*, 231.
(12) Stahlberg, J.; Furangen, A. *Chromatographia* **1987**, *24*, 78.
(13) Stahlberg, J.; Hagglund, I. *Anal. Chem.* **1988**, *60*, 1958.
(14) Bartha, A.; Stahlberg, J.; Szokoli, F. *J. Chromatogr.* **1991**, *552*, 13.
(15) Stahlberg, J.; Jonsson, B.; Horvath, C. *Anal. Chem.* **1991**, *63*, 1867.
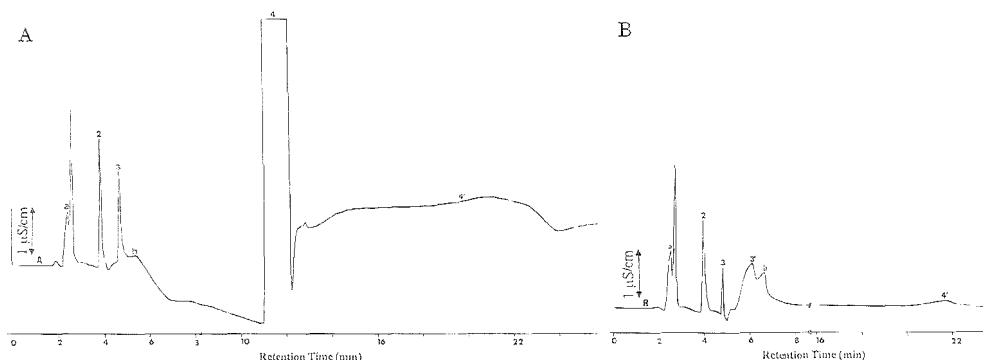(16) Stahlberg, J.; Jonsson, B.; Horvath, C. *Anal. Chem.* **1992**, *64*, 3118.
(17) Stahlberg, J. *Anal. Chem.* **1994**, *66*, 440.
(18) Weber, S. G.; Orr, J. D. *J. Chromatogr.* **1991**, *332*, 433.
(19) Weber, S. G. *Talanta* **1989**, *36*, 99.

Figure 2. (A) Chromatogram of an aqueous solution containing 1.0 μM each of $CaCl_2$, $CaBr_2$, and $Ca(NO_3)_2$ with the addition of a "sacrifice" of CaI_2 (1000 μM): (1) $Ca^{2+}-2Cl^-$, (2) $Ca^{2+}-2Br^-$, (3) $Ca^{2+}-2NO_3^-$, (4, 4') $Ca^{2+}-2I^-$, (a) unknown peak, (b) peak presumably due to CO_2. Separation conditions are the same as in Figure 1. (B) Chromatogram of an aqueous solution containing 1.0 μM each of $CaCl_2$, $CaBr_2$, Ca-$(NO_3)_2$, and CaI_2: (1) $Ca^{2+}-2Cl^-$, (2) $Ca^{2+}-2Br^-$, (3, 3') $Ca^{2+}-2NO_3^-$, (4') $Ca^{2+}-2I^-$, (a) unknown peak, (b) peak presumably due to CO_2. Separation conditions are the same as in Figure 1.
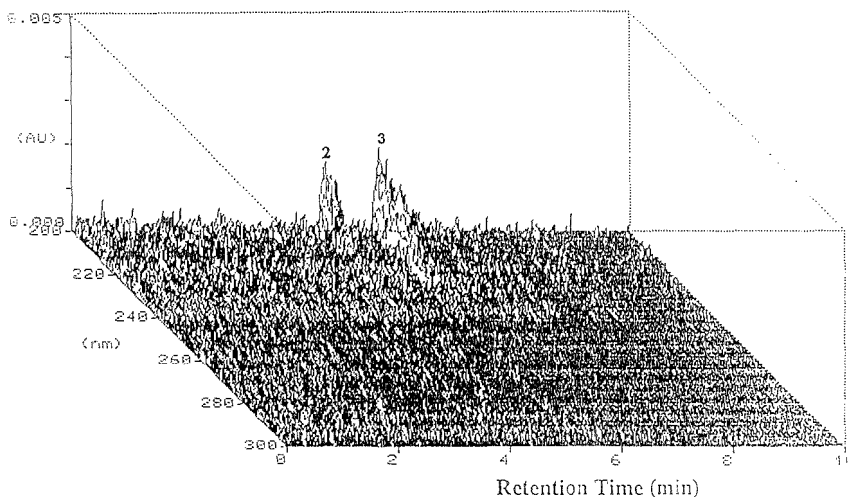
Figure 3. Chromatogram of an aqueous solution containing 0.1 μM each of $CaCl_2$, $CaBr_2$, and $Ca(NO_3)_2$ with the addition of a sacrifice species of CaI_2 (100 μM), obtained using a UV−vis detector: (2) $Ca^{2+}-2Br^-$, (3) $Ca^{2+}-2NO_3^-$. $Ca^{2+}-2Cl^-$ could not be detected. Separation conditions are the same as in Figure 1.

The occurrence of two elutions is important in understanding the mechanism, but it is a drawback in the determination of trace level ions because the volumes of both elutions must be calculated.

To obtain a single peak, analyte ions were released from the Stern layer to the diffuse layer. This was achieved by introducing a new species of salt with a longer retention time into the original sample solution to replace analyte ions in the Stern layer. Because this new salt is only used to release analyte ions, it will be referred to as a "sacrifice" species. Seven aqueous solutions containing 1.0 μmol/L each of $CaCl_2$, $CaBr_2$, and $Ca(NO_3)_2$ and X μmol/L of CaI_2 [X = 1.0 (1), 10 (2), 100 (3), 500 (4), 800 (5), 1000 (6), and 2000 (7)] were prepared and separated under the same conditions. The areas of the peaks corresponding to $Ca^{2+}-2Cl^-$, $Ca^{2+}-2Br^-$, and $Ca^{2+}-2NO_3^-$ eluted from the diffuse layer were plotted as a function of the concentration of CaI_2 in the original sample

solutions. For $Ca^{2+}-2Br^-$ and $Ca^{2+}-2NO_3$, with increasing concentrations of CaI_2 in the original sample solution, the peak areas increased and became constant. For $Ca^{2+}-2Cl^-$, the peak areas increased only slightly. Typical chromatograms for these separations with the addition of a "sacrifice" species are shown in Figure 2. The areas of the peaks corresponding to $Ca^{2+}-2Cl^-$, $Ca^{2+}-2Br^-$, and $Ca^{2+}-2NO_3^-$, calculated from chromatogram A, were 0.8%, 8.9%, and 57% larger than the peak areas calculated from chromatogram B.

Standard solutions containing $CaCl_2$, $CaBr_2$, and $Ca(NO_3)_2$ (concentration ranges from 0.01 μmol/L to 10.0 μmol/L) with the addition of the sacrifice CaI_2 (always 0.1 mmol/L) were prepared and separated to derive calibration graphs (peak areas versus concentrations). The linearities (r) were found to be 0.991, 0.999, and 0.999 for the ion combinations of $Ca^{2+}-2Cl^-$, $Ca^{2+}-$

$2Br^-$, and $Ca^{2+}-2NO_3^-$, respectively, eluted from the diffuse layer. For $Ca^{2+}-2Cl^-$, the linearity was unsatisfactory due to the appearance of a peak (a) which is of unknown provenance. The good linearities of the calibration lines indicate that the presence of the analytes [$CaCl_2$, $CaBr_2$, and $Ca(NO_3)_2$] in the Stern layer was insignificant when the proportion of the sacrifice species in the sample solution was relatively high. In other words, the analytes were released from the Stern layer when a large number of sacrifice salts were present.

Using water as the mobile phase also improves detection of trace lelvels of UV-absorbing ions when a UV–vis detector is used. Figure 3 shows a chromatogram of an aqueous solution containing 0.1 μmol/L each of $CaCl_2$, $CaBr_2$. and $Ca(NO_3)_2$ with CaI_2 (0.1 mmol/L) as the sacrifice. The UV-absorbing ion combinations of $Ca^{2+}-2Br^-$ and $Ca^{2+}-2NO_3^-$ were successfully detected.

Chromatography of Proteins Using Polybutadiene-Coated Zirconia

Lifang Sun[†] and Peter W. Carr*,‡

Physical and Analytical Research Division, Eastman Chemical Company, Kingsport, Tennessee 37662 and Department of Chemistry and Institute for Advanced Studies in Bioprocess Technology, University of Minnesota, 207 Pleasant Street SE, Minneapolis, Minnesota 55455

Polybutadiene-coated zirconia (PBD-ZrO$_2$), when used as a stationary phase in conjunction with a mobile phase containing phosphates, constitutes a reversed-phase/cation-exchange mixed-mode chromatographic system. The separation of proteins on this phase can be achieved only through the use of mobile phases containing the correct combination of phosphoric acid, displacing salt, and organic cosolvent. We found that *excessive* Coulombic interactions between proteins and the stationary phase impair the system performance for the separation of proteins. The effects of mobile phase conditions on the separation of proteins using phosphate-adsorbed PBD-ZrO$_2$ are studied in this work. Factors such as the presence of a multivalent cation, mobile phase pH, phosphate concentration, and salt concentration can be manipulated to reduce the net negative charge on the surface and thereby improve the performance of the system toward the separation of proteins.

Silica-based bonded phases have been widely used for reversed-phase protein separations.[1–4] However, the narrow range of pH stability of silica-based packing materials limits their use to pHs between 2 and 7. For large-scale protein separations, silica-based columns may become fouled and deactivated upon irreversible adsorption of proteins and cell debris. Due to their instability, silica-based columns cannot be regenerated by washing with hot acids or bases.[5,6] In addition, silica-based phases cannot be sterilized or depyrogenated by washing with hot acids or bases.[7] Although polymeric stationary phases are generally used where high pH mobile phase conditions are necessary, they shrink and swell in organic solvents. The cost of a separation can be greatly reduced if the lifetime of the chromatographic column can be prolonged. Therefore, the need for a pH and mechanically stable packing motivated this study of polybutadiene-coated zirconia (PBD-ZrO$_2$)[8–10] for protein separations.

PBD-ZrO$_2$ is acid and base stable.[8–10] It is also mechanically strong and stable in organic solvents. The main difficulty in using zirconia-based packing materials for the separation of proteins is the energetic inhomogeneity of their surfaces.[8–10] The Lewis acid sites on zirconia's surface strongly interact with solutes that have Lewis base moieties, such as carboxyl groups, thereby causing peak broadening, tailing, and low recovery.[11–14] Previous work has shown that the separation of proteins on PBD-ZrO$_2$ using typical reversed-phase type mobile phases (acetonitrile, trifluoroacetic acid, etc.) was not at all successful due to the extremely strong and irreversible adsorption of all proteins examined.[8,15] This irreversibility leads to almost zero recovery of the injected proteins under all elution conditions previously examined. Although zirconia's Lewis acid sites can be effectively blocked by adsorbing phosphate ions,[12,13,16] proteins still could not be eluted from PBD-coated, phosphate-modified zirconia phases under typical reversed-phase type mobile phase conditions.[17] Recently we found[18] that the irreversible adsorption of proteins on phosphate-adsorbed PBD-ZrO$_2$ is primarily due to a mixed-mode reversed-phase/cation-exchange retention mechanism. Negatively charged phosphate ions in the mobile phase adsorb onto zirconia, thereby causing the surface of the PBD-ZrO$_2$ to become so highly charged that it acts, even at low pH, as a cation exchanger.[18] Thus, proteins are retained on phosphate-adsorbed PBD-ZrO$_2$ due to both hydrophobic and Coulombic interactions. To use PBD-ZrO$_2$ for protein and peptide separations, both *phosphoric acid* and a *displacing salt* must be added to a conventional reversed-phase type mobile phase (acetonitrile/water) to block zirconia's Lewis acid sites and to suppress Coulombic interactions.[18]

Mixed-mode stationary phases have been used in protein separations to improve selectivity.[19,20] We have shown that the reversed-phase/cation-exchange mixed-mode phosphate-adsorbed PBD-ZrO$_2$ phase exhibits a unique selectivity in the separation of peptides.[18] However, the problem of using a mixed-mode stationary phase is low recovery or totally irreversible adsorption of proteins.[19,21] We found that the performance of this mixed-mode

† Eastman Chemical Co.
‡ University of Minnesota.
(1) Aguilar, M. I.; Hearn, M. T. W. In *HPLC of Proteins, Peptides and Polynucleotides*; Hearn, M. T. W., Ed.; VCH Publishers, Inc.: New York, NY, 1991; pp 247–275.
(2) Janzen, R.; Unger, K. K.; Giesche, H.; Kinkel, J. N.; Hearn, M. T. W. *J. Chromatogr.* 1987, 397, 81.
(3) Stadalius, M. A.; Ghris, B. F. D.; Snyder, L. R. *J. Chromatogr.* 1987, 387, 21.
(4) Hearn, M. T. W. *J. Chromatogr.* 1987, 418, 3.
(5) Wilson, T. D.; Simmons, D. M. *Chromatographia* 1991, 31, 362–366.
(6) Glajch, J. L.; Kirkland, J. J.; Köhler, J. *J. Chromatogr.* 1987, 384, 81–90.
(7) Weary, M.; Pearson, F. *Bio. Pharm.* 1988, 1, 22–29.
(8) Rigney, M. P. Ph.D. Thesis, University of Minnesota, Minneapolis, MN, 1988.
(9) Rigney, M. P.; Weber, T. P.; Carr, P. W. *J. Chromatogr.* 1989, 484, 273–291.

(10) Nawrocki, J.; Carr, P. W.; Rigney, M. P.; McCormick, A. V. *J. Chromatogr.* 1993, 657, 229–282.
(11) Blackwell, J. A.; Carr, P. W. *J. Liq. Chromatogr.* 1991, 14, 2875–2889.
(12) Blackwell, J. A.; Carr, P. W. *Anal. Chem.* 1992, 64, 863–873.
(13) Blackwell, J. A.; Carr, P. W. *J. Chromatogr.* 1991, 549, 59–75.
(14) Blackwell, J. A. *Chromatographia* 1993, 35, 133–138.
(15) Sun, L.; McCormick, A. V.; Carr, P. W. *J. Chromatogr.* 1994, 658, 465–473.
(16) Schafer, W. A.; Carr, P. W. *J. Chromatogr.* 1991, 587, 149–160.
(17) Schafer, W. A. University of Minnesota, Minneapolis, MN, private communication, 1990.
(18) Sun, L.; Carr, P. W. *Anal. Chem.* 1995, 67, 2517–2523.
(19) Nau, D. R. In *HPLC of Proteins Peptides and Polynucleotides*; Hearn, M. T. W., Ed.; VCH Publishers, Inc.: New York, NY, 1991; pp 331–395.
(20) Zhu, B. Y.; Mant, C. T.; Hodges, R. S. *J. Chromatogr.* 1992, 594, 75–86.
(21) Berkowitz, S. A.; Baker, J. T. *Adv. Chromatogr.* 1989, 29, 175–219.

Table 1. Characteristics of the Proteins Studied

protein	MW	pI[a]	ΣR_c[b]	no. of NH$_2$[c]	no. of COOH[d]	N[e]
insulin	6 030	5.7	0.79	4	4	51
cytochrome c	11 700	9.4	1.00	23	18	104
ribonuclease b	13 690	9.3	1.10	18	27	124
lysozyme	14 310	11.0	1.62	18	26	129
hemoglobin	62 912	7.1	9.33	91	57	577

[a] Isoelectric point. [b] Relative hydrophobicity, calculated as $\Sigma R_c^{\text{protein}}/\Sigma R_c^{\text{cytochrome }c}$, where ΣR_c is the sum of the retention coefficient of the amino acid residues reported by Guo et al.[31] [c] Total number of basic residues in the protein. [d] Total number of acidic residues in the protein. [e] Total number of residues in the protein.

phosphate-adsorbed PBD-ZrO$_2$ phase for peptide separations is limited by the extra peak broadening due to secondary equilibrium.[18] In this work, we find that this is also a problem for separating proteins that carry a high positive charge.

We have shown[18] that the surface charge of the phosphate-adsorbed PBD-ZrO$_2$ phase is altered by a number of factors. The objective of this work was to understand the effect of mobile phase variables on the separation of proteins using a phosphate-adsorbed PBD-ZrO$_2$ stationary phase. This will allow us to understand the limitations and enable us to optimize the separation conditions.

EXPERIMENTAL SECTION

Chemicals. All solvents used in this work were HPLC grade and were obtained from Fisher Scientific (Fairlawn, NJ). HPLC water was prepared by passing house deionized water through a Barnstead Nanopure deionizing system with an organic-free cartridge and a 0.2 μm filter. Trifluoroacetic acid (TFA), trichloroacetic acid, sodium methyl sulfate, sodium perchlorate, and calcium chloride were obtained from Aldrich (Milwaukee, WI). Phosphoric acid was from Fisher Scientific. Perchloric acid was from Mallinckrodt Inc. (Paris, KY). Proteins, listed in Table 1, were from Sigma (St. Louis, MO). The sodium perchlorate/acetonitrile system is a potential hazard and should be handled with care. Water should be mixed with perchlorate-containing organic wastes.

Chromatographic Columns. HPLC-quality zirconia particles were prepared by the "polymer-induced colloid aggregation" method.[22,23] The main advantage of this method is that the resulting particles have a narrow particle size distribution. The zirconia particles used in this work (Batch Coac-14) have an average diameter of 6 μm, a surface area of 22 m^2/g, and an average pore diameter (4 times the ratio of pore volume over surface area) of 170 Å based on nitrogen sorptometry. The polybutadiene coating was prepared according to a modified procedure based on Rigney's work.[9] A PBD loading of 0.6 mg of PBD/m^2 of total surface area was used. The detailed preparation procedure was described in a previous paper.[18] The final carbon loading of the PBD-ZrO$_2$ is 0.45 mg/m^2 based on carbon combustion analysis.

Two gram portions of PBD-ZrO$_2$ particles were used to pack each of the 5 cm × 0.46 cm i.d. columns that are typically used in this work. Column dimensions other than 5 cm × 0.46 cm will be specified in context. Stainless steel blank columns, end fittings, and 2 μm stainless steel screens used in this work were obtained

(22) Sun, L.; Annen, M. J.; Lorenzaro, F.; Carr, P. W.; McCormick, A. V. *J. Colloid Interface Sci.* 1994, *163*, 464–473.
(23) Annen, M. J.; Kizhappali, R.; Lorenzano-Porras, F.; Carr, P. W.; McCormick, A. V., submitted to *J. Colloid Interface Sci.*
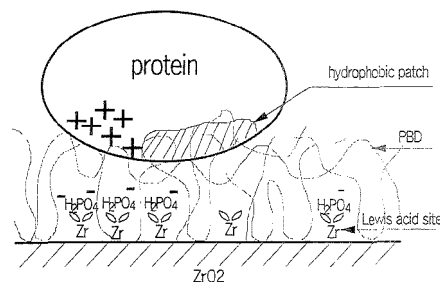
Figure 1. Schematic of interactions between a protein molecule and phosphate-adsorbed PBD-ZrO$_2$.

from Alltech (Deerfield, IL). Columns were packed by a magnetically stirred upward slurry technique in which particles are slurried in a solvent and forced into a column at 350 bar by pure isopropyl alcohol. The slurry solvent used for PBD-ZrO$_2$ was 90:10 isopropyl alcohol/hexane.

Chromatographic Experiments. All chromatographic studies were conducted on a Perkin-Elmer 3B series chromatograph at room temperature. Detection was at 280 nm. Protein samples were typically prepared as 0.5% (w/v) in 0.1% aqueous TFA. The injection volume was typically 10 μL.

Acid and Base Washing. The effect of acid and base washing of phosphate-adsorbed PBD-ZrO$_2$ was studied in this work. During acid washing, 0.1 M nitric acid at 80 °C was pumped through the column at a flow rate of 0.2 mL/min for 8 h. After the column was flushed with water until the eluent became neutral, 10 mL of 0.1 M sodium hydroxide was pumped through the column. The column was then washed with water.
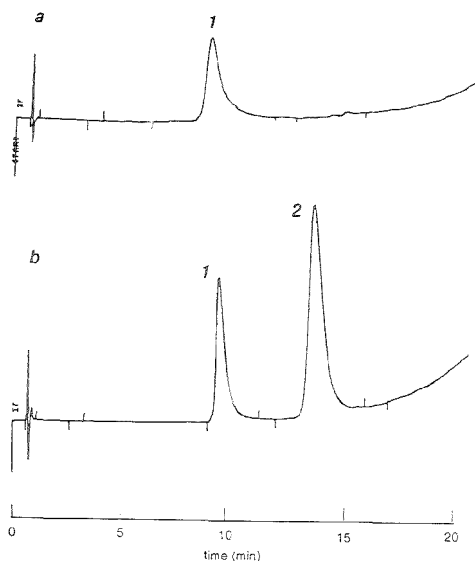
RESULTS AND DISCUSSION

Mobile Phase Composition. Phosphate-adsorbed PBD-ZrO$_2$ is a reversed-phase/cation-exchange mixed-mode stationary phase.[18] The hydrophobic moieties on a protein molecule interact with the cross-linked polybutadiene coating, and the protein's positively charged moieties interact with the negatively charged phosphate ions adsorbed on zirconia's surface (Figure 1). In contrast to conventional silica-based RPLC, a reversed-phase mobile phase containing both phosphoric acid and a displacing salt must be used to elute proteins from a phosphate-adsorbed PBD-ZrO$_2$ phase.

The most important findings of the present work are that a wide variety of proteins can be eluted from the stationary phase when both phosphoric acid and sodium perchlorate are present in the mobile phase, and in the absence of either phosphoric acid or sodium perchlorate, none of the proteins tested can be eluted. Most importantly, for those proteins which do elute under the conditions described in this work, the peak shape is usually quite acceptable (vide infra).

The typical elution gradient used in this work is a 20 min A–B linear gradient from 20% mobile phase B to 90% mobile phase B. Mobile phase A is an aqueous solution of 0.1 M phosphoric acid, 1 M sodium perchlorate, and 0.1% TFA; mobile phase B is a solution of 1 M sodium perchlorate and 0.1% TFA in acetonitrile. The pH of mobile phase A is 1.5. Variations of this protocol were used to study the effect of each mobile phase component. We used insulin and lysozyme as test solutes in many of the studies described in this work. These two proteins were chosen due to the fact that they have quite different isoelectric points and molecular weights (Table 1).
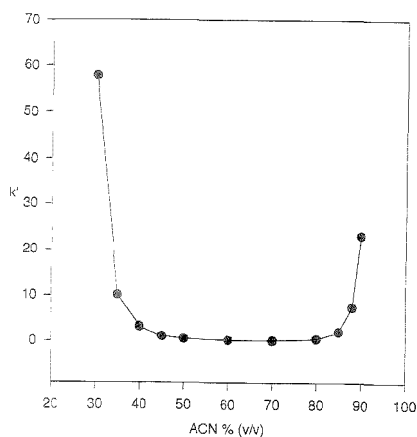
Figure 2. Retention of insulin versus mobile phase composition. Mobile phase A is an aqueous solution of 0.1 M phosphoric acid, 1 M sodium perchlorate, and 0.1% TFA; mobile phase B is a solution of 1 M sodium perchlorate and 0.1% TFA in acetonitrile. Isocratic elution at different A–B composition; 1 mL/min; 254 nm detection; 30 °C.

Retention Mapping for Insulin. To obtain a retention map for insulin on phosphate-adsorbed PBD-ZrO$_2$, the retention of insulin was measured *isocratically* at different acetonitrile compositions in the mobile phase. As shown in Figure 2, the retention of insulin decreased dramatically as the volume fraction of the acetonitrile phase was increased from 30% to 40%. This rapid drop in k' as the amount of organic modifier is increased is quite typical of reversed-phase protein chromatography.[24] As the volume fraction of the acetonitrile phase was further increased from 40% to 80%, the k' of insulin remained quite small ($k' < 1$). Finally, an increase in the volume fraction of acetonitrile phase from 80% to 90% caused a dramatic increase in insulin's retention. This increase in retention indicates the presence of a secondary retention mechanism, which we postulate to be due to Coulombic interactions. Because salts are incompletely dissociated in non-aqueous media, that is, they are ion-paired, the decrease in the volume fraction of water phase decreases the ionic strength of the mobile phase. This results in an increase in Coulombic interactions between insulin and the stationary phase, causing the significant increase in retention.

Concentration of Displacing Salt. With a mobile phase containing 0.5 M sodium perchlorate, insulin could be eluted from the phosphate-adsorbed PBD-ZrO$_2$, whereas lysozyme was irreversibly adsorbed (Figure 3a). By increasing the concentration of sodium perchlorate to 1 M, both insulin and lysozyme were eluted with acceptable peak shapes (Figure 3b). The need for a higher ionic strength for the elution of lysozyme is consistent with the fact that lysozyme has more basic amino acids (more positive charges) and a higher isoelectric point than does insulin (Table 1). We will show below that the higher positive charge on cytochrome c does not permit elution from phosphate-adsorbed PBD-ZrO$_2$ using a mobile phase containing 1 M sodium perchlorate at pH 1.5. Additional increases in the ionic strength of the mobile phases can suppress Coulombic interactions even more; however, the solubility of sodium perchlorate in acetonitrile is

(24) Hearn, M. T.; Grego, B. *J. Chromatogr.* **1981**, *218*, 497–507.
(25) Hjertén, S. *Adv. Chromatogr.* **1981**, *19*, 111–123.

Figure 3. Effect of salt concentration on protein elution: 1, insulin; 2, lysozyme. Mobile phase A is an aqueous solution of 0.1 M phosphoric acid, 0.1% TFA, and sodium perchlorate; mobile phase B is a solution of 0.1% TFA and sodium perchlorate in acetonitrile. Linear A–B gradient from 20% B to 90% B; 20 min at 1 mL/min; 254 nm detection; 25 °C. (a) 1 M sodium perchlorate in mobile phase A and B. (b) 0.5 M sodium perchlorate in mobile phase A and B.

limited. Therefore, keeping other mobile phase conditions constant, 1 M is close to the highest possible concentration of sodium perchlorate that can be used. While mobile phases with a high salt concentration diminish Coulombic interactions, they concomitantly strengthen hydrophobic interactions between proteins and stationary phases due to the well-known "salting out" effect used in hydrophobic interaction chromatography.[25] Therefore, the lowest possible salt concentration should be used.

Mobile Phase pH. The pH of the mobile phase can affect the retention of proteins by altering the net charge on both the protein and the stationary phase. The typical pH used in reversed-phase protein chromatography with silica-based bonded phases is pH 2. At this pH, the silica surface is essentially uncharged and proteins are fully protonated, which prevents secondary ionic interactions. For the phosphate-adsorbed PBD-ZrO$_2$ system, the mobile phase pH can affect (1) the adsorption of phosphate on zirconia (thereby affecting the number of accessible Lewis acid sites on the solid surface and the degree of surface negative charge) and (2) the protein surface charge.

Chromatograms of a mixture of insulin and lysozyme obtained at pH 0.6, 1.5, 4.2, and 7.1 are shown in Figure 4. Clearly, pH 1.5 gave the best peak shape for both insulin and lysozyme (Figure 4b). At pH 0.6, the retention times of both proteins decreased, but both peaks became broader and less symmetric (Figure 4a) compared to the results at pH 1.5. We have shown[18] that the amount of surface negative charge on phosphate-adsorbed PBD-ZrO$_2$ decreases upon decreasing the mobile phase pH. This is probably due to protonation of the adsorbed phosphate ions and a decrease in the amount of phosphate adsorbed. Therefore, the decrease in retention of proteins as the pH decreases is likely due to a decrease in the strength of Coulombic interactions. It is
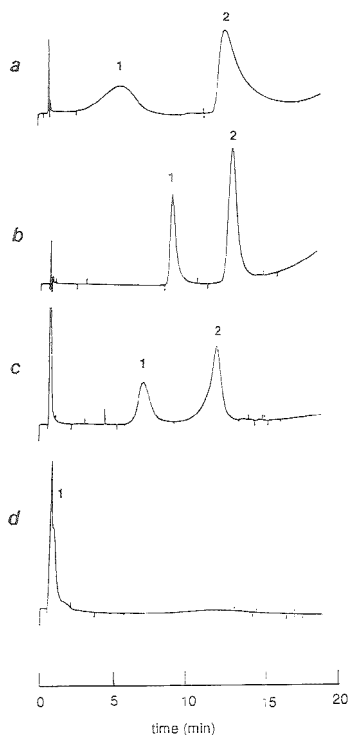
Figure 4. Effect of mobile phase pH on the elution of insulin and lysozyme: 1, insulin; 2, lysozyme. Mobile phase A is an aqueous solution of 0.1 M phosphoric acid and 1 M sodium perchlorate; mobile phase B is a solution of 1 M sodium perchlorate in acetonitrile. Linear A–B gradient from 20% B to 90% B; 20 min at 1 mL/min; 254 nm detection; 25 °C. (a) pH 0.6 (0.5 M sodium perchlorate in mobile phase A was replaced by 0.5 M perchloric acid). (b) pH 1.5. (c) pH 4.2 (the pH of mobile phase A was adjusted by 50% (w/w) sodium hydroxide). (d) pH 7.1 (the pH of mobile phase A was adjusted by 50% (w/w) sodium hydroxide).

very important to note that cytochrome c, which *could not* be eluted at pH 1.5, does elute at pH 0.6. This is consistent with our expectations because cytochrome c has more positive charges than does lysozyme (Table 1).

Hingston et al. and Stumm et al. predicted that maximal adsorption of a Lewis base on a metal oxide occurs when the solution pH is equal to the pK_a of the conjugate acid of the Lewis base.[10,26,27] The fact that maximal adsorption of fluoride and borate on zirconia occurred at a pH close to the corresponding pK_a[28] confirmed this prediction. The pK_{a1} of phosphoric acid is 2.1. This implies that zirconia adsorbs more phosphate ions at pH 1.5 than at pH 0.6. Therefore, the peak broadening and asymmetry of insulin and lysozyme at pH 0.6 relative to that at pH 1.5 is more likely due to an increased possibility of the adsorption of proteins on zirconia's Lewis acid sites. A gradual deterioration in the peak shapes of both insulin and lysozyme was observed over a period of about 1 h at a 1 mL/min flow after the mobile phase pH was

(26) Stumm, W.; Kummert, R.; Sigg, L. *Croat. Chem. Acta* **1980**, *53*, 291.
(27) Hingston, F. J.; Atkinson, R. J.; Posner, A. M.; Quirk, J. P. *Nature* **1967**, *215*, 1459.
(28) Blackwell, J. A.; Carr, P. W. *J. Chromatogr.* **1991**, *549*, 43–57.
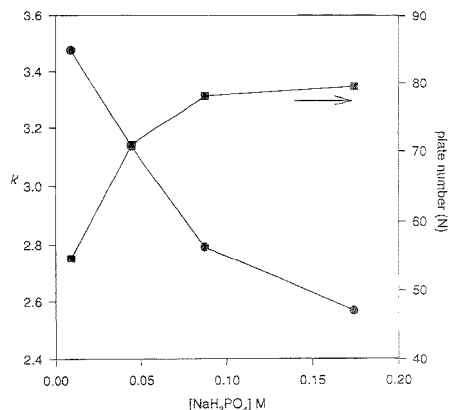
Figure 5. Effect of phosphate concentration on the retention of insulin. ●, capacity factor; ■, plate number. Isocratic elution, mobile phase is water/acetonitrile 65.2:34.8 with 0.1% TFA. [NaH$_2$PO$_4$] — [NaClO$_4$] = 1 M; pH 2; 1 mL/min; 254 nm detection; 25 °C.

changed from 1.5 to 0.6. This slow change is attributed to the slow desorption of phosphate from zirconia at the lower pH.[29]

In contrast to the effect of a decrease in pH, an increase in pH causes an increase in surface negative charge on phosphate-adsorbed PBD-ZrO$_2$ due to further deprotonation of the surface phosphate groups.[18] Therefore, compared to the performance at pH 1.5 (Figure 4b), peak broadening and asymmetry at pH 4.2 (Figure 4c) are likely due to stronger Coulombic interactions. Because lysozyme has more basic amino acids than does insulin (Table 1), its peak shape is more severely distorted than that of insulin. A further increase of pH to 7.1 (Figure 4d) causes irreversible adsorption of lysozyme on phosphate-adsorbed PBD-ZrO$_2$. Insulin, which has an isoelectric point of 4.5, is not retained at pH 7.1. This is probably due to the fact that insulin bears the same sign (negative) charge as does the stationary phase at pH 7.1, and therefore it is repelled from the stationary phase. Many other proteins such as hemoglobin and ribonuclease b that can be eluted at pH 1.5 irreversibly adsorb on the phosphate-adsorbed PBD-ZrO$_2$ at pH 7.1. These results can be attributed to the increase in the surface charge.

Phosphate Concentration. As described earlier, the purpose of adding phosphate in the mobile phase is to block zirconia's Lewis acid sites so as to prevent the irreversible adsorption of proteins on PBD-ZrO$_2$.[18] Therefore, the extent of blockage of Lewis acid sites by phosphate ions greatly affects the elution of proteins. Figure 5 shows the effect of the concentration of phosphate on insulin's retention time and column efficiency. Isocratic elution conditions with constant ionic strength and organic modifier concentration were used in this study. As the phosphate concentration was increased from 0.09 to 0.17 M, the retention of insulin decreased and the plate number increased. The plate number remains relatively constant, provided that the concentration of phosphate exceeds 0.1 M. In the absence of phosphate in the mobile phase, elution of insulin was not observed within 10 min.

We believe that the above results are due to an increase in the number of accessible Lewis acid sites on the surface as the concentration of phosphate is decreased. Therefore, protein molecules experience stronger Lewis acid–base interactions with

(29) Schafer, W. A.; Carr, P. W. *J. Chromatogr.* **1991**, *587*, 137–147.
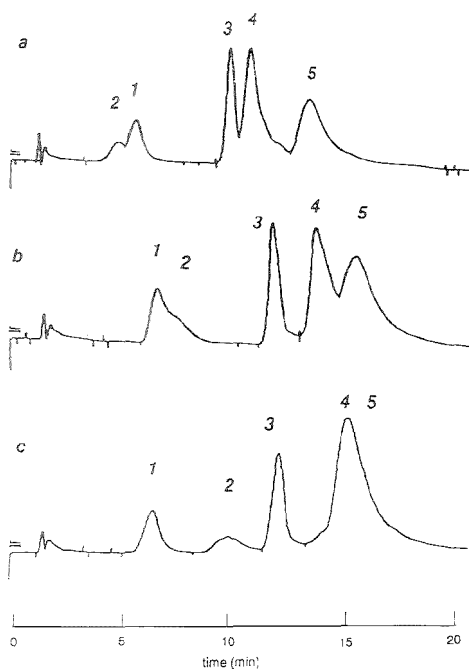
Figure 6. Separation of a protein mixture on phosphate-adsorbed PBD-ZrO$_2$ by both salt and ACN gradient. The column was acid and base washed: 1, insulin; 2, ribonuclease b; 3, lysozyme; 4, cytochrome c; 5, hemoglobin. Mobile phase A is an aqueous solution of 0.1 M phosphoric acid, sodium perchlorate, and 0.1% TFA. Mobile phase B is a solution of 1 M sodium perchlorate and 0.1% TFA in acetonitrile. Linear A–B gradient from 20% B to 90% B; 20 min at 1 mL/min; 254 nm detection; 25 °C. (a) No salt gradient; 1 M sodium perchlorate in mobile phase A. (b) Salt gradient of 0.76 to 0.97 M sodium perchlorate in 20 min; 0.7 M sodium perchlorate in mobile phase A. (c) Salt gradient of 0.6 to 0.95 M sodium perchlorate in 20 min; 0.5 M sodium perchlorate in mobile phase A.

the stationary phase as the concentration of phosphate decreases, resulting in an increase in retention and peak broadening.

Adsorption of Multivalent Cations. Multivalent cations have been used to modify the surface properties of silica. Adsorption of 100 mM thorium(IV)[30] on silica can change the net surface charge from negative (due to the presence of ionized silanol groups) to positive. We believed that by adsorbing multivalent cations on the phosphate-adsorbed PBD-ZrO$_2$, we could greatly reduce or even reverse the surface negative charge. Because proteins carry a net positive charge at the optimal chromatographic pH (pH 1.5), a positively charged stationary phase should be advantageous because attractive Coulombic interactions toward proteins would then be avoided.

We studied the effect of adding calcium(II) to the mobile phase to demonstrate the effectiveness of adsorbing multivalent cations to eliminate surface negative charge on phosphate-adsorbed PBD-ZrO$_2$. After the phosphate-adsorbed PBD-ZrO$_2$ was equilibrated with a mobile phase containing 10 mM calcium chloride, the

(30) MacDougall, F. H. *Physical Chemistry*, 3rd ed.; Macmillan Co.: New York, 1952; p 724.
(31) Guo, D.; Mant, C. T.; Taneja, A. K.; Parker, J. M. R.; Hodges, R. S. *J. Chromatogr.* 1986, 359, 499.

capacity factor of benzylamine decreased from 4.7 to 3.6. This indicates that adsorption of calcium(II) decreases the surface negative charge on phosphate-adsorbed PBD-ZrO$_2$. The most significant improvement in performance after introducing calcium-(II) is the successful elution of cytochrome c at pH 1.5. The decrease in surface charge decreased the Coulombic interactions between the cytochrome c and the phosphate-adsorbed PBD-ZrO$_2$. This again indicates that the failure to elute cytochrome c at pH 1.5 is due to excessive Coulombic interactions. The effect of calcium(II) on the retention of insulin and lysozyme, both of which elute in the absence of calcium(II), is minor.

Selectivity of Acid and Base Treated Phosphate-Adsorbed PBD-ZrO$_2$. We found that the column performance toward protein separations was greatly improved after the column was washed with acid and base. Cytochrome c, which could not be eluted prior to the acid and base washing, eluted in a sharp peak with a pH 1.5 calcium-free mobile phase (Figure 6). The results indicate that the Lewis acid site concentration on PBD-ZrO$_2$ changed upon extensive acid and base washing.

Insulin and lysozyme were less retained and eluted with much narrower peaks. A chromatogram of a mixture of insulin, ribonuclease b, lysozyme, cytochrome c, and hemoglobin on an phosphate-adsorbed PBD-ZrO$_2$ column is shown in Figure 6. Although the mixed-mode retention mechanism does cause band broadening, it has the advantage of affording a unique separation selectivity. Because the retention of proteins bearing different net charges respond to the change in mobile phase ionic strength differently, separations can be optimized by varying either the organic solvent or the salt concentration in the mobile phase. For example, instead of keeping the salt concentration constant at 1 M during the gradient (Figure 6a), we can use a linear gradient of salt concentration from 0.76 to 0.97 M to allow the separation of lysozyme and cytochrome c (Figure 6b). By programming a steeper salt gradient from 0.60 to 0.95 M, we achieved the separation of insulin and ribonuclease b (Figure 6c).

CONCLUSION

The surface chemistry of zirconia requires a strong Lewis base to be added to the mobile phase to block interactions of surface Lewis acid sites with carboxylate groups in a protein. The resulting negatively charged solid surface induces strong attractive Coulombic interactions with the positively charged amino groups in proteins. As a consequence, proteins cannot be eluted from hydrophobically coated zirconia particles until elution conditions are adjusted to control all possible interactions. Except for the Lewis acid–base interactions, the situation is not fundamentally different from that encountered in the elution of proteins from reversed-phase silica; that is, we must make provisions for weakening both the primary and the secondary types of interaction. As a consequence, retention, peak width, and recovery of proteins on polybutadiene-coated zirconia depend on solution pH, ionic strength, concentration of phosphate, and, of course, organic modifier.

Multivariate Curve Resolution Applied to Continuous-Flow Spectrophotometric Titrations. Reaction between Amino Acids and 1,2-Naphthoquinone-4-sulfonic Acid

J. Saurina, S. Hernández-Cassou,* and R. Tauler

Departament de Química Analítica, Universitat de Barcelona, Diagonal 647, 08028 Barcelona, Spain

A continuous-flow acid–base titration system has been developed for the study and analytical application of chemical reactions between amino acids and 1,2-naph-thoquinone-4-sulfonate. For each titration, a set of spectra are obtained at pH values from 6.5 to 12.5. Multivariate curve resolution is applied to provide an optimal estimation of concentration and spectra profiles of the species formed during the chemical reaction. Resolution of these chemical species is greatly improved when several runs of different spectrophotometric titrations of the same chemical reaction system (multiple correlated data matrices) are analyzed simultaneously, allowing the quantitative determination of the concentration of amino acid that has reacted in each case.

It has been pointed out that most traditional wet chemistry methods of analysis can be easily implemented using modern flow technologies. The term flow chemography[1] has been proposed for chemical techniques which exploit controlled flow and flow injection methodologies and translate the information obtained thereby into a graph or image. All these techniques, including chromatography, flow injection analysis, and flow injection synthesis, require control of the reaction conditions by the flow. Similarly to these methods, spectrophotometric titrations can be implemented using controlled flow methodologies. With any of these flow-based methods, a vector of ordered data (first-order tensor) or a matrix of ordered data (second-order tensor) is produced. The treatment of these types of data by computerized means, like multivariate calibration[2–5] and multivariate curve resolution methods,[6,7] permits the resolution and quantification of the components present in unknown mixtures.

The goal of multivariate curve resolution methods is the recovery of the true underlying concentration and spectra profiles of the individual species in the unresolved mixture. However, in general, the pure mathematical solutions obtained by multivariate curve resolution and other factor analysis-based methods are not

the true solutions but a linear combination of them,[7,8] and a certain level of ambiguity persists (factor analysis ambiguity). Conditions to remove these ambiguities have been studied.[9] Detection of selectivity and zero concentration regions are important aspects to consider. Depending on the cases, additional constraints like non-negativity, unimodality, and closure considerably reduce the ambiguity of possible mathematical solutions.

The study of a single data matrix of an unresolved mixture by multivariate curve resolution is problematic, even applying the mentioned constraints. However, the simultaneous treatment of several sets of correlated data matrices having one or more orders in common by multivariate curve resolution[9–12] is a powerful way to improve the results with respect to those obtained by individual analysis of a single data matrix. This requires that the different data matrices simultaneously analyzed have at least one of the orders in common (i.e., the spectral order is easily maintained if the pure spectrum of common species is unique in the different titrations). Optimum resolution is achieved when the data present a trilinear structure,[13] which means that every species is defined by the same spectral and concentration vectors in the different experiments. Experimentally, this requires precise synchronization of the two orders of measurement for all data sets to be simultaneously analyzed.

In the present work, a recently developed multivariate curve resolution method is used for the analysis of reaction-based data obtained from a continuous-flow spectrophotometric titration. This iterative method is a general tool for the resolution and quantitation of the species present in different kinds of bilinear data systems, like multiequilibria and macromolecular spectrophotometric titrations,[10,11] process analysis,[12] coeluted chromatographic peaks,[14] and chemical sensors.[15] The reaction under study is the derivatization of amino acids with 1,2-naphthoquinone-4-sulfonate (NQS)[16] shown in the following scheme:
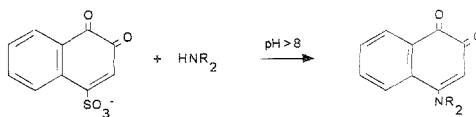
The reaction takes place at 70 °C in a three-channel continuous-flow system. The pH for the development of the reaction can be varied in a controlled manner. A previous continuous-flow titration

(1) Kowalski, D. R.; Ruzicka, J.; Christian, G. D. *Trends Anal. Chem.* **1990**, *9*, 8–13.
(2) Sekulik, S.; Seaholtz, M. B.; Wang, Z.; Kowalski, B. R.; Lee, S. E.; Holt, B. R. *Anal. Chem.* **1993**, *65*, 835A–845A.
(3) Whitman, D. A.; Seaholtz, M. B.; Christian, G. D.; Ruzicka, J.; Kowalski, B. R. *Anal. Chem.* **1991**, *63*, 775–781.
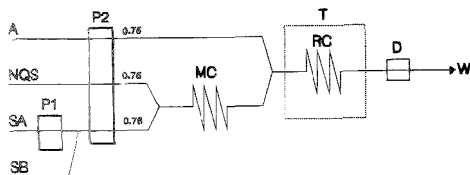(4) Lukkari, I.; Lindberg, W. *Anal. Chim. Acta* **1988**, *211*, 1–10.
(5) Lindberg, W.; Kowalski, B. R. *Anal. Chim. Acta* **1988**, *206*, 125–135.
(6) Erickson, B. C.; Ruzicka, J.; Kowalski, B. R. *Anal. Chim. Acta* **1989**, *218*, 303–311.
(7) Lawton, W. H.; Sylvestre, E. A. *Technometrics* **1971**, *13*, 617–632.

(8) Malinowski, E. R. *Factor Analysis in Chemistry*, 2nd ed.; John Wiley: New York, 1991.

Figure 1. Continuous-flow manifold. P1, variable speed pump; P2, constant speed pump; MC, mixing coil of 2 m × 0.5 mm i.d.; RC, reaction coil of 10 m × 0.5 mm i.d.; T, thermostatic bath; D, spectrophotometric detector; A, amino acid channel; NQS, NQS channel; SA, stock solution A; SB, stock solution B; W waste. Flow rates of buffer, NQS, and amino acid solutions are 0.75 mL/min. Flow rates of stock solutions SA and SB are variable.

system[17] was designed to study the acid—base equilibria of the NQS reagent, demonstrating that flow systems allow titration of unstable analytes such as NQS. Although data produced were also spectra at different pH values, the data structures differ considerably in both cases. For a particular acid—base equilibrium, the relative concentrations of species depend only on the pH variation. This means that the simultaneous treatment of these data, apart from signal averaging, will not improve the resolution with respect to a single data matrix. However, in reaction-based systems, such as amino acids and NQS, different experiments can provide new and complementary information, reducing in this way the ambiguities of the mathematical solutions. Moreover, the present study is also focused on developing new constraints to be applied to the alternating least-squares optimization, profiting from the characteristics of the data structure in which the trilinearity is maintained only for some species.

EXPERIMENTAL SECTION

Reagents. All chemicals were of analytical-reagent grade. Amino acids were supplied by Merck. Sodium 1,2-naphthoquinone-4-sulfonate (NQS, Aldrich) was used to prepare a stock solution 1.1×10^{-3} M reagent in 0.1 M hydrochloric acid (Merck). Solution SA was 0.05 M NaH_2PO_4 + 0.05 M H_3BO_3 + 0.05 M $NaHCO_3$ + 0.05 M NaOH. Solution SB was 0.05 M NaH_2PO_4 + 0.05 M H_3BO_3 + 0.05 M $NaHCO_3$ + 0.35 M NaOH (all from Merck).

Apparatus. A Perkin-Elmer UV/vis/near-IR Lambda 19 spectrophotometer with a Hellma flow cell (10 mm path length and 18 μL volume) was used. Spectra were collected and translated to JCAMP ASCII files by means of Perkin-Elmer software. pH was measured with an Orion ROSS combined glass electrode connected to a Radiometer PHM84 pH meter.

Continuous-Flow System. The continuous-flow system developed in the present study is shown in Figure 1. All solutions were pumped through standard Tygon tubing by means of two

low-pressure peristaltic pumps (Scharlau HP4). Connections, T-pieces, and reaction coils were made of PTFE. Buffer and reagent solutions merged in a mixing coil (MC) of 2 m × 0.5 mm i.d. The reaction between amino acids and NQS reagent took place in a reaction coil (RC) of 10 m × 0.5 mm i.d. immersed in a thermostatic bath (SBS TFB-3) at 70 °C.

The final buffer solution was generated on-line from two different stock solutions, SA and SB. Its composition was varied during the process by modifying the ratio of the flow rates of the two solutions. Therefore, the pH in the RC was varied in a controlled manner. Flow rates of amino acid, reagent, and buffer solutions were kept at 0.75 mL/min for all of them, while those of solutions SA and SB were varied during the process (from 0.65 to 0.1 mL/min for SA, and from 0.1 to 0.65 mL/min for SB).

At every titration point, the corresponding spectrum for each amino acid concentration was registered when the system achieved the steady state. The pH of each point was experimentally measured in the waste solution (W). The composition of solutions SA and SB was suitable to work in a buffered medium during the entire titration (from pH 6.5 to 12.5), increasing, therefore, the robustness of the method. The pH synchronization between different runs of titrations of the same chemical system was experimentally achieved by pumping sequentially through the system, at every pH, each solution with different amino acid concentration. When the corresponding spectra had been registered, the pH was modified and the whole procedure repeated for a new pH.

Chemical Reaction Systems under Study. Four amino acids were taken as models to study the reaction with NQS: proline (Pro) as a secondary amino acid, lysine (Lys) as a basic amino acid, aspartic acid (Asp) as an acidic amino acid, and phenylalanine (Phe) as a model for other amino acids. Every amino acid was assayed at three concentration levels: 5×10^{-5}, 1×10^{-4}, and 2.5×10^{-4} M (except for Asp, where the concentrations were 1×10^{-4}, 2.5×10^{-4}, and 5×10^{-4} M. In this case, the concentrations were higher because the sensitivity of the reaction for Asp is lower).

Validation. To validate the results obtained by multivariate curve resolution, the pure responses of the species present in the system were obtained by an independent method. Pure species spectra of the NQS were directly registered from a NQS solution at 70 °C at pH 6.5 (acidic NQS species, **I**) and 12.5 (NQS decomposition product, **II**). Pure spectra of amino acid derivatives were determined in the absence of the NQS reagent to avoid its interfering effect. This was done by chromatographic separation of the different amino acid derivatives after their corresponding precolumn derivatization. It was carried out in a vial (batch procedure) by mixing equal volumes of reagent, buffer, and amino acid solution containing Phe, Lys, Pro, and Asp. The reagent solution was 0.03 M NQS + 0.1 M HCl and buffer solution was 0.05 M H_3BO_3 + 0.24 M NaOH, providing a final pH of 10.0 in the reaction medium, and the concentration of every amino acid in the mixture solution was 0.002 M. The reaction was developed for 5 min in a water bath set at 65 °C. Under these conditions, the formation of derivatives was quantitative. Next, 50 μL of solution containing the amino acid derivatives was injected into a C_{18} column. Separation was achieved using an acetic acid/acetate mobile phase (pH 4.75). Every amino acid derivative was recovered by collecting the corresponding fraction of the eluate from the chromatographic system. For the characterization of

(9) Tauler, R.; Smilde, A.; Kowalski, B. R. *J. Chemom.* **1995**, *9*, 31–58.
(10) Tauler, R.; Izquierdo-Ridorsa, A.; Casassas, E. *Chemom. Intell. Lab. Syst.* **1993**, *18*, 293–300.
(11) Casassas, E.; Tauler, R.; Marqués, I. *Macromolecules* **1994**, *27*, 1729–1737.
(12) Tauler, R.; Kowalski, B. R.; Fleming, S. *Anal. Chem.* **1993**, *65*, 2040–2047.
(13) Sánchez, E.; Kowalski, B. R. *J. Chemom.* **1988**, *2*, 265–280.
(14) Lacorte, S.; Barceló, D.; Tauler, R. *J. Chromatogr.*, in press.
(15) Tauler, R.; Smilde, A. K.; Henshaw, J. M.; Burgess, L. W.; Kowalski, B. R. *Anal. Chem.* **1994**, *66*, 3337–3344.
(16) Saurina, J.; Hernández-Cassou, S. *J. Chromatogr.* **1994**, *676*, 311–319.
(17) Saurina, J.; Hernández-Cassou, S.; Tauler, R. *Anal. Chim. Acta*, in press.

the acidic (species **III**) and basic (species **IV**) amino acid derivative species, the pH of each fraction collected was adjusted to 4.8 or 13.0, respectively, setting the final volume to 5 mL in each case. These solutions were used to record the corresponding spectrum.

DATA TREATMENT

Data generated by the continuous-flow method consisted of independent sets of spectra at different pH values. Although spectra were initially registered from 290 to 590 nm in steps of 1 nm, data reduction was performed in steps of 6 nm; thus, 51 working wavelengths were finally used. The data were treated using MATLAB for Windows (version 4.0).

Although more detailed descriptions are given in other papers,[9-11,13-15] the steps of the multivariate curve resolution procedure are summarized as follows: (1) arrangement of spectral data in matrices; (2) determination of the number of species present in the system from the analysis of the singular values; (3) obtention of an initial estimation of pH profiles or pure spectra of these species either from evolving factor analysis[18] or by pure variable detection methods;[19] (4) detection of selective (rank one) windows using fixed-size moving window evolving factor analysis or local rank analysis;[20,21] and (5) alternating least-squares optimization of the pH or concentration profiles and of the pure spectra based on the compliance of Beer's law. Depending on the nature and structure of the data, different constraints are applied during the optimization.[9-11,13-15]

Points 1 and 5 deserve more attention, owing to the pecularities of the continuous-flow reaction system used in the present study.

Data Structure. Spectral data belonging to different titrations of the same amino acid were analyzed simultaneously by arranging the individual data matrices in a new augmented data matrix, one on top of the other, keeping common wavelengths in the same columns, assuming therefore that the spectra in different experiments were registered at the same wavelengths (spectral synchronization). This augmented data matrix has a trilinear structure[8] when every species is described by the same unique diad of vectors in the different experiments: a pure spectrum and a pH or concentration profile. Thus, trilinearity requires both pH and wavelength synchronization. Departures from strictly trilinear data structures are quite common in analytical chemistry, for instance, when different data matrices share only one of the two orders of measurement, or when one of these orders is not reproducible enough. In the present work, although there are synchronization and reproducibility in both orders of measure, concentration profiles have strictly equal shapes for only some species (amino acid derivative species **III** and **IV**), while for reagent species (species **I** and **II**), the shapes in their concentration profiles are slightly different in the different experiments.

Constraints Developed for Reaction-Based Systems. (A) Closure Constraint. Two closures must be simultaneously fulfilled at every point of the reaction process: (a) The sum of the concentrations of unreacted and derivative amino acid species must be equal to its total analytical concentration, which is kept constant during the experiment. However, only the amino acid derivative species are spectrophotometrically active, while the

(18) Gampp, H.; Maeder, M.; Meyer, Ch.; Zurberbühler, A. D. *Talanta* **1985**, *32*, 1133−1139.
(19) Windig, W.; Stephenson, D. A. *Anal. Chem.* **1992**, *64*, 2735−2742.
(20) Keller, H. R.; Massart, D. L. *Anal. Chim. Acta* **1991**, *246*, 379−390.
(21) Geladi, P.; Wold, S. *Chemom. Intell. Lab. Syst.* **1987**, *2*, 273−281.

unreacted amino acid species do not absorb in the wavelength range under study. In practice, during the ALS optimization, if the sum of the concentrations of amino acid derivative absorbing species exceeds the total amino acid concentration, the pH or concentration profiles of the amino acid derivatives are suitably rescaled. (b) The sum of concentrations of all detected species containing the NQS reagent (including NQS species I and II and amino acid derivative species III and IV) must be equal to the analytical concentration of the NQS reagent.

(B) Equal Shape of pH Profiles Constraint. Equal shape contraints for concentration profiles have been previously developed.[9,13,17] In the present study, a new constraint has been implemented considering of some particularities of the reaction between amino acids and NQS. In this reaction, only the amino acid derivative species keeps the same shape of pH profiles in the different experiments, whereas the unreacted NQS species have pH profiles that depend on the amino acid concentration. This occurs because a certain amount of the reagent is consumed to produce the amino acid derivatives, which thus changes the pH profiles of the NQS reagent species. Therefore, the equal shape constraint is selectively applied to only those species whose pH profiles remain unchanged in the different experiments (amino acid derivative species).

Estimation of the Residual Degree of Ambiguity. The estimation of the residual degree of rotational ambiguity in the recovered solutions obtained by multivariate curve resolution has been calculated from the cosine of the angle between the two vectors representing the known spectrum vector (see Validation, above) and the estimated one by multivariate curve resolution. Cosine values equal to 1.0 indicate that the shapes of both vector profiles are equal, and the rotational ambiguity of that species is totally solved. Conversely, cosine values lower than 1 indicate that a certain degree of rotational ambiguity remains. Quantitative information is obtained by comparing the area of the pH profiles recovered, as is explained in Table 1.

RESULTS AND DISCUSSION

(A) Study of the NQS at 70 °C. Spectra of pure NQS reagent were obtained by pumping water instead of amino acid solution through channel A (see Figure 1). The spectra were ordered in a matrix, and they described the behavior of this reagent at 70 °C in the pH range from 6.5 to 12.5. Eigenanalysis of this data matrix reveals that two main factors are responsible for data variation, which is interpreted as the formation of two species during the titration. This analysis differs considerably from results obtained in previous studies performed at 20 °C, where three species were found.[17] This difference shows clearly that the process in both cases is different. At 70 °C, NQS quickly decomposes at pH values higher than 9, giving an orange-brown product. Conversely, at 20 °C, the decomposition of NQS is avoided, and the process observed was the acid−base equilibria of NQS. The initial purest spectra used in the alternating least-squares optimization were (a) spectrum at pH 6.5 for the NQS acidic species and (b) spectrum at pH 12.5 for the NQS decomposition species.

(B) Study of the Reaction between Phe and NQS. Figure 2 shows the spectral data set when a solution of 2.5×10^{-4} M Phe was pumped through channel A (see Figure 1) and a 1.1×10^{-3} M NQS solution was used as reagent (NQS channel). Eigenanalysis of the corresponding spectral data matrix indicates that four absorbing chemical species are present. According to

Table 1. Effect of Constraints on the Recovery of Pure Species Spectra by Multivariate Curve Resolution in the Simultaneous Analysis of Four Continuous-Flow Acid—Base Spectrophotometric Titrations of the Phe—NQS Reaction System[a]

option[b]	cosine values[c]				% error[d]		
	I	II	III	IV	III	IV	total[e]
a		0.996	0.951	0.732	3.8	3.7	3.8
b		0.997	0.949	0.981	12.2	12.4	12.3
c		0.993	0.976	0.978	4.5	3.9	4.9
d		0.998	0.943	0.982	5.1	3.0	4.2
e		0.996	0.987	0.973	5.0	4.3	4.7

[a] Reaction conditions: NQS concentration, 1.1×10^{-3} M; Phe concentration, 0, 5×10^{-5}, 1×10^{-4}, and 2.5×10^{-4} M; pH range, 6.5–12.5 [b] Constraints applied in the ALS optimization: a, without applying any closure constraint or equal shape of pH profiles constraint; b, applying closure constraint with respect to the NQS reagent; c, applying closure constraint with respect to the NQS reagent and equal shape constraint of all the pH profiles; d, applying closure constraint with respect to the reagent and equal shape constraint to only the pH profiles of the amino acid derivative species; e, applying closure constraint with respect to both reagent and analyte and equal shape constraint to only the pH profiles of the amino acid derivative species. [c] Cosine values between experimental and calculated pure spectra. [d] Percentage of error in quantitative estimations of relative concentrations of amino acid derivative species III and IV: % error = $(\sum (C_{known} - C_{calcd})^2)^{1/2} / (\sum C_{known}^2)^{1/2}) \times 100$, where C_{known} is the relative concentration of an amino acid species known from the experimental concentration ratios of Phe solution used in the different experiments, and C_{calcd} is the calculated relative concentration of an amino acid species obtained from the area ratios of the recovered pH profiles of the species in the different experiments by multivariant curve resolution. [e] Total percentage of error considering both species III and IV simultaneously (using the same equation for % error described in d).
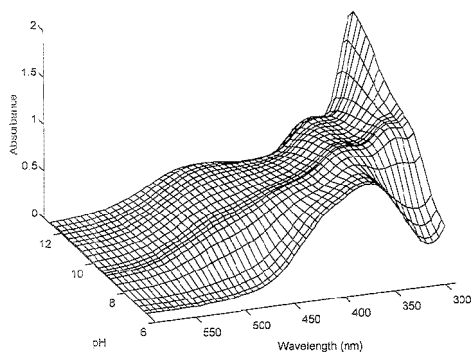
Figure 2. Experimental spectra obtained in a continuous-flow acid-base spectrophotometric titration of the Phe—NQS reaction system when a 2.5×10^{-4} M Phe solution is pumped through channel A. Conditions: NQS concentration, 1.1×10^{-3} M; pH range, 6.5–12.5.

the results of the previous study of the NQS decomposition, two of these species can be assigned to the NQS reagent, while the other two are assigned to the amino acid derivative species or reaction products. The spectra used as initial estimation of these two reaction products were those measured at pH 9.0 and 12.3, corrected (subtracted) for the NQS absorption spectra at these pH values.

In the resolution of this single data matrix by multivariate curve resolution, two closure constraints were simultaneously applied to the total analytical concentration of NQS and amino acid. The cosine values between the known pure spectra (obtained from independent experiments) and those recovered from the optimiza-
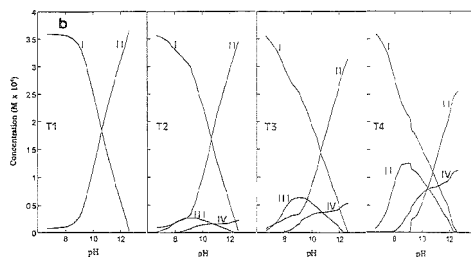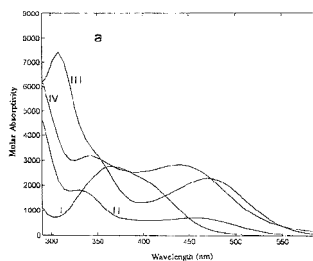
Figure 3. Results of the study of the reaction between Phe and NQS by simultaneous multivariate curve resolution analysis of four continuous-flow acid—base spectrophotometric titrations (T1, T2, T3, and T4). Titration conditions: NQS concentration, 1.1×10^{-3} M; pH range, 6.5–12.5; Phe concentrations, 0 in T1 (water instead Phe solution is pumped), 5×10^{-5} M in T2, 1×10^{-4} M in T3, and 2.5×10^{-4} M in T4. Constraints applied: (i) closure with respect to reagent and amino acid, (ii) equal shape for the pH profiles of the amino acid derivative species III and IV. (a) Recovered pure spectra of species I, II, III, and IV. (b) Recovered pH profiles of species I, II, III, and IV for the different experiments.

tion procedure were 1 for species I, 0.971 for species II, 0.986 for species III, and 0.941 for species IV. From these results, species I is correctly recovered, while especially species IV still shows a certain degree of rotational ambiguity.

To improve the previous resolution of the system, a simultaneous analysis of several experiments is needed. Four different solutions pumped through channel A of Figure 1 (Phe solutions at 5×10^{-5}, 1×10^{-4}, and 2.5×10^{-4} M and water) were used to generate four acid—base spectrophotometric titrations. Eigenanalysis of the column-wise augmented data matrix (wavelength common) gives four major contributions, similarly to the eigenanalysis of the individual data matrices containing the amino acid and the NQS reagent. No rank augmentation is observed when more data matrices are included in the analysis, showing that a maximum of four independent absorbing species are detected in the system within the pH range under study (6.5–12.5). Eigenanalysis of the rowwise augmented data matrix indicates a contribution of a fifth singular, which is interpreted as if the shapes of the pH profiles of the two NQS reagent species in the different experiments are not exactly equal in all the titrations but slightly modified by the reaction with the amino acid. The excess of NQS reagent concentration with respect to the amino acid was not enough to neglect its consumption by the reaction with Phe.

The effect of different constraints on the recovery of pure spectra and pH profiles of the species present has been evaluated (Table 1). In practice, because of random and systematic errors such as baseline drift and variations in the flow rates, it is difficult

Table 2. Effect of Constraints on the Recovery of Pure Species by Multivariate Curve Resolution in the Simultaneous Analysis of Four Continuous-Flow Acid–Base Spectrophotometric Titrations of Several Amino Acid–NQS Reaction Systems[a]

amino acid	cosine value				% error		
	I	II	III	IV	III	IV	total
Pro	1	0.997	0.973	0.940	2.2	1.1	1.8
Lys	1	0.997	0.976	0.961	0.6	9.9	7.2
Asp	1	0.999	0.964	0.775	1.4	41.3	32.8

[a] Constraints applied: closure constraint with respect to both reagent and analyte and equal shape constraint to only the pH profiles of the amino acid derivative species. See Table 1 for information.

to obtain the complete recoveries of these profiles. Thus, in this study, cosine values higher than 0.95 are considered to be related with good recoveries of spectra. In Table 1, a summary of results is given. In all cases, the spectral profiles of the reagent species I and II are correctly recovered, showing clearly that the inclusion of the response matrix of the pure NQS reagent provides the selective information needed for the resolution of these two NQS species. Using equal shapes of the pH profiles constraint and the closure constraint (approaches c, d, and e), the best results are obtained. Option e (closure constraint with respect to both reagent and Phe and equal shape constraint to only pH profiles of Phe derivative species) is the most powerful for the resolution of this reaction system. Figure 3 shows pure spectra and pH profiles obtained with this option. The shapes of the pH profiles recovered for species I are slightly different in the four experiments. This agrees with the fact that NQS is consumed by the reaction with the amino acid.

(C) Study of the Reactions between Pro, Lys, and Asp with NQS. The reaction between NQS and three other amino acids (Pro, Lys, and Asp) was also studied by multivariate curve resolution in the same way as for Phe. For every amino acid, four spectrophotometric titrations were analyzed simultaneously using the proposed method. Table 2 shows a summary of the results obtained, demonstrating the general use of the method. Under the experimental conditions of the spectrophotometric titrations, the formation of the amino acid derivatives is nearly quantitative for Phe, Pro, and Lys, while for Asp it is low. Species

IV (Table 2) is the most difficult to resolve, since its pH profile is always embedded below the pH profile of species II. Moreover, the two pure spectra of species IV and II are very similar, with a high degree of overlap. In particular, species IV of the NQS–Asp system is the poorest recovered because, in this case, a very low amount of derivative species is generated in the reaction (<15%). A longer reaction time and higher temperature may be required for completion of the reaction in the case of Asp.

CONCLUSIONS

The continuous-flow titration method proposed in the present work is able to provide highly structured second-order data, thus allowing improved resolution of unknown chemical reaction-based systems. The multivariate curve resolution procedure allows the recovery of important analytical information about these reaction-based systems, such as the pure spectra profiles of the reagent and product species, the pH profiles of all species present in the system, the percentage of analyte that has been reacted, and the optimum pH for the maximum development of the reaction.

Results of the reactions between NQS and amino acids indicate that constraints like closure and equal shape of profiles selectively applied to only some of the products of the reaction (amino acid derivatives) lead to improved recovery of pure spectra and pH profiles. The method proposed can easily be extended to the characterization and analytical application of other types of chemical reactions.

SUPPORTING INFORMATION AVAILABLE

Two tables and three figures concerning the experimental results (5 pages). See any current masthead page for ordering information.

Gas Sensing Properties of Porous Silicon

Israel Schechter*

Department of Chemistry, Technion—Israel Institute of Technology, Haifa 32 000, Israel

Moshe Ben-Chorin and Andreas Kux

Department of Physics—E16, Technical University of Munich, D-85747 Garching, Germany

Conductivity of porous silicon layers (p-type) has been investigated for organic vapor sensing. A many orders of magnitude increase in conductivity in response to a vapor pressure change from 0 to 100% has been measured for some compounds. The conductivity (at a constant pressure) varies exponentially with the compound's dipole moment. The temporal response of the porous silicon layers is in the seconds range, and the recovery is much slower (minutes). However, due to the tremendous conductivity changes and the low background noise, a complete recovery is not needed for sensing purposes. The mechanism of conductivity enhancement has been studied using several methods. It is attributed to an increase in the density of charge carriers. An additional mechanism based on increased diffusivity may take place in microporous silicon. The observed characteristics suggest the application of porous silicon to future chemical sensors. The sensors have the potential to be integrated monolithically with other silicon devices using current technologies.

Porous silicon (PS) is becoming an increasingly important electronic material in current fabrication technology. It has been suggested as a potential optical material for new silicon light emitting devices.[1-9] The fabrication of this material is carried out by a very simple electrochemical etching of silicon, which creates a network of nanometer-sized Si structures. Extensive studies have already been carried out on the electro- and photoluminescence properties of this material. Several models have been proposed to explain the origin of light emission, including quantum confinement effects,[1,2,10,11] radiative recombination via surface states,[12] and silicon-based compounds like SiH_x,[13] siloxene,[14] and amorphous silicon.[15] Only a few researches have been interested in chemical effects on the emitted light.[16-18]

This study is focused on the chemical sensing properties of PS. Silicon-based chemical sensors would be of extreme practical importance: a number of new devices are possible. The sensing activity of PS is based on its large internal surface area of ~500 $m^2\ cm^{-3}$, which implies possible adsorbate effects. Characterization of these surfaces and measurements of their specific area have been carried out by means of several techniques.[19-21] The quenching of PS photoluminescence by chemicals has been already suggested for application in chemical sensors.[16,17] Nevertheless, sensors based on photoluminescence changes are unlikely to be realized, due to their high cost: such devices include complex and expensive (time-resolved) spectroscopic setup. We suggest a different chemical approach, based on the conductivity of PS rather than on the photoluminescence quenching. This study is based on our discovery of the tremendous changes in the electrical conductivity of PS exposure to various chemicals in the gas phase. Chemical sensors based on the electrical conductivity of other semiconductors are well known (e.g., ref 22), and their contribution has been recognized.[23] The advantages of PS sensors are the simplicity of fabrication, low cost, and a possibility for integration with other silicon-based devices.

Actually, a similar application has already been proposed by Anderson et al.[24] They investigated capacitance variations of PS layers under exposure to vapors. The reported capacitance variations were within 1 order of magnitude only (factor of 4.4), and the temporal responses were in the 5–10 min range. Here

(1) Canham, L. T. *Appl. Phys. Lett.* 1990, *57*, 1046–1048.
(2) Lehmann, V.; Gösele, U. *Appl. Phys. Lett.* 1991, *58*, 856–858.
(3) Richter, A.; Steiner, P.; Kozlowski, F.; Lang, W. *IEEE Electron Device Lett.* 1991, *12*, 691–692. Steiner, P.; Kozlowski, F.; Lang, W. *Appl. Phys. Lett.* 1993, *62*, 2700–2702.
(4) Koshida, N.; Koyama, H. *Appl. Phys. Lett.* 1992, *60*, 347–349.
(5) Halimaoui, A.; Oules, C.; Bomchil, G.; Bsiesy, A.; Gaspard, F.; Herino, R.; Ligeon, M.; Muller, F. *Appl. Phys. Lett.* 1991, *59*, 304–306.
(6) Bressers, P. M. M. C.; Knapen, J. W. J.; Meulenkamp, E. A.; Kelly. J. J. *Appl. Phys. Lett.* 1992, *61*, 108–110.
(7) Canham, L. T.; Leong, W. Y.; Beale, M. I. J.; Cox, T. I.; Taylor, L. *Appl. Phys. Lett.* 1992, *61*, 2563–2565.
(8) Bomchil, G.; Halimaoui, A.; Sagnes, I.; Badoz, P. A.; Berbezier, I.; Perret, P.; Lambert, B.; Vincent, G.; Garchery, L.; Regolini, J. L. *Appl. Surf. Sci.* 1993, *65*, 394–407.
(9) Canham, L. T. *MRS Bull.* 1993, *18* (July), 22–28.
(10) Calcott, P. D. J.; Nash, K. J.; Canham, L. T.; Kane, M. J.; Brumhead, D. *J. Phys. C* 1993, *5*, L91.
(11) Suemoto, T.; Tanaka, K.; Nakajima, A.; Itakura, T. *Phys. Rev. Lett.* 1993, *70*, 3659–3662.
(12) Koch, F.; Petrova-Koch, V.; Muschik. T.; Nikolov, A.; Gavrilenko. V. *MRS Proc.* 1993, *283*, 197–202. Koch F. *MRS Proc.* 1993, *298*, 319.
(13) Prokes, S. M.; Glembocki, O. J.; Bermudez, V. M.; Kaplan, R.; Friedersdorf, L. E.; Searson, P. C. *Phys. Rev. B* 1992, *45*, 13788. Prokes, S. M.; Carlos, W. E.; Bermudez, V. M. *Appl. Phys. Lett.* 1992, *61*, 1447–1449.
(14) Brandt, M. S.; Fuchs. H. D.; Stutzmann, M.; Weber, J.; Cardona, M. *Solid State Commun.* 1992, *81*, 307–312.
(15) Perez, J. M.; Villalobos, J.; McNeill, P.; Prasad, J.; Cheek, R.; Kelber, J.; Estrera, P.; Stevens, P. D.; Glosser, R. *Appl. Phys. Lett.* 1992, *61*, 563–565.
(16) Lauerhaas, J. M.; Credo, G. M.; Heinrich, J. L.; Sailor, M. J. *J. Am. Phys. Soc.* 1992, *114*, 1911–1912.
(17) Lauerhaas, J. M.; Sailor, M. J. *Science* 1993, *261*, 1567–1568.
(18) Ben-Chorin, M.; Kux, A.; Schechter, I. *Appl. Phys. Lett.* 1994, *64*, 481.
(19) Herino, R.; Bomchil, G.; Barla, K.; Bertrand, C.; Ginoux, J. L. *J. Electrochem. Soc.* 1987, *134*, 1994.
(20) Canham, L. T.; Groszek, A. J. *J. Appl. Phys.* 1992, *72*, 1558–1565.
(21) Bard, A. J. *J. Electrochem. Soc.* 1994, *141*, 402–409.
(22) Bott, B.; Jones, T. A. *Sens. Actuators* 1984, *5*, 43–53.
(23) Janata, J. *Anal. Chem.* 1992, *64*, 196R–218R.
(24) Anderson, R. C.; Muller, R. S.; Tobias, C. W. *Sens. Actuators* 1990, *A23*, 835–839.

we compare these figures with the conductivity responses. Capacitance variations were attributed to condensation of liquid in the pores. In the following, we show that the mechanism of conductance increase is different and is not based on condensation at all. Furthermore, the dynamic range of conductivity is much larger than that of the capacitance. An attempt to develop a humidity sensor based on the hydrophobic and hydrophilic properties of PS has also been carried out;[25] however, no other effects have been tested.

EXPERIMENTAL SECTION

The microporous silicon (micro-PS) layers were prepared by anodization of a (100) p-type, B-doped Si wafer with resistivity of 5 Ω cm in a 1:1 volume solution of HF (49% in water)−ethanol. The etch current density was 30 mA cm^{-2}. The anodization time was chosen to form layers of 10−20 μm thickness. For conductivity measurements, aluminum contacts (area of ∼4 mm^2, thickness of a few micrometers) were evaporated on top of the porous silicon layer and were connected to metal wires.

Current was measured using a Keithley 236 source-measure unit in a two-terminal sandwich configuration. The source unit provided a stabilized voltage that was applied between the evaporated contact and an ohmic contact on the back of the Si wafer. The measured currents were in the range of nano- to microamperes. The instrument was equipped with an IEEE-488 interface, and all data were transferred to a microcomputer for analysis.

For some of the studies, meso-porous silicon (meso-PS) layers were used. These layers were prepared from a p$^+$ (100) substrate with a resistivity of 10 mΩ cm. The etching conditions were the same as those used for the micro-PS samples. Following anodization, the meso-PS layers were separated from the underlying silicon substrate by an electropolishing step (same acid concentration, but 0.3 A cm^{-2} anodization current). In-plane conductivity of the free-standing meso-PS layers was measured in the two-terminal configuration, between two evaporated aluminum contacts (a few micrometers thick).

Exposure to chemical gases was carried out in a small vacuum chamber. Samples were kept in ambient conditions and were introduced into the vacuum chamber just for the chemical exposure measurements. The sample was first flushed with clean nitrogen and evacuated using a rotary pump. Proper gas mixtures, containing the desired partial pressure of the organic gases and clean and dry nitrogen, were prepared in a large container and introduced into the sample chamber by a valve. The valve was closed when the desired gas pressure in the chamber was reached. Nitrogen was then added (in a few seconds) in order to perform the measurements at a fixed total pressure of ∼1 bar and in order to keep a well-defined gas composition and to prevent penetration of other gases from the outside.

RESULTS AND DISCUSSION

Current−Voltage Profile. The current−voltage profile of our PS samples is approximately symmetrical with respect to zero voltage, as shown in Figure 1, for both vacuum or nitrogen atmosphere. Nitrogen has no influence on conductivity and photoluminescence properties, so it can be used for dilution. For low methanol partial pressures, the current−voltage curve remains symmetrical, and only the current amplitude increases. Exposure

(25) Yamana, A. J. Electrochem. Soc. 1995, 137, 2925.
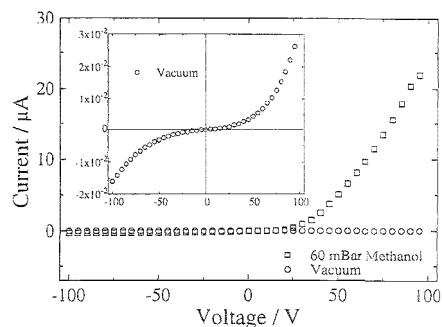
Figure 1. Current−voltage profile of a typical porous silicon sample. The inset shows current in vacuum (magnified by a factor of ∼700). Note the remarkable effect of methanol on the current and the rectifying characteristics.

Table 1

compound	dipole moment/D	vapor pressure/Torr
benzene	0	110
cyclohexane	0	104
fluorobenzene	1.6	70
toluene	0.36	29
trichloroethylene	0.8	77
chloroform	1.01	210
diethyl ether	1.25	587
2-propanol	1.66	43
methanol	1.7	128
ethanol	1.69	59
n-propanol	1.68	17
acetone	2.88	233
methyl ethyl ketone	2.7	105
N,N-dimethylformamide	3.82	4

to higher pressures has a remarkable effect and introduces rectifying characteristics.

Analysis of these characteristics, for various gas concentrations and for various thicknesses of PS layers,[18] suggests that the current in forward bias is a correct measure of the PS resistance. The change from symmetrical to rectifying behavior with increasing methanol pressure is due to the electrical structure of the device, which may be described as a serial combination of a resistor (PS layer) with a diode (Schottky barrier at the interface between Si and PS). At low methanol concentration, the PS resistance is so high that it limits the current, resulting in symmetrical current−voltage curves. At higher concentrations, the resistance is much reduced and the current in the reverse bias is limited by the interface, giving rise to rectifying behavior. However, in forward bias, the limiting element is the PS resistance, and thus, the sensing characteristics of the PS were measured with a forward voltage bias.

Vapor Effects. We measure the effect of 14 compounds, as listed in Table 1. The relative current changes (at 5 V) caused by exposure to these compounds (compared to clean nitrogen) are given in Figure 2, for 10 mbar and for half of the vapor pressure at room temperature. Following Lauerhaas et al.,[16] who showed a correlation of the luminescence quenching with the dipole moment of the adsorbate, we plot the current increase on a logarithmic scale as a function of the dipole moment of the molecules. While the effect on the luminescence was linear,[16] the conductivity increase is exponential. A many orders of
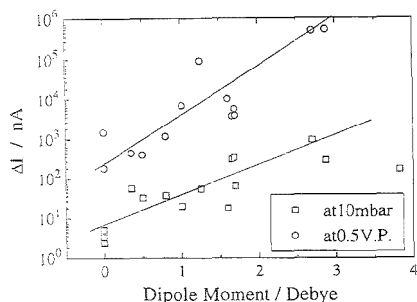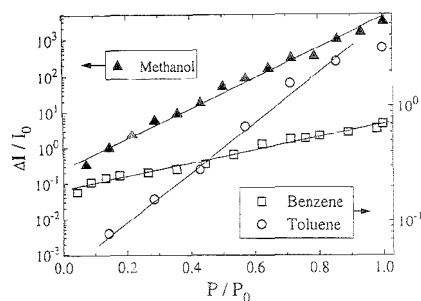
Figure 2. Current changes (relative to nitrogen) induced by several compounds, at 10 mbar and at half the vapor pressure. The applied voltage was 5 V. The point on the right, at 3.82 D, was measured at 4 Torr only (its vapor pressure at room temperature), which accounts for the deviation. Note the many orders of magnitude effects of both the dipole moment and pressure.

Figure 3. Exponential dependence of current changes (relative to vacuum) on the gas pressure (relative to vapor pressure) for several solvents. The curves of benzene and toluene do not cross when presented against absolute pressure.

Figure 4. Temporal response and recovery of the porous silicon conductivity on exposure to methanol. Due to the intense response, there is no practical need to wait for full recovery. The inset shows a schematic drawing of the PS sensor and its electric connections.

magnitude effect was observed for acetone and for methyl ethyl ketone, which have large dipole moments, while benzene, with zero dipole moment, has a very low influence on the conductivity of PS. This exponential dependence of the conductivity change (at the same gas pressure) on the dipole moment is of considerable importance for sensor development.

However, the spread of the data in Figure 2 shows that the dipole moment is not the only physical factor that affects the conductivity. Water vapor, for example, has only a negligible effect, although the dipole moment is very large. This is attributed to the hydrophobic nature of the hydrogen-passivated surface of PS crystallites. After we removed this surface coverage by means of a 400 °C annealing step (in air), a large increase in the conductivity was observed following exposure to water. In a similar manner, Lauerhaas and Sailor[17] reported enhancement of the photoluminescence quenching by water vapor following a chemical treatment, which makes the hydrophobic surface more hydrophilic. The insensitivity of the hydrated surface to water vapor is an additional advantage for sensor applications. Furthermore, the possibility to control the device selectivity by surface treatment allows for optimizing the sensitivity to specific chemical compounds.

Pressure Dependence. In addition to the above-mentioned exponential dependence on the dipole moment, there is another exponential dependence: the current as a function of the gas pressure for each of the separate compounds. This is shown in Figure 3 for methanol (on the left axis) and for other compounds with lower dipole moments (right axis). Again we see that the change in the conductivity is not directly related to the dipole moment, since even for benzene, which has zero dipole moment, an increase in the conductivity as a function of concentration is observed. This suggests that there exists a mechanism of conductivity enhancement which is not related to the dipole moment. Two different routes have also been proposed for luminescence quenching due to polar and nonpolar adsorbates.[17]

Temporal Response. An additional important feature is the time response and recovery of the PS conductivity following gas exposure. In order to study these characteristics, we exposed a PS sample to methanol in the following way. The sample chamber was evacuated and exposed to clean nitrogen. The chamber was
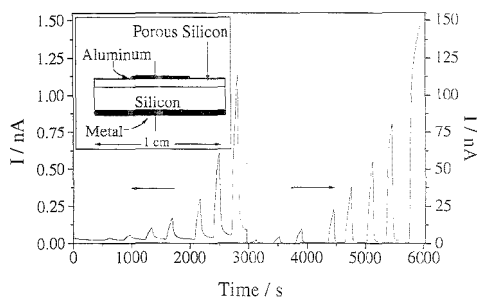
then evacuated again and exposed to a mixture of nitrogen with 10 mbar of methanol, at the same total pressure (~1 bar). After a defined time of ~2 min, the chamber was evacuated again for a few minutes and then filled with a new mixture of nitrogen and methanol, at a higher concentration. This concentration was kept for exactly the same period inside the chamber before the chamber was evacuated again. The procedure described above was repeated for several cycles. The results are shown in Figure 4. An increase in the current immediately after the exposure is observed, followed by a recovery after evacuation. The response and the recovery times, as a function of the methanol concentration, can be obtained from this figure. A *complete* recovery of the signal is not fast,[18] probably due to the fractal nature of the micro-PS surface. The long full-recovery time gives rise to a slight elevation of the baseline during measurements. However, the results of Figure 4 demonstrate that the main part of the recovery occurs on a quite short time scale. Usually, 10% recovery is obtained in 30 s, and 90% recovery takes ~100 s. The derivative of the signal, for instance, would indicate the change in the methanol concentration. Therefore, for practical purpose, both the response and the recovery can be considered fast.

The measured temporal characteristics can be rationalized by a simple model. The adsorption rate is generally given by[26]

(26) Morrison, S. R. *The Chemical Physics of Surfaces*; Plenum Press: New York. 1977.

$$\frac{d\Gamma}{dt} = -k_1\Gamma - k_2(\Gamma_t - \Gamma)p \tag{1}$$

where Γ_t is the density of adsorption sites, p is the pressure, and Γ is the adsorbate density (per area or volume unit). The first term describes the desorption process, and the second one describes the adsorption.

At relatively low adsorption, k_1 and k_2 are pressure independent, and we can derive the steady state ($d\Gamma/dt = 0$) adsorbate concentration,

$$\Gamma = \Gamma_t p/(p + k_1/k_2) \tag{2}$$

which can be simplified in the low-pressure range:

$$\Gamma = \Gamma_t(k_2/k_1)p \tag{3}$$

The exponential characteristics of Figure 3 can be expressed in the following form:

$$\sigma = \sigma_0 e^{p/p_0} \tag{4}$$

where p_0 is adsorbate dependent. By eqs 3 and 4, we get

$$\sigma = \sigma_0 e^{\Gamma/\Gamma_0} \tag{5}$$

Our pumping procedure starts at surface concentration $\Gamma(0)$, given by the steady state condition $\Gamma(0) = \Gamma_t(k_2/k_1)p$ ($t = 0$), and we pump down to low pressures. Thus, the second term in eq 1 vanishes, and the solution of this equation (at $p \approx 0$) is

$$\Gamma(t) = \Gamma(0)e^{-k_1 t} \tag{6}$$

Provided that the conductivity instantaneously responds to the concentrations, eqs 5 and 6 give

$$\ln\frac{\sigma(t)}{\sigma_0} = \frac{\Gamma(0)}{\Gamma_0}e^{-k_1 t} = \frac{p(0)}{p_0}e^{-k_1 t} \tag{7}$$

Equation 7 has been fitted to our data, and good results have been obtained for the conductivity as a function of time, after a fast pumping down of the vapors. Deviations have been observed at longer times, probably due to contribution of the second term in eq 1, which was neglected here. At longer times (>1000 min), the readsorption cannot be neglected.

Mechanism of Conductivity Enhancement. We discuss now the origin of the enhancement of PS conductivity by the adsorbed molecules. We first examine one suggestion made by Anderson et al.[24] They have argued that the change in the electrical properties of PS following adsorption (capacitance in their study) is due to liquid condensation inside the microcapillaries of the PS. This would lead to an increased capacitance as well as an extra current flowing through the liquid, resulting in an "artificial" conductivity enhancement. In order to check this mechanism, we have measured the refractive index of our PS layers, using FT-IR spectroscopy. The existence of liquid inside the pores should increase the effective refractive index. Such an
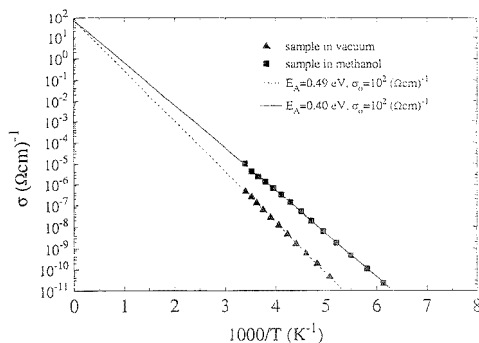
Figure 5. Temperature dependence of meso-PS conductivity (at 5 V) in vacuum and in methanol vapor. The activation energy is lowered in the presence of the methanol vapor, while the conductivity prefactor is not changed.

increase was observed only above methanol pressure of 80 mbar, suggesting that below this pressure no condensation occurs. Nevertheless, conductivity enhancement was observed at much lower methanol pressures. Moreover, the recovery of the refractive index following evacuation was faster than the current relaxation.

A full understanding of the mechanism of the conductivity enhancement requires a knowledge of both the electrical transport properties of the PS and the charge transfer reaction that occurs during the adsorption at the silicon surface. Unfortunately, the conductivity in micro-PS is influenced by a variety of parameters. The material is a fractal network of nanometer-sized crystallites. Quantum confinement causes spatial fluctuations of the effective band gap. As a result, internal energy barriers exist between the crystallites, which electrons have to overcome. Electrons move through the system on the most favorable route. Even without the presence of adsorbate molecules, the conductivity mechanism is not trivial, and their addition further complicates the situation.

In order to shed some light on the question of the conductivity enhancement, we simplified the problem by examining meso-PS layers. The silicon structures in these samples are larger (10−20 nm),[2,17] and therefore quantum size effects are negligible. They also lack the fractal topology possessed by the micro-PS.[28] This allowed us to treat meso-PS as a usual semiconductor.[29] The main difference between a meso-PS layer and a piece of bulk crystalline silicon is the large surface area of the first. On the other hand, this is the common feature it shares with micro-PS. Thus, one might expect to learn about the conductivity enhancement problem by looking at meso-PS, since the charge transfer processes in both materials are probably similar, because they depend mostly on the local environment of the adsorption sites.

Figure 5 is an Arrhenius plot of the conductivity as a function of temperature. When the sample is kept in vacuum, the activation energy is 0.49 eV, and the conductivity prefactor is $\sim 10^2 \ \Omega \ cm^{-1}$. When methanol is introduced into the chamber, the activation energy decreases (to 0.4 eV), but the conductivity prefactor is

(27) Cullis, A. G.; Canham, L. T. *Nature* **1991**, *253*, 335−338.
(28) Goudeau, P.; Naudon, A.; Bomchil, G.; Herino, R. *J. Appl. Phys.* **1989**, *66*, 625.
(29) Schwarz, R.; Wang, F.; Ben-Chorin, M.; Grebner, S.; Nikolou, A.; Koch, F. *Thin Solid Films* **1995**, *255*, 23−26.

not affected. Assuming semiconductor behavior, the conductivity can be approximated by[30]

$$\sigma = N_c e\mu e^{-(E_c - E_f)/kT}$$

where N_c is the effective density of states at the band edge, e is the electron charge, μ is the free electron mobility, and E_c and E_f are the band edge and Fermi energies, respectively. We assume that only the majority carriers contribute to the conductivity and that N_c and μ are only weakly dependent on the temperature. In a doped semiconductor, E_f might be a function of the temperature. However, in our case, the activation energy is constant over the whole range of the measurement, and therefore the Fermi level is pinned at a fixed point with respect to the band edge. In vacuum, the activation energy is approximately half the band gap of crystalline silicon (~1.1 eV), suggesting that the Fermi level is near mid-gap position. Therefore, we can conclude that the material behaves like a compensated semiconductor. When methanol is introduced, the Fermi level shifts to a new position and is fixed closer to the band edge. The meaning of this result is that methanol injects extra carriers into the PS. The sign of these carriers was determined by thermopower measurements. A small temperature gardient was applied to the sample, and the sign of the induced voltage indicated that the majority carriers are electrons for this material prepared from highly p-doped substrate. Thus, adsorbed methanol (as well as other vapors discussed here) behaves like an electron donor.

There are two possible mechanisms to account for the methanol effect. It might be that during adsorption, the methanol is oxidized, thus giving an extra electron to the silicon skeleton. Since oxidation of methanol (and of ketones, which also show a large conductivity effect) is questionable, another mechanism has to be considered. It is possible that the existence of methanol with its high polarizability at the vicinity of the PS internal surfaces give rise to local fields, shifting the energy position of other surface states. Thus, the energy distribution of density of states inside the gap changes, shifting the Fermi level position with respect to the conduction band edge.

The mechanism suggested above is based on a strong change in the density of charge carriers, while their mobility (diffusivity) is kept constant. This seems to be the case for meso-PS; however, for micro-PS, another mechanism might contribute as well. As we have stated before, conduction in micro-PS is limited by barriers between particles. A preferential adsorption of polarizable molecules on such sites might reduce the barriers, increasing the effective diffusivity of the carriers and thus the conductivity. It is probable that both mechanisms contribute to the conductivity enhancement in micro-PS.

Finally, it is interesting to discuss the changes observed in photoluminescence properties of micro-PS and their relation to the conductivity enhancement. A shift to the Fermi level, caused by addition of carriers, will increase the nonradiative recombination rate and therefore quench the conductivity. It has been already shown that PS luminescence can be quenched by the application of voltage, due to an injection of extra carriers into the crystallites.[5,8] This process increases the probability for Auger recombination. However, it has been observed that this process

selectively suppresses the red part of the photoluminescence band, because injection into the larger particles that are responsible for this light is easier. The other mechanism we have suggested for the micro-PS conductivity effect, the lowering of barriers between particles, would also give rise to luminescence quenching, since excited carriers have easier access to nonradiative centers. However, in this case, one would expect that a similar decrease in the photoluminescence intensity would take place all over the spectrum, as observed in the experiments. Further investigation is needed to clarify these points.

Comparison to Other Measurements. Anderson et al.[24] have examined PS devices for vapor sensing, mainly as a humidity sensor. They have found a 440% increase in the capacitance of PS layers in response to a humidity change from 0 to 100%. In addition, they have found only weak sensitivity to methanol and acetone. This is not in disagreement with our results. since their samples were prepared in such a way that the internal surfaces were oxidized and therefore hydrophilic.[24] Another batch of their samples, prepared in a special way which restored the original hydrophobic nature, showed no response to water vapor, but a large effect was induced by methanol. As we have discussed before, the humidity response can be easily changed by simple pretreatment or aging of the samples. We chose samples that do not respond to water vapor, since we were interested in sensing the organic materials. Water vapor is expected to influence the conductivity of hydrophobic PS only at a high humidity level and prolonged exposure. Mares et al.[31] reported on conductivity changes as a function of humidity for relative humidities larger than 25%. Even in that case, the wetting of the inner surfaces occurred only after exposure for several days. We believe that the prolonged exposure also results in partial oxidation, which allows wetting to occur. This effect is negligible in our samples, due to the relatively short exposure times we used.

The vapor condensation-based mechanism, proposed by Anderson et al.[24] and by Mares et al.,[31] was eliminated in our case by measuring the refractive index of the PS layer, carried out using FT-IR spectroscopy. It should be mentioned that even in the capacitance study, the internal condensation is not the only possible explanation, since capacitance may be changed by adsorption of molecules with a high dipole moment, even under submonolayer coverage.

CONCLUDING REMARKS

PS has many of the characteristics required for chemical sensor development. First, its electrical response varies by many orders of magnitude for different gases at the same partial pressure. In addition. for each of the gases, an exponential current enhancement has been observed as a function of partial pressure. This means that the chemical nature of the adsorbates has a considerable influence on conductivity, which is favorable for sensor applications. Preparation of PS samples is very simple, much simpler than for other semiconductor- and metal oxide-based sensors. Since this layer is constructed on a standard silicon wafer, the final sensors can be integrated with other silicon-based devices.

The proposed PS device is easily handled, since it is not affected by exposure to oxygen and other ambient gases. Actually, very similar results were obtained when pure nitrogen was

---

(30) Seeger, K. *Semiconductor Physics*, 5th ed.; Springer: New York, 1988.

(31) Mares, J. J.; Kristofic, J.; Hulicius, E. *Thin Solid Films* 1995, 255, 272–275.

replaced with air. (Nitrogen was used just to ensure a stable and well-defined environment.) The PS device is rather stable, although variations could be observed after a few months (probably due to a slow process of internal oxidation).

The mechanism of conductivity enhancement is not completely clear. In the case of meso-PS, where no quantum effects are expected, it is probably based on carriers activation, while in the case of micro-PS, an additional mechanism of increased diffusivity may take place. However, it is clear from the construction of the device that the conductivity takes place vertically (across the surface). Experiments with photoconductivity of these samples support this concept. Probably, the organic gases penetrate into the PS layer under the aluminum contacts and contribute to the observed conductivity enhancement. Nevertheless, more experimental evidence is needed for a final conclusion on the mechanism and the active sites.

Further investigation of the performance of n-type porous silicon, which is known to possess a different microstructure, is of interest. The effects of preparation procedure on the final sensitivity and response have still to be studied. This procedure consists of many variables, such as etching current and time or composition of the etching solution, that probably should influence the final characteristics. Further understanding of the physical effects involved in the current enhancement may contribute to sensor development, regarding its selectivity, temporal response, and concentration sensitivity.

Solvent Effects on the Redox-Dependent Binding Properties of a Viologen-Based Receptor for Neutral Organic Molecules

Ronald R. Lilienthal and Diane K. Smith*

Department of Chemistry, San Diego State University, San Diego, California 92182-1030

Cyclic voltammetry of a viologen-based cyclophane receptor, VH, in water, 10% acetonitrile/water, and acetonitrile is described. Minimal electrolyte was necessary in order to prevent precipitation of the reduced VH in aqueous solutions. Shifts in the half-wave potential of the first viologen reduction are observed in the presence of various substituted benzenes. The direction and magnitude of the shifts are explained in terms of two competing factors: (i) the change in the electron donor–acceptor character of the host that occurs upon reduction and (ii) the change in the hydrophobic/hydrophilic character of the host upon reduction. The first factor promotes binding of acceptor-substituted guests to the reduced host and donor-substituted guests to the oxidized host. The second factor promotes binding of all the guests to the reduced host in aqueous solution. Large potential shifts are observed when both factors work in the same direction.

A redox-dependent receptor is a receptor that undergoes a reversible redox process that changes the binding properties of the receptor. Such receptors have several potential applications in analytical chemistry. For example, they could function as the primary components in electrochemical sensors, providing both substrate recognition and a means for electrochemical detection. Redox-dependent receptors could also be utilized in membrane separation systems that employ a potential gradient to effect selective transport across the membrane.

In previous reports, we have described some of the redox-dependent binding properties of the viologen-based receptor, VH, in acetonitrile.[1,2] VH, originally prepared and studied by Stoddart
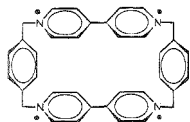
VH

and co-workers,[3] binds benzene-size aromatics in the cavity between the 4,4′-bipyridiniums,[3–6] commonly known as viologens. Like other viologens, the viologens in VH undergo two reversible reductions, first to a stable radical cation and then to a neutral

quinoid structure. eqs 1 and 2.[1,2,4] Although not much change in
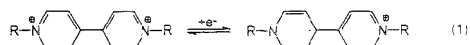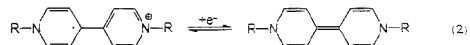
the size or shape of the binding cavity is expected upon reduction, we reasoned that the changes in charge and electronic structure which do occur would alter the binding properties of VH, and, indeed, this turned out to be the case.

Although numerous redox-dependent receptors for ionic species have been described,[7] VH is one of only a few redox-dependent receptors for neutral compounds which have been reported to date.[7,8] Of these, it is the only example where binding strength changes in a straightforward and predictable manner upon reduction/oxidation. In our previous work, we showed that the oxidation state which is preferred by a particular substrate or guest molecule in acetonitrile can be predicted on the basis of the ability of the guest to interact with the positive charges on VH and on electron donor–acceptor considerations. Specifically, benzene derivatives with ethoxy ether side chains that interact with the positively charged sites bind more strongly to the oxidized VH^{4+} form, which has a greater positive charge. This was determined from the negative shift in the half-wave potential of the first viologen reduction in the presence of these guests. Smaller but still significant shifts are observed with guests which do not specifically interact with the positive charges. In these cases, the preferences are controlled by electron donor–acceptor considerations. Donor-substituted guests, which bind more strongly to the relatively electron poor VH^{4-}, cause negative shifts in the observed half-wave potential of the $VH^{4+/2+}$ couple. In contrast, acceptor-substituted guests, which bind more strongly to the reduced VH^{2+} form, cause positive shifts in the half-wave potential.

(1) Fonseca, R. J.; Colina, J. T.; Smith, D. K. J. Electroanal. Chem. 1992, 340, 34L.
(2) Smith, E. A.; Lilienthal, R. R.; Fonseca, R. J. Anal. Chem. 1994, 66, 3013.
(3) Odell, B.; Reddington. M. V.; Slawin, A. M. Z.; Spencer, N.; Stoddart, J. F.; Williams, D. J. Angew. Chem., Int. Ed. Engl. 1988, 27, 1547.

(4) Anelli, P. L.; Ashton, P. R.; Ballardini, R.; Delgado, M.; Gandolfi, M. T.; Goodnow, T. T.; Kaifer, A. E.; Philp, D.; Pietraszkiewicz, M.; Prodi, L.; Reddington, M. V.; Slawin, A. M. Z.; Spencer, N.; Stoddart, J. F.; Vicent, C.; Williams, D. J. J. Am. Chem. Soc. 1992, 114, 193.
(5) (a) Goodnow, T. T.; Reddington, M. V.; Stoddart, J. F.; Kaifer, A. E. J. Am. Chem. Soc. 1991, 113, 4335. (b) Philp, D.; Slawin, A. M. Z.; Spencer, N.; Stoddart, J. F.; Williams, D. J. J. Chem. Soc., Chem. Commun. 1991, 1584. (c) Cordova, E.; Bissell, R. A.; Spencer, N.; Ashton, P. R.; Stoddart, J. F.; Kaifer, A. E. J. Org. Chem. 1993, 58, 6550.
(6) Bernardo, A. R.; Stoddart, J. F.; Kaifer, A. E. J. Am. Chem. Soc. 1992, 114, 10624.
(7) Beer, P. Adv. Inorg. Chem. 1992, 39, 79.
(8) Seward, E. M.; Hopkins, R. B.; Sauerer, W.; Tam, S.-W.; Diederich, F. J. Am. Chem. Soc. 1990, 112, 1783.

In this paper, we explore the influence of solvent on the redox-dependent binding properties of VH. Solvent typically has a strong influence on binding in organic host–guest systems.[9,10] Indeed, solvation forces are often the primary driving force for binding in these systems. This is particularly true in aqueous solution, where the unfavorable solvation of an apolar guest and apolar binding site strongly promote binding. Since viologens become more hydrophobic upon reduction, the solvation properties of the binding site in VH will change considerably in aqueous solution, and this could lead to large changes in binding strengths.

Unfortunately, it is not straightforward to investigate the electrochemistry of VH in aqueous electrolyte for the very reason that it would be interesting to do so. The increased hydrophobicity of the radical cation promotes precipitation of the radical onto the electrode surface, leading to distorted voltammograms which can not be simply interpreted in terms of binding equilibria. The tendency to precipitate is much greater for VH than for simpler viologens, making it nearly impossible to observe undistorted voltammograms in aqueous electrolyte solution.

Bernardo et al. avoided this difficulty by exchanging the viologen host into a Nafion film coated on an electrode surface.[6] This allowed them to examine the undistorted voltammetry of VH in the presence of different guests in aqueous solution. However, the interior of a Nafion film is a considerably different environment than water, so their results do not necessarily reflect the influence of solvation forces which we wish to explore. In addition, although the Nafion approach will be useful for practical applications such as sensors or membrane separation systems, it increases the complexity of the experimental system, making it more difficult to extract fundamental information regarding the redox-dependent binding.

We took another approach to solving the precipitation problem which avoids the added complexity of a surface-modified electrode system. By using microelectrodes, we have studied the voltammetry of VH in water, with minimal electrolyte. Under these conditions, no distortion is observed, and the electrochemistry can be examined in the presence of different guests. In many cases, we observe a positive shift in the redox potential in the presence of the guests, implying stronger binding to the reduced form of the host. The positive shift is consistent with solvation-controlled binding, since the reduced VH^{2+} state is more hydrophobic and is therefore less favorably solvated by water than the VH^{4+} state. The observation that even guests which give negative potential shifts in acetonitrile give positive shifts in water underscores the significance of solvation forces in this system.

EXPERIMENTAL SECTION

Compound Preparation. VH was prepared and purified as described in the literature.[3] ^{1}H NMR and ^{13}C NMR of the purified product agreed with the reported chemical shifts. The initial PF$_6^-$ salt was converted to the chloride salt by dissolving in acetonitrile and adding excess tetraethylammonium chloride. Methylviologen (MV) was prepared by reacting excess methyl iodide with 4,4'-bipyridine in acetonitrile. The resulting iodide salt was converted to the PF$_6^-$ salt by adding excess NH$_4$PF$_6$ to an aqueous solution of the iodide. The PF$_6^-$ salt was converted to the chloride as

described above. 1,4-Bis[2-(2-hydroxyethoxy)ethoxy]benzene (**1b**) was prepared and purified according to the literature procedure.[4]

$$HO(CH_2CH_2O)_n \!\!-\!\!\langle \bigcirc \rangle\!\!-\!\! (OCH_2CH_2)_nOH$$

$$\textbf{1a}\ \ n=1, \ \textbf{1b}\ \ n=2$$
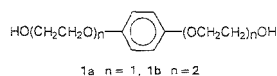
All other guest compounds were purchased from commercial sources and further purified as follows. 1,4-Diaminobenzene, 1,2-diaminobenzene, and 1,2-dihydroxybenzene were sublimed in vacuo. 1,4-Dihydroxybenzene was recrystallized from acetonitrile under N$_2$.

Electrochemical Studies. The microelectrode experiments were performed using a Pine Instrument Co. RDE4 bipotentiostat with a Kipp and Zonen $X-Y$ chart recorder. Both the electrochemical cell and the potentiostat were placed in a copper mesh faraday cage to reduce signal noise. For the nonmicroelectrode experiments, a PAR Model 173 potentiostat connected to a PAR Model 175 universal potential programmer was used. All electrochemical measurements were made under Ar or N$_2$ in a one-compartment cell with a Pt or Au disk working electrode (2 mm or 25 μm diameter) and a Pt wire counter electrode. A SCE reference electrode was used for the aqueous experiments, and a Ag/AgNO$_3$ reference electrode was used for the acetonitrile work.

Water from a Millipore Milli-Q water purification system was used for aqueous electrochemical experiments. HPLC-grade acetonitrile was used for the nonaqueous experiments. For the 100% acetonitrile experiments, the acetonitrile was passed through a small column of activated alumina directly into the electrochemical cell. Tetrabutylammonium hexafluorophosphate, previously recrystallized 3 times from 95% ethanol and dried in vacuo for 24 h at 70 °C, was used as the electrolyte in the nonmicroelectrode experiments.

Binding Constant Measurements. Binding constants for all guests with VH^{4+} were estimated from NMR data using the following procedure. A D$_2$O or 10% CD$_3$CN/D$_2$O solution which contained a known concentration of VH ($\sim$0.5 mM) and a known concentration of guest (0.3–1.0 mM) was prepared, and its ^{1}H NMR spectrum was recorded (Chem Magnetics 200 MHz FT NMR spectrometer). Enough guest was then added to the NMR tube to increase the concentration to $\sim$10 mM, and another NMR was recorded. Finally, the guest concentration was increased to $\sim$20 mM, and a final NMR was recorded. With most guests, little change in chemical shift (<3%) was observed between the 10 and 20 mM guest solutions, indicating saturation binding. To calculate the binding constant, we measured the change in chemical shift in hertz (ΔHz) of the VH^{4+} xylyl protons in the VH solution containing a low concentration of guest relative to a VH^{4+} solution with no added guest. The methylene VH^{4+} protons were used as an internal standard for this calculation since they did not shift significantly with added guest. These data were then plugged into the 1:1 NMR binding isotherm, eq 3,[11] where [G] is taken to

$$\Delta Hz = \frac{\Delta Hz_{max}K[G]}{1 + K[G]} \tag{3}$$

be the total guest concentration in the original solution, ΔHz is the change in chemical shift in hertz in the original solution, and

(9) Diederich, F. *Cyclophanes*; Royal Society of Chemistry: London, 1991; Chapter 7.

(10) (a) Smithrud, D. B.; Diederich, F. *J. Am. Chem. Soc.* **1990**, *112*, 339. (b) Smithrud, D. B.; Wyman, T. B.; Diederich, F. *J. Am. Chem. Soc.* **1991**, *113*, 5420.

(11) Connors, K. A. *Binding Constants*; John Wiley: New York, 1987; Chapter 5.
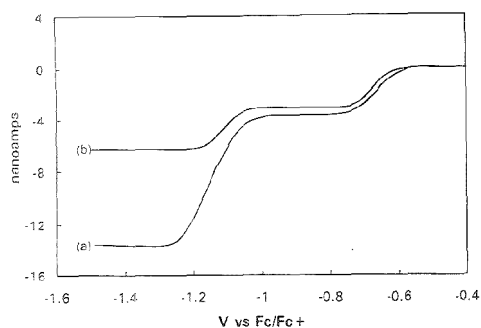
Figure 1. Voltammograms of 0.5 mM VH in acetonitrile with (a) no electrolyte and (b) 100 mM NBu₄PF₆. Other conditions: 25 μm Pt disk electrode, 50 mV/s scan rate.

ΔHz_{max} is the change in chemical shift in hertz in the 20 mM guest solution. (With benzonitrile and nitrobenzene, it did not appear that saturation binding had been reached at 20 mM, so instead the average ΔHz_{max} observed for all the other guests was used for the ΔHz_{max} of these two guests.) Since the [G] term in eq 3 represents the free guest concentration and not the total guest concentration, this calculation gives only an initial estimate of K. An iterative procedure was used to get a better estimate of K. First, the initial K was used to calculate the free guest concentration at a given value of G_{tot} and H_{tot} using eq 4. This value of [G]

$$[G] = \frac{KG_{tot} - KH_{tot} - 1 + \sqrt{(KH_{tot} - KG_{tot} + 1)^2 + 4\,KG_{tot}}}{2K} \quad (4)$$

was then plugged back in to eq 3 to get a better estimate of K, and the new K was used to recalculate [G]. The process was repeated until the values of K and [G] converged. We estimate that the resulting K values have an error on the order of 35% as a result of large uncertainties in the host and guest concentrations, due to the small amounts of material used. Three replicate measurements were made with **1a** in D₂O, and the resulting experimental value, 11 000 ± 3400 (90% confidence limits), agrees with the error analysis.

RESULTS

Cyclic Voltammetry of VH in Acetonitrile with No Electrolyte. Microelectrodes were required for this work because the larger currents at "normal"-size electrodes (millimeter diameter), coupled with high solution resistance without electrolyte, lead to large IR drops and the accompanying distortion in the voltammetry. The low currents at micrometer-size electrodes minimize the IR drop, making it possible to do voltammetry in quite resistive media.[12] However, use of microelectrodes does not eliminate another complication of removing the electrolyte, i.e., with no electrolyte and a charged species like VH, migration effects cannot be conveniently ignored as they typically are.

The effect of migration is illustrated in Figure 1, which shows voltammograms of VH at a 25 μm diameter Pt disk electrode in acetonitrile with no electrolyte present and with excess electrolyte.

Both voltammograms show the expected sigmoidal-shaped waves characteristic of microelectrodes at slow scan rates. The two reduction waves at −0.66 and −1.10 V are for the first and second reductions of VH. At high electrolyte concentrations, the limiting current after the second viologen reduction is approximately twice that after the first viologen reduction, consistent with both reduction processes involving equal number of electrons (in this case, two). However, at lower electrolyte concentrations, the limiting current after the second reduction is more than twice that of the first reduction, and both currents are greater than that observed in the presence of electrolyte.

The observed changes in the voltammetry with different electrolyte concentrations can largely be explained by migration effects. Qualitatively, reduction of the cationic host makes the region near the electrode surface relatively negatively charged compared to the bulk. This creates a potential field which pulls in more VH⁴⁺ from the bulk, leading to enhanced mass transport and enhanced currents compared to the excess electrolyte situation, where diffusion is the only form of mass transport. The effect is even greater at the potential of the second reduction, because there is a greater charge differential between the surface region and the bulk.

Amatore has derived a series of equations for predicting the expected current enhancements for charged species when no electrolyte is present.[13] These equations predict the observed current fairly well in several real systems.[13,14] For the first reduction of VH, the equations predict that the limiting current without electrolyte will be 1.35 times greater than the limiting current in the presence of a large excess of electrolyte. This is reasonably close to the observed value of 1.26 (from Figure 1). However, for the second reduction, Amatore's equations predict an enhancement of 5.0 in the absence of electrolyte, whereas the observed enhancement is only 2.2. Qualitatively similar results were observed by Norton and White for MV under the same experimental conditions.[15] They showed that the smaller than expected current for the second reduction could be explained by consideration of the comproportionation reaction between MV²⁺ and MV⁰. The large favorable equilibrium constant ($K = 8.5 \times 10^6$) means that at potentials where MV⁰ is produced at the electrode, there is mainly MV⁺ in the diffusion layer, so the electric field is not as great as expected and the migration current is less. We assume that a similar explanation holds for VH, since the equilibrium constant for the comproportionation would also be large ($K = 2.7 \times 10^7$ from the difference in the $E_{1/2}$'s).

Cyclic Voltammetry of VH in Water with No Electrolyte. Unlike in acetonitrile, we are not able to observe the effect of electrolyte in water, nor are we able to observe a difference in limiting current between the first and second reductions. This is because either adding excess electrolyte or scanning into the second reduction leads to highly distorted voltammetric waves, as shown in Figure 2. The large stripping peaks observed on the return scan are definitive evidence for precipitation of the reduced species under these conditions. However, the key point for the present study is that, without electrolyte, we are able to at least scan through the first reduction with no evidence of precipitation onto the electrode surface. Under these conditions, the steady state wave is broader than that observed for the first reduction in

(12) Wightman, R. M.; Wipf, D. O. In *Electroanalytical Chemistry, Vol. 15*; Bard, A. J., Ed.; Marcel Dekker: New York, 1989; pp 308–316.

(13) Amatore, C.; Fosset, B.; Bartelt, J.; Deakin, M. R.; Wightman, R. M. *J. Electroanal. Chem.* **1988**, *256*, 255.
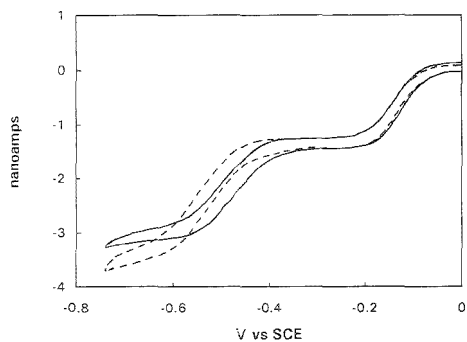
(14) Lee, C.; Anson, F. C. *J. Electroanal. Chem.* **1992**, *323*, 381.

(15) Norton, J. D.; White, H. S. *J. Electroanal. Chem.* **1992**, *325*, 341.
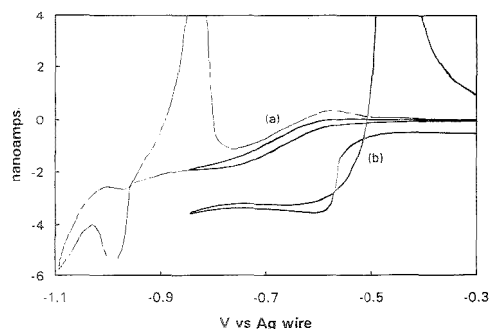
Figure 2. Voltammograms of 0.5 mM VH in water with (a) no electrolyte and (b) 100 mM KCl. Other conditions: 25 μm Pt disk electrode, 50 mV/s scan rate.

Figure 3. Voltammograms of 0.5 mM VH and 1 mM Ru(NH$_3$)$_6$Cl$_3$ in water with no electrolyte. Dashed line, no guest. Solid line, +10 mM **1b**. Other conditions: 25 μm Pt disk electrode, 50 mV/s scan rate.

acetonitrile in the presence of excess electrolyte, suggesting that some IR drop is occurring. However, for most of the work, we also added 1 mM Ru(NH$_3$)$_6$Cl$_3$ as an internal potential reference. With the additional ions present, the IR drop is minimal since the log plot slope in this case (Figure 3) is identical to that observed in acetonitrile with excess electrolyte.

Potential Shifts in the Presence of Guest Molecules. Upon addition of suitable guest molecules to an aqueous solution of VH, significant shifts in the VH$^{4+/2+}$ redox potential are typically observed. This is illustrated in Figure 3 with **1b** as the guest molecule. The solid line is the voltammogram observed for 0.5 mM VH^{4+} and 1 mM Ru(NH$_3$)$_6^{3-}$ in water. The reduction at −0.13 V is for the Ru$^{3+/2+}$ couple, and that at −0.51 V is for the VH$^{4+/2+}$ couple. Upon addition of 10 mM **1b** (solid line in Figure 3), the $E_{1/2}$ of Ru$^{3+/2+}$ remains the same, but the $E_{1/2}$ of VH$^{4+/2+}$ shifts positive by 34 mV. The fact that the Ru potential does not shift upon addition of the guest, along with the fact that no shift is observed for 1 mM MV under the same experimental conditions (Table 1), suggests that this shift is due to binding of **1b** in VH and not to experimental artifacts such as changes in liquid junction potentials or solution resistance.

Interestingly, the potential shift observed upon addition of **1b** to the aqueous solution of VH^{4+} is in the direction opposite to that observed in 0.05 M NBu$_4$PF$_6$/MeCN. In the latter solvent system, a negative shift of −49 mV is observed upon addition of 10 mM

Table 1. Observed Shifts in Half-Wave Potential (in mV) for the First Viologen Reduction in the Presence of Different Guests under Different Solvent Conditions

| | | | $\Delta E_{1/2}$ VH$^{4+/2+}$ | | |
| | | $\Delta E_{1/2}$ MV$^{2+/+}$, 10 mM guest, H$_2$O | 10 mM guest | | 100 mM guest, MeCN[a] |
entry	guest		H$_2$O	10% MeCN/ H$_2$O	
1	1a	−2	+41	0	−35
2	1b	+2	+34	−3	−80
3	1,4-dihydroxybenzene	−2	+20	−27	−21
4	1,2-dihydroxybenzene	0	−23	−47	−34
5	phenol		−13	−36	
6	1,4-diaminobenzene	−1	+10	−22	−42
7	1,2-diaminobenzene	0	−13	−36	−45
8	aniline	−4	−6	−13	−34
9	benzene	+4	0	−6	−13
10	cyanobenzene	+2	−60	+40	+11
11	nitrobenzene	b	+87	+55	+10

[a] With 0.05 M NBu$_4$PF$_6$. [b] Potential obscured by guest electrochemistry.

1b. Analysis of the dependence of the potential shift on **1b** concentration indicates that the binding constant of **1b** with VH^{4+} in 0.05 M NBu$_4$PF$_6$/MeCN is 4000 M^{-1}, while the binding constant of **1b** with VH^{2+} is essentially 0 M^{-1}, within experimental error.[2] The strong binding of **1b** to VH^{4+} in acetonitrile is largely due to the favorable electrostatic interaction between the ethoxy ether side chains and the positive charges on the viologens. Reduction to VH^{2+} decreases the charge, and this evidently weakens the interaction to a level where binding does not occur. The opposite behavior observed for VH in water indicates that in this solvent, not only does **1b** bind to VH^{2+} but the binding is stronger than that to VH^{4+}!

As shown in Table 1, a number of other benzene derivatives show similar behavior similar to that of **1b**. Consider first the oxygen-substituted guests, entries 1–5. These guests all cause the $E_{1/2}$ of VH$^{4+/2+}$ to shift negative in acetonitrile, but, like **1b**, **1a** and 1,4-dihydroxybenzene (hydroquinone) both cause a positive shift in water. In contrast, 1,2-dihydroxybenzene (catechol) and phenol both cause negative shifts in water. With all the guests, the shift moves in a negative direction in 10% acetonitrile/water. With **1a,b**, this results in essentially no shift in 10% acetonitrile/water, but with 1,4-dihydroxybenzene, the shift becomes negative, and with 1,2-dihydroxybenzene and phenol, the shift becomes even more negative. Interestingly, both of these guests give a larger negative shift in 10% acetonitrile/water than they do in pure acetonitrile with 10 times more guest. Under the same conditions (no electrolyte, 10 mM guest), the potential shift observed with 1,2-dihydroxybenzene in 10% acetonitrile/water is −47 mV, compared to −17 mV in pure acetonitrile.

We also examined three amino-substituted benzenes, entries 6–8. Like the oxygen guests, these all give negative shifts in acetonitrile, as expected on the basis of donor−acceptor considerations. Smaller shifts are observed with these guests in water than with the oxygen-substituted guests. However, the trends observed with the amino guests are exactly the same as those observed with the hydroxy guests: a positive shift with the 1,4-substituted guest, a negative shift with the 1,2-substituted guest, and a smaller negative shift with the monosubstituted guest. Again, the shifts become more negative in 10% acetonitrile.

As might be expected, the largest positive shifts are observed with the two guests that also give positive shifts in acetonitrile,
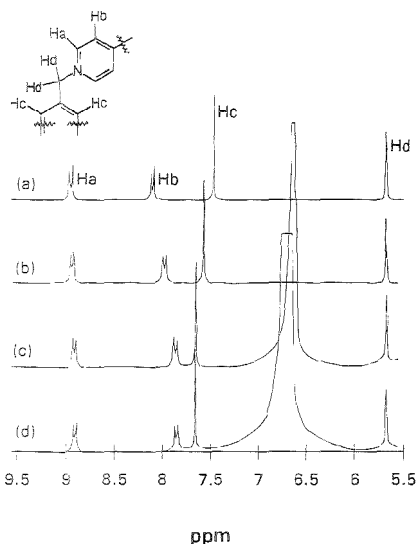
Figure 4. ^{1}H NMR spectra of VH in D_2O in the presence of (a) 0, (b) 0.3, (c) 10, and (d) 20 mM 1,2-dihydroxybenzene.

benzonitrile, and nitrobenzene. The shift with nitrobenzene is most impressive: 90 mV with only 10 mM added guest! Like the other guests, with both of these guests, the shift is less positive in 10% acetonitrile and even less positive in pure acetonitrile.

With all the guests, blank experiments were run in water with MV. No significant shift in the $E_{1/2}$ of MV was observed with any of these guests, indicating that the shifts observed with VH are, indeed, due to binding in the cavity and not to other experimental artifacts, such as changes in liquid junction potentials or solution pH.[16]

NMR Studies. Although we suspected strong binding in aqueous solution, we were initially surprised to find that addition of more guest to aqueous solutions of 0.5 mM VH and 10 mM **1a,b** caused no further changes in $E_{1/2}$, indicating saturation binding at these concentrations.[17] This conclusion was confirmed by NMR studies, which suggest that most of the guests give saturation binding under the conditions of the electrochemical experiments.

Figure 4 illustrates typical results with ^{1}H NMR spectra of a 0.5 mM D_2O solution of VH in the presence of 0, 0.3, 10, and 20

mM 1,2-dihydroxybenzene. Upon addition of guest, definite downfield shifts are observed in the xylyl protons (H_C) of VH and upfield shifts in the inner bipyridinium protons (H_B). Much smaller changes are observed in the outer bipyridinium protons (H_A), and there is essentially no change at all in the methylene protons (H_D). All these changes are completely consistent with binding of the guest in the central cavity of the host. The xylyl protons of VH fall in the deshielding region of the aromatic system of the guest and therefore move downfield, whereas the bipyridinium H_B protons fall in the shielding region of the guest and, as a result, move upfield. Smaller changes would be expected for the bipyridinium H_A protons, since they lie intermediate between the shielding and deshielding regions of the guest, and no change would be expected for the methylene protons, since they are pointing away from the binding cavity and should have little interaction with the guest.

Upon increasing the guest concentration from 0.3 to 10 mM, increased shifts are observed in the host protons, but no further changes are observed upon doubling the concentration to 20 mM. Similar results are observed for **1a,b** and all the other hydroxy- and amino-substituted guests in both D_2O and 10% CD_3CN/D_2O. This is good evidence that, for these guests, saturation binding occurs at 0.5 mM VH and 10 mM guest, the conditions of the voltammetric measurements.

The fact that we observe saturation binding and therefore know the maximum change in chemical shift allows us to use data such as those shown in Figure 4 to make a rough estimate of binding constants. The details of the calculations are described in the Experimental Section, and the results are tabulated in Table 2 under K_{ox}. Bernardo et al. report a value (from a UV/vis titration) of 3850 M^{-1} for VH with 1,2-dihydroxybenzene in pH 7 (0.3 M) phosphate buffer.[6] This is considerably smaller than the value of 22 000 M^{-1} we estimate from the NMR in D_2O. It is doubtful that the buffer system would have that large an effect, so it is possible that we are overestimating the binding constants, perhaps by assuming too low a value for the maximum change in chemical shift. Nonetheless, we believe it likely that the relative order of binding strengths is correct, and additional understanding can be gathered by examining the trends in the estimated K_{ox}'s.

(16) Since the solutions are unbuffered, the addition of some of the guests will cause small changes in solution pH. For example, addition of 10 mM 1,2-diaminobenzene causes a pH change from 7.2 to 7.5, and addition of 10 mM 1,4-diaminobenzene causes a pH change from 7.2 to 8.6. (Both values measured with a pH electrode.) However, since protons are not directly involved in the viologen reduction, these changes should not have a direct effect on the viologen electrochemistry. The lack of a potential shift with MV indicates that there is also no indirect effect.

(17) At lower guest concentrations, the $E_{1/2}$ does shift with increasing guest concentration. In our earlier work (ref 2), we were able to use this type of information to determine K_{ox} and K_{red}. We are not able to do this in this case because, given the magnitude of the binding constants measured with NMR, we should be in the regime where, at <1 equiv of guest, we see two CV waves, one for bound and one for unbound host. (see ref 18.) Unfortunately, we cannot observe this, because the waves are too close together. Simple spreadsheet calculations indicate that we would need at least a 120 mV difference in $E_{1/2}$ in order to observe a clear inflection in the steady state CV wave, and the largest difference we observe is only 90 mV.

In many respects, these trends agree with our expectations, although there are some interesting surprises. To begin, it appears that the OR- and NH$_2$-substituted guests bind more strongly to VH^{4+} than benzene, benzonitrile, and nitrobenzene, as expected on the basis of donor–acceptor considerations. However, since N is generally considered a stronger π-donating substituent than O, we would have guessed that the NH$_2$ guests would bind more strongly than the OH guests. In fact, the opposite is true in most cases. This may reflect the importance of an electrostatic interaction between the heteroatom on the guest and the H's on the bipyridinium ring. These H's, which have partial positive charge, would interact more strongly with O than with N, since the former has more negative charge character due to the greater electronegativity of O.

Another unexpected result is the sensitivity to substitution patterns. Under most circumstances, both 1,2-dihydroxybenzene and 1,2-diaminobenzene bind substantially more weakly than their respective 1,4-isomers. This may be attributed to the increased water solubility of the more polar 1,2-isomers. Another intriguing possibility is that it is an entropic effect. The 1,2-isomers may be locked more tightly in the binding cavity than the 1,4-isomers, making binding more entropically unfavorable with the ortho isomers.

DISCUSSION

By combining the K_{ox}'s estimated from the NMR data with the $\Delta E_{1/2}$'s in Table 1, and assuming the latter to be the maximum shifts, the binding constants to the reduced host, K_{red}, can also be estimated by using eq 5.[18] These data, tabulated in Table 2,

$$\Delta E_{1/2,max} = (29.6 \text{ mV}) \log(K_{red}/K_{ox}) \qquad (5)$$

cannot be taken quantitatively due to the uncertainty in the estimated binding constants. However, the relative order of binding strength is likely correct, giving an overall qualitative view of the redox-dependent binding.

In general, there are three factors which can promote binding in a host–guest system.[9] One is favorable interactions between the host and guest. This is determined by the stereoelectronic complementarity of host and guest. The other two factors are related to solvation. One is the release of solvent molecules from the surface of the binding cavity into bulk solution upon binding of a guest in the cavity, and the other is the release of solvent molecules from the surface of the guest into bulk solution upon binding. The last two factors should be favorable from both enthalpic and entropic standpoints for apolar guests and an apolar binding site in water.[10]

The second solvation factor, release of solvent molecules from the guest, depends only on the guest, and it therefore will not vary with oxidation state of the host and cannot directly affect redox-dependent binding. However, it can affect the magnitude of the binding constants and, through them, the magnitude of the observed potential shift at a given guest concentration. This factor undoubtedly contributes substantially to the strong binding which is observed in water, since the guests are relatively apolar and are not solvated particularly well by water. On average, the estimated K_{ox}'s decrease by 54% on going from water to 10%

acetonitrile/water, and this is likely due to the better solvation of the guests by the acetonitrile.

The other important solvation factor promoting host–guest binding is the release of solvent molecules from the binding cavity into bulk solution. This should always be a favorable process for an apolar binding site in water. How favorable it is will depend on the hydrophobic/hydrophilic character of the binding site, and this can vary with oxidation state of the host and, therefore, can directly affect the redox-dependent binding. Since the viologen host becomes more hydrophobic on reduction, this factor will always promote binding to the reduced host and will tend to cause a positive shift in redox potential with any hydrophobic guest.

The estimated binding constants of the donor-substituted guests decrease by an average of 67% on going from oxidized to reduced VH in 10% acetonitrile/water, whereas in pure water they *increase* by an average of 490%. We attribute the generally stronger binding of the reduced host in water to the poor solvation of the biradical cavity by water. Again, the acetonitrile molecules solvate the reduced cavity more effectively, and so the binding is weaker in the presence of acetonitrile. An alternate way to look at this is that the acetonitrile also acts as a guest and, due in part to its large concentration, competes favorably with the benzene derivative for the reduced cavity.

The other factor promoting binding, favorable interactions between the host and guest, is determined by the stereoelectronic complementarity of host and guest. This will vary depending on the oxidation state of the host. As discussed earlier, this factor explains the observed potential shifts in acetonitrile quite nicely. Specifically, the shifts with all the guests agree with predictions based on electron donor–acceptor considerations. The larger shifts observed with **1a,b** are due to the additional strong electrostatic interaction between the ethoxy ether side chains and the positive charge on the host.

For the acceptor-substituted guests, benzonitrile and nitrobenzene, the two factors discussed above both promote binding to the reduced host, so its not surprising that these guests give the largest magnitude potential shifts in water. With the donor-substituted guests, the two factors pull in opposite directions, resulting in smaller shifts. The direction of the shift indicates which factor wins out. In the case of **1a,b**, 1,4-dihydroxybenzene, and 1,4-diaminobenzene, the solvation factor is apparently stronger, because positive shifts are observed. With aniline and benzene, the two forces balance each other out in water, because almost no shift is observed. However, with 1,2-dihydroxybenzene, 1,2-diaminobenzene, and phenol, host–guest interactions are more important than the hydrophilic/hydrophobic state of the binding site, because negative potential shifts are observed.

Why are there these differences between the donor-substituted guests? Although we have framed the argument that host–guest interaction considerations should favor binding to the oxidized host for donor guests, there are also interactions with the reduced biradical host, and it would seem that differences in these interactions must explain the differences between the donor guests. The general trend that the 1,4-isomers bind more strongly than the 1,2-isomers is even more pronounced in the reduced state, resulting in negative potential shifts for the ortho guests. One possible explaination for this is that the delocalized radical interacts more favorably with the less polarized, more polarizable π-system of the completely symmetric para isomers. It is perhaps significant that the different potential shifts of the 1,4-oxygen-

(18) Miller, S. R.; Gustowski, D. A.; Chen, Z.-H.; Gokel, G. W.; Echegoyen, L.; Kaifer, A. E. *Anal. Chem.* 1988, *60*, 2021.

substituted guests, **1a,b** and 1,4-dihydroxybenzene, appear to be due almost entirely to differences in K_{ox}. The π-systems of all three guests should have similar electronic structures, and this results in K_{red}'s that are identical within experimental error.

CONCLUSIONS

The data presented in this paper clearly demonstrate the significant role solvent plays in redox-dependent binding. Changes in both magnitude and direction of potential shift are observed with VH and the same guests in water, 10% acetonitrile/water, and acetonitrile. These changes are consistent with increased overall binding in water and with relatively stronger binding to the reduced host in water. The latter observation is most easily explained by the change in hydrophobic/hydrophilic character of the host. The increased hydrophobicity of the reduced host promotes binding of the guest. However, although this factor is clearly very important in determining which oxidation state is preferred, our results also show that it does not overwhelm electron donor—acceptor considerations. The largest potential shifts are observed when both solvation forces and donor—acceptor forces pull in the same direction. When they pull in opposite directions, sometimes the solvation factor wins, and sometimes the donor—acceptor factor wins.

Designing redox-dependent receptors for neutral molecules is inherently a more challenging task than designing receptors for ionic compounds. Since reduction or oxidation typically involves a change in charge, receptors for ionic compounds can rely on the perturbation of a strong electrostatic interaction to alter the binding properties. Receptors for neutral guests must rely on the perturbation of weaker interactions to alter the binding properties. Nevertheless, our work with the viologen host clearly shows that redox-dependent binding with neutral guests is possible. Furthermore, we have now demonstrated three general ways in which binding control can be achieved: (i) by using changes in electron donor—acceptor character, (ii) by perturbation of strong ion—dipole interactions, and (iii) by altering the solvation properties of the binding site. By designing redox-dependent host—guest systems where multiple factors work in the same direction, significant binding differences and large potential shifts should be possible with neutral guests.

Electrocatalytic Oxidation and Amperometric Detection of Aliphatic and Furanic Aldehydes at a Mixed-Valent Ruthenium Oxide–Ruthenium Cyanide Film on Glassy Carbon Electrodes

Tommaso R. I. Cataldi,* Cristiana Campa, and Diego Centonze

Dipartimento di Chimica, Università degli Studi della Basilicata, Via N. Sauro, 85, 85100 Potenza, Italy

The electrocatalytic oxidation and amperometric detection of simple and furanic aldehydes at a mixed-valent ruthenium oxide–ruthenium cyanide (mvRuO–RuCN) modified glassy carbon (GC) electrode is described. The oxoruthenium centers cross-linked with ruthenium cyanide are believed to be the electroactive surface species in acidic media. The capability of mvRuO–RuCN films to catalyze the slow electrode reaction of aldehydic compounds is illustrated in cyclic voltammetry and flowing streams amperometric detection. A sensitive quantitation of aliphatic and furanic aldehydes without the need of derivatization steps was achieved by coupling ion exclusion chromatography (IEC) with electrochemical detection, using the mvRuO–RuCN film electrode. The presence of low $RuCl_3$ and $K_4Ru(CN)_6$ levels in the mobile phase considerably improves the response stability. Of practical importance is that this modified electrode can be used without detrimental effects at a column temperature of 60 °C. At room temperature, the detection limits of aliphatic aldehydes such as acetaldehyde, propionaldehyde, and butyraldehyde in IEC with amperometric detection ($E_{appl} = +1.08$ V vs Ag/AgCl) were 1.0, 0.8, and 0.8 nmol injected (S/N = 3), respectively.

Even though virtually all organic compounds are predicted thermodynamically to be oxidized at potentials available at bare solid electrodes, kinetically inhibited electrochemical processes are very often encountered. Low molecular weight aliphatic aldehydes, inherently difficult to detect due to the lack of a strong chromophore or fluorophore group, are also scarcely electrooxidizable at unmodified glassy carbon (GC) electrodes. Moreover, at a gold electrode, the oxidation strongly depends on pH with an electrochemical process that is particularly effective only in alkaline solutions,[1–3] and though the platinum electrode in acidic solutions has been used, it requires pulsed amperometric detection in order to address surface fouling problems.[4] Therefore, the most commonly used method for aldehydes determination is through derivatization with 2,4-dinitrophenylhydrazine and subsequent liquid chromatographic separation with ultraviolet photometric detection.[5–7]

A simple and sensitive analytical method, avoiding the need for troublesome derivatization reactions, is still a major research goal for aliphatic aldehydes quantitation with constant-potential electrochemical (EC) detection. An interesting strategy for their amperometric monitoring in flowing solutions is to employ modified electrodes with a catalytically active surface. One of the most promising and valuable methods of electrode modification uses electropolymerization to produce an adherent, conducting, and electroactive film.[8] Kulesza[9] showed that coatings of mixed-valent ruthenium oxide cross-linked with ruthenium cyanide (mvRuO–RuCN) exhibit considerable electrocatalytic activity in the oxidation of methanol. This inorganic film is believed to contain mixtures of oxo- and cyano-bridged ruthenium centers in mixed oxidation states.[10–13] Kulesza et al.[14] later described a composite film of cobalt tetra(p-tolyl)porphyrin and mvRuO–RuCN, which shows good electrocatalytic activity toward propionaldehyde. As we have demonstrated previously, the mvRuO–RuCN sensing electrode can be used as an electrocatalytic amperometric sensor in liquid chromatography and flow injection analysis of primary aliphatic alcohols in acidic media.[15] The modified electrode surface exhibited excellent stability under vigorous hydrodynamic conditions, provided that low levels of the electroplating solution were present in the mobile phase.[16] This operation mode provides great potential for amperometric monitoring of flowing streams, even if relatively high analyte concentrations are injected.[17]

In this work, the action of the mvRuO–RuCN is further pursued for the detection of simple aliphatic aldehydes and furanic compounds such as 2-furaldehyde (2-F), 5-(hydroxymethyl)-2-furaldehyde (5-HMF), and 5-methyl-2-furaldehyde (5-MF). These

(1) Sibille, S.; Moiroux, J.; Marot, J.-C.; Deycard, S. *J. Electroanal. Chem.* **1978**, *88*, 105.
(2) Vitt, J. E.; Larew, L. A.; Johnson, D. C. *Electroanalysis* **1990**, *2*, 21.
(3) Olivi, P.; Bulhões, L. O. S.; Beden, B.; Hahn, F.; Leger, J.-M.; Lamy, C. *J. Electroanal. Chem.* **1992**, *330*, 583.
(4) Rocklin, R. D. In *Formaldehyde: Analytical Chemistry and Toxicology*; Turoski, V., Ed.; Advances in Chemistry Series 210; American Chemical Society: Washington, DC, 1985; Chapter 2, p 13.
(5) Grosjean, D.; Fung, K. *Anal. Chem.* **1982**, *54*, 1221.
(6) Takami, K.; Kuwata, K.; Sugimae, A.; Nakamoto, M. *Anal. Chem.* **1985**, *57*, 243.
(7) Ogawa, I.; Fritz, J. S. *J. Chromatogr.* **1985**, *329*, 81.
(8) Murray, R. W. In *Molecular Design of Electrode Surfaces*; Murray, R. W., Ed.; Techniques of Chemistry Series XXII; John Wiley & Sons, Inc.: Chichester, UK, 1992.
(9) Kulesza, P. J. *J. Electroanal. Chem.* **1987**, *220*, 295.
(10) Cox, J. A.; Kulesza, P. J. *Anal. Chem.* **1984**, *56*, 1021.
(11) Cox, J. A.; Gray, T. *Electroanalysis* **1990**, *2*, 107.
(12) Cox, J. A.; Jaworski, R. K.; Kulesza, P. J. *Electroanalysis* **1991**, *3*, 869.
(13) Kulesza, P. J.; Bandoch, M. *J. Electroanal. Chem.* **1992**, *323*, 131.
(14) Kulesza, P. J.; Mlodnicka, T.; Haber, J. *J. Electroanal. Chem.* **1988**, *257*, 167.
(15) Cataldi, T. R. I.; Centonze, D.; Guerrieri, A. *Anal. Chem.* **1995**, *67*, 101.
(16) Cataldi, T. R. I.; Centonze, D.; Desimoni, E.; Forastiero, V. *Anal. Chim. Acta* **1995**, *310*, 257.
(17) Cataldi, T. R. I.; Centonze, D.; Desimoni, E. *Food Chem.*, in press.

latter substances are relevant compounds in food control and processing.[18-22] For most practical applications, furanic aldehydes can be conveniently detected by liquid chromatography at 280 nm. The electrochemical oxidation of these solutes, as well as aliphatic aldehydes, at carbon electrodes is very poor. Therefore, the scope of their inclusion in this work was to verify the electrochemical capability of mvRuO—RuCN-modified electrodes to promote the oxidation of a wider range of scarcely electroactive aldehydic compounds.

EXPERIMENTAL SECTION

Reagents and Samples. Acetaldehyde (99%), propionaldehyde (97%), isobutyraldehyde (99+%), butyraldehyde (99%), valeraldehyde (97%), 5-methylfurfural (99%), 2-furaldehyde (99%), 5-(hydroxymethyl)furfural (99%), ruthenium(III) chloride hydrate, and potassium hexacyanoruthenate(II) hydrate (Aldrich Chemical Co.) were used as received. Other chemicals employed were of analytical grade and were used without further purification. Solutions were prepared in deionized and doubly distilled water.

Electrode Modification. Several conducting substrates such as Pt, Au, and glassy carbon (GC) can be coated with mvRuO-RuCN inorganic films in mineral acid solutions without the need for alkali metal ions.[15] GC electrodes were always employed throughout this work. Before each modification, the electrode surface was wet polished with 0.05 μm α-alumina powder, rinsed with a stream of deionized water, and sonicated for a few minutes. Electrochemical deposition can be easily accomplished in a solution containing 0.5–2 mM $RuCl_3$ and $K_4Ru(CN)_6$ in dilute H_2SO_4 (e.g., 10–25 mM), either by holding a polished GC electrode at a constant potential of 1.05 V or by cycling the potential between −0.2 and 1.1 V vs SCE. Figure 1 shows a set of cyclic voltammograms (CVs) obtained when the GC electrode was cycled continuously at 50 mV s^{-1}. The CVs are characteristic of accumulating electroactive species on the electrode surface with increasing surface coverage with time. The modification procedure was effected in freshly prepared and not deaereated solutions. Film deposition by controlled potential consistently yields results similar to those obtained from films prepared by potential cycling.

Apparatus. Cyclic voltammetry was performed with an Amel Instruments (Milan, Italy) Model System 5000, equipped with a Linseis $X-Y$ recorder, Model LY 18100. Electrochemical experiments were made at room temperature using a conventional single-compartment glass cell. The GC disk electrode (3-mm diameter) used in cyclic voltammetry was purchased from Amel, Model 493. Amperometric detection was performed with an EG&G Princeton Applied Research (PAR) Model 400 electrochemical detector and a flow-through thin-layer electrochemical cell with a single GC working electrode (MP 1305) modified with mvRuO—RuCN films, a Ag/AgCl reference electrode, and a stainless steel auxiliary electrode. The detector time constant was set at 1 s. The output signal was recorded on an $X-t$ Amel Model 868 recorder. All measurements were performed by applying the desired operating potential and allowing the transient current to decay before the amperometric monitoring.
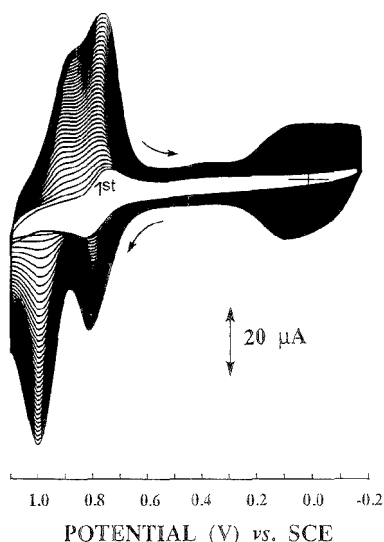
(18) Jeuring, H. P.; Kuppers, F. J. E. M. *J. Assoc. Off. Anal. Chem.* **1980**, *63*, 1215.
(19) Porretta, S.; Sandei, L. *Food Chem.* **1991**, *39*, 51.
(20) Kim, H.-J.; Richardson, M. *J. Chromatogr.* **1992**, *593*, 153.
(21) Blanco Gomis, D.; Gutiérrez Alvarez, M. D.; Sopeña Naredo, L.; Mangas Alonso, J. J. *Chromatographia* **1991**, *32*, 45.
(22) Villalón Mir, M.; Quesada Granados, J.; López G.; De La Serrana, H.; López Martínez, M. C. *J. Liq. Chromatogr.* **1992**, *15*, 513.

Figure 1. CVs recorded continuously at a glassy carbon electrode (12.5 mm^2) between −0.2 and 1.1 V vs SCE in 25 mM H_2SO_4 solution containing 1 mM $RuCl_3$ and 1 mM $K_4Ru(CN)_6$. Scan rate, 50 mV s^{-1}.

The chromatographic system consisted of a Hewlett Packard 1050 pump equipped with an on-line degasser system and a Rheodyne (Berkeley, CA) Model 7125 injector. A Timberline Instruments Inc. Model H-500 (Boulder, CO) was used as column heater. Chromatographic separations were effected with an Aminex HPX-87-H (Bio-Rad Labs, Richmond, CA) cation-exchange resin column, 300 mm × 7.8 mm i.d. (9-μm particle size), using diluted solutions of H_2SO_4 as the eluent spiked with low concentrations of $RuCl_3$ and $K_4Ru(CN)_6$.

RESULTS AND DISCUSSION

The deposit of mvRuO—RuCN on GC electrodes is attributed to the growth of a compact and conducting film with extended Ru—O—Ru and Ru—CN—Ru bridging in the structure. Indeed, it seems that the growth of ruthenium-containing inorganic films is propitiated by the ability of Ru to form oxo and cyano bridges in acidic media.[23] This modified electrode prepared in dilute sulfuric acid solutions exhibits three well-defined redox transitions (see Figure 1) with anodic peak potentials at +0.05, +0.78, and +1.00 V vs SCE, which probably correspond to Ru(II/III)—oxo, cyanoruthenate(II/III), and Ru(III/IV)—oxo centers, respectively.[9] Similar electrochemical behavior was observed in buffered solutions at pH 2.[9,11] In particular, the more positive oxidation peak was assigned to ruthenium species in the ruthenium oxide portion of the inorganic film, and the involvement of these species in several oxygen-transfer oxidations of organic compounds was suggested.[12-14]

Electrocatalytic Oxidation of Aliphatic and Furanic Aldehydes. To assess the potential electrocatalytic activity of this electroactive inorganic film toward the oxidation of aldehydic compounds, the voltammetric behavior was initially investigated.

(23) Cotton, F. A.; Wilkinson, G. *Advanced Inorganic Chemistry*, 5th ed.; John Wiley & Sons Inc.: New York, 1988; pp 878–890, 253–255.
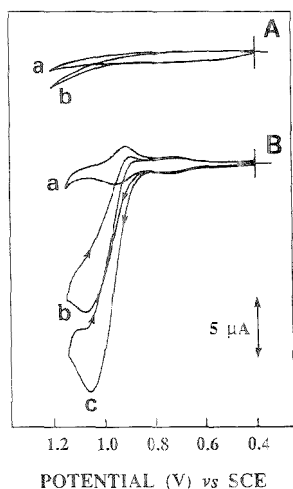
Figure 2. (A) CVs at a bare GC electrode between +0.4 and +1.20 V (a) in the blank supporting electrolyte, 25 mM H_2SO_4, and (b) upon addition of 0.93 M propionaldehyde. (B) Electrocatalytic oxidation at a GC/mvRuO−RuCN film electrode (0.4−1.15 V) in the absence (a) and the presence of (b) 5 and (c) 10 mM propionaldehyde. Scan rate, 2 mV s^{-1}.

Figure 3. (A) CVs at a bare GC electrode between +0.4 and +1.10 V (a) in the blank supporting electrolyte, 25 mM H_3PO_4, and (b) upon the addition of 2 mM 2-furaldehyde. (B) Electrocatalytic oxidation at a GC/mvRuO−RuCN film electrode in the absence (a) and the presence of (b) 1 and (c) 2 mM 2-furaldehyde. Scan rate, 5 mV s^{-1}.

Figure 2B shows typical cyclic voltammograms (CVs) obtained with a GC/mvRuO−RuCN-modified electrode and recorded at 2 mV s^{-1} in a 25 mM H_2SO_4 solution containing 5 and 10 mM propionaldehyde (curves b and c, respectively). Curve a was recorded in the blank supporting electrolyte. Acetaldehyde and butyraldehyde exhibited similar qualitative voltammetric behavior. Under identical conditions, aldehydes are not effectively oxidized at bare GC electrodes and require much higher concentrations to produce an observable voltammetric response. Curve b in Figure 2A was obtained at a GC electrode in the presence of 0.93 M propionaldehyde. Formaldehyde and longer chain aliphatic aldehydes were not examined because reagent grade solutions of the former contain an elevated percentage of methanol as a preservative, while the latter are sparingly soluble in aqueous solutions. Upon propionaldehyde additions, the catalytic oxidation is evidenced by a strong enhancement of the anodic current that increases on increasing propionaldehyde concentration (voltammograms b and c). This behavior implies a catalytic mechanism that involves the cycling of the catalyst between oxidation states. The anodic peak potential in the presence of propionaldehyde occurs at about +1.05 V, a value that is more positive (about 80−100 mV) than the third anodic peak of the mvRuO−RuCN film electrode. At higher scan rates, the CVs exhibited drawn out oxidation waves instead of peak-shaped profiles, likely due to kinetic limitations of the electrocatalytic process.

It has been shown that the mvRuO−RuCN film electrode exhibits better activity and above all good stability in a moderately acid environment.[13] For most of the experiments, a 10 or 25 mM H_2SO_4 solution was used as supporting electrolyte/mobile phase (see next section). However, the effect of some mineral acid solutions in the pH range 1.5−2.5 was also evaluated. Apparently, the electrochemical behavior of the mvRuO−RuCN film electrode and the catalytic oxidation of aldehydic compounds is similar in
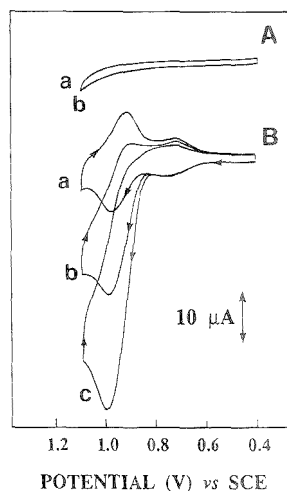
dilute solutions of H_2SO_4, H_3PO_4, HCl, and $HClO_4$. Indeed, the overvoltage for the oxidation process is also much lower for furanic aldehydes. Figure 3 displays CVs recorded at 5 mV s^{-1} in 25 mM H_3PO_4 for 2-furaldehyde at the mvRuO−RuCN-modified electrode (B) and at an unmodified GC electrode (A). As mentioned earlier, also in this case, no oxidation peak was observed at the bare GC electrode (curves a and b in Figure 3A are indistinguishable). On the contrary, curves b and c of Figure 3B, which refer to cyclic voltammograms obtained upon the addition of 1.0 and 2.0 mM 2-furaldehyde, respectively, exhibit a large increase in the anodic current with peak potential at +1.0 V. The catalytic oxidation currents observed were proportional to the concentration of 2-furaldehyde. It follows that also in this case the inorganic film participates catalytically within the oxidation mechanism. Apparently, the electrocatalytic oxidation occurs through the high-valent oxoruthenium species formed in the potential region of the third oxidation wave of the modified electrode. As outlined earlier in the oxidation of aliphatic alcohols,[15] the specific catalytic activity of the mvRuO−RuCN-modified electrode is presumably related to the formation of oxoruthenium(IV) or higher oxidation states of ruthenium. Very recently, Ru(VI) has also been suggested as the active oxidant in the catalytic process at the modified electrode surface.[24]

Electrochemical Detection in Flow-Through Analysis of Aldehydic Compounds. On the basis of the voltammetric results, an electrocatalytic sensor seems very attractive for greatly enhancing the amperometric detection of underivatized aliphatic aldehydes. However, before we illustrate the applications of the mvRuO−RuCN film electrode in chromatographic separations with EC detection, some features of the flow injection response will be given. Hydrodynamic voltammetry under flowing stream operations, which possesses a much higher current sensitivity

---

(24) Gorski, G.; Cox, J. A. *Anal. Chem.* **1994**, *66*, 2771.
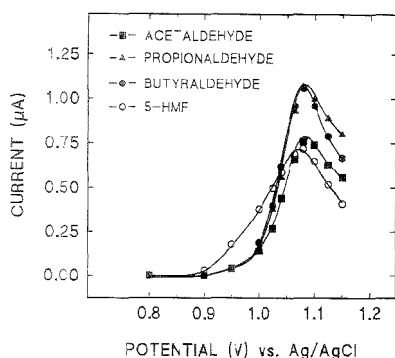
Figure 4. Hydrodynamic voltammograms of 2.0 mM acetaldehyde, 2.4 mM propionaldehyde, 2.0 mM butyraldehyde, and 0.3 mM 5-HMF in ion exclusion chromatography at a GC/mvRuO$-$RuCN-modified electrode. Column, Aminex HPX-87-H, 300 mm × 7.8 mm i.d.; isocratic elution at room temperature with 10 mM H$_2$SO$_4$ containing 5 μM RuCl$_3$ and 5 μM K$_4$Ru(CN)$_6$; flow rate, 0.8 mL min^{-1}; loop, 20 μL; thin-layer electrochemical cell. The mvRUO-RuCN film was grown at constant applied potential for 15 min in a solution containing 1 mM RuCl$_3$ and 1 mM K$_4$Ru(CN)$_6$ in 25 mM sulfuric acid.
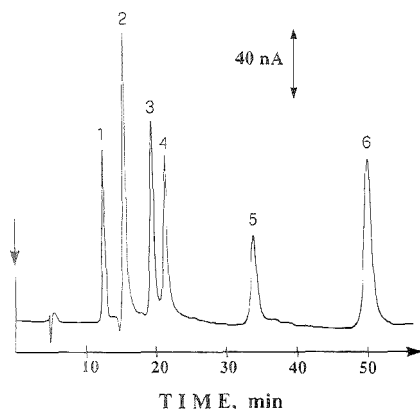
Figure 5. Ion exclusion chromatographic separation with EC detection of aliphatic aldehydes at a mvRuO$-$RuCN CME. Detection potential, $+$1.08 V vs Ag/AgCl; loop, 50 μL. Sample solution injected: (1) 18 nmol of acetaldehyde, (2) 21 nmol of propionaldehyde, (3) 15 nmol of isobutyraldehyde, (4) 14 nmol of butyraldehyde, (5) 10 nmol of valeraldehyde, and (6) 0.75 nmol of 2-F. Temperature, ambient; column back pressure, 814 psi. Other conditions as in Figure 4.

than CV, was used to characterize the electrochemical oxidation of simple aldehydes. The GC/mvRuO$-$RuCN film electrode in a thin-layer electrochemical cell maintained its catalytic stability under constant-potential operation. The repeatability of response, expressed as the relative standard deviation (RSD) of the peak height for a set of 20 consecutive injections using a test solution containing 20 nmol (2 mM × 10 μL) of acetaldehyde, was about ±0.8% at an applied potential of $+$1.08 V, indicating good short-term stability. The examination of the peak profile in flow injection yielded a throughput of ~40 injections/h at a flow rate of 1.0 mL min^{-1}. Very recently, it was successfully demonstrated that the presence of low concentrations of the electroplating mixture in
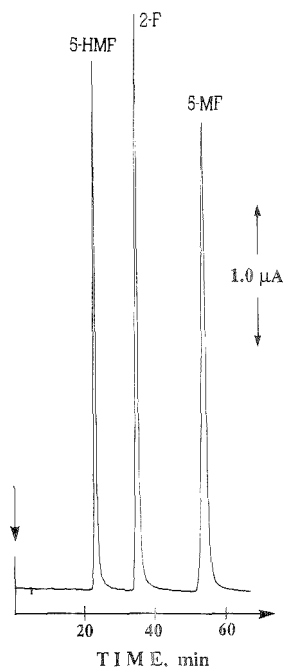
Figure 6. Chromatographic separation and amperometric detection of furanic aldehydes at a mvRuO$-$RuCN CME. Sample mixture injected: 26 nmol of 5-HMF, 24 nmol of 2-F, and 26 nmol of 5-MF. Detection potential, $+$1.05 V; column temperature, 60 °C; back pressure, 520 psi; loop, 20 μL. Other experimental conditions were the same as those described in Figure 5.

the carrier streams provides a constant response to ethanol injections over an 8-h working time when the mvRuO$-$RuCN film on the GC electrode is continuously used as amperometric sensor.[16] Consequently, also in this case, a carrier electrolyte of 25 mM H$_2$SO$_4$ containing RuCl$_3$ and K$_4$Ru(CN)$_6$ at equimolar low levels (i.e., 5 μM) was delivered through the electrochemical cell.

Figure 4 shows the hydrodynamic voltammograms (HDVs) obtained for acetaldehyde, propionaldehyde, butyraldehyde, and 5-HMF by liquid chromatographic amperometric detection with the mvRuO$-$RuCN-modified electrode. The experiments were performed with an Aminex HPX-87-H ion exclusion column in the H$^+$ form using 10 mM H$_2$SO$_4$ spiked with RuCl$_3$ and K$_4$Ru(CN)$_6$ at equimolar concentrations (5 μM) as the mobile phase. After each change in applied potential, 5$-$15 min of stabilization time was allowed prior to injection of the sample. Each point in the hydrodynamic voltammetric curves represents an average of two or three separate injections. The mvRuO$-$RuCN-modified electrode exhibited a peak-shaped HDV, with a maximum response at 1.07$-$1.08 V vs Ag/AgCl for all aliphatic and furanic aldehydes examined. The data were collected over a period of about 9 h with the flow rate set at 0.8 mL/min. These findings demonstrate that the mvRuO$-$RuCN-modified electrode is suitable for amperometric detection of aldehydic compounds. Moreover, the stability of response was greatly improved with the use of an appropriate mobile phase/supporting electrolyte. While the ion exclusion column imposes the use of dilute solutions of sulfuric

Table 1. Quantitative Parameters of Aldehydic Compounds in IEC[a] with Amperometric Detection at a GC/ mvRuO–RuCN Film Electrode Evaluated at Different Temperatures

| compound | capacity factor (k') | i (μA) $= a + bc$ (mM)[b] | | r^c | LOD[d] (nmol) |
		$b \pm t_{95}s_b$	$a \pm t_{95}s_a$		
		$T = 22 \pm 2$ °C			
acetaldehyde	1.55	0.20 ± 0.01	0.03 ± 0.05	0.9983	1.0
propionaldehyde	2.18	0.25 ± 0.01	0.05 ± 0.05	0.9979	0.8
isobutyraldehyde	2.98	0.35 ± 0.03	0.05 ± 0.07	0.9973	0.8
butyraldehyde	3.39	0.32 ± 0.03	0.04 ± 0.07	0.9961	0.8
valeraldehyde	5.80	0.24 ± 0.02	0.01 ± 0.03	0.9982	1.1
2-furaldehyde	9.20	6.91 ± 0.06	0.01 ± 0.01	0.9999	0.05
		$T = 60 \pm 1$ °C			
acetaldehyde	1.71	0.20 ± 0.01	0.01 ± 0.02	0.9998	1.6
propionaldehyde	2.37	0.20 ± 0.01	0.04 ± 0.02	0.9994	1.5
isobutyraldehyde	3.17	0.32 ± 0.01	0.01 ± 0.03	0.9994	1.6
butyraldehyde	3.48	0.33 ± 0.02	-0.00 ± 0.04	0.9989	1.6
valeraldehyde	5.53	0.23 ± 0.01	0.00 ± 0.01	0.9996	2.0
2-furaldehyde	6.03	8.2 ± 0.1	-0.01 ± 0.01	0.9999	0.04

[a] Column, Aminex HPX-87-H, 300 mm $\times$ 7.8 mm i.d.; eluent, 10 mM H_2SO_4, 5 μM RuCl$_3$, and 5 μM K$_4$Ru(CN)$_6$; flow rate, 0.8 mL min^{-1}; loop, 50 μL; thin-layer electrochemical cell with a GC/mvRuO–RuCN CME; applied potential, +1.08 V as Ag/AgCl; the same deposit was used at room temperature and at 60 °C. The mvRuO–RuCN film was grown electrochemically for 15 min at +1.05 V vs SCE in 25 mM H_2SO_4 solution containing 1 mM RuCl$_3$ and 1 mM K$_4$Ru(CN)$_6$. [b] Regression lines calculated by linear least-squares analysis using six or seven data points spaced over the linear range; t is taken at the 95% confidence level. [c] Correlation coefficient. [d] Limit of detection determined for S/N = 3 from the lowest injected concentration.

acid as the mobile phase, the electrode stability of the ruthenium-based electrode was considerably enhanced in the presence of micromolar concentrations of the electroplating salts. It is noteworthy that low Ru(III) and Ru(CN)$_6^{4-}$ levels in the mobile phase did not influence the retention of compounds and, above all, column selectivity and lifetime. Indeed, no detrimental effects on the column's performance were observed even after intensive use lasting about 3 months. For example, no differences were observed in the retention times, capacity factors, and selectivity of aliphatic aldehydes during the operations with this mobile phase. The presence of RuCl$_3$ do not affect the column's performance probably because, as mentioned earlier, the moderately acid media tend to form and stabilize ruthenium oxo species.[23]

A valuable technique for the separation of undissociated compounds such as weak acids, alcohols, aldehydes, ect. is through ion-exclusion chromatography (IEC) using a cation-exchange resin in the H$^+$ form with an acidic eluent.[25,26] The application of the ruthenium-based electrode as an amperometric sensor in IEC with EC detection of aliphatic aldehydes is illustrated in Figure 5. The chromatogram was obtained for a sample mixture containing acetaldehyde, propionaldehyde, isobutyraldehyde, butyraldehyde, valeraldehyde, and 2-furaldehyde. Taking into account the HDVs, an operating potential of +1.08 V was applied. The capacity factors (k') and limits of detection (LOD) are summarized in Table 1. Linear plots of peak current vs concentration were obtained for concentrations up to 5–10 mM. The LODs of aliphatic aldehydes, evaluated at room temperature as the concentration that yields a signal 3 times the background noise from the lowest injected concentration, range from 0.8 to 1.1 nmol. The linear dynamic ranges, expressed as the ratio of the upper limits and the LODs, span 2–3 orders of magnitude. The correlation coefficients (r) of linear least-squares fitting of the calibration curves were in the range of 0.9973–0.9999. As

may be seen from the chromatogram, the peaks are fairly symmetric in shape with an asymmetry value of 1.20, 1.15, and 1.22 estimated for isobutyraldehyde, valeraldehyde, and 2-furaldehyde, respectively. When 10 mM H_3PO_4 was used as mobile phase, a pronounced tailed response was observed for all compounds.

Effect of Column Temperature. The effect of temperature on the column separation and amperometric detection was evaluated by performing determinations of aliphatic and furanic aldehydes at 60 °C. The retention times of furanic compounds are greatly influenced by column temperature; thus, the next step was to verify whether the mvRuO–RuCN-modified electrode may be influenced by higher temperatures compared to room temperature. A chromatographic separation, carried out at the column temperature of 60 °C for a sample mixture containing 5-HMF, 2-F, and 5-MF, is shown in Figure 6. Increasing column temperature is accompanied by a noticeable decrease in retention times of furanic aldehydes, while aliphatic aldehydes are much less influenced by temperature changes (see Table 1). The capacity factors evaluated for 5-HMF, 2-F, and 5-MF were respectively 5.2, 9.2, and 14.4 at room temperature and 3.9, 6.0, and 9.7 at 60 °C. Accordingly, the increase in temperature also has an impact on peak resolution by increasing the number of theoretical plates. For example, the number of plates ($\pm$SD) evaluated at the two temperatures were 4900 ± 300 and 7800 ± 500, at 22 and 60 °C, respectively. These data compared very well with those reported by Pecina et al.[25]

A systematic investigation of the ruthenium oxide-based modified electrode at 60 °C column temperature was made. Temperature does not have a significant effect on sensor response, as shown by the data in Table 1. The slopes of the calibration graphs were almost unchanged for aliphatic aldehydes, but the background noise increased by a factor of 3, i.e., 5 nA compared to 1.8 nA at 22 °C. Therefore, the S/N ratio decreased, leading to slightly higher LODs for the aldehydes tested. It is worthwhile mentioning that the same deposit was used for both runs, at 22 and 60 °C, on two consecutive days. Finally, the stability of the

(25) Pecina, R.; Bonn, G.; Burtscher, E.; Bobleter, O. *J. Chromatogr.* **1984**, *287*, 245.
(26) Fritz, J. S. *J. Chromatogr.* **1991**, *546*, 111.

mvRuO−RuCN was also evaluated at 60 °C. A series of four repeated chromatographic injections of a furanic aldehyde mixture (1.2 mM) yielded RSDs of 1.7%, 1.5%, and 2.1% for 2-F, 5-HMF, and 5-MF, respectively. These data were collected during a 4 h time, with the last injection producing peak heights almost identical to those exhibited by the first injection.

CONCLUSIONS

The present study demonstrates that a chemically modified electrode based on the mvRuO−RuCN inorganic film is capable of electrocatalytically oxidizing aliphatic and furanic aldehydes in acidic media. This modified electrode surface can be used as an amperometric sensor in flow-through analysis of aldehydic compounds with excellent sensitivity. It should be emphasized that not only does this modified electrode provide a simple and sensitive sensor for aliphatic aldehydes, but also column temperature can be employed to some extent for controlling the selectivity in ion exclusion chromatographic separations. The reliability and stability of mvRuO−RuCN films offer a valid alternative to UV or fluorescence detection of aliphatic aldehydes, where derivatization steps are needed.

Dual-Analyte Fiber-Optic Sensor for the Simultaneous and Continuous Measurement of Glucose and Oxygen

Lin Li and David R. Walt*

Max Tishler Laboratory for Organic Chemistry, Department of Chemistry, Tufts University, Medford, Massachusetts 02155

A fiber-optic sensor for the continuous and simultaneous determination of glucose and oxygen is described. The sensor is comprised of dual-analyte sensing sites in defined positions on the distal end of an imaging fiber (350 μm o.d.). Each sensing site is an individual polymer cone covalently attached to the activated fiber surface using localized photopolymerization. The oxygen sensor consists of a double-layer polymer cone. The inner polymer cone is a hydrophobic gas-permeable copolymer containing an oxygen-sensitive ruthenium dye, and the outer layer is a poly(hydroxyethyl methacrylate) (HEMA) polymer. The glucose sensor is an oxygen sensor with a poly-HEMA outer layer containing immobilized glucose oxidase. The fluorescence images of both sensing sites are captured with a CCD camera, and the measured fluorescence intensities are related to analyte concentrations. Oxygen quenching data for both sensing sites fit a two-site Stern–Volmer quenching model. The sensor has been used to simultaneously monitor independent changes in glucose and oxygen concentrations. Glucose calibration curves were obtained under varying oxygen tensions, and the detection limit is 0.6 mM glucose. The effect of fluctuations in oxygen partial pressure on the glucose response can be used to calibrate the sensor. The sensor response time varies from 9 to 28 s, depending on the different thicknesses of the enzyme layer. The sensor maintains the same sensitivity for 2 days. Multiple glucose sensing sites with different enzymatic activities can be immobilized on the distal end of the fiber, affording control of the linear range.

Glucose biosensors have been utilized widely in clinical analysis, biomedical research, and biotechnology.[1–5] In most cases, the sensing scheme is based on the enzymatic oxidation of glucose by glucose oxidase. Glucose can be monitored by analyzing either the reaction products or the oxygen consumption. The response of these sensors depends on the local oxygen concentration, which limits their application. For example, in neurochemical applications, fluctuations in sensor response can

be caused by changes in oxygen tension during synaptic events.[6] In addition, the sensor's in vivo performance can be affected by the availability of local oxygen, which varies due to the uneven distribution of oxygen within the tissue and the degree of tissue damage caused by sensor implantation.[7,8]

Oxygen-independent glucose biosensors have been developed in order to overcome these problems. Glucose enzyme electrodes have been described which use mediators or redox polymers instead of oxygen to transfer electrons between the reduced enzyme and an electrode surface.[9–12] Such sensors are much less sensitive to oxygen, but the oxygen dependence has not been eliminated completely. An alternative approach is to employ glucose sensors in which a constant oxygen supply is provided internally. A glucose microsensor has been fabricated by locating the sensing surface in an oxygenated microenvironment; therefore, the glucose measurement is independent of the oxygen concentration in the sample.[13] Other newly designed glucose sensors are based on an unlimited oxygen supply from the atmosphere.[5,14] Many of these sensors are not optimal for either in vivo or in vitro glucose monitoring due to incompatible sensor sizes or complicated configurations. For some applications, the concentration of oxygen must be known in order to understand biological events involving glucose.[15,16]

We have developed a novel technique for fabricating compact multianalyte fiber-optic chemical sensors.[17–19] Multiple analyte sensing sites are placed in precise positions using localized photopolymerization of appropriate dye indicators or enzymes on the distal end of an optical imaging fiber. The changes in the optical properties at each site are transmitted through an imaging fiber through distinct optical pathways and simultaneously moni-

(1) Michael, A. C.; Justice, J., Jr. Anal. Chem. 1987, 59, 405–410.
(2) Dermal, B. A. A.; Il, S.-Y.; Schmid, R. D. Biosens. Bioelectron. 1992, 7, 133–139.
(3) Bindra, D. S.; Zhang, Y. N.; Wilson, G. S.; Sternberg, R.; Thevenot, D. R.; Moatti, D.; Reach, G. Anal. Chem. 1991, 63, 1692–1696.
(4) Amine, A.; Patriarche, G. J.; Marrazza, G.; Mascini, M. Anal. Chim. Acta 1991, 242, 91–98.
(5) Rishpon, J.; Shabtai, Y.; Rosen, I.; Zibenberg, Y.; Tor, R.; Freeman, A. Biotechnol. Bioeng. 1990, 35, 103–107.

(6) Zimmerman, J. B.; Wightman, R. M. Anal. Chem. 1991, 63, 24–28.
(7) Zhang, Y.; Wilson, G. S. Anal. Chim. Acta 1993, 281, 513–520.
(8) Brunstein, E.; Abel, P.; Gens, A.; Eich, K.; Woedtke, T. V. Biomed. Biochim. Acta 1989, 48, 911–917.
(9) Cass, A. E. G.; Davis, G.; Francis, G. D.; Hill, H. A. O.; Aston, W. J.; Higgins, I. J.; Plotkin, E. V.; Scott, L. D. L.; Turner, A. P. F. Anal. Chem. 1984, 56, 667–671.
(10) Yokoyama, K.; Tamiya, E.; Karube, I. Anal. Lett. 1989, 22, 2949–2959.
(11) Gregg, B. A.; Heller, A. Anal. Chem. 1990, 62, 258–263.
(12) Pishko, M. V.; Michael, A. C.; Heller, A. Anal. Chem. 1991, 63, 2268–2272.
(13) Cronenberg, C.; Groen, B. V.; Beer, D. D.; Heuvel, H. V. D. Anal. Chim. Acta 1991, 242, 275–278.
(14) Kusano, H. Clin. Phys. Physiol. Meas. 1989, 10, 1–9.
(15) Casciari, J. J.; Sotirchos, S. V.; Sutherland, R. M. J. Cell. Physiol. 1992, 151, 386–394.
(16) Zinker, D.; Namdaran, K.; Wilson, R.; Dracy, D.; Lacy, D.; Wassaerman, D. Diabetes 1993, 42, A44.
(17) Barnard, S. M.; Walt, D. R. Nature 1991, 353, 338–340.
(18) Walt, D. R.; Agayn, V.; Bronk, K.; Branard, S. Appl. Biochem. Biotechnol. 1993, 41, 129–137.
(19) Bronk, K. S.; Walt, D. R. Anal. Chem. 1994, 66, 3519–3520.

tored with a charged-coupled device (CCD) camera. This strategy is used here to develop a dual-analyte fiber-optic sensor for glucose and oxygen. The oxygen sensing site consists of an oxygen-sensitive ruthenium complex in a hydrophobic gas-permeable copolymer on the distal end of an imaging fiber. The glucose sensing site is composed of a second oxygen sensing polymer cone coated with poly(hydroxyethyl methacrylate) (HEMA) containing immobilized glucose oxidase. The concentrations of glucose and oxygen are proportional to the changes in the fluorescence intensities of the ruthenium complex at each sensing site. The response characteristics of this dual-analyte sensor for glucose and oxygen are presented.

EXPERIMENTAL SECTION

Materials. Tris(2,2'-bipyridyl (bpy))ruthenium(II) chloride, tris(phenanthroline (phen))ruthenium(II) chloride, benzoin ethyl ether (BEE), and α-D-glucose were all purchased from Aldrich Chemical Co. (Milwaukee, WI). Glucose oxidase (β-D-Glucose, oxygen 1-oxidoreductase; EC 1.1.3.4) (162 units/mg type VII, *Aspergillus niger*) and fumed silica (0.014 μm o.d.) were obtained from Sigma Chemical Co. (St. Louis, MO). (Acryloxy)propylmethylsiloxane (15–20%) and dimethylsiloxane (80–85%) copolymer (ps802) were obtained from Gelest, Inc. (Tullytown, PA). Ethylene glycol dimethacrylate (EGDMA) and 2-hydroxyethyl methacrylate (HEMA) were obtained from Polysciences Inc. (Warrington, PA). Ru(4,7-diphenyl(Ph)-1,10-phen)₃(Cl)₂ was synthesized and purified as described previously.[20] All the other reagents were used as received. Oxygen and nitrogen were purchased from Northeast Airgas, Inc. (Salem, NH). Solutions of varying oxygen tension were prepared by bubbling 0.1 M pH 7.4 phosphate buffers with appropriate gas for at least 15 min. All reagent solutions were prepared with distilled, deionized water purified with a Barnstead Nanopure system. Glucose solutions were prepared in 0.1 M pH 7.4 phosphate buffer and stored in the refrigerator for 24 h before use to allow equilibration between α-D-glucose and β-D-glucose.

The immobilization of Ru(bpy)₃²⁺ or Ru(phen)₃²⁺ on fumed silica (0.014 μm o.d.) was done as follows. Initially, 30 mg of Ru(II) dye was added to 60 mg/mL fumed silica/methylene chloride solution. The solution was stirred overnight to adsorb the Ru(II) complex on silica. The silica particles containing Ru(II) dye were washed with 150 mL of methanol and dried in an oven at 135 °C. The Ru(II)/silica particles were stored in the dark at room temperature.

The single-core step-index hard clad silica (HCS) fibers (750 μm o.d., 550 μm i.d.) were purchased from Ensign-Bickford Optics Co. (Avon, CT). Silica imaging fibers with an outer core diameter of 350 μm, containing 6000 sensing elements, were purchased from Sumitomo Electric U.S.A., Inc. (Torrance, CA). All fibers were polished before use on lapping films purchased from General Fiber Optics, Inc. (Fairfield, NJ).

Fabrication of Oxygen Sensor. An oxygen sensor was prepared by immobilizing an oxygen-sensitive Ru(II) complex in a gas-permeable siloxane polymer on the distal end of a single-core silica fiber using photopolymerization. These sensors were used to examine the optimal experimental conditions. The photopolymerization approaches and procedures have been described previously.[21] The oxygen-sensitive copolymer solution was

prepared by dissolving 30 mg of BEE in 0.25 mL of methylene chloride solution containing varying amounts of Ru(II) complex and 0.5 mL of ps802 siloxane copolymer.

Fabrication of Glucose and Oxygen Sensing Arrays. The imaging fiber was silanized in a 10% (v/v) 3-(trimethoxysilyl)propyl methacrylate/acetone solution to activate the fiber surface before use. The instrumentation of the photodeposition system has been detailed previously.[19] Briefly, the oxygen sensing cone was formed at a precise location on the distal end of the fiber by site-selectively photopolymerizing the oxygen-sensitive poly(dimethylsiloxane) copolymer. The copolymer solution was prepared as described above with 1 mg/mL Ru(Ph₂phen)₃²⁺/methylene chloride stock solution. Excitation light (wavelength, 350 ± 80 nm) from a xenon–mercury arc lamp was focused through a 400 μm diameter pinhole and a 15× reflective objective onto the proximal end of the fiber. The light was transmitted to the other end of the fiber in a 27 μm diameter circular area of the fiber. An electronic shutter was used to control the light illumination time on the fiber surface. The distal end of the fiber was dipped into the oxygen-sensitive polymer solution and removed, leaving a drop on the surface. The electronic shutter was then opened for 3 s to initiate photopolymerization on the fiber surface. The oxygen sensing polymer cone was formed only at the illuminated area. The distal end of the fiber was rinsed with ethanol to remove excess monomer solution. After polymerization was complete, the fiber was repositioned for a subsequent polymerization. Four siloxane polymer cones were photodeposited on the distal end.

The glucose sensing cone was prepared by depositing HEMA polymer containing glucose oxidase on the surface of the oxygen-sensitive siloxane polymer cone. The immobilization of glucose oxidase in HEMA polymer was unsuccessful when the enzyme was dissolved in an aqueous HEMA polymerization solution. Therefore, the following procedure was used, which was found to be effective for enzyme immobilization in poly-HEMA.[22] Glucose oxidase (2 mg) was suspended in 0.5 mL of a 10% dextran solution and lyophilized. The dry particles of lyophilized enzyme were stored in a desiccator at 5 °C. The lyophilized glucose oxidase was suspended in 0.5 mL of a HEMA polymerization solution containing 4% EGDMA cross-linker and 30 mg of BEE photoinitiator. Since photopolymerization is inhibited by oxygen, the solution was deoxygenated by bubbling with nitrogen for 15 min before use. A 100 μL aliquot of this monomer solution containing glucose oxidase was first illuminated for 60 s with 366 nm light to form a viscous oligomer. The distal end of the fiber was then immersed in this oligomer solution. A pinhole with a diameter of 800 μm (giving a focused spot with a diameter of 54 μm) was used to allow enough light to illuminate the entire oxygen polymer sensing cone. The fiber was illuminated for 15 s, and glucose oxidase-containing HEMA was polymerized on the surface of the oxygen cone. The distal end of the fiber was rinsed with ethanol until the excess monomer solution was washed off the fiber. Generally, 30 s illumination is required to deposit a HEMA polymer on the imaging fiber without the prepolymerization step. The purpose of prepolymerizing the HEMA monomer solution before photodeposition is to minimize the light exposure time of the oxygen sensing cone, since the Ru(II) dye is photolabile.

The second glucose sensing polymer cone was deposited using the same procedure as the first one but with a 14 s illumination time on the fiber surface. The remaining two oxygen sensing

(20) Watts, R. J.; Crosby, G. A. *J. Am. Chem. Soc.* **1971**, 93, 3184–3188.
(21) Barnard, S. M. Ph.D. Thesis, Tufts University, Medford, MA, 1992.

(22) Healey, B. G.; Walt, D. R., Tufts University, unpublished results.
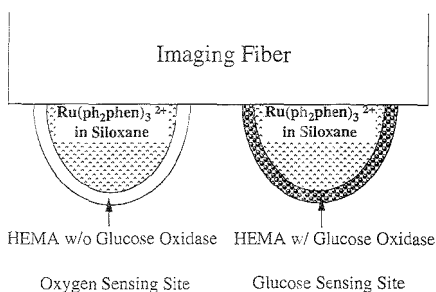
Figure 1. Schematic showing the cross-sectional view of the glucose and oxygen sensing sites.

cones were coated with a HEMA polymer without glucose oxidase using the same procedure as that used for the first glucose sensing cone. The extra layer of HEMA hydrogel provides better resiliency than ps802 siloxane polymer. All the sensors were soaked in pH 7.4 phosphate buffer for 2 h before use. Figure 1 shows schematically the cross section of oxygen and glucose sensing sites on the distal end of an imaging fiber.

Sensor Response Measurements. The oxygen sensor response on the single-core HCS silica fiber was monitored on a double-monochromator fluorescence system.[23] The excitation wavelength was 480 nm, and the emission wavelengths were 590, 600, and 610 for $Ru(bpy)_3^{2+}$, $Ru(phen)_3^{2+}$, and $Ru(Ph_2phen)_3^{2+}$, respectively. The sensor response at different oxygen concentrations was monitored until steady-state signals were obtained.

The imaging sensor response was measured with use of a modified fluorescence microscope. The instrumentation has been described elsewhere.[19] The distal end of the fiber was immersed in an appropriate test solution, and the images of the distal end of the optical fibers were captured by a CCD camera. The excitation and emission filters were 470 ± 35 and ≥ 600 nm, respectively. The fluorescence intensities at the sensing cones were obtained as a function of time by analyzing the captured images using appropriate imaging processing software (IPlab, Signal Analytics, Vienna, VA). The fluorescence intensities of sensing cones reported at different analyte concentrations were steady-state signals. For the stability experiment, the sensor was stored in pH 7.4 phosphate buffer in the dark at 4 °C overnight.

RESULTS AND DISCUSSION

The placement of both glucose and oxygen sensors on the same optical fiber provides this biosensor array with the ability to measure both enzyme substrates simultaneously. Therefore, variations in oxygen do not compromise sensor performance. Sensor preparation involves a photopolymerization technique. First, oxygen-sensitive sensors are deposited in a hydrophobic siloxane polymer. Next, an enzyme-containing hydrogel layer is photodeposited on top of some of the oxygen sensors. The resulting sensors are ~50 μm in diameter. The ability to precisely control the position and architecture of each sensing layer provides an entry into a wide range of sensor and biosensor arrays.

Oxygen Sensor. The oxygen sensitivity of each polymer sensing cone directly influences the performance of the dual-

(23) Walt, D. R.; Gabor, G.; Goyet, C. *Anal. Chim. Acta* **1993**, *274*, 47–52.

analyte sensor. Several key parameters have been investigated to optimize the response properties of oxygen sensors based on fluorescence quenching of Ru(II) complexes under our experimental conditions. These parameters include the polymer support, the coordinating ligands (L) of the $Ru^{II}(L)_3$ complex, the photopolymerization time, and the amount of dye in the polymer matrix.

The magnitude of the oxygen sensor response in pH 7.4 phosphate buffer was dependent on the photopolymerization time. By increasing the photopolymerization time from 5 to 10 s, a 50% decrease in the sensor fluorescence intensities was observed (data not shown). Ru(II) complexes in siloxane polymers decompose upon irradiation with visible or UV light. Therefore, increasing the light exposure time of the Ru(II) complex during sensor fabrication caused more decomposition and diminished the fluorescence intensity. A photopolymerization time of 3 s was used for oxygen sensor fabrication.

The dye loading in the siloxane polymer also influenced the magnitude of the sensor response and its sensitivity. The fluorescence signal of the oxygen sensor increased with increasing concentrations of Ru(II) complex in the siloxane monomer solution. However, more dye did not produce better sensitivity. The optimal dye loading for the highest sensitivity was as follows: $Ru(bpy)_3^{2+}$–silica/siloxane of 20 mg/mL, $Ru(phen)_3^{2+}$–silica/siloxane of 32 mg/mL, and $Ru(Ph_2phen)_3^{2+}$/siloxane of 0.33 mg/mL in the siloxane copolymer solutions. Further increases in the dye concentration resulted in larger background signals and lower sensitivity. Immobilization of the Ru(II) complex on silica resulted in a heterogeneous medium for oxygen quenching, and a linear Stern–Volmer plot was obtained. $Ru(Ph_2phen)_3^{2+}$ was not adsorbed on silica due to the limited amount of this commercially unavailable dye.

The influences of polymer supports and coordinating ligands on the quenching of Ru(II) complexes by oxygen have been studied in detail by Demas et al.[24,25] Under the present experimental conditions, the best oxygen-sensitive dye for the sensor was found to be $Ru(Ph_2phen)_3^{2+}$ in the ps802 siloxane polymer. $Ru(Ph_2phen)_3^{2+}$ has the longest excited-state lifetime and the largest solution Stern–Volmer quenching constant. The oxygen sensor based on this complex is extremely sensitive to oxygen.[24] Figure 2 shows that this dye is 4 times more sensitive than either $Ru(bpy)_3^{2+}$ or $Ru(phen)_3^{2+}$. The sensitivity observed here is lower than that reported by Demas. The loss of sensitivity is caused mainly by the polymer used and photolysis of the Ru(II) complex during sensor fabrication. As a result, $Ru(Ph_2phen)_3^{2+}$ was used exclusively to prepare all the sensors described below.

Glucose and Oxygen Sensing Array. Figure 3 shows the fluorescence image of a four-spot sensor captured in a pH 7.4 air-saturated phosphate buffer. Spots 1 and 2 are glucose sensitive; spots 3 and 4 are oxygen sensitive only. Glucose sensing cone 1 was prepared with a longer photopolymerization time than that for cone 2, resulting in a larger polymer cone and thus more glucose oxidase immobilized in the polymer matrix. At the oxygen sensing sites, the Ru(II) complex fluorescence intensity is related to both the oxygen concentration in the sample solution
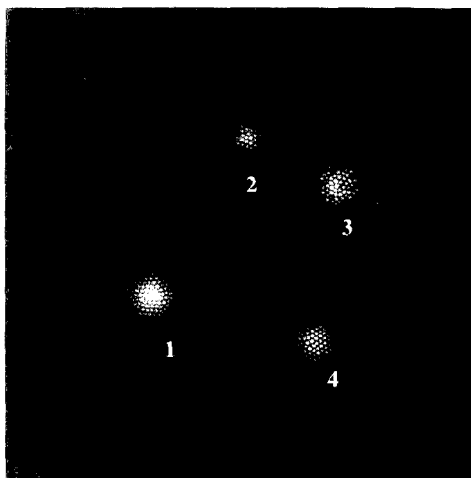
(24) Bacon, J. R.; Demas, J. N. *Anal. Chem.* **1987**, *59*, 2780–2785.
(25) Xu, W.; McDonough, R. C.; Langsdorf, B.; Demas, J. N.; DeGraff, B. A. *Anal. Chem.* **1994**, *66*, 4133–4141.
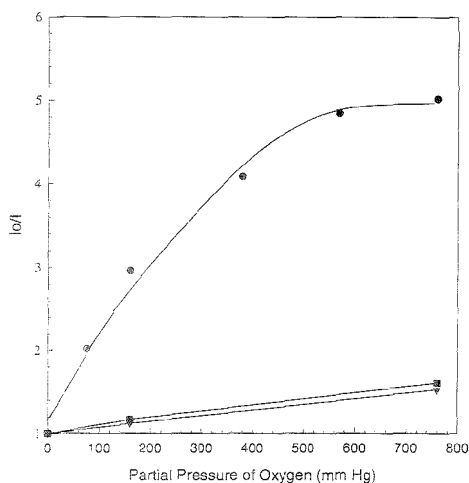
Figure 2. Stern—Volmer plots of oxygen sensors with Ru(bpy)$_3^{2+}$ — silica/siloxane of 20 mg/mL (▼), Ru(phen)$_3^{2+}$—silica/siloxane of 32 mg/mL (■), and Ru(Ph$_2$phen)$_3^{2+}$/siloxane of 0.33 mg/mL (●).

Figure 3. Fluorescence image of a four-spot fiber-optic sensor in pH 7.4 phosphate buffer. Spots 1 and 2 are glucose sensitive, and spots 3 and 4 are oxygen sensitive only.

and the diffusion of oxygen within the polymer. At the glucose sensing sites, glucose oxidation is catalyzed by glucose oxidase within the HEMA polymer layer as glucose diffuses into the polymer matrix. Catalysis causes depletion of oxygen in the HEMA polymer, leading to depletion in the inner siloxane cone, resulting in a fluorescence intensity increase. The changes in fluorescence intensity are related to both glucose and oxygen concentrations in the sample solution and the diffusion of both glucose and oxygen in the polymers. Since oxygen fluctuations in the sample solution can be monitored by analyzing the fluorescence intensity at the oxygen sensing site, the oxygen effect on the glucose sensor can be determined on the basis of the
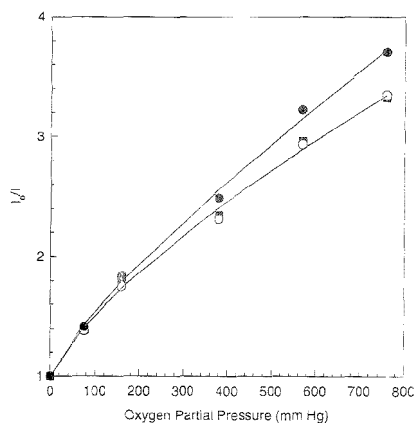
Figure 4. Oxygen quenching of Ru(Ph$_2$phen)$_3^{2+}$ in oxygen sensing cone 4 (■) and glucose sensing cones 1 (○) and 2 (●). The simulated curves (—) for oxygen cone 4 and glucose cone 1 and for glucose cone 2 were generated using the two-site Stern—Volmer quenching model. For oxygen cone 4 and glucose cone 1, $f_{01} = 0.47$, $f_{02} = 0.53$, $K_{sv1} = 0.0133$, and $K_{sv2} = 0.0014$. For glucose cone 2, $f_{01} = 0.51$, $f_{02} = 0.49$, $K_{sv1} = 0.0131$, and $K_{sv2} = 0.0016$.

measured oxygen concentrations in the sample solution. The concentrations of oxygen and glucose, therefore, can be monitored simultaneously.

Figure 4 shows the oxygen quenching data for one oxygen (spot 4) and two glucose (spots 1 and 2) sensing cones. The nonlinear curves suggest multiple quenching sites within the polymer matrix having different sensitivities to oxygen quenching.[25] Spots 1 and 4 were prepared under exactly the same conditions, and the oxygen sensitivities of both the glucose and oxygen sensing sites are virtually identical. Spot 2 was prepared using a shorter photopolymerization time. It is more sensitive to oxygen since the oxygen-sensitive dye within the polymer matrix was exposed to less light during polymerization.

A two-site Stern—Volmer quenching model was used to fit the oxygen quenching data (eq 1):[24]

$$I_o/I = 1/(f_{01}/(1 + K_{sv1}[O_2]) + f_{02}/(1 + K_{sv2}[O_2])) \quad (1)$$

where I is the fluorescence intensity at an oxygen concentration of $[O_2]$, I_o is the value in the absence of quencher oxygen, f_{0j} is the fraction of quenching site j contributing to the unquenched intensity I, and the K_{svj} values are the Stern—Volmer quenching constants at quenching site j.[24] Figure 4 presents the best-fitting curves, with $f_{01} = 0.47 \pm 0.03$, $K_{sv1} = 0.013 \pm 0.015$ mmHg^{-1}, $f_{02} = 0.53 \pm 0.03$, and $K_{sv2} = 0.0014 \pm 0.0009$ mmHg^{-1} for glucose cone 1 and oxygen cone 4, and $f_{01} = 0.51 \pm 0.39$, $K_{sv1} = 0.013 \pm 0.016$ mmHg^{-1}, $f_{02} = 0.49 \pm 0.04$, and $K_{sv2} = 0.0016 \pm 0.0013$ mmHg^{-1} for glucose cone 2.

In order to examine the effect of oxygen on the glucose sensor response, glucose responses were measured under different oxygen tensions with the dual-analyte sensor. The fluorescence intensities (I) at glucose or oxygen sensing sites for different concentrations of glucose and oxygen were measured, and I_o/I values were calculated. With each value of I_o/I, the corresponding quencher oxygen concentration was calculated by solving the
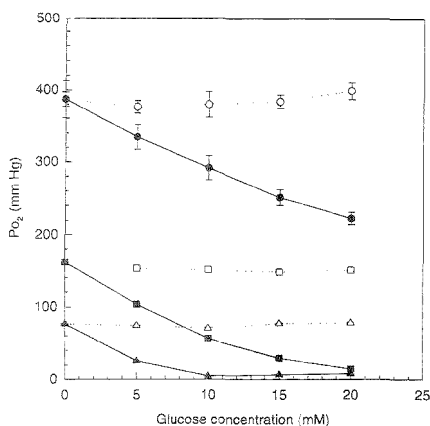
Figure 5. Dual-analyte sensor responses to oxygen (open symbols) and glucose (solid symbols) with oxygen partial pressures of 76 (triangles), 159.6 (squares), and 380 (circles) mmHg.
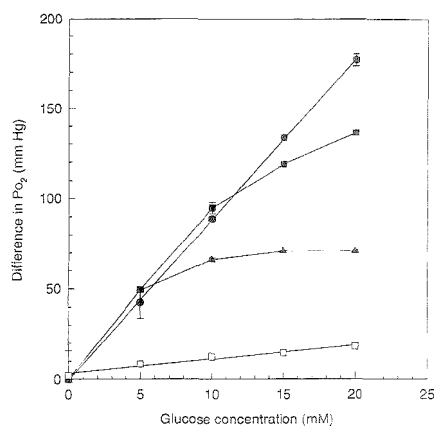
Figure 6. Glucose calibration curves at oxygen pressures of 76 (▲), 159.6 (■), and 380 (●) mmHg for glucose cone 1 and 159.6 mmHg (□) for glucose cone 2.

following quadratic equation derived from eq 1:

$$(I_o/I)^{-1}K_{sv1}K_{sv2}[O_2]^2 + \{(I_o/I)^{-1}K_{sv1} + (I_o/I)^{-1}K_{sv2} - f_{01}K_{sv2} - f_{02}K_{sv1}\}[O_2] - (I_o/I)^{-1} - f_{01} - f_{02} = 0 \quad (2)$$

Since the concentration of oxygen in the polymer matrix was unknown, the partial pressure of oxygen in the gas used to saturate the calibrated buffer was applied in the above equations. Figure 5 presents glucose response curves of a glucose-sensitive polymer matrix (spot 1) and an oxygen-sensitive polymer matrix (spot 4) under varying oxygen tensions.

At a fixed oxygen concentration, the response of the oxygen sensor is virtually constant with increasing glucose concentration, while the response at the glucose sensor decreases due to consumption of oxygen during glucose oxidation. The difference (ΔP_{O_2}) between the oxygen concentrations in the medium and in the glucose-sensitive polymer matrix corresponds to the glucose concentration. From Figure 5, the oxygen concentration within the glucose sensing cone drops to almost zero at a glucose concentration of 10 mM, and further increases in glucose concentration do not affect the glucose sensor response at an oxygen tension of 76 mmHg. This result indicates that oxygen depletion inside the glucose sensing cone is complete at glucose concentrations ≥10 mM. Similarly, oxygen depletion is complete at glucose concentrations ≥20 mM at an oxygen tension of 159 mmHg. Thus, the dynamic range of the sensor can be extended by increasing the oxygen partial pressure.

Calibration curves of glucose were made by plotting ΔP_{O_2} versus glucose concentration (see Figure 6). For glucose sensing cone 1, a linear calibration curve is obtained with an oxygen partial pressure of 380 mmHg over the entire glucose concentration range of 0–20 mM. However, calibration curves at lower oxygen tensions are somewhat downward curved at high glucose concentrations, due to depletion of oxygen within the glucose sensing cone, as discussed above. The slopes of the calibration curves over the linear ranges for three different oxygen tensions are almost the same, indicating that sensitivity to glucose is

independent of the oxygen concentration outside the sensing layer. As can be seen in Figure 6, the linear ranges of the glucose calibration curves increase with increasing oxygen partial pressures. The detection limit (DL) is estimated to be 0.6 mM (S/N = 3) for glucose sensing cone 1.

The glucose response can be altered by changing the amount of glucose oxidase immobilized in the HEMA matrix. Figure 6 shows a glucose calibration curve at an oxygen partial pressure of 159.6 mmHg for glucose sensing cone 2. Compared to glucose cone 1, glucose cone 2 is less sensitive (DL, 1.5 mM) because less enzyme was immobilized. Although the sensitivity of this sensor is lower, it possesses a wider dynamic range due to less oxygen depletion at a given glucose concentration. Glucose cone 2 afforded a linear glucose response curve over the glucose concentration range of 0–20 mM. This result indicates that the dynamic range of glucose response can be increased by using a lower enzyme loading. With an imaging fiber, multiple glucose sensing sites with different enzymatic activities can be placed on a single fiber surface. The sensitivity and dynamic range at a particular glucose sensing site varies according to its enzymatic activity. Therefore, any desired dynamic range of glucose response can be obtained by photodepositing the appropriate amount of glucose oxidase.

The dual-analyte sensor has been used to predict glucose concentrations under different oxygen pressures. The fluorescence images of glucose and oxygen sensing polymer cones were collected with sample solutions containing different concentrations of glucose and oxygen. The steady-state fluorescence intensities were measured and converted to corresponding P_{O_2} on the basis of the two-site quenching model. Glucose concentrations were predicted using the calibration curves of ΔP_{O_2} versus glucose concentration. Figure 7 shows the plot of the predicted glucose concentration versus the actual glucose concentration. The excellent correlation proves the utility of the sensor calibration scheme.

The sensor was also tested for its response to interfering substances usually found in biological samples, such as ascorbic acid (AA), uric acid, and acetaminophen. These three compounds are known to be major interferents in electrochemical measure-
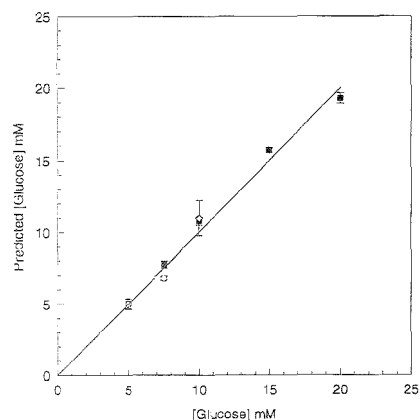
Figure 7. Predicted concentrations of glucose at oxygen tensions of 159.6 (O), 380 (■), and 570 mmHg (◊) versus actual glucose concentrations.
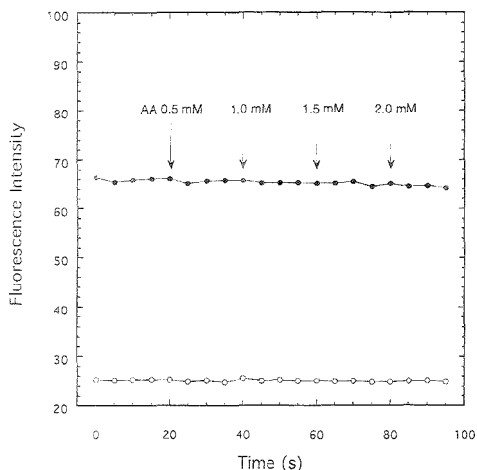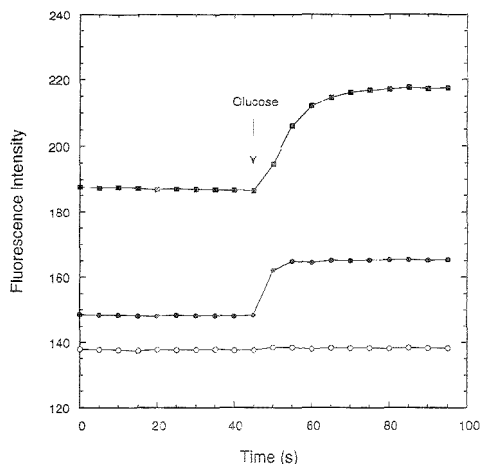

Figure 8. Glucose (●) and oxygen (O) sensor responses to 50 mM glucose with AA concentrations of 0.5–2.0 mM. Arrow indicates the injection of AA.
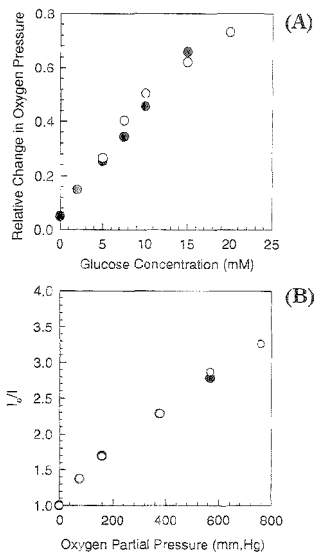

Figure 9. Response time curves for glucose sensors with thicker (■) and thinner (●) poly-HEMA layers and oxygen (O) sensing polymer matrices. The arrow indicates the injection of glucose (50 mM).

Figure 10. Stability of the dual-analyte sensor. (A) Stern–Volmer plots for oxygen sensing polymer matrix on the first (O) and second (●) days. (B) Glucose calibration curves for glucose sensing polymer matrix on the first (O) and second (●) days.

ments of glucose because they are oxidized at the same potential as hydrogen peroxide. Our experimental results indicate that both saturated uric acid and acetaminophen solutions do not interfere with glucose and oxygen responses (data not shown). In biological samples, extracellular AA concentrations vary between 100 and 500 μM.[26,27] The sensor's response to 50 mM glucose was measured at AA concentrations within this range. No significant interference on either oxygen or glucose sensors was observed with AA concentrations up to 2 mM (see Figure 8). Therefore, the sensor is applicable to biological measurements. AA samples with much larger concentrations were found to influence responses of both oxygen and glucose sensors because AA can be

oxidized spontaneously in aqueous solution by either oxygen or hydrogen peroxide (data not shown).[28-30]

Sensor response times and stability were also examined. Figure 9 shows the dynamic response curves of glucose monitored by injecting 0.5 mL of 1.0 M glucose solution into 5 mL of pH 7.4

(26) Grunewald, R. A.; O'Neil, R. D.; Fillenz, M.; Albery, W. J. *J. Neurochem. Int.* **1983**, *5*, 773–778.
(27) Grunewald, R. A. *Brain Res. Rev.* **1993**, *18*, 123–133.

(28) Hughes, D. E. *Anal. Chem.* **1985**, *57*, 555–558.
(29) Mushran, S. P.; Agrawal, M. C. *J. Sci. Ind. Res.* **1977**, *36*, 274–283.
(30) Lowry, J. P.; O'Neil, R. D. *Anal. Chem.* **1992**, *64*, 456–459.

phosphate buffer. The sensor response time increases with the thickness of the enzymatic polymer layer. The glucose sensor with a thicker glucose oxidase-containing poly-HEMA layer has a response time (time required to reach 95% of the steady state signal) of 28.3 ± 1.7 s (three measurements), and the sensor with a thinner layer has a response time of 8.8 ± 1.3 s (four measurements). The sensor recovery time is ~1 min (data not shown). Figure 10A shows the response to oxygen, and Figure 10B shows the glucose calibration curves for a sensor on two consecutive days. The fluorescence intensity at each sensing site decreases when the sensor is exposed to excitation light because the Ru(II) complex photodecomposes. However, the results in Figure 10 indicate that the sensitivity of this dual-analyte sensor to both oxygen and glucose is maintained over 2 days.

CONCLUSIONS

The dual-analyte sensor reported here is capable of simultaneously and continuously monitoring glucose and oxygen. Glucose concentrations can be monitored precisely under unknown oxygen concentrations by calibrating the fluctuations resulting from oxygen. Since the images are captured by a CCD camera, both quantitative information and spatial distribution of substrates are obtained simultaneously. In addition, a sensor with a wide dynamic range can be obtained by photodepositing multiple sensing sites with varying enzymatic activities. This compact dual-analyte sensor (350 μm o.d.) has a fast response time (<30 s) and is relatively stable. The sensor may be suitable for both in vivo and in vitro measurements of simultaneous changes in both glucose and oxygen in biological samples. The sensing system can be generalized for other biologically important compounds catalyzed by oxidase-type enzymes.

Identification of Plastics among Nonplastics in Mixed Waste by Remote Sensing Near-Infrared Imaging Spectroscopy. 1. Image Improvement and Analysis by Singular Value Decomposition

W. H. A. M. van den Broek, D. Wienke, W. J. Meissen, C. W. A. de Crom, and L. Buydens*

Catholic University of Nijmegen, Laboratory for Analytical Chemistry, Toernooiveld 1, NL-6525 ED Nijmegen, The Netherlands

A near-IR camera has been installed in an experimental setup for real-time plastic identification. Singular value decomposition (SVD) has been used for qualitative analysis and substantial improvement of the measured multivariate images. The obtained score plots provided spatial correlations between different pixel structures caused by sample material on the one hand and image artifacts on the other. In this way, the score plots have been used as a tool to optimize the experimental setup and image quality. The improved images were offered to a new classification algorithm called multivariate image rank analysis, based on SVD, as described in part 2 of this series of articles, which follows in this issue (Wienke, D.; et al. *Anal. Chem.* 1995, *67*, 3760).

There are several ways for postconsumer plastics to reach their final destiny. In the past, landfilling was a common way to dump plastics waste. Now, product recycling, material recycling, thermal recycling, and chemical recycling are among the methods to reuse plastics. However, for each of these methods, it would be better to sort the plastics before further processing.[1-3] Presently, the University of Nijmegen, The Netherlands, and the Institute for Chemical and Biochemical Sensor Research, Münster, Germany, are investigating the possibility for sorting plastics on the basis of their chemical–physical properties.[4] One part of the project involves the discrimination of plastics from nonplastics by means of infrared imaging spectroscopy. More about near-IR imaging can be found in refs 12–14. The principle of discrimination lies in the differences of absorption spectra in particular wavelength regions for plastics and nonplastics. Therefore, a set or stack of images are measured at specific wavelength regions ("multivariate image"). These regions need to be chosen in a way to give maximum discrimination. An additional aspect of the technique is that all measurements need to be recorded in real-time remote sensing to be independent of size, position, shape, and movement of the waste sample on a conveyor belt. Another advantage of the use of a camera lies in the ability to obtain geometric information about the samples. This is conserved in the local pixel correlation in the image. In this way, sample composition can be used as an additional sorting criterion in recycling. The developed

experimental setup should be able to detect single macroscopic plastic samples on a conveyor belt. Further, it should be able to discriminate these from nonplastic waste samples. To extract the important information from the images, multivariate statistical methods will be used. The aim of this paper is to check whether it is possible to remove or separate artifacts, such as background, noise, shadow, specular reflections, and spikes, from the important material information in the image. This can be achieved in two ways: by optimizing the hardware and by applying multivariate statistics. An experimental design and singular value decomposition (SVD) will be applied to optimize the sample-to-background signal ratio and to remove or minimize artifacts such as shadow and specular reflection. The significantly improved images will be classified with a new technique, multivariate image rank analysis (MIRA). This classifier must be seen as a mathematical method that is able to extract sufficient information from the stack of images that it can determine whether the sample is a plastic material or not.[5] Because software solutions are very (computation) time consuming, optimization of the hardware was given higher priority. A high-quality image will facilitate the future material identification.

THEORY

Image Correction. Infrared images, obtained with an optical infrared camera, can be described mathematically by two-dimensional light intensity functions, $F(x,y)$, where x and y represent respectively the x and y coordinates in a two-dimensional plane, and F represents the chromatic notion of intensity called brightness or, equivalently, the gray level of the image at a particular point (x,y).[6] The intensity is caused by infrared light reflected from the image plane, and it is related to the physical–chemical property of absorption measured from the considered samples and background material. The more a material in the image plane can absorb, the higher its brightness within $F(x,y)$. Since the images need to be processed and analyzed by a computer, they need to be discretized. A discretized image can be considered as a matrix, expressed as I, with n image rows and m image columns. The content of the elements i (referred to as pixels) of the matrix $I_{r,m}$ represents the gray level. For example, the detector of the camera used in the described experiments has a matrix size of 64×64 pixels and a 10 bits

(1) Menges, G. *Gummi, Fasern, Kunstst.* 1993, *46* (2), 62–68.
(2) Brandrup, J. *Gummi, Fasern, Kunstst.* 1993, *46* (9), 732–738.
(3) Wagemann, K. *Nachr. Chem., Tech. Lab.* 1994, *42* (1), 28–34.
(4) Huth-Fehre, T.; Feldhoff, R.; Kantimm, T.; Quick, I.; Winter, F.; Cammann, K.; van den Broek, W.; Wienke, D.; Meissen, W.; Buydens, L. *J. Mol. Struct.* 1995, *348*, 143–146.

(5) Wienke, D.; Broek van den, W.; Meissen, W.; Buydens, L. *Anal. Chem.* 1995, *67*, 3760–3766.
(6) Gonzalez, R. C.; Woods, R. E. *Digital Image Processing*; Addison-Wesley: Reading, MA, 1992

(1024) gray level representation. Every single detector element can measure the reflection at a certain area in the image plane. The whole matrix of 64 × 64 pixels can measure the reflection enclosed by the image plane. Measuring the images at p different wavelengths results in a three-dimensional stack of images, expressed by a boldface, underlined, capitalized letter, $\underline{\mathbf{X}}_{64,64,p}$. Wavelengths can be chosen by interference filters or, more advanced, by an acoustic optical tunable filter (AOTF).[7] In order to compare the images measured at p different variables (wavelengths), these need to be corrected for background and dark current contributions. The raw image, $\mathbf{I}_{raw}$, is the sum of the reflected light from the sample or background and the dark current, $\mathbf{I}_{dark}$. The latter is a contribution of the background signal level of the detector array, caused by always present heat radiation. For example, a dark current level of around 25% of the total dynamic detector range is normal for infrared cameras with semiconductor diode arrays. The absorption spectrum of materials used as image background causes different wavelength-dependent background reflections. Therefore, reference images per filter, $\mathbf{I}_{ref}$, need to be measured. This is done by recording the same scene as in the raw image but without sample. The corrected net images $\mathbf{I}_{n,m}$, which are used for further investigation, can be calculated using

$$\mathbf{I}_{n,m} = \frac{\mathbf{I}_{raw} - \mathbf{I}_{dark}}{\mathbf{I}_{ref} - \mathbf{I}_{dark}} \tag{1}$$

When there is no absorption of the sample, $\mathbf{I}_{raw}$ is about equal to $\mathbf{I}_{ref}$, and thus $\mathbf{I}_{n,m}$ will be equal to ~1. If one desires to measure the sample absorption, the following correction needs to be made:

$$\mathbf{I}_{n,m} = 1 - \frac{\mathbf{I}_{raw} - \mathbf{I}_{dark}}{\mathbf{I}_{ref} - \mathbf{I}_{dark}} = \frac{\mathbf{I}_{ref} - \mathbf{I}_{raw}}{\mathbf{I}_{ref} - \mathbf{I}_{dark}} \tag{2}$$

Image Analysis by Singular Value Decomposition (SVD).
As mentioned in the previous paragraph, the data measured from a single sample are collected as a three-dimensional stack of images $\underline{\mathbf{X}}_{n,m,p}$ at p wavelengths. To facilitate the interpretation of this stack, a decomposition of $\underline{\mathbf{X}}_{n,m,p}$ is proposed. According to Geladi et al.,[8] it is usually necessary for practical reasons to unfold this three-dimensional stack of images into a two-dimensional matrix before decomposition. All images measured at p variables are first unfolded into p vectors having $n \times m$ elements, called objects. These vectors are arranged in a 2D matrix $\mathbf{Z}_{nm,p}$. One method for doing such a decomposition is by a SVD, as given by eq 3, where $\mathbf{Z}_{nm,p}$ is the unfolded stack of images (as explained

$$\mathbf{Z}_{nm,p} = \mathbf{U}_{nm,p}\mathbf{S}_{p,p}\mathbf{V}^{\mathrm{T}}_{p,p} \tag{3}$$

below), $\mathbf{U}_{nm,p}$ and $\mathbf{V}^{\mathrm{T}}_{p,p}$ are orthogonal matrices containing respectively left and right singular vectors, and $\mathbf{S}_{p,p}$ is a diagonal matrix with the corresponding singular values. This method does not require a priori knowledge of a statistical distribution of $\mathbf{Z}$. The $\mathbf{Z}$ matrix can be decomposed into eigenvalues and eigenvectors. The maximum number of eigenvectors that can be obtained mathematically is p (provided that $p \leq \min(p, nm)$, correspond-

ing to the number of variables (wavelengths). However, to reproduce the original data matrix, at least q eigenvectors are needed, with $q \leq p$. This number q is called the rank of the matrix $\mathbf{Z}_{nm,p}$. Because it is not possible to avoid experimental artifacts completely, the remaining $p - q$ eigenvectors will merely account for experimental error, such as nonlinearities of the optical system and inhomogeneous illumination,[11] and will be left out according to eq 4, where $\mathbf{U}_{nm,q}$, $\mathbf{V}_{p,q}$, and $\mathbf{S}_{q,q}$ have reduced dimensions q

$$\mathbf{Z}_{nm,p} = \mathbf{U}_{nm,q}\mathbf{S}_{q,q}\mathbf{V}^{\mathrm{T}}_{q,p} + \mathbf{E}_{nm,p} \tag{4}$$

and $\mathbf{E}_{nm,p}$ is the residual matrix, accounting for the experimental error. Often the right singular vectors are called "loadings" whereas the left singular vectors multiplied with the singular values (US) are called "scores". These scores are equivalent to the ones calculated in principle component analysis (PCA):[9]

$$\mathbf{Z}^{\mathrm{T}}\mathbf{Z} = \mathbf{V}\mathbf{S}^{1/2}\mathbf{V}^{\mathrm{T}} \tag{5}$$

$$\mathbf{Z}\mathbf{Z}^{\mathrm{T}} = \mathbf{U}\mathbf{S}^{1/2}\mathbf{U}^{\mathrm{T}} \tag{6}$$

In imaging, one is mostly interested in the correlation (structure) between the objects or pixels. In the present work, these pixels give information about the material composition of the measured samples. Besides this, information about experimental artifacts can be obtained, too, such as shadow effects, specular reflection, and background inhomogeneity. All these effects form structures in the stack of images. In order to visualize these effects, score plots can be used. A score plot is a graph of two score vectors from the US matrix. It demonstrates the correlation between pixels representing the same material or artifact effects. Here, a score plot is graphically represented by only the vectors in $\mathbf{U}$, since the scaling with $\mathbf{S}$ will not have an effect on the graph. Clusters can be formed only when the information is preserved in the data, which means that the choice of variables is very important for an appropriate cluster discrimination. The inherent power of a score plot is that clusters can be extracted independently and transformed back to the original image space, called reconstructed fractional images (Figure 1). This is done by first selecting the desired cluster with a border line. Only the pixels within the border are used to fill the new score matrix. All other pixel values are set to zero. The new score matrix has to be multiplied with $\mathbf{S}\mathbf{V}^{\mathrm{T}}$ to get a fractional reconstructed image matrix, which is built up only by the pixels belonging to the selected cluster. In this way, underlying pixel correlations in the stack of images can be found which were not detected or were difficult to detect in the original data. Score plots can now be used for qualitative investigation of a large amount of image information.

Criterion for Image Optimization. In order to check whether an image has been improved by practical adaptation of the experimental setup or by software processing, the images need to be evaluated. Since the main goal of the project is to discriminate plastics from nonplastics, an evaluation criterion must be defined which is able to assess the quality of discrimination. We have chosen to use the gray level ratio of the objects in the images. The ratio is calculated in such a way that the numerator

(7) McClure, W. F. *Anal. Chem.* 1994, *66*, 43A–53A.
(8) Geladi, P.; Isaksson, H.; Lindqvist, L.; Wold, S.; Esbensen, K. *Chemom. Intell. Lab. Syst.* 1989, *5*, 209–220.
(9) Faber, N. Contributions to Multivariate Data Analysis in Chemometrics. Ph.D. Thesis, University of Nijmegen, The Netherlands, 1994.
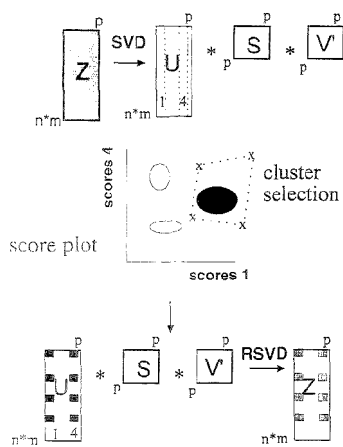
Figure 1. Image information extraction using score plots. A score plot is a graph comprising only two vectors from the **U** matrix. Depending on the problem, a certain combination of vectors may give clustering of the pixels. An arbitrary cluster can be extracted from the plot and projected back to the original image space by a reversed SVD (RSVD). The only pixels shown in the so-called fractional reconstructed image belong to the extracted cluster in the score plot. Note that, for these selected pixels, all their p scores vectors from **U** are used in the RSVD step.

of the ratio is higher than the denominator. This can be achieved by choosing the appropriate filters.[10] Because the whole optimization process will be performed with the same filters, the only differences in ratios can be caused by changes in the experimental setup, such as light source position and light source illumination power, by mirror reflection, or by shadow artifacts.

An easy way to calculate the gray level ratio of the objects in both images is to calculate the norms of both images after eliminating the background contribution. The background has to be eliminated because it can give a large contribution to the norm when a small sample is present in the image. The background noise is eliminated by making all pixel values zero below a certain threshold value. The threshold value has been chosen as 3 times the average standard deviation of the background. Ideally, when no artifacts are present, the only gray levels that remain originate from the sample. The norm of the filtered image is now only calculated from the gray levels of the sample. The evaluation criterion (A) can be calculated by

$$A = \frac{||\text{filtered image at filter 1}||}{||\text{ filtered image at filter 2}||} \quad (7)$$

When there are artifacts present in the image, these will decrease the ratio due to independency of wavelength. Different filters will not affect the artifact contribution. This results in an increasing norm for both images, which will lower the ratio. This can be illustrated when two filter combinations are compared. Suppose filters 1 and 2 have the following norm contributions: 0.400/0.200 = 2.00 au and 10.4/10.2 = 1.02 au, respectively. The absolute differences are 0.2, but a significant difference will be obtained

(10) van den Broek, W.; Wienke, D.; Kraak, A.; Melssen, W.; Buydens, L. *Appl. Spectrosc.*, submitted for publication.

upon calculating the ratios. Artifacts will cause extra contributions to the norm and lower the ratio. The evaluation criterion can be interpreted as finding the highest ratio for the best image quality.

EXPERIMENTAL SECTION

The experimental macro setup for discrimination between plastics and nonplastics is shown schematically in Figure 2. A near-IR camera, provided with a 64×64 pixel focal plane array detector is able to detect spectroscopic information over the wavelength range from 1 to 5.5 μm. Each pixel is a semiconductor device which is able to register incoming photons. Contrary to conventional detector materials,[11-13] the detector used in this experiment was made of InSb (Cincinnati Electronics Inc., Mason, OH). In front of the detector array, inside the camera, a cold shield filter has been positioned to prevent the detector from sensing background light emitted by the optical components. This cold shield filter has to be cooled with N_2. The wavelength range of the cold shield filter has been extended to 1.1−4.6 μm.

Two objective lenses are needed for operation in the whole wavelength range. The first is the original objective lens made from CaF_2, and it has a standard 50 mm EFL $f/2.3$ multiple element lens (Cincinnati Electronics Inc.), which is transparent from 1.8 to 4.6 μm. The second objective lens is made of boron crown glass (BK-7), with a standard 50 mm EFL $f/1.8$ multiple element lens (Pentacon). This objective lens is transparent from 0.3 to 2.7 μm.

The output of the camera is a 12 bit digital data port which is able to send 51.44 frames (complete images) per second. Each pixel exhibits a sensitivity range of 10 bits, resulting in 1024 gray levels. No framegrabber is used since the digital output of the camera is sent indirectly, via an external interface SC-01 (electronic buffer) and a high-speed 16 bit S16D I/O interface (Engineering Design Team, Inc., Beaverton, OR), to the memory of the computer. The computer is a SUN SPARC 10 workstation containing 32 MB RAM. By avoiding a time delaying device such as a framegrabber, the high frame speed of the camera can almost be conserved. This is an important step in real-time measurements. A heat source is used to illuminate the sample with infrared light. The total distance between sample and detector is about 2 m (remote sensing mode), and therefore a powerful light source is required (600−1800 W) to get sufficient photons on the detector for a safe identification of the samples. Because of this, the turning filter wheel has to be positioned between the camera and sample. If placed between sample and light source, the filters would become damaged due to the emitted heat of the light source. However, our implementation involves the problem of refocusing the BK-7 objective lens for each filter because the refraction index of this lens material is wavelength dependent. The filter wheel is prepared for eight filters maximum. At present, six filters can be used which are transparent in the following wavelength regions: 1548−1578, 1545−1655, 1655−1745, 1700−2150, 2207−2321, and 2115−2550 nm, respectively. Several materials have been investigated for background material in the experimental setup. Sanded aluminum gave the highest contrast for macroscopical plastic samples.

(11) Geladi, P.; Grahn, H.; Lindgren, F. In *Chemical Multivariate Image Analysis: Some Case Studies, Applied Multivariate Analysis in SAR and Environmental Studies*; Devilers, J., Karcher, W., Ed.; Kluwer Scientific Publishers: Dordrecht, 1991; pp 447-478.
(12) Robert, P.; Bertrand, D.; Devaux, M. F. *NIR News* **1991**, *2* (2), 9−10.
(13) McClure, W. F. *NIR News* **1991**, *2* (2), 8.
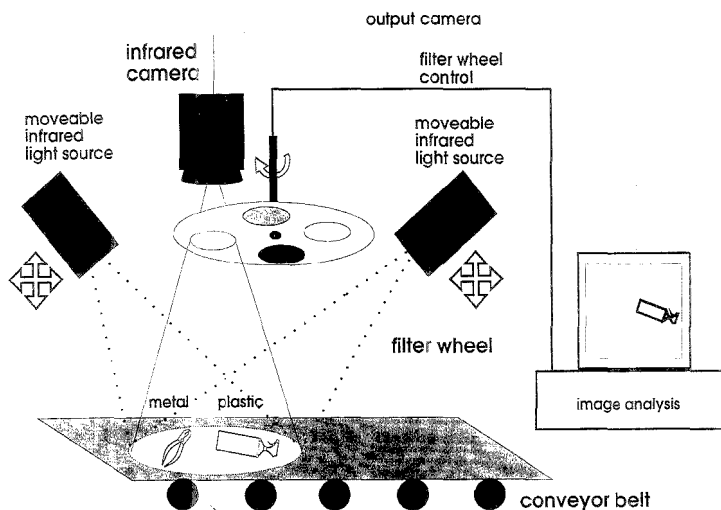
Figure 2. Experimental macro setup for the identification of plastics in mixed waste. Two light sources illuminate the image plane on a conveyor belt. The reflected radiation is passed through interference filters and detected by the IR camera. The plastic samples will show a characteristic reflection spectrum for the irradiated light from the light sources. The output of the camera is recorded and processed by a computer. Only the plastic samples have been made visible on the screen due to different absorption properties of the materials.

SOFTWARE AND COMPUTATIONS

The images can be recorded and processed using the Khoros 1.0 software environment (The Khoros Group, University of New Mexico, Albuquerque, NM), with its accompanying graphical user interface CANTATA. Khoros can be used as a visual programming tool for software development in scientific image visualization. This package entails a library of over 260 routines to facilitate research in image processing, pattern recognition, remote sensing, and machine vision.

Also, a way exists for direct data access using the S16D interface combined with a library of C procedures. The library enables real-time image acquisition by self-written software. The necessary acquisition software and external interface SC-01 were developed and installed by Starling Consultancy (Hengelo, The Netherlands).

The score plot program software was in-house developed using C for a SUN SPARC 10 workstation. Additional XITE software procedures (Torr Lonnestad and Otto Milvang, Image Processing Laboratory, Department of Informatics, University of Oslo, Norway) were included for graphical display of the images. Matlab (The MathWorks, Inc., Natick, MA) was used for further calculations and image representations.

RESULTS AND DISCUSSIONS

First, it was found that the dark current image, I_{dark}, of the camera is about 25% of the total signal, which is too large to ignore. Second, the reference image, I_{ref}, needs to be measured because for three reasons: First, the optical width of the filters are different, so different amounts of light per filter (flux) are falling on the detector. In order to compare samples in different images, there has to be correction for this effect. Second, the light source has a wavelength-dependent emission spectrum in the optical near-IR region. Third, the transmission spectrum of the camera lens is wavelength dependent, too. Therefore, both correction images, I_{dark} and I_{ref}, need to be used in eqs 1 and 2.

The assumption we make in the corrected images is that both the background and the sample material have similar surface scattering properties. Although this will not be the case in all measurements, we found that it did not influence our evaluation criterion, since this entailed the calculation of gray level ratios of the object.

The appropriate choice for the background material can help to maximize the background-to-sample contrast in the image. Geladi et al.[14b] have chosen black velvet because of the low specular reflection. We found that this was not the only variable of influence in our measurements. Also, the gray level contrast needs to be taken into account. Therefore, we have chosen aluminum as background material because it has low absorption coefficients for near-IR radiation. For both filters, the sanded aluminum gave the highest brightness (contrast) after image correction (Table 1). To avoid specular reflection, the aluminum was sanded to give a smooth diffuse reflected near-IR background. After this successful treatment, the only specular reflection found was caused by the samples. Furthermore, we have tried to reduce this disturbing effect by optimizing the light source position, as will be demonstrated in the following section.

Another problem that arises in reflection mode measurements is due to shadows caused by the sample in the image plane. Due to a large variety in height, size, and shape of these samples and due to illumination, different shadow patterns may occur. For flat samples, shadow effects are negligible, but for higher samples this effect cannot be ignored. In theory, there are two kinds of shadows (Figure 3). The first is called cast shadow (umbra), caused in an area which cannot be illuminated by the light source. The second is called self-shadow (penumbra), caused in an area which can only be partly illuminated.[17] The aim of the following

(14) (a) Geladi, P.; Bengtsson, E.; Esbensen, K. Grahn, H. *Trends Anal. Chem.* **1992**, *11* (1), 41–52. (b) Geladi, P.; Grahn, H.; Esbensen, K.; Bengtsson, E. *Trends Anal. Chem.* **1992**, *11* (3), 121–130.

Table 1. Results for Optimal Selection of Background Material, Given by Numbers That Represent the Mean Pixel Gray Level Values for the Corrected Reflection Intensities of the Measured Tile Sample[a]

background material	filter 1, 1545–1655 nm mean intensity	filter 2, 1655–1745 nm mean intensity
sanded aluminum	0.77	0.79
wood	0.60	0.61
black cloth	0.57	0.59
green velvet	0.49	0.49
green velvet on aluminum	0.47	0.44
smooth iron	0.57	0.56
black carbon	−0.25	−0.39

[a] A high positive value corresponds to a good diffuse reflecting background material. The negative values found for black carbon are due to a better reflection of the background compared to the sample.
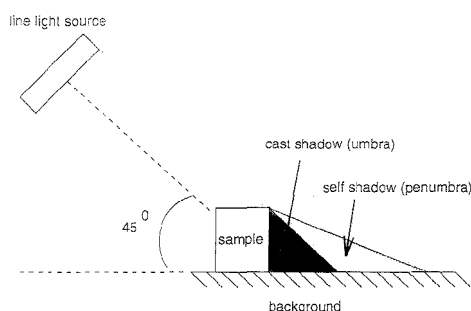
Figure 3. Schematic representation of two kinds of shadow, cast shadows and self-shadow, respectively. The cast shadow is caused in an area which cannot be reached by radiation from the light source. The self-shadow is caused in an area which can be only partly reached by light from the light source.

Table 2. Results of the Experimental Design for Optimization of the Light Source Position[a]

variable number	variable name or interaction term	calcd regression coeffs
a_0	intercept	4.2100
a_1	horizontal (H)	−0.6544
a_2	vertical (V)	−0.6056
a_3	intensity (I)	−0.8869
a_4	HH	0.0050
a_5	VV	−0.0300
a_6	II	−0.0100
a_7	VH	0.1375
a_8	VI	0.2825
a_9	HI	0.1800
a_{10}	VHI	−0.0513

[a] Three factors have been investigated: horizontal (H) and vertical (V) position of the light source and its intensity (I). A second-order model including all interactions has been chosen. Low values for H and V mean the light source is farthest away from the sample. A low value for the intensity means a low radiation.

Table 3. Mean Gray Level Values and Their Corresponding Variances, Calculated from the Five Fractional Reconstructed Images[a]

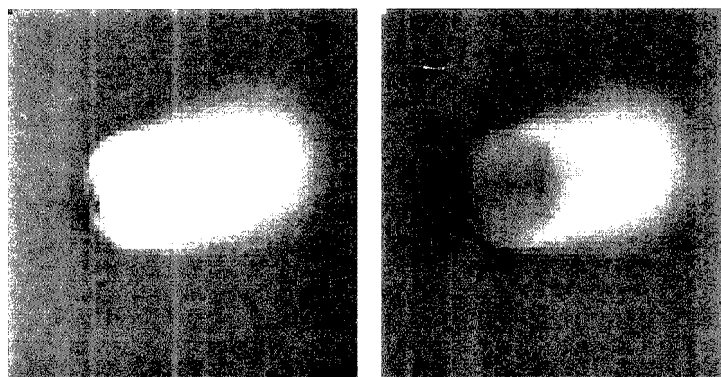| cluster	image 1		image 2	
	mean (au)	variance	mean (au)	variance
background	−0.0424	0.0011	−0.0214	0.0021
umbra	0.6069	0.0014	0.5282	0.0039
penumbra	0.2582	0.0223	0.2359	0.0176
specular refln	−0.1718	0.0078	−0.6380	0.0300
sample	0.5216	0.0025	0.1090	0.0121

[a] It can be seen that the variances for the background are very low, which means that the image quality is very good. The variances of the penumbra are much higher because these are decreasing in the opposite direction from the light source (Figure 3). Specular reflection can cause oversaturation of the pixels, leading to large negative values after image correction.

experiment is to investigate whether it is possible to separate shadow patterns mathematically from the sample absorption pattern within the image. If this would be possible with a multivariate technique, it will not be necessary to spend much effort on homogeneous image illumination or mathematical shadow removal, e.g., using an erosion filter, as mentioned by Geladi et al.[16] Multivariate image rank analysis (MIRA),[5] as, e.g., a classifier tolerates these shadow artifacts. To demonstrate that both shadow types are additive effects that can be separated from the sample pattern in the image, score plots from singular value decomposition eqs 3 and 4, were used. Even without preprocessing (mean centering and variable scaling) of the original data (Figure 4), five different clusters were formed in the score plot in Figure 5: two significant distant shadow clusters, two significant distinguishable clusters for background and sample, and one distant cluster for specular reflection. Specular reflection is caused by direct projection of the illuminated light onto the camera detector by the smoothness of the sample surface for certain angles of incidence. The umbra and penumbra clusters can be

clearly distinguished from the remaining clusters, although penumbra shows some overlap with the background pixels. This score plot shows that shadow effects can be separated from other pixel structures by using decorrelated eigenvectors (eqs 3 and 4). Figure 6 shows the reconstructed fractional images, calculated from the score matrix U, in one single combination image. The five clusters were given arbitrary gray levels in order to visualize them. With this in mind, it can be understood why multivariate classifiers are able to extract a desired sample pattern out of a shadowed image. Table 3 shows the mean gray level values and their variances for the five fractional reconstructed images.

For the optimization of the light source position, a statistical central composite design[15] was carried out on a representative sample, providing a second-order model including all interaction terms for three factors. These factors were the horizontal (H) and vertical (V) positions and the intensity (I) of the light source:

$$g(V,H,I) = a_0 + a_1H + a_2V + a_3I + a_4H^2 + a_5V^2 + a_6I^2 + a_7HV + a_8III + a_9VI + a_{10}HVI \quad (3)$$

As response, g, the absorption ratio of the sample at two distinct wavelengths (1545–1655 and 1655–1745 nm, respectively), was chosen. The higher the ratio, the better the image quality. A high value for the horizontal and vertical position means that the

(15) Deming, S. N.; Morgan, S. L. *Experimental Design: A Chemometric Approach*; Elsevier: Amsterdam, 1987.
(16) Geladi, P.; Swerts, J.; Lindgren, F. *Chemom. Intell. Lab. Syst.* 1994, 24, 145–167.
(17) Jiang, C.; Ward, M. O. *CVGIP (Computer, Vision, Graphics, and Image Processing): Image Understanding*; Academic: San Diego, CA, 1994; pp 213–225.
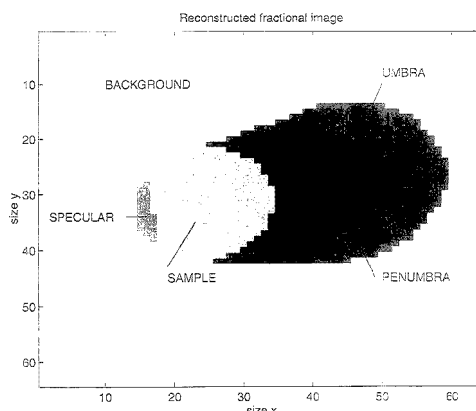
Figure 4. Two typical images measured from a high round plastic cap showing clearly the original disturbances, such as specular reflection on the left edge and shadow effects on the right side of the sample. The filters used were transparent in the wavelength regions (left) 1545–1655 and (right) 1655–1745 nm. Only one light source was used, which was positioned on the left side of the sample.
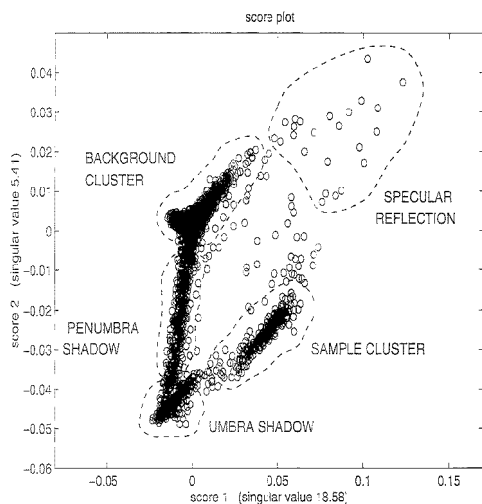
Figure 5. Score plot from score vectors 1 and 2, calculated from the stack of images shown in Figure 4. Five clusters can be extracted: two for shadow effects, one for specular reflection, and two respectively for background and sample correlations.

Figure 6. Five reconstructed fractional images superimposed on a single image. The gray level values were chosen arbitrarily to visualize the different clusters. These clearly represent the mentioned effects in the original images (see also Figure 5). A few intermediate pixels (not belonging to any cluster) were filtered out.

light source is farthest away from the sample or image plane. The terms in the model were able to describe 94% of the factor residuals, and it turned out that there was no lack of fit. The calculated model is given in Table 2. The model optimum was found at maximum values for V and H and a minimum value for I. This means that it is more favorable to position the light source farther away from the image plane (a larger angle between the triangle of light source, sample, and camera) for both the horizontal and vertical positions. Although the first introduces a larger shadow effect, it will be compensated by a much better brightness of the image in the pixels. The optimal position of the light source found for the macro setup in the present work is different to that for the micro setup (e.g., microscopy). In the latter, an illumination ring of glass fiber is commonly used for homogeneous image plane illumination.[15] This ring is attached

close to the objective, which gives a small angle of incidence. The opposite is true for an optimal position in the macro setup, where a large angle gives significantly better results. Although a large angle generates more shadow contributions, these can easily be separated by multivariate techniques from sample patterns, as has already been successfully proven using SVD.

CONCLUSIONS

Two ways to remove or reduce experimental artifacts in a multivariate stack of remote sensing near-infrared images have been presented. Inhomogeneity of the background illumination, lamp source intensity, and fluctuating optical transmission characteristics can be reduced by correcting the raw images via reference and dark current images. Shadow artifacts and specular reflection can be separated from the important sample structures in the images using singular value decomposition. This is a powerful tool for analyzing and improving multivariate images and optimizing the experimental setup with respect to undesired

artifacts. In the optimization of the experimental setup, we showed that the position of the light source differs fundamentally from that of a micro setup. After this optimization, the background material showed no further specular reflection and provided the desired high contrast for the measured samples within the stack of images.

ACKNOWLEDGMENT

Identification of Plastics among Nonplastics in Mixed Waste by Remote Sensing Near-Infrared Imaging Spectroscopy. 2. Multivariate Image Rank Analysis for Rapid Classification

D. Wienke,* W. van den Broek, and L. Buydens

Laboratory for Analytical Chemistry, Catholic University of Nijmegen, Toernooiveld 1, 6525 ED Nijmegen, The Netherlands

Macroscopic samples of household waste were experimentally characterized by a sequence of images, taken in four distinct wavelength regions by NIRIS. The obtained three-dimensional stack of images serves as individual fingerprint for each sample. A rapid data compression, followed by an abstract factor rotation of this stack into a spectroscopically meaningful intermediate four-element vector by a method called multivariate image rank analysis (MIRA), finally provided a single number. This number serves as decision limit for detection of plastics among nonplastic waste. The MIRA results are independent of sample size and sample position within the camera image. They are sensitive to only the type of sample material. MIRA was also found to be robust against image errors such as shadow or slight sample replacements between measurements.

Environmental and economic reasons make recycling of mixed industrial and household waste more attractive. The usually low value of waste can significantly be increased by sorting. Purer fractions of glass, metal, paper, and plastic waste can easier be reused, because they may be more easily reprocessed to higher valued products. Recently, spectroscopic and sensor methods in combination with rapid pattern recognition techniques were proposed for fine sortation of distinct types of postconsumer plastics.[1-3] Our laboratory has also developed an automated identification device for distinct types of plastics, based on a rapid remote near-IR diode array spectrometer combined with artificial neural networks as a real-time classifier.[4-6]

However, presorting of waste is a necessary step to get a stream of plastics for further fine sorting. Technologically, presorting is a more difficult step. Therefore, our laboratory is also developing an optical sensor device for presorting of mixed waste, and this will be described in the present work. This sensor

device should be able to identify the plastics within the stream of mixed waste. This research is part of European project SIRIUS (Sensors and Artificial Intelligence for Recognition and Identification of Used Plastics), in cooperation with the Institute for Chemical and Biochemical Sensor Research (ICB) in Münster, Germany.

Based on a feasibility study on infrared spectra of several materials in household waste, the idea has been developed by the authors to use near-infrared imaging spectroscopy (NIRIS) for discrimination between plastics and nonplastics in waste. This idea is based on distinct spectroscopic fingerprints of plastics and nonplastics in the optical near-IR region (Figure 1a,b). Near-IR spectra of plastics (Figure 1a) show two significant peaks: one in the central near-IR region (first overtone around 1600 nm) and one at the upper end of the wavelength scale (combination bands, around 2300 nm). Nonplastics from household garbage such as glass, ceramics, and metals provide decreasing spectral patterns with increasing near-IR wavelength. Only natural polymers such as paper and wood give a spectral peak structure that is more similar to that of particular plastics than to metal, glass, and ceramics (Figure 1b).

One could ask, why not use a rapid scan near-IR spectrometer for this classification task? What would be the added value of NIRIS compared to a classical near-IR spectrometer? The answer lies less in the analytical−spectroscopic field and more in the process−analytical field. NIRIS provides more than the type of sample material. An near-IR image additionally gives an estimate of sample shape and sample size. In recycling technology, sample shape and sample size are additional important descriptors for identification and sorting. One may be interested, for example, in forming separate fractions of bottles and cans from the same material. NIRIS has a second technological advantage compared with classical "single spot" near-IR spectroscopy. Varying size and position from sample to sample at the moving conveyor belt cause focus problems for a remote spectrometer with a single focused measuring spot. In contrast to that, a spectroscopic camera with a wide angle of view can solve the focus problem better than a single spectrometer beam. It provides a particular redundance in analytical information, giving somewhat more freedom to on-line process analysis. The redundancy in NIRIS data can be removed again afterward with chemometrical tools, as will be demonstrated in the present study. However, the alternative idea, to use a rapid scan near-IR spectrometer for presorting of waste instead of a spectroscopic imaging camera, is under consideration within the SIRIUS project, too. The results

(1) Eisenreich, N.; Knull, H.; Theines, E. Presented at the 23rd Annual Waste Management Conference of Energetic Materials and Polymers, Inst. Chem. Tech Karlsruhe, Germany. 1992; 59/1−59/12.
(2) Ritzmann, H. P.; Schudel, D. *Kunststoffe* **1994**, *84*, 582−584.
(3) Alam, M. K.; Stanton, S. L. *Process Control Quality* **1993**, *4*, 245−252.
(4) Wienke, D.; van den Broek, W.; Melssen, W.; Buydens, L.; Feldhoff, R.; Kantimm, T.; Huth-Fehre, T.; Quick, L.; Winter, F.; Cammann, K. *Anal. Chim. Acta*. in press.
(5) Huth-Fehre, T.; Feldhoff, R.; Kantimm, Th.; Quick, L.; Winter, F.; Cammann, K.; van den Broek, W.; Wienke, D.; Melssen, W.; Buydens, L. *J. Mol. Struct.* **1995**, *348*, 143−146.
(6) Wienke, D.; van den Broek, W.; Schoenmakers, J.-W.; Buydens, L.; Huth-Fehre, T.; Feldhoff, R.; Kantimm, T.; Cammann, K. *Chemom. Intell. Lab. Syst*, in press.
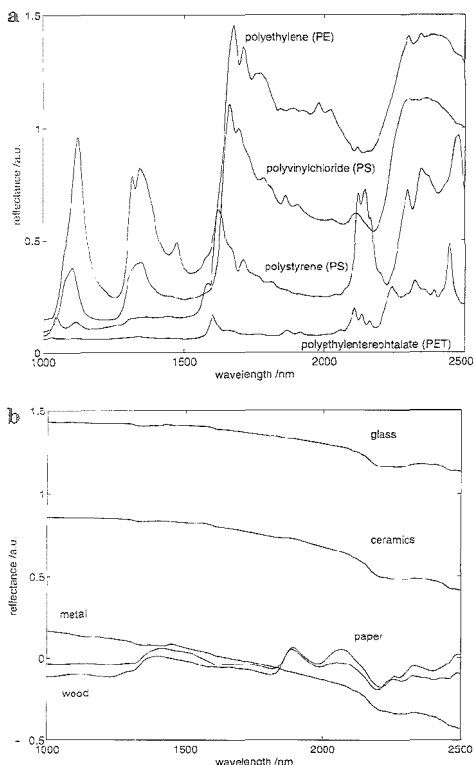
Figure 1. Near-infrared reflectance spectra that are typical for important types of postconsumer plastics (a) and postconsumer nonplastics (b). Spectra were taken by a NIRSystems 6500 spectrometer using a DRIFT unit for transflectance measurements.

will reported later. The present work will focus on the use of a remote operating wide optical range high-speed digital (near-)IR camera as a multivariate optical sensor.

Such fast digital (near-)IR imaging devices, based on advanced semiconductor materials (InSb, InGaAs, HgCdTe), became available in the last few years for civil research as rather typical products from military and space technology. They substitute the near-IR videcons used, for example, by Robert et al.[7], McClure,[8,9] and Geladi et al.[12] in their pioneering studies of NIRIS. Recently, Lewis, Levin, and Treado[13,14] reported first results with their InSb focal plane diode array for spectroscopic near-IR microscopy.

(7) Robert, P.; Bertrand, D.; Devaux, M. F. *NIR News* **1991**, *2* (2), 9–10.
(8) McClure, W. F. *NIR News* **1991**, *2* (2), 8.
(9) McClure, W. F. *Anal. Chem.* **1994**, *66*, 43A–53A.
(10) Geladi, P.; Isaksson, H.; Lindquist, L.; Wold, S.; Esbensen, K. *Chemom. Intell. Lab. Syst.* **1989**, *5*, 209–220.
(11) Geladi, P.; Esbensen, K. In *SAR and Environmental Studies*; Devillers, J., Karcher, W., Eds.; Kluwer Scientific Publishers: Amsterdam, 1991; pp 415–445.
(12) Geladi, P.; Grahn, H.; Lindgren, F. In *Applied Multivariate Analysis in SAR and Environmental Studies*; Devillers, J., Karcher, W., Eds.; Kluwer Scientific Publishers: Amsterdam, 1991; pp 447–478.
(13) Lewis, E. N.; Levin, I. A. *Appl. Spectrosc.* **1995**, *49* (5) 673–678.
(14) Treado, P. J.; Levin, I. W.; Lewis, E. N. *Appl. Spectrosc.* **1994**, *48* (5), 607–615.

In the present macroscopic application, the (near-)IR cameras need to be fast enough for use on a running conveyor belt with a typical transportation speed for waste of 2 m/s. Another requirement is that the data processing has to be done in real-time. This can be reached by optical data processing or by fast computers and efficient chemometrical algorithms.

The present work will describe such an experimental presorter developed in our laboratory. Furthermore, the MIRA algorithm will be introduced as one chemometrical possibility to extract the correct material type (plastics versus nonplastics) from a three-dimensional stack of near-IR images.

THEORY

Assumptions. NIRIS measurements of chemical samples by a camera in the optical near-IR range can be compared with an absorption measurement (or a reflectance measurement) in optical spectroscopy. Namely, to get the single desired netto image of a sample, $I_{n,m}$, forming a data matrix of intensity values, measured with $n \times m$ pixels, one needs in total three measurements: first, the brutto image, $I_{n,m}^{ref+sample}$, showing the sample placed in a sample background (single piece of waste material at the conveyor belt); second, the pure image of the neutral background, $I_{n,m}^{ref}$, that simultaneously will serve as an independent reference image (usually the empty conveyor belt). (As in spectroscopy, a reference image corrects for the spectrum of the camera optics, for the spectrum of the illumination source and for characteristical sensitivity function of the detector array.); third, the dark current level image of the camera itself, $I_{n,m}^{dark}$, to correct for a noise offset of the detector array. As in absorption theory for optical spectroscopy, the netto image is obtained, then, by combining all three measured images:

$$ I_{n,m} = 1 - (I_{n,m}^{ref+sample} - I_{n,m}^{dark})/(I_{n,m}^{ref} - I_{n,m}^{dark}) \qquad (1) $$

An example helps to explain this expression. Assume a camera with a focal plane array of 64×64 pixels, each having 10-bits pixel resolution (see also Experimental Section). Each pixel can thus provide digital measurements (integers) between 0 and 1023 (respectively 1 and 1024). If one closes the shutter of the camera lens, one gets the dark image of the detector. For a near-IR camera with a semiconductor array (InSb, InGaAs, HgCdTe, etc.), it usually has a noise level between 100 and 400 gray values. Assume, for example, a noise level of 256 gray values: the maximum range of 1024 possible intensity values shrinks to the real range of $1024 - 256 = 768$. This is, in fact, only a dynamical detector range of 9.5-bit instead of the announced 10-bit. Additionally, one has to divide by a reference image, $I_{n,m}^{ref}$, that plays the role of the 100% reference intensity in optical spectroscopy, sent through an empty spectrometer (without sample). Finally, a zero background level is obtained for the netto image $I_{n,m}$ in eq 1 by substracting the whole right expression from 1.

If the same sample will be imaged at p distinct wavelength at identical position and with identical background, one will get a so-called stack of images. A capitalized, underlined, boldface letter, $\underline{\mathbf{X}}_{n,m,p}$, is used for such a three-dimensional data array. Two directions of this data stack originate from image geometry $n \times m$ and the third direction from the p distinct wavelengths.

Such multiwavelength images have been taken for many years by civil and military space satellites from the earth's surface and evaluated by rather classical image processing techniques and

by multivariate methods such as principal component analysis (PCA). The same idea of multiwavelength imaging (or "imaging spectroscopy") and PCA, extended by other multivariate methods such as PLS regression, was proposed for numerous chemical applications by Geladi et al.,[10–12] Esbensen and Geladi,[15] and Grahn et al.[16] Under the mathematical assumption that such a stack of images is a linear combination of individual images from several chemical or physical "hidden components", these authors demonstrated that PCA is an excellent tool to find the hidden component images by decomposing this three-dimensional stack. The elegance of this is that the principal components (scores) can be presented as images again after a suitable backtransformation, which helps in gaining a visual understanding of the nature of the hidden components. The present MIRA approach basically uses a comparable idea under very different experimental assumptions. First, in contrast to the former, only one chemical sample is expected in the image. (Technically, this can be guaranteed in each modern mechanical waste sortation plant.) Second, according to eq 1, the pixels belonging to the pure background (nonobject pixels) have values close to zero. Third, artifacts such as shadow, specular reflectance, and interferences cannot be completely avoided. In the preceding work,[17] it has been proven that most of these effects can be linearly separated from the sample part by singular value decomposition. Fourth, the single waste sample will move slightly in time during the p measurements, caused by the conveyor belt movement.

Multivariate Image Rank Analysis (MIRA). A three-dimensional stack of images from a single waste sample forms a three-dimensional data array $\underline{X}_{n,m,p}$ with $i = i-n$ image pixels in one image direction and $j = 1-m$ image pixels in the other image direction, and with $k = 1-p$ wavelength slides in the third direction. $\underline{X}_{n,m,p}$ is unfolded to a two-dimensional data array (matrix), $Z_{nm,p}$, with p columns and $n \times m$ rows. In practice, unfolding costs no extra computation time, because a digital camera is read out pixel by pixel, which means that the images always already unfolded reach the computer memory. Each of the p image slices thus forms a single column vector inside $Z_{nm,p}$, and all former rows of the original image form behind each other a long, one-dimensional data string. In this way, the geometrical information about the object shape and its position is lost because the unfolding operation destroyed the pixel neighborhood interrelationships. However, at this moment, we were interested only in the material type. The required spectroscopic information is still present in $Z_{nm,p}$. The p columns of $Z_{nm,p}$ form a small spectrum for each image pixel (row). One possible means of material analysis would be a row-by-row scan of $Z_{nm,p}$, combined with a check of each of the $n \times m$ spectra. Simple statistics for all $n \times m$ rows would provide the number of background spectra, the number of sample spectra, and the spectra. However, such simple counting works only for simulated images where noise, shadow, and mirror effects are absent. In the MIRA approach, we assume that $Z_{nm,p}$ contains the desired information but in a hidden way among these several undesired influences.

Multiplying pixel i by itself can be considered as multiplication of the transpose z_i^T of its spectral patterns with this pattern z_i to a matrix $C_{p,p}^{\text{sample},i,i}$ of dimension $p \times p$. This matrix can be

written by the square of a new vector s of standard length 1 and a scaling constant a with

$$z_i^T z_i = C_{p,p}^{\text{sample},i,i} = (z_i^T/||z_i||)||z_i||^2(z_i/||z_i||) = s_i^T a s_i \quad (2)$$

This constant a is thus the squared length of z_i. Because z_i is the spectrum of the sample pixel, then s_i is a standardized spectrum of length 1 of the pixel. A pairwise multiplication over all pixels belonging to the sample within the entire image,

$$C_{p,p}^{\text{sample}} = \sum_{i=1}^{\text{sample pixels}} (z_i^{\text{sample},T} z_i^{\text{sample}}) =$$
$$\sum_{i=1}^{\text{sample pixels}} (s_i^{\text{sample},T} a^{\text{sample}} s_i^{\text{sample}}) \quad (3)$$

still provides a matrix $C_{p,p}^{\text{sample}}$ of dimension $p \times p$, which is now the total sum of all the pairwise vector products. Another matrix of dimensions $p \times p$ can be found for all pixels of the image background, $C_{p,p}^{\text{bg}}$, with

$$C_{p,p}^{\text{bg}} = \sum_{i=1}^{\text{bg pixels}} (z_i^{\text{bg},T} z_i^{\text{bg}}) = \sum_{i=1}^{\text{bg pixels}} (s_i^{\text{bg},T} a^{\text{bg}} s_i^{\text{bg}}) \quad (4)$$

A similar expression can be given for pixels from a shadow, $C_{p,p}^{\text{shadow}}$:

$$C_{p,p}^{\text{shadow}} = \sum_{i=1}^{\text{shadow pixels}} (z_i^{\text{shadow},T} z_i^{\text{shadow}}) =$$
$$\sum_{i=1}^{\text{shadow pixels}} (s_i^{\text{shadow},T} a^{\text{shadow}} s_i^{\text{shadow}}) \quad (5)$$

and for pixels that changed from sample pixels to background pixels because of the conveyor belt movement, $C_{p,p}^{\text{move}}$, measurement noise, $C_{p,p}^{\text{noise}}$, and other artifacts and undesired image effects. Thus, the unfolded stack of images, multiplied by its left transpose, can thus be rewritten as a sum:

$$(Z^T Z)_{p,p} = C_{p,p}^{\text{sample}} + C_{p,p}^{\text{bg}} + C_{p,p}^{\text{shadow}} + C_{p,p}^{\text{move}} + \cdots + C_{p,p}^{\text{noise}} \quad (6)$$

As already mentioned, this linear separability of several undesired image artifacts, such as distinct types of shadow, background, or specular reflection, has already been experimentally demonstrated.[17] It forms an important basis for the applicability of the entire MIRA approach.

According to eqs 2–5, these individual matrices in eq 6 can be further decomposed into their standardized spectral profiles s and the scaling factor a, giving the following expression:

$$(Z^T Z)_{p,p} = s^{\text{sample},T} a^{\text{sample}} s^{\text{sample}} + s^{\text{bg},T} a^{\text{bg}} s^{\text{bg}} + s^{\text{shadow},T} a^{\text{shadow}} s^{\text{shadow}} + \cdots + s^{\text{noise},T} a^{\text{noise}} s^{\text{noise}} \quad (7)$$

On the other hand, a classical singular value decomposition

(15) Esbensen, K.; Geladi, P. *Chemom. Intell. Lab. Syst.* **1989**, *7*, 67–86.
(16) Grahn, H.; Szevenyi, N. M.; Roggenbuck, M. W. *Chemom. Intell. Lab. Syst.* **1989**, *7*, 87–93.
(17) van den Broek, W.; Wienke, D.; Melssen, W.; de Crom, K.; Buydens, L. *Anal. Chem.* **1995**, *67*, 3753–3759.

(SVD) of $(\mathbf{Z}^T\mathbf{Z})_{p,p}$ would be written as

$$(\mathbf{Z}^T\mathbf{Z})_{p,p} = \mathbf{u}^{\text{source1}}\lambda^{\text{source1}}\mathbf{e}^{\text{source1,T}} + \mathbf{u}^{\text{source2}}\lambda^{\text{source2}}\mathbf{e}^{\text{source2,T}} +$$
$$\mathbf{u}^{\text{source3}}\lambda^{\text{source3}}\mathbf{e}^{\text{source3,T}} + \cdots + \mathbf{u}^{\text{source4}}\lambda^{\text{source4}}\mathbf{e}^{\text{source4,T}} \quad (8)$$

with matrix $\mathbf{U}$ = singular vectors $(\mathbf{Z}^T\mathbf{Z})_{p,p}^T(\mathbf{Z}^T\mathbf{Z})_{p,p}$, matrix $\mathbf{E}$ = singular vectors $(\mathbf{Z}^T\mathbf{Z})_{p,p}(\mathbf{Z}^T\mathbf{Z})_{p,p}^T$, and λ the diagonal matrix of singular values.

Equation 8 is a decomposition of the image stack into abstract sources of variation. A chemically meaningful rotation of this abstract solution is required. However, eqs 7 and 8 show a high similarity and offer a way to estimate the desired standardized spectral profiles $\mathbf{s}$ by a SVD under well-defined experimental assumptions (see below). Geladi et al.[10] discussed this way as a rapid numerical possibility to estimate the desired scores images T from a PCA decomposition of $\mathbf{Z}$:

$$\mathbf{Z} = \mathbf{TL} \quad (9)$$

via their PCA loadings $\mathbf{L}$ and PCA eigenvalues $\mathbf{D}$ obtained by

$$(\mathbf{Z}^T\mathbf{Z}) = \mathbf{L}^T\mathbf{DL} \quad (10)$$

However, we were less interested in the scores image $\mathbf{t}$ but more in a quantitative prediction of the waste sample's individual spectral profile $\mathbf{e}^{\text{sample}}$ (identical with $\mathbf{u}^{\text{T,sample}}$) from the image stack to extract the correct material type.

The point of the MIRA approach to maximize the contribution of the matrix $\mathbf{C}_{p,p}^{\text{sample}}$ in expression 6 while minimizing the contribution of the remaining terms by experiment. In other words, the MIRA approach tries to force $(\mathbf{Z}^T\mathbf{Z})_{p,p}$ into a matrix of rank $r = 1$. Expression 1, for example, helps to force the background term $\mathbf{C}_{p,p}^{\text{bg}}$ toward a zero matrix. The shadow term in eq 6 becomes small with an intelligent sample illumination. The term $\mathbf{C}_{p,p}^{\text{move}}$ can be minimized if the measurement speed is some magnitude higher than the movement of the conveyor belt with the sample. If the object of interest has a significant absorption within the total image, it will always dominate the first-rank component. One can consider the SVD step also as a rotation of the matrix $(\mathbf{Z}_{n\times m,p}^T\mathbf{Z}_{n\times m,p})_{p,p}$ into a new coordinate system $\mathbf{U}_{p,f}$ whereby the rotation matrix is equal to

$$\mathbf{R}_{f,p} = \mathbf{V}_{f,f}\mathbf{E}_{f,p}^T \quad (11)$$

providing the new axis that corresponds to the order f of rank components. As mentioned above, the dominating rank of the sample in the image will force this rotation in a spectroscopically desired direction. The ideal case would be for the column vector $\mathbf{u}_1$ to approximate $\mathbf{s}^{\text{sample}}$ as close as possible. Clearly, the more dominant the rank-one component, the better this approximation will be.

The last step of the MIRA model is the extraction of a decision limit from the predicted spectra $\mathbf{u}$ profile of the sample. For this we make use of the normality property of $\mathbf{u}_1$ (length = 1) and of an additional spectroscopic trick. The p filters are placed in such a way in the spectrum that for each filter that is placed at a characteristic absorption peak (Figure 1a), a second one is placed in a valley (absorption minimum) close to the peak. In the case of plastics identification, we used two peaks in the near-IR
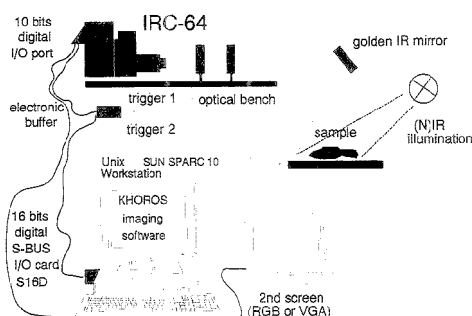
Figure 2. Experimentally realized laboratory setup for presorting of mixed postconsumer waste. Near-infrared images from the same sample, placed and illuminated on a conveyor belt, can be taken in p wavelength regions. The wavelength regions are selected by a rotating wheel with interference filters, placed in front of the camera. The obtained image stack is on-line processed by a dedicated Unix workstation, running in stand-alone mode.
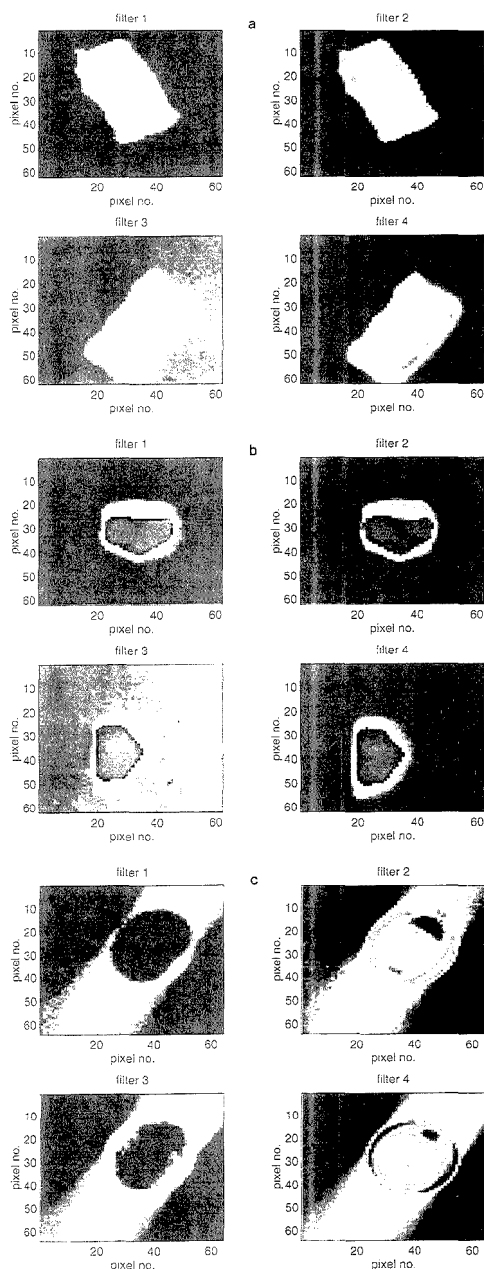
spectrum where plastics show a high absorbance compared to nonplastics. According to Figure 1a, the high-intensity filters can be placed, for example, around 1700 and 2400 nm (see Experimental Section). Based on this trick and on the normality property of $\mathbf{u}_1$, the calculated decision value for an arbitrary sample,

$$B^{\text{sample}} = \left(\sum_{k=1}^{p/2}u_{k,\text{peaks}}^2 / \sum_{k=1}^{p/2}u_{k,\text{valleys}}^2\right) \quad (12)$$

summarizes all elements in the predicted $\mathbf{u}$ vector corresponding to peak wavelengths, divided by the sum over all elements in $\mathbf{u}$ corresponding to non-peak wavelength. The value for B will thus for spectra like that in Figure 1a be much larger than 1 (plastics). For spectra like that in Figure 1b, the predicted value for B will be significantly smaller than 1 (metal, stone, ceramics) or close to 1 for wood and paper (a little bit larger or smaller than 1). In this way, the former original three-way data array, $\underline{X}_{n,m,p}$ from the camera measurement of one waste sample is compressed to a single number B as a scalar decision limit for future control of an automated waste sorter.

EXPERIMENTAL SECTION

A digital infrared diode array camera IRC-64 (Cincinatti Electronics Inc., Mason, OH) has been mounted at an optical bench on the laboratory wall (Figure 2). The camera has a 64 × 64 pixels focal plane diode array of nitrogen-cooled InSb that is sensitive in the wavelength region from 1.1 to 5.0 μm. A cold shield inside the camera blocks undesired infrared background radiation above 4.6 μm but allows radiation to pass between 1.0 and 4.6 μm. An IR optics (CaF$_2$, transparent at 2.3–4.5 μm) and a near-IR optics (BK7 glass, transparent at 0.3–2.75 μm) allow us to obtain mid- and near-IR measurements. Via an electronic buffer, concerning a trigger input/output, the camera has been connected to a high-speed 16-bit digital interface S16D (S-Bus card made by EDT Inc., Beaverton, OR). The stream of digital image data is written by the S16D I/O card directly into the 32 MB RAM of a SUN Sparc 10 (Unix workstation) in real-time. This enables us, via the digital I/O port (10 and 12 bits, respectively), the technical

filter 1   a   filter 2

filter 3   filter 4

filter 1   b   filter 2

filter 3   filter 4

filter 1   c   filter 2

filter 3   filter 4

Figure 3. Stacks of $p = 4$ experimental near-infrared images (size 64×64 pixels/image) for several pieces of nonplastics and plastics, taken by the experimental setup in Figure 2 (filter 1, 1600 ±110 nm; filter 2, 1700 ±90 nm; filter 3, 1700–2150 nm; filter 4, 2115–2550 nm. (a) Piece of paper (moved and rotated), (b) piece of ceramics (moved and rotated), and (c) circular piece of polystyrene (moved, two strong shadows).

possibility of high-speed measurements with up to 52 images/s. Simultaneously, the less well resolved 8-bit analog infrared image can be visualized on a second screen in real-time by using the alternative RGB or the VGA output port of the IRC. Reading the digital data directly from the camera avoids any further analog–digital conversion (or vice versa). An additional advantage is that no framegrabber is needed. In this way, the digital images are not disturbed by any noise caused by data conversion processes. Simultaneously, the maximum camera speed of 52 digital images/s of size 64×64 pixels is used. The real-time measurement is done under the large KHOROS imaging software package (University of New Mexico, Albuquerque, NM). The IRC-64 can be directly on-line called under KHOROS by a computer mouse-supported operation. A symbolic camera icon appears within the graphical CANTATA user interface of KHOROS on the workstation screen. In this way, the camera becomes operational. The data stream from the camera can be linked on-line via the workstation's 32 MB RAM to all software devices available in KHOROS, such as mathematical filters, image transformations, image analysis algorithms, and multivariate data analysis. Communication software between the S16D card and KHOROS and the electronic installation has been realized by Starling Consultancy (Hengelo, The Netherlands). Complete infrared movies can be measured by the IRC-64 and then presented by KHOROS by real-time visualization of the movie out of the workstation's RAM. IRC-64 images can be saved to disk in several formats by KHOROS. In this way the images can be read into other imaging software, such as MATLAB, and into self-written programs under the Unix operating system. A rotable filter wheel at the optical bench with up to $p = 8$ filters helps to measure the same sample in distinct desired wavelength regions. For the present experiments, we used four near-IR interference filters from Spectrogon (Sweden) with the following parameters (compare with spectra in Figure 1): narrow band pass filter 1 (1600 ± 110 nm), narrow band pass filter 2 (1700 ± 90 nm), broad band filter 3 (1700–2150 nm), and broad band filter 4 (2115–2550 nm).

Further equipment, such as a pin-hole setup, mirrors, and (near-)IR-illumination sources, were mounted. The pixelwise recalibration of the camera is done by a so-called uniformity module using a cool and a hot emission sources. A sanded plate, made from aluminum, provides a neutral, scattering, metallic background for (near-)IR radiation and for measurement of the reference image, $I_{64,64}^{ref}$.

SOFTWARE AND COMPUTATIONS

Four images per sample were saved by KHOROS to hard disk and then read into MATLAB (Unix). The MIRA algorithm, as described in the Theory section, has been completely developed and implemented in MATLAB by the author. In the mean time, MIRA has been also implemented and tested in C language. This now allows use of MIRA outside KHOROS by direct access in real-time and in on-line mode to the IRC-64 camera to run the complete presorter setup automatically.

RESULTS AND DISCUSSION

Different but typical waste materials were analyzed by the described experimental setup. Macroscopic pieces of several centimeters in size made from paper, wood, glass, metal, ceramics, and stone served as typical nonplastics. Pieces of white polystyrene, yellow polyethylene, and dark blue polypropene were

Table 1. Experimental Image Stacks of Size 64 × 64 × 4 for Distinct Plastics and Nonplastic Samples (Partly Given in Figure 3), Decomposed by the MIRA Approach via Eqs 1−8[a]

true material type	sample moved during measurement?	predicted dicision border B	corresponding eigenvalue λ_1	λ_2	λ_3	λ_4
white polystyrene	no	3.73	374.6	109.3	9.7	2.43
white polystyrene	yes	1.41	670.1	70.1	23.3	16.1
dark blue polypropene	no	1.96	615.9	23.8	4.6	3.0
dark blue polypropene	yes	1.59	659.3	34.5	12.1	4.6
stone	yes	0.88	688.2	200.9	10.9	1.5
ceramics	no	0.90	339.5	7.3	3.9	1.5
paper	no	0.25	256.7	29.9	14.1	2.3
paper	yes	1.13	331.3	138.2	19.04	6.6
yellow polyethylene	no	2.22	696.1	22.89	9.7	3.91
yellow polyethylene	yes	1.96	598.7	138.2	41.0	13.6
aluminum	no	1.10	640.8	207.6	166.8	71.0
aluminum	yes	0.82	597.8	212.7	96.6	63.1
copper	no	0.87	316.9	33.3	9.5	5.3
copper	yes	0.90	302.6	28.7	14.0	3.0
brown glass	no	0.82	570.1	55.7	15.6	12.4
brown glass	yes	0.80	535.5	60.0	19.8	8.7
white glass	no	1.07	53.8	26.9	5.9	2.9
white glass	yes	0.00	517.8	38.7	17.9	13.7
wood	no	1.53	156.7	19.3	9.2	1.9
wood	yes	0.02	401.2	130.9	20.7	2.0

[a] If the calculated decision value B for the images is large, a plastic is found. See Table 2 for the corresponding standardized spectral patterns, u_1, for selected samples.

Table 2. Predicted Spectral Elements of u_1 Profiles for the samples, Given in Table 1, Extracted by the MIRA Approach from the Image Stacks[a]

true material type	sample moved during measurement?	u profile u_1	u_2	u_3	u_4
white polystyrene	no	0.15	0.55	0.30	0.76
white polystyrene	yes	0.37	0.49	0.38	0.70
dark blue polypropene	no	0.26	0.50	0.52	0.65
dark blue polypropene	yes	0.35	0.48	0.51	0.62
stone	yes	0.50	0.49	0.52	0.47
ceramics	no	0.52	0.51	0.50	0.46
paper	no	0.88	0.41	0.12	0.18
paper	yes	0.30	0.06	0.62	0.73
yellow polyethylene	no	0.15	0.42	0.54	0.71
yellow polyethylene	yes	0.16	0.39	0.56	0.71
aluminum	no	0.53	0.58	0.44	0.44
aluminum	yes	0.54	0.48	0.51	0.47
copper	no	0.52	0.46	0.51	0.51
copper	yes	0.53	0.49	0.49	0.48
brown glass	no	0.53	0.50	0.52	0.44
brown glass	yes	0.55	0.49	0.51	0.46
white glass	no	0.40	0.52	0.57	0.50
white glass	yes	0.98	−0.02	0.19	−0.02
wood	no	0.34	0.27	0.53	0.73
wood	yes	0.98	0.13	−0.15	−0.06

[a] Compare the u_1 profiles with corresponding near-IR spectra in Figure 1.

characterized as easy and as a difficult plastic samples (dark colored samples give near-IR spectra with a bad S/N ratio). Looking to selected near-IR images (Figure 3), one can already see the difference in absorption ratios between the different wavelength regions for different materials. The piece of paper (Figure 3a) shows an absorption pattern that lies between those of ceramics (Figure 3b, nearly no differences) and the piece of plastic (Figure 3c, remarkable absorption contrasts). Realistic situations at a moving conveyor belt in a waste sortation plant (sample shadow, sample replacement, mirror reflection) were simulated by irregular sample illumination and sample movement during measurement (rotation, translation).

The summarized results for all experimental images and additional samples (Tables 1 and 2) show that the MIRA approach works for almost all samples, as theoretically predicted. For all plastics, the predicted B value is, as desired, significant larger than 1 and often close to or larger than 2. The reverse trend (smaller than or around 1) was found for all nonplastics. However, in some cases, the B value for some nonplastics deviates a little from the expectations. An example is the piece of polished aluminum ($B = 1.10$). One reason could be that the background was a sanded aluminum plate giving only minimal contrast. A second example is the piece of paper. After a strong rotation by 90° and a moderate movement, the former correct B value for paper of 0.25 raised over the decision border to a value of 1.13. This is still lower as for all plastics but gives the general impression that small changes in position are tolerated by the MIRA approach. But if the overlap between sample pixels is lost within the same image stack by too much sample movement, then the correlation between them is lost and a second significant

singular value is generated, providing a wrong u-profile. One can see this, for example, for paper in Table 1; the second eigenvalue is raised if a sample is moved between two filter measurements. A third negative example is the piece of wood ($B = 1.53$).

However, the first eigenvalue dominates in all cases the other three for all measured sample image stacks (Table 1). This one condition is necessary to get a suitable estimate u of the searched spectral profile s in order to obtain in this way a correct prediction of the material class via the B criterion.

Another interesting result has been found. Shadows, mirror reflections, and other types of irregular illumination obviously do not play as negative a role as expected. In other words, these effects seem to be nearly independent of wavelength, so they form together with the background a linear independent hidden component with minor influence. The constancy of their absorption intensity decouples these effects in the components space from the variation of the sample absorption with wavelength. For recycling practice, that means that the conveyor belt does not need to be illuminated by an extreme homogeneous light source, but only by a simple near-IR lamp.

The estimates u for the desired standardized spectral profiles s (Table 2) show a good correlation with the true near-IR spectra, as given in Figure 1a for plastics and in Figure 1b for nonplastics. The u profiles for plastics correctly reflect the theoretically expected spectral pattern low−high−low−high determined from the placement of the four filters. The decreasing intensity trend with increasing wavelength of the u profiles for stone and ceramics agrees almost perfectly with the spectra of ceramics (or glass) (Figure 1b). For paper and metal, the general trend is also correct, but differences in some details are stronger than for the other materials. Most of the problems are caused by the optical system (transmission spectrum of the camera lens, emission spectrum of the near-IR illumination source). At this moment, a boron crown glass lens (BK7) is used that shows between 2100 and 2700 nm a significant decrease in transmission. This loss of

transmission has been partly compensated for by using small band pass filters for filters 1 and 2 and a more than 4 times wider broad band filter for the filters 3 and 4. However, according to eq 1, the real dynamic range for the pixel resolution is mainly determined by a maximum S/N ratio. At this time, an alternative (near-)IR lens material (MgF$_2$) is in experimental testing. This material has at 2500 nm >90% transmission compared to BK7 (30%). It is expected that with the new optics, the influence of the peak between 2300 and 2500 nm in eq 12 will increase, giving finally better discriminating B values.

CONCLUSIONS

Remote spectroscopic near-infrared imaging spectroscopy, if combined with robust chemometric methods, can serve as a tool for identification of plastics among nonplastics in mixed household waste. The presented mathematical method MIRA helps to extract the spectral fingerprint of a sample from its three-dimensional stack of near-IR images. MIRA provides a rotation of the abstract principal component space into a spectroscopically interpretable solution. MIRA provides identical classifications for differently sized, distinctly shaped, and distinctly located samples made from the same material (plastics detection among nonplastics). Further, MIRA suppresses the negative influences of irregular illumination and shadows in the images. MIRA tolerates a slight sample movement (from conveyor belt) during one measurement. All these properties make the new approach attractive for a real-world implementation in a future real-time, on-line sorting device for mixed postconsumer waste based on remote near-IR imaging spectroscopy.

Variable Index of Refraction Ultrathin Films Formed from Self-Assembled Zirconium Phosphonate Multilayers: Characterization by Surface Plasmon Resonance Measurements and Polarization/Modulation FT-IR Spectroscopy

Dennis G. Hanken and Robert M. Corn*

Department of Chemistry, University of Wisconsin—Madison, 1101 University Avenue, Madison, Wisconsin 53706

Ultrathin (submicrometer) organic films of specified index of refraction are constructed by the sequential deposition of self-assembled zirconium phosphonate (ZP) molecular monolayers that contain two different bisphosphonate ions, 1,10-decanediylbis(phosphonate) (DBP) and 4,4'-azobis[(p-phenylene)methylene]bis(phosphonate) (AZO). By varying the ratio of DBP to AZO monolayers in the ZP multilayer film, the index of refraction can be controlled. A combination of surface plasmon resonance (SPR) measurements and polarization/modulation Fourier transform infrared reflection—absorption spectroscopy (PM/FT-IRRAS) is used to examine the structure of the ZP multilayers on vapor-deposited gold substrates, and ellipsometric measurements are utilized to determine the index of refraction of the ZP multilayers on transparent substrates. ZP films consisting of 100% DBP and 100% AZO molecules are found to have indices of refraction of 1.51 and 1.64, respectively, at an optical wavelength of 632.8 nm. In both the 100% DBP and the 100% AZO multilayers, an average monolayer thickness of 16 ± 0.5 Å is determined from the SPR measurements. The spectroscopic and ellipsometric data indicate that the index of refraction of mixed ZP multilayer films (i.e., films with both DBP and AZO self-assembled monolayers) can be varied systematically between 1.51 and 1.64, but that the average thickness of the self-assembled monolayers is greater in the mixed films than in either of the 100% DBP or 100% AZO multilayers.

The formation of ultrathin (submicrometer) organic films by the sequential deposition of molecular monolayers is currently being pursued as a means of fabricating thin-film optical devices such as optical waveguides, photoactive switches, electrooptical components, and nonlinear optical films.[1,2] The versatility of this deposition methodology stems from (i) the fine control of film thickness that can be achieved by forming the thin film one monolayer at a time and (ii) the ease with which different chemical functionalities can be incorporated into the thin film in order to control its linear and nonlinear optical properties. Currently, the most common method of forming ultrathin organic films one monolayer at a time is the Langmuir—Blodgett (LB) technique of repeatedly transferring monolayer structures from a water surface to a substrate.[3,4] In 1988, Mallouk and co-workers demonstrated a new strategy for forming organic thin films on metal and oxide substrates by the spontaneous adsorption and self-assembly of zirconium phosphonate (ZP) multilayers.[5,6] These films contained alternate layers of organic (n-alkyl) and inorganic (zirconium phosphonate) structures and appeared to be both thermally robust and highly reproducible. A variety of metal phosphonate multilayer structures are currently being examined for use as ultrathin organic films in both optical and chemical applications.[7-35]

(1) Ulman, A. An Introduction to Ultrathin Organic Films; Academic: New York, 1991.
(2) Swalen, J. D.; Allara, D. L.; Andrade, J. D.; Chandross, E. A.; Garoff, S.; Israelachvili, J.; McCarthy, T. J.; Murray, R.; Pease, R. F.; Rabolt, J. F.; Wynne, K. J.; Yu, H. Langmuir 1987, 3, 932.

(3) Blodgett, K. B. J. Am. Chem. Soc. 1935, 57, 1007.
(4) Blodgett, K. B.; Langmuir, I. Phys. Rev. 1937, 51, 964.
(5) Lee, H.; Hong, H.-G.; Mallouk, T. E.; Kepley, L. J. J. Am. Chem. Soc. 1988, 110, 618.
(6) Lee, H.; Mallouk, T. E.; Kepley, L. J.; Hong, H.-G.; Akhter, S. J. Phys. Chem. 1988, 92, 2597.
(7) Putvinski, T. M.; Schilling, M. L.; Katz, H. E.; Chidsey, C. E. D.; Mujsce, A. M.; Emerson, A. B. Langmuir 1990, 6, 1567.
(8) Katz, H. E.; Scheller, G.; Putvinski, T. M.; Schilling, M. L.; Wilson, W. L.; Chidsey, C. E. D. Science 1991, 254, 1485.
(9) Katz, H. E.; Schilling, M. L.; Chidsey, C. E. D.; Putvinski, T. M.; Hutton, R. S. Chem. Mater. 1991, 3, 699.
(10) Ungashe, S. B.; Wilson, W. L.; Katz, H. E.; Scheller, G. R.; Putvinski, T. M. J. Am. Chem. Soc. 1992, 114, 8717.
(11) Schilling, M. L.; Katz, H. E.; Stein, S. M.; Shane, S. F.; Wilson, W. L.; Buratto, S.; Ungashe, S. B.; Taylor, G. N.; Putvinski, T. M.; Chidsey, C. E. D. Langmuir 1993, 9, 2156.
(12) Katz, H. E.; Schilling, M. L. Chem. Mater. 1993, 5, 1162.
(13) Bent, S. F.; Schilling, M. L.; Wilson, W. L.; Katz, H. E.; Harris, A. L. Chem. Mater. 1994, 6, 122.
(14) Katz, H. E.; Wilson, W. L.; Scheller, G. J. Am. Chem. Soc. 1994, 116, 6636.
(15) Katz, H. E.; Brent, S. F.; Wilson, W. L.; Schilling, M. L.; Ungashe, S. B. J. Am. Chem. Soc. 1994, 116, 6631.
(16) Katz, H. E. Chem. Mater. 1994, 6, 2227.
(17) Akhter, S.; Lee, H.; Hong, H.-G.; Mallouk. T. E.; White, J. M. J. Vac. Sci. Technol., A 1989, 7, 1608.
(18) Cao, G.; Mallouk, T. E. Inorg. Chem. 1991, 30, 1434.
(19) Hong, H.-G.; Mallouk, T. E. Langmuir 1991, 7, 2362.
(20) Hong, H.-G.; Sackett, D. D.; Mallouk, T. E. Chem. Mater. 1991, 3, 521.
(21) Cao, G.; Rabenberg, L. K.; Nunn, C. M.; Mallouk, T. E. Chem. Mater. 1991, 3, 149.
(22) Yang, H. C.; Aoki, K.; Hong, H.-G.; Sackett, D. D.; Arendt, M. F.; Yau, S.-L.; Bell, C. M.; Mallouk, T. E. J. Am. Chem. Soc. 1993, 115, 11855.
(23) Xu, X.-H.; Yang, H. C.; Mallouk, T. E.; Bard, A. J. J. Am. Chem. Soc. 1994, 116, 8386.
(24) Burwell, D. A.; Thompson, M. E. Chem. Mater. 1991, 3, 730.
(25) Vermeulen, L. A.; Thompson, M. E. Nature 1992, 358, 656.
(26) Vermeulen, L. A.; Snover, J. L.; Sapochak, L. S.; Thompson, M. E. J. Am. Chem. Soc. 1993, 115, 11767.

$^2O_3P\text{-}(CH_2)_{10}\text{-}PO_3^{2-}$ DBP

$R=CH_2\text{-}PO_3^{2-}$ AZO

$R= CH_2\text{-}PO_3^{2-}$

$\text{-S-}(CH_2)_{11}\text{-O-}PO_3^{2-}$

$= Zr^{4-}$

etc.

1:1 AZO/DBP
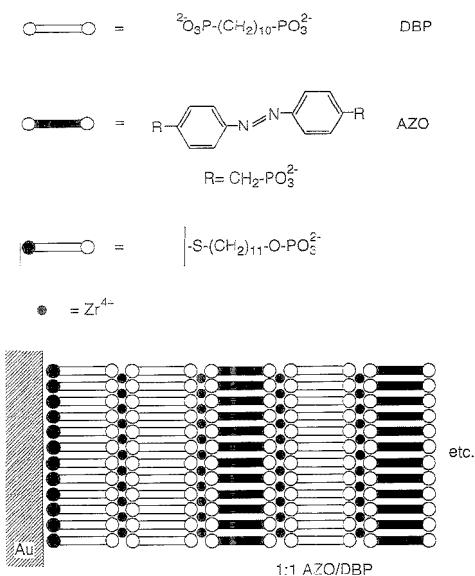
Figure 1. Schematic diagram for the construction of mixed zirconium phosphonate multilayer films. The ZP films are created on vapor-deposited gold substrates that have been first primed with a self-assembled monolayer of phosphorylated 11-mercaptoundecanol (MUD) and one self-assembled monolayer of 1,10-decanediylbis-(phosphonate) (DBP). Mixed multilayers are formed by the sequential self-assembly of either 1,10-decanediylbis(phosphonate) (DBP) or 4,4′-azobis[(p-phenylene)methylene]bis(phosphonate) (AZO) molecules onto the surface. For example, the 1:1 AZO/DBP multilayer film will have alternating self-assembled monolayers of AZO and DBP.

Perhaps the two most fundamental characteristics of an ultrathin organic film are its thickness (d) and its index of refraction (n). For example, both d and n need to be specified when creating a thin-film optical waveguide for a given wavelength of light. In this paper, we demonstrate that the self-assembly of ZP multilayers can be used to construct ultrathin organic films with both a specific thickness and an index of refraction that can be set in a given range ($1.51 \leq n \leq 1.64$ at $\lambda = 632.8$ nm). To accomplish this, we create ZP multilayers which contain two different bisphosphonate ions, 1,10-decanediylbis(phosphonate) (DBP) and 4,4′-azobis[(p-phenylene)methylene]bis(phosphonate) (AZO). As depicted in Figure 1, monolayers of either DBP or AZO are deposited sequentially onto a substrate primed with a monolayer of a phosphate-terminated species and one self-assembled monolayer of DBP. For example, a 1:1 AZO/DBP film will consist of alternating self-assembled monolayers of AZO and

DBP. By varying the AZO/DBP ratio in the ZP multilayer, we can control the overall index of refraction of the thin film.

ZP multilayers formed on vapor-deposited gold substrates are characterized with a combination of polarization/modulation Fourier transform infrared reflection–absorption spectroscopy (PM/FT-IRRAS) for molecular structure information and surface plasmon resonance (SPR) measurements for the optical determination of film thickness. We recently employed this combination of techniques to characterize the adsorption of biopolymers onto self-assembled monolayers at gold surfaces,[36] and both methods have been applied by a number of other research groups in the study of self-assembled monolayers.[35,37–45] In addition to the experiments on gold substrates, the indices of refraction for ZP multilayer films formed on transparent silica substrates were determined from ellipsometry. The combined spectroscopic characterization experiments reveal that the mixed ZP multilayer deposition strategy for the formation of variable index of refraction organic films is deceptively simple: while the index of refraction of the thin film varies in a systematic fashion, unexpected changes are observed in the molecular structure and thickness of the mixed ZP multilayers.

EXPERIMENTAL CONSIDERATIONS

Materials. Diethyl 4-aminobenzylphosphonate (99%), pyridine (99%), 2,4,6-collidine (99%), phosphorus oxychloride (99%), bromotrimethylsilane (97%), zirconyl chloride octahydrate (98%), anhydrous octane (99+%), anhydrous tetrahydrofuran (THF) (99.9%), and lithium aluminum hydride (1 M in THF) were obtained from Aldrich. Other reactants and solvents included CuCl (Mallinckrodt), (10-carbomethoxydecyl)dimethylchlorosilane (United Chemical Technologies), methylene chloride and UV grade acetonitrile (Burdick and Jackson), ethyl acetate (Fisher), and absolute ethanol (Quantum). All chemicals were used as received. Mercaptoundecanol (MUD) and 1,10-decanediylbis-(phosphonic acid) (DBP) were synthesized as described previously.[35] All aqueous solutions were prepared from 18 MΩ·cm Millipore-filtered water.

Synthesis of Azobis[(p-phenylene)methylene]bis(phosphonic acid) (AZO). AZO was prepared from an autoxidation reaction of diethyl 4-aminobenzylphosphonate (2 g, 8.2 mmol in 20 mL of pyridine) and oxygen (bubbled through the solution at 10 psi) in the presence of CuCl (0.25 g, 2.5 mmol) as a catalyst.[46] The reaction was determined to be complete in 3 h by TLC in 1:1 hexane/ethyl acetate. The pyridine solution was added to a separatory funnel containing 100 mL each of a 10% HCl aqueous solution and ethyl acetate; the ethyl acetate extract was subsequently dried with Na$_2$SO$_4$, and the solvent was removed by rotary evaporation to give a red crystalline solid. Hydrolysis of the bis-
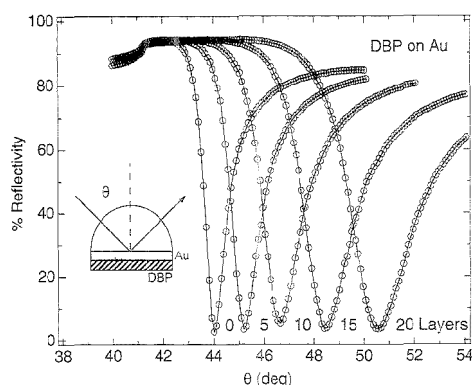
(27) Vermeulen, L. A.; Thompson, M. E. *Chem. Mater.* **1994**, *6*, 77.
(28) Thompson, M. E. *Chem. Mater.* **1994**, *6*, 1168.
(29) Snover, J. L.; Thompson, M. E. *J. Am. Chem. Soc.* **1994**, *116*, 765.
(30) Byrd, H.; Pike, J. K.; Talham, D. R. *Chem. Mater.* **1993**, *5*, 709.
(31) Byrd, H.; Whipps, S.; Pike, J. K.; Ma, J.; Nagler, S. E.; Talham, D. R. *J. Am. Chem. Soc.* **1994**, *116*, 295.
(32) Zeppenfeld, A. C.; Fiddler, S. L.; Ham, W. K.; Klopfenstein, B. J.; Page, C. J. *J. Am. Chem. Soc.* **1994**, *116*, 9158.
(33) O'Brien, J. T.; Zeppenfeld, A. C.; Richmond, G. L.; Page, C. J. *Langmuir* **1994**, *10*, 4657.
(34) Kumar, C. V.; Chaudhari, A.; Rosenthal, G. L. *J. Am. Chem. Soc.* **1994**, *116*, 403.
(35) Frey, B. L.; Hanken, D. G.; Corn, R. M. *Langmuir* **1993**, *9*, 1815.

(36) Jordan, C. E.; Frey, B. L.; Kornguth, S.; Corn, R. M. *Langmuir* **1994**, *10*, 3642.
(37) Haussling, L.; Ringsdorf, H.; Schmitt, F. J.; Knoll, W. *Langmuir* **1991**, *7*, 1837.
(38) Cooke, S. J.; Roberts, G. G. *Thin Solid Films* **1992**, *210/211*, 685.
(39) Liedberg, B.; Lundstrom, I.; Stenberg, E. *Sens. Actuators B* **1993**, *11*, 63.
(40) Porter, M. D. *Anal. Chem.* **1988**, *60*, 1143.
(41) Troughton, E. B.; Porter, M. D.; Nuzzo, R. G.; Allara, D. L.; Bain, C. D.; Whitesides, G. M. *Langmuir* **1988**, *4*, 365.
(42) Ulman, A.; Tillman, N. *Langmuir* **1989**, *5*, 1418.
(43) Dubois, L. H.; Nuzzo, R. G. *Annu. Rev. Phys. Chem.* **1992**, *43*, 437.
(44) Duevel, R. V.; Corn, R. M. *Anal. Chem.* **1992**, *64*, 337.
(45) Xu, C. J.; Sun, L.; Kepley, L. J.; Crooks, R. M.; Ricco, A. J. *Anal. Chem.* **1992**, *64*, 3191.
(46) Terent'ev, A. P.; Mogilianskii, I. D. *J. Gen. Chem. U.S.S.R.* **1958**, *28*, 2002.

(diester) was performed by reaction with bromotrimethylsilane (7.5 g, 49 mmol) in methylene chloride (30 mL) under N_2 at room temperature for 12 h.[47] The solvent and excess bromotrimethylsilane were removed under vacuum to yield an orange paste that was converted to a fine orange/brown precipitate upon the addition of 50 mL of a 10% HCl aqueous solution. This precipitate was extracted with ethyl acetate as in the case of the pyridine solution to yield a brown/orange powder (1.32 g, 87% yield): ^1H NMR (DMSO-d_6), δ 3.1 (d, 4 H, CH$_2$-P), δ 7.45 (d, 4 H, ArH), δ 7.80 (d, 4 H, ArH); Raman (H$_2$O) 1616, 1477, 1433, and 1160 cm^{-1}; IR (KBr) 1602, 1499, 984, and 581 cm^{-1}; UV–vis λ_{max} (aqueous, pH = 10) 348 nm.

Substrate Preparation and Primer Layer Formation. Gold substrates for the SPR and PM/FT-IRRAS measurements were prepared by the vapor deposition of thin (47 nm) gold films onto glass microscope slide covers as reported previously.[36,48,49] Prior to ZP multilayer deposition, a monolayer of MUD was first self-assembled on the gold surface by immersion in a 1 mM ethanolic solution for 48–72 h. The resulting alcohol-terminated surface was then phosphorylated using previously described methods,[35] followed by zirconation in 5 mM ZrOCl$_2$ aqueous solution and the self-assembly of one DBP monolayer (by immersion in a 1.2 mM aqueous solution for 16 h). The surface was rinsed thoroughly with Millipore-filtered water between all deposition steps. This resultant "primer layer" was prepared on all of the gold substrates prior to the formation of a ZP multilayer film. Silica substrates for the ellipsometry measurements were prepared from fused silica disks (Laser Optics, Inc., 1 in. diameter × 0.25 in., λ/20). The silica surface was prepared according to the following procedure: (i) immersion in 150 mL of 30/70 (v/v) 30% H$_2$O$_2$/ concentrated H$_2$SO$_4$ (Fluka, puriss) for 1 h with sonication [*Caution*: This solution is a highly oxidizing mixture that should only be prepared immediately before use and not stored],[50] (ii) extensive rinsing with water and absolute EtOH, (iii) heating at 110 °C for 4 h, (iv) silanization with a 10 mM (10-carbomethoxy-decyl)dimethylchlorosilane solution in octane heated to reflux for 24 h under nitrogen,[51] (v) rinsing in absolute EtOH for 1 h with sonication, (vi) heating at 110 °C for 1 h, and (vii) reaction with LiAlH$_4$ in THF for 2 min under nitrogen to reduce the terminal methyl ester on the silanized surface to an alcohol.[52] As in the case of the gold substrates, prior to ZP multilayer formation, this alcohol-terminated surface was first phosphorylated, zirconated, and then coated with a single DBP monolayer.

ZP Multilayer Formation Methodology. ZP multilayers were assembled on the primed gold and silica substrates by alternate exposure of the surface to an aqueous 5 mM ZrOCl$_2$ solution (1–2 h) and an aqueous 1.2 mM bisphosphonate (either DBP or AZO) solution (9–18 h). The surface was rinsed extensively with water after each deposition step. The extended exposure time to the DBP or AZO solution was required for complete self-assembly of the monolayer onto the surface at room temperature; shorter self-assembly times have been observed for elevated temperatures.[8,26]

(47) McKenna, C. E.; Higa, M. T.; Cheung, N. H.; McKenna, M. C. *Tetrahedron Lett.* **1977**, *2*, 155.
(48) Barner, B. J.; Corn, R. M. *Langmuir* **1990**, *6*, 1023.
(49) Goss, C. A.; Charych, D. H.; Majda, M. *Anal. Chem.* **1991**, *63*, 85.
(50) Finklea, H. O.; Robinson, L. R.; Blackburn, A.; Richter, B.; Allara, D.; Bright, T. *Langmuir* **1986**, *2*, 239.
(51) Wirth, M. J.; Fatunmbi, H. O. *Anal. Chem.* **1993**, *65*, 822.
(52) Tillman, N.; Ulman, A.; Penner, T. L. *Langmuir* **1989**, *5*, 101.

Figure 2. SPR reflectivity curves obtained during the formation of a 100% DBP multilayer film. The DBP multilayer is self-assembled onto a thin (47 nm) gold film that is in optical contact with a BK7 prism. The reflectivity of p-polarized light at 632.8 nm from the BK7/Au/DBP sample is monitored as a function of incident angle, θ (see inset). A sharp minimum in the reflectivity is observed at the SPR angle corresponding to the coupling of the incident laser light with surface plasmons at the Au/DBP interface. SPR reflectivity curves after the self-assembly of 0, 5, 10, 15, and 20 DBP monolayers are plotted. The shifts observed in the SPR angle can be quantitatively related to the thickness and index of refraction of the ZP multilayer.

PM/FT-IRRAS Measurements on Gold Substrates. All PM/FT-IRRAS differential reflectance spectra (%$\Delta R/R$) were obtained without a background or reference spectrum on a Mattson RS-1 spectrometer utilizing a methodology and optical layout that have been described previously.[53,54] The differential reflectance spectra were converted to absorbance units in order to compare them with normal FT-IRRAS spectra.[35] Spectra in the CH stretching region (3100–2700 cm^{-1}) were obtained with an InSb detector, and spectra in the mid-infrared region (1800–850 cm^{-1}) were obtained using a narrow band HgCdTe detector. All spectra were acquired at 2 cm^{-1} resolution from 1024 interferometer scans.

SPR Measurements on Gold Substrates. SPR reflectivity measurements were obtained with an SPR apparatus that has been described previously.[36] The thin gold film samples were brought into optical contact with a BK7 hemispherical prism using a drop of methyl salicylate (as an index matching fluid) between the prism and the back side of the gold-coated microscope slide cover. As shown schematically in the inset of Figure 2, the reflectivity of p-polarized light from a HeNe laser (632.8 nm, 1 mW, Newport Corp.) from the BK7/Au/ZP film sample was monitored as a function of incident angle, θ. Figure 2 plots a series of reflectivity curves obtained during the formation of a 20 monolayer DBP film. The reflectivity curves all exhibit a cusp at 41.3° corresponding to the critical angle of the BK7 hemispherical prism. Beyond the critical angle, a sharp dip in the reflectivity was observed that is associated with the formation of surface plasmons at the gold/ZP film surface. The position of the reflectivity minimum is denoted as the SPR angle and is shifted with the deposition of successive ZP multilayers onto the surface. The reflectivity curve

(53) Green, M. J.; Barner, B. J.; Corn, R. M. *Rev. Sci. Instrum.* **1991**, *62*, 1426.
(54) Barner, B. J.; Green, M. J.; Saez, E. I.; Corn, R. M. *Anal. Chem.* **1991**, *63*, 55.
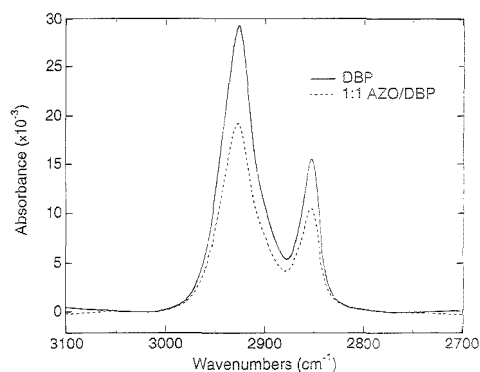
labeled "0 Layers" corresponds to a gold surface that has been modified with the primer layer mentioned above (phosphorylated MUD and 1 DBP monolayer). Shifts in the SPR angle ($\Delta\theta$) after the deposition of subsequent DBP monolayers were defined relative to the SPR angle for this surface. These shifts in the SPR angle were modeled with a six-phase [BK7 ($n = 1.52$), Au ($n = 0.154 + 3.55i$), MUD ($n = 1.45$), DBP ($n = 1.51$), ZP film, air] complex Fresnel calculation using a Pascal program described previously.[36]

UV–Vis Absorption and Ellipsometry Measurements on Silica Substrates. The deposition of AZO molecules onto transparent substrates was monitored by UV–vis spectra obtained from a Hewlett-Packard Model 8452A diode array spectrophotometer. Micromolar aqueous AZO solutions exhibited an absorption maximum at 348 nm, and ZP multilayer films exhibited an absorption maxiumum at 340 nm. The amount of absorbance at 340 nm increased linearly with the number of AZO monolayers for both the 100% AZO and the 1:1 AZO/DBP films. The slight blue shift in the absorption maximum upon deposition suggests that the AZO molecules are interacting slightly in the ZP multilayers. However, no UV photochemistry, i.e., trans to cis isomerization,[55-57] was observed in any of the AZO multilayers, even though a large photoactivity was observed for AZO molecules in an aqueous solution. Ellipsometry measurements for the various ZP films on fused silica were obtained with a Rudolph Research Model AutoEL II ellipsometer employing 633 nm light at an incident angle of 70°. The ellipsometric parameters Δ (the phase difference upon reflection) and Ψ (the arctangent of the amplitude ratio for the s and p components of light upon reflection) were measured as a function of ZP film thickness. These Δ and Ψ values were then compared with the results of a three-phase [SiO$_2$ ($n = 1.46$), ZP film, air] Fresnel calculation to determine an index of refraction for the ZP film.

RESULTS AND DISCUSSION

Characterization of a 100% DBP Multilayer Film. The CH stretching and mid-IR regions of the PM/FT-IRRAS spectrum for a ZP multilayer formed from the sequential self-assembly of 20 DBP monolayers onto a primer layer on a gold substrate are shown in Figures 3 and 4, respectively. The positions and relative intensities of the infrared bands in this spectrum did not change with the number of DBP multilayers, indicating that each self-assembled DBP monolayer had an equivalent molecular structure. The frequencies and assignments of the various infrared bands are listed in Table 1, and agree with the PM/FT-IRRAS spectrum obtained previously.[35] Three items in the PM/FT-IRRAS spectrum are of particular value in the determination of the molecular structure of the DBP multilayer film:

(i) The antisymmetric and symmetric methylene CH stretching bands occur at 2927 and 2854 cm^{-1}, respectively. The positions of these bands indicate that the self-assembled monolayers are not tightly packed in an all-trans configuration; instead, the DBP monolayers are thought to be disordered to accommodate the zirconium phosphonate lattice spacing in the inorganic portions of the ZP film.[11,13,35]

(55) Rau, H. In *Photochromism*; Durr, H., Laurent, H. B., Eds.; Elsevier: New York, 1990, pp 165–192.
(56) Ichimura, K.; Suzuki, Y.; Seki, T. *Langmuir* 1988, 4, 1214.
(57) Liu, Z.-F.; Morigaki, K.; Enomoto, T.; Hashimoto, K.; Fujishima, A. *J. Phys. Chem.* 1992, 96, 1875.

Figure 3. CH stretching region of the PM/FT-IRRAS spectra of a 20 monolayer 100% DBP film (solid line) and a 20 monolayer 1:1 AZO/DBP film (dashed line) on a vapor-deposited thin gold film. The gold surface was primed with a self-assembled monolayer of phosphorylated MUD and one self-assembled DBP monolayer before the formation of the ZP films. The antisymmetric and symmetric methylene stretching bands occur at 2927 and 2854 cm^{-1}, respectively, in both of the ZP films. The integrated area for the 1:1 AZO/DBP film is 70% of the 100% DBP film, which is higher than expected.
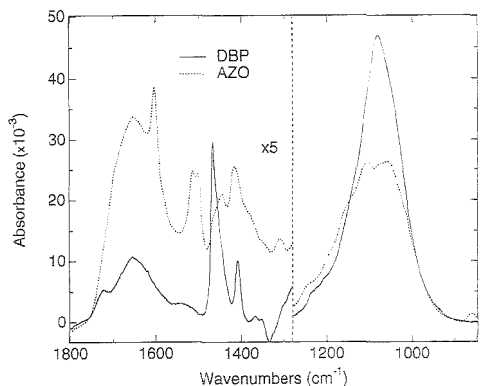
Figure 4. Mid-infrared region of the PM/FT-IRRAS spectra of a 20 monolayer 100% DBP film (solid line) and a 20 monolayer 100% AZO film (dashed line) on a vapor-deposited thin gold film. The gold surface was primed with a self-assembled monolayer of phosphorylated MUD and one self-assembled DBP monolayer before the formation of the ZP films. The frequencies and band assignments for the two spectra are listed in Table 1.

(ii) A single, sharp, well-defined phosphonate band is observed at 1080 cm^{-1}. The position of this band is representative of the structure of the inorganic portion of the ZP multilayer and becomes sharp and well-defined on densely packed primer monolayers.[35]

(iii) A broad and weak absorption band (corresponding to an intensity of ~1 × 10^{-4} AU/monolayer) is observed at 1654 cm^{-1}. This broad band is attributed to the bending vibration of water and indicates that some water molecules have been incorporated into the ZP multilayer (most likely in the inorganic portions of the film). The incorporation of water molecules into ZP multilayers has been observed previously.[12] Heating the film to 105 °C for 72 h under vacuum did not alter the intensity of this band.

Table 1. Vibrational Band Frequencies and Assignments for the DBP and AZO Multilayers[62-65]

frequency (cm^{-1})	band	assignment
	DBP Film	
2927 ± 1	$\nu_a(CH_2)$	methylene stretch
2854	$\nu_s(CH_2)$	methylene stretch
1654	$\delta(H_2O)$	water bending
1467	$\delta(CH_2)$	CH$_2$ scissoring def.
1409	$\delta(\alpha\text{-}CH_2)$	α-CH$_2$ scissoring def.
1080	$\nu_a(PO_3{}^{2-})$	phosphonate stretch
	AZO Film	
3060	$\nu_{20}(C-H)^a$	aromatic CH stretch
2930	$\nu_a(CH_2)$	methylene stretch
2856	$\nu_s(CH_2)$	methylene stretch
1653	$\delta(H_2O)$	water bending
1604	$\nu_{8a}(CC)^a$	ring stretch
1508	$\nu_{19a}(CC)^a$	ring stretch
1415	$\delta(\alpha\text{-}CH_2)$,	α-CH$_2$ scissoring def.,
	$\nu_{19b}(CC)^a$	ring stretch
1102, 1065	$\nu_a(PO_3{}^{2-})$	phosphonate stretch

^{a} Frequency modes and assignments follow the numbering convention of Wilson for para-substituted benzenes[66] and azobenzenes.[67]
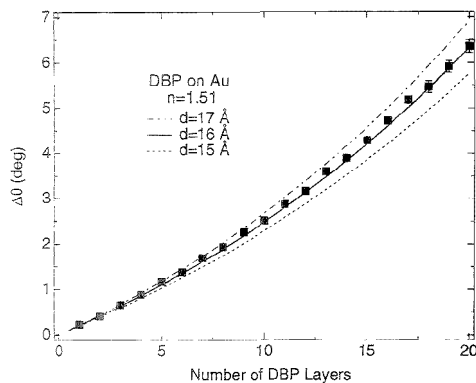
Figure 5. Shifts in the SPR angle ($\Delta\theta$) measured during the formation of a 20 monolayer 100% DBP film. The shifts $\Delta\theta$ were determined from SPR reflectivity curves such as those shown in Figure 2, with the SPR angle of the "0 Layer" surface defined as $\Delta\theta = 0$. The three lines in the figure are the results of complex Fresnel calculations using an index of refraction of 1.51 (as determined from ellipsometric experiments) for the ZP multilayer and a DBP monolayer thickness of 15, 16, or 17 Å. From the experimental data, a DBP monolayer thickness of 16 ± 0.5 Å is determined.

In order to determine the thickness of the DBP multilayer film, a series of SPR measurements were performed during the film deposition process. Figure 5 plots the shift ($\Delta\theta$) in the SPR angle observed after the addition of each self-assembled monolayer during the formation of a DBP multilayer film. As mentioned in the previous section, the SPR angle is determined from the minimum in the SPR reflectivity curve obtained with a HeNe laser at $\lambda = 632.8$ nm. In addition, the x-axis in the figure is defined as the number of monolayers that have been deposited onto a primer layer that consists of one DBP monolayer self-assembled onto a phosphorylated MUD monolayer. This primer layer was used for all of the ZP multilayers on gold substrates in this paper.

The shift in the SPR angle observed during the formation of the DBP multilayer can be used to determine the film thickness
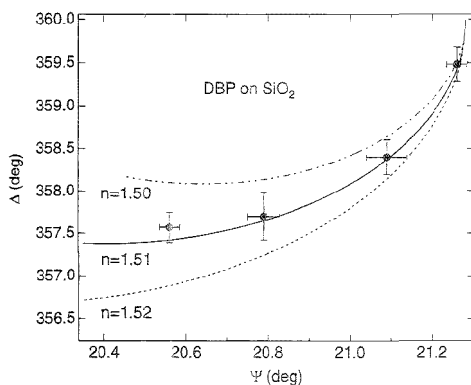
Figure 6. Ellipsometry measurements for 100% DBP multilayers formed on a fused silica substrate. Values of Δ and Ψ after the self-assembly of 10, 15, 20, and 25 DBP monolayers onto the silica surface are plotted as solid circles. The three curves in the figure are the results of complex Fresnel calculations for a three-phase system (SiO$_2$, film, air) as the film thickness is varied and its index of refraction is set to 1.50, 1.51, or 1.52. The film thickness for the three curves increases from right to left. From the experimental data, an index of refraction of 1.51 ± 0.01 is obtained for the 100% DBP multilayer. The results of ellipsometry measurements on other ZP multilayers are listed in Table 2.

if the index of refraction of the film (n) is known.[36] One possibility is to use the bulk index of refraction of $n = 1.54$; this approach was employed by Mallouk et al. to obtain a monolayer thickness of 16.4 Å from ellipsometric data.[22] In principle, ellipsometric measurements of the DBP multilayer on the gold substrate could be used to determine n and d simultaneously; in practice, however, the small shifts in Δ and Ψ observed from monolayers on metal surfaces make this determination difficult.[6,7] An alternate approach employed in this paper is to determine n for the various films by ellipsometric measurements on ZP multilayers that have been deposited onto a transparent silica substrate. The primer layer used for the transparent substrates is not as well-defined as the alkanethiol monolayer employed on the gold substrates and results in larger sample-to-sample variations in film thickness for a given number of monolayers. However, for films of 10–30 monolayers, the changes in Δ and Ψ are large enough to determine the index of refraction to ±0.01. For example, the ellipsometric (Δ,Ψ) values for 10, 15, 20, and 25 DBP multilayers deposited onto a silica substrate are plotted in Figure 6. Also plotted in the figure (the solid and dashed lines) are the theoretical (Δ,Ψ) values expected as a function of film thickness with n fixed at either 1.50, 1.51, or 1.52. The experimental data clearly show that n for the DBP multilayer film is determined to be equal to 1.51 ± 0.01. Similar ellipsometric measurements were used to determine n for the other ZP multilayers described in this paper and are listed along with the value for the 100% DBP film in Table 2.

Now that it has been determined that the index of refraction for the DBP multilayers is equal to 1.51, the SPR angle shifts in Figure 5 can be analyzed to ascertain the thickness of the self-assembled DBP monolayers. Using a six-phase Fresnel calculation, the theoretical curves for $\Delta\theta$ as a function of the number of ZP monolayers are plotted in Figure 5 for monolayer thicknesses of 15, 16, and 17 Å. A comparison of the experimental data points

Table 2. Monolayer Thicknesses and Indices of Refraction for the ZP Multilayer Films

film	n^a	d (Å/layer)^b	$\Delta\theta_{20}$ (deg)	d_{20} (Å)
DBP	1.51 ± 0.01	16 ± 0.5	6.36 ± 0.15^c	320 ± 5
AZO	1.64	16	8.33	320
1:1	1.57	19	9.65	380

^{a} Determined by ellipsometry on fused silica substrates. ^{b} Determined by SPR on vapor-deposited gold slides. ^{c} Reported uncertainty is the standard deviation of three gold-ZP film samples.

and the theoretical $\Delta\theta$ curves demonstrate that a DBP monolayer thickness of 16 ± 0.5 Å can be obtained from the SPR measurements. This thickness agrees favorably with values reported previously.[22] The accuracy of better than ± 1 Å is typical for the SPR technique[36] and is remarkable for an optical measurement at $\lambda = 632.8$ nm. On the basis of a space-filling model, the inorganic portion of the DBP monolayer from the center of the first carbon above to the first carbon below the layer is determined to be about 6.5 Å. In an all-trans configuration that is oriented perpendicular to the surface, the additional nine methylene groups contribute about 11.4 Å, for a total thickness of ~17–18 Å.[32,58] An experimentally determined average monolayer thickness of 16 Å is plausible given the possibility of tilting and the presence of alkyl chain disorder in the DBP monolayer as observed in the PM/FT-IRRAS spectrum.

Characterization of a 100% AZO Multilayer Film. For comparison with the 100% DBP monolayer, a second ZP multilayer was created by the sequential self-assembly of AZO monolayers onto a primer layer on a gold substrate. The CH stretching region of the PM/FT-IRRAS spectrum for the 100% AZO multilayer (not shown) was dominated by the antisymmetric and symmetric methylene stretches of the primer layer at 2925 and 2852 cm^{-1}, respectively. Moreover, the integrated area of these methylene bands did not change significantly after the deposition of the first three AZO monolayers and was only slightly larger after the deposition of 20 AZO monolayers. The constant intensities of the primer layer bands suggest that (i) no changes in band intensity due to local field effects were observed in the ultrathin ZP films, as expected given the relatively long wavelength of the infrared light, and (ii) the methylene stretches of the two methylene groups in the AZO molecule were very weak ($< 3 \times 10^{-5}$ AU/monolayer). After the deposition of 20 AZO monolayers, a weak, broad aryl CH stretching band was observed at 3060 cm^{-1}.

The mid-IR region of the PM/FT-IRRAS spectrum for the 100% AZO multilayer is plotted as the dashed line in Figure 4. As in the case of the DBP multilayer, the positions and relative intensities of the various infrared bands in this spectrum did not change with film thickness, indicating that each self-assembled AZO monolayer possessed an equivalent molecular structure. The frequencies and assignments of the various infrared bands are listed in Table 1. New bands from the azobenzyl functionality appear at 1604 and 1508 cm^{-1}. The water bending band at 1652 cm^{-1} is more intense than that in the PM/FT-IRRAS spectrum of the DBP multilayer film, and the phosphonate band at ~1100 cm^{-1} is smaller and split into two bands. These last two comparisons suggest that the AZO multilayer film is more disordered than the DBP multilayer film.[11]

(58) Dines, M. B.; DiGiacomo, P. M. *Inorg. Chem.* **1981**, *20*, 92.
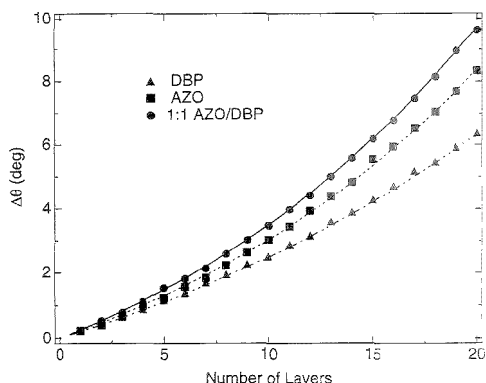
Figure 7. Shifts in the SPR angle ($\Delta\theta$) measured during the formation of 20 monolayer ZP films of 100% DBP (triangles), 100% AZO (squares), and 1:1 AZO/DBP (circles). The shifts $\Delta\theta$ were determined from SPR reflectivity curves, with $\Delta\theta = 0$ defined as the SPR angle for the primed gold surface (see text for details). The solid and dashed lines are the results of complex Fresnel calculations using the indices of refraction and average monolayer thicknesses for DBP, AZO, and 1:1 AZO/DBP films listed in Table 2. An unexpectedly large average monolayer thickness of 19 Å is observed for the 1:1 AZO/DBP film.

In order to determine the film thickness, SPR measurements were performed during the deposition of the AZO multilayer film, and the shift ($\Delta\theta$) in the SPR angle observed after the addition of each self-assembled monolayer is plotted as the squares in Figure 7. For comparison, the SPR data for the DBP film from Figure 5 are plotted in the figure as the triangles. A larger $\Delta\theta$ per monolayer is observed for the AZO multilayer film; this larger shift is attributed to a higher index of refraction of the AZO multilayer. As listed in Table 2, ellipsometric measurements of AZO multilayer films on a transparent substrate yield an index of refraction of $n = 1.64 \pm 0.01$. This value is within the range observed for azobenzene-derivatized polymers (1.623–1.758)[59] and is significantly higher than the value of 1.51 observed for the DBP film. Using an index of refraction of 1.64, the six-phase Fresnel calculations can be used to analyze the SPR shifts and determine an average AZO monolayer thickness of 16 ± 0.5 Å, which is the same value obtained for the DBP monolayer. The similarity of these two numbers suggests that mixed monolayers of these two molecules may yield stable ZP multilayer films. On the basis of a space-filling model with an inorganic section thickness of 6.5 Å, the AZO monolayer in which the azobenzene is oriented perpendicular to the surface (9–10 Å) should have a total thickness of ~17–18 Å.[32,58] The smaller experimentally determined value of 16 Å again suggests tilting and disorder in the ZP film.

Characterization of a 1:1 AZO/DBP Multilayer Film. Having determined that a DBP multilayer film has an index of refraction $n = 1.51$ and that an AZO multilayer film has an index of refraction $n = 1.64$, one would expect that a ZP multilayer film formed from alternating self-assembled monolayers of AZO and DBP would possess an index of refraction of $n = (1.64 + 1.51)/2 = 1.575$. Indeed, the ellipsometric measurements of a 1:1 AZO/

(59) Kohler, W.; Robello, D. R.; Willand, C. S.; Williams, D. J. *Macromolecules* **1991**, *24*, 4589.
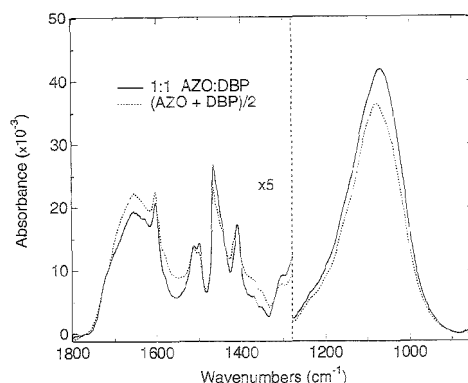
DBP multilayer film on a transparent substrate yield a value of n = 1.57 (see Table).

However, SPR measurements on the 1:1 AZO/DBP multilayer suggest that even though $n = 1.57$ as expected, the structure and thickness of the ZP film have changed. As with the previous two ZP films, SPR measurements were performed during the deposition of the 1:1 AZO/DBP multilayer film in order to determine the average monolayer thickness. The shift $\Delta\theta$ observed after the addition of each self-assembled monolayer is plotted as circles in Figure 7 along with the data from the DBP and AZO multilayers. Given that $n = 1.57$ for this film, one would expect that the $\Delta\theta$ curve for this film would fall in between the curves from the AZO and DBP multilayers. Unexpectedly, the data for the 1:1 AZO/DBP multilayer systematically show a *larger* $\Delta\theta$ shift than either of the other two films. Using $n = 1.57$, this $\Delta\theta$ curve corresponds to an average monolayer thickness of 19 Å, which is a 19% increase in the average thickness as compared to the 16 Å obtained for both the AZO and DBP monolayers. To demonstrate how unusual this number is, if the monolayer thickness is fixed at 16 Å, the $\Delta\theta$ curve for the 1:1 AZO/DBP multilayer can only be fit using an index of refraction of 1.70, which is clearly an unreasonable number given $n = 1.64$ for the 100% AZO multilayer.

What structural changes have occurred that result in a new average thickness of 19 Å/monolayer for the 1:1 AZO/DBP multilayers? The UV–vis experiments on the 1:1 AZO/DBP multilayers used to characterize the ZP film formation on the transparent substrates showed no unusual behavior: the absorption spectra were the same as those obtained from the 100% AZO monolayers except that the overall absorbance was half as intense, as expected. The PM/FT-IRRAS spectrum of the 1:1 AZO/DBP film, however, was not quite what was expected. The CH stretching region for the 1:1 AZO/DBP multilayer is plotted as the dashed line in Figure 3 along with the spectrum for the 100% DBP multilayer. The frequencies of the methylene bands are the same in the two samples, indicating that there are no large structural changes in the DBP monolayers of the mixed film. However, the integrated intensity of the methylene bands for the 1:1 film is 70% of that observed for the pure DBP multilayer. This value is ~20% higher than expected.[60]

The mid-IR region of the PM/FT-IRRAS spectrum for the 1:1 AZO/DBP multilayer is plotted in Figure 8 (the solid line) and confirms the discrepancy observed in the methylene stretching bands. Also plotted in the figure is a spectrum labeled "(AZO + DBP)/2" (the dashed line). This artificial spectrum is synthesized from the spectra of the 100% AZO and 100% DBP multilayers and represents what should have been observed if the picture in Figure 1 were correct. Instead, the phosphonate band at 1080 cm^{-1} and the DBP methylene scissoring band at 1466 cm^{-1} are more intense in the spectrum of the true 1:1 AZO/DBP multilayer by ~18%. The aryl bands of the azobenzene functionality are about the same intensity in the two spectra, and the water band in the true spectrum is smaller than expected.

Note that only intensity changes are observed in the PM/FT-IRRAS spectrum of the 1:1 AZO/DBP multilayer. No changes in vibrational band frequencies are observed, indicating that there

(60) The expected value for the CH stretching region is based on an artificial spectrum derived by taking the average of the 100% AZO and the 100% DBP spectra. The integrated intensity of the methylene stretching bands for the synthesized spectrum is 57% of that observed for the pure DBP multilayer. This value is 20% lower than the intensity of the measured 1:1 AZO/DBP spectrum.

Figure 8. Mid-infrared region of the PM/FT-IRRAS spectrum of a 20 monolayer 1:1 AZO/DBP ZP film (solid line). The gold surface was primed with a self-assembled monolayer of phosphorylated MUD and one self-assembled DBP monolayer before the formation of the ZP film. This spectrum contains contributions from both the AZO and DBP portions of the multilayer, although the DBP bands are 18% more intense than expected. For comparison, a synthetic spectrum denoted as "(AZO + DBP)/2" (dashed line) that was generated from the spectra of the 100% DBP and 100% AZO multilayers is also plotted.

are no large changes in the molecular structure of the 1:1 AZO/DBP multilayer. The changes in band intensity can be attributed to one of two effects: either there has been a change in the orientation of the molecules in the AZO and DBP monolayers, or there has been a change in the number density of molecules in the ZP multilayers. Most of the change in intensity arises from changes in the vibrational bands associated with the DBP molecules; very little change is observed in the intensity of the vibrational bands of the AZO molecules in the ZP film. The SPR data clearly show that the average monolayer thickness has increased by 19% in the 1:1 AZO/DBP multilayer film. If this increase were to arise from a more perpendicular orientation of the DBP multilayers, one would expect to see a *decrease* in the intensity of the methylene stretching bands. Such decreases are often observed in the well-oriented samples of *n*-alkanethiol monolayers self-assembled onto gold surfaces.[41,43] The fact that we instead observe an *increase* in the stretching band intensities (but no change in the band frequencies) implies that 19% more DBP has been incorporated into the 1:1 AZO/DBP film than the amount suggested in the simple picture in Figure 1. It is this additional DBP that must lead to the increased average film thickness of 19 Å/monolayer. In fact, a reexamination of the SPR data in Figure 7 also shows this to be true. The amount of shift in the SPR angle uniformly increases for the 1:1 AZO/DBP film with each additional monolayer deposition. If the same amount of AZO and DBP were deposited with each monolayer, we would expect to see a larger shift for the AZO monolayers (due to its higher index of refraction) than for the DBP monolayers.

How does the additional 19% of DBP get incorporated into the 1:1 AZO/DBP multilayer film? It is important to remember that all of the optical measurements employed in this paper to analyze the ZP films are average measurements over the entire surface. Thus an average monolayer thickness of 16 Å/monolayer could mean that a significant portion of a given DBP or AZO self-assembled monolayer has a thickness of 19 Å, while the rest of

the film is significantly thinner; increasing the average film thickness just means that the amount of thicker monolayer regions has increased. Another possibility is that changes in the packing structure of the inorganic zirconium phosphonate lattice for the mixed monolayers are responsible for changes in the packing density of the organic sections of the monolayer. This may also provide a possible explanation for the observed decrease in the intensity of the water band at 1653 cm^{-1}, since it is likely that the water resides in the inorganic regions of the film. Similar arguments of changes in the structure of the zirconium phosphonate lattice have been suggested by Byrd et al. and Zeppenfeld et al. in their studies of metal phosphonate multilayers.[30,32] In addition, a third possibility is that excess DBP intercalates into the preceding AZO regions of the 1:1 AZO/DBP multilayer film. This results from the inability to form pure well-ordered AZO monolayers due to the azo dye substituent area being greater than that of the phosphonate headgroup area of 24 Å^2. The incorporation of excess DBP molecules into the AZO regions may then cause both sets of molecules to stand straighter, i.e., more perpendicular, resulting in the observed larger 1:1 AZO/DBP multilayer film thickness. An analogous bulk system in which large tetramethyl biphenylphosphonate groups are surrounded by smaller phosphite groups has been reported by Alberti et al.[61]

SUMMARY AND CONCLUSIONS

In summary, we have demonstrated that mixed zirconium phosphonate multilayer films can be used to create ultrathin

organic films with a specified thickness and index of refraction. In particular, the two molecules DBP and AZO can be used to create mixed ZP multilayer films of index of refraction at 632.8 nm between 1.51 and 1.64. In principle, one could construct graded index of refraction ZP films by systematically changing the AZO/DBP ratio during the multilayer film formation. A second potential application of these DBP and AZO monolayers would be to mix them with SHG-active ZP multilayers in order to tune the index of refraction and phase matching characteristics of the resultant ZP multilayer. We are currently pursuing the synthesis and self-assembly of SHG-active ZP multilayers that employ an additional phosphorylation step during deposition, as first demonstrated by Katz et al.[7]

The studies reported in this paper demonstrate that SPR and PM/FT-IRRAS measurements are a pair of well-matched, highly sensitive methods for determining the molecular structure and the thickness of the ZP multilayers. In particular, it was shown that the 1:1 mixed AZO/DBP monolayer did not exhibit the thickness expected from the 100% DBP and 100% AZO multilayers; additional DBP molecules are apparently incorporated into the mixed ZP multilayer film. In preliminary experiments on 2:1 and 1:2 AZO/DBP multilayer films, we have seen similar effects in the average film thickness. It is clear from these initial results that the optical and spectroscopic characterization measurements employed in this work are essential tools for the rational design of ultrathin optical films via the self-assembly of organic monolayers.

(61) Alberti, G.; Costantino, U.; Marmottini, F.; Vivani, R.; Zappelli, P. *Angew. Chem., Int. Ed. Engl.* 1993, *32*, 1357.
(62) Bellamy, L. J. *The Infra-red Spectra of Complex Molecules*; Wiley: New York, 1975.
(63) Socrates, G. *Infrared Characteristic Group Frequencies*; Wiley: Chichester, 1980.
(64) Lin-Vien, D.; et al. *The Handbook of Infrared and Raman Characteristic Frequencies of Organic Molecules*; Academic: Boston, 1991.
(65) Thomas, L. C. *Interpretation of the Infrared Spectra of Organophosphorus Compounds*; Heyden: London, 1974.
(66) Sverdlov, L. M.; Kovner, M. A.; Krainov, E. P. *Vibrational Spectra of Polyatomic Molecules*; John Wiley & Sons: New York, 1974; pp 341.
(67) Klima, M. I.; Kotov, A. V.; Gribov, L. A. *J. Struct. Chem.* 1972, *13*, 987.

Dynamics of Acrylodan-Labeled Bovine and Human Serum Albumin Sequestered within Aerosol-OT Reverse Micelles

Jeffrey S. Lundgren, Mark P. Heitz, and Frank V. Bright*

Department of Chemistry, Natural Sciences and Mathematics Complex, State University of New York at Buffalo, Buffalo, New York 14260-3000

We investigate the effects of hydration on acrylodan-labeled bovine and human serum albumin (BSA-Ac and HSA-Ac) in aerosol-OT (AOT) reverse micelles solubilized in *n*-heptane. Time-resolved fluorescence intensity decay experiments reveal a dipolar relaxation process surrounding the acrylodan cybotactic region. This process is best described by a two-term rate law wherein the *average* relaxation increases with increased hydration. However, the actual rate constants describing the relaxation process either remain unchanged or actually *decrease* with increased hydration. The results illustrate that the fractional contribution associated with the individual relaxation pathways causes the observed changes in relaxation dynamics. The recovered rotational reorientation dynamics of the acrylodan residue are also affected by the extent of protein hydration. As hydration is increased, the semiangle through which the acrylodan residue precesses *increases* by 10° for both protein systems. Interestingly, the recovered semiangles for the native proteins equal those recovered at *lower* hydration when the proteins are sequestered within the AOT reverse micelle. These results demonstrate the importance of hydration on protein behavior in environments where water is limited (e.g., biosensor interfaces and sol–gel-derived biocomposites).

At the most elementary level, proteins are identified by their amino acid sequence or primary structure.[1-3] This structure can be altered only by breaking and/or forming new covalent bonds within the peptide chain. To a first approximation, protein conformation, function, and stability depend strongly on primary structure, but secondary, tertiary, and quaternary structures also affect protein behavior/function.[1-3] Plasma proteins, enzymes, and antibodies are systems in which ultimate function/performance are governed by subtle structural changes within the protein microdomains.[4]

A portion of the research in our group has focused on the development of analytical biosensors.[5-7] During the course of this work, we have become acutely aware of the need to understand and thus control the behavior of a biorecognition element (e.g., enzymes and antibodies) at or within a sensor interface. For example, it has become evident that the act of immobilizing/entrapping the biorecognition element to form the biosensor can alter its function, behavior, performance, and/or stability and ultimately affect a biosensor's analytical figures of merit. We have also shown that a complex interdependence exists between the biorecognition element and the behavior of the reporter group (i.e., fluorophore) used to "sense" target analyte–biorecognition element binding.

Many studies have shown that "hydration" plays a key role in protein structure and performance.[8-17] Thus, the degree of protein hydration and/or local solvent composition can affect a protein's structure and dynamics and, in turn, its performance. For example, Goryunov and co-workers[13] have illustrated how human serum albumin (HSA) is affected by solvation. These authors followed the spin–spin relaxation times of water protons and found that they were a function of the percent age of D_2O in the system, demonstrating that the stability of HSA is influenced by the degree of hydration. Bolton and Scherer[18] have shown that the structure of bovine serum albumin (BSA), cast as a thin film, is affected by the relative humidity (RH). In this work, Raman spectroscopy was used to follow changes in the α-helicity of BSA as a function of RH. Together these results demonstrate that protein hydration can control protein conformation and behavior. Thus, it seems clear that any attempt toward exploiting proteins as chemical

---

(1) Stryer, L. *Biochemistry;* W. H. Freeman and Co.: New York, 1988.
(2) Schultze, H. E.; Heremans, J. F. *Molecular Biology of Human Proteins;* Elsevier Publishing Co.: New York, 1966; Vol. 1, Chapter 1, pp 7–40.
(3) DeVoe, H. In *Structure and Stability of Biological Macromolecules: Theory of the Conformation of Biological Macromolecules in Solution;* Timasheff, N. S., Fasman, G. D., Eds.: New York, 1969; pp 2–63.
(4) Creighton, T. E. *Protein Function: A Practical Approach;* Oxford University Press: New York, 1989.

(5) (a) Bright, F. V.; Litwiler, K. S.; Vargo, T. G.; Gardella, J. A., Jr. *Anal. Chim. Acta* 1992, *262*, 323–30. (b) Betts T. A.; Catena, G. C.; Huang, J.; Litwiler, K. S.; Zhang, J.; Zagrobelny, J.; Bright, F. V. *Anal. Chim. Acta* 1991, *246*, 55–63. (c) Bright, F. V.; Betts, T. A.; Litwiler, K. A. *Anal. Chem.* 1990, *62*, 1065–9.
(6) (a) Lundgren, J. S.; Bekos, E. J.; Wang, R.; Bright, F. V. *Anal. Chem.* 1994, *66*, 2433–40. (b) Wang, R.; Narang, U.; Prasad, P. N.; Bright F. V. *Anal. Chem.* 1993, *65*, 2671–5. (c) Narang, U.; Wang, R.; Prasad, P. N.; Bright, F. V. *J. Phys. Chem.* 1994, *98*, 17–22. (d) Jordan, J. D.; Dunbar, R. A.; Bright, F. V. *Anal. Chem.* 1995, *67*, 2436–43.
(7) Wang, R.; Sun, S.; Bekos, E. J.; Bright, F. V. *Anal. Chem.* 1995, *67*, 149–59.
(8) Steinmann, B.; Jäckle, H.; Luisi, P. L. *Biopolymers* 1986, *25*, 1133–56.
(9) Gekko. K.; Morikawa, T. *J. Biochem.* 1981, *90*, 39–50.
(10) Otting, G.; Liepinish, E.; Wüthrich, K. *Science* 1991, *254*, 974–80.
(11) Berndt, K. D.; Beunink, J.; Schröder, W.; Wüthrich, K. *Biochemistry* 1993, *32*, 4564–70.
(12) Khurgin, Y.; Maksareva, E. *FEBS Lett.* 1993, *315*, 149–52.
(13) Kaivarainen, A. I.; Sukhanova, G.; Goryunov, A. S. *Folia [Biol.]* 1984, *30*, 84–92.
(14) Gallay, J.; Vincent, M.; Nicot, C.; Waks, M. *Biochemistry* 1987, *26*, 5738–47.
(15) Holmberg, K. *Adv. Colloid Interface Sci.* 1994, *51*, 137–74.
(16) Ruckenstein, E.; Karpe, P. *Biotechnol. Lett.* 1990, *12*, 241–6.
(17) Han, D.; Rhee, J. S. *Biotechnol. Bioeng.* 1986, *28*, 1250–5.
(18) Bolton, B. A.; Scherer, J. R. *J. Phys. Chem.* 1989, *93*, 7635–40.

recognition elements should be carried out with attention to the effect of hydration on the protein–reporter group couple.

Aerosol-OT (AOT) reverse micelles allow one to simultaneously solubilize proteins within a defined domain *and* control the extent of protein hydration.[19,20] AOT reverse micelles consist of a polar core surrounded by ionic head groups that are, in turn, attached to aliphatic tails, suspended in an organic liquid phase.[21,22] Thus, by adding protein and the desired amount of water to this system, both of which are sequestered within the reverse micelle, one can effectively control the degree of protein hydration.

In this paper, we report on the effects of hydration on BSA and HSA. These proteins were selected because they have been used previously as models[6a,7,13,18,21,22] and they both have a single, free cysteine residue at position 34.[23,24] This particular site provides a convenient target for site-selective labeling[25] with the fluorescent probe 6-acryloyl-2-(dimethylamino)naphthalene (acrylodan, Ac). Thus, these systems serve as simple biorecognition element–reporter group couples. Further, because all fluorescence results from a single, well-defined site within the protein, we can follow how protein hydration influences the dynamics surrounding the cysteine-34 residue.

Previous work from our group on BSA-Ac has demonstrated that there are nanosecond and subnanosecond dipolar relaxation processes within the cybotactic region surrounding the acrylodan reporter group.[7] Complementary time-resolved decays of anisotropy revealed that the rotational motion of the acrylodan reporter group in the native protein is limited to a semiangle of 23 ± 1°. In the current work, our goals are to determine the effects of hydration on (1) the average local environment surrounding the acrylodan reporter group, (2) the dynamics of the cybotactic region surrounding the acrylodan residue, and (3) the rotational dynamics associated with the acrylodan probe. Steady-state and time-resolved fluorescence are used to address these issues, and AOT reverse micelles formed in *n*-heptane serve to control the extent of protein hydration.

THEORY

The theory of frequency-domain fluorescence for recovering intensity and anisotropy decays and determining the time evolution of the fluorescence emission spectrum (e.g., dipolar relaxation of the cybotactic region) has been described elsewhere.[7,26–29] The interested reader is referred to the aforementioned references for a more thorough description of the acquisition techniques, data analysis schemes, and basic interpretation.

Time-Dependent Spectral Relaxation. Photoexcitation of a fluorophore generally leads to an instantaneous change in the

(19) Marzola, P.; Pinzino, C.; Veracini, C. A. *Langmuir* 1991, 7, 238–42.
(20) Marzola, P.; Gratton, E. *J. Phys. Chem.* 1991, 95, 9488–95.
(21) Costantino, L.; Volpe, C. D.; Ortona, O.; Vitagliano, V. *J. Chem. Soc., Faraday Trans.* 1992, 88, 61–3.
(22) Fletcher, P. D. I. *J. Chem. Soc., Faraday Trans.* 1987, 83, 1493–506.
(23) Rosenoer, V. M.; Oratz, M. *Albumin Structure, Function, and Uses*; Pergamon Press: New York, 1977.
(24) Bing, D. H. *The Chemistry and Physiology of Human Plasma Proteins*; Pergamon Press: New York, 1979.
(25) Garrison, M. D.; Iuliano, D. J.; Saavedra, S. S.; Truskey, G. A.; Reichert, W. M. *J. Colloid Interface Sci.* 1992, 148, 415–24.
(26) (a) *Topics in Fluorescence Spectroscopy*; Lakowicz, J. R., Ed.; Plenum Press: New York, 1991; Vols. 1–3. (b) Bright, F. V.; Betts, T. A.; Litwiler, K. S. *CRC Crit. Rev. Anal. Chem.* 1990, 21, 389–405.
(27) Gratton, E.; Jameson, D. M.; Hall, R. D. *Annu. Rev. Biophys. Bioeng.* 1984, 13, 105–24.
(28) Lakowicz, J. R. *Principles of Fluorescence Spectroscopy*; Plenum Press: New York, 1983; Chapter 6, pp 155–85.
(29) Lakowicz, J. R.; Cherek H. *Chem. Phys. Lett.* 1985, 122, 380–4.

fluorophore's dipole moment.[26a] This disrupts the equilibrium between the fluorophore and its surrounding environment. In order to reestablish equilibrium, the solvent molecules and/or local groups within the cybotactic region "relax" or "reorganize" to minimize the unfavorable interactions produced following the sudden change in the fluorophore dipole moment. If this relaxation process occurs on a time scale similar to the fluorophore excited-state lifetime, it results in a quantifiable, time-dependent shifting of the emission spectrum.[7,27–32] In turn, this provides information on the dynamics of the local environment surrounding the fluorescent reporter group.[7,27–32]

Decay of Fluorescence Anisotropy. Time-resolved fluorescence anisotropy measurements on biomolecule–reporter group systems provides information on the global motion of the protein and local motion of the fluorescent reporter group. Our previous work[7] on BSA-Ac showed that the decay of anisotropy, r(t), was described by a double exponential decay of the form

$$r(t) = r_o[\beta_1 \exp^{-t/\phi_1} + \beta_2 \exp^{-t/\phi_2}]$$

where r_o is the limiting anisotropy, ϕ_1 is the rotational correlation time associated with the local motion of the probe, and ϕ_2 is the rotational correlation time of the global motion of the protein. The terms β_1 and β_2 are the fractional contributions to the total anisotropy decay from the local and global motions, respectively ($\sum \beta_i = 1$).

If the probe precesses about its axis, *and* the protein is free to rotationally reorient, one can associate a semiangle (θ) with the range of motion that the probe experiences over the course of the excited-state lifetime:[7,26a]

$$\theta = \cos^{-1}\{^1/_2[(8\beta_2{}^{1/2} + 1)^{1/2} - 1]\}$$

Thus, if the cybotactic region surrounding the reporter group were totally restrictive to the local motion of the fluorescent reporter group, θ would approach 0°. In contrast, an increase in the semiangle indicates that the probe has more local mobility.

EXPERIMENTAL SECTION

Reagents. The following chemicals were used: 6-acryloyl-2-(dimethylamino)naphthalene (acrylodan, Molecular Probes); essentially fatty acid-free BSA, HSA, and 12 000 MW cutoff cellulose dialysis tubing (Sigma Chemical Co.); sodium bis(2-ethylhexyl)-sulfosuccinate and 1,4-bis(4-methyl-5-phenyl-2-oxazolyl)benzene (Me_2POPOP) (Aldrich Chemical Co.); *n*-heptane (Mallinckrodt Specialty Chemicals Co.); $Na_2HPO_4 \cdot 7H_2O$, $NaNO_3$, and $NaClO_4 \cdot H_2O$ (Fisher Chemical); and $NaH_2PO_4 \cdot H_2O$ (J. T. Baker Inc.).

Preparation of BSA- and HSA-Ac. BSA- and HSA-Ac were prepared according to published protocols.[7,25]

Encapsulation of BSA- and HSA-Ac in AOT. A stock solution of 0.2 M AOT was prepared by adding the dry AOT solid to a 250 mL volumetric flask. Two hundred milliliters of *n*-heptane was then added, the solution was sonicated until all of the AOT had dissolved and diluted to volume with *n*-heptane. Protein was loaded into the reverse micelles by first placing an aliquot of the

(30) Maroncelli, M.; Fleming, G. R. *J. Chem. Phys.* 1987, 86, 6221–9.
(31) Maroncelli, M.; Castner, E. W.; Bagchi, B.; Fleming, G. R. *Faraday Discuss. Chem. Soc.* 1988, 85, 199–210.
(32) Maroncelli, M.; MacInnis, J.; Flemming, G. R. *Science* 1989, 3, 1674–81.

stock AOT solution into a quartz cuvette. In a second step, we added a known volume of distilled, deionized water to the micelle solution. In the final step, we added a known volume of the protein stock solution. The total water added to the system, defined as the water loading ($R = [water]/[AOT]$), is the sum of the water added in step 2 and the water from the protein stock solution. The final concentration of the acrylodan-labeled serum albumin was always 0.5 μM. All samples were equilibrated at 20 °C for at least 12 h prior to fluorescence measurements. Under these particular conditions, there is little probability of two or more proteins being sequestered within a single micelle.

Fluorescence Measurements. All steady-state measurements were performed with a SLM 48000 MHF spectrofluorometer using a Xe arc lamp as the excitation source. All measurements were made at 20 °C, and spectra were background subtracted.

Time-resolved intensity and anisotropy decay data were acquired in the frequency domain using a SLM 48000 MHF multifrequency phase–modulation fluorometer. An argon ion laser (Coherent, Model Innova 400-10) operating at 351.1 nm was used as the excitation source. A 340 ± 20 nm bandpass filter was placed in the excitation path to eliminate extraneous plasma discharge. Magic angle polarization was used for all excited-state intensity decay experiments.[33] Me$_2$POPOP in ethanol served as the reference lifetime standard; its lifetime was assigned a value of 1.45 ns.[28] For all experiments, the Pockels cell was operated at a repetition rate of 5 MHz. Typically data were collected for 60–90 s over a frequency range of 5–125 MHz (25 frequencies). All multifrequency phase and modulation data were analyzed according to the global analysis method described elsewhere.[7,34-36]

RESULTS AND DISCUSSION

Steady-State Fluorescence. The site-selective labeling of the serum albumin at the cysteine-34 (loop 1, domain I) defines the cybotactic region of the acrylodan report group.[7] Thus, by using the reverse micelle system and controlling R, we are able to follow the way protein hydration affects the cybotactic region surrounding cysteine-34. Figure 1A presents the steady-state emission spectra of HSA-Ac in AOT at six different water loadings and compares them to the native protein in 0.1 M phosphate buffer (pH 7.0). Clearly, as R increases, there are several changes in the *average* local environment surrounding the acrylodan residue. First, the emission spectra shift from 440 nm at $R = 2.78$ to 465 nm at $R = 22.2$. Second, the emission spectra broaden and the total fluorescence decreases with increasing R. The same trend is observed for BSA-Ac (data not shown). Third, as the protein is hydrated (R is increased), the average environment surrounding the Ac group apparently becomes more similar to the environment seen for the native protein. However, even above $R = 22.2$, the emission spectra are unchanged and do not reach those seen for native BSA- or HSA-Ac.

In order to better compare the effects of hydration on the BSA- and HSA-Ac emission, Figure 1B presents the emission center of
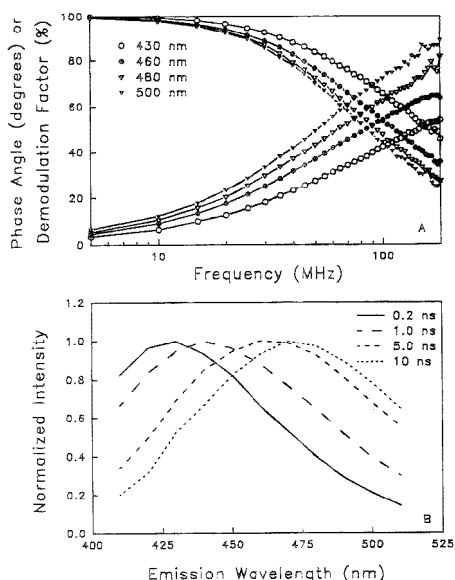
(33) Spencer, R. D.; Weber, G. J. *Chem Phys.* **1970**, *52*, 1654–67.
(34) (a) Wang, R.; Bright, F. V. *J. Phys. Chem.* **1993**, *97*, 4231–8. (b) Wang, R.; Bright, F. V. *J. Phys. Chem.* **1993**, *97*, 10872–8. (c) Wang, R.; Bright, F. V. *Appl. Spectrosc.* **1993**, *47*, 800–6. (d) Wang, R.; Bright, F. V. *Appl. Spectrosc.* **1993**, *47*, 792–9.
(35) Beecham, J. M.; Gratton, E. *Proc. SPIE–Int. Soc. Opt. Eng.* **1988**, *909*, 70–81.
(36) Beecham, J. M.; Graton. E.; Ameloot, M.; Knutson, J. R.; Brand, L. In *Topics in Fluorescence Spectroscopy*; Lakowicz, J. R., Ed.; Plenum Press: New York, 1991; Vol. 2, Chapter 5, pp 241–305.

Figure 1. Steady-state emission spectra of HSA-Ac (panel A), and the emission center of gravity for BSA-Ac (O) and HSA-Ac (●) in AOT reverse micelles solubilized in *n*-heptane as a function of R (panel B).

gravity (ECOG) as a function of R. The ECOG[37] is simply the weighted average emission. Interestingly, when these serum albumins are sequestered within the AOT micelle, there are no statistical differences in the steady-state ECOGs between BSA- and HSA-Ac over the R values investigated (Figure 1B). However, the ECOGs of BSA- and HSA-Ac in 0.1 M phosphate buffer (pH 7.0) are 20 240 ± 100 and 20 920 ± 100 cm^{-1}, respectively. Thus, these steady-state experiments reveal that BSA- and HSA-Ac are more similar when sequestered within the AOT micelle than they are in their native forms. This suggests that the native protein structure is not achieved within even the hydrated reverse micelle systems.

Time-Resolved Fluorescence. Previous work from our group[7] on native, chemically denatured, and silica-adsorbed BSA-Ac has shown that the acrylodan ground state is homogeneous and the excited state is influenced by dipolar relaxation processes. When BSA- and HSA-Ac are sequestered within AOT micelles, this same pattern persists at all R values. Thus, dipolar relaxation within the environment surrounding the acrylodan reporter group continues when these proteins are placed in a restricted, dehydrated environment.

In order to determine the relaxation rate law and recover the kinetics of this relaxation process,[7] we carried out a series of emission wavelength-dependent multifrequency phase and modulation (MPM) experiments on BSA- and HSA-Ac in the AOT micelles as a function of R. Figure 2A presents a typical series of wavelength-dependent MPM traces for HSA-Ac sequestered within AOT at $R = 11.1$. The fact that the traces are not superimposible

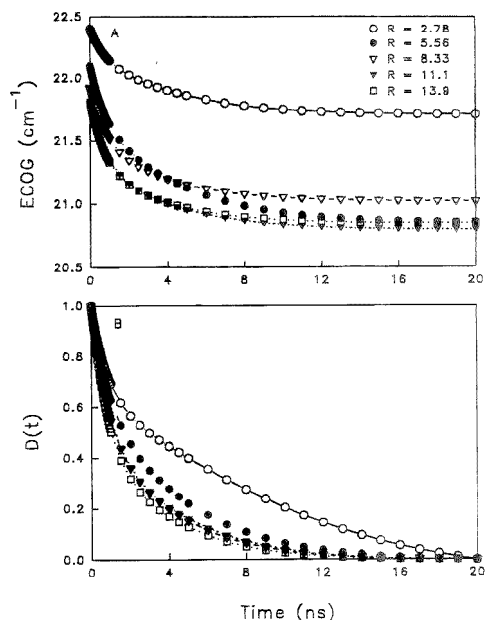(37) Lakowicz, J. R.; Hogen, D. *Biochemistry* **1981**, *20*, 1366–73.

Figure 2. Wavelength-dependent multifrequency phase and modulation traces (panel A), and the recovered time-resolved emission spectra for HSA-Ac ($R = 11.1$) in AOT reverse micelles solubilized in *n*-heptane (panel B).

Figure 3. Recovered time-resolved emission center of gravity (panel A), and $D(t)$ for HSA-Ac in AOT reverse micelles solubilized in *n*-heptane (panel B) as a function of R.

Figure 4. Effects of R on the recovered dipolar relaxation rates (panel A) and fractional contributions to the rates (panel B) for BSA- and HSA-Ac.

demonstrates that the acrylodan excited-state decay kinetics are heterogeneous. Detailed analysis of the data following our earlier protocol[7] yield the time-dependent emission spectra of the acrylodan reporter group (Figure 2B). Dipolar relaxation is clearly evident as a red shift (i.e., relaxation) in the emission spectra with time.

Figure 3A presents the actual time-resolved ECOG for HSA-Ac in AOT as a function of R. Several aspects of these data merit special mention. First, following optical excitation, there is a red-shifting of the spectrum at all R values. Second, at our first time point (~20 ps), the ECOG traces do not all begin at the same ECOG. This suggests that there is at least one faster (<20 ps), unresolved relaxation term that contributes to the acrylodan relaxation process. Third, the greatest shift occurs during the first 4 ns following excitation.

To better illustrate the effects of hydration on the dipolar relaxation process, we present, in Figure 3B, the dipolar relaxation function, $D(t)$,[7] for the same data shown in Figure 3A. $D(t)$ is a convenient normalization function that allows one to compare directly relaxation process that occur over different spectral windows. Qualitative inspection of Figure 3B shows that the average relaxation becomes more rapid as R is increased. For example, the average decay constant at $R = 2.78$ is ~6 ns, whereas it is near 2 ns at $R = 13.9$. Thus, hydration either increases the relaxation rate(s) or provides another pathway for dipolar relaxation.

In order to quantitatively determine the effects of hydration on the relaxation kinetics, we modeled the $D(t)$ data with a series of simple kinetic schemes.[7] The results of the analysis are illustrated in Figure 4 and can be summarized as follows. First, the dipolar relaxation process is best described by a double-

exponential decay law at all R values. This indicates that at least *two* independent processes are responsible for the spectral relaxation of the acrylodan fluorescence in BSA- and HSA-Ac. Similar conclusions were reached for native, chemically denatured,
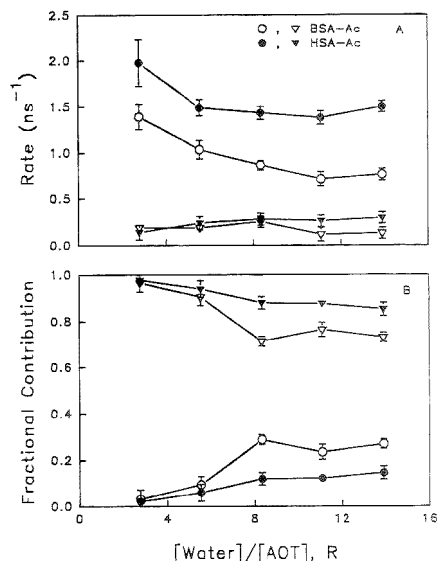
and silica-adsorbed BSA-Ac.[7] Second, the slower of the two relaxation rates is affected little by changes in R. Third, the faster rate term *decreases* as R increases, especially in the low R region. Fourth, the faster of the two relaxation rates in HSA-Ac is always greater than the faster rate associated with BSA-Ac. Fifth, on increasing protein hydration, there is an increase in the contribution from the faster relaxation rate to the overall dipolar relaxation processes. Initially, at $R = 2.78$, the contribution from the faster rate term contributes <5% to the overall dipolar relaxation process. However, at the highest R values studied, the contribution from the faster relaxation rate contributes between 25 (HSA-Ac) and 35% (BSA-Ac). Interestingly, when compared to our previous work on BSA-Ac,[7] the two sets of recovered rates are approximately the same. The difference is that the faster rate term for native BSA-Ac in solution contributes ~60% to the $D(t)$. Thus, the relative contribution from this faster relaxation rate is *arrested* by a factor of at least 2 and up to an order of magnitude when the proteins are sequestered within the AOT micelles. Together, these results show that hydration does not affect the dipolar relaxation rates alone but actually influences the distribution of these relaxation pathways *and* the rates.

Rotational Reorientation Kinetics. Previous work on native BSA-Ac demonstrated that the decay of anisotropy was best described by a model having two independent rotational motions.[7] The slower motion was associated with the rotational reorientation of the entire protein (i.e., global motion). The faster motion was associated with local motion of the acrylodan reporter group attached at cysteine-34. Figure 5 presents typical differential polarized phase angle (panel A), polarized modulation ratio data (panel B), and fits corresponding to one- and two-component models for HSA-Ac in AOT at $R = 11.1$. The double-exponential decay law clearly best describes the decay of anisotropy at this and all R values.

Marzola and Gratton[20] previously studied the effects of hydration on the rotational dynamics of HSA sequestered in reverse micelles. In that work, the authors monitored the fluorescence from the lone HSA tryptophan and reported a decrease in the longer rotational correlation time (global motion) as R increased. The rotational correlation time for the global protein motion systematically varied from 68 ± 6 to 48 ± 3 ns as R increased from 4.1 to 25.2, respectively. However, the authors saw no observable change in the faster rotational correlation time with R. The authors attributed the decrease in the global rotational correlation time (as R is increased) to a decrease in the interaction between the micelle and the protein at higher R.

Our experimental data on BSA- or HSA-Ac show that the longer rotational correlation time does not differ statistically over the range of R values studied. Similarly, the faster rotational correlation time remains unaffected by R. These particular results are somewhat at odds with the Marzola–Gratton work,[20] but they most likely reflect the fact that the local environments surrounding the two reporter groups (tryptophan and acrylodan) are quite different from one another.

Because the rotational correlation times we recovered for BSA- and HSA-Ac do not vary with R, we carried out a linked global analysis of these data files (associated with a given protein), wherein the rotational correlation times were linked across the entire range of R values studied. The results of this linking scheme are summarized in Figure 6A and illustrate that, while the rotational correlation times are not a function of R, the
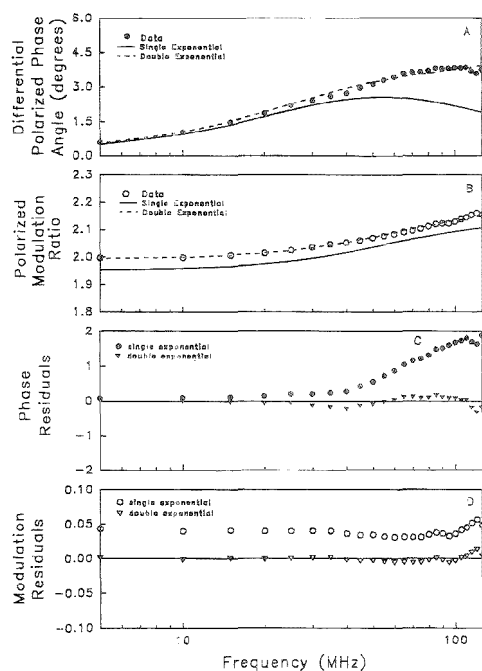
Figure 5. Rotational reorientation data for HSA-Ac in AOT reverse micelles at $R = 11.1$. (A) Differential polarized phase angle. (B) Polarized modulation ratio. The lines represent the best fits to an isotropic (- - -) and an anisotropic (—) rotor model. (C and D) Corresponding residual plots (isotropic rotor, ●, ○: anisotropic rotor, ▼,▽).

fractional contributions of the individual rotational correlation times *are* a strong, systematic function of R. Specifically, we see that (1) at low R values, most (~80%) of the decay of anisotropy results from the global motion of the protein and (2) at the higher R values, the contributions from the local and global motion become comparable.

The recovered fractional contribution data provide a means to compute the semiangle through which the acrylodan residue precesses.[7,26a] The effects of R on this semiangle are summarized in Figure 6B and show several interesting trends. First, at the lowest hydration levels, the acrylodan semiangle in BSA- and HSA-Ac is 21 ± 1.5°. This value is statistically equivalent (at the 99.9% confidence level) to the recovered semiangle for the *native* forms of these proteins in buffer. Second, as water is added to the system, the recovered semiangle *increases*, indicating that acrylodan reporter group exhibits a greater range of motions at higher R values. Third, the cybotactic region is affected most below $R = 15$. We attribute these observations to a hydration-induced change in the protein structure such that the cybotactic region "opens" when the protein is within AOT and R is increased (Figure 7). Static circular dichroism (CD) work by Luisi and co-workers[8] on lysozyme hydration in AOT supports these observations. Specifically, these authors found that the lysozyme CD spectra in aqueous buffer were more similar to those of the same protein, when sequestered in AOT, at the lowest R values. These authors
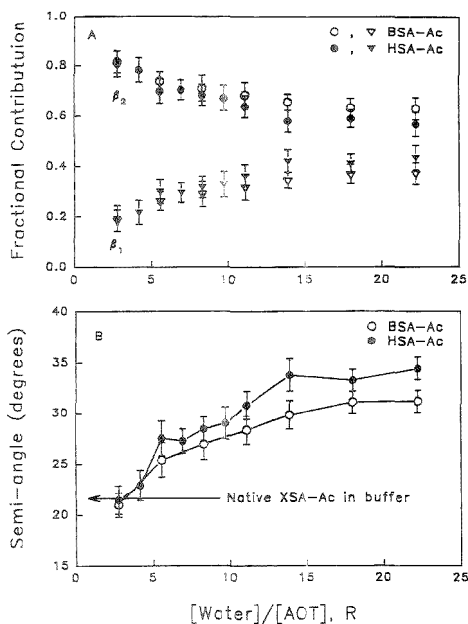
Figure 6. Effect of R on the fractional contribution to the decay of anisotropy (β_2, $\bigcirc$, $\bullet$; β_1, $\triangledown$, $\blacktriangledown$) (panel A) and the semiangle (panel B). See text for further discussion.

low R or native   high R
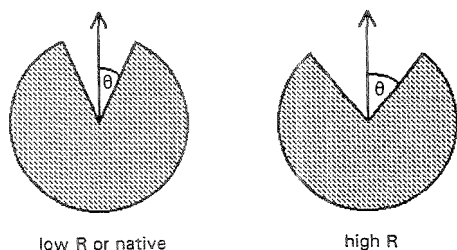
Figure 7. Simplified model illustrating the effect of protein hydration, within AOT, on acrylodan precessional angle.

attributed this phenomenon to denaturation of AOT-sequestered lysozyme as water is added.

Effects of AOT on Albumins. Serum albumins are known to bind fatty acids, and the aliphatic chains can penetrate within the hydrophobic interior of the protein.[23] Thus, we considered the possibility that the AOT monomer tails may partition into our proteins, causing structural changes within the cybotactic region, and alter the systems dynamics. In order to address this issue, we prepared an aqueous BSA-Ac solution and titrated it with AOT. Although we observed an 800 cm^{-1} blue shift in the emission spectra and an increase in the fluorescence on adding AOT, there were no detectable differences in the recovered rotational reorientation dynamics. The recovered semiangle remained constant at $21 \pm 1.5°$ at all AOT concentrations. These results are consistent with the AOT hydrocarbon tails not influencing the rotational relaxation of the acrylodan reporter group within these particular proteins.

Effects of Ionic Strength on Albumins. We have also considered the possibility that ionic strength within the AOT might influence BSA- and HSA-Ac. In the current system, all of the charged species (e.g., the sulfonate head groups of the AOT monomers and counterions) are sequestered within the small micelle core region along with the protein. As a result, the ionic strength within the reverse micelle can range between 2 and 20 M over the range of water loadings investigated. In an effort to isolate the effects of ionic strength on BSA- and HSA-Ac, we added varying amounts of NaNO$_3$ or NaClO$_4$ to the aqueous protein solutions and investigated the fluorescence. The concentration of the sodium salts ranged from 0 to 4 M; solubility problems limited use of higher salt concentrations. No significant changes were observed in the steady-state or time-resolved fluorescence emission spectra over the concentrations studied. This suggests that these particular serum albumins can maintain their native structures at these salt concentrations. However, when BSA-Ac is denatured with 8 M guanidine hydrochloride,[7] the recovered $D(t)$ increased by ~2-fold, and the faster dipolar relaxation rate contributes nearly 80% to the overall relaxation process. We speculate that the greatest influence under these denatured conditions is a direct result of the greater accessibility of the acrylodan residue to bulk water.

CONCLUSIONS

We illustrate how hydration influences the dynamics of biomolecules in environments with limited water. The results of these experiments can be summarized as follows. First, there is dipolar relaxation of the acrylodan fluorescence in BSA- and HSA-Ac when these proteins are sequestered within a reverse micelle. Second, two rate terms are required to describe this relaxation process. The faster term is on the subnanosecond time scale, while the slower relaxation term is in nanoseconds. Third, at the lowest degree of hydration ($R = 2.78$), the faster relaxation process contributes <5% to the total dipolar relaxation process. However, as water is added (up to $R = 13-15$), the contribution to the total dipolar relaxation from the faster relaxation process increases 5- and 3-fold for BSA- and HSA-Ac, respectively. Fourth, the faster of the two rate terms actually decreases slightly over this same region. This demonstrates that hydration affects the rates *and* their contributions to the dipolar relaxation process. Fifth, the cybotactic region surrounding the acrylodan residue is never truly equivalent to native proteins at any R when the protein is sequestered within the AOT reverse micelle. Sixth, compared to previous work,[7] dipolar relaxation occurs faster in the native protein. Seventh, the decay of anisotropy is best described by an anisotropic rotor model at all R values, and the two rotational correlation times are independent of protein hydration. Eighth, the semiangle through which the reporter group is able to precess changes significantly with hydration. At the lowest R values, the semiangle is statistically equivalent to the value recovered for the native proteins. However, as water is added, the semiangle increases systematically by 10°.

Together these results demonstrate the complexity of the interplay between hydration and protein function and dynamics. They further show that it is not enough to simply keep the protein hydrated in order to maintain their integrity. One must simultaneously control the immediate environment surrounding the protein/recognition element *and* its degree of hydration. Our fluoropolymer surfaces[5a] apparently achieve this balancing act, but optical properties are poor and protein surface coverages are low.

More recent work[3b,d] on sol–gel-derived biocomposites may provide a more viable means to simultaneously increase the available concentration of biorecognition element, control its hydration, and control its immediate environment. Work in this area is continuing.

ACKNOWLEDGMENT

[⊗] Abstract published in *Advance ACS Abstracts*, September 1, 1995.

Quantitative Aspects of FT-IR Emission Spectroscopy and Simulation of Emission–Absorption Spectra

Gábor Keresztury,*,† János Mink,‡,§ and János Kristóf‡

Central Research Institute for Chemistry, Hungarian Academy of Sciences, P.O. Box 17, H-1525 Budapest, Hungary, Department of Analytical Chemistry, University of Veszprém, P.O. Box 158, H-8201, Veszprém, Hungary, and Institute of Isotopes, Hungarian Academy of Sciences, P.O. Box 77, H-1525 Budapest, Hungary

Recent advances in FT-IR emission spectroscopy of solids are briefly reviewed, and some neglected points concerning the measurement of blackbody radiation are dealt with. A corrected equation describing the single-beam emission spectra is given, taking into account the possible thermal radiation of the detector. Similarities between the effect of self-absorption and that of "illegal" data manipulations on emittance spectra are pointed out, both giving rise to spectral distortions like inverted or split peaks or altered band shapes and intensities. To avoid some of these problems, the use of a linear emission intensity scale, emissivity, is advocated, especially for quantitative work. A special case of self-absorption, namely, that of multilayer samples, is discussed, in which the spectral distributions of emitted and absorbed radiation are significantly different. Simulations of the emission–absorption spectra observed in such cases are shown to help with spectral and structural interpretation.

With the proliferation of modern FT-IR instruments in the last two decades, an increasing number of laboratories turned to infrared emission spectroscopy (IRES) as an alternative spectroscopic technique for condensed materials and bulk, opaque samples for which transmission or reflection techniques proved to be inadequate. Following the pioneering work of Low and Coleman,[1,2] some basic considerations and exploratory measurements were published by Griffiths[3,4] and Chase[5] to test the capabilities and limitations of IRES using IR interferometry. More recently, several other workers checked the influence of sampling conditions (such as sample thickness and temperature, geometry of sample arrangement, etc.) on the quality of IR emission spectra, essentially confirming the earlier results. The prime objective of these works, surveyed by Chalmers and Mackenzie,[6] was to develop solid sampling techniques and methods that would produce good quality spectra free from the known inherent spectral distortions.

It has been noted repeatedly that IR emission spectra of condensed samples often suffer from severe distortions (mainly in the regions of strong emission bands) that could be attributed either to surface reflectivity or to self-absorption.[3,6–8] To eliminate band distortions due to selective reflection, the use of thick (opaque) samples as reference has been proposed by Rytter and co-workers.[9,10] Another recent major advancement in IRES sampling technique is the application of transient heating[11,12] of the sample surface in order to get rid of self-absorption and to increase spectral contrast in the case of bulky samples by means of exciting only a thin surface layer temporarily. Most recently, the feasibility of measuring IR emission spectra of highly opaque solids by modulated emission spectroscopy was demonstrated by Guillois et al.[13]

Less attention has been paid to practical aspects of FT-IR emission spectroscopy in relation to the fundamental theory of thermal radiation (e.g., measurement of sample temperature[14,15]) and to the presentation (choice of intensity scale) and data processing of emission spectra. The main aims of this paper are to clarify some key issues that have created controversy or have been glossed over in the literature and to advocate the use of a linear intensity scale, emissivity, for quantitative work. In addition, we would like to draw attention to potential sources of spectral distortions or errors in quantitative applications stemming from improper operations over emittance spectra. It will also be shown on an example that, in special cases, one can take advantage of self-absorption, for instance, to detect the formation of a layered structure on the basis of interpreting the spectrum as an emission–absorption spectrum.

Central Research Institute for Chemistry, Hungarian Academy of Sciences.
† Department of Analytical Chemistry, University of Veszprém.
§ Institute of Isotopes, Hungarian Academy of Sciences.
(1) Low, M. J. D. *Nature* 1965, *208*, 1089–1090.
(2) Low, M. J. D.; Coleman, I. *Spectrochim. Acta* 1966, *22*, 396–376.
(3) Griffiths, P. R. *Appl. Spectrosc.* 1972, *26*, 73–76.
(4) Griffiths, P. R. *Am. Lab.* 1975, *7*, 37–45.
(5) Chase, D. B. *Appl. Spectrosc.* 1981, *35*, 77–81.
(6) Chalmers, J. M.; Mackenzie, M. W. In *Advances in Applied Fourier Transform Infrared Spectroscopy*; Mackenzie, M. W., Ed.; Wiley: New York, 1988; pp 105–188.

(7) Kember, D.; Sheppard, N. *Appl. Spectrosc.* 1975, *29*, 496–500.
(8) Willis, H. A.; Sheppard, N.; Chalmers, J. In *7th International Conference on Fourier Transform Spectroscopy*; Cameron, D. P., Ed. *Proc. SPIE-Int. Soc. Opt. Eng.* 1989, *1145*, 431–432.
(9) Hvistendahl, J.; Rytter, E.; Øye, H. A. *Appl. Spectrosc.* 1983, *37*, 182–187.
(10) Rytter, E. *Spectrochim. Acta* 1987, *43A*, 523–529.
(11) Jones, R. W.; McClelland, J. F. *Anal. Chem.* 1989, *61*, 650–656.
(12) Jones, R. W.; McClelland, J. F. *Anal. Chem.* 1990, *62*, 2074–2079.
(13) Guillois, O.; Nenner, I.; Papoular, R.; Reynaud, C. *Appl. Spectrosc.* 1994, *48*, 297–306.
(14) DeBlase, F. J.; Compton, S. *Appl. Spectrosc.* 1991, *45*, 611–618; Erratum, 1991, *45*, 1209.
(15) Keresztury, G.; Mink, J. *Appl. Spectrosc.* 1992, *46*, 1747–1749.
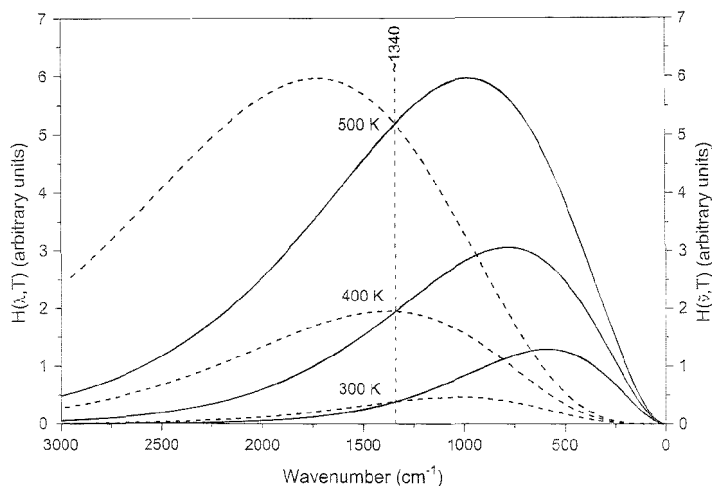
Figure 1. Comparison of Planck functions given in wavenumber representation ($H(\tilde{\nu}, T)$, solid lines) with those in wavelength representation ($H(\lambda, T)$, broken lines) for three different temperatures.

EXPERIMENTAL SECTION

Infrared emission and emission–absorption spectra were measured with a Bomem MB-102 spectrometer equipped with a DTGS detector. The emission accessory attached to the side port of the instrument consisted of a sample holder (an electrically heated, polished stainless steel plate) and an off-axis paraboloid mirror to collect the radiation. Double beam emittance or emittance–transmittance spectra were obtained by ratioing the single-beam emission spectrum of the sample against that of a blackbody reference (a metal plate painted with matte black paint) recorded at identical conditions.

Spectral simulations were performed either on a Nicolet 1180 computer (programmed in Fortran) equipped with a Zeta Series 100 digital plotter or on IBM PCs.

RESULTS AND DISCUSSION

Theoretical Background, with Modifications. *Blackbody Radiation: Wavenumber vs Wavelength Representation.* The fundamental law governing thermal emission is expressed by Planck's distribution function, H, which describes the *spectral radiance* (or spectral density of radiant power, often designated as ϱ) of a blackbody at absolute temperature T. This function is given in textbooks (see, e.g., refs 16–18) and review papers on IRES[14,19,20] in various (often erroneous) forms, either as a function of wavelength, λ, or frequency, ν, or as a function of wavenumber, $\tilde{\nu}$. For the sake of completeness, we present here all three mutually consistent forms that give the radiant power emitted from

(16) Goody, R. M.; Yung, Y. L. *Atmospheric Radiation: Theoretical Basis I*; Oxford University Press: New York, 1989; pp 29–33.
(17) Lenoble, J. *Atmospheric Radiative Transfer*; A. DEEPAC Publishing: Hampton, 1993.
(18) Schrader, B., Ed. *Infrared and Raman Spectroscopy. Methods and Applications*; VCH: Weinheim, 1995.
(19) Bates, J. B. In *Fourier Transform Infrared Spectroscopy*; Ferraro, J., Ed.; Academic Press: New York, 1978; Vol. 1, pp 99–142.
(20) Huong, P. V. In *Advances in Infrared and Raman Spectroscopy*; Clark, R. J. H., Hester, R. E., Eds.; Heyden: London, 1978; Vol. 4, Chapter 3, pp 85–107.

a unit area, per solid angle, in elementary spectral intervals $d\lambda$, $d\nu$, and $d\tilde{\nu}$, respectively:

$$H(\lambda, T) \ d\lambda = 2hc^2\{\lambda^5[\exp(hc/\lambda kT) - 1]\}^{-1} \ d\lambda \quad (1)$$

$$H(\nu, T) \ d\nu = 2hc^{-2}\nu^3/[\exp(h\nu/kT) - 1]^{-1} \ d\nu \quad (2)$$

$$H(\tilde{\nu}, T) \ d\tilde{\nu} = 2hc^2\tilde{\nu}^3/[\exp(hc\tilde{\nu}/kT) - 1]^{-1} \ d\tilde{\nu} \quad (3)$$

where h, c, and k are universal constants. The inclusion of spectral elements $d\lambda$, $d\nu$, and $d\tilde{\nu}$ in these equations ensures the correct conversion between the various expressions of spectral radiance. (Note also that versions of the Planck function containing a factor 8π instead of 2 in the above equations refer to radiance in the whole solid angle.) In practical applications of the Planck function in IRES, however, it is not so much the constant factors but the general form of the function that must be chosen properly.

Figure 1 shows the two most often used functions corresponding to eqs 1 and 3 for three different temperatures, plotted in a common linear wavenumber scale for easy comparison. It is quite apparent that they describe curves of essentially different shapes, with their maxima shifted considerably to higher wavenumbers in the case of the wavelength representation. This becomes well understandable if we consider the curves described by eq 1 as spectra scanned with a spectral slit width constant in wavelength (λ) and the curves described by eq 3 as spectra scanned with a spectral slit width constant in wavenumber ($\tilde{\nu}$). Due to the relation $d\lambda/ = d\tilde{\nu}/\tilde{\nu}^2$ (derived from $\lambda = 1/\tilde{\nu}$), a spectral slit width constant in wavelength ($d\lambda$) means an increasing spectral interval in the wavenumber scale ($d\tilde{\nu}$) with decreasing wavenumbers. Thus, the integral of the two curves (the total energy detected) in the whole spectrum will be the same for both representations, in accordance with the Stefan–Boltzmann law. The intensity scales of the two series of curves in Figure 1 are arbitrary, but the relative intensities *within* both series are correct. The correctness of the curves is testified to by the fact that the pairs of $H(\lambda, T)$ and $H(\tilde{\nu}, T)$ curves corresponding to the same temperature cross each other at the

same frequency for all temperatures (at the frequency where the "physical slit width" is the same for both representations).

Regarding FT-IR emission spectrometry, it should be pointed out that since FT-IR spectrometers produce spectra *at constant resolution in wavenumber*, it is the wavelength representation, eq 3, that should be used as theoretical reference blackbody radiation.[15]

Measurement of Emission: Temperature of the Detector and Instrument Response. If the radiation of a blackbody at absolute temperature T is detected by an ideal FT-IR spectrometer having 100% throughput, no stray light, and detector with blackbody characteristics kept at 0 K, spectra coincident with a Planck function, $H(\tilde{\nu},T)$, would be obtained.

Radiation emitted by a non-blackbody having emittance $E(\tilde{\nu})$ is described by the function $E(\tilde{\nu})H(\tilde{\nu},T)$, which can be viewed as the emittance spectrum of the sample modulated by the Planck function. If the detector in *not* at 0 K, only the radiation *balance* between the detector and sample (plus surroundings) is measured. Although this principle is stated by Chase[1] and quoted by DeBlase and Compton,[14] the expression they have given for the radiation detected by the spectrometer *does not reflect* this circumstance:

$$L(\tilde{\nu},T) = R(\tilde{\nu})[E_s(\tilde{\nu})H(\tilde{\nu},T) + B(\tilde{\nu}) + I(\tilde{\nu})\varrho(\tilde{\nu})] \quad (4)$$

where $R(\tilde{\nu})$ is the instrument response function, and $B(\tilde{\nu})$ and $I(\tilde{\nu})\varrho(\tilde{\nu})$ represent stray radiation (background radiation and instrument self-emission reflected off the sample surface, respectively). To be correct, in place of $E_s(\tilde{\nu})H(\tilde{\nu},T)$, eq 4 should contain the difference of radiation fluxes coming from the sample and from the detector:

$$L_s(\tilde{\nu},T) = R(\tilde{\nu})\{[E_s(\tilde{\nu})H(\tilde{\nu},T_s) - E_d(\tilde{\nu})H(\tilde{\nu},T_d)] + B(\tilde{\nu}) + I(\tilde{\nu})\varrho(\tilde{\nu})\} \quad (5)$$

where subscripts s and d denote sample and detector, respectively. The above correction, however, has no consequence on the measurement of sample emittance if it is done according to the two−temperature, four-measurement approach.[5,21] It gains real significance when single-beam emission spectra are studied using a room temperature detector. In this case, stray radiation originating from room temperature parts of the spectrometer can be neglected, and, if $E_d(\tilde{\nu})$ is close to unity (most detectors are good approximations to a blackbody radiator), the measured single-beam spectrum can be described as

$$L_s(\tilde{\nu},T) = R(\tilde{\nu})[E_s(\tilde{\nu})H(\tilde{\nu},T_s) - H(\tilde{\nu},T_d)] \quad (6)$$

When both the sample and the detector are blackbodies ($E_s(\tilde{\nu}) = E_d(\tilde{\nu}) = 1$) kept at two different temperatures, we arrive at an even simpler formula,

$$L_s(\tilde{\nu},T) = R(\tilde{\nu})[H(\tilde{\nu},T_s) - H(\tilde{\nu},T_d)] \quad (7)$$

The correction scheme we proposed in a recent note[15] to achieve a fair comparison between measured and theoretical blackbody curves (e.g., for the measurement of the sample temperature)

(21) Kember, D.; Chenery, D. H.; Sheppard, N.; Fell, J. *Spectrochim. Acta* 1979, 35A, 445−459.

corresponds to the use of eq 7. It appears to be an effective way of correcting for detector temperature.

From eq 7, it follows that if the sample is at a lower temperature than the detector, $L(\tilde{\nu},T)$ will be negative, showing that the net radiation flux is directed from the detector toward the sample. In this case, the interferogram appears inverted (turned upside down), but the single-beam spectrum obtained after Fourier transformation and phase correction will be the same as in the case of positive temperature difference, $T_s - T_d$.

It is interesting to note that according to eq 6, for a room temperature detector and heated sample having strong discrete emission bands, $L(\tilde{\nu},T)$ can be *positive at some frequencies* (at the peaks of the emission bands of the sample) *and negative at others* (in transparent regions of the sample spectrum), meaning that *radiation of different frequencies can travel in opposite directions*. We wonder if this possible state of events born out by sheer speculation will ever receive experimental confirmation.

Intensity Scales and Quantitative Evaluation. Thermally excited FT-IR emission spectra recorded in the conventional way, with the sample at elevated temperature, are usually presented in one of the following intensity scales: (i) single-beam emission (energy) spectrum; (ii) relative emittance, i.e., emission of the sample relative to that of a reference or background material (e.g., the empty heater plate, the untreated sample, etc.); (iii) emittance, E or $E\%$, i.e., the single-beam emission spectrum of the sample divided by that of a laboratory blackbody measured at the same temperature, or emittance spectra obtained by the four-measurement, two-temperature approach;[5,21] and (iv) reflection-corrected emittance, E^*, i.e., same as iii above, but with the use of an optically opaque (very thick) reference *of the same material* as the sample instead of the blackbody.[9,10]

Of these, presentation i is not really acceptable because its band intensities are modulated by the shape of the Planck blackbody radiation and by the instrument response function, which can mask useful spectral information. Spectral presentation ii eliminates the wavenumber dependence of the instrument response but may produce unpredictably high intensity values, and the noise level may increase enormously in regions of low (near zero) emission of the reference material. Emission spectra obtained using a blackbody reference (as under iii) ensures true relative band intensities, but distortions due to dispersion of surface reflectivity or self-absorption may still be present. In order to eliminate such distortions from the spectra, the so-called reflection-corrected emittance, E^*, was proposed by Hvistendahl et al.[9] and Rytter.[10] This way, true relative band intensities are obtained with no distortions at all.

Note, however, that the emittance scale, E, or rather $1 - E$, is analogous to transmittance in absorption spectroscopy in the sense that it is *not* linearly proportional to thickness (d) or concentration (c), and its maximum value, in principle, is 1. In order to convert the emittance spectrum, $E(\tilde{\nu})$, to a linear intensity scale termed by us *emissivity*, $\epsilon(\tilde{\nu})$, the negative logarithm of $1 - E(\tilde{\nu})$ has to be taken:

$$-\log_{10}[1 - E(\tilde{\nu})] = \epsilon(\tilde{\nu})cd \quad (8)$$

Equation 8 can be called the Lambert−Beer law of emission spectroscopy. If we are concerned only with the internal properties of the sample and exclude surface effects (reflection), $1 - E(\tilde{\nu})$ can be replaced by the transmittance of the sample, $t(\tilde{\nu})$,

and we get the customary form of the Lambert—Beer law used in absorption spectrometry, where $\epsilon(\tilde{\nu})$ denotes the molar (decadic) absorption coefficient. Thus, if reflection can be neglected, eq 8 defines the decadic absorbance, A_{10}, and can be used for quantitative determinations.

The transformation of emittance spectra to absorbance according to eq 8 is similar to, but unfortunately not quite the same as, conversion of transmittance spectra to absorbance, because the argument of log is $1 - E(\tilde{\nu})$, which requires an operation (constant array minus spectrum) not readily available in the FT-IR software of many commercial instruments. In the lack of the proper operation (and perhaps because of the similarity of the terms emittance and absorbance), emittance data are often treated like absorbance data, and all kinds of data manipulations allowed for absorbance spectra are performed with emittance spectra. However, it is important to realize that most operations, like spectral subtraction, baseline correction, deconvolution, curve fitting, etc., are "illegal" in the emittance scale because they require a linear intensity scale. Although an expression similar to eq 8 appeared (with a printing error) in an early paper by Griffiths,[4] it has been ignored even in some works dealing with quantitative determinations.[22]

Equation 8 assumes that the measured emittance spectrum, $E(\tilde{\nu})$, is connected to the internal property of the sample, emissivity, $\epsilon(\tilde{\nu})$, as

$$E(\tilde{\nu}) = 1 - 10^{-\epsilon(\tilde{\nu})x} \qquad (9)$$

where $x = dc$ is the effective thickness (i.e., sample thickness times concentration). Note that it is $\epsilon(\tilde{\nu})$, not $E(\tilde{\nu})$, that can be approximated by a sum of Lorentzian/Gaussian functions. It it most unfortunate and may add to the confusion of these two quantities that the accepted IUPAC nomenclature[23] uses the same symbol, ϵ, for both emittance (E in this paper) and molar decadic absorption coefficient, quantities appearing simultaneously in both eqs 8 and 9.

Spectral Distortions Due to Self-Absorption or Improper Data Manipulations. In view of the previous discussion, eq 9 can be written in short as

$$E(\tilde{\nu}) = 1 - t(\tilde{\nu}) \qquad (10)$$

where $t(\tilde{\nu})$ is the transmittance of the sample. Rytter[10] has shown (using a different notation) that the effect of reabsorption of bulk emission by a cooler surface layer manifested in splitting or inversion of the centers of strong emission bands can be modeled by the expression

$$E(\tilde{\nu}) = (1 - t_b^2)t_s \qquad (11)$$

where t_b and t_s are transmittances of the bulk and of the surface layer, respectively. In fact, a simpler expression,

(22) Tiloca, D. C.; Busch, M. A.; Busch, K. W. Appl. Spectrosc. 1991, 45, 178–185.
(23) Mills, I.; Cvitas, T.; Homann, K.; Kallay, N.; Kuchitsu, K. Quantities, Units and Symbols in Physical Chemistry, IUPAC, 2nd ed.; Blackwell Scientific Publications: Oxford, 1993; pp 31–32.
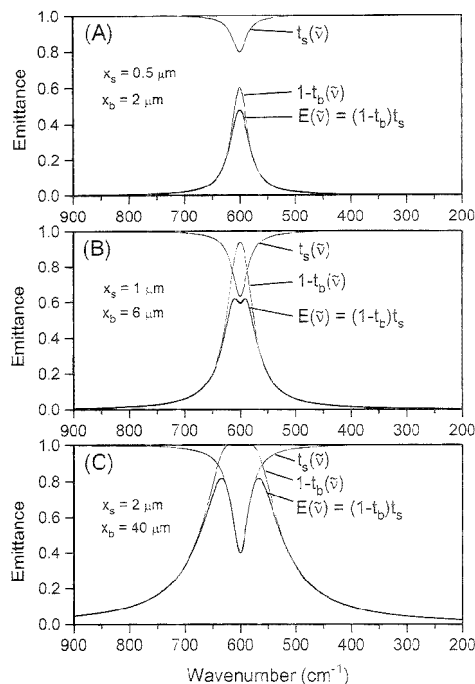
Figure 2. Simulation of the effect of self-absorption using eq 12 for different effective thicknesses of emitting bulk (x_b) and absorbing surface layer (x_s). (Lorentzian band shapes with $\tilde{\nu}_0 = 600$, $i_0 = 2000$, and $w = 30$ cm^{-1}.)

$$E(\tilde{\nu}) = (1 - t_b)t_s \qquad (12)$$

referring to a single pass of the emitted radiation through the sample (i.e., no reflecting back plate) can describe the effect of self-absorption and simulate the inversion or splitting of emission bands just as well. The successful simulation shown on the examples of Figure 2 proves that *this effect of self-absorption is due to the interplay of nonlinearity of both emittance and transmittance scales and their opposite directions.*

Furthermore, it can be readily shown that illegal spectral manipulations such as subtraction done in a nonlinear intensity scale (e.g., emittance or all those listed under i—iv) can lead to distortions that can be mistaken for the effect of surface reflectivity or reabsorption.

The only way to avoid the spectral artifacts of illegal data manipulation is to transform the emittance spectra in accordance with eq 8 to a linear intensity scale, emissivity, before spectral manipulations. The incorporation of the corresponding operation (i.e., a constant minus double-beam spectrum) into FT-IR emission spectroscopy software packages is strongly recommended to instrument manufacturers.

Emission—Absorption Spectroscopy of Multilayer Samples. The starting point of our discussion here is the assumption that self-absorption is a common phenomenon occurring most of the time when the sample is heated from the rear side so that the cooler surface layer can absorb radiation emitted by the inner parts or deeper-lying layers.
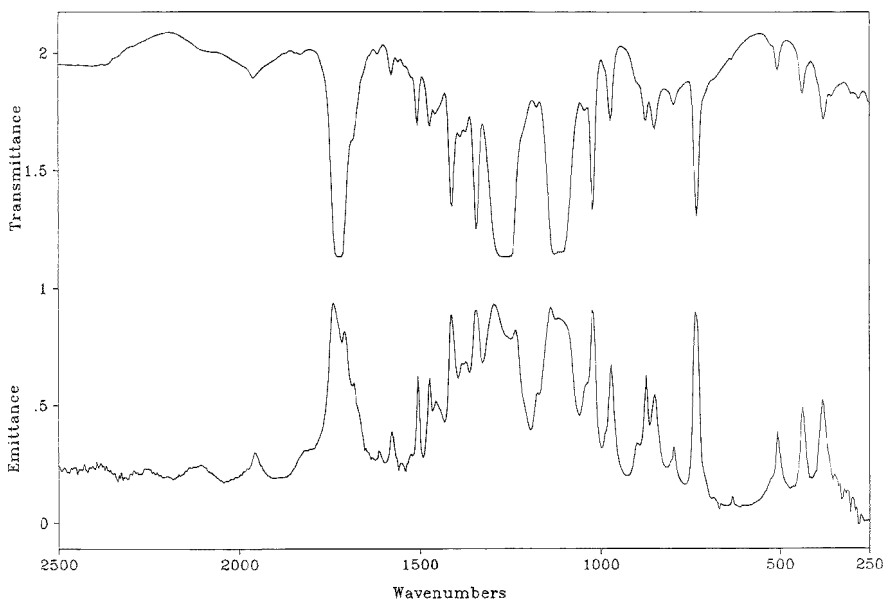
Figure 3. Emission spectrum of a 6 μm Mylar sheet on a heated shiny metal plate (lower trace), and emission–absorption spectrum of the same Mylar sheet on a heated metal plate covered with matte black paint (upper trace).
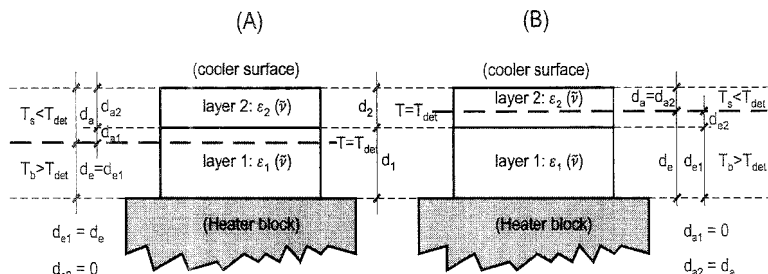
Figure 4. Notation of layers in a two-layer sample depending on the temperature gradient within the sample in an emission–absorption experiment. (A) The cool absorbing surface layer is thicker than layer 2 ($d_a > d_2$). (B) The absorbing layer is thinner than layer 2 ($d_a < d_2$).

This assumption has been verified by two simple measurements, the results of which are shown in Figure 3. In the first case (Figure 3, lower trace), a 6 μm thick Mylar sheet was attached to the sample holder (a heated, polished metal plate), while in the second case (Figure 3, upper trace), the Mylar sheet was attached to a laboratory blackbody (a similar metal plate covered with matte black paint). Both spectra were measured at the same temperature and ratioed against the same single-beam blackbody emission spectrum. The resulting spectra show clearly that while the lower spectral trace in Figure 3 is a usual emittance spectrum (with signs of self-absorption near the peaks of the strongest bands), the other one can be regarded as the absorption (transmittance) spectrum of the Mylar sheet, or more correctly, as an *emission–absorption spectrum* where the deeper-lying layer of the sample (the black paint) is emitting while the upper layer of the sample (the Mylar sheet) is absorbing radiation.

It is quite natural that when a homogeneous or *single-layer* sample is studied by IR emission, the distorting effect of self-

absorption can occur only at the center of (strong) emission bands. In *multilayer samples*, however, when the emitting bulk and the absorbing surface layer are structurally or even chemically different, the emission and absorption bands may be at very different frequencies, the combination of which produces a complicated picture: this is a single-beam absorption spectrum in which the source radiation may be far from continuous. The observed spectrum of such samples will depend on the thicknesses of the different layers (d_1, d_2, etc.) within the composite sample on the one hand, and on the distribution of temperature, i.e., on the thicknesses of emitting (d_e) and absorbing portions (d_a), on the other.

Absorption–emission spectra (AES) of multilayer samples can be simulated using a mathematical approach similar to eq 12, taking into account that layers that are chemically (structurally)

(24) Jones, R. W.; McClelland, J. F. *Anal. Chem.* **1990**, *62*, 2247–2251.
(25) Kristóf, J.; Mink, J.; DeBattist, A.; Liszi, J. *Electrochim. Acta* **1994**, *39*, 1531–1536.
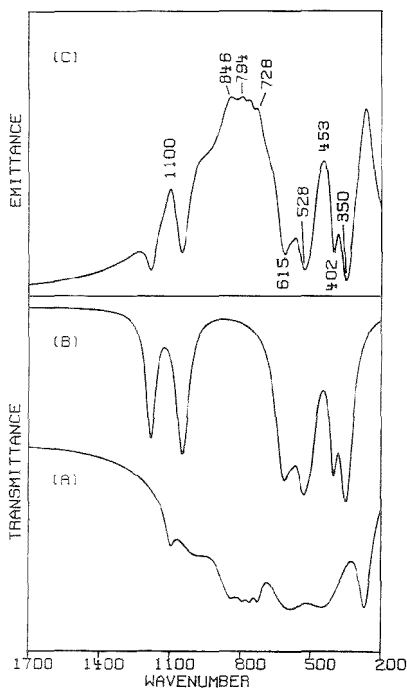
Figure 5. Simulation of the IR emission—absorption spectrum of an electrocatalytic IrO$_2$/TiO$_2$ film having a layered structure. The hypothetical absorption spectra of layers 1 and 2 (lower two traces) were chosen to produce an emission—absorption spectrum (upper trace) closely resembling the measured emission spectrum (see Figure 6 of ref 25).

different have different spectral distributions (see Figure 4 for notations used in the case of two layers):

$$E = [1 - 10^{-\epsilon_1(\tilde{\nu})d_{e1} - \epsilon_2(\tilde{\nu})d_{e2}}] \times 10^{-\epsilon_1(\tilde{\nu})d_{a1} - \epsilon_2(\tilde{\nu})d_{a2}} \quad (13)$$

On varying the thicknesses of emitting and absorbing layers, this equation can lead to very different results. Naturally, the conditions of the IR emission experiment can be varied as well, applying different cooling and heating regimes as in TIRES[11,12] or TIRTS.[2]

As an example, the simulation of IR emission spectra of mixed IrO$_2$/TiO$_2$ electrocatalytic layers on a Ti plate is shown in Figure 5. The "theoretical" spectrum closest to the measured one (see Figure 6 of ref 25) is that in Figure 5C, which was obtained on the assumptions that a 5 μm TiO$_2$ layer is formed on top of a 10 μm IrO$_2$ layer and that the upper layer is only absorbing the radiation emitted by the lower layer.

In principle, if the absorption spectra of the pure components (layers) making up the sample are known, a kind of *depth profiling* can be carried out by varying the heating—cooling equilibrium in the sample, accompanied by simulations of emission—absorption spectra. These capabilities of IRES are not explored yet completely. Although it is not expected that this method can compete with the depth profiling potential of the photoacoustic (PA) technique, it may be handy when PA cannot be used, e.g., under conditions of remote sensing or in on line or in situ measurements.

Further refinement of the procedure is envisaged by taking into account also the population of the vibrational energy levels, depending on the temperature of the layers.

Correspondence

Exact Mass Determination for Elemental Analysis of Ions Produced by Matrix-Assisted Laser Desorption

Jiangyue Wu, Steven T. Fannin, Melanie A. Franklin, Tadeusz F. Molinski, and Carlito B. Lebrilla*

Department of Chemistry, University of California, Davis, California 95616

The exact masses of bastadins, cyclic peptides from marine sponges *Ianthella basta*, are determined using matrix-assisted laser desorption ionization (MALDI) coupled to a Fourier transform mass spectrometer. Two known compounds were mixed with the unknown to serve as internal calibrants. The mass of the calibrants bracketed the mass of the unknown compound. With this method, exact masses were obtained to within 5 ppm for single determinations, and less than 3 ppm for multiple determinations, allowing the derivation of elemental composition. This method is viable for routinely obtaining the exact masses of new compounds with MALDI.

One of the most important features of mass spectrometry (MS) is the capability for providing exact masses, thereby allowing the determination of elemental composition. The analyses can be performed with high sensitivity and more importantly when the compound contains several impurities. For this reason, mass spectral data are often allowed in place of elemental composition as a requirement for the characterization of new compounds. Accurate mass determination is typically performed with mutiple sector instruments using a known ionic species in the spectrum (internal calibration) as a reference point.[1]

The recent development of matrix-assisted laser desorption ionization (MALDI) has provided greater versatility in MS analyses by allowing formation of large ionic species from thermally labile compounds.[2-5] An impressive mass range has been demonstrated surpassing 10^6 daltons. Although MALDI produces very little fragmentation, favoring instead strong signals of quasimolecular ions, accurate mass determination remains a difficult task. Several recent attempts have shown the progress in assigning exact masses using a variety of MS techniques. Beavis and Chait showed mass accuracy of 0.01% with MALDI-time-of-flight (TOF)

MS.[5] This has been improved to less than 50 ppm using careful sample preparation and a reflectron/time of light.[6] MALDI-sector mass spectrometry of CsI clusters has yielded mass assignments within 0.015% of actual values.[7,8] MALDI-quadrupole ion trap mass spectrometry (ITMS) was used to obtain mass accuracy of less than 0.05%.[9] Unfortunately, all of these examples are still well above the 5 ppm (0.0005%) necessary for the identification and the subsequent publication of new compounds.

Wilkins has shown that MALDI-Fourier transform mass spectrometry is a viable method for obtaining high mass and high resolution of MALDI-produced ions.[10,11] With an external source MALDI-FTMS, McIver has shown deviation of less than 10 ppm between known and determined mass with external calibration and by including the trapping plate potential in the mass calibration equation.[12,13] In this regard, FTMS may provide the most immediate and accessible method for obtaining exact masses of MALDI-produced ions.

In this report we illustrate a two-calibrant technique for obtaining the exact masses of a group of compounds called bastadins with an external source MALDI-FTMS. We are not aware of other examples where the exact mass of an unknown compound was determined from MALDI within the acceptable limit for the characterization (by elemental composition) of new compounds. The compounds are cyclic peptides isolated from marine sponges. They are particularly difficult to analyze with MS because the compounds contain several bromine atoms that contribute to significant isotopic peaks to make the lightest isotopmer, the most important for exact mass determination, also the least abundant.

(1) *Tandem Mass Spectrometry*; McLafferty, F. W., Ed.; John Wiley & Sons, Inc.: New York, 1983.
(2) Karas, M.; Hillenkamp, F. *Anal. Chem.* 1988, 60, 2299−301.
(3) Beavis, R. C.; Chait, B. T. *Rapid Commun. Mass Spectrom.* 1989, 3, 432−5.
(4) Beavis, R. C.; Chait, B. T. *Rapid Commun. Mass Spectrom.* 1989, 3, 436−9.
(5) Beavis, R. C.; Chait, B. T. *Anal. Chem.* 1990, 62, 1836−40.
(6) Vorm, O.; Mann, M. *J. Am. Soc. Mass Spectrom.* 1994, 5, 955−8.
(7) Annan, R. S.; Kochling, H. J.; Hill, J. A.; Biemann, K. *Rapid Commun. Mass Spectrom.* 1992, 6, 298−302.
(8) Hill, J. A.; Annan, R. S.; Biemann, K. *Rapid Commun. Mass Spectrom.* 1991, 5, 395−9.
(9) Chambers, D. M.; Goeringer, D. E.; McLuckey, S. A.; Glish, G. L. *Anal. Chem.* 1993, 65, 14−20.
(10) Koster, C.; Castoro, J. A.; Wilkins, C. L. *J. Am. Chem. Soc.* 1992, 114, 7572−4.
(11) Walker, K. L.; Kahr, M. S.; Wilkins, C. L.; Xu, Z.; Moore, J. S. *J. Am. Soc. Mass Spectrom.* 1994, 5, 731−9.
(12) Li, Y.; McIver, R. T., Jr.; Hunter, R. L. *Anal. Chem.* 1994, 66, 2077−83.
(13) McIver, R. T., Jr.; Li, Y.; Hunter, R. L. *Proc. Natl. Acad. Sci. U.S.A.* 1994, 91, 4801−5.

Top View

Figure 1. Top view of FTMS instrument with MALDI source. A nitrogen laser (with 337 nm wavelength) is aimed at a sample probe in the source region of the instrument. The ions are formed and guided into the analyzer cell using a single-stage quadrupole rod assembly. The analyzer cell rests in the homogeneous region of a 3 T superconducting magnet.

Exact mass determination with this particular FTMS is notable for several reasons. To our knowledge, it is the first determination of the exact mass of an unknown compound. It is performed with a relatively low field (3 T) superconducting magnet which has average homogeneity; the magnet does not contain shim coils for adjustment. It has not also been possible to obtain exact masses of MALDI-produced ions.

EXPERIMENTAL SECTION

The experiments were performed on an external source FTMS instrument described earlier.[14,15] The MALDI source was fabricated using an existing LSIMS source. The ionization source was modified by removing a stainless steel mesh which functioned as part of a side electrode (Figure 1). Removal of the mesh did not significantly appear to affect ion intensities. A Laser Science Inc. nitrogen laser with a maximum 230 μJ/pulse was mounted directly on the instrument and pointed toward the ion source. The beam was attenuated with a single quartz disk placed directly in the path of the beam and a quartz window that allowed the beam access to the source. The total attenuation by the window and the quartz disk totaled between 10 and 20% of the maximum output.

As discussed previously by McIver and co-workers, the timing of the pulse sequences is important for the MALDI experiments.[12,13] The experiment is started by a 1.0 ms pulse of N_2 gas. With the reservoir at 22 Torr, the maximum pressure obtained in the analyzer cell was in the low 10^{-5} Torr. Simultaneously, the quadrupole rods were activated for ion transmission. The laser is pulsed 50 ms after the pulsed gas. The front trapping plate is set initially to 0 V; at 0.5 ms after the laser pulse, the front trapping plate is rapidly raised to 10 V. The rear trapping plate is maintained at 10 V at the beginning of the experiment. Both trapping plates are maintained at 10 V for 10 s to allow ions to translationally cool by collisions with the N_2 gas. After the cooling

period, the trapping plates were dropped to a final voltage of 1.0 V, unless specified. The analyzer pressure during the detection period is typically 2×10^{-8} Torr. These are conditions that have been established by Li et al.[12,13]

The bastadins were obtained from samples of the marine sponge *Ianthella basta* and were purified by HPLC as described elsewhere.[16,17] Since they are derived from one basic structure, their molecular formulas fall within a limited number of combinations. This facilitated the assignments of the molecular formulas for given exact masses.

RESULTS

Accurate mass determinations in FTMS require that the frequencies of the ions be stable. If external calibrants are to be used, then the frequencies must remain constant for a long period of time. With internal calibrants, the frequencies must be stable during the detection period (typically less than a few seconds). Several factors can affect the stability of the ion's cyclotron frequency. The most important include the homogeneity of the magnetic and the electric field within the analyzer cell. With a 6

(14) McCullough, S. M.; Gard, E.; Lebrilla, C. B. *Int. J. Mass Spectrom. Ion Processes* **1991**, *107*, 91−102.

(15) Carroll, J.; Lebrilla, C. B. *Anal. Chem.* **1993**, *65*, 1582−7.

(16) Mack, M.; Molinski, T. F.; Buck, E. D.; Pessah, I. N. *J. Biol. Chem.* **1994**, *269*, 23236−48.

(17) Franklin, M. A.; Molinski, T. F., unpublished results.

Table 1. Exact Mass (m/z) Determination of a Known Compound, α-Cyclodextrin, Using the Sodiated Parent and the Fragment of Gramicidin S as Internal Calibrants

theor mass	determination		av of determns	dev (ppm)
	1 (dev, ppm)	2 (dev, ppm)		
995.3067	995.3033 (−3.4)	995.3122 (5.5)	995.3078	1.1

[a] Reference compounds: gramicidin S (MH+ m/z 1141.7138 and MNa+ m/z 1163.6957) + fragment (m/z 717.4214 and 571.3608).

T magnet and low trapping potentials (less than 1.0 V), Li et al. showed that use of an external reference provides a maximum deviation of less than 10 ppm between the observed and actual masses.[12,13] An external reference is naturally advantageous. It decreases the number of necessary manipulations and minimizes the inadvertent introduction of impurities. However, many FTMS instruments have magnets with lower and in many cases less homogeneous magnetic fields. The superconducting magnet in this laboratory, for example, has a field strength of only 3 T. Although this field strength and the available homogeneity provide adequate mass accuracy, less than 20 ppm is routinely attainable with external calibration; it does not fulfill the rigorous requirement for publications of new compounds (5 ppm or less). In these cases, internal calibration is necessary to obtain more accurate masses.

Selection of a calibrant depends primarily on the desired mass range. The compounds were chosen to bracket the mass of the sample as closely as possible. Rigorous experiments have not yet been performed to determine the largest possible mass range between the two calibrants that would still provide acceptable results. The two calibrants need not be structurally similar to the unknown compound, although a calibrant that exhibits good sensitivity to MALDI is desirable. When fragment ions from one calibrant is abundant, the quasimolecular parent and a strong fragment ion signal may suffice for calibration. This is illustrated with the determination of a known compound, a cyclic hexasaccharide α-cyclodextrin, whose exact mass is measured by using the quasimolecular peak (MH+, m/z 1141.7138 and MNa+, m/z 1163.6957) and fragments (m/z 717.4214 and 571.3608) of the gramicidin S calibrant (Table 1). The average of two determinations produce a value (m/z 995.3078) that varies by only 1.1 ppm from the theoretical mass (m/z 995.3067). The largest single deviation is 5.5 ppm for the lowest mass isotopmer. The major problem with using fragments stems from the unpredictability of MALDI for producing fragment ions. The use of two compounds that bracket the expected mass is more desirable.

The mass spectrum of a mixture is shown (Figure 2) derived from ~1 pmol of a bastadin, which we designate as unknown 1, and 0.1 pmol each of the two calibrant compounds maltopentaose (a linear oligosaccharide, left arrow) and gramicidin S (a cyclic decapeptide, right arrow). Although the mass spectrum was obtained in the low-resolution broad-band mode, the isotopic envelope contains easily resolvable peaks with a corresponding resolution of 5000 (fwhh, inset). The large number of Br atoms produces a complicated quasimolecular ion region. However, with the resolution and the high S/N, the isotopic pattern is less of a hindrance and is useful for determining the number of Br atoms. The isotopic pattern corresponds to the presence of four bromine
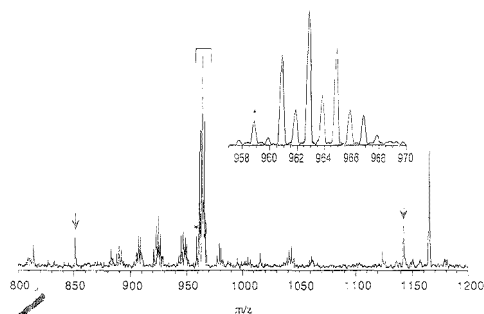
Figure 2. MALDI-FTMS of unknown 1 (given the name bastadin-20). The labeled peaks are the lowest mass isotopmer of the calibrant compounds maltopentaose (sodiated, left arrow) and gramicidin S (protonated, right arrow). Both protonated and sodiated gramicidin S are observed, and either one could be used for calibration. The lowest mass isotopmer (asterisk) and the pseudomolecular ion region are shown (inset). The ionic bastadin species correspond to sodium adducts.

atoms on the bastadin ring. The high S/N of the spectrum also facilitates the assignment of the lightest isotopmer (asterisk). The identification of this peak is key in providing accurate masses because it has the least interference from isobaric peaks of other isotopmers. In the fast atom bombardment (FAB) spectrum, the matrix background often makes this peak less prominent.

The exact mass of unknown 1 has been independently verified using standard methods that employ a double-sector instrument. In this procedure, fast atom bombardment was used in a vacuum generator ZAB-2F and the quasimolecular ion was peak matched, by overlaying the signals, to a known reference signal. In MALDI-FTMS, the quasimolecular ion cluster corresponds to the sodiated species. The cyclic peptides appear to strongly coordinate alkali metal ions. All the bastadins we have analyzed to date appear as sodium-coordinated species as do the two quasimolecular ions of the calibrants (arrow).

With the known masses of sodiated gramicidin S and maltopentaose, the mass of the sodiated bastadin (unknown 1) is determined to be (m/z 958.8588). This value deviates by only 5.2 ppm from the exact mass of the lowest isotopmer for a compound with the corresponding molecular formula $C_{34}H_{28}$-$Br_4N_4O_8Na$ (m/z 958.8538). The discrepancy lies within the acceptable limit for the identification and publication of new compounds.

In the past, only a single accurate mass determination was necessary for new compounds. More recently, multiple determinations have been encouraged. With multiple analyses, FTMS gives numbers with even better agreement. Unknown 2 is a compound obtained by permethylating unknown 1 (diazomethane, 4 °C, 24 h). The permethylation reaction allows the determination of the number of hydroxyl groups on the ring. The sodiated parent is observed to have a m/z 1015 (Figure 3). The summary of three determinations is tabulated (Table 2). An average value of the exact mass was obtained corresponding to m/z 1014.9143. The closest molecular formula for unknown 2 is $C_{38}H_{36}Br_4N_4O_8$-Na, which has a theoretical mass of m/z 1014.9164 producing a deviation of only 2.1 ± 1.5 ppm. The mass change from unknown 1 to unknown 2 corresponds to the addition of four methyl groups. The analysis was performed over a period of several days,
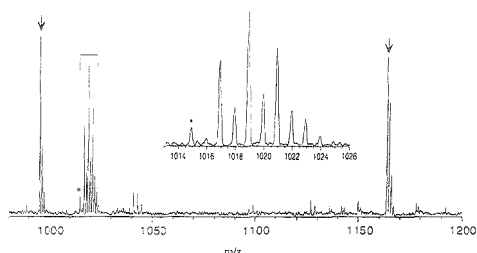
Figure 3. MALDI-FTMS of unknown 2 (bastadin-20 tetramethyl ether). The calibrants used are α-cyclodextrin (sodiated, left arrow) and gramicidin S (sodiated, right arrow). The lowest mass isotopmer (asterisk) and the quasimolecular ion region are shown (inset). The most abundant quasimolecular ions are typically sodium adducts.

Table 2. Exact Mass (m/z) Determination of a Bastadin, Unknown 2, Obtained by Permethylation of Unknown 1[a]

theor mass	absol dev (ppm) of each determn			av of determns	dev[b] (ppm)
	1	2	3		
1014.9164	−3.4	−0.4	−2.4	1014.9143	2.1 ± 1.5
1016.9144	2.6	3.5	9.4	1016.9197	5.2 ± 3.7
1018.9124	2.6	2.6	5.5	1018.9160	3.5 ± 1.7
1020.9103	2.6	5.6	7.5	1020.9157	5.3 ± 2.5
1022.9083	1.7	−3.2	−1.3	1022.9073	1.0 ± 2.3

[a] Reference compounds: α-cyclodextrin (MNa+, m/z 995.3067) + gramicidin S (MNa+, m/z 1163.6957). [b] Deviation of average values from theoretical mass.

Table 3. Exact Mass Determination of a Bastadin, Unknown 3

theor mass	absol deviation (ppm) of each determn		av of two determns	dev[b] (ppm)
	1	2		
1036.7642	1.2	3.4	1036.7666	2.3
1038.7623	8.1	1.1	1038.7671	4.6
1040.7603	1.9	−2.4	1040.7601	−0.2
1042.7582	2.4	−1.3	1042.7588	0.6
1044.7562	−3.0	2.4	1044.7559	−0.3
1046.7542	−7.5	−7.9	1046.7461	−7.7

[a] Reference compounds: α-cyclodextrin (MNa+, m/z 995.3067) + gramicidin S (MNa+, m/z 1163.6957). [b] Deviation of average values from theoretical mass.

Figure 4. Plot of difference between the calculated and determined mass for ions in the quasimolecular ion region of mass spectrum for unknown 3 (later identified as bastadin-19). The smallest differences occur when the trapping voltages are set to 1.0 V or less. Large differences are observed with trapping plate voltages set to 1.5 V and greater.

illustrating good instrumental stability. With the given molecular formula, the deviation of the determined mass from the exact mass for the entire pseudomolecular region is provided (Table 2). There is excellent reproducibility when the internal standard is used. The largest deviations are observed in determination 3 for the heavier isotopmers having m/z 1017 and 1021. As mentioned, the higher masses may contain isobaric species of other naturally occurring isotopes such as ^{13}C and ^{18}O. For this reason, it is better to chose the lightest isotopmer for exact mass determinations. The heavier isotopmers, however, are useful for confirmation of the assigned molecular formula.

Based on the above results and the NMR data,[17] unknown 1 was shown to be a new compound and given the name bastadin-20, where X = H and R = H (see structure). Unknown 2 is the tetramethyl derivative of bastadin-20 where X = H and R = CH$_3$.

A third compound, unknown 3, was also separated by HPLC from extracts of *Ianthella basta*. The average value obtained from the MALDI is m/z 1036.7666 corresponding to a molecular formula of C$_{34}$H$_{27}$Br$_3$N$_4$O$_8$Na (Table 3). The calculated mass for the given formula corresponds to m/z 1036.7642 for the lightest isotopmer and lies only 2.3 ppm from the experimentally determined value. Most of the values for each isotopmer in the two determinations vary by less than 5 ppm from the calculated values except for the heaviest isotopmer, which is 7.7 ppm away from its calculated value. The determined mass was key to identifying this compound. Based on this value and the NMR of unknown 3,[16] it is identified as the previously characterized bastadin-19 where X = Br and R = H.

In all the spectra, a cluster of peaks 16 u larger than the sodiated quasimolecular peaks is observed (See, for example,

Figures 2 and 3.). These signals correspond to the potassiated parent and could provide further confirmation of the assignment of the quasimolecular ions. More importantly, these species illustrate that the exact masses of mixtures can be determined simultaneously. These determinations are aided by the propensity of MALDI-FTMS to produce primarily quasimolecular ions. The determination of mixtures will greatly facilitate the speed of the analysis particularly for compounds or groups of compounds that are chemical homologues.

The values of the trapping plate voltage are important for exact mass determination and must be kept as low as possible. The observed natural frequencies of the ions are known to shift as the trapping plate voltages are increased.[12,18] Even with the internal standard, care must be taken to use low trapping voltages. Figure 4 shows the differences between the exact mass and the determined mass (in ppm) as a function of trapping plate voltage. The largest deviations occur with 2.0 V, which is also the largest voltage investigated (Table 4). The most useful trapping voltages appear to be between 0.5 and 1.0 V as these conditions exhibit the least scatter and maintain the lowest deviation between determined and actual mass for the lowest mass isotopmer. With 0.5 V trapping the largest deviation is 7.8 ppm, for the heaviest isotopmer, while with 1.0 V of trapping potential the largest deviation is 5.2 ppm. The difference between the observed mass

(18) Grosshans, P. B.; Marshall, A. G. *Int. J. Mass Spectrom. Ion Processes* 1990, 100, 347−79.

Table 4. Differences between Theoretical Mass and Determined Mass as a Function of Trapping Plate Voltages for Bastadin-19[a]

theor mass (m/z)	Δ (m/z)			
	0.5 V	1.0 V	1.5 V	2.0 V
1036.7642	2.2	−1.2	−18.2	−136.5
1038.7623	5.0	−0.7	−9.9	−0.3
1040.7603	−0.3	−5.2	−10.6	10.1
1042.7582	0.3	−5.0	−10.5	8.2
1044.7562	−0.2	−1.1	−4.3	22.0
1046.7542	−7.8	−2.0	13.7	22.6

[a] Reference compounds: α-cyclodextrin (MNa$^+$, m/z 995.3067) + gramicidin S (MNa$^+$, m/z 1163.6957).

of the lightest isotopmer and the known mass is less than 3 ppm with 0.5 and 1.0 V of trapping. With 1.5 V, nearly all masses have deviations that are greater than 10 ppm. The deviations increase further with 2.0 V on the trapping plates. Below 0.5 V the ion intensities decrease significantly, but there is no observable effect on signal strength between 0.5 and 2.0 V.

MALDI-FTMS is useful for determining the exact masses of compounds. The method described is relatively simple requiring only the addition of the calibrants. All other conditions are typical for MALDI-FTMS. The method does not require modifications in either the hardware or the software to implement. The low fragmentation yield allows simple assignments of the pseudomolecular ions. More importantly, there is a real potential for performing mixture analyses and obtaining exact masses of several compounds simultaneously. Furthermore, there is little tuning required between samples as the internal calibrant helps minimize varying instrumental conditions.

Approaches and Limits for Accurate Mass Characterization of Large Biomolecules

Roman A. Zubarev,* Plamen A. Demirev, Per Håkansson, and Bo U. R. Sundqvist

Ion Physics Department, Institute for Radiation Sciences, Uppsala University, Box 535, 75121 Uppsala, Sweden

The use of the average mass for mass characterization of large biomolecules is examined in light of the latest achievements in mass spectrometry, and factors affecting the accuracy of both theoretical calculation and experimental determination are analyzed. It is concluded that, in practice, the accuracy of average mass measurements is limited to ±0.1 Da for molecular masses below 10 000 Da and to 10 ppm for masses above that value. Inherent properties of the isotopic distributions lead to a systematic underestimation of the average mass during the measurements. The procedure proposed earlier (Zubarev, R. A. Int. J. Mass. Spectrom. Ion Processes 1991, 107, 17–27) in order to correct for this effect is now extended to the case of multiply-charged ions and their use for mass scale calibration. A formula is derived for the relationship between mass accuracy and both the instrumental resolving power and molecular ion peak statistics. Monoisotopic mass measurements are recommended to be used whenever possible. As a complement to that, other additive quantities, such as the ratio of intensities of the first isotopic peak to the monoisotopic peak, can be employed.

Recent advances in mass spectrometry of biomolecules bring to life the old issue about the "most comprehensive" mass spectrometric characteristics of molecular weight (MW).[1] The following well-known quantities are usually applied to characterize MW: nominal, monoisotopic, most abundant, and average (chemical) mass.[1] Previously, the average mass (AM), defined as the centroid of the biomolecules isotopic distribution, was found to be the least ambiguous for MW of large biomolecules.[1] Later, it was realized that, because of the natural variations of isotopic abundances of the elements, AM can only be determined, even theoretically, with limited accuracy.[2] Carbon atoms alone, contributing ~50% of a polypeptide's mass and 70% of the isotopic shift (difference between the AM and monoisotopic mass), give ±8 ppm uncertainty in the AM of a protein.[3] It is not an overestimation to assume that other elements raise the total uncertainty up to 10 ppm. Thus, the theoretical AM of the natural protein horse myoglobin lies within the interval 16 951.3–16 951.7 Da, although a straightforward calculation from the sequence gives a value of 16 951.49 Da.[4] Since the theoretical value itself is

defined with ±10 ppm uncertainty, any comparison of the experimental results with theoretical calculations is only meaningful if the difference exceeds that value.

Another finding concerning the AM is that its experimental determination almost inevitably leads to a systematic error that can be as large as 1 Da.[5] The origin of this systematic error can be rationalized through the consideration of the shape of the biomolecules' isotopic distribution. The latter is nonsymmetric and has a "tail" stretching toward higher masses. Because of its low abundance, this tail is generally ignored during the measurements in order to suppress interferences from the noise that is always present in real mass spectra. Therefore, the mass obtained as the centroid of the isotopic distribution in such measurements is always "lighter" than the true AM. The remarkable feature of this systematic error, or shift between the theoretical and measured AM, is that it is almost independent upon the MW or elemental composition of a biomolecule. Instead, it is determined by what fraction of the isotopic distribution is used for the measurements. If, for instance, one considers only the upper half of the distribution, the shift will be 0.5 ± 0.1 Da for biomolecules with MW > 700.[5] So far, no attempts have been made to rationalize this particular behavior of AM. This work proposes an explanation based on the consideration of the properties of the binomial distribution. The explanation found confirms that the considered shift is, in fact, an inherent feature of the biomolecules' isotopic distribution and that the "measure-and-correct" approach proposed in ref 5 is valid for a wide range of biomolecules. An extension of the approach for multiply-charged ions and reference peaks used for mass scale calibration is also given.

In experimentally obtained mass spectra, one observes isotopic distributions "simulated" by nature. Because of the limited number of ions accumulated in the peaks and other instrumental factors, the obtained distributions deviate from the theoretically calculated one and so does the measured AM. Limited mass resolution of the instrument leads to a "fusion" of the isotopic peaks which might also shift the centroid of the distribution. Of analytical interest is what knowledge of instrumental resolution and accumulated statistics is necessary in order to achieve the desired mass accuracy. In the current work, an attempt is made to find the answer to this question using Monte Carlo simulations.

EXPERIMENTAL SECTION

Computational Methods. Isotopic distributions of bovine insulin were calculated on an IBM PC AT with Borland C v. 2.0 compiler using an approach similar to that described by Yergey et al.[6] Different threshold values were used to limit the total

(1) Yergey, J.; Heller, D.; Hansen, G.; Cotter, R. J.; Fenselau, C. Anal. Chem. 1983, 55, 353–356.
(2) Pomerantz, S. C.; McCloskey, J. A. Org. Mass Spectrom. 1987, 22, 251–253.
(3) Beavis, R. C. Anal. Chem. 1993, 65, 496–497.
(4) Zaia, J.; Annan, R. S.; Biemann, K. Rapid Commun. Mass Spectrom. 1992, 6, 32–26.

(5) Zubarev, R. A. Int. J. Mass Spectrom. Ion Processes 1991, 107, 17–27.
(6) Yergey, J. A. Int. J. Mass Spectrom. Ion Phys. 1983, 52, 337–349.

number of permutations involved, ranging from 0.001% to 1% of the intensity of the most abundant permutation. The Monte Carlo simulations were performed on a Macintosh IIci using a program written on the THINK C v. 4.0 (Symantec). These simulations involved the computation of isotopic distributions of C_N clusters with $N = 100-1000$ carbon atoms and totally 10^2-10^4 molecules (clusters) in each distribution.

Instrumentation. The in-house built DIPLOMA time-of-flight plasma desorption mass spectrometer was used in this study; it is described in detail elsewhere.[7] The instrument employs a single-stage mass reflectron and provides a typical mass resolution of 5000 fwhm for organic ions and 10 000 for CsI. The total effective length of the flight path of ions is 2.3 m. The primary 72.3 MeV $^{127}I^{13+}$ ions come from a tandem Van de Graaf accelerator at a typical rate of 2500 s^{-1}. Spectra were taken at acceleration voltage for secondary ions of +15 kV.

Samples. The peptide thymosin was obtained from a commercial source and was used without further purification. The samples were prepared in the following way. First, a nitrocellulose (NC) layer of 400-700 Å thickness was deposited by spin coating from an acetone solution on a 1 × 1 cm^2 silicon slice (chip). Peptide molecules were dissolved in water and were dried on top of the backing. Finally, the samples were washed with water in order to remove salts and low-mass contaminants.[8]

RESULTS AND DISCUSSION

Peculiarities of the Theoretical Calculation of AM. The theoretical AM can be calculated in two ways: (i) by multiplying the coefficients in the elemental composition formula by the chemical masses of the elements and (ii) by generating the isotopic distribution and calculating its centroid.

$$AM = \sum_{i=0}^{m} M_i I_i / \sum I_i \qquad (1)$$

where M_i and I_i are the masses and corresponding intensities of the spectrum points (bins of a line histogram). In theory, the two computational approaches for AM calculations are equivalent. In practice, however, the second way may involve complications because of the huge number of permutations involved. For the relatively simple molecule of glucagon (MW = 3483.8), for instance, the calculation of 7.9×10^9 unique permutations is needed.[6] A commonly employed method to avoid excessive calculations is to generate only permutations exceeding a threshold value.[6] The introduction of a threshold may introduce an error: the isotopic distribution of bovine insulin, calculated with 0.1% threshold relative to the most abundant permutation, gives an average mass of 5733.521 Da.[6] The result deviates from the theoretical value AM = 5733.585 Da calculated from the elemental chemical masses, by 0.064 Da or 11 ppm. That is, the error obtained is of the order of the uncertainty from the isotopic abundance variations! We have found that, in fact, a threshold as low as 0.001% is needed to achieve an agreement of better than 0.001 Da between the average masses calculated by the two approaches.
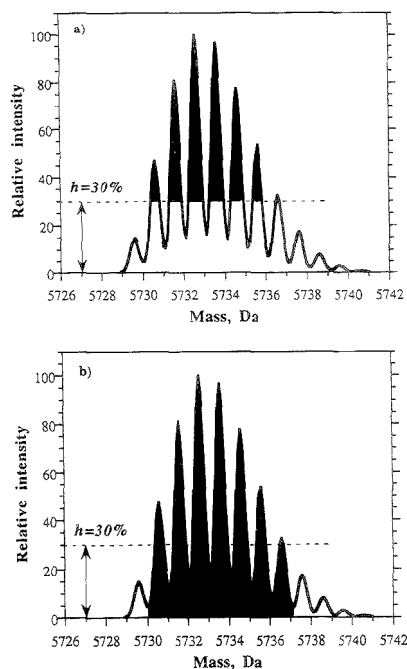
Figure 1. Centroid determination of the bovine insulin isotopic distribution: (a) top-fitting method, a cutoff at a level h and averaging only the upper part of the distribution, i.e., background subtraction; (b) integration down to the base line of all prominent isotopic peaks exceeding h (no background subtraction).

Another constraint may arise from the number m of significant isotopic peaks in the obtained distribution. Calculations for bovine insulin show that, in order to obtain better than ±0.1 Da accuracy, one needs to measure *both* masses and intensities of at least $m = 11$ isotopic peaks, the smallest of which is just 3% of the maximum intensity (provided that both masses and intensities are measured exactly). It should be noted that m increases rapidly with MW: for MW = 12 000, $m = 20$ if ±0.1 Da accuracy is desired. The above results suggest that proper care should be taken while using computer programs (including commercial ones) for generating the isotopic distributions in order to avoid miscalculations. The best strategy would be to calculate the centroid of the obtained distribution and compare it with the AM value obtained through the chemical masses of elements.

Experimental Measurements of AM. *Two Approaches to Centroid Measurements.* In order to suppress interferences from the noise in experimentally obtained spectra, one has to select the "most prominent" peaks by setting up a suitable threshold. In Figure 1, two possible approaches for centroid determination are shown: (a) "top-fitting",[5,9,10] a cutoff at a certain level h and averaging only the upper part of the distribution, i.e., background subtraction; (b) integration down to the base line of all prominent isotopic peaks exceeding h, i.e., no background subtraction. The

(7) Brinkmalm, G.; Håkansson, P.; Kjellberg, J.; Demirev, P.; Sundqvist, B. U. R.; Ens, W. *Int. J. Mass Spectrom. Ion Processes* **1992**, *114*, 183−207.
(8) Jonsson, G. P.; Hedin, A. B.; Håkansson, P. L.; Sundqvist, B. U. R.; Säve, B. G. S.; F. P.; Nielsen, P. F.; Roepstorff, P.; Johansson, K.-E.; Kamensky, I.; Lindberg, M. S. L. *Anal. Chem.* **1986**, *58*, 1084−1087.

(9) Feng, R.; Konishi, Y.; Bell, A. W. *J Am. Soc. Mass Spectrom.* **1992**, *2*, 387−401.
(10) McEwen, C. N.; Larsen, B. S. *Rapid Commun. Mass Spectrom.* **1992**, *6*, 173−178.

centroid obtained in both approaches is always "lighter" than the true average mass, because the high-mass tail is not included in the calculations. Both cases, therefore, lead to a negative systematic error. For a cutoff level $h = 50\%$ and top-fitting, this systematic error is almost independent of the mass and amino acid composition of polypeptides with MW > 700 and lies within 0.45 ± 0.10 Da.[5] Thus, an obvious approach for improving the accuracy of the average mass is to add a correction factor ($\Delta m_{50\%} = 0.45$ Da) to the experimentally determined value. The uncertainty ± 0.1 Da of the correction factor remains, however, as a possible mass error. The "down-to-base line" integration (Figure 1b) is, in fact, a combination of two figures: the top-fitting part (as in Figure 1a) and an under-the-threshold part. The comparison of the two approaches will be given later.

Origin of the Systematic Shift in Measured AM Values. The source of systematic deviation of the measured centroid from the theoretical AM is best illustrated with the example of the isotopic distribution of single-element two-isotope molecules, e.g., pure carbon clusters C_N (including fullerenes). The isotopic peak abundances of such a distribution are described by the binomial distribution

$$P(n) = \frac{N!}{n!\,(N-n)!}\, p^n (1-p)^{N-n}$$

where $P(n)$ is the relative intensity of the nth peak (the monoisotopic peak is denoted as the 0th peak) and $p < 1$ is the relative abundance of the less abundant isotope. The position n_{max} of the most abundant peak in the distribution satisfies the following relation:

$$\mu - (1-p) < n_{max} < \mu + p$$

Here $\mu = pN$ is the mean value of the binomial distribution, i.e., its centroid. Making an assumption $p \ll 1$ (for carbon, $p = 0.011$), we obtain

$$\mu - 1 < n_{max} < \mu \quad \text{or} \quad 0 < \mu - n_{max} < 1$$

In other words, the position of the most abundant peak in the binomial distribution is always "lighter" than the centroid, and the difference $(\mu - n_{max})$ between these two values never exceeds unity. The behavior of $\mu - n_{max}$ for carbon clusters as a function of the total number N of atoms in the cluster is shown in Figure 2. The discrete character of the binomial distribution causes $\mu - n_{max}$ to "oscillate" with an amplitude 1 as N increases. The period of the "oscillations" is equal to $1/p$.

Let us now consider the difference between the average value μ of the distribution and the centroid $\bar{n}$ of its upper part taken above the cutoff level h (top-fitting). The behavior of $\mu - \bar{n}$ as a function of N for different h is shown in Figure 3. At $h = 50\%$, $\mu - \bar{n}$ approaches a value of ~ 0.4 and oscillates around it with a relatively small amplitude, <0.1 Da. Another remarkable feature of that dependence is that, even at low cutoff levels, the magnitude of $\mu - \bar{n}$ is significant: it already reaches ~ 0.1 Da at $h = 3\%$.

Figure 4 represents the comparison made for carbon clusters between the top-fitting and down-to-base line integration with the threshold taken at $h = 50\%$. As can clearly be seen, the latter approach exhibits ~ 3 times larger variation of the magnitude,
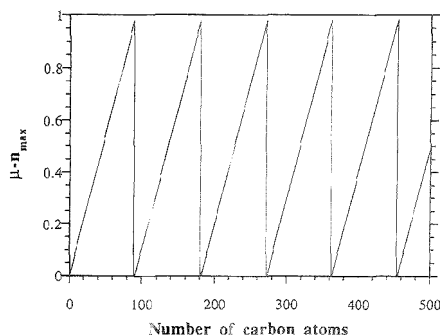
Figure 2. Dependence of $\mu - n_{max}$ for carbon clusters as a function of the total number N of atoms in the cluster (μ, true position of the isotopic distribution centroid; n_{max}, position of the maximum peak). The period of "oscillations" is equal to $1/p$, where p is the relative abundance of the less abundant isotope.
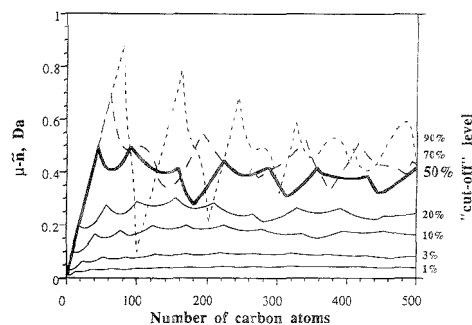
Figure 3. Dependence of $\mu - \bar{n}$ for carbon clusters as a function of the total number N of atoms in the cluster at different cutoff levels h (μ, true position of the isotopic distribution centroid; $\bar{n}$, centroid of its upper part taken above the cutoff level h).

ranging from 0.1 to 0.6 Da. Because of the large oscillations, the correction Δm_h cannot be implemented for down-to-base line integration, and we will not consider this approach further.

Application for Peak Position Determination. As shown in the above considerations, the systematic shift $\mu - \bar{n}$ is an inherent feature of any binomial distribution with $p \ll 1$. The isotopic distribution characterizing biomolecules is in fact a complex binomial one, where binomial distributions of single elements are superimposed. Although a strict mathematical proof is difficult to present, it is intuitively clear that the properties of a peptide isotopic distribution will be dominated by the 70% contribution from carbon atoms. Indeed, our calculations show that the isotopic distribution of bovine insulin exhibits behavior very similar to that of carbon. For example, a cutoff level of 3% was found to give an error in AM of 0.1 Da. Therefore, the "measure-and-correct" approach proposed in ref 5 might be valid for a wide range of biomolecules. This approach is employed on a routine basis in our work, involving mostly TOF measurements. The cutoff level $h = 50\%$ and the corresponding correction value $\Delta m_{50\%} = 0.5$ Da are found to represent a reasonable tradeoff between two opposite desires. The first one is to suppress interferences by chosing a high cutoff level; the other one is the precision consideration demanding lower h for better statistics. An
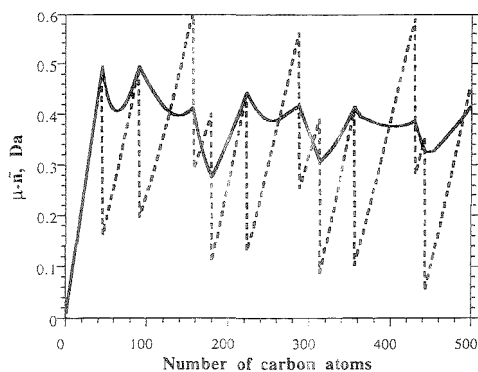
Figure 4. Dependence of $\mu - \bar{n}$ for carbon clusters as a function of the total number N of atoms in the cluster at cutoff level $h = 50\%$ for two centroid determination procedures: top-fitting (solid line) and down-to-base line (dashed line). In the latter case, variation of the $\mu - \bar{n}$ magnitude is much larger than in the former (from 0.1 to 0.6 Da). The correction Δm_h, therefore, cannot be implemented there.
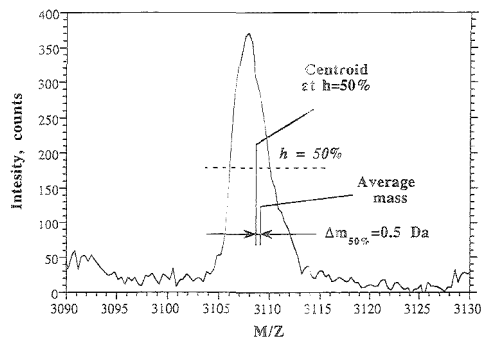
Figure 5. Plasma desorption TOF spectrum of the MH^+ ion region of thymosin (theoretical MW = 3108.1). Average m/z measured at $h = 50\%$ − 3108.5, corresponding to measured average mass of 3107.5 Da. Adding the correction value $\Delta m_{50\%} = 0.5$ Da results in average mass 3108.0 ± 0.1 Da, in good agreement with the theoretical value.

application of the proposed approach is shown in Figure 5, where the plasma desorption TOF spectrum of the MH^+ ion of thymosin (AM = 3108.1 Da) is presented. The position of the centroid measured at $h = 50\%$ is m/z 3108.5, corresponding to a measured AM of 3107.5 Da. After adding the correction value $\Delta m_{50\%} = 0.5$ Da, the resulting AM becomes 3108.0 ± 0.1 Da, in good agreement with the theoretical value.

When the background is low compared to the signal, the intermediate cutoff region, $3\% < h < 25\%$, where the oscillations of $\mu - \bar{n}$ are minimal (Figure 3), is more convenient for choosing the correction value Δm_h (corresponding Δm_h values for different h are given in ref 5). This, however, might not mean better accuracy, because the dependence $\Delta m_h(h)$ is much steeper for those values of h, and an error in h leads to more significant error in Δm_h than at $h = 50\%$.[5]

It should be noted that the method is applicable for any MW greater than ~700. Although the isotopic distribution of a biomolecule becomes relatively more symmetric with molecular mass increase,[1] the discrepancy between the AM and the peak

position remains the same in terms of the absolute value, i.e., $\mu - \bar{n} \approx 0.5$ Da at $h = 50\%$.[5] The discrepancy can be significantly higher, up to 1 Da, at higher h (see Figure 3).

Application for Multiply-Charged Ions and Mass Scale Calibration. For multiply-charged ions ($z > 1$), the discrepancy between the theoretical m/z value and the "top-fitted" position was found to be z times smaller than in the case of $z = 1$:

$$\Delta(m/z)_h = (1/z)\ \Delta(m/(z=1))_h$$

This implies that the charge state of ions, z, must be known before the appropriate correction can be applied.

In various mass spectrometric techniques, standard compounds (calibrants) are used for the purpose of better mass calibration. There, undesirable errors in the AM determination may also arise if one does not take into account the Δm_h factor. For instance, if the mass scale is calibrated using known AM of singly-charged calibrant peaks with positions determined at $h = 50\%$, the whole mass scale will be shifted by ~0.5 Da. If the ions to be measured are also singly-charged, direct measurement of their centroids yields the right answer without any further corrections. If, however, the ions have $z > 1$ charges, their measured centroid will be shifted by $(-0.5/z + 0.5)$ Da. After deconvolution (multiplication of the measured centroid values by z), one obtains an error of $0.5(z - 1)$ Da. In the general case, when ions with $z = n$ are used for the calibration with centroids determined above threshold h, the corresponding error of q-charged ion peak centroids will be $\Delta m_h(q - n)$.

Influence of Instrumental Parameters on AM Measurements. Monte Carlo simulations of the isotopic distributions of carbon clusters C_N were performed in order to determine how resolution and statistics affect the mass accuracy. The distributions containing N_c molecules were "observed" with an instrumental resolution of R; i.e., every isotopic peak was replaced by a Gaussian distribution with dispersion $\sigma_0 = AM/(2.35R)$. The latter expression originates from the definition of resolving power $R = AM/\text{fwhm}$, where fwhm = $2.35\sigma_0$ is the full width at half-maximum of a single isotopic peak. Masses of the individual isotopic peaks M_i were assumed to be known exactly, while intensities (abundances) I_i were allowed to deviate randomly from their theoretical values by up to $\pm 2\sqrt{I_i}$ (Poisson statistics was assumed). For every simulated distribution, the centroid was calculated at $h = 0\%$ using eq 1 and compared with the theoretical AM. Every kind of distribution was simulated 10^4 times, and the standard deviation σ_{AM} from the theoretical AM was calculated. Based on the results of the simulations, an empirical formula was found for σ_{AM}^2:

$$\sigma_{AM}^2 \approx AM/(1000N_c) + (0.15/N_c)(AM/R)^2 \qquad (2)$$

Equation 2 implies that, in order to obtain an accuracy of $\Delta M_a = 2\sigma = 0.1$ Da in average mass measurement of a compound with AM ≈ 10 000 Da, one should accumulate at least $N_c \approx 4000$ ions in the molecular ion peak, provided the isotopic peaks are well resolved. Therefore, high sensitivity does not necessarily lead to high accuracy of mass determination. Even though single molecules can be trapped in the FTICR cell,[11] and excellent

(11) Cheng, X.; Bakhtiar, R.; Van Orden, S.; Smith, R. D. *Anal. Chem.* 1994, 66, 2084–2087.

resolution can be achieved, accurate AM measurements still will require a collection of thousands of ions.

Another conclusion that can be drawn is that, in terms of the error in AM measurements, the requirements on the resolving power of an instrument are rather modest. It is easy to see from eq 2 that, with equal statistics accumulated in the molecular ion peak, a resolving power of $R \geq (150 \cdot AM)^{1/2}$ provides an accuracy comparable with that obtained with much higher resolution. From that point of view, the "sufficient" resolution is $R = 1200$ for MW < 10 000 and $R = 3900$ for MW up to 100 000: in both cases, the accuracy of the AM determination will not be compromised by the resolution.

Comparison of AM with Other Mass Spectrometric Characteristics. From a practical point of view, the use of *additive* quantities for biomolecule characterization is preferable. Nominal, monoisotopic, and average mass are additive: their values for the parts of a molecule, summed together, yield the corresponding values for the whole molecule. On the contrary, the mass of the most abundant isotopic peak, as well as any other peak besides a monoisotopic one, is not additive (see below). Another example of a nonadditive quantity is the width of the isotopic distribution. Additive quantities are linear functions of the elemental composition for all biomolecules and monomer composition for biopolymers and thus allow a wider range of mathematical techniques to be implemented for molecule recognition than those nonadditive.[12]

Monoisotopic Mass. The monoisotopic mass carries information on the elemental composition of the molecule but not on isotopic abundances. This is, in fact, an advantage, unless deuteration or similar procedures are used. There are no basic limitations on the accuracy in the monoisotopic mass measurements of a biomolecule, except for that the abundance of the monoisotopic peak is very low at high MW. Generally, it is hard to establish the position of the monoisotopic peak at MW > 5000, even though the isotopic pattern might be well resolved. Erratic monoisotopic mass assignment leads to an error of at least 1 Da. The way out has been shown by the approach based on an a priori relationship between the AM and the most probable position M_m of the monoisotopic peak:[13]

$$M_m = AM - (AM/K) \tag{3}$$

where $K = 1463$ for proteins and $K = 2092$ for polynucleotides. Here it was assumed that the monomers (amino acids and nucleotides, respectively) are equally abundant in biopolymers. Formula 3 works satisfactorily, i.e., gives an error less than ± 0.5 Da for proteins below 10 kDa and polynucleotides below 100 kDa. Senko et. al. improved the approach for peptides by constructing the model amino acid *averagine*, $C_{4.9384}H_{7.7583}N_{1.3577}O_{1.4773}S_{0.0417}$, which takes into account the natural abundances of different amino acids.[14] The factor K, calculated through the averagine, turns out to be 1741.5. The difference in K reflects relatively low natural abundance of S-containing amino acids, methionine and cysteine. The Senko's value gives a better estimation for the *most probable*

(12) Berdnikov, A. S. Ph.D. Thesis, Institute for Analytical Instrumentation, USSR Academy of Sciences, Leningrad, 1990.

(13) Zubarev, R. A.; Bondarenko, P. V. *Rapid Commun. Mass Spectrom.* **1991**, *5*, 276–277.

(14) Senko, M. W.; Beu, S. C.; McLafferty, F. W. *J. Am. Soc. Mass Spectrom.* **1995**, *6*, 229–233.

monoisotopic mass of natural peptides, but otherwise does not extend the mass range of the validity of eq 3, because the *spread* of monoisotopic masses at MW = 10 000 remains to be ± 0.5 Da.

Masses of Individual Isotopic Peaks. Since every isotopic peak except the monoisotopic consists of many closely situated components (isobars),[1] the mass of each of those peaks is, in fact, a centroid of the isobar distribution. This makes the mass of an individual isotopic peak a nonadditive quantity. The width of that distribution depends on the distance from the monoisotopic peak and usually is in the range of several millidaltons.[15,16] The calculation of the exact mass of an isotopic peak must involve, therefore, a full-scale generation of the isotopic distribution; it is not enough just to calculate the position of the ^{13}C components. Obviously, the natural spread in the isotopic abundances will influence the exact position of an isotopic peak, although it is not yet clear to what extent. For high-mass compounds, no individual isotopic peak can always be recognized as the most intense,[1] and therefore, the mass of the most abundant peak hardly can serve as a characteristics of MW. However, the exact masses of individual isotopic peaks can be measured with an accuracy of a few ppm.[17] It has been suggested therefore that the set of masses of individual peaks can be used for the biomolecular mass characterization.[17] It is not clear yet how big an error in the molecular characterization could arise from even 1 ppm error in the mass of an individual isotopic peak. The main difficulty here is to identify the "origin of the coordinates", i.e., to find the position of the monoisotopic peak. Again, a mistake in assignment "costs" at least 1 Da error in MW determination. It is therefore doubtful that the set of individual isotopic peak masses alone can be a sufficient characteristic of MW, although it might be a useful complement to other mass spectrometric characteristics, e.g., the average mass.

Other Additive Characteristics of MW. There is yet another additive quantity that can be useful for the mass spectrometric characterization of molecules provided the isotopic peaks are resolved and the intensity of the monoisotopic peak can be measured. This is $K_{1/0}$, the ratio of intensities of the first isotopic peak, usually referred to as the $^{13}C_1$ peak, to the monoisotopic one. $K_{1/0}$ is a linear function of the molecular elemental composition (except for elements without M+1 isotopes, like Cl or P) and isotopic abundances:

$$K_{1/0} = \sum E_i A_{1E_i}/A_{0E_i}$$

where E_i are the numbers of atoms in the elemental formula and A_{0E_i} and A_{1E_i} are the corresponding abundances of the M and M + 1 isotopes for each element, respectively. For average natural isotopic abundances, it follows

$$K_{1/0} = 0.0111E_C + 0.00015E_H + 0.0037E_N +$$
$$0.0004E_O + 0.0079E_S$$

Theoretically, $K_{1/0}$ contains information on both the elemental composition and abundances and thus is a valuable mass spec-

(15) Werlen, R. C. *Rapid Commun. Mass Spectrom.* **1994**, *8*, 976–980.

(16) Yergey, J.; Cotter, R. J.; Heller, D.; Fenselau, C. *Anal. Chem.* **1984**, *56*, 2262–2263.

(17) Dobberstein, P.; Schroeder, E. *Rapid Commun. Mass Spectrom.* **1993**, *7*, 861–864.

trometric characteristic. In practice, however, it might be difficult to measure this parameter with sufficient accuracy due to resolution and statistics constraints. Besides, the 10 ppm limit in accuracy due to natural variation in the isotopic abundances applies also to that quantity.

CONCLUSION

Accurate average molecular weight characterization of biomolecules faces substantial difficulties when the desired accuracy approaches 0.1 Da for MW below 10 000 or 10 ppm above that limit. Even theoretically calculated isotopic distributions may deviate from the "true" shape if an insufficiently low threshold is chosen to limit the number of permutations. In practice, measurements of the average mass inevitably lead to an underestimation of its value; even with a proper correction, the residual uncertainty is still of the order of ±0.1 Da. Such a correction can only be made if the top-fitting approach is used for centroid measurements; the down-to-base line method leads to a greater, and not correctable, error. One should be aware of the origin of the systematic shift between the theoretical and measured AM, which is in the very nature of the isotopic distribution of biomolecules. Statistics accumulated in the molecular ion peak, together with limited resolving power of the instrument, can compromise the accuracy of high-sensitivity AM measurements. An equation is obtained (eq 2) allowing one to estimate the statistical error arising due to these reasons. The use of the monoisotopic mass, whenever it is possible, is preferable. Other additive quantities, such as $K_{1/0}$, can also be used in combination with monoisotopic or average mass, to characterize biomolecules. As for the set of exact masses of the individual isotopic peaks, it is doubtful that it can serve as a sole MW characteristic.

Failure of ^{29}Si NMR To Detect Increased Blood Silicon Levels in Silicone Gel Breast Implant Recipients

Peter Macdonald,*,† Nick Plavac,† Walter Peters,‡ Stanley Lugowski,§ and Dennis Smith§

Department of Chemistry, Division of Plastic Surgery, and Centre for Biomaterials, University of Toronto, Toronto, Ontario, Canada M5S 1A2

We have compared directly the results of atomic absorption (AA) spectroscopy and a ^{29}Si magic angle spinning (MAS) nuclear magnetic resonance (NMR) technique reported in the literature by Garrido et al. (Garrido, L.; et al. *Magn. Reson. Med.* 1994, 31, 328−330) for analyzing blood silicon levels in control patients versus patients with silicone gel breast implants. AA spectroscopy yielded blood silicon levels in the nanogram per milliliter range for control patients, while somewhat higher values were found in patients with implants. The ^{29}Si MAS NMR technique applied to the identical blood samples was unable to detect silicon in any of the samples. Sensitivity calculations demonstrate that ^{29}Si MAS NMR should not be expected to detect silicon at the levels determined by AA spectroscopy under the spectroscopic conditions employed and that the concentration of silicon-containing compounds would need to be 10^4 times the level detected by AA in order to be detected by this NMR method.

The fate of silicone leaked from silicone gel breast implants has become the focus of intense scrutiny. Free silicone can "bleed" into the tissues immediately adjacent to implants[1,2] and can migrate further via the lymphatic system.[3] The silicones, or polysiloxanes, of which implant materials are composed are generally rather inert chemically. Nevertheless, immunological sensitization to silicone could possibly contribute to the development of autoimmune connective tissue disease.[4] A recent report by Garrido and colleagues suggested that biodegradation and chemical modification of silicone accompanies its migration among tissues and organs and that measurable amounts of silicon, on the order of 100 mM total silicon (corresponding to approximately 2.8 mg/mL), were found circulating in the blood of some implant patients.[5]

The studies of Garrido et al.[5] were conducted using ^{29}Si magic angle spinning (MAS) nuclear magnetic resonance (NMR) spec-

troscopy to assess levels of silicone in blood and to identify any chemical modifications that had occurred. NMR spectroscopy is ideally suited for chemical identification, because there is a rich variety of spectral parameters sensitive to structural and dynamic details and because it is possible to perform the analysis from within the midst of a complex mixture, such as a biological fluid. However, NMR spectroscopy is not a particularly sensitive technique in comparison to others.[6] When lower absolute amounts of an analyte are present, sensitivity considerations inevitably restrict the utility of NMR spectroscopy.

More recent atomic absorption (AA) spectroscopy measurements of blood silicon levels indicate that total elemental silicon concentrations fall in the 10−20 ng/mL range for control patients, while statistically significant higher levels (20−40 ng/mL) are found in patients with silicone gel breast implants.[7] Nevertheless, even the highest levels of silicon determined using AA are 5 orders of magnitude lower than those reported using ^{29}Si MAS NMR.[5]

In order to address this discrepancy between the findings of the two techniques, we have performed a direct comparison of blood silicon levels determined by AA and ^{29}Si MAS NMR analyses. Levels of blood silicon were determined in both control patients and patients having silicone gel breast implants. The details of the AA and ^{29}Si MAS NMR techniques employed matched as closely as possible those described in the conflicting reports.

EXPERIMENTAL SECTION

Blood Collection. Blood was collected from seven volunteers having silicone gel breast implants and six control patients without implant exposure. No patients with diabetes or autoimmune disease, or patients taking any known silicate-containing medications, were included in the study. The implants had been in place for a median of 13 years (range 7−20 years). Five of the seven patients subsequently demonstrated implant rupture at explantation. All blood samples were taken in a fashion designed to eliminate silicon contamination, using a meticulously clean collection room and "silicone-decontaminated" syringes and plasticware as described previously.[7] Heparinized blood samples were stored at 4 °C prior to analysis by AA and ^{29}Si NMR spectroscopies.

AA Spectroscopy. Silicon measurements were carried out with a Varian Model 875 atomic absorption spectrophotometer

* Phone: 905-828-3805. Fax: 905-828-5425. E-mail: pmacdona@credit.erin. utoronto.ca.
  † Department of Chemistry.
  ‡ Division of Plastic Surgery.
  § Centre for Biomaterials.
(1) Nelson, G. D. *Plast. Reconstr. Surg.* 1980, 66, 969−970.
(2) Barker, D. E.; Retsky, M. I.; Schultz, S. *Plast. Reconstr. Surg.* 1978, 61, 836−841.
(3) Hausner, R. J.; Schoen, F. J.; Pierson, K. K. *Plast. Reconstr. Surg.* 1978, 62, 381−384.
(4) Peters, W. *Ann. Plast. Surg.* 1995, 34, 103−109.
(5) Garrido, L.; Pfleiderer, B.; Jenkins, B. G.; Hulka, C. A.; Kopans, D. B. *Magn. Reson. Med.* 1994, 31, 328−330.

(6) Abragam, A. *Principles of Nuclear Magnetism*; Oxford Press: Hong Kong. 1961.
(7) Peters, W.; Smith, D.; Lugowski, S.; McHugh, A. *Ann. Plast. Surg.* 1995, 34, 343−347.

	controls (ng/mL)	implants (ng/mL)
number	6	7
minimum	5.30	7.10
maximum	57.70	57.50
mean	25.42	27.11
median	21.75	25.31
standard deviation	20.41	17.77
standard error	8.33	6.72

equipped with a graphite furnace Model GTA 95 and autosampler, using procedures and protocols described elsewhere.[7]

^{29}Si MAS NMR. ^{29}Si NMR spectra were recorded under conditions matching as closely as possible those described by Garrido et al.[5] Specifically, spectra were obtained using a Varian 9.4 T VXRS 400 NMR spectrometer equipped with a Doty MAS probe tuned to the resonance frequency of ^{29}Si (79.459 MHz). Typically, a 200 μL volume of whole blood was transferred into a standard Doty 7 mm (i.d.) zirconium MAS rotor, and the ^{29}Si NMR spectrum was acquired using acquisition parameters as follows: slow spinning of the MAS rotor (~1000 Hz), single-pulse excitation with a 3.5 μs radio-frequency pulse (~45° tip angle), a recycle delay of 10 s, with a sweep width of 33 000 Hz digitized into 2048 data points. Eight thousand such scans were signal-averaged (~22 h total acquisition time).

RESULTS AND DISCUSSION

AA Spectroscopy. Table 1 summarizes the results of the AA spectroscopy measurements of silicon levels in blood samples for the control patients versus those with silicone gel breast implants. For the control group, blood silicon levels were in the nanogram per milliliter range, the mean value being 25.42 ng/mL, in agreement with previous determinations using the same methodology.[7] For the implant group, blood silicon levels were somewhat higher, the mean value being 27.11 ng/mL, again agreeing with previous determinations in a similar, albeit larger, patient group.[7]

^{29}Si MAS NMR Spectroscopy. Figure 1 shows a series of ^{29}Si MAS NMR spectra obtained as described in the Experimental Section. Spectrum A is a positive control acquired using silicon oil (Dow Corning 360 Medical Fluid; viscosity 350 cs, average molecular weight 12 000). A single broad resonance line is visible ($\delta = -21$ ppm relative to tetramethylsilane, TMS) and is assigned to the dimethylsiloxanes of poly(dimethylsiloxane).[8] Other possible silicon resonances, such as hydrolyzed and methyl-terminated silicone, or silica, or high-coordinated silicon, are not observed. Either these compounds are present in amounts too small to be detected or their signals are broadened beyond the detection limit under the processing conditions used to generate the ^{29}Si NMR spectra. Of particular note is our use of an exponential multiplication of the free induction decay signal prior to Fourier transformation, corresponding to a line broadening of 400 Hz, exactly as employed by Garrido et al.[5]

Spectrum B is typical of the blood samples tested here in that the only ^{29}Si NMR resonance that is visible is a broad, featureless

(8) Coleman, B. *NMR of Newly Accessible Nuclei*; Laszlo, P., Ed.; Academic Press: New York, 1983; Vol. 2, p 197.
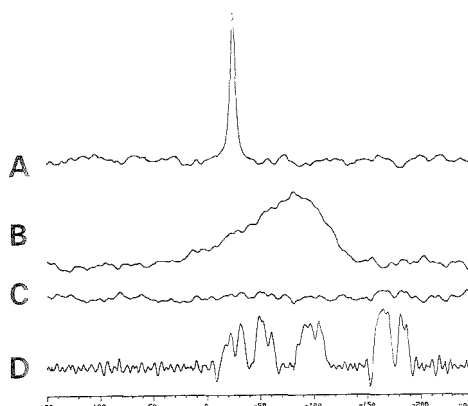
Figure 1. ^{29}Si MAS NMR spectra: (A) 200 μL of silicon oil, 4 scans, line broadening (lb) 400 Hz, no data points removed from the FID, and vertical scale (vs) 1500; (B) 200 μL of whole blood from implant patient, 8000 scans, lb 400 Hz, no data points removed from the FID, and vs 75 000; (C) 200 μL of whole blood from implant patient [same sample as (B)], 8000 scans, lb 400 Hz, first 10 data points removed from the FID, and vs 75 000; (D) 200 μL of whole blood from implant patient [same sample as (B)], 8000 scans, lb 400 Hz, first 10 data points removed from the FID, and vs 600 000; selected integration and phasing of particular regions of spectrum as described in the text.

line centered at ~−100 ppm, corresponding to the expected resonance frequency of silicon dioxide (otherwise known as silica). This same broad resonance line is observed in all blood samples, both implants and controls, and even in a blank sample containing only water. It must arise, therefore, from background silica present in the NMR probe itself.

A common means of removing such broad background resonances from NMR spectra is to eliminate the first few data points from the free induction decay (FID) prior to Fourier transformation. When we removed the first 10 data points of the FID, exactly according to Garrido et al.[5] (Garrido, L., personal communication), we obtained spectrum C shown in Figure 1, from which the broad resonance assigned to background silicon in the probe is now clearly absent. More significant is the absence of any other silicon resonances, whatsoever, under these acquisition and signal processing conditions. The same result is obtained in all blood samples tested, whether from control patients or patients having silicone gel breast implants.

We would mention, in addition, an eighth patient, who had subcutaneous silicone injections rather than silicone gel implants. AA spectroscopy results indicate that blood silicon levels for this patient were in the high end of the range displayed by the silicone gel breast implant group. (The AA results for this eighth patient are not included in the data or the statistical analysis of Table 1.) Even using blood from this eighth patient, we were unable to detect any ^{29}Si NMR signal.

One difficulty arising from eliminating the initial data points in an FID is the necessity of correcting for the substantial first-order phase shift that is an unavoidable side effect of employing such a signal-processing routine. Spectrum D in Figure 1 shows that it is possible to generate what appear to be broad resonance signals in the ^{29}Si NMR spectrum simply by employing the spectral baseline correction and phasing routines which are a standard

part of the data-processing software offered by every modern NMR spectrometer manufacturer. In the spectrum shown, we chose four particular regions of the spectrum for integration. After selecting the desired range of frequencies for integration, the phase of the signal within that region is adjusted as desired, and the computer "corrects" the intervening regions for apparent baseline anomalies. The resulting phased and baseline-corrected spectrum apparently contains resonances within the selected frequency ranges. These arise purely as a result of computer manipulation. The difficulty here originates with the fact that there is no "real" signal in the spectrum upon which to base a judgment regarding the correct phase and baseline treatment. Note that we could have chosen any region of the spectrum, performed the same manipulations, and generated similar anomalies.

A simple calculation supports our experimental finding that ^{29}Si NMR, under the conditions described by Garrido et al.[5] and reproduced here, is incapable of detecting levels of silicon consistent with those reported by AA spectroscopy. The detection limit is a function of the signal to noise ratio (S/N) in the NMR spectrum. Signal increases directly with the number of NMR-sensitive nuclei in the sample coil of the NMR probe and the number of scans that are averaged together. Noise, on the other hand, increases only as the square root of the number of scans. Consequently, S/N increases with the square root of the number of scans. The spectrum of silicon oil in Figure 1 has a S/N ratio of 33, obtained with a 200 μL volume and signal averaging just four scans. Using the density of silicon oil (1.05 g/mL), the weight fraction of Si in poly(dimethylsiloxane) (37.8 wt %), and the natural abundance of ^{29}Si (4.7%), one calculates that such a volume of silicon oil contains ~3.4 mg of ^{29}Si. If the number of scans were increased to 8000 from 4, then the S/N ratio would increase by a factor of $(8000/4)^{1/2}$ to equal ~1476. The absolute lower limit of sensitivity corresponds to a S/N ratio of 1. Under conditions identical to those under which the various blood samples were tested, this would equate to approximately (3.4 mg /1476) = 2.3 μg of $^{29}Si/200 \mu$L, corresponding to ~245 μg/mL total elemental silicon. For signal detection a S/N ratio of 2 or more is desirable,

while for quantification a minimum S/N of 3 is generally considered necessary. Clearly, these ^{29}Si NMR sensitivity limits are a factor of 10^4 higher than the blood silicon levels determined from AA spectroscopy. We would point out that a further calculation shows that to detect such low levels of silicon using the described ^{29}Si NMR technique would require multiple centuries of signal acquisition time. Even allowing for differences in the sensitivity of one NMR probe versus another, and the approximate nature of the calculation, it seems impossible that ^{29}Si MAS NMR could detect the silicon levels reported by AA spectroscopy.

More appropriate conditions for ^{29}Si NMR spectroscopy of blood samples than those described by Garrido et al.[5] are readily conceived. In particular, MAS of liquid samples is a poor means of eliminating $^{29}Si-^1H$ dipolar coupling, one of the main sources of loss of S/N through line broadening in ^{29}Si NMR spectra. A better approach would be to directly decouple ^1H using a radio-frequency decoupling field while employing an inverse-gated sequence to avoid deleterious nuclear Overhauser enhancements due to silicon's spin $I = -^1/_2$. Larger sample sizes and a higher sensitivity solution-state NMR probe would also seem to be a necessary prerequisite to better signal-to-noise ratios. Finally, recent advances in NMR radio-frequency coil design[9,10] may eventually permit routine detection of such low levels of analyte, but these are not yet widely available.

The question remains as to why Garrido et al.[5] observed silicon NMR resonances in their blood samples. If the published spectra were due to real signals rather than artifacts from data processing, then contamination from extraneous sources during the collection and/or sample-handling process seems the most likely explanation.

ACKNOWLEDGMENT

(9) Wu, N.; Peck, T.; Webb, A.; Magin, R.; Sweedler, J. *Anal. Chem.* 1994, 66, 3849–3857.
(10) Black, R. D.; Early, T. A.; Roemer, P. B.; Mueller, O. M.; Mogro-Campero, A.; Turner, L. G.; Johnson, G. A. *Science* 1993, 259, 793.

Attomole-Sensitivity Electrospray Source for Large-Molecule Mass Spectrometry

Gary A. Valaskovic, Neil L. Kelleher, Daniel P. Little, David J. Aaserud, and Fred W. McLafferty*

Baker Chemistry Laboratory, Cornell University, Ithaca, New York 14853-1301

Full mass spectra of high resolving power are obtained from 0.2 nL sample volumes of large (>10 kDa) nucleotides and proteins using a new electrospray ionization (ESI) system combined with Fourier transform mass spectrometry. The ESI needles are fabricated by laser-heated pulling of fused-silica tubing (5–20 μm i.d.), followed by chemical etching and surface metalization. Total analyte *loaded* at the instrument of 8.6 fmol and 216 amol produces signal-to-noise ratios of 400:1 and 60:1, respectively, and resolving power of >10^5 for full mass spectra, while the total amount of material consumed is ~150 and 10 amol, respectively.

Exciting advances in biomedicine have been made possible recently by ultrasensitive techniques for single cell[1] and subcellular[2] analyses that correlate imaging[3,4] and separation[1,5] methodologies with selective, sensitive chemical analysis. For example, subattomole sensitivity has been demonstrated with capillary electrophoresis (CE) but with low chemical specificity.[1] Integration of CE with electrospray ionization,[6,7] especially[8] with Fourier transform (FT) MS,[9–11] improves specificity dramatically; recent reports describe hemoglobin mass spectra from 10 red blood cells (5 fmol, FTMS)[12] and peptide mass spectra of limited mass range from 0.3 fmol samples (consuming only ~10 amol).[13] The sample requirements for such ESI-MS systems (50 fmol achieved for

normal ESI-MS)[14] have been substantially lowered by the discovery[15–17] that reducing ESI sample flow rates from 1 μL/min to as low as 25 nL/min ("μESI")[17] yields a far smaller reduction in the signal-to-noise ratio (S/N). Matrix-assisted laser desorption (MALDI),[18] the other exciting new method for the ionization of large (>10 kDa) molecules, has low attomole sample requirements attained by analysis of femtogram samples.[19,20] The ESI system presented here extends this capability to ESI-FTMS by reducing sample size to the picoliter level, realizing the small sampling requirements for single-cell analysis by MS.

One type of these μESI glass "needles" is fabricated from fused-silica capillary tubing (5–250 μm inside diameter, i.d.), forming a sharp tip by etching or grinding;[15,16,21] these needles can utilize much smaller (and observable) sample volumes. For the second type, 0.5–1 mm i.d. glass capillary tubing is heat softened and pulled down to form tips of 1–3 μm i.d.;[17] the much smaller droplets from these yield a stable spray at lower flow rates (25–50 nL/min), with improved desolvation and ionization efficiency. Combining these approaches, the μESI needles described here are fabricated by pulling down fused-silica capillary tubing to minimize further both sample volume and droplet size.

EXPERIMENTAL SECTION

For electrospray tip preparation, short lengths of small-bore (5, 10, and 20 μm i.d.; 150 μm outside diameter, o.d.) fused-silica capillary tubing (Polymico Technologies, Phoenix, AZ) were mounted in a modified micropipet puller (Sutter Instruments, Model P-87, Novato, CA) with the standard platinum–iridium heating element replaced with a 25 W CO_2 laser (Synrad, Inc., Bothell, WA); apparatus details are described elsewhere.[22] The

(1) Yeung, E. S. *Acc. Chem. Res.* 1994, *27*, 409–414.
(2) Sakmann, B.; Neher, E., Eds. *Single-Channel Recording*; Plenum Press: New York, 1983.
(3) Foskett, J. K.; Grinstein, S., Eds. *Noninvasive Techniques in Cell Biology*; Wiley-Liss: New York, 1990; Vol. 9.
(4) Herman, B., Jacobsen, K., Eds. *Optical Microscopy for Biology*; John Wiley & Sons: New York, 1990.
(5) Gilman, S. D.; Ewing, A. G. *Anal. Chem.* 1995, *67*, 58–64.
(6) Fenn, J. B.; Mann, M.; Wang, C. K.; Wong, S. F.; Whitehouse, C. M. *Science* 1989, *246*, 64–71.
(7) Smith, R. D.; Wahl, J. H.; Goodlett, D. R.; Hofstadler, S. A. *Anal. Chem.* 1993, *65*, 574A–584A.
(8) Hofstadler, S. A.; Wahl, J. H.; Bruce, J. E.; Smith, R. D. *J. Am. Chem. Soc.* 1993, *115*, 6983–6984.
(9) McLafferty, F. W. *Acc. Chem. Res.* 1994, *27*, 379–386.
(10) Speir, J. P.; Senko, M. W.; Little, D. P.; Loo, J. A.; McLafferty, F. W. *J. Mass Spectrom.* 1995, *30*, 39–42.
(11) O'Connor, P. B.; Speir, J. P.; Senko, M. W.; Little, D. P.; McLafferty, F. W. *J. Mass Spectrom.* 1995, *30*, 88–93.
(12) Hofstadler, S. A.; Swanek, F. D.; Gale, D. C.; Ewing, A. G.; Smith, R. D. *Anal. Chem.* 1995, *67*, 1477–1480.
(13) Andren, P. E.; Emmett, M. R.; Caprioli, R. M. *J. Am. Soc. Mass Spectrom.* 1994, *5*, 867–869.

(14) Kelleher, N. L.; Senko, M. W.; Little, D. P.; O'Connor, P. B.; McLafferty, F. W. *J. Am. Soc. Mass Spectrom.* 1995, *6*, 220–221.
(15) Gale, D. C.; Smith, R. D. *Rapid Commun. Mass Spectrom.* 1993, *7*, 1017–1021.
(16) Emmett, M. R.; Caprioli, R. M. *J. Am. Soc. Mass Spectrom.* 1994, *5*, 605–613.
(17) Wilm, M. S.; Mann, M. *Int. J. Mass Spectrom. Ion Processes* 1994, *136*, 167–180.
(18) Hillenkamp, F.; Karas, M.; Beavis, R. C.; Chait, B. T. *Anal. Chem.* 1991, *63*, 193A–202A.
(19) Li, Y.; McIver, R. T. *Rapid Commun. Mass Spectrom.* 1994, *8*, 743–749.
(20) Jespersen, S.; Niessen, W. M. A.; Tjaden, U. R.; Greef, J. v. d.; Litborn, E.; Lindberg, U.; Roeraade, J. *Rapid Commun. Mass Spectrom.* 1994, *8*, 581–584.
(21) Kriger, M. S.; Cook, K. D.; Ramsey, R. S. *Anal. Chem.* 1995, *67*, 385–389.
(22) Valaskovic, G. A.; Holton, M.; Morrison, G. H. *Appl. Opt.* 1995, *34*, 1215–1228.
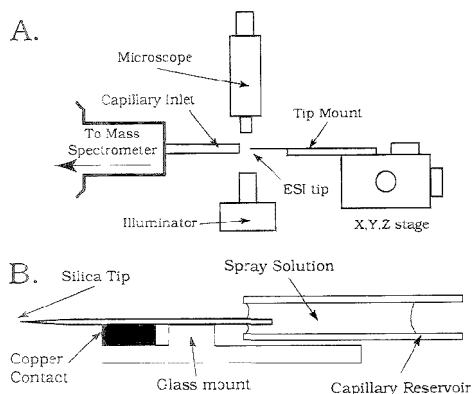
Figure 1. (A) Electrospray inlet system. (B) Detail of the needle mount.

Figure 2. (A) Light photomicrograph of a needle from 5 μm i.d. tubing after pulling and (B) after etching, tip i.d. ~2 μm. (C) SEM photomicrograph of a 2.3 μm i.d. tip; note the extremely thin wall.

laser first burns off the polyimide coating (11 W for 5–15 s) and softens the silica (16 W); the puller then reduces the tubing diameter to yield a short (<1 mm) taper, separating the tube into two tips of 50–100 nm i.d. as measured by high-resolution scanning electron microscopy (SEM). After trimming and cleaving the distal end of each needle for a 1–4 cm tube length, tips were immersed in 49% HF (Fisher Chemicals, Fairlawn, NJ) for 30–60 s and flushed multiple times with 0.2 μm membrane-filtered, 16 MΩ H_2O over a period of 20–30 min. Tip i.d.'s ranged from 1 to 5 μm, depending on the silica tubing i.d. and the HF immersion time. After drying in air, a thin-film sputter deposition system (Denton Vacuum, Model DV-502, Cherry Hill, NJ) deposited a 25–150 nm thick gold film on the needle in a 60 mTorr Ar atmosphere with a 20 mA sputter current.

The mass spectrometer was a modified 6 T Extrel-Waters (Madison, WI) FTMS-2000 instrument with Odyssey data station, introducing the electrosprayed ions with quadrupolar transport through five stages of differential pumping into a cylindrical trapped ion cell held at 10^{-9} Torr.[23,24] To aid ion trapping and cooling during acquisition, a gas pulse [Ar or N_2 at (~2–5) × 10^{-6} Torr] is admitted into the vacuum chamber. Spectra are acquired in broad-band acquisition mode after base pressure is restored, usually in 20–30 s. The fused-silica ESI needles (Figure 1) are glued on the end of a glass/copper mount; electrical contact between the Au-coated portion of the tip and the copper plate was made with silver paint. The tip mount is attached to an X,Y,Z stage for fine positioning with respect to the heated capillary inlet (~100 °C); as observed with a transmitted light microscope (Olympus Optical Co.), the optimum tip–inlet distance is 0.25–1.5 mm. A positive or negative tip–inlet potential, typically 600–1300 V, was applied with 5 kV supply (Bertran Associates, Hicksville, NY).

Immediately before use, samples were centrifuged at 16000g for 5–10 min to minimize suspended particles. Analyte is delivered to the distal end of the needle with a clean glass capillary, with flow monitored by the light microscope. Filling the needle

is completed with solvent, and the capillary "reservoir" is added (Figure 1). After the tip voltage is turned on, a stable ESI current is usually obtained in 1–15 s. Following spectral acquisition, the capillary reservoir is removed and the remaining solution is sprayed until "dry". Fresh needles are used when analyte or analyte concentration is changed.

Equine cytochrome c and bovine ubiquitin (Sigma Chemical) were dissolved in 2% acetic acid (99.9%, Aldrich Chemical). Single-stranded 50-mer DNA (Cornell Peptide/DNA synthesis facility) was desalted with high-performance liquid chromatography (HPLC) and dissolved (20 μM) in 70% acetonitrile (Aldrich Chemical) and 0.015% triethylammonium acetate (TEA).[25]

The mass spectrometer was externally calibrated prior to acquisition of analyte spectra. Molecular weights reported here are for the most abundant isotopic peak; incorrect peak assignment, which can yield a ±1 Da error, is minimized by statistically comparing the measured and theoretical isotopic distributions.[26]

Safety Considerations: Hydrofluoric acid can cause serious burns; it should be handled in a fume hood with protective clothing and eye wear and disposed of with excess calcium chloride. Carbon dioxide lasers can cause ignition of flammable materials and require protective eye wear and beam path enclosure.

(23) Beu, S. C.; Senko, M. W.; Quinn, J. P.; Wampler, F. M.; McLafferty, F. W. *J. Am. Soc. Mass Spectrom.* **1993**, *4*, 557–565.

(24) Senko, M. W.; Speir, J. P.; McLafferty, F. W. *Anal. Chem.* **1994**, *66*, 2801–2808.

(25) Little, D. P.; Thannhauser, T. W.; McLafferty, F. W. *Proc. Natl. Acad. Sci. U.S.A.* **1995**, *92*, 2318–2322.

(26) Senko, M. W.; Beu, S. C.; McLafferty, F. W. *J. Am. Soc. Mass Spectrom.* **1995**, *6*, 229–233.
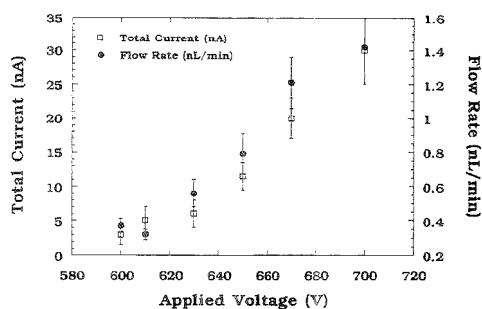
Figure 3. Total spray current (□) and flow rate (●) vs applied voltage: ESI needle 2 μm i.d. tip, from 5 μm i.d. tubing; 1.0 mm between tip and counterelectrode.
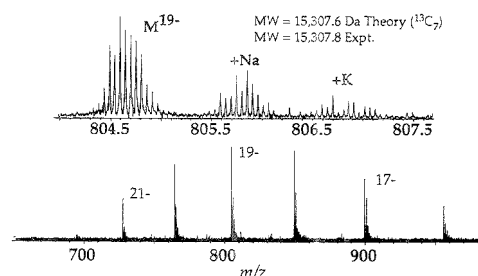
Figure 4. Mass spectrum of 50 mer DNA (14 nL of 20 μM solution): ESI needle 2.8 μm i.d. tip, 20 μm i.d. tubing; flow rate $\sim$3 nL/min; data acquisition time 3 s.

RESULTS AND DISCUSSION

Needle Fabrication and Spray Characteristics. A 15% batch-to-batch flow reproducibility can be achieved by holding the pulling and etching parameters constant. The pulling process is much more easily controlled to generate submicrometer tips. Etching these in HF (Table 1) results in a terminal wall of 50–80 nm thickness (Figure 2) that generates the high electric fields required for stable ESI. As found by Wilm and Mann,[17] sample flow starts when the electrical potential is applied at the tip. At a fixed potential between the tip and inlet capillary, decreasing the distance increases the flow rate, with the lower limit determined by the onset of corona discharge. Flow rate and total spray current are also determined by the applied voltage (Figure 3). Flow rates were measured by the duration of the spray current from a completely filled needle without the reservoir.

An ESI spray rate of 25 nL/min is the lowest previously reported;[17] a spray rate 2 orders of magnitude lower is achieved here with a similar tip size. This appears to be due mainly to the viscous flow within the small-bore capillary tube; note that the flow reduction (Table 1) is more dependent on needle capillary inside diameter than on tip orifice inside diameter. Solutions of large molecular weight proteins spray at rates 10–50% lower than with solvent alone in the same silica tip.

Needle Durability. Lifetimes for continuous spraying are generally 20–60 min. There are two modes of tip failure: clogging by particle impurities or precipitated analyte, and loss of electrical contact with the spray solution from degradation of the gold coating at the tip. Particle clogging can be greatly reduced by submicrometer filtration and centrifugation of solutions. Organic
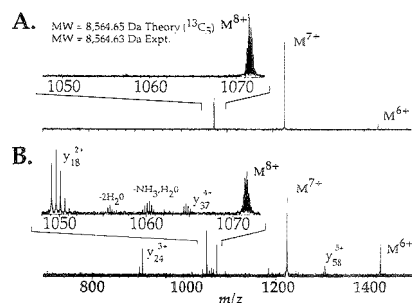
Figure 5. Mass spectra of bovine ubiquitin (20 μM): nozzle–skimmer capillary voltage, (A) 80 V, (B) 180 V; ESI needle, 2.6 μm i.d. tip, 5 μm tubing; flow rate $\sim$0.5 nL/min; data acquisition 3 s.
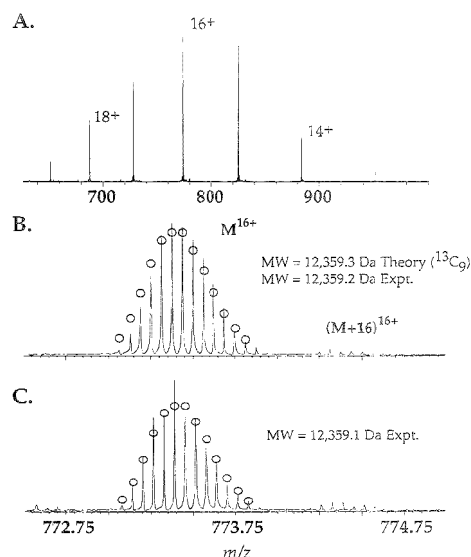
Figure 6. Mass spectra (3 s data acquisition) of equine cytochrome c: ESI needle, 2 μm i.d. tip, 5 μm tubing. (A) and (B) 0.86 nL of 10 μM (8.6 fmol), 0.3 nL/min. (C) 0.22 nL of 1 μM (0.22 fmol), 0.23 nL/min. (O) Theoretical isotopic peak abundances.

cosolvents can cause much more rapid precipitation of analyte during the spray process, apparently from preferential evaporative loss of cosolvent at the tip. Loss of electrical contact with the gold coating is likely due to the poor adhesion of gold to the silica substrate and corona discharge. The silanization technique of Kriger et al.[21] resulted in only a modest improvement (10–20%) in tip lifetime. Better results were obtained with thick ($\geq$150 nm) gold films, but thin (<35 nm) gold films allow viewing the contents directly with the microscope. Needles with thin films yield $\sim$15–30 min (10–20 sample injections) of continuous spraying; thick films last from 45 to 60 min.

ESI with 20 μm Tubing. The μESI-FTMS spectrum of the 50 mer DNA (Figure 4) $A_{10}T_{10}C_{17}G_{13}$ (MW — 15 307.6 theory, 15 307.8 experiment), required additional TEA (0.015%) to displace impurities from the needle tip. Despite a 3 nL/min flow rate, the total 50 mer ion current measured behind the cell was 20–30 pA, vs 75–150 pA from the standard ESI source (1 μL/min). Further,

the spectra from the two sources show similar S/N. With their pioneering source, Emmett and Caprioli[16] also found that a far greater percentage of ions yields a meaningful (analyte) signal.

Reduced Thermal Stress. An unexpected advantage of μESI was shown by the spectrum of single-stranded DNA T_{60}, which exhibits little fragmentation as well as good S/N (data not shown). In contrast, the normal ESI spectrum shows substantial fragmentation. The electrospray is directed at a capillary (Figure 1) that is heated to aid in droplet desolvation; μESI, with its far lower flow rate, requires a capillary heating wattage 25–50% less than that normally used, consistent with the decreased dissociation. μESI of longer strand DNAs ($\geq$100 bases) are currently under investigation.

μESI with 5 μm Tubing. A sample of 0.76 nL of 20 μM bovine ubiquitin (15 fmol) electrosprayed from a 5 μm needle (2.0 μm tip) at a 0.5 nL/min flow rate gave the Figure 5 spectra (MW = 8564.65 theory, 8564.63 experiment). These were acquired sequentially, each with a 3×10^{-6} Torr N_2 pulse prior to a 3 s ion acquisition and a 20 s delay before the excite/detect event. The 80 V capillary voltage was changed to 180 V between spectra to effect nozzle–skimmer ion dissociation, with the y_{18}, y_{24}, y_{37}, and y_{58} ions further characterizing the analyte.[23,27,28] The ~90 s spray time would be sufficient for further tandem MS experiments; also, ion trapping requires only a few seconds, so that the ESI high voltage could be turned off between trapping events, stopping sample flow. The extended spray time of this source should also benefit the long data acquisition times of scanning instruments.[13,16]

Further sample reduction still yields useful spectra (Figure 6) of cytochrome c (0.3 nL/min, total sample of 8.6 fmol, 150 amol consumed, current at the ion cell of 20–30 pA). The unexpectedly high S/N (400:1), high resolving power (>10^6), and mass accuracy (12 359.3 Da theory, 12 359.2 Da experiment) is maintained even though the analyte delivery rate is $^1/_{3000}$ of that with conventional ESI. A total of 0.22 fmol delivered to the instrument (10 amol consumed) yielded a spectrum of S/N 60:1–80:1, experimental MW = 12 359.1. A cytochrome c spectrum of 3:1 S/N should require 10 amol loaded and 0.5 amol consumed. Thus, the spectrum quality obtained with microvolume sampling and conventional ESI on the same mass spectrometer[14] should be duplicated with this ESI source using 3 orders of magnitude less sample.

CONCLUSIONS

This source demonstrates both picoliter sample volume and picoliter/min flow rates for high-sensitivity electrospray ionization, truly "picospray" ESI. Its needles are easily produced from commercial fused-silica tubing and can be used in standard ESI sources. Femtomole samples of large ($\geq$10 kDa) molecules routinely yield full mass spectra at high S/N, RP $\approx$ 10^5, and MW errors <0.3 Da. These capabilities are far better than those acheived for MALDI, even with FTMS,[19,29] and the projected detection limit of ~10 amol of material loaded is comparable to that reported for MALDI.[20] Particularly promising would be use of picospray ESI with capillary electrophoresis, maintaining spray stability at ultralow flow rates, using directly its narrow-bore (5–75 μm) silica tubing.[8,12,21] When combined with CE, the analysis of complex protein mixtures in practical "real world" samples will be possible. MS protein charting,[30] in which known proteins are identified in complex biological samples using only molecular weight and fragment ion masses from tandem MS, could be possible at the single-cell level.

(27) Loo, J. A.; Quinn, J. P.; Ryu, S. I.; Henry, K. D.; Senko, M. W.; McLafferty, F. W. *Proc. Natl. Acad. Sci. U.S.A.* **1992**, *89*, 286–289.
(28) Little, D. P.; Speir, J. P.; Senko, M. W.; O'Connor, P. B.; McLafferty, F. W. *Anal. Chem.* **1994**, *66*, 2809–2815.
(29) Li, Y.; Hunter, R. L.; McLver, R. T. *Nature* **1994**, *370*, 393–395.
(30) Feistner, G. J.; Faull, K. F.; Barofsky, D. F.; Roepstorff, P. *J. Mass Spectrom.* **1995**, *30*, 519–530.

Poly(vinyl alcohol) as Solid Substrate Material for Room-Temperature Phosphorimetry

Tatsuya Kitade,* **Keisuke Kitamura, Junko Hayakawa, Emiko Nakamoto,** and **Noriko Kishimoto**

Kyoto Pharmaceutical University, 5 Nakauchi-cho, Misasagi, Yamashina-ku, Kyoto 607, Japan

A mixture of poly(vinyl alcohol) (PVA) and a small amount (5%) of cellulose (CLL) was pressed under ~280 kg/cm^2 to form a disk of 1 mm thickness, and the prepared disk was used as a solid substrate for room-temperature phosphorescence (RTP). The addition of CLL was to reduce the fragility of the disk and enhance the permeability of sample solutions into the disk surface. The sample solution spotted PVA–CLL solid substrates were dried in a microwave oven conveniently. The efficiency of PVA–CLL solid substrates was monitored by RTP intensity of *p*-aminobenzoic acid (PABA) spotted on them, and the results showed that the RTP signal of PABA was largely enhanced as compared to that on the conventional paper solid substrates. Another prominent feature of the PVA–CLL solid substrate is that the RTP signal can be observed sufficiently even without a dry gas flush during the RTP measurement, while a dry gas flush is essential for the conventional substrates. A calibration curve for PABA was linear from 7.3 to 1200 pmol/spot. The results for the RTP measurements of chlorpromazine hydrochloride and tetracaine hydrochloride were also reported. The limits of detection of PABA and the other two drugs were 0.03, 0.16 and 1.26 ng, respectively.

Room-temperature phosphorimetry on solid substrates has been investigated to develop a sensitive and selective method for determination of trace amounts of organic compounds. This technique was first reported by Roth, who obtained room-temperature phosphorescence (RTP) from aromatic compounds adsorbed on filter paper and cellulose.[1] Schulman and Walling reported on other substrates, such as silica, alumina, paper, and asbestos.[2,3] Since then, a great deal of effort has been focused on the search for suitable substrate materials.[4-11] Recently, ion-exchange resins have been used in the flow-through RTP optosensor that is based on transient immobilization on the resin of metal chelates.[12-14] Among the materials investigated, filter and

chromatography paper have appeared to be the most convenient substrates for the RTP measurements. Thus, several investigations on paper substrate RTP have been performed.[15-18] Campiglia et al. adopted filter paper as the substrate for the solid substrate RTP detection of caffeine, theophylline, and theobromine in liquid chromatography.[19] Recently, Gioia et al. showed that the addition of sodium dodecyl sulfate and heavy atom salts can enhance paper substrate RTP of biogenic indoles.[20]

However, paper substrates have some disadvantages; i.e., they are not always identical in their qualities and frequently have background emissions. In addition, continuous gas flow through the sample compartment of a spectrophotometer is necessary during measurement of RTP emissions because moisture can quench them.

This paper describes the preparation of a moisture- and oxygen-insensitive RTP solid substrate by using poly(vinyl alcohol) (PVA) mixed with a small amount of cellulose (CLL). The efficiency of prepared solid substrates was evaluated by the RTP intensity of *p*-aminobenzoic acid (PABA) spotted on them. The method of drying samples was also investigated.

EXPERIMENTAL SECTION

Reagents. Poly(vinyl alcohol) 2000 (Kanto Chemical Inc.), fibriform cellulose (CLL) (Nacalai Tesque Inc.), extra pure grade PABA (Kanto Chemical Inc.), chlorpromazine hydrochloride (Sigma Chemical Co.), and tetracaine hydrochloride (Wako Pure Chemical Industries Ltd.) were used as purchased without further purification. Deionized water was distilled and used as the solvent to prepare stock solutions of the drugs.

Procedure. The PVA granules were ground with a motor-driven mill and then sifted through a 250 mesh sieve. The obtained fine powder having less than 63 μm particle size was mixed with an appropriate amount of CLL. After the mixture was well ground in an agate mortar with a pestle, 50 mg of the mixture was pressed for a few minutes with a die used to make KBr disks for IR spectrophotometry. The disk was 13 mm in diameter and ~1 mm in thickness. After reinforcing the back side of the disk

(1) Roth, M. *J. Chromatogr.* **1967**, *30*, 276–278.
(2) Schulman, E. M.; Walling, C. *Science* **1972**, *178*, 53–54.
(3) Schulman, E. M.; Walling, C. *J. Phys. Chem.* **1973**, *77*, 902–905.
(4) Von Wandruszka, R. M. A.; Hurtubise, R. J. *Anal. Chem.* **1976**, *48*, 1784–1788.
(5) Von Wandruszka, R. M. A.; Hurtubise, R. J. *Anal. Chim. Acta* **1977**, *93*, 331–333.
(6) Von Wandruszka, R. M. A.; Hurtubise, R. J. *Anal. Chem.* **1977**, *49*, 2164–2169.
(7) Ford, C. D.; Hurtubise, R. J. *Anal. Chem.* **1978**, *50*, 610–612.
(8) Ford, C. D.; Hurtubise, R. J. *Anal. Chem.* **1979**, *51*, 659–663.
(9) Aaron, J. J.; Andino, M.; Winefordner, J. D. *Anal. Chim. Acta* **1984**, *160*, 171–184.
(10) Andino, M.; Aaron, J. J.; Winefordner, J. D. *Talanta* **1986**, *33*, 27–33.
(11) Kuroda, N.; Nohta, H.; Ohkura, Y. *Anal. Chim. Acta* **1987**, *197*, 169–176.

(12) Pereiro-Garcia, R.; Liu, Y. M.; Diaz-Garcia, M. E.; Sanz-Medel, A. *Anal. Chem.* **1991**, *63*, 1759–1763.
(13) Alava-Moreno, F.; Diaz-Garcia, M. E.; Sanz-Medel, A. *Anal. Chim. Acta* **1993**, *281*, 637–644.
(14) Liu, Y. M.; Pereiro-Garcia, R.; Valencia-Gonzalez, M. J.; Diaz-Garcia, M. E.; Sanz-Medel, A. *Anal. Chem.* **1994**, *66*, 836–840.
(15) McAleese, D. L.; Dunlap, R. B. *Anal. Chem.* **1984**, *56*, 600–601.
(16) De Lima, C. G.; Andino, M. M.; Winefordner, J. D. *Anal. Chem.* **1986**, *58*, 2867–2869.
(17) Campiglia, A. D.; de Lima, C. G. *Anal. Chem.* **1987**, *59*, 2822–2827.
(18) Garcia Alvarez-Coque, M. C.; Ramis Ramos, G.; O'Reilly, A. M.; Winefordner, J. D. *Anal. Chim. Acta* **1988**, *204*, 247–258.
(19) Campiglia, A. D.; Laserna, J. J.; Berthod, A.; Winefordner, J. D. *Anal. Chim. Acta* **1991**, *244*, 215–222.
(20) Gioia, S. M. C.; Campiglia, A. D. *Anal. Chim. Acta* **1994**, *287*, 89–94.
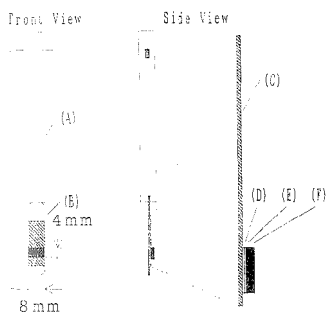
Figure 1. Structure of spindle-type sample holder and substrate: (A) threaded brass rod; (B) flat brass plastic base holder; (C) plastic base; (D) double-faced tape; (E) cellophane tape; (F) solid substrate.
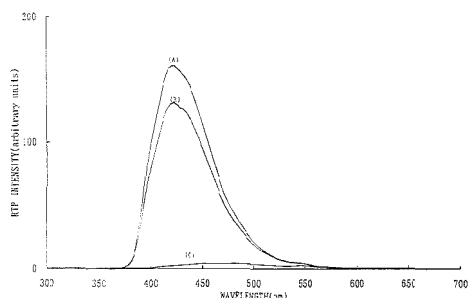
Figure 2. Comparison of RTP emission spectra of PABA spotted on several kinds of substrates. ([PABA], 0.2 nmol/20 μL): (A) PVA; (B) PVA–CLL (95:5); (C) CLL.

with cellophane tape, it was cut into 4 × 8 mm pieces and stuck to a plastic plate (8 × 30 mm) with double-faced tape as shown in Figure 1. A 20 μL aliquot of the sample solution was spotted on the whole surface of the substrate by using a microsyringe. Then the substrate was placed in the preheated microwave oven and dried for 5 min. After drying, the substrate was stuck to a spindle-type holder (see Figure 1) with a double-faced tape and cooled to room temperature in air. The RTP signal was measured by a spectrofluorometer (Hitachi F-3010) equipped with a phosphorescence accessory. Excitation and emission slits were set at 5 nm.

RESULTS AND DISCUSSION

RTP Emissions of PABA on a PVA Solid Substrate. A typical RTP emission spectrum of PABA spotted on a PVA solid substrate is shown in Figure 2. The wavelengths of excitation and emission maxima were 273 and 421 nm, respectively. The results apparently show that the PVA substrate dramatically enhances the phosphorescence intensity as compared to the CLL substrate. Furthermore, it should be noted that the RTP spectrum on the PVA substrate was obtained without passing dry gas through the sample compartment of the spectrophotometer during the measurement.

Another advantage of the PVA substrate is that it does not have any RTP signal. The RTP emission spectrum of PVA substrate itself is depicted in Figure 3 together with those of CLL and distilled water (solvent for sample preparation). The results
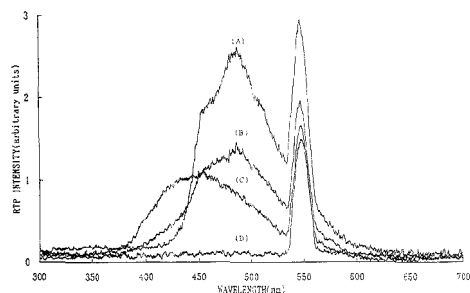
Figure 3. Comparison of RTP emission spectra of several kinds of substrates and distilled water: (A) CLL, (B) PVA–CLL (95:5); (C) Distilled Water (substrate–PVA; sample amount, 20 μL); (D) PVA.

show that PVA does not display any RTP emission (excited at 273 nm) from 300 to 700 nm except the signal at 546 nm, which is assigned to the secondary scattered excitation beam, while CLL and the distilled water have weak RTP signals arising from impurities contained in them.

These results of PVA indicate that PVA can possibly be used as a superior RTP solid substrate material. However, the solid substrate made from PVA alone has two defects for practical use. One is that the PVA disk is very fragile so that it is difficult to cut it into pieces having suitable area. The other is that the PVA disk is so tightly formed that the spotted sample solution penetrates into it very gradually. In order to overcome these defects, addition of a small amount of CLL to PVA was investigated.

Effect of Mixing CLL. PVA solid substrates containing CLL in several ratios were formed under varied pressures. The intensities at the RTP emission maximum of PABA on these substrates were measured. The results indicated that the pressure to form the substrates did not largely affect the RTP intensity of PABA, but the addition of CLL apparently decreased the RTP intensity of PABA as the amount of CLL in the mix increased. Thus, the amount of CLL to be mixed should be as small as possible. Therefore we decided to use a mixture of 95% PVA and 5% CLL as the solid substrate material. The addition of even 5% CLL could practically reduce the fragility of the solid substrate disk and enhance the permeability of the sample solution into it.

The pressure to be applied to form the substrate disks was set at 280 kg/cm^2, since this pressure seemed to give better results than the other values although there is not remarkable difference in the effect of the disk-forming pressure on the RTP intensity of PABA.

The RTP spectrum of PABA on the PVA–CLL (95:5) substrate thus prepared is depicted in Figure 2 and shows that the decrease in the RTP intensity caused by mixing CLL is very small as compared with that on the substrate made from PVA alone. The effect of the emission of the added CLL will not interfere the evaluation of the efficiency of PVA solid substrate because its intensity is negligibly weak as compared with that of PABA on the PVA–CLL substrate and its maximum is located away from that of PABA (421 nm), as seen in Figure 3.

Even if an analyte has its emission maximum at or near the wavelength of this background emission maximum, the extent of the interference will also depend on the relative intensity of the emission maximum of the analyte to that of the background
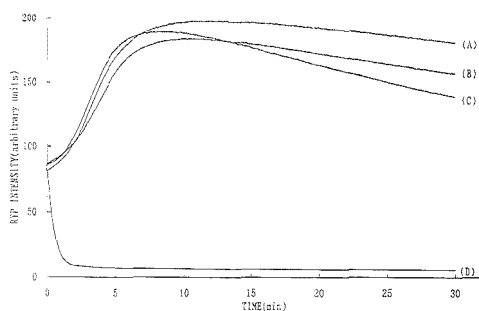
Figure 4. Time courses of the RTP signal of PABA measured with and without He gas or dry air flush: [PABA] (A–C) 0.2 nmol/20 μL; (D) 2 nmol/20 μL. (A) He, PVA–CLL (95:5); (B) dry air, PVA–CLL (95:5); (C) without gas flush, PVA–CLL (95:5); (D) without gas flush, filter paper (Toyo, Filter Paper No. 2).

Table 1. RTP Spectral Characteristics of PABA and Other Drugs on PVA–CLL Solid Substrate

compound	excitation peak (max) (nm)		emission peak (max) (nm)		limit of detection[a] (ng)	
	PVA–CLL	lit.	PVA–CLL	lit.	PVA–CLL	lit.
p-aminobenzoic acid	273	277[b]	421	435[b]	0.03	0.08[b]
chlorpromazine hydrochloride	259 317	260[b] 313[b]	512	522[b]	0.16	1.6[b]
tetracaine hydrochloride	219		443		1.26	

[a] Calculated as the concentration corresponding to three times the background noise, which was taken as the mean of three blank measurements. [b] Measured on TlNO₃ and sodium dodecyl sulfate-impregnated filter paper.[18]

emission. Taking account the noise level in Figure 3, the intensity of the background emission of the PVA–CLL substrate itself may be considered to be not so intense.

Though the substrate prepared from PVA alone has practical inconveniences as described above, use of the PVA substrate may not be impossible as a background emission-free substrate.

Sample Drying. After a sample solution is spotted, the solid substrate is to be sufficiently dried. Several methods have been used for this purpose, e.g., blowing dry gases, vacuum drying, etc. In this study, desiccator (with a silica gel for 3 days), blowing Ar gas (for 1 h), vacuum drying (with a rotary pump for 10 min), hot air blower (for 10 min), and microwave oven (for 5 min) methods were investigated by monitoring the RTP intensity of PABA on PVA–CLL (95:5) substrate. Remarkably strong RTP intensity was obtained when the sample was dried by using a hot air blower and a microwave oven. In both methods, the temperature of the samples were elevated in the process of drying; thus, heating in drying samples may be also necessary to enhance the RTP intensity. We preferred to use the microwave oven for drying samples for its practical conveniences. The time of drying samples in a microwave oven should be properly selected, because too long time drying cause sample carbonization. In this study, 5 min drying gave the best results.

Effect of Gas Flush into the Sample Compartment. It has been considered to be essential to flush an inert gas or dry air into the sample compartment during the measurement of RTP on solid substrates, since moisture can quench the RTP emissions.[3,21–23] A typical instance of the PABA RTP on filter paper measured without the gas flush is shown in Figure 4. Usually a very large amount of dry gas is required to observe RTP. However, though being measured without the gas flush, the RTP on the PVA–CLL substrate does not show a notable decrease in its intensity as compared to those measured with He gas or dry air flush, as shown in Figure 4. The reason for this may be that the PVA matrix which holds the PABA molecules will become a very hard structure by drying in the microwave

oven and behave as a barrier to the penetration of moisture and/or oxygen into the substrate. This prominent feature of the PVA–CLL solid substrate is a large advantage for practical use of the RTP technique.

The RTP intensity change with time after drying in the microwave oven is shown in Figure 4, and the results indicate that the intensity of RTP on the PVA–CLL substrate increases for the initial 6–7 min regardless of use of the gas flow. This phenomenon may be induced by the fact that the sample temperature was quite high at the time just after the sample was dried in the microwave oven and fell gradually to the ambient temperature.

Relationship between the RTP Intensity and the Amount of PABA on the PVA–CLL Solid Substrate. The RTP intensity of PABA of 11 samples ranging from 7.3 to 1600 pmol/spot was measured at the emission maximum to investigate the relationship between the RTP intensity and its amount on the PVA–CLL solid substrate. The calibration curve was linear up to 1200 pmol/spot with a correlation coefficient of 0.999 for 22 data points and nearly intercepted the origin. The relative standard deviation of the five successive determinations was 19.1% at a level of 200 pmol/spot. This result is not so satisfactory and improvement of the reproducibility is under investigation.

To confirm that the PVA–CLL solid substrate is effective for the RTP measurement of phosphors other than PABA, chlorpromazine hydrochloride and tetracaine hydrochloride were examined as instances. The results summarized together with that of PABA in Table 1 confirm that the dry gas flush is also not necessary for these drugs and show that the limits of detection are enhanced several times as compared to the values on the filter paper.[18]

Consequently, it can be clearly shown that PVA is a superior material for the solid substrate of RTP measurements, which enhances RTP intensity and does not require the dry gas flush into the sample compartment during the RTP measurement.

(21) Paynter, R. A.; Wellons, R. S.; Winefordner, J. D. Anal. Chem. **1974**, 46, 736–738.
(22) Parker, R. T.; Freedlander, R. S.; Schulman, E. M.; Dunlap, R. B. Anal. Chem. **1979**, 51, 1921–1926.
(23) Schulman, E. M. J. Chem. Educ. **1976**, 53, 522–524.

Simple Preparation of a C₈ HPLC Stationary Phase with an Internal Polar Functional Group

John E. O'Gara,* Bonnie A. Alden, Thomas H. Walter,* John S. Petersen,[†]
Carsten L. Niederländer,[‡] and Uwe D. Neue*

Chromatography Chemical Division, Waters Corporation, 34 Maple Street, Milford, Massachusetts 01757-3696

A novel HPLC stationary phase is described that possesses an internal carbamate functional group. The reversed-phase material is prepared via bonding of silica with 3-(chlorodimethylsilyl)propyl *N*-octylcarbamate, which is prepared in two steps from octylamine and allyl chloroformate. The resultant bonded silica has a reproducible ligand surface concentration of 3.2–3.3 μmol/m². The methodology is an alternative to the reaction of acid chlorides with aminopropyl bonded phases, where an inhomogeneous mixture of derivatized and underivatized amine groups results. The chromatographic properties of the octylcarbamate bonded phase were compared to those of an end-capped octyldimethylsilyl bonded phase using a variety of neutral, acidic, polar, and basic compounds under different mobile-phase conditions. The octylcarbamate phase exhibited dramatically reduced retentions for polar and basic compounds. The reductions are attributed to the embedded carbamate group's weakening of the interaction between unbonded silanols and the analytes.

The separation of basic analytes by reversed-phase HPLC continues to challenge chromatographers.[1,2] Acceptable separations have been achieved using high-purity silica,[3] silica coated with a polymeric layer,[4] silica end-capped with short-chain alkyl silanes,[5] and mobile-phase conditions that suppress analyte/silanol interactions.[6] Another solution is to use a reversed-phase silica possessing a ligand with an internal polar functional group. An internal polar group appears to weaken the interaction between basic analytes and residual silanol groups on the silica surface. Silica packings of this type have been prepared by the acylation of aminopropyl bonded phases.[7,8] For example, Bayer and co-workers have reported the reaction of aminopropyl silica with acid chlorides, phenylsulfonyl chloride, or alkyl isocyanates in a solid phase reaction.[7a] The bonded phases were reportedly useful for

the separation of basic substances, although the extent of amidization was not unambiguously determined.[7b] Functionalized reversed-phase ligands are commonly prepared via aminopropyl coupling,[9–11] but the methodology suffers from the difficulty in modifying the silica surface reproducibly over two successive reactions. As outlined in Figure 1, a poorly defined mixture of derivatized and underivatized amine groups may exist on the silica surface. Furthermore, the underivatized aminopropyl ligands possess anion-exchange characteristics at low pH which can negatively influence their chromatographic behavior for acidic compounds.[12]

In this report, a novel silica bonded phase is described which contains an internal polar carbamate functional group. The carbamate group is incorporated into an octyldimethylchlorosilane compound, which is synthesized in two organic reaction steps. Conventional monofunctional bonding chemistry then yields a derivatized silica with a uniform surface composition. Cyclodextrin stationary phases prepared in a similar manner have been shown to increase surface concentration 2-fold versus the two-step amidization protocol.[13] The novel octylcarbamate bonded phase has been found to exhibit reduced retention for basic and polar analytes compared to an end-capped octyldimethylsilyl stationary phase.

EXPERIMENTAL SECTION

General. NMR spectra were recorded on a Bruker MSL-300 NMR spectrometer. ¹H and ¹³C spectra were recorded in chloroform-*d* (dried over 4 Å molecular sieves) with chloroform as an internal standard at 7.24 and 77.7 ppm, respectively. ²⁹Si spectra were recorded as neat samples with TMS as an external standard at 0.0 ppm. ¹³C NMR spectra of the bonded silica were obtained using the CP-MAS technique with a spinning speed of 4.0 kHz and a cross-polarization contact time of 0.5 ms. Chemical shifts were referenced to an external sample of adamantane, with the peak for the methylene carbons assigned a chemical shift of 29.5 ppm. Elemental analyses were recorded using a Control Equipment Corp. Model 240XA analyzer. IR spectra were recorded on a Mattson Polaris FT-IR spectrometer. Bonded silica

Present address: GelTex Pharmaceuticals, Inc., Waltham, MA 02154.
† Present address: Sandoz AG, CH-4002 Basel, Switzerland.
(1) Nicholls, G.; Clark, B. J.; Brown, J. E. Anal. Proc. 1993, 30, 51–54.
(2) McCalley, D. V. J. Chromatogr. 1993, 636, 213–220.
(3) Hanai, T.; Ohhira, M.; Tamura, T. LC-GC 1988, 6, 922–928.
(4) Ohtsu, Y.; Shiojima, Y.; Okumura, T.; Koyama, J.-I.; Nakamura, K.; Nakata, O.; Kimata, K.; Tanaka, N. J. Chromatogr. 1989, 481, 147–157.
(5) Freiser, H. H.; Nowlan, M. P.; Gooding, D. L. J. Liq. Chromatogr. 1989, 12, 827–843.
(6) Sadalius, M. A.; Berus, J. S.; Snyder, L. R. LC-GC 1988, 6, 494–500.
(7) (a) Buszewski, B.; Schmid, J.; Albert, K.; Bayer, E. J. Chromatogr. 1991, 552, 415–427. (b) Kasturi, P.; Buszewski, B.; Jaroniec, M.; Gilpin, R. K. J. Chromatogr. 1994, 659, 261–265.
(8) Ascah, T. L.; Feibush, B. J. Chromatogr. 1990, 506, 357–369.

(9) Unger, K. K. Chromatographia 1991, 31, 507–511 and references cited therein.
(10) Dohtsu, K.; Ohmori, K.; Fukuda, R.; Takenaka, S.; Takagi, M. Anal. Sci. 1988, 4, 371–376.
(11) Su, W.; Gregory, R. B.; Gilpin, R. K. J. Chromatogr. Sci. 1993, 31, 285–290 and references cited therein.
(12) Czajkowska, T.; Hrabovsky, I.; Buszewski, B.; Gilpin, R. K.; Jaroniec, M. J. Chromatogr. A 1995, 691, 217–224.
(13) Fujimura, K.; Kitagawa, M.; Takayanagi, H.; Ando, T. J. Liq. Chromatogr. 1986, 9, 607–620.
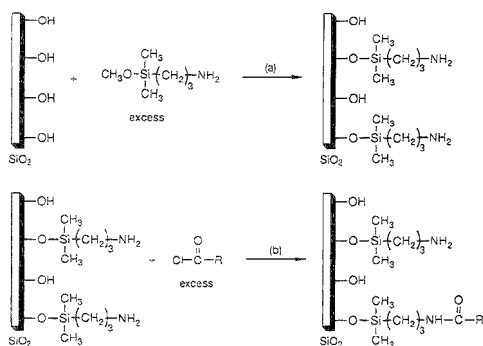
Figure 1. Previous methodology for the synthesis of functionalized reversed-phase ligands. In step a, an aminopropylsilane is bonded to the silica surface. In step b, the amine group is partially derivatized with an acylating agent. A mixture of reacted and unreacted amine groups results in the final product.

was packed into 3.9 mn × 150 mm stainless steel columns using conventional high-pressure slurry techniques.[14]

Dimethylchlorosilane (98% by ^{29}Si NMR spectroscopy, Hüls America), hexachloroplatinic acid (99.995%, Aldrich), allyl chloroformate (97%, Aldrich), and octylamine (99%, Aldrich) were used as received. Symmetry silica was supplied by Waters Corp. and had the following physical properties prior to derivatization: average particle diameter, 5.0 μm; specific surface area, 341 m^2/g; mean pore diameter, 9.8 nm; pore volume, 0.83 cm^3/g; and metal content, Fe, 1 μg/g, Na, 8 μg/g, and Al, 1 μg/g. All solvents were HPLC grade. Octyldimethylsilyl (C$_8$) reversed-phase silica was prepared from the Symmetry silica described above and n-octyldimethylchlorosilane (%C = 11.64; C$_8$ surface concentration, 3.41 μmol/m^2). The material was end-capped (final %C = 12.02) with chlorotrimethylsilane prior to column packing and chromatographic evaluation.

Chromatographic Analyses. Chromatographic data were recorded on a modular HPLC system with a Euramark Mistral thermostated column oven maintained at 23 ± 0.5 °C, a Waters 490E programmable wavelength absorbance detector, a Waters Model 712 WISP autoinjector, and a Waters 626 solvent delivery module. Isocratic separations were performed at a flow rate of 1.0 mL/min in a methanol/20 mM KH$_2$PO$_4$/K$_2$HPO$_4$, pH 7.00 (65:35 v/v) mobile phase or an acetonitrile/50 mM KH$_2$PO$_4$, pH 3.00 (20:80 v/v) mobile phase. Chromatographic data were collected and analyzed using Waters ExpertEase chromatography software (v3.2) installed on a DEC VAX 3100 workstation.

Hydrolytic Stability. Bonded phases were tested for hydrolytic stability by storage in a methanol/20 mM KH$_2$PO$_4$/K$_2$HPO$_4$, pH 7.00 (65:35 v/v) mobile phase and a methanol/20 mM KH$_2$-PO$_4$, pH 3.00 (65:35 v/v) mobile phase. Columns were equilibrated with 50 column volumes of the mobile phase, and the k value of acenaphthene was determined using the average of three injections. Columns were retested periodically over the course of 25–30 days. Prior to testing, each column was flushed with 20 column volumes of water and methanol and then reequilibrated with 50 column volumes of the mobile phase. See Figure 4 for results.

(14) Snyder, L. R.; Kirkland, J. J. *An Introduction to Modern Liquid Chromatography*, 2nd ed.; Wiley-Interscience: New York, 1979; Chapter 6.

Scheme 1
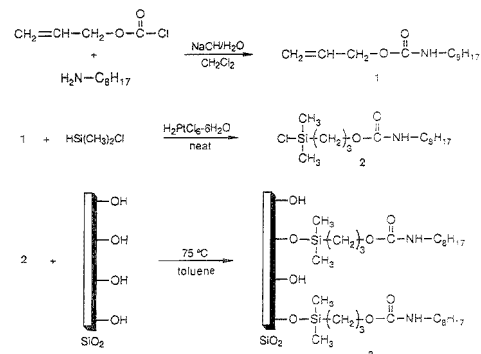
Allyl *N*-Octylcarbamate (1). Octylamine and allyl chloroformate were reacted in the traditional manner.[15] The synthesis of **1** has been described elsewhere:[16] bp 130 °C at 0.5 Torr; ^{1}H NMR δ 5.90 (m, 1H), 5.23 (m, 2H), 4.65 (br s, 1H), 4.52 (d, $J =$ 5.4 Hz, 2H), 3.15 (m, 2H), 1.47 (m, 2H), 1.25 (br s, 10H), 0.85 (t, $J =$ 6.7 Hz, 3H); ^{13}C NMR δ 156.9, 133.6, 117.6, 65.7, 41.5, 32.2, 30.4, 29.7, 27.1, 23.1, 14.4; IR (NaCl, film) 3337, 2932, 1703, 1649, 1537, 1252 cm^{-1}. Anal. Calcd for C$_{12}$H$_{23}$NO$_2$: C, 67.57; H, 10.87. Found: C, 67.56, H, 11.22.

3-(Chlorodimethylsilyl)propyl *N*-Octylcarbamate (2). The hydrosilylation of olefin **1** with chlorodimethylsilane was conducted in the normal way using Speier's catalyst.[17] The synthesis of **2** has been described elsewhere:[16] ^{1}H NMR δ 4.63 (br s, 1H), 4.00 (t, $J =$ 6.6 Hz, 2H), 3.11 (m, 2H), 1.68 (m, 2H), 1.45 (m, 2H), 1.24 (br s, 10H), 0.84 (m, 5H), 0.38 (s, 6H); ^{13}C NMR δ 157.0, 67.0, 41.6, 32.3, 30.6, 29.8, 29.7, 27.3, 23.4, 23.1, 15.6, 14.6, 2.1; ^{29}Si NMR δ 31.4. Anal. Calcd for C$_{14}$H$_{29}$NO$_2$SiCl: C, 54.60; H, 9.82. Found: C, 54.11, H, 9.82.

Caution: Chlorosilanes are corrosive and moisture-sensitive.

Silica Bonded Phase 3. 3-(Chlorodimethylsilyl)propyl *N*-octylcarbamate (**2**) was bonded to Symmetry silica. The bonding procedure was performed in the conventional way on a 10 g scale, where silane **2** (12.0–15 μmol/m^2 of silica surface) and an excess of a base catalyst were added to dry silica suspended in dry toluene.[18] After the mixture was stirred for 4 h at 75 °C, the bonded silica was isolated via vacuum filtration and purified by repeated washings with toluene, acetone/water (1:1 v/v), and acetone. All bonded samples of **3** were dried in a vacuum oven (0.1 Torr, 75 °C) for 16 h prior to characterization. ^{13}C CP-MAS NMR δ 158, 68, 41, 31–29, 23, 13, 1 (see also Figure 2); IR (KBr, pellet) 2932, 1698, 1547 cm^{-1}.

RESULTS AND DISCUSSION

Preparation of Reversed-Phase Silica. The preparation of the octylcarbamate reversed-phase silica is outlined in Scheme 1. Allyl *N*-octylcarbamate (**1**) was prepared from the condensation

(15) Blatt, A. H., Ed. *Organic Syntheses;* Wiley: New York, 1943; Collect. Vol. II, p 278.

(16) Neue, U. D.; Niederländer, C. L.; Petersen, J. U.S. Patent 5,374,755, 1994.

(17) Armitage, D. A. In *Comprehensive Organometallic Chemistry;* Wilkinson, G., Ed.; Pergamon Press: New York, 1982; Vol. 2, pp 117–120 and references cited therein.

(18) Kinkel, J. N.; Unger, K. K. *J. Chromatogr.* **1984,** *316,* 193–200.

Table 1. Coverage and Chromatographic Data Comparison of Octylcarbamate-Derivatized Silica 3A D[a] Prepared from Different Batches of Chlorosilane 2

	octylcarbamate reversed-phase silica			
	3A	3B	3C	3D
	Coverage Data[b]			
%C	14.44	14.38	14.17	14.22
%H	3.16	3.02	2.98	3.08
%N	1.29	1.27	1.25	1.23
surface concn[c]	3.29	3.27	3.21	3.23
	Chromatographic Data[d]			
acenapthene k	7.64	8.15	7.66	7.58
relative retention (tailing)				
propranolol	0.210 (1.3)	0.188 (1.2)	0.208 (1.2)	0.207 (1.4)
butyl paraben	0.383 (1.1)	0.391 (1.0)	0.385 (1.0)	0.385 (1.0)
dipropyl phthalate	0.425 (1.1)	0.429 (0.9)	0.432 (1.0)	0.432 (1.0)
naphthalene	0.518 (1.1)	0.508 (1.0)	0.512 (1.0)	0.512 (1.0)
amitriptyline	1.09 (1.1)	1.02 (1.1)	1.12 (1.5)	1.12 (1.3)

[a] The starting silica was the same in all cases. [b] Average of two determinations. [c] Calculated from %C, see ref 19. [d] Void volume marker, uracil. Tailing determined by USP method, see ref 20.

of octylamine and allyl chloroformate. The olefin was dried prior to the hydrosilylation reaction to minimize hydrolysis side products in the subsequent reaction. Chlorosilane 2 was made by addition of 0.1 molar equiv of chlorodimethylsilane to 0.04 molar % hexachloroplatinic acid dissolved in olefin 1 at room temperature. After an induction period, the hydrosilylation began, as evidenced by an exotherm. An additional 1.4 molar equiv chlorodimethylsilane was then added slowly, and the reaction temperature was maintained below the boiling point of chlorodimethylsilane (36 °C). No olefin remained upon completion of chlorodimethylsilane addition, and excess silane was removed in vacuo to yield 2.

The bonding reaction was conducted in the conventional way for monofunctional chlorosilanes and yielded a reversed-phase silica with a calculated ligand surface concentration of 3.2–3.3 μmol/m²[19] Table 1 shows the carbon, hydrogen, and nitrogen contents measured for four bonded samples (3A–D) prepared from different batches of chlorosilane 2. Multiple bondings using the same batch of silane had identical surface concentrations within experimental error. Because the propyl N-octylcarbamate chain attached to the dimethylsilyl moiety is 14 atom units long, a bonded-phase surface concentration of 3.3 μmol/m² was anticipated for 3, based on the reported surface concentration of C_{14} dimethylsilyl bonded phases on 10 nm pore diameter silica (3.26–3.43 μmol/m²).[19]

Bonded samples 3A–D were also nearly indistinguishable when compared chromatographically (Table 1). A mixture of neutral, acidic, and basic compounds had very similar selectivity and tailing values when separated on columns packed with the four reversed-phase samples. The tailing factor for the strong base amitriptyline ($pK_a = 9.2$) was slightly larger for 3C,D, and the increase is attributed to the slightly lower ligand surface concentration for these two samples. Amitriptyline tailing has been shown to be very sensitive to silica surface differences when used in a pH 7 buffered mobile phase.[21]

(19) Berendsen, G. E.; Pikaart, K. A.; de Galan, L. *J. Liq. Chromatogr.* **1980**, *3*, 1437–1464.
(20) *The United States Pharmacopeia*, 22nd revision; Mack Printing Co.: Easton, PA, 1990; pp 1558–1568.
(21) Neue, U. D.; Phillips, D. J.; Walter, T. H.; Capparella, M.; Alden, B. A.; Fisk, R. *LC-GC* **1994**, *12*, 468–480.
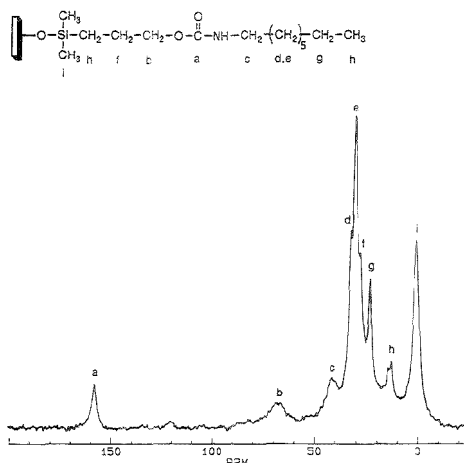
Figure 2. ¹³C CP-MAS NMR spectrum of 3-(dimethylsilyl)propyl N-octylcarbamate bonded-phase silica **3A**.

The ¹³C CP-MAS NMR spectrum of the bonded phase 3A is shown in Figure 2. The spectrum is consistent with the ligand structure, and no unassigned resonances were observed by ¹³C or ²⁹Si CP-MAS NMR spectroscopy for the bonded silica. The IR spectra of the bonded samples were also consistent with the assigned product. No evidence for other ligand types was observed.

Silyl ligands containing an internal functional group linkage are more reproducibly bonded to silica using the methodology described above in comparison to the traditional two-step heterogeneous amidization process. By synthesizing a monofunctional chlorosilane with the desired substituents and then bonding the silane to silica, only one heterogeneous reaction is required to obtain product. Replacement of the second heterogeneous step by a homogeneous reaction provides better control over intermediate and final product purity. This methodology has been shown to be applicable to the preparation of a variety of differently substituted silanes and their concomitant bonded phases.[16]

Table 2. Chromatographic Comparison Using pH 7.00, pH 3.00,[a] and Engelhardt[b] Test Conditions: Octylcarbamate 3B Reversed-Phase Silica versus End-Capped Octyldimethylsilyl Reversed-Phase Silica

compound	octylcarbamate 3B	end-capped octyl
	pH 7.00, k (Tailing)[c]	
propranolol	1.54 (1.2)	1.98 (1.1)
butyl paraben	3.19 (1.0)	2.73 (1.2)
dipropyl phthalate	3.50 (0.9)	5.20 (1.1)
napthalene	4.14 (1.0)	4.34 (1.1)
acenapthene	8.15 (0.9)	8.83 (1.0)
amitriptyline	8.34 (1.1)	15.37 (1.5)
	pH 3.00, k (Tailing)	
toluamide	1.12 (1.2)	1.46 (1.2)
chlorpheniramine	1.60 (1.2)	3.26 (1.3)
propranolol	4.40 (1.3)	8.23 (1.3)
	Engelhardt Test, k (Tailing)	
aniline	0.630 (1.5)	0.673 (1.4)
o,m,p-toluidines[d]	1.07 (1.3)	1.23 (1.4)
phenol[e]	1.13	1.05
N,N-dimethylaniline	3.42 (1.3)	4.45 (1.1)
ethyl benzoate	4.41 (1.2)	6.03 (1.1)
toluene	4.98 (1.1)	6.69 (1.0)
ethylbenzene	8.57 (0.8)	12.28 (1.0)

[a] Void volume marker, maleate. [b] See ref 22 for description of conditions. [c] Tailing determined by USP method, see ref 20. [d] Isomeric toluidines coeluted. [e] Unable to measure tailing due to low resolution.

Chromatographic Evaluation. The efficacy of the carbamate bonded phase in interacting with unreacted silanols on the silica surface was measured by comparison to an end-capped C_8 bonded phase (Table 2 and Figure 3). The comparison was made by separating neutral, acidic, polar, and basic compounds under pH 7 and pH 3 mobile phase conditions, as well as using Engelhardt's test for the evaluation of reversed phases.[22] Under all three test conditions, polar and basic analytes had markedly lower capacity factors (k) on the octylcarbamate phase versus the end-capped C_8 phase. The decreased capacity factors for the polar and basic compounds in all three tests are attributed to a weakening of the interaction with unbonded silanols due to the presence of the embedded carbamate group.

Neutral analytes were also less retained on the octylcarbamate phase. The decrease is attributed to the lower surface concentration of the octylcarbamate ligand versus the end-capped C_8 phase, and hence less hydrophobic interaction between bonded-phase and hydrocarbon analytes.[22] The polar acidic compounds phenol and butyl paraben were both slightly more retained on the octylcarbamate phase. A concise explanation for this small shift remains unavailable, but an interaction between the phenolic proton and the highly polarized carbonyl oxygen of the carbamate group may be operative.

The octylcarbamate ligand was also compared to the end-capped C_8 phase for hydrolytic stability under pH 3 and pH 7 buffered mobile-phase conditions (65:35 methanol/buffer). The change in acenaphthene k was used as a measure of surface ligand changes, because the retention of this analyte is a sensitive measure of ligand hydrolysis. As the plots in Figure 4 show, no large difference in chemical stability was observed between the octylcarbamate and the C_8 bonded phases. Under pH 3 buffer conditions, the acenaphthene k decreased by ~0.9% for the end-capped C_8 bonded phase and by ~1.6% for the octylcarbamate

(22) Engelhardt, H.; Jungheim, M. *Chromatographia* 1990, 29, 59−68.
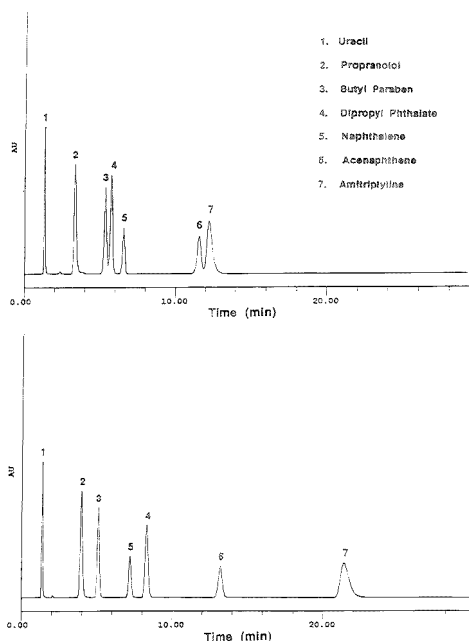
Figure 3. Chromatogram of uracil, propranolol, butyl paraben, dipropyl phthalate, naphthalene, acenaphthene, and amitriptyline separated in 65:35 methanol/20 mM KH$_2$PO$_4$/K$_2$HPO$_4$ at pH 7.00. (Top) 3-(Dimethylsilyl)propyl N-octylcarbamate bonded phase. (Bottom) Trimethylsilyl end-capped C_8 bonded phase.
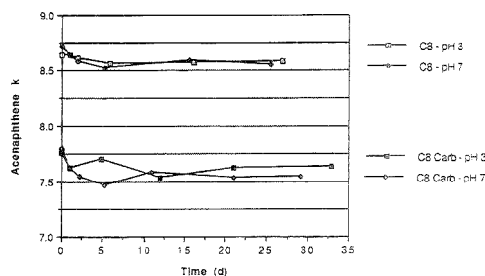
Figure 4. Acenaphthene k vs time (days) under pH 3.00 and 7.00 test conditions. Octylcarbamate reversed-phase silica versus end-capped octyldimethylsilyl reversed-phase silica.

bonded phase. At pH 7, both ligands were slightly less stable, where the acenaphthene k decreased by ~2.0% and 3.2% for the C_8 and octylcarbamate phases, respectively.

SUMMARY

A simple procedure has been described for the preparation of a C_8 stationary phase that contains an internal polar functional group. Two organic reactions and a single monofunctional chlorosilane bonding step lead to a reproducible and homogeneous silica surface. This methodology offers an alternative to the aminopropyl acylation approach previously used to prepare

functionalized silica ligands, where the extent of amidization is often incomplete and variable. Compared to an end-capped C_8 bonded phase, the bonded phase prepared from 3-(chlorodimethylsilyl)propyl N-octylcarbamate gave reduced k values for neutral, polar, and basic compounds. The octylcarbamate bonded phase may be useful in the separation of compounds that have undesirable interactions with silanols, or where a packing material with a selectivity different from that of a conventional C_8 bonded phase is needed. HPLC applications using this novel C_8 reversed-phase silica are in progress, and results will be reported in due course.

Evaluation of the Precision and Accuracy of a Uranium Isotopic Analysis Using Glow Discharge Optogalvanic Spectroscopy

C. M. Barshick,* R. W. Shaw, J. P. Young, and J. M. Ramsey

Chemical and Analytical Sciences Division, Oak Ridge National Laboratory, Oak Ridge, Tennessee 37831-6375

The measurement precision and accuracy were evaluated for an isotopic analysis of uranium using diode laser-excited optogalvanic spectroscopy. The ratio of $^{235}U/(^{235}U + ^{238}U)$ was measured using the 776 nm uranium isotope line for five samples ranging from depleted to enriched ^{235}U composition. The percent relative error (accuracy) with respect to thermal ionization measurements ranged from 2.38% for a nominally 20% enriched ^{235}U sample to slightly greater than 30% error for a depleted one. Run-to-run, day-to-day, and sample-to-sample precision (repeatability) were measured using an enriched sample; the run-to-run precision ranged from $\pm1.9\%$ to $\pm5.5\%$ RSD, and the day-to-day precision was $\pm2.6\%$ RSD. The sample-to-sample precision, determined using three different cathodes, was found to be $\pm3.5\%$ RSD. The ratios showed no trends or biases, varying about a mean of 0.21 and ranging from a high of ~0.23 to a low of 0.18. A search was conducted for a stronger atomic line and a matching higher power diode laser in an attempt to improve the signal-to-noise ratio for the depleted case. Using a 150 mW diode laser that produced nominally 42 mW chopped power at 831.84 nm, a depleted uranium oxide sample was found to contain 0.26% ^{235}U, within 3.7% of the value found using thermal ionization mass analysis. Using this same laser, the run-to-run reproducibility improved to $\pm7.8\%$ from $\pm13.6\%$. This level of accuracy and precision is sufficient for screening applications, where preliminary information about the isotopic composition of a sample provides the incentive for additional analysis using more precise techniques.

Several techniques have been developed for isotopic analysis, including decay-counting[1,2] and mass spectrometry,[3–5] as well as methods that rely on the accessibility of optical transitions to provide isotopic selectivity (e.g., laser-induced fluorescence[6] and

optogalvanic spectroscopy[7,8]). It is this latter technique that we have investigated, focusing on the use of a dc glow discharge (GD) for atomization, a demountable discharge cell with a novel cathode arrangement[9,10] for rapid sample exchange, and rugged, fieldable, high-power (>30 mW) diode lasers to excite optical transitions. Our goal is a fieldable instrument that will provide uranium isotope ratio information; in this report, we describe the laboratory-based precision and accuracy results that influence the design.

The GD is well suited for optogalvanic spectroscopy. Sample preparation is minimal, and the GD is amenable to a variety of sample types. Sputtered neutral species are produced in relatively large abundance ($>10^8$ cm^{-3}), providing a sufficient population for optical excitation to higher lying energy levels. Because the GD operates at pressures between 100 and 1500 Pa, the collision frequency is quite high ($0.6 \times 10^7 - 9 \times 10^7$ collisions/s); this is suitable for optogalvanic spectroscopy because ionizing collisions can bring about the change in discharge voltage necessary to produce a signal. By scanning the wavelength of a narrow bandwidth laser over a resonant transition, individual isotopes can be excited and quantified. Diode lasers are well suited for this purpose. These semiconductor coherent light sources operate in the near-infrared (630 nm to 1.5 μm) and are conveniently tunable over a few nanometers by changing their temperature or drive current. Diode lasers are also rugged, an attractive feature when the goal is field deployment.

Several hundred uranium transitions have been identified in the diode laser accessible range; Gagne and co-workers,[11–13] as well as others,[14–16] have performed a number of fundamental spectroscopic investigations of uranium. Data concerning isotope shifts and relative emission intensities of many optical transitions[14] are available. In this paper, we assess the relative optogalvanic strength of several transitions and identify suitable candidates for practical uranium isotopic analysis. We have limited our investigation to transitions that are accessible to commercially available

(1) Knoll, G. F. Radiation Detection and Measurement; John Wiley & Sons: New York, 1989. Overman, R. T.; Clark, H. M. Radioisotope Techniques; McGraw-Hill Book Co., Inc.: New York, 1960.
(2) El-Assaly, F. M. Methods of Low-Level Counting and Spectrometry, Proceedings of an International Symposium on Methods of Low-Level Counting and Spectrometry, Berlin, Germany; International Atomic Energy Agency: Vienna, 6-10 April, 1981.
(3) Heumann, K. G. In Inorganic Mass Spectrometry; Adams, F., Gijbels, R., Van Grieken, R., Eds.; John Wiley & Sons: New York, 1988.
(4) Dubois, J. C.; Retail, G.; Cesario, J. Int. J. Mass Spectrom. Ion Processes 1992, 120, 163–177.
(5) Turner, P. J. In Applications of Plasma Source Mass Spectrometry II; Holland, G., Eaton, A. N., Eds.; Royal Society of Chemistry: Cambridge, 1993.

(6) Cannon, B. D. Personal communication, 1995.
(7) Keller, R. A.; Engleman, R.; Zalewski, E. F. J. Opt. Soc. Am. 1979, 69, 738–742.
(8) Lipert, R. J.; Lee, S. C.; Edelson, M. C. Appl. Spectrosc. 1992, 46, 1307–1308.
(9) Barshick, C. M.; Shaw, R. W.; Young, J. P.; Ramsey, J. M. Anal. Chem. 1994, 66, 4154–4158.
(10) Tong, W. G.; Shaw, R. W. Appl. Spectrosc. 1986, 40, 494–497.
(11) Demers, Y.; Gagne, J. M.; Dreze, C.; Pianarosa, P. J. Opt. Soc. B 1986, 3, 1678–1680.
(12) Piyakis, K. N.; Gagne, J. M. J. Opt. Soc. B 1989, 6, 2289–2294.
(13) David, E.; Gagne, J. M. Appl. Opt. 1990, 29, 4489–4493.
(14) Blaise, J.; Radziemski, L. J., Jr. J. Opt. Soc. Am. 1976, 66, 644–659.
(15) Engleman, R.; Palmer, B. A. J. Opt. Soc. Am. 1980, 70, 308–317.
(16) Palmer, B. A.; Keller, R. A.; Engleman, R. Informal Report No. LA-8251-MS; Los Alamos Scientific Laboratory: Los Alamos, NM, 1980.
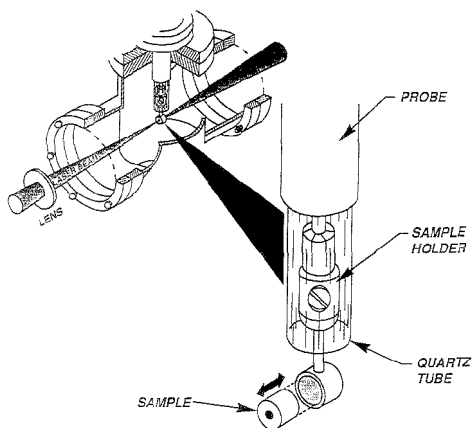
Figure 1. Sample configuration in the discharge cell.

diode lasers and that will provide adequate sensitivity. Run-to-run, day-to-day, and sample-to-sample repeatability are reported for a transition at 776.19 nm. A transition at 831.84 nm was also examined because of the availability of high-power diode lasers (>100 mW) in this region. Samples included machined uranium metal, uranium metal powder, uranium oxide, and uranium fluoride; both enriched and depleted ^{235}U compositions were examined.

EXPERIMENTAL SECTION

Sample Preparation. Glow discharge cathodes were fabricated in the shape of hollow cylinders 4.85 mm in diameter × 2.54 mm in length, with an inner diameter of 2.38 mm. The 10% enriched ^{235}U sample was machined from uranium metal; all other cathodes were formed by pressing powder in a hollow cathode die at 3.4 × 10^7 Pa for 5 min. Although any pure conducting powder can be used as a binder, a 50/50 wt % mixture of silver powder (325 Mesh, 99.99+%; Aldrich Chemical Co., Milwaukee, WI) and tantalum powder (325 Mesh, 99.98%; Alfa Aesar Johnson Matthey, Ward Hill, MA) was used in this investigation. Silver was chosen because it is available in relatively high purity and is malleable; tantalum was added to the silver because of its ability to getter oxygen. This gettering action helps to reduce the analyte oxides and hydroxides in the discharge.[17] The cathode comprised a 50/50 wt % mixture of binder and sample (~0.25 g).

Special precautions are necessary when handling uranium due to its radioactivity. Uranium is primarily an α emitter, but it also emits low to moderate β—γ energy; care must be taken to prevent ingestion or inhalation and to minimize exposure. Uranium is also pyrophoric when finely divided, and anyone contemplating research with uranium or uranium compounds is well advised to seek the help of a health physicist and industrial hygienist before beginning.

Glow Discharge Source. The GD cell with demountable cathode has been described in a previous publication.[9] Figure 1 illustrates the position of the sample relative to its holder and vacuum insertion probe. The sample cathodes were held in a stainless steel ring welded to a 1.59 mm diameter rod. This rod is inserted in a sample holder that is shielded by a quartz tube to

keep the discharge from arcing near the high-voltage feedthrough. A discharge forms over the entire cathode and holder assembly and is most intense at the center of the cylinder bore, where the atom density is reported to be highest;[18] it was in this region that uranium atoms were measured. Sample manipulation was accomplished by means of a probe inserted through an O-ring seal. The discharge current was held at a constant 20 mA. With a 50 kΩ ballast resistor in the circuit, the applied voltage was 500 V. The vacuum chamber housing served as the counter electrode. The cell was maintained nominally at 1050 Pa of argon with a gas flow rate of 3 cm^3(STP) min^{-1}. To reduce further the level of oxides and hydroxides in the discharge, a liquid nitrogen-filled cooling ring was positioned near the cathode; this aids in the removal of water vapor from the discharge.[19,20]

Laser Spectroscopy. A continuous wave (CW) argon ion laser-pumped titanium—sapphire ring laser[9] was used for exploratory spectroscopy and to provide the data on relative optogalvanic signal intensities for the transitions investigated. Two single-longitudinal-mode AlGaAs diode lasers were used in this study: a Model ML-64110N (Mitsubishi Electric Corp., Tokyo, Japan) with a nominal room temperature output of 30 mW at 777 nm and a Model SDL-5422-H1 (SDL Inc., San Jose, CA) with a nominal room temperature output of 150 mW at 834 nm. These diode lasers were used in conjunction with commercial control electronics.[9] For the 776 nm spectral study, the diode laser was maintained at 25.0 °C and 130 mA for an approximate power at the sample of 8 mW (400 W/cm^2). For the 832 nm study, the diode laser was maintained at 18.8 °C and 136 mA for an approximate power at the sample of 42 mW (2100 W/cm^2).

The diode laser frequency was scanned using a sawtooth signal generator to vary the drive current;[9] a 7.5 mA current scan (corresponding to 21.9 GHz) was used for the 776 nm line, and a 14 mA current scan (corresponding to 15 GHz) was used for the 832 nm line. Wavelengths were determined using a wavemeter (Model WA-20 VIS; Burleigh Instruments, Inc., Fisher, NY) with readout of ±0.001 nm.

The CW laser light was chopped at 1000 Hz with a mechanical chopper (Model SR540; Stanford Research Systems, Inc., Sunnyvale, CA). The ac component of the cathode voltage was monitored with a digital oscilloscope (Model 2246A; Tektronix Inc., Beaverton, OR) and a lock-in amplifier (Model SR510 or SR850; Stanford Research Systems, Inc.; 1 s time constant). In the titanium—sapphire laser experiments, the output from the lock-in amplifier was digitized using the same computer that was used to control the laser. The lock-in amplifier used for the diode laser experiments (Model SR850) included data collection and storage capabilities. Data were collected in ASCII form and processed off-line using commercially available software (KaleidaGraph; Synergy Software, Reading, PA).

The lasers used in this investigation were Class 4 (titanium—sapphire) and Class 3b (diode) devices. Safe operating practices consistent with these classifications were followed.

RESULTS AND DISCUSSION

Measurement Accuracy. Isotopc ratio measurements using a magnetic sector mass spectrometer have the advantage that all

---

(17) Mei, Y.; Harrison, W. W. *Spectrochim. Acta* **1991**, *46B*, 175—182.

(18) Caroli, S.; Alimonti, A.; Petrucci, F. In *Improved Hollow Cathode Lamps for Atomic Spectroscopy*; Caroli, S., Ed.; Ellis Horwood Limited Publishers, Halsted Press: New York, 1985.

(19) Ohorodnik, S. K.; DeGendt, S.; Tong, S. L.; Harrison, W. W. *J. Anal. At. Spectrom.* **1993**, *8*, 859—865.

(20) Ohorodnik, S. K.; Harrison, W. W. *Anal. Chem.* **1993**, *65*, 2542—2544.

Table 1. Isotopic Abundances of Samples Studied (Atom %)

sample	^{233}U	^{234}U	^{235}U	^{236}U	^{238}U
powder depleted uranium metal		0.0012 ± 0.0002	0.268 ± 0.005	0.0030 ± 0.0002	99.728 ± 0.005
powder depleted uranium tetrafluoride (UF$_4$)		0.0027 ± 0.0002	0.490 ± 0.003		99.507 ± 0.003
powder natural uranium metal		0.0054 ± 0.0004	0.716 ± 0.005		99.279 ± 0.005
machined solid enriched uranium metal	<0.001	0.064 ± 0.001	10.054 ± 0.022	0.059 ± 0.001	89.824 ± 0.022
powder enriched uranium oxide (U$_3$O$_8$) NIST SRM U-200		0.1246 ± 0.0003	20.013 ± 0.020	0.2116 ± 0.0006	79.651 ± 0.021

Table 2. Optogalvanic Data Recorded Using the 776 nm Diode Laser

sample	optogalvanic value $^{235}U/(^{235}U + {}^{238}U)$	measurement precision (%)	thermal ionization value $^{235}U/(^{235}U + {}^{238}U)$
depleted uranium tetrafluoride (UF$_4$)	0.0034	11.6	0.00490 ± 0.00003
natural uranium metal powder	0.0090	14.4	0.00716 ± 0.00005
enriched uranium metal	0.10	3.14	0.101 ± 0.002
enriched uranium oxide NIST SRM U-200	0.20	1.84	0.201 ± 0.002
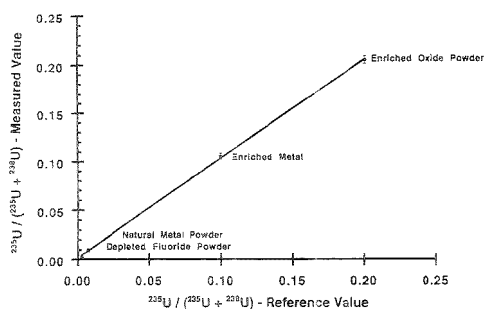
Figure 2. Measured $^{235}U/(^{235}U + {}^{238}U)$ ratio versus the reference value (certified value or thermal ionization mass spectrometric measurement) for four of the five materials listed in Table 1.

Figure 3. $^{235}U/(^{235}U + {}^{238}U)$ ratio for three samples and 77 measurements.

the peaks exhibit nominally the same Gaussian shape. In optogalvanic spectroscopy, the line shape is complicated by effects that include odd-mass isotope hyperfine structure. If the signal is integrated over all the area of the hyperfine structure, no loss of accuracy should result; however, as the elemental concentration decreases or the odd-mass isotope composition decreases, some of the structure is lost in the baseline noise, and the accuracy suffers. To evaluate the utility of optogalvanic spectroscopy for uranium isotope ratio measurements, four cathodes (fabricated from a ^{235}U-enriched oxide powder, a ^{235}U-enriched metal, a natural metal powder, and a ^{235}U-depleted fluoride powder) were prepared using materials listed in Table 1. By choosing four different isotopic compositions and three different uranium compounds, we addressed samples with a wide variety of characteristics.

Figure 2 shows a calibration curve developed from data (see Table 2) recorded using the 776 nm diode laser. The measured $^{235}U/(^{235}U + {}^{238}U)$ values (peak areas) are plotted versus either the certified values, as in the case of the National Institute of Standards and Technology (NIST) U-200 (nominally 20% enriched in ^{235}U), or versus thermal ionization mass spectrometric values, as measured in the Inorganic Mass Spectrometry Laboratories at the Oak Ridge National Laboratory. Eleven isotope ratio measurements were made for each cathode. The error bars correspond to 1σ relative standard deviation. The data show a good linear fit, with an R value of 0.999 86 for a line with slope 1.019 and y-intercept 0.0018. For the four samples analyzed, the percent relative error with respect to the thermal ionization measurements
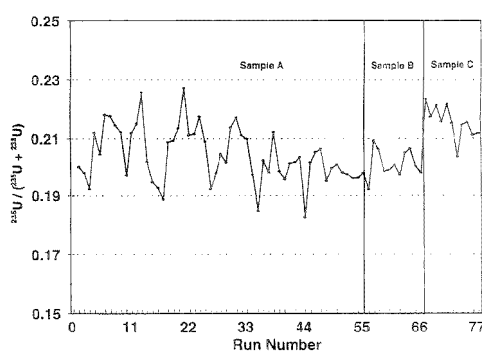
ranged from 2.38% for the nominally 20% enriched ^{235}U sample, where the signal-to-noise ratio was $>500:1$, to $>30\%$ error for the natural and depleted samples, where the signal-to-noise ratio was $<5:1$. Although this degree of accuracy was encouraging, we searched for a stronger atomic line, as well as higher power diode lasers, in an effort to improve the signal-to-noise ratio for the depleted sample case.

Measurement Precision. Run-to-run, day-to-day, and sample-to-sample precision (repeatability) were also evaluated using a 776 nm, 30 mW diode laser (400 W/cm^2 at the cathode). The cathode was formed from the NIST U-200 standard. In total, the $^{235}U/(^{235}U + {}^{238}U)$ data plotted in Figure 3 comprise 77 measurements taken over seven days with three different sample cathodes. Each measurement is the average of 11 $^{235}U/(^{235}U + {}^{238}U)$ ratios. The signals corresponding to ^{235}U and ^{238}U were measured as the area of the peaks, from baseline to baseline, using off-line processing. The run-to-run precision is defined as the percent relative standard deviation at 1σ for $n = 11$ measurements of the same cathode. This value ranged from $\pm 1.9\%$ to $\pm 5.5\%$ over five consecutive days. The mean was computed each day and used to determine the day-to-day precision; this was $\pm 2.6\%$ RSD. Sample-to-sample precision was based on measurements from three different cathodes (55 from sample A and 11 each from samples B and C); this value was $\pm 3.5\%$ RSD. The ratios show no trends or biases, varying about a mean of 0.21 and ranging from a high of 0.23 to a low of 0.18. This level of precision will suffice for many
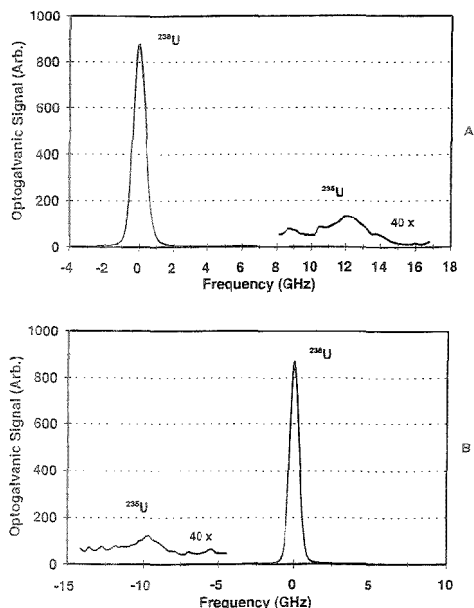
Figure 4. Uranium optogalvanic spectra (averages of five scans) recorded for (A) the 776.19 nm line using a titanium−sapphire laser of ~2.5 × 10⁴ W/cm² power density and (B) the 831.84 nm line using a titanium−sapphire laser of ~1.9 × 10³ W/cm² power density. The sample was depleted uranium metal powder (0.27% ²³⁵U). The discharge conditions were 1050 Pa of argon, 20 mA, and 500 V. The lock-in gain setting was altered by 40× at the indicated positions.

Figure 5. Uranium optogalvanic spectrum (average of five scans) recorded for the 831.84 nm line using a diode laser with a power density of ~2.1 × 10³ W/cm². The sample was the same as that used for Figure 4, a depleted uranium metal powder (0.27% ²³⁵U). The discharge conditions were 1050 Pa of argon, 20 mA, and 500 V.

applications where information about the isotopic composition of a sample provides a basis for determining if further investigations are desirable.

Optogalvanic Intensities. In a previous publication,[9] we showed 776 nm spectra for a nominally 10% ²³⁵U-enriched uranium metal sample obtained with use of both the titanium−sapphire and diode lasers. A goal of the present study was to evaluate the analytical usefulness of the technique for determining isotope ratios of uranium samples with depleted, natural, or enriched abundances of ²³⁵U. The data in Figure 3 indicate that such measurements can be made with a reasonable degree of accuracy and precision. However, we wanted to achieve better than 10% accuracy and precision for samples that contain >0.3% ²³⁵U relative abundance. The quality of the measurements suffered from lack of signal strength at the 776 nm (12 879.981 cm⁻¹) line. One potential solution was to increase the laser power (as in the case of the spectrum in Figure 4A, excited using the 500 mW titanium−sapphire laser). Because higher power diode lasers were not readily available for the 776 nm transition, an alternative transition was sought. Several parameters restricted the search for a different line. Transitions accessible to diode lasers (630−1000 nm) were required for which high-power (>30 mW) devices were commercially available. Transitions that had a relatively large ²³⁵U isotope shift (>10 GHz; see Table 3) and a relatively large strength (stronger than the 776 nm line) were preferred. Table 3 shows the transitions[16] that were considered as optogalvanic candidates, along with the relative emission intensities[16] and isotope shifts.[15]

Our experimentally determined optogalvanic intensities for these transitions are also shown. To generate these data, three 10 GHz scans were recorded over the ²³⁸U line using the titanium−sapphire laser (~500 mW at the sample). As anticipated, there is no strong correlation between relative emission and optogalvanic signal intensities. Of the eight transitions examined, the one at 832 nm (12 018.3089 cm⁻¹) was the most promising. The optogalvanic signal intensity was 2.5 times greater than that at 776 nm for the same laser power, and a 150 mW diode laser was commercially available in the 834 nm region. In addition, the magnitude of the isotope shift was approximately the same as for the line at 776 nm. Figure 4B shows a spectrum for a depleted ²³⁵U oxide sample at 832 nm, obtained with use of the titanium−sapphire laser attenuated to 38 mW (the anticipated power of the 832 nm diode laser). The ²³⁵U signal is clearly observed, and the signal-to-noise ratio is comparable to that for the 500 mW, 776 nm case.

Precision and Accuracy of a Measurement at 832 nm. Figure 5 shows a depleted uranium metal spectrum recorded using a 150 mW SDL diode laser operating with a nominal output power of 42 mW at the discharge cathode. The spectrum is similar to the one shown in Figure 4B, an anticipated result given

that the line widths of the lasers are at least an order of magnitude narrower than the Doppler-limited spectral line width. The signal-to-noise ratios are comparable. The measured $^{235}U/(^{235}U + ^{238}U)$ ratio was 0.0026, within 3.7% of the thermal ionization mass analysis value.

For enriched samples, precision was not expected to improve significantly for the 832 nm line. The increase in signal-to-noise ratio, however, should have an impact on the measurement precision for a depleted sample. The run-to-run reproducibility, as defined previously, did improve to ±7.8% from ±13.6% RSD (1σ for 11 measurements). This is the direct result of the more powerful diode laser and the stronger optogalvanic transition (compared to the 776 nm line).

CONCLUSIONS

Precision and accuracy of a uranium isotope ratio measurement have been evaluated for diode laser-excited optogalvanic spectroscopy. Samples that were enriched, natural, or depleted in ^{235}U were easily distinguishable from one another. Determined with use of a 150 mW diode laser at 832 nm, the measured $^{235}U/(^{235}U + ^{238}U)$ ratio for a depleted uranium metal sample was 0.0026, within 3.7% of the thermal ionization mass analysis value. The run-to-run reproducibility was ±7.8%, a 2-fold improvement from the measurement obtained with use of a 30 mW diode laser at 776 nm. These results are sufficient for many applications where preliminary data concerning isotopic composition of a sample provide the basis for deciding whether further investigations are warranted.

Single-Piece All-Solid-State Ion-Selective Electrode

Johan Bobacka,*,† Tom Lindfors,‡ Mary McCarrick,‡,§ Ari Ivaska,‡ and Andrzej Lewenstam‡

KONE Instruments Corporation, Ruukintie 18, FIN-02320 Espoo, Finland, and Laboratory of Analytical Chemistry, Åbo Akademi University, FIN-20500 Turku-Åbo, Finland

A novel concept of a single-piece all-solid-state ion-selective electrode (SPE) is introduced. A processable conjugated (electronically conducting or semiconducting) polymer (CP) is dissolved in a cocktail containing the components used for a conventional ion-selective poly-(vinyl chloride) matrix membrane. The cocktail, containing the CP, is cast directly on a solid substrate (glassy carbon), resulting in a SPE. The role of the CP is to mediate the charge transfer between the substrate and the membrane. Two soluble CPs are studied: (i) poly(3-octylthiophene) in its undoped state and (ii) polyaniline doped (protonated) with bis(2-ethylhexyl) hydrogen phosphate. Experimental results obtained for lithium-selective SPEs and calcium-selective SPEs are discussed. All the SPEs studied show near-Nernstian responses, and no redox interference is observed as long as the concentration of the CP is sufficiently low. The incorporation of a CP, particularly polyaniline, in the membrane is shown to improve the stability of the standard potential of the SPE compared to the corresponding coated-wire electrode (membrane without CP). Impedance measurements provide information about the charge transfer processes of the electrodes.

In the so-called conventional ion-selective electrode (ISE), the on-selective membrane is in electrical contact with the inner reference electrode through the inner reference solution. The transfer from ionic conductivity (in the membrane and the inner reference solution) to electronic conductivity (in the inner reference electrode and external instrumentation) is provided by the reversible electrode reaction of the inner reference electrode, resulting in an ISE exhibiting a stable and reproducible standard potential.

For some applications, it is advantageous to replace the inner reference solution by a solid contact, giving an all-solid-state ISE that can be fabricated in various shapes and sizes and needs no refilling.[1] One such approach is to contact the ion-selective membrane directly to a solid substrate, resulting in the coated-wire electrode (CWE).[2,3] A disadvantage of the CWE is the irreproducibility and drift of the electrode potential that can be related to the poorly defined charge transfer process(es) at the

(blocked) interface between the ionically conducting membrane and the electronically conducting substrate.[4]

A more stable electrode potential can be obtained by contacting the ion-selective membrane to the solid substrate via an intermediate layer having mixed ionic and electronic conductivity.[1] In such an all-solid-state ISE, the transfer from ionic to electronic conductivity is possible through the intermediate layer. Several electrochemically synthesized polymers, such as poly(p,p'-biphenol),[5] poly(1-pyreneamine),[5] polypyrrole,[6] and poly(3-octylthiophene),[7] have been used as the intermediate layer in this type of ISE. However, the additional step required to produce the intermediate layer makes this type of electrode more complicated to fabricate than the CWE.

Active research in the field of synthetic metals has resulted in solution-processable conducting polymers such as poly(3-alkylthiophenes)[8] and recently polyaniline (PANI).[9] Undoped poly(3-alkylthiophenes) with alkyl side chains longer than three carbon atoms are soluble in common organic solvents. In their undoped (unintentionally doped) state, poly(3-alkylthiophenes) have been characterized as p-type semiconductors, expected to form an ohmic contact with materials having a high work function.[10] Additionally, undoped poly(3-octylthiophene) (POT) was found to give a nonselective cationic response to several alkali and alkaline earth metal cations.[11] These electrical and ion-sensitive properties of POT prompted us to investigate the possibility of enhancing the signal transduction of the CWE by incorporation of POT in the membrane, resulting in a single-piece all-solid-state ion-selective electrode (SPE). A lithium-selective electrode with the poly(vinyl chloride) (PVC)–POT matrix membrane will be described in this work. The concept of the SPE is illustrated further by using PANI as the conducting polymer. The emeraldine base form of PANI can be doped (protonated) by functionalized protonic acids, resulting in an electrically conducting form of PANI that is soluble in common organic solvents.[9] By choosing bis(2-ethylhexyl) hydrogen phosphate (DiOHP) as the protonic acid, the resulting doped PANI is compatible with plasticized PVC.[12] In this work, PANI doped with DiOHP is used to prepare calcium-selective SPEs.

(5) Oyama, N.; Ohsaka, T.; Yoshimura, F.; Mizunuma, M.; Yamaguchi, S.; Ushizawa, N.; Shimomura, T. *J. Macromol. Sci.-Chem.* **1988**, *A25*, 1463–1473.
(6) Cadogan, A.; Gao, Z.; Lewenstam, A.; Ivaska, A.; Diamond, D. *Anal. Chem.* **1992**, *64*, 2496–2501.
(7) Bobacka, J.; McCarrick, M.; Lewenstam, A.; Ivaska, A. *Analyst* **1994**, *119*, 1985–1991.
(8) Elsenbaumer, R. L.; Jen, K. Y.; Oboodi, R. *Synth. Met.* **1986**, *15*, 169–174.
(9) Cao, Y.; Smith, P.; Heeger, A. J. *Synth. Met.* **1992**, *48*, 91–97.
(10) Tomozawa, H.; Braun, D.; Phillips, S.; Heeger, A. J.; Kroemer, H. *Synth. Met.* **1987**, *22*, 63–69.
(11) Bobacka, J.; Lewenstam, A.; Ivaska, A. *Talanta* **1993**, *40*, 1437–1444.
(12) Pron, A.; Österholm, J.-E.; Smith, P.; Heeger, A. J.; Laska, J.; Zagorska, M. *Synth. Met.* **1993**, *57*, 3520–3525.

(1) Nikolskii, B. P.; Materova, E. A. *Ion-Sel. Electrode Rev.* **1985**, *7*, 3–39.
(2) Cattrall, R. W.; Freiser, H. *Anal. Chem.* **1971**, *43*, 1905–1906.
(3) Cattrall, R. W.; Hamilton, I. C. *Ion-Sel. Electrode Rev.* **1984**, *6*, 125–172.
(4) Buck, R. P. In *Ion Selective Electrodes in Analytical Chemistry*; Freiser, H., Ed.; Plenum: New York, 1978; Vol. 1, p 58.

EXPERIMENTAL SECTION

Reagents. Chemically synthesized poly(3-octylthiophene) (POT) in powder form was obtained from Neste Oy (Research Centre, Kulloo, Finland). The fraction of POT that was insoluble in tetrahydrofuran (THF) was removed by filtration, and the THF-soluble fraction was used in electrode preparation. Emeraldine base was purchased from AC&T (Applications, Chemistry & Technologies, St. Egrève, France). Bis(2-ethylhexyl) hydrogen phosphate (DiOHP) was obtained from Aldrich. Soluble PANI was obtained as follows: 99.1 mg of emeraldine base was added to 0.05 M DiOHP–THF solution (10 mL). In this PANI–DiOHP mixture, the molar ratio between DiOHP and the repeat unit of PANI was equal to 0.5. The insoluble fraction was removed by filtration, and the THF-soluble fraction of the PANI–DiOHP mixture was used in electrode preparation. Analytical grade reagent salts were used as received from Merck or Fluka and dissolved in distilled, deionized water.

Cocktail Preparation. The composition (w/w) of the Li cocktail was the following: lithium ionophore ETH 2137 (2.0%), bis(1-butylpentyl) adipate (65.6%), and PVC (32.4%), dissolved in THF. The composition (w/w) of the Ca cocktail was the following: calcium ionophore ETH 1001 (3.4%), bis(2-ethylhexyl) sebacate (62.9%), PVC (31.7%), and potassium tetrakis(4-chlorophenyl)borate (2.0%), dissolved in THF. Different amounts of soluble POT or PANI were added to the cocktails, resulting in the modified cocktails used for the Li- and Ca-selective SPEs (Li- and Ca-SPEs). Li cocktails containing 5–25% POT (w/w) and Ca cocktails containing 1 or 2% PANI (w/w) were prepared.

Electrode Fabrication. The electrode substrate was a glassy carbon (GC) disk electrode (area, 0.07 cm^2) that was polished with 0.3 μm Al$_2$O$_3$ paste and rinsed with water and CHCl$_3$ or THF. The Li-SPEs were fabricated by applying Li cocktail, containing POT (5–25%), on the GC disk electrode and then allowing the solvent (THF) to evaporate at room temperature for at least 5 h. The volume of the Li cocktail applied, typically 100–200 μL, was adjusted to obtain a mass of the dry membrane of about 12–13 mg for each Li-SPE. The Ca-SPEs were made analogously by applying Ca cocktail (100–200 μL), containing PANI (1 or 2%), to obtain a mass of the dry membrane of about 7 mg for each Ca-SPE. For comparison, lithium and calcium electrodes were also prepared from cocktails without conducting polymer, cast on GC. In this paper, these electrodes are called Li- and Ca-CWEs, although they are actually coated-disk electrodes. The dry masses of the CWE membranes were the same as for the respective SPEs. The thickness of the resulting membranes was in the range 0.1–0.2 mm. Prior to use, all electrodes were conditioned for at least 12 h in 10^{-1} M chloride solutions of the primary ion.

Potentiometric Measurements. Potentiometric measurements were carried out by using the SPE (or CWE) as the indicator electrode and Ag/AgCl/KCl (3 M) as the reference electrode. The potentiometric selectivity coefficients (K_{ij}^{pot}) were determined by the separate solution method using 0.01 M chloride solutions of the cations involved. The detection limit was obtained from the point of intersection of the extrapolated linear region and the low-concentration-level region of the calibration curve. The redox sensitivity was investigated by measuring the potential of the SPE in a solution of a constant ionic background (0.1 M), 1 mM in the Fe(CN)$_6^{3-/4-}$ redox couple, with different ratios of Fe(III)/Fe(II), ranging from 1:10 to 10:1.
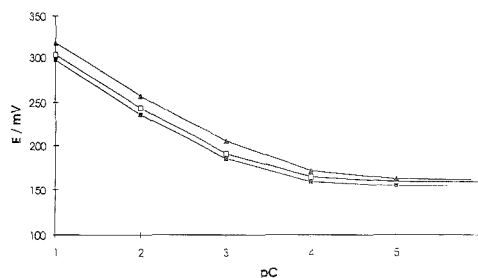
Figure 1. Calibration curves for (■) Li-CWE and Li-SPEs containing (□) 5 and (▲) 20% POT. Background salt, 0.1 M KNO$_3$.

Table 1. Response Characteristics of Li-SPEs with Membranes Containing Different Amounts of POT^a

[POT], % (w/w)	slope, mV/decade	detectn limit, M	log K_{ij}^{pot}			
			$j = $ Na$^+$	$j = $ K$^+$	$j = $ NH$_4^+$	$j = $ Mg^{2+}
0	56.0	2.1 × 10^{-4}	−1.24	−1.29	−1.33	−2.33
5	56.0	2.6 × 10^{-4}	−1.27	−1.29	−1.39	−2.39
10	56.8	1.7 × 10^{-4}	−1.31	−1.46	−1.49	−2.43
15	57.8	1.8 × 10^{-4}	−1.40	−1.48	−1.61	−2.58
20	55.5	1.6 × 10^{-4}	−1.37	−1.47	−1.57	−2.49
25	56.8	1.8 × 10^{-4}	−1.40	−1.47	−1.62	−2.45

^{a} Results for the Li-CWE (0% POT) are shown for comparison. The slopes were calculated in the concentration range 10^{-1}–10^{-3} M Li$^+$.

Impedance Measurements. Impedance mesurements were performed on SPEs and CWEs by using a S-5720B frequency response analyzer connected to a Model 2000 potentiostat/galvanostat (NF Circuit Instruments). The reference electrode was a calomel electrode (3 M KCl), and the auxiliary electrode was a glassy carbon rod. The solution was 0.1 M in the primary ion. The impedance spectra included frequencies from 100 kHz to 16 mHz. Occasionally, frequencies down to 1 mHz were used. The amplitude of the sinusoidal excitation signal was 100 or 200 mV. A relatively high amplitude was used in order to obtain an acceptable S/N ratio. All experiments were performed at room temperature (23 ± 2 °C).

RESULTS AND DISCUSSION

Ionic Response. Examples of the calibration curves for the Li-CWE and some Li-SPEs are shown in Figure 1. The response characteristics of the electrodes studied are collected in Table 1. The Li-SPEs containing 5–25% POT and the Li-CWE showed near-Nernstian responses, and the limit of detection and selectivity were approximately the same for both types of electrodes.

Examples of the calibration curves for the Ca-SPEs containing 1 and 2% PANI and the Ca-CWE (0% PANI) are shown in Figure 2. The slopes of the calibration curves in the concentration range 10^{-1}–10^{-4} M Ca^{2+} for the electrodes containing 0, 1, and 2% PANI (average of three electrodes of each type) were 28.2 ± 0.7, 28.0 ± 0.2, and 27.0 ± 1.6 mV/decade, respectively. The Ca-SPEs containing 1 and 2% PANI were found to show essentially the same selectivity as the Ca-CWE with respect to Li$^+$, Na$^+$, K$^+$, Mg^{2+}, Cu^{2+}, and Co^{2+}.

Redox Response. The Li-SPEs containing 5–25% POT and the Li-CWE did not show any redox response, indicating that ion
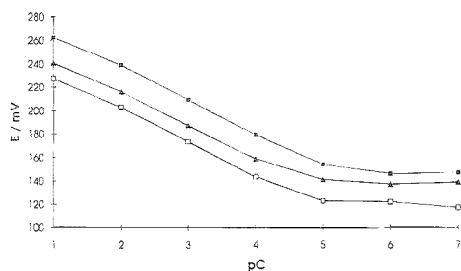
Figure 2. Calibration curves for (■) Ca-CWE and Ca-SPEs containing (□) 1 and (▲) 2% PANI. Background salt, 0.1 M KCl.

transfer dominates over electron transfer at the membrane–solution interface, under the experimental conditions used. However, if the concentration of POT in the membrane was increased to 75 or 100%, the electrodes showed some redox sensitivity, with slopes of about 20 mV/decade, suggesting that electron transfer can take place through the semiconducting POT. A 100% POT concentration means that the membrane consists of pure POT (no other materials are present). These results agree with previous observations that electrochemically synthesized POT in its undoped state shows some redox sensitivity in solutions containing 1 mM $Fe(CN)_6^{3-/4-}$.[11]

Similarly, the Ca-SPEs containing only 1–10% PANI, as studied in this work, and the Ca-CWE did not show any redox sensitivity. The electrode containing 100% PANI, i.e., pure PANI, was redox sensitive, giving a slope of about 40 mV/decade, reflecting the electronic conductivity of doped PANI.

Potential Stability. The stability of the Ca-SPEs was studied by comparing the potential drift for the Ca-SPEs containing 1 and 2% PANI with that of the Ca-CWE. The potential of the electrodes was measured over 14 days, and the average drift for each type of electrode (three electrodes of each type) was calculated. The Ca-SPEs containing 1 and 2% PANI showed drifts of 0.2 ± 0.2 and -0.5 ± 0.5 mV/day, respectively. The Ca-CWEs showed a drift of -1.0 ± 0.8 mV/day. These results show that the Ca-SPEs, especially the electrode containing 1% PANI, have a more stable standard potential than the Ca-CWE. Interestingly, a very small concentration (1%) of PANI seems to be enough to significantly improve the stability of the electrode. This can be related to the unique property of processable PANI to form connected pathways at very low volume fractions in bulk polymers.[9]

Also, the SPEs containing POT were found to show a relatively stable standard potential. For example, the potential stability of the Li-SPE containing 15% POT was studied by measuring the potential over a time period of 8 days. After an initial conditioning time of 3 days, the potential of the Li-SPE drifted by ~0.8 mV/day. The Li-CWE showed a drift of about 2.3 mV/day over the same period of time. These results indicate that the presence of POT in the membrane may improve the stability of the electrode potential but maybe not to the same extent as doped PANI.

Impedance Measurements. Impedance measurements were performed on Ca-SPEs immersed in 0.1 M $CaCl_2$ solution. Examples of the impedance spectra for the Ca-CWE and the Ca-SPEs containing 1 and 2% PANI are shown in Figure 3. The high-frequency semicircle can be related to the bulk impedance of the

(13) Nahir, T. M.; Buck, R. P. *Electrochim. Acta* **1993**, *38*, 2691–2697.
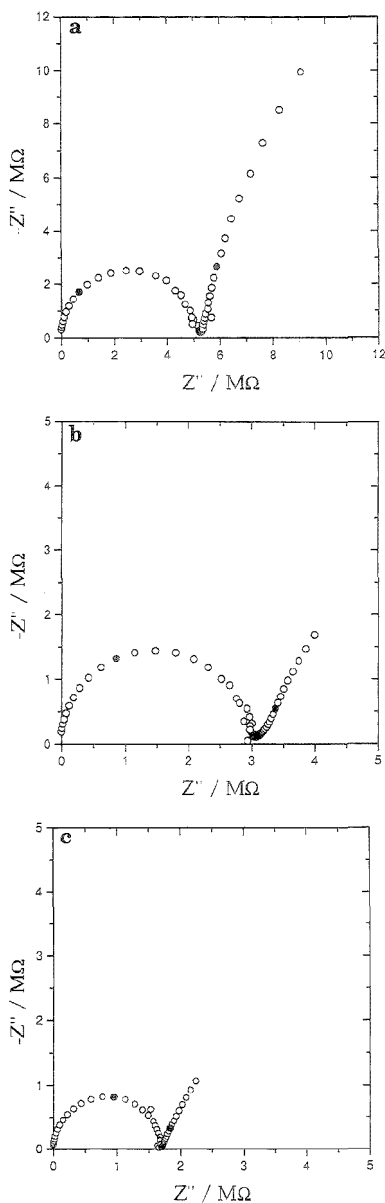
Figure 3. Impedance spectra for (a) the Ca-CWE and the Ca-SPEs containing (b) 1 and (c) 2% PANI. Frequency range, 100 kHz–16 mHz. Filled symbols (from left to right): 1 kHz, 100 mHz. Applied dc potential, 200 mV (vs calomel reference electrode).

membrane.[13] The bulk resistance of the membrane was found to decrease with increasing amount of PANI (Figure 3). The time constant (τ_b) of the bulk process was calculated from the impedance spectra presented in Figure 3 by using the frequency (f_{max}) at the top of the high-frequency semicircle:

Figure 4. Impedance spectra for (a) the Li-CWE and the Li-SPEs containing (b) 5, (c) 10, (d) 15, and (e) 25% POT . Frequency range, 100 kHz–10 mHz. Filled symbols (from left to right): 1 kHz, 100 mHz. Applied dc potential: (a) 270, (b) 225, (c) 225, (d) 235, and (e) 380 mV (vs calomel reference electrode).

$$\tau_b = (2\pi f_{max})^{-1} \qquad (1)$$

The Ca-CWE showed a time constant of 0.40 ms, while the Ca-SPEs containing 1 and 2% PANI showed time constants of 0.25 and 0.13 ms, respectively. These results suggest that the bulk process of the electrodes becomes faster with increasing concentration of PANI.

At low frequencies, the beginning of a second semicircle is observed for the Ca-SPEs and Ca-CWE. When the calcium membrane (0% PANI) was contacted by electrolyte solution on both sides (conventional Ca-ISE), the second semicircle was

absent.[7] Therefore, it seems plausible that this second semicircle is related to charge transfer process(es) at the substrate—membrane interface. As can be seen in Figure 3, this low-frequency semicircle is significantly smaller for the Ca-SPEs than for the Ca-CWE, indicating that the charge transfer impedance is decreased by incorporation of PANI in the membrane. This may be the reason for the improved potential stability discussed above.

Impedance measurements were also performed on the Li-CWE and the Li-SPEs containing 5–25% POT in 0.1 M LiCl solution. The results are shown in Figure 4. The bulk resistance of the

Li-SPEs was found to increase with an increasing amount of POT. This may be related to a relatively low electronic and/or ionic conductivity of undoped POT compared to doped (protonated) PANI.

At low frequencies, the Li-SPEs give a straight line in the complex impedance plane. The angle between the straight line and the real impedance axis decreases with increasing concentration of POT in the membrane, and at 25% POT, the straight line is more or less parallel to the real impedance axis (Figure 4). The introduction of POT into the membrane thus seems to influence the charge transfer process(es) at the substrate–membrane interface, but the simultaneous increase in the bulk resistance makes the interpretation difficult. Clearly, the analytical performance of the Li-SPE was improved by incorporation of undoped POT in the membrane (Table 1), but the impedance measurements reveal some disadvantages of POT compared to PANI.

Response Mechanism. The response mechanism of the type of SPEs studied in this work may be explained analogously to that suggested for solid-contact ISEs (SCISEs) using the conducting polymer (CP) as the intermediate layer.[6,7] The main difference between the SPE and the SCISE is the integration of the CP into the PVC matrix membrane (M) phase of the latter. Ideally, the charge transfer process (ion recognition and signal transduction) in the SPE can be described by the following steps: (i) ion transfer at the membrane–solution interface, (ii) ion transport in the membrane, (iii) coupling of ion and electron transfer in the membrane, (iv) electron transport in the membrane, (v) electron transfer at the substrate–membrane interface, and (vi) electron transport in the substrate. Steps i and ii are taken care of by the neutral carrier in the membrane, as for conventional ISEs. Based on the mixed ionic and redox sensitivity of p-type CPs, it can be suggested that the CP plays a central role in step iii.[14,15] Due to its electronic conductivity, the CP is expected to facilitate steps iv and v. Step vi is obvious. A common feature of the response mechanism of the SPE and the SCISE is that the coupling of ion and electron transfer and the transport of electrons to the substrate, steps iii–v, are expected to occur through the CP either as a separate layer (SCISE) or integrated in the PVC membrane phase (SPE).

Step iii is perhaps the most interesting in the chain of charge transfer processes because it couples the ionic and electronic signals analogously to the redox reaction occurring at a conventional reference electrode, e.g., the Ag/AgCl electrode:

$$AgCl(s) + e^- = Ag(s) + Cl^-(aq) \tag{2}$$
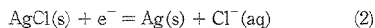
A similar reaction may take place at the interface between a p-type CP and a PVC matrix membrane. If the anions are mobile,

the reaction can be written as[14,15]

$$P^+A^-_{(CP)} + e^- = P_{(CP)} + A^-_{(M)} \tag{3}$$
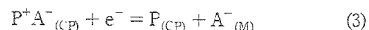
where P^+ is the oxidized CP segment (1 polaron or $^1/_2$ bipolaron), P is the electrically neutral CP segment, A^- is the doping anion, and e^- is the electron. The subscript (CP) indicates the conducting polymer phase, and subscript (M) indicates the PVC matrix membrane phase. If the anions (A^-) are immobile, the reaction can be written as

$$P^+A^-_{(CP)} + e^- + N^-_{(M)} = PA^-N^+_{(CP)} \tag{4}$$
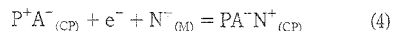
$N^+_{(M)}$ is used to indicate both free and ionophore-complexed cation. In the case of the cation-selective membranes studied in this work, where cations are the mobile species, reaction 4 is more probable than reaction 3. In general, the relative contributions from reactions 3 and 4 will depend on the relative mobilities of A^- and N^+ in the membrane (both A^- and N^+ may be mobile). Based on the response mechanism outlined above, the electronic conductivity of the CP phase and the ionic conductivity of the M phase, together with the rate of ion (A^- or N^+) transfer at the CP–M interface, are expected to influence the stability and reproducibility of the standard potential of the SPE (and SCISE).

CONCLUSIONS

The concept of including a soluble conducting polymer in the membrane phase may be useful in the production of single-piece all-solid-state ion-selective electrodes. Results from impedance measurements suggest that doped PANI enhances the transduction of the chemical signal (ion activity) into the electrical signal (potential), resulting in improved potential stability of the electrode compared to the CWE. Introducing POT into the membrane was found to improve the analytical performance of the SPE but resulted in an increased bulk resistance. It should be pointed out that PANI was used in its doped (protonated) state, whereas POT was used in its undoped state. Doped POT was not used in the SPEs because of its limited solubility in THF and the instability due to its high redox potential. In general, properties such as the electronic conductivity and ion sensitivity of the conjugated polymer are expected to play a central role concerning the proper functioning of SPEs. Although this research is still at an early stage, we believe that the concept introduced in this paper will open up new possibilities for the design of single-piece all-solid-state ion-selective electrodes.

(14) Lewenstam, A.; Bobacka, J.; Ivaska, A. *J. Electroanal. Chem.* **1994**, *368*, 23–31.
(15) Bobacka, J.; Gao, Z.; Ivaska, A.; Lewenstam, A. *J. Electroanal. Chem.* **1994**, *368*, 33–41.

Hydrazine Detection Using a Tyrosinase-Based Inhibition Biosensor

Joseph Wang* and Liang Chen

Department of Chemistry and Biochemistry, New Mexico State University, Las Cruces, New Mexico 88003

An amperometric biosensor for the determination of hydrazine compounds, based on their inhibitory effect on the activity of immobilized tyrosinase, has been developed. The hydrazine–tyrosinase interaction can be modeled as a reversible competitive inhibition. Kinetic parameters (K_i and $I_{0.5}$) have been determined for various hydrazine compounds. The tyrosinase-based carbon paste electrode offers sensitive measurements to the low-micromolar level and good precision. The trend in sensitivity, methylhydrazine > hydrazine > dimethylhydrazine, reflects the degree of inhibition. The applicability to assays of unaltered river and drinking water samples is illustrated. Analogous measurements at disposable thick-film sensors are also reported. These inhibitor biosensors hold great promise for field-based monitoring of various hydrazines.

Hydrazine compounds are widely used as fuels (in rocket propulsion systems), corrosion inhibitors, catalysts, emulsifiers, or dyes. In view of major concerns regarding the toxicity of these compounds, there are growing needs for innovative devices for monitoring of hydrazines. Field measurements are preferred, as they afford the option of a rapid warning capability while avoiding the errors, delays, and cost of laboratory-based measurements. The miniaturized nature of electrochemical probes, and the portability of associated instrumentation, make them very attractive for the task of on-site monitoring of hydrazine compounds. Various chemically modified electrodes, based on different electrocatalytic moieties, have thus been developed for the detection of different hydrazines.[1–4] Analogous biosensing schemes for measuring hydrazines have not been developed, despite the great promise of biosensor technology for on-site analyses.

This paper describes a biosensor approach for amperometric monitoring of hydrazine compounds. The new procedure relies on the inhibitory action that various hydrazines exert on the activity of the enzyme tyrosinase. Inhibitor biosensors have been widely used for monitoring toxic substances, such as organophosphate pesticides,[5,6] cyanide,[7,8] or heavy metals.[9] The modulated biocatalytic activity accrued from the inhibitor–enzyme interaction has been monitored from the decreased current response to the

corresponding substrate. Similarly, we have discovered that tyrosinase is inactivated by hydrazine compounds and have exploited this behavior for developing useful hydrazine sensors.

EXPERIMENTAL SECTION

Apparatus. Amperometric and chronoamperometric measurements were performed with an EG&G PAR Model 264A voltammetric analyzer, in connection with a Houston Omniscribe strip-chart recorder. All studies were carried out in a 10-mL cell (Model VC-2, BAS). The enzyme electrode, reference one (Model RE-1, BAS), and platinum wire auxiliary electrode were inserted through holes in the cell Teflon cover. A magnetic stirrer provided the convective transport during the amperometric experiments.

Electrode Preparation. The carbon-paste bioelectrode was prepared by hand mixing the desired amount (3% w/w) of tyrosinase with ordinary carbon paste, made of 60% graphite powder (Acheson 38, Fisher) and mineral oil (Aldrich). A portion of the resulting paste was then packed into the 3-mm-diameter cavity of a Teflon body. A copper wire, inserted through the opposite side, provided the electrical contact. New bioelectrode surfaces were smoothed on a weighing paper.

The fabrication of the screen-printed biosensor was described previously.[10] A semiautomatic printer (Model TF-100) was used, in connection with a tyrosinase-containing ink. The latter was prepared by mixing 2 g of the carbon ink (Gwent, UK) with 14 mg (50 000 units) of tyrosinase.

Reagents. All chemicals were reagent grade and were used as received. Solutions were prepared daily with double-distilled water. Methylhydrazine, and 1,2-dimethylhydrazine dihydrochloride were obtained from Aldrich, while hydrazine sulfate and phenol were received from Baker. Tyrosinase (EC 1.14.18.1, 3900 units/mg) was obtained from Sigma. A phosphate buffer solution (0.05 M, pH 7.4) served as the supporting electrolyte. The river water sample (Rio Grande) was collected in Las Cruces, NM, while the drinking water sample was obtained at the NMSU laboratory.

Procedure. Amperometric experiments were performed by holding the working electrode at the operating potential (−0.1 V) and allowing the transient current to decay in the presence of the stirred blank solution. Addition of the substrate (usually at 1×10^{-5} M) was followed by successive additions of the target analyte (inhibitor). Chronoamperometry was performed by stepping the potential from open circuit to −0.1 V and recording the current transient. All experiments were carried out at room temperature (22 °C).

RESULTS AND DISCUSSION

Amperometric hydrazine detection is based on the modulated biocatalytic activity of tyrosinase in the presence of its substrate

(1) Zegal, J.; Fierro, C.; Rozas, R. J. Electroanal. Chem. 1981, 119, 403.
(2) Wang, J.; Lu, Z. Electroanalysis 1989, 1, 517.
(3) Zen, J.; Tang, J. Anal. Chem. 1995, 67, 208.
(4) Zhou, J.; Wang, E. Electroanalysis 1992, 4, 473.
(5) Skladal, P. Anal. Chim. Acta 1992, 269, 281.
(6) Marty, J.; Sode, K.; Karube, I. Electroanalysis 1992, 4, 249.
(7) Smit, M. H.; Cass, A. E. Anal. Chem. 1990, 62, 2429.
(8) Smit, M. H.; Rechnitz, G. A. Anal. Chem. 1993, 65, 380.
(9) Dolmanova, I. F.; Shekhovtsova, T. N.; Kutcheryaeva, V. V. Talanta 1987, 34, 201.

(10) Wang, J.; Chen, Q. Anal. Lett. 1995, 28, 1131.
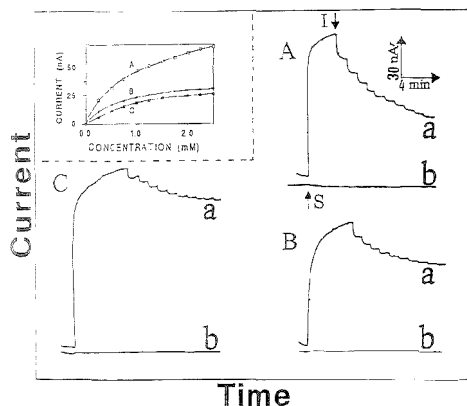
Figure 1. Current–time recordings at the ordinary (b) and tyrosinase-modified (a) electrodes upon increasing the methylhydrazine (A), hydrazine (B), and dimethylhydrazine (C) concentration in 2.5 × 10^{-4} M steps. Operating potential, −0.1 V; stirring rate, 300 rpm; solution, 0.05 M phosphate buffer containing 1 × 10^{-5} M phenol. Also shown (as inset), the resulting calibration plots.

and inhibitor. Mushroom tyrosinase is a copper-containing monooxygenase that converts phenolic compounds to the corresponding quinones at the expense of oxygen:[11]

$$\text{phenol} + \text{oxygen} \xrightarrow{\text{tyrosinase}} o\text{-quinone} + \text{water}$$
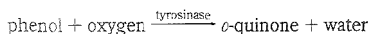
The liberated quinone species can be conveniently detected by a low-potential reduction. The addition of hydrazine causes inhibition of the enzyme, consequently decreasing the amount of liberated quinone. Tyrosinase offers several advantages for such application. It is highly stable, can be used in both aqueous and nonaqueous environments, and allows detection at low potentials where potential interferences are minimal.

Figure 1a illustrates the effect of various hydrazines upon the tyrosinase-generated amperometric response. It shows the response to 1 × 10^{-5} M (S), followed by successive 2.5 × 10^{-4} M additions of the inhibitors (I) methylhydrazine (A), hydrazine (B), and dimethylhydrazine (C). The sensor responds rapidly to these submillimolar hydrazine concentrations, as indicated from the decreased response to the substrate. Steady-state responses for the inhibitors are produced within ~20 (A) and ~15 (B, C) s. Note also that in the absence of biocatalytic activity the enzyme-free electrode is not responsive to the substrate or inhibitor (b). No chemical reaction between hydrazines and phenol was indicated from monitoring the direct (nonenzymatic) oxidation current of phenol at the bare electrode (+0.9 V; not shown). Also shown in Figure 1 (inset) are the resulting calibration plots. As expected for inhibition processes, such plots are not linear with a significant curvature at high hydrazine concentrations. The trend in sensitivity, methylhydrazine > hydrazine > dimethylhydrazine, reflects the extent of the inhibitor−enzyme interaction, i.e., the degree of inhibition. These profiles were used also to estimate the coefficient of inhibition, $I_{0.5}$: 4.5 × 10^{-4} M (hydrazine), 5.5 × 10^{-4} M (methylhydrazine), and 6.3 × 10^{-4} M (dimethylhydrazine).

(11) Rodriquez, M.; Flurkey, W. J. Chem Educ. **1992**, 69, 767.
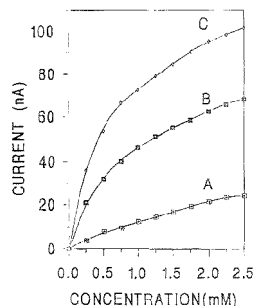
Figure 2. Effect of enzyme loading upon the response to methylhydrazine: calibration plots for pastes containing 1 (A), 3 (B), and 5 (C) wt % tyrosinase. Conditions as in Figure 1.

Since there have not been earlier reports on the inhibitory effect of hydrazine on tyrosinase, we examined the nature of this inhibition process. Lineweaver−Burk plots for the phenol−tyrosinase reaction in the presence of different concentrations of the hydrazine inhibitors [(1−3) × 10^{-3} M] were characterized by a fixed intercept (i.e., V_{max}), a behavior consistent with a competitive inhibition process[12] (not shown; conditions, as in Figure 1, for successive additions of the phenol substrate to the hydrazine solution). Such competitive inhibition is in agreement with the early suggestion that the inhibition of tyrosinase proceeds through interaction with the active copper site.[13] These kinetics data were used for determining the inhibition constant (K_i). Secondary replots of the slopes of the Lineweaver−Burk plots for various concentrations of hydrazine, methylhydrazine, and dimethylhydrazine thus yielded K_i values of 7.1 × 10^{-4}, 1.38 × 10^{-3}, and 3.02 × 10^{-3} M, respectively (as was calculated from the x-intercept).

The hydrazine inhibition is reversible, and the sensor can be reused after rinsing. For example, six successive measurements of 5 × 10^{-5} M methylhydrazine using the same electrode surface (and 1 × 10^{-5} M phenol) yielded a mean steady-state current response of 52.4 nA with a range of 48.6−53.6 nA (not shown; conditions, as in Figure 1a). The relative standard deviation over the entire series, 3.8%, as well as the good reproducibility of the substrate response, indicated that the sensor is fully recovered from these repetitive 2-min exposures. The reversibility of the biosensor was indicated also from the fact that the calibration data (e.g., of Figure 1) hold regardless of the direction of the concentration change.

The enzyme loading has a profound effect upon the sensitivity of the hydrazine biosensor. Figure 2 shows calibration plot for methylhydrazine at carbon pastes containing 1 (A), 3 (B), and 5 (C) wt % tyrosinase. The response is nearly proportional to the biocatalytic activity. The influence of other experimental variables, such as the operating potential or substrate concentration, was explored and optimized (not shown). Most favorable response characteristics were obtained at −0.1 V and using 1 × 10^{-5} M phenol.

Chronoamperometry represents another useful mode of operating hydrazine biosensors. Figure 3 displays chronoampero-

(12) Rawn, J. D. Biochemistry; Neil Patterson Publishers: Burlington, VT, 1989; p 179.
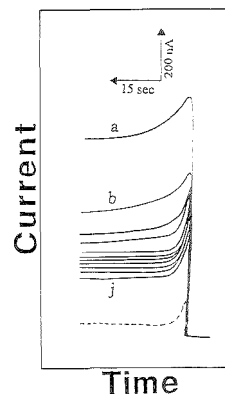(13) Lerch, K. Mol. Cell. Biochem. **1983**, 5, 125.
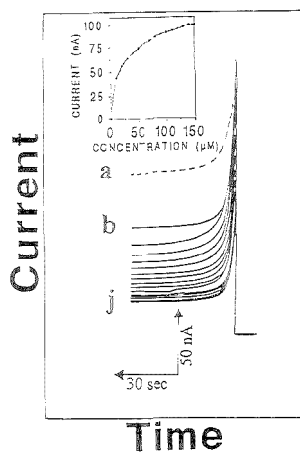
Figure 3. Chronoamperometric calibration data; response to successive additions of 1×10^{-5} M methylhydrazine (b–j) in the presence of 1×10^{-5} M phenol (a). Potential step to -0.1 V. Electrolyte, as in Figure 1.
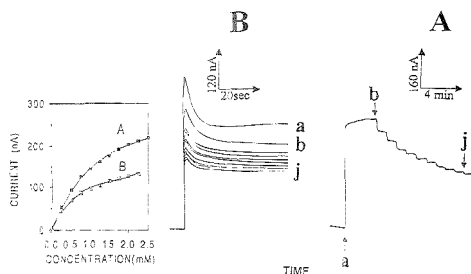
Figure 4. Assays of an unaltered river water sample: amperometric (A) and chronoamperometric (B) response to additions of 1×10^{-4} M phenol (a) and 2.5×10^{-4} M methylhydrazine (b–j). Conditions, as in Figures 1A and 3, with the exception of not using a supporting electrolyte.

Figure 5. Chronoamerometric response of the screen-printed tyrosinase electrode to addition of 5×10^{-3} M phenol (a), followed by successive additions of 2.5×10^{-4} M methylhydrazine (b–j). The dotted line corresponds to the response to the blank solution (in the absence of phenol or methylhydrazine. Conditions as in Figure 3.

grams for phenol (a) and successive 1×10^{-5} M increments of methylhydrazine (b–j). The phenol peak decreases rapidly upon increasing the hydrazine concentration at first and then more slowly (see inset for the resulting calibration plot). Convenient measurements of micromolar hydrazine concentrations can thus be realized. Such quantitation relies on the reproducibility of the chronoamperometric response. A prolonged series of 15 successive measurements of 1×10^{-5} M methylhydrazine (in the presence of 1×10^{-5} M phenol) resulted in a stable response, with a relative standard deviation of 4.9% (not shown). Such chronoamperometric operation obviates the need for solution stirring, hence facilitating various field applications. Bioamplification schemes may be useful for similar measurements of submicromolar concentrations.

The new sensor was tested in connection with various real samples. Figure 4 displays the amperometric (A) and chronoamperometric (B) response to a river water sample spiked with different levels of methylhydrazine [$(2.5-22.5) \times 10^{-4}$ M, b–j]. Both techniques offer convenient assays of this natural water sample, with a fast and sensitive response. Note also that the

sample was unaltered (i.e., use of the natural pH and ionic strength). Similar favorable response characteristics were observed for a spiked drinking water sample (not shown). The blank chronoamperometric response (without phenol) was very low, indicating lack of major interferences in these samples. No response for hydrazine or phenol was observed for both water samples without the enzyme. With storage in air at 4 °C, the hydrazine sensor had a lifetime of ~30 days; surface renewal can be accomplished rapidly, as common for carbon-paste electrodes.

In addition to carbon-paste electrodes, we examined the detection of hydrazine compounds at single-use screen-printed sensor strips. Such low-cost microfabricated sensors should facilitate the on-site environmental and industrial monitoring of hydrazine compounds. We have recently developed disposable phenol biosensors based on tyrosinase-containing carbon inks.[5] The suitability of these sensors for hydrazine detection, based on the perturbed bioactivity of the printed tyrosinase layer, was thus tested. Figure 5 displays the chronoamperometric response of the thick-film tyrosinase strip to the phenol substrate (a), as well as for successive concentration increments of 2.5×10^{-4} M methylhydrazine (b–j). The current difference rises sharply with the inhibitor concentration at first and then more slowly. The operation of these sensor strips may be coupled to light, battery-operated analyzers, as desired for monitoring hydrazine exposure.

In conclusion, it has been illustrated for the first time that hydrazine biosensors can be designed based on the perturbed bioactivity of tyrosinase. Such devices offer a fast and sensitive response and hold great promise for early warning against hydrazine contamination. Applicability to hydrazine measurements in nonaqueous environments is also anticipated based on the organic-phase activity of the enzyme. Tyrosinase activity in extreme environments may lead also to the detection of hydrazines in air. Such monitoring of hydrazine vapors should be extremely useful for aerospace applications. It is realized that tyrosinase is susceptible to a variety of inhibitors. Whenever needed, improved selectivity may be achieved by incorporating various permselective surface coatings. The small size of hydrazine compounds may thus be advantageous in connection with different size exclusion

films. Alternately, it may be possible to employ a multianalyte–chemometric approach in connection to an enzyme array biosensor. Several enzymes, which are inhibited to varying degrees by different toxic analytes, can thus be employed to give a distinct fingerprint pattern and mixture analysis. Such schemes should be useful for simple mixtures (such as those common in the aerospace industry). More detailed quantitative information can be achieved by coupling with another analytical system (e.g., liquid chromatography or mass spectroscopy), with the biosensor serving mainly as an alarm that initiates the additional work. It is hoped that these developments should facilitate the on-site environmental and industrial monitoring of hydrazine compounds.

[®] Abstract published in *Advance ACS Abstracts*, September 15, 1995.

Author Index

New Optima DV
The best view from any angle

200 Samples. 30 Elements. 4 Hours. One Instrument.

We've said it before: the Optima 3000 is the only ICP-OES to combine the speed of simultaneous with the flexibility of sequential. Today, only a year after its introduction, hundreds of chemists agree.

And now, building on the success of the original Optima, we're introducing our newest model, the Optima 3000 XL. Featuring axial plasma viewing, for unmatched performance in ICP detection limits.

Whichever Optima model you choose, all the ICP elements are measured in less than a minute—at multiple wavelengths. And the high sample throughput dramatically lowers your cost of analysis.

Optima includes over 5,000 emission lines, giving you the flexibility to select alternate interference-free lines, improving your accuracy. It measures the spectral background every time it measures the analyte line—simultaneously—increasing your throughput.

And the Optima 3000 and 3000 XL are not only fast and flexible. They're also powerful, easy to use, and easy to afford.

However many samples, elements, or applications you have to handle, there's only one name you have to remember: Optima 3000.

For sales information or literature in the U.S., call 1-800-762-4000. Outside the U.S., contact your Perkin-Elmer representative.

ISO 9001 CERTIFIED

PERKIN ELMER